Higher-Order Resummation and Precision Predictions for Color-Singlet Transverse Momentum Distributions at the LHC

Dissertation

zur Erlangung des Doktorgrades
an der Fakultät für Mathematik,
Informatik und Naturwissenschaften

Fachbereich Physik

der Universität Hamburg

vorgelegt von

Georgios Billis

Hamburg
2021

Gutachterïnnen der Dissertation:	Dr. Frank J. Tackmann
	Prof. Dr. Géraldine Servant
Zusammensetzung der Prüfungskommission:	Dr. Frank J. Tackmann
	Prof. Dr. Géraldine Servant
	Prof. Dr. Elisabetta Gallo
	Prof. Dr. Sven-Olaf Moch
	Prof. Dr. Georg Weiglein
Vorsitzender der Prüfungskommission:	Prof. Dr. Sven-Olaf Moch
Datum der Disputation:	22. 10. 2021
Vorsitzender des Promotionsausschusses Physik:	Prof. Dr. Wolfgang Hansen
Leiter des Fachbereichs Physik:	Prof. Dr. Günter H. W. Sigl
Dekan der Fakultät MIN:	Prof. Dr. Heinrich Graener

To Vangelis, Aleka, Evi, and Angelika.

Abstract

With the entire potential of the Large Hadron Collider (LHC) expected to be fully realized in the near future (High-Luminosity LHC), theoretical predictions that match the ever-increasing precision of its experimental measurements are more imperative than ever. A central part of the LHC program is the study of differential distributions for color-singlet processes (e.g. Drell-Yan and Higgs production) since they allow for rigorous tests of the Standard Model and possible deviations from it. In this thesis, we focus on technical aspects of higher-order resummation for differential distributions as well as on providing precision predictions for color-singlet processes at the LHC in the framework of Soft-Collinear Effective Theory (SCET).

We first discuss the solution of the Sudakov evolution factor which is a central ingredient in every resummation framework. For the single gauge interaction case (QCD), all available approximate analytic solutions are studied with an emphasis on the accuracy they achieve. We find that at higher logarithmic orders none of the analytic methods meet the criteria for (sub-)percent level precision, and to this end we propose a semi-numerical method for its evaluation. We then apply this method and study the solution of the Sudakov factor in the presence of multiple gauge interactions (QCD$\otimes$QED), where its precision is found to be at the permil level. An indispensable ingredient in this approach is an analytic solution of the coupled β-functions for the running of the couplings, which we provide.

We then study the leading-power singular structure of the transverse momentum (q_T) and 0-jettiness ($\mathcal{T}_0$) resolution variables for generic color-singlet processes in QCD. We exploit that the logarithmic structure of beam and soft functions is predicted by the renormalization group equations (RGE) they satisfy, and we solve them to three loops. These are necessary ingredients for the q_T and $\mathcal{T}_0$ resummation at N^{3}LL$'$ and N^{4}LL as well as for the extension of the corresponding subtraction methods to N^{3}LO. In addition, by employing consistency relations between different factorization limits, we predict the threshold limit of the q_T and $\mathcal{T}_0$ beam function boundary coefficients at N^{3}LO, results that go beyond their RGE-predicted terms. Furthermore, motivated by the nontrivial functional form of the full N^{3}LO beam boundary terms, we propose a cost-optimal and precision-driven strategy for the numerical implementation of kernels that bear such functional signature.

Finally, we present predictions for the inclusive and fiducial gluon-fusion Higgs q_T spectrum at N^{3}LL$'$+N^{3}LO at the LHC. For the latter, we compare to ATLAS preliminary data, finding good agreement throughout the spectrum. Part of our discussion focuses on the presence of linear (fiducial) power corrections that stem from the experimental cuts and how they can be included in the resummation framework. We then apply differential q_T subtractions to predict, for the first time, the Higgs total fiducial cross section at N^{3}LO and improved by timelike and q_T resummation. Of major importance for the precision of our results are the quadratic (nonsingular) power suppressed contributions, which we obtain via a dedicated fitting procedure. We conclude by discussing the caveats that apply to the commonly used q_T-slicing method at this high perturbative order and in the presence of fiducial cuts. Both the q_T spectrum and the total fiducial cross section are the highest-order predictions with a realistic description of all decay products at a hadron collider to date.

Zusammenfassung

Da sich die großen experimentellen Möglichkeiten des Large Hadron Collider (LHC) in naher Zukunft immer deutlicher abzeichnen (High-Luminosity LHC), sind theoretische Vorhersagen, die der ständig zunehmenden Präzision experimenteller Messungen gerecht werden, wichtiger denn je. Zentraler Bestandteil des LHC-Programms ist die Untersuchung von differentiellen Wirkungsquerschnitten für farbneutrale Prozesse (z.B. Drell-Yan- oder Higgs-Produktion), da sie exakte Tests des Standardmodells und möglicher Abweichungen von ihm ermöglichen. In dieser Arbeit werden technische Aspekte der Resummation von differentiellen Wirkungsquerschnitten höherer Ordnung ausgearbeitet und Präzisionsvorhersagen für farbneutrale Prozesse am LHC im Rahmen der Soft-Collinear Effective Theory (SCET) erstellt.

Wir diskutieren zuerst die Lösung des Sudakov-Evolutionsfaktors, der eine zentrale Rolle in allen Formulierungen von Resummation spielt. Für den Fall einer einzelnen Eichwechselwirkung (QCD) werden alle verfügbaren analytischen Näherungslösungen auf die erreichte Genauigkeit untersucht. Auf höheren logarithmischen Ordnungen erfüllt keine der analytischen Methoden die erforderliche Präzision auf oder unterhalb Prozentniveau. Stattdessen wird eine halbnumerische Methode vorgestellt, die dieses Ziel erreicht. Anschließend wird diese Methode angewendet auf den Fall mehrerer Eichwechselwirkungen (QCD$\otimes$QED), wo erneut eine Genauigkeit auf dem Promilleniveau festgestellt wird. Ein unverzichtbarer Bestandteil dieses Ansatzes ist die hier erarbeitete analytische Lösung der gekoppelten β-Funktionen für die laufenden Kopplungskonstanten.

Weiterhin werden die führenden singulären Terme im Transversalimpuls (q_T) und 0-Jettiness-Spektrum ($\mathcal{T}_0$) für generische farbneutrale Prozesse in der QCD hergeleitet. Die Herleitung basiert auf der Renormierungsgruppe (RG), deren rekursive Lösung zu dritter Ordnung die logarithmische Struktur von kollinearen und soften Matrixelementen vorhersagt. Dies sind notwendige Zutaten für die Resummation von q_T und $\mathcal{T}_0$ auf $\mathrm{N^3LL'}$ und $\mathrm{N^4LL}$ sowie für die Erweiterung der entsprechenden Subtraktionsmethoden auf $\mathrm{N^3LO}$ in fester Ordnung. Zudem werden Konsistenzbeziehungen zwischen verschiedenen Faktorisierungstheoremen benutzt, um die führenden eikonalen Terme in den kollinearen Proton-Matrixelementen für q_T und $\mathcal{T}_0$ auf $\mathrm{N^3LO}$ zu ermitteln, was über die aus der RG bestimmten Terme hinausgeht. Motiviert durch die nichttriviale funktionale Form der vollständigen kollinearen Randbedingung auf $\mathrm{N^3LO}$ wird eine kostenoptimale Strategie mit kontrolliertem Fehlerterm für die numerische Implementierung von Integralkernen entwickelt, die eine solche funktionale Signatur tragen.

Schließlich werden theoretische Vorhersagen für das Higgs-q_T-Spektrum in Gluonenfusion auf $\mathrm{N^3LL'}$+$\mathrm{N^3LO}$ am LHC errechnet, sowohl für den inklusiven Fall wie für eine realistische experimentelle Detektorakzeptanz. Die letztere Vorhersage wird mit vorläufigen Daten aus Messungen des ATLAS Experiments verglichen und zeigt gute Übereinstimmung im gesamten Spektrum. Ein Teil unserer Diskussion konzentriert sich auf das Phänomen linearer Korrekturen im Spektrum, die sich aus der Detektorakzeptanz ergeben, aber im Resummationsformalismus berücksichtigt werden können. Weiter wird eine differentielle

q_T-Subtraktion angewendet, um zum ersten Mal den gesamten Wirkungsquerschnitt für Gluonenfusion mit realistischer Akzeptanz auf dritter Ordnung zu errechnen, sowohl in fester Ordnung wie unter Einbeziehung von q_T-Resummation und der Resummation sogenannter zeitartiger Logarithmen. Von großer Bedeutung für die Genauigkeit dieser Ergebnisse sind die quadratischen (nicht singulären) Korrekturen im Spektrum, die mithilfe einer Regressionsanalyse ermittelt werden. Abschließend diskutieren wir die teils gravierenden Nachteile der üblichen q_T-Slicing-Methode auf dieser hohen Ordnung und bei nichttrivialer Detektorakzeptanz. Sowohl das q_T-Spektrum als auch der gesamte Wirkungsquerschnitt stellen die höchsten störungstheoretischen Ordnungen dar, die für theoretische Vorhersagen mit einer realistischen Beschreibung aller Zerfallsprodukte je für einen Hadronenbeschleuniger erreicht wurden.

List of publications

Journal articles:

[1] G. Billis, F. J. Tackmann and J. Talbert, *Higher-Order Sudakov Resummation in Coupled Gauge Theories*, *JHEP* **03** (2020) 182 [1907.02971].

[2] G. Billis, M. A. Ebert, J. K. L. Michel and F. J. Tackmann, *A toolbox for q_T and 0-jettiness subtractions at N^3LO*, *Eur. Phys. J. Plus* **136** (2021) 214 [1909.00811].

[3] G. Billis, B. Dehnadi, M. A. Ebert, J. K. L. Michel and F. J. Tackmann, *Higgs pT Spectrum and Total Cross Section with Fiducial Cuts at Third Resummed and Fixed Order in QCD*, *Phys. Rev. Lett.* **127** (2021) 072001 [2102.08039].

Acknowledgements

First and foremost, I would like to express my deep gratitude to my supervisor, Frank Tackmann, for his guidance during my PhD. Frank taught me a huge amount of physics, passed on his enthusiasm for it, and had his office door *always* open, encouraging questions and discussions from which I profited a lot. It has been a great experience being his student. I would also like to thank Prof. Dr. Géraldine Servant for her willingness to co-referee my thesis and Prof. Dr. Elisabetta Gallo, Prof. Dr. Sven-Olaf Moch, and Prof. Dr. Georg Weiglein for agreeing to be part of my PhD disputation committee.

Another reason why this journey was great, is due to my collaborators, Bahman Dehnadi, Markus Ebert, Johannes Michel, and Jim Talbert. They taught me that, while figuring out things in physics is rewarding, it can also be fun. I would like to thank all of them for always being willing to answer my (sometimes annoyingly a lot) questions and for passing on their knowledge and experience. Furthermore, I am grateful to Johannes and Markus for their valuable suggestions and feedback on this manuscript.

I would also like to thank all the past and present residents of the 1b-penthouse, Aron Bodor, Pia Bredt, Bahman Dehnadi, Markus Diehl, Juhi Dutta, Florian Fabry, Daniel Meuser, Riccardo Nagar, Ivan Novikov, Davide Pagani, Peter Plößl, Maria Olalla Olea Romacho, Alejo Rossia, Laís Sharem Schunk, Frank Tackmann, Jim Talbert and Lorenzo Zoppi for creating a nice working atmosphere and for our interesting discussions during coffee.

Finally, I would like to thank my parents, Vangelis and Aleka, my sister Evi, and Angelika. None of this would have been possible without your constant, unconditional support and love.

Contents

List of figures

List of acronyms

Pages with relevant material are listed after the entry where applicable.

ATLAS A Toroidal LHC Apparatus, *LHC experiment*

BEH Brout-Englert-Higgs, *mechanism* 1

BPS Bauer-Pirjol-Stewart, *field redefinitions* 32, 36

BSM Beyond the Standard Model

CMS Compact Muon Solenoid, *LHC experiment*

COM Center Of Mass, *reference frame*

CSS Collins-Soper-Sterman, *formalism* 14, 103

DGLAP Dokshitzer-Gribov-Lipatov-Altarelli-Parisi, *equation* 20, 179

d.o.f degrees of freedom

DY Drell-Yan, *process*

EFT Effective Field Theory

EoM Equations of Motion

EW Electroweak

EWSB Electroweak Symmetry Breaking

FO Fixed-Order

FSR Final State Radiation 47

FT Fourier Transform

HL-LHC High-Luminosity LHC

HPL Harmonic Polylogarithm, *function* 125

IFI Initial Final State Interference, *radiation* 47

IR Infrared, *divergences* 9

IRC Infrared-Collinear, *safety* 20

ISR Initial State Radiation 47

KLN Kinoshita–Lee–Nauenberg, *theorem* 14

LHC Large Hadron Collider

MPL Multiple Polylogarithm, *function* 133

$\overline{\text{MS}}$ Modified Minimal Subtraction, *renormalization scheme* 9

N^{k}LL (Next-to-)^k Leading Logarithm
N^{k}LO (Next-to-)^k Leading Order
N^{k}LP (Next-to-)^k Leading Power
NWA Narrow Width Approximation 140
OPE Operator Product Expansion 92, 109
PDF Parton Distribution Function 14
PS Parton Shower
QCD Quantum Chromodynamics 9
QED Quantum Electrodynamics
rEFT rescaled Effective Field Theory, *Higgs* 140
RGE Renormalization Group Equation 13, 65
RPI Reparametrization Invariance 31, 32
RRGE Rapidity Renormalization Group Equation 41
SCET Soft-Collinear Effective Theory 22
SM Standard Model
TMD Transverse Momentum Dependent 103
TMDPDF Transverse Momentum Dependent PDF 103
UV Ultraviolet, *divergences* 9
VEV Vacuum Expectation Value

Chapter 1

Introduction

In July 2012 the last piece of the Standard Model (SM) jigsaw puzzle was put in place. The discovery of a SM-compatible Higgs boson at the Large Hadron Collider (LHC) by the ATLAS [4] and CMS [5] experiments is among the most important breakthroughs in the field of high-energy physics that undoubtedly has opened the door to a new era. Its significance lies in the fact that it allows for the SM to be considered complete and self-consistent.

The SM is a quantum field theory invariant under a local $\mathrm{SU}(3)_c \otimes \mathrm{SU}(2)_L \otimes \mathrm{U}(1)_Y$ symmetry. It dictates the dynamics and interactions of matter particles (quarks and leptons) and gauge bosons, with the latter corresponding to the carriers of the strong, weak and electromagnetic forces. At face value, these symmetries demand that all gauge bosons are massless, something that is not on par with experimental observations; weak interactions are mediated by massive gauge bosons. The only known way that masses are introduced without spoiling the underlying symmetries is via *spontaneous* electroweak symmetry breaking (EWSB) [6–8] by the vacuum, which is realized through the Brout-Englert-Higgs (BEH) mechanism [9–11]. The Higgs boson is the imprint of EWSB, an actual prediction of the model and instrumental in elucidating the origin of the particles' masses, both for gauge bosons and matter fields. In addition, the Higgs boson plays a central role in preserving unitarity in the SM which would be otherwise violated in the scattering of longitudinal gauge bosons $W_L^+W_L^- \to W_L^+W_L^-$.

Despite the success and triumphs of the SM, there are quite a few open questions that the SM fails to address. In the SM only left-handed neutrinos are accounted for, something that explicitly excludes a mass term for them. Contrary to this theoretical prediction, it is known from the observed neutrino oscillations [12, 13] that they have small, non-zero masses. In principle, the SM could accommodate right-handed neutrinos such that the corresponding Yukawa terms give rise to masses, but this opens yet another door to questions on why neutrinos are that much lighter than the rest of the leptons and what is the underlying mechanism responsible for it. A different shortcoming of the SM is that it does not contain a candidate particle for Dark matter, which could be part in explaining various cosmological and astrophysical observations related to (among others) the formation of structures in the universe. There is also the puzzle of the matter-antimatter asymmetry in the universe, which in addition to other conditions [14], the amount of CP-violation it requires in order to be explained is not sufficiently generated within the SM hadron sector and therefore its origin must lie in physics beyond it.

But there are also aspects directly related to the SM itself, which at first sight appear arbitrary and naturally spawn even more questions. For example, the known fermion masses exhibit a strong hierarchy, where the lightest has a mass $m_e \simeq 0.51\,\text{MeV}$ whereas the heaviest $m_t \simeq 173.0\,\text{GeV}$ [15]. Furthermore, it is quite unclear how gravity can be reconciled with the SM, where the interactions of the former are expected to be of the same size as gauge interactions at the Planck scale $M_{\text{Planck}} \sim 10^{19}\,\text{GeV}$. Closely related is the famous hierarchy problem in which radiative corrections to the Higgs boson mass have a quadratic sensitivity to the cut-off scale $\Lambda \overset{?}{\sim} M_{\text{Planck}}$ where physics beyond the SM (BSM) are expected to appear. Given the experimentally measured value of the Higgs mass $m_H = 125.18 \pm 0.16\,\text{GeV}$ [15], this implies that either a significant amount of cancellations (fine tuning) has to take place or some new symmetry must protect it from said radiative corrections.

In any case, all of the previous arguments, theoretically or observationally motivated, point to the fact that the SM cannot be the final answer and BSM phenomena should manifest themselves one way or another. The study of the Higgs boson gives access to the EWSB mechanism, which it merely parametrizes, but it can also answer the question whether the observed Higgs boson is *the one* predicted by the SM.

The precision frontier at the LHC. Given that so far direct BSM manifestations have been elusive, a possible way to hunt for new physics is via *precision measurements*. While Run 1 of the LHC resulted in the discovery of the Higgs, due to limited statistics and the lower center of mass energy (7, 8 TeV), searches were mainly focused on total cross sections. In Run 2, the increased energy (13 TeV) and larger instantaneous luminosity resulted in a richer data set to be explored. A direct consequence is that now, differential distributions can be studied with significantly lower uncertainties. Differential distributions are important because they allow for fine-grained tests of the SM and they can be more sensitive to BSM effects, which may impact only parts or different regions of the spectrum and in turn can be highly suppressed in total cross sections.

Take for example the transverse momenta p_T^H of the Higgs boson. The dominant production channel of the Higgs at the LHC is via gluon-fusion, which is a loop-induced process with quarks mediating its effective coupling to the gluons. It is known that the high-p_T^H region is particularly sensitive to new physics, see e.g. ref. [16], whereas the low-p_T^H region provides stringent tests of perturbative Quantum Chromodynamics (QCD). In addition, it has been shown in refs. [17, 18] that the small and intermediate-p_T^H region is sensitive to modifications of the Yukawa couplings between light quarks and the Higgs. The presence of new physics modifying these couplings, thus translates into a deviation from the SM-predicted p_T^H spectra. This provides an indirect way to set constraints on various BSM models that predict such modifications. An important requirement, though, especially if the couplings are only lightly influenced by BSM physics, is a high-precision measurement that will allow for the smallest possible deviation to be inferred. The left panels of figure 1.1 show the measurement of p_T^H by the CMS [19] (top) and ATLAS [21] (bottom) experiments, where it is clear that even though no incompatibility with the SM predictions is observed,

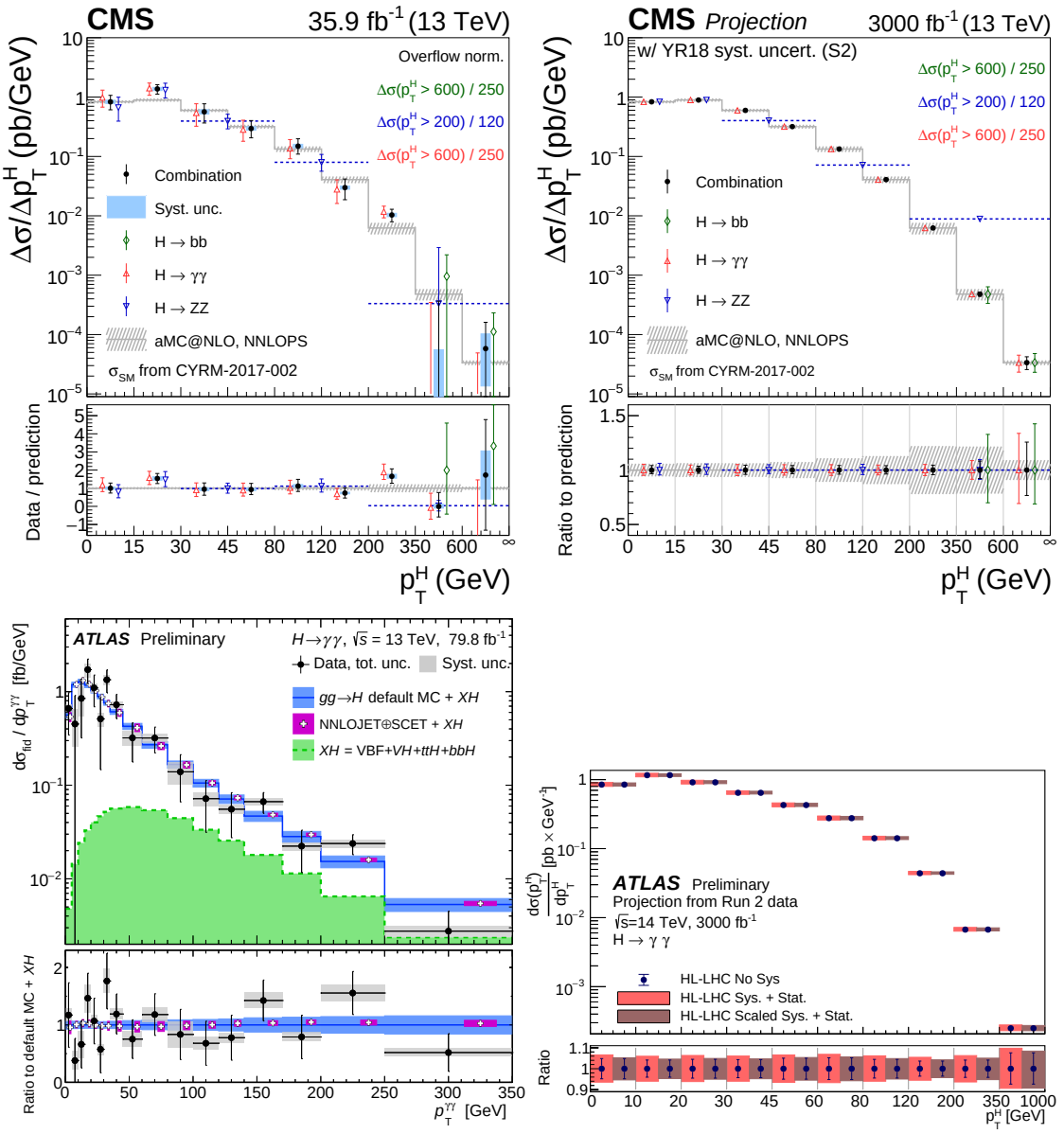

Figure 1.1: Measurement at the LHC (left) and projection in the High-Luminosity LHC (right) for the Higgs transverse momentum distribution by the CMS [19, 20] (top) and ATLAS [21, 22] (bottom) experiments.

the experimental uncertainties are still significant and mainly statistically dominated. This picture is expected to change dramatically with the High-Luminosity LHC (HL-LHC) [23]. The instantaneous luminosity will increase such that the final data set in the late-2030s will correspond to 3000 fb^{-1} and both experiments will undergo significant upgrades to improve their performance [23–25]. This is also what the right panels of figure 1.1 suggest, which show the HL-LHC projections for p_T^H [20, 22], where the resulting uncertainties for the measured spectra will be significantly reduced and expected to be at $\sim 5 - 10\%$.

Of course, precision measurements require at least equally *precise theory predictions* in order to exploit the full potential of the LHC. This is primarily achieved with the calculation of higher-order dominant QCD corrections in cross sections, aiming for a perturbative convergence and a reduction of theoretical uncertainties to the same or better level as the experimental ones. For typical hard scattering processes at the LHC, the total cross section is expanded in the strong coupling constant $\alpha_s \sim 0.1$ as

$$\sigma = \sigma^{(0)} + \alpha_s\,\sigma^{(1)} + \alpha_s^2\,\sigma^{(2)} + \alpha_s^3\,\sigma^{(3)} + \dots\,, \tag{1.1}$$

where it is clear that as long as $\sigma^{(n)} \sim \mathcal{O}(1)$, the convergence of the total cross section σ is guaranteed due to the smallness of α_s. The perturbative expansion in eq. (1.1) can then be safely truncated at a certain order based on the required precision. However, achieving higher-order predictions for total cross sections is quite a hard endeavour and even more so for differential distributions, where the calculational and computational complexity increases severely. Furthermore, additional complications arise in theoretical predictions for observables that are sensitive to soft and collinear QCD radiation. One such observable is the transverse momenta p_T^H of the Higgs. The expansion of the differential cross section in the strong coupling constant α_s is plagued at each order in perturbation theory by logarithms of the form

$$\frac{\mathrm{d}\sigma}{\mathrm{d}p_T^H} \;\sim\; \sum_{n=1}^{\infty}\sum_{m=0}^{2n-1} \alpha_s^n \frac{1}{p_T^H} \ln^m \frac{p_T^H}{m_H}\,, \tag{1.2}$$

which are known as Sudakov double logarithms. While such terms are innocuous for the parts of the spectrum where $p_T^H \sim m_H$, since they can be considered small in these regions, in the region $p_T^H \ll m_H$ where the bulk of the cross section is, these logarithms grow large and overcome the α_s suppression, rendering the perturbative expansion divergent. For these parts of the spectrum, such terms have to be accounted for to *all orders* in perturbation theory. This requires a re-organization of the cross section's perturbative expansion, a procedure known as *resummation*. Resumming such terms restores the convergence and results in a physical spectrum as $p_T^H \to 0$. There are various ways that resummation can be performed and in this thesis we work in the framework of effective field theories (EFT).

Another way to increase the precision of theory predictions is to include effects that are subleading compared to QCD, and thus often neglected. This would be the case for example for electroweak (EW) or pure Quantum Electrodynamics (QED) effects. A good rule of the thumb relates the relative importance of the QED coupling constant $\alpha_e \sim 1/127$ at typical LHC scattering energies to that of QCD, $\alpha_e \sim \alpha_s^2$, which roughly implies that at two-loops and beyond in QCD, the corresponding QED contributions (in principle) should be also taken into account. In addition, since photons are massless, much like the gluons in QCD, soft and collinear QED radiation will contribute the same logarithmic structure as that in eq. (1.2), and also has to be resummed in order to obtain a convergent perturbative expansion in α_e. While such effects are not (yet) relevant for the dominant production channel of the Higgs boson, since it is gluon induced, they are already becoming important

for other well-studied color-singlet processes at the LHC such as the Drell-Yan (DY) process $pp \to Z/\gamma^* \to \ell^+\ell^-$ [26]. The importance of the DY process is understood from that its non-strongly interacting decay products provide a uniquely clean experimental signature that is measured with great precision. Therefore, it is considered a 'standard candle' for the extraction of various SM parameters [27–29] and the parametrization of the universal parton distribution functions (PDFs) (see e.g. ref. [30] for relevant discussion), which are necessary inputs for practically any prediction at the LHC, but also is an important background in various BSM searches (see e.g. ref. [27]).

In light of the above and given the vast theory challenges of the upcoming HL-LHC era, this thesis is devoted to further enriching the theoretical toolbox of resummation and provide precision predictions relevant for the LHC. In the following we give an overview of the topics that are studied in this thesis, along with its main results.

Resummation in the presence of multiple gauge interactions. In chapter 3 we focus on extending the resummation framework from the case of a single gauge interaction to a multi-gauge interaction. Of central importance for the resummation of Sudakov double logarithms in every method (EFT-based or not), and for every resolution variable, is the evaluation of the Sudakov evolution kernel and of the β-function that dictates the running of the coupling. In a multi-gauge environment, the β-functions of the couplings become a coupled system of differential equations for which we provide an analytic solution up to three loops. Our method is directly extendable to arbitrary order. Turning to the evolution kernel, we point out that while its analytic form is common in every framework, the strategies for its evaluation differ considerably with an increasing amount of approximating assumptions. We find that such assumptions already result in significant systematic errors for the case of a single gauge interaction (pure QCD) and cannot be neglected when aiming for (sub-)percent precision, as would be the case in higher-order resummation and/or when considering in addition QED or EW effects. We solve this issue by proposing a semi-numerical method that employs our analytic solution for the coupled β-functions together with a numerical evaluation of the evolution kernel, addressing both aspects of low computational cost and high precision. Our strategy directly applies for the resummation of QCD⊗QED or QCD⊗EW mixed effects. As an illustration we obtain the complete NNLL Sudakov evolution factor in QCD⊗QED.

Subtractions at N^{3}LO. In chapter 4 we study the leading-power singular structure for the total transverse momentum (q_T) and 0-jettiness ($\mathcal{T}_0$) resolution variables in color-singlet production processes (e.g. $pp \to Z, W^\pm, H$) in the framework of Soft-Collinear Effective Theory (SCET). The q_T and $\mathcal{T}_0$ dependence of the factorized cross section is encoded in so-called beam and soft functions that are universal objects, appearing also as part of more complicated factorization theorems. Exploiting the fact that their logarithmic structure in q_T and $\mathcal{T}_0$ is entirely dictated by the renormalization group equations (RGEs) they satisfy, we solve the latter up to N^{3}LO in QCD to obtain their fixed-order structure. These results

are necessary ingredients for carrying out resummation at $\mathrm{N^3LL'}$ and $\mathrm{N^4LL}$ order, for the corresponding differential subtractions at $\mathrm{N^3LO}$, and for the matching of $\mathrm{N^3LO}$ predictions to Parton Showers (PS).

Consistency relations of various factorization limits relate both q_T and $\mathcal{T}_0$ beam functions in the eikonal limit ($z \to 1$) to known soft functions. Exploiting such relations, we derive the $\mathrm{N^3LO}$ singular terms of the beam function nonlogarithmic boundary coefficients, results that go substantially beyond the RGE-predicted terms and have been confirmed by explicit three-loop calculations since their original publication.

The complicated form of the beam function boundary terms as a function of the momentum fraction z makes their numerical evaluation particularly challenging. Motivated by their importance in precision phenomenological analyses, we present a method for an improved approximation of kernels that bear such functional signature, achieving a cost-optimal, close to machine-precision numerical implementation.

Higgs physics. The transverse momentum spectrum of the Higgs boson, $q_T \equiv p_T^H$, arguably is the most important differential distribution measured at the LHC. In chapter 5 we present predictions for the gluon-fusion Higgs q_T spectrum at $\mathrm{N^3LL'}$+$\mathrm{N^3LO}$. This order includes the complete $\mathcal{O}(\alpha_s^3)$ contributions throughout the small, intermediate, and large q_T-region. We show results both for the inclusive and the fiducial case, i.e. according to fully realistic experimental kinematic selection and acceptance cuts on the Higgs decay products. A direct consequence of the fiducial cuts is the emergence of linearly enhanced (fiducial) power corrections which we explicitly resum at the same order, together with Sudakov (timelike) double logarithms $\ln^2(-1-\mathrm{i}0) = -\pi^2$ that timelike processes such as $gg \to H$ are known to exhibit. We employ the experimental cuts used by the ATLAS collaboration [31, 32] and directly compare to ATLAS preliminary results [32], finding good agreement throughout the spectrum.

In addition, by employing differential q_T subtractions we are able to integrate the fiducial q_T spectrum to predict, for the first time, the Higgs total fiducial cross section at $\mathrm{N^3LO}$ order. We investigate both cases of including or not resummation. While for the latter we find a poor convergence caused by cut-induced logarithmic effects, q_T resummation successfully addresses them, and together with timelike resummation they result in a significantly improved convergence for the total cross section. Finally, we show that the commonly used q_T-slicing method can severely worsen the accuracy of results, especially if the enhanced fiducial power corrections are only included via fixed-order matching. Both the q_T spectrum and the total fiducial cross section are the highest-order predictions differential in the decay products at a hadron collider to date.

Thesis outline.
This thesis is structured as follows. In chapter 2 we give a review of the theoretical concepts that this thesis relies on. This includes a brief overview of QCD, a discussion of its universal soft and collinear limits, and a short introduction to SCET, the effective field theory that describes these limits. In chapter 3 we apply SCET to derive the extension of the q_T factorization to the case of QCD⊗QED in order to motivate the RGE structure that emerges when multiple gauge interactions are involved. We move on to solving the coupled β-function RGEs that serve as an important input both for the study and the evaluation of the Sudakov evolution kernel in a multi-gauge environment. In chapter 4 we provide a detailed derivation of the N^{3}LO singular structure for the q_T and $\mathcal{T}_0$ beam and soft functions and study the numerical impact of the newly calculated terms. We then discuss the extraction of the beam function boundary coefficients in the $z \to 1$ limit, from which we construct ansätze that are valid beyond the eikonal limit. In the final part we describe a method for an improved approximation of kernels with complicated functional form like that of the q_T beam function boundary coefficients, and exemplify numerically the advantages of our method. In chapter 5 we present predictions for the inclusive and fiducial q_T spectrum of the Higgs boson in the gluon-fusion channel at the LHC. Part of the chapter is a detailed review of the framework that our phenomenological study is based on, which includes all aspects of resummation and fixed-order matching as well as our uncertainty estimation and the extraction of the nonsingular cross section. Finally, we obtain the total fiducial cross section and discuss the impact of the linearly enhanced power corrections in the context of the q_T-slicing method. We conclude in chapter 6. In appendix A we summarize various conventions used throughout this thesis and in appendix B we collect all relevant perturbative ingredients. Appendix C is devoted to the extraction of three-loop mixed QCD⊗QED β-function coefficients, while in appendix D we further elaborate on the extraction of beam function coefficients in the eikonal limit.

Chapter 2

Collider physics

In this chapter we aim to provide a brief introduction to the theoretical concepts that this thesis is based on. In section 2.1 we review the very basics of the theory of strong interactions, in section 2.2 we discuss its soft and collinear limits, and finally in section 2.3 we introduce the effective field theory that describes these limits.

2.1 Quantum Chromodynamics

The theory of strong interactions is described by Quantum Chromodynamics (QCD). It is a non-abelian gauge field theory with symmetry group $\mathrm{SU}(N)_c$, where $N = 3$ is the number of colors. In QCD the fundamental degrees of freedom are the *quarks* and *gluons* whose dynamics are described by the Lagrangian density

$$\mathcal{L} = \sum_q \bar{\psi}_{q,i}\big(\mathrm{i}\not{D}_{ij} - m_q\,\delta_{ij}\big)\psi_{q,j} - \frac{1}{2}\,\mathrm{tr}\,F_{\mu\nu}F^{\mu\nu}\,. \tag{2.1}$$

The quarks $\psi_{q,i}$ are Dirac fermions of flavor $q = \{u, d, s, c, b, t\}$ that carry *color* quantum number $i = 1, 2, 3$. Under a local $\mathrm{SU}(N)_c$ rotation they transform according to the fundamental (triplet) representation[1]

$$\psi_q(x) \mapsto U(x)\psi_q(x)\,, \qquad U(x) = e^{\mathrm{i}\alpha(x)^a T^a}\,, \tag{2.2}$$

where T^a_{ij} are the generators of the $\mathrm{SU}(N)_c$ Lie group in the fundamental representation and $\alpha^a(x)$ are arbitrary, space-dependent phases.

The gluons, A^a_μ, are massless spin-1 fields that correspond to the quanta of $\mathrm{SU}(N)_c$ and transform according to the adjoint (octet) representation

$$A^a_\mu(x)T^a \mapsto U(x)\left(A^a_\mu(x)T^a + \frac{\mathrm{i}}{g}\partial_\mu\right)U^\dagger(x)\,, \tag{2.3}$$

where $a = 1, \ldots, 8$ and we use an Einstein-type summation convention for all repeated indices.

The covariant derivative in eq. (2.1) is constructed via the minimal coupling prescription with the gluon field

$$D^\mu_{ij} = \partial^\mu\,\delta_{ij} - \mathrm{i}g A^{\mu\,a} T^a_{ij}\,, \tag{2.4}$$

[1] From now on, we suppress color indices i except in expressions whose presence is either helpful or mandatory.

where g is the strong coupling constant, most commonly expressed as $\alpha_s = g^2/(4\pi)$.

The Lagrangian in eq. (2.1) is invariant both under *global* and *local* $\mathrm{SU}(N)_c$ transformations. Global transformations, $\alpha^a(x) \equiv \text{const.}$, are a manifestation of color conservation while it is the local transformations in eq. (2.2) that give rise to the rich QCD dynamics and its complex structure.

The generators T^a of $\mathrm{SU}(N)_c$ in the fundamental representation are given by 3×3 traceless Hermitian matrices that satisfy the algebra commutation relation

$$[T^a, T^b] = \mathrm{i} f^{abc} T^c \,, \tag{2.5}$$

where f^{abc} are the completely antisymmetric structure constants and T^a are conventionally normalized to

$$\mathrm{tr}[T^a T^b] = T_F \delta^{ab} \equiv \frac{1}{2}\delta^{ab} \,. \tag{2.6}$$

In addition, the generators satisfy the famous Jacobi identity

$$\begin{aligned} & \big[T^a, [T^b, T^c]\big] + \big[T^b, [T^c, T^a]\big] + \big[T^c, [T^a, T^b]\big] = 0 \\ \Rightarrow \quad & f^{ade} \; f^{bcd} \; + f^{bde} \; f^{cad} \; + f^{cde} \; f^{abd} \; = 0 \,. \end{aligned} \tag{2.7}$$

Another important representation is the *adjoint representation* in which the generators T^a_A are given by the structure constants and eq. (2.7) makes it clear that they also satisfy the algebra commutation relations

$$(T^b_A)_{ac} = \mathrm{i} f^{abc} \,, \qquad [T^a_A, T^b_A] = \mathrm{i} f^{abc} T^c_A \,. \tag{2.8}$$

Quantities that are ubiquitous in QCD theoretical predictions are the *Casimir invariants* of $\mathrm{SU}(N)_c$ that label different representations and commute with the group's generators. The quadratic Casimirs already appear at the lowest order calculations, where for the fundamental and the adjoint representation they respectively read

$$(T^a T^a)_{ij} = C_F \delta_{ij} \,, \qquad f^{abc} f^{abd} = C_A \delta^{cd} \,, \tag{2.9}$$

which for $N = 3$ the color structure constants C_F and C_A evaluate to

$$C_F = \frac{N^2 - 1}{2N} = \frac{4}{3} \,, \qquad C_A = N = 3 \,. \tag{2.10}$$

The second term in eq. (2.1) is the famous *Yang-Mills* Lagrangian and corresponds to the kinetic term of the gluons. It is understood that the trace is over color indices in order to satisfy gauge invariance and the field strength tensor reads

$$F_{\mu\nu} \equiv F^a_{\mu\nu} T^a = \frac{\mathrm{i}}{g}[D_\mu, D_\nu] = \partial_\mu A^a_\nu T^a - \partial_\nu A^a_\mu T^a + g f^{abc} A^b_\mu A^c_\nu T^a \,. \tag{2.11}$$

It is noteworthy that although the Yang-Mills Lagrangian appears like a generalization of Maxwell's Lagrangian in Quantum Electrodynamics (QED) there is an important difference:

the former does not correspond to a free theory Lagrangian since it also contains interaction terms. As a part of it, we find cubic and quartic local gluon field interactions, $\propto f^{abc}$ or $\propto f^{ade}f^{bce} + \ldots$, which stem as a direct consequence of their non-abelian nature, i.e. due to the fact that they also carry color charge.

The quantization of QCD proceeds via the path integral formalism in which all the possible field configurations for all fields are integrated over. At this point, we come across a subtlety innate to theories that are invariant under local gauge transformations as those in eqs. (2.2) and (2.3): integrating over all possible gauge field configurations for A^a_μ, we are bound to also integrate over redundant ones, i.e. those that are connected to each other via gauge transformations. To address this issue we have to isolate the physical configurations, a procedure achieved via the *Fadeev–Popov method* and involves introducing the gauge-fixing term

$$\mathcal{L}_{\mathrm{GF}} = \frac{1}{2\tau}(\mathrm{i}\partial^\mu A^a_\mu)^2\,, \tag{2.12}$$

where τ is a free parameter. The choice $\tau = 1$ corresponds to the *Feynman gauge* whereas $\tau = 0$ is known as the *Landau gauge*. While for practical calculations it is convenient to work with a specific value for τ, we stress that correlation functions of any gauge invariant operator must be independent of τ irrespectively of its value.

While eq. (2.12) explicitly breaks gauge invariance and thus the aforementioned redundancy, introducing it has an important implication. The Fadeev–Popov method leaves behind a gauge field-dependent determinant which can be conveniently represented as a path integral over Grassmann variables $c, \bar{c}$ and allows to incorporate the corresponding Lagrangian as part of eq. (2.1). This procedure gives rise to the so-called *ghost fields* whose dynamics are dictated by

$$\mathcal{L}_{\mathrm{ghost}} = \bar{c}^a(\mathrm{i}\partial^\mu \mathrm{i}\mathcal{D}^{ab}_\mu)c^b\,, \tag{2.13}$$

where the covariant derivative $\mathcal{D}^{ab}_\mu$ is in the adjoint representation

$$\begin{aligned}\mathcal{D}^{ab}_\mu &= \partial_\mu\delta^{ab} - \mathrm{i}gA^c_\mu(T^c_A)_{ab} \\ &\equiv \partial_\mu\delta^{ab} - gf^{abc}A^c_\mu\,.\end{aligned} \tag{2.14}$$

The ghost fields c^a do not correspond to physical particles as they do not satisfy the correct spin-statistics theorem. Their inclusion though in perturbative calculations is crucial since they serve as propagating modes that cancel the otherwise unphysical timelike and longitudinal polarizations of the gauge fields A^a_μ.[2]

It should be stressed that the appearance of the ghost fields is a consequence of the non-abelian gauge symmetry and absent in the abelian case, best exemplified by QED. The

[2]The fact that the ghost fields correspond to dynamical degrees of freedom in QCD coupled to gauge fields, is specific to the gauge fixing term in eq. (2.12) which belongs to the family of *covariant gauges*. Another possible family of gauges is the *axial gauge*, which corresponds to a 'physical gauge' in the sense that the resulting determinant from the Fadeev–Popov method is gauge field independent and thus it can be neglected in the normalized partition function.

easiest way to see this, is realizing that the structure constants in abelian case are zero, $f^{abc} \equiv 0$, and thus the interaction term in eq. (2.13) is absent. Thus, in abelian gauge theories ghost and gauge fields do not couple and we can treat the determinant induced by the Fadeev–Popov method as an overall multiplicative factor which eventually drops out in the normalized partition function.

Having described the dynamics of matter and gauge fields in eq. (2.1) as well as all the intricacies of their quantization that give rise to eqs. (2.12) and (2.13), we are now in position to write the complete QCD Lagrangian

$$\mathcal{L}_{\text{QCD}} = \sum_q \bar{\psi}_{q,i}\big(\mathrm{i}\not{D}_{ij} - m_q\,\delta_{ij}\big)\psi_{q,j} - \frac{1}{2}\,\mathrm{tr}\,F_{\mu\nu}F^{\mu\nu} + \frac{1}{2\tau}(\mathrm{i}\partial^\mu A^a_\mu)^2 + \bar{c}^a(\mathrm{i}\partial^\mu \mathrm{i}\mathcal{D}^{ab}_\mu)c^b\,. \quad (2.15)$$

Eq. (2.15) contains only two independent parameters: the quark masses m_q and the strong coupling constant g. From experimental measurements it is known that m_q exhibit a strong hierarchy among the different flavors, with $m_t \simeq 173\,\text{GeV}$ and $m_u \simeq 2.2\,\text{MeV}$ being the heaviest and the lightest respectively [15]. In this thesis we will be considering the environment of collider experiments such as that of the Large Hadron Collider (LHC), where typical energies and characteristic momentum scales in the processes of interest allow us to neglect the masses of light quark flavors $q=\{u,d,s,c,b\}$ to good approximation. Therefore, for the rest of the thesis we consider eq. (2.15) for $n_f \equiv n_q = 5$ massless quark flavors.

Another important aspect of relativistic interacting quantum field theories with far reaching implications is that of *regularization* and *renormalization*. These two procedures emerge as a necessity due to the appearance of *ultraviolet divergences* (UV) in higher-order perturbative calculations. UV divergences have their origin in unconstrained large momenta in quantum loops which have to be regularized and systematically eliminated (renormalized) by a redefinition of the fields and the parameters in eq. (2.15). While there are many ways to regularize and tame such infinities (e.g. Pauli-Villars, Wilsonian cut-off Λ, finite lattice spacing, etc.), the most elegant one is *dimensional regularization*. Not only it respects both Lorentz and gauge invariance, but it also allows to simultaneously regularize another class of divergences, the *infrared divergences* (IR), that appear in massless field theories. All of the above make it quite appealing when it comes to practical calculations. In dimensional regularization divergent four-dimensional integrals are evaluated in non-integer dimensions $d=4-2\epsilon$ and their result is expressed as a Laurent series in ϵ with divergences appearing explicitly as poles $\propto 1/\epsilon^n$, $n>0$. Subsequently, these poles are 'absorbed' in the redefined fields and parameters and in the end the limit $\epsilon \to 0$ is taken, retrieving the $d=4$ result.

An important relation is that between the *bare* strong coupling constant as it appears in eq. (2.15) and the *renormalized* coupling

$$\alpha_s^{\text{bare}} = \Big(\frac{\mu^2 e^{\gamma_E}}{4\pi}\Big)^\epsilon Z_{\alpha_s}(\epsilon,\mu)\,\alpha_s(\mu)\,, \quad (2.16)$$

where Z_{α_s} is the counterterm responsible for canceling the poles at all orders in perturbation theory. The *renormalization scale* μ is a parameter of mass dimension $[\mu]=1$ introduced

such that the QCD action $[S_{\rm QCD}] = 0$ in d-dimensions. The awkward prefactor $e^{\epsilon\gamma_E}/(4\pi)^\epsilon$ defines the *modified minimal subtraction* ($\overline{\rm MS}$) renormalization scheme. It is interesting to notice the appearance of the scale μ out of a Lagrangian which, for the case of massless quarks, contains no explicit scale. This is known as *dimensional transmutation*.

The left hand side of eq. (2.16) is independent of μ, which implies its exact cancellation on the right hand side. Exploiting this, we can derive the famous renormalization group equation (RGE) for the strong coupling constant

$$\frac{{\rm d}\alpha_s(\mu)}{{\rm d}\ln\mu} = \beta[\alpha_s(\mu)] = -2\epsilon\alpha_s(\mu) - 2\alpha_s(\mu)\sum_{n=0}^{\infty}\beta_n\Big[\frac{\alpha_s(\mu)}{4\pi}\Big]^{n+1}\,, \tag{2.17}$$

where β_n are the beta function coefficients that dictate the *running* of α_s. At lowest order the coefficient reads

$$\beta_0 = \frac{11}{3}C_A - \frac{4}{3}T_F n_f\,, \tag{2.18}$$

and they are found to be scheme independent up to two loops. The term $\propto\epsilon$ in eq. (2.17) does not contribute to the $\alpha_s(\mu)$ running but it plays an important role in the derivation of the RGEs for various perturbative quantities.

Neglecting terms $\sim\mathcal{O}(\alpha_s^3)$ in eq. (2.17) we can solve it exactly and obtain the one-loop running for the strong coupling

$$\alpha_s(\mu) = \frac{\alpha_s(\mu_0)}{1 + \frac{\alpha_s(\mu_0)}{2\pi}\beta_0\ln\frac{\mu}{\mu_0}}\,, \tag{2.19}$$

where $\alpha_s(\mu_0)$ is a boundary condition at some characteristic scale μ_0. Usually it is set to be $\mu_0 \equiv m_Z = 91.1876\,{\rm GeV}$ [15] where the measured experimental value is $\alpha_s(m_Z) = 0.1181$ [15].

A phenomenologically crucial observation of eq. (2.18) is that $\beta_0 > 0$ for $N = 3$ and $n_f \leq 16$, which in turn implies that $\alpha_s(\mu)$ decreases for increasing values of μ, that is at short scales. This is the much celebrated result known as *asymptotic freedom* and it is a characteristic of non-abelian gauge theories, owing to the self interaction terms of the gauge bosons A^a_μ. It is precisely this feature that established QCD, a non-abelian gauge theory, as a viable candidate for the description of the strong interactions which allows at sufficiently short distances a quantitative description of quarks and gluons as a collection of almost free particles, usually referred to as *partons*.

Contrary to its high energy behavior $\alpha_s(\mu)$ diverges at large distances. This is most easily seen in eq. (2.19) where $\alpha_s \to \infty$ as the denominator tends to zero and allows to identify the scale that this happens

$$\Lambda_{\rm QCD} = \mu_0\exp\left[-\frac{2\pi}{\beta_0\alpha_s(\mu_0)}\right] \simeq 0.08\,{\rm GeV}\,. \tag{2.20}$$

This scale is known as the *Landau pole* and it is the point where the onset of color confinement and hadronization effects take place, i.e. where the perturbative description of QCD no longer applies. The value of $\Lambda_{\rm QCD}$ in eq. (2.20) is not entirely representative

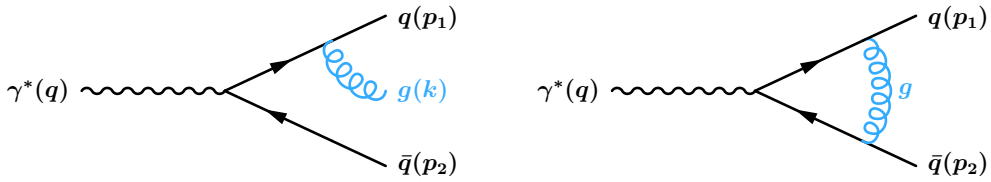

Figure 2.1: Feynman diagrams contributing to the next-to-leading order cross section for the process $e^+e^- \to \gamma^* \to$ jets where only the decay of the virtual photon is shown. Left panel corresponds to the real emission amplitude while the right panel corresponds to the one-loop virtual correction.

since it doubtful whether the QCD beta function — which is calculated in perturbation theory — still provides a good description of $\alpha_s(\mu)$ in this regime. Furthermore, even the fact that it is a physical pole is unclear since it is expected that the increasing trend of $\alpha_s(\mu)$ should stop at distances of typical hadron sizes $\sim \Lambda_{\rm QCD}^{-1}$, as it originally results from pair creation of particles which towards the non-perturbative regime obtain a natural IR cut-off [33]. Nevertheless, in practical perturbative calculations it is customary to work with $\Lambda_{\rm QCD} \simeq 1\,\text{GeV}$ where non-perturbative effects are expected to become important.

2.2 Soft and collinear limits of QCD

Neglecting the quark masses m_q is on the one hand well motivated for collider experiment environments where the characteristic momentum scale for the processes of interest, Q, is much larger $Q \gg m_q$. On the other hand, it is in this limit that a certain class of divergences appear, the so-called *soft and collinear divergences*.[3] They emerge in radiative corrections and correspond to a universal feature of QCD in the sense that they are independent of the details of the underlying hard scattering process. To better understand how they emerge and how they are treated, we discuss them in what follows in the context of two prototypical examples in collider physics (e.g. see refs. [34–36]), that of $e^+e^- \to$ jets and $pp \to X$.

$e^+e^- \to$ jets. At lepton colliders the initial state is a color-singlet and therefore they have provided with a uniquely clean environment in studying both experimentally and theoretically the dynamics of QCD. In this example we consider the process $e^+e^- \to \gamma^*(q) \to$ jets at the center of mass (COM) frame. At leading order (LO) in perturbation theory it involves the production of a quark-antiquark pair, while at next-to-leading order (NLO) in QCD it involves a single gluon emission $e^+e^- \to \gamma^*(q) \to q(p_1)\bar{q}(p_2)g(k)$. The Born (lowest order) and two real emission amplitudes for this process read,

$$\mathrm{i}\mathcal{M}_{\rm Born} = \bar{u}(p_1)\mathrm{i}eQ_q\gamma^\mu v(p_2)\, I_\mu(q) \tag{2.21}$$

$$\mathrm{i}\mathcal{M}_1 = \bar{u}(p_1)\mathrm{i}gT^a \not{\epsilon}^*(k)\frac{\mathrm{i}(\not{p}_1 + \not{k})}{(p_1+k)^2}\mathrm{i}eQ_q\gamma^\mu v(p_2)\, I_\mu(q)\,, \tag{2.22}$$

[3] They are also referred to as IR divergences in much of the literature.

$$\mathrm{i}\mathcal{M}_2 = \bar{u}(p_1)\mathrm{i}eQ_q\gamma^\mu \frac{-\mathrm{i}(\not{p}_2 + \not{k})}{(p_2+k)^2}\mathrm{i}gT^a \not{\epsilon}^*(k) v(p_2)\, I_\mu(q)\,, \tag{2.23}$$

where we suppress any color and Dirac indices for the sake of readability. Here, e is the electromagnetic coupling constant and Q_q is the charge of the quark with flavor q. All the information for the initial state subprocess $e^+e^- \to \gamma^*(q)$, including the photon propagator, is part of the tensor $I_\mu(q)$ whose precise form is irrelevant for this example. Left panel of figure 2.1 shows the Feynman diagram for the real emission amplitude $\mathrm{i}\mathcal{M}_1$, excluding the production subprocess, and $\mathrm{i}\mathcal{M}_2$ is understood to correspond to the mirrored diagram. Taking the soft limit $k^\mu \ll p_{1,2}^\mu$ of both radiative amplitudes in eqs. (2.22) and (2.23) we find,

$$\mathrm{i}\mathcal{M}_{\mathrm{tot}} = \mathrm{i}\mathcal{M}_1 + \mathrm{i}\mathcal{M}_2 = \left[g\frac{p_2\cdot\epsilon^*(k)}{p_2\cdot k} - g\frac{p_1\cdot\epsilon^*(k)}{p_1\cdot k}\right] \times \bar{u}(p_1)\mathrm{i}eQ_q\gamma^\mu T^a v(p_2)\, I_\mu(q)\,, \tag{2.24}$$

where we used the usual gamma matrix anti-commutation relation $\{\gamma^\mu, \gamma^\nu\} = 2g^{\mu\nu}$ along with the fact that the partons are massless, $p_{1,2}^2 = k^2 = 0$ and $\bar{u}(p_1)\not{p}_1 = \not{p}_2 v(p_2) = 0$. Now squaring eq. (2.24), summing and averaging over polarizations and color, after some algebra we find

$$\sum_{\text{col.,pol.}} \left|\mathrm{i}\mathcal{M}_{\mathrm{tot}}\right|^2 = g^2 C_F \frac{2p_1\cdot p_2}{(p_1\cdot k)(p_2\cdot k)} \times \sum_{\text{pol.}} \left|\mathrm{i}\mathcal{M}_{\mathrm{Born}}\right|^2, \tag{2.25}$$

where for the polarization sum we used $\sum_\lambda \epsilon_\lambda^\mu(k)\epsilon_\lambda^{\nu*}(k) = -g^{\mu\nu} + \mathcal{O}(k)$ which is an appropriate approximation in the soft limit. At this point we come to an important observation, namely that in the soft limit the part of the (squared) amplitude responsible for the soft real emission has completely factorized from the (squared) Born amplitude into an overall factor. Inspecting also the three-body massless decay phase space in the soft limit we find it to factorize,

$$\begin{aligned}\mathrm{d}\Phi_3(q) &= \left[\prod_{i=1}^{2}\frac{\mathrm{d}^4p_i}{(2\pi)^4}(2\pi)\,\delta(p_i^2)\,\theta(p_i^0)\right]\frac{\mathrm{d}^4k}{(2\pi)^4}(2\pi)\,\delta(k^2)\,\theta(k^0)\,(2\pi)^4\,\delta^{(4)}(q-p_1-p_2-k)\\ &\approx \mathrm{d}\Phi_2(q) \times \frac{\mathrm{d}^4k}{(2\pi)^4}(2\pi)\,\delta(k^2)\,\theta(k^0)\,,\end{aligned} \tag{2.26}$$

where $\mathrm{d}\Phi_2(q)$ is the two-body decay phase space. The assumption that $k^\mu \ll p_{1,2}^\mu$ allows for the statements that the two quarks are produced in a back-to-back configuration and they are parametrized by Born kinematics, since the recoil provided by the gluon emission can be neglected. Therefore, quark and antiquark momenta can be parametrized as $p_1^\mu = Q/2\,(1,\vec{n})$ and $p_2^\mu = Q/2\,(1,-\vec{n})$ with the unit vector $\vec{n}$ chosen along the direction of the quark and Q being the COM energy. Under these considerations and using eqs. (2.25) and (2.26), the cross section for the real emission reads

$$\sigma_R^{(1)} = \sigma^{(0)} \times \frac{2\alpha_s C_F}{\pi}\int_0^\infty \frac{\mathrm{d}k^0}{k^0}\int_0^\pi \frac{\mathrm{d}\theta}{\sin\theta}\,, \tag{2.27}$$

where θ is the polar angle between $\vec{n}$ and the emitted gluon while $\sigma^{(0)}$ is the Born cross section,

$$\sigma^{(0)} = \frac{1}{2Q^2}\int \mathrm{d}\Phi_2(q) \sum_{\text{pol.}} \left|\mathrm{i}\mathcal{M}_{\text{Born}}\right|^2 . \tag{2.28}$$

In eq. (2.27) the integrals over the energy k^0 and the polar angle θ are singular with the singularities occurring when $k^0 \to 0$ and/or $\theta \to 0, \pi$. The former corresponds to a *soft singularity* as it essentially emerges for vanishing momenta of the gluon $k^\mu \to 0$, whereas the latter corresponds to a *collinear singularity* since it is realized when the gluon emission is almost parallel to the direction of the parent quark. Note that the collinear singularity is also referred to as *mass singularity*, a name whose origin stems from the fact that the neglected quark masses m_q would provide a natural IR cut-off to it. This can be understood by considering the case of massive quarks and by looking at the propagator of either eq. (2.22) or eq. (2.23), which in that case would be

$$\frac{\pm\mathrm{i}(\not{p}_i + \not{k})}{(p_i + k)^2 - m_q^2} = \frac{\pm\mathrm{i}(\not{p}_i + \not{k})}{k^0 Q\Big(1 \mp \cos\theta\sqrt{1 - \big(m_q/Q\big)^2}\Big)} , \qquad \text{for} \quad i = 1, 2 , \tag{2.29}$$

where now the singularity $\theta \to 0, \pi$ is completely screened by the nonzero m_q.

While the divergences appearing in eq. (2.27) could pose a problem for QCD, there is one more contribution that we have not yet taken into account. This involves the soft limit of the one-loop virtual correction, depicted in the right panel of figure 2.1, interfered with the Born amplitude. In this, the loop integral is also IR divergent since the momenta of the virtual gluon can become arbitrarily soft and/or collimated to one of the fermions. Therefore, summing both real and virtual contributions we would then find that the IR divergences cancel exactly between them. This is based on the celebrated Kinoshita–Lee–Nauenberg (KLN) theorem [37–39] which states that for sufficiently inclusive observables such as the total cross section, IR singularities completely cancel out leaving behind finite perturbative corrections.

pp → X. Another important class of experiments is that of hadron colliders such as the LHC. The physical picture there is fundamentally different since the colliding protons are bound states of partons and the scales appearing in such cross sections are quite disparate; proton states are governed by nonperturbative effects $\sim \Lambda_{\text{QCD}}$ whereas the typical scale of a hard scattering process, Q, is considered much larger $Q \gg \Lambda_{\text{QCD}}$. The seminal work of Collins, Soper and Sterman provided a formal way of disentangling contributions coming from such different regimes in terms of the *collinear factorization theorem* [40], under which the hadronic cross section for the production of any final state X can be schematically expressed as

$$\sigma(pp \to X) = \sum_{ij} \int_0^1 \mathrm{d}x_1 \mathrm{d}x_2 \; f_i(x_1) f_j(x_2) \; \hat{\sigma}_{ij}(x_1 x_2 s) + \mathcal{O}\Big(\frac{\Lambda_{\text{QCD}}}{Q}\Big) , \tag{2.30}$$

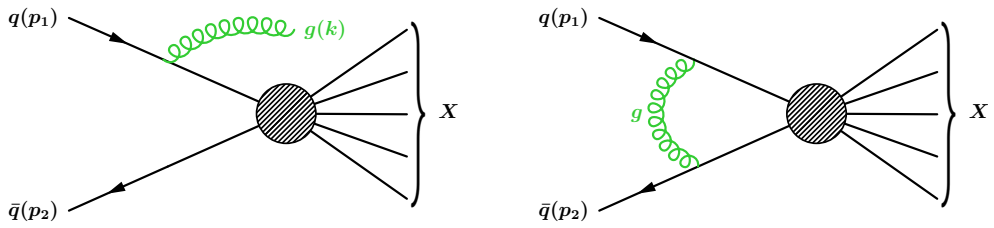

Figure 2.2: Feynman diagrams contributing to the next-to-leading order partonic cross section for the process $q\bar{q} \to X$ where X is any final state. The hard scattering vertex Γ is depicted as a black blob. Left panel shows the real emission amplitude while the right panel shows the one-loop virtual correction.

where s is the COM energy and $f_i(x)$ is the parton distribution function (PDF). It encodes the probability of extracting a parton i from the proton p with longitudinal momentum fraction x that subsequently participates in the hard scattering. Accordingly, $\hat{\sigma}_{ij}$ denotes the partonic cross section for the process $ij \to X$. The factorization in eq. (2.30) is among the most important results in QCD since it separates universal nonperturbative quantities (PDFs) that are fitted from experimental data from those that can be calculated in perturbative QCD (partonic cross section).

At this point, a natural question that may be posed is whether the same cancellation of soft and collinear divergences that we discussed in the $e^+e^- \to$ jets example, also happens for cross sections at proton colliders. To answer that, we consider a typical process at the LHC, $pp \to X$, where at lowest order we assume that it is mediated by the partonic channel of quark-antiquark annihilation $q(p_1)\bar{q}(p_2) \to X(p_X)$. At NLO there is a single real gluon emission whose momenta k^μ can be conveniently expressed in terms of the Sudakov decomposition,

$$k^\mu = (1-z)p_1^\mu + (1-y)p_2^\mu + k_\perp^\mu \,, \tag{2.31}$$

where $k_\perp \cdot p_{1,2} = 0$ and $\vec{k}_T^{\,2} = -\vec{k}_\perp^{\,2}$ are the Euclidian transverse momenta. Furthermore, from the on-shell condition $p_1^2 = p_2^2 = k^2 = 0$ we obtain $(1-z)(1-y)(p_1 \cdot p_2) = k_T^2$. In principle there are two amplitudes contributing at NLO for this process, where the gluon is radiated either from the quark or the antiquark, but we are interested in the p_1-collinear limit and this amounts to considering only the emission off the quark, shown in left panel of figure 2.2 (the emission off the antiquark is power suppressed in this limit). The Born and the real emission amplitudes read,

$$\mathrm{i}\mathcal{M}_{\mathrm{Born}} = \bar{v}(p_2)\mathrm{i}\Gamma(p_1,p_2)u(p_1)\,, \tag{2.32}$$

$$\mathrm{i}\mathcal{M}_1 = \bar{v}(p_2)\mathrm{i}\Gamma(p_1-k,p_2)\frac{\mathrm{i}(\not{p}_1 - \not{k})}{(p_1-k)^2}\mathrm{i}gT^a \not{\epsilon}^*(k)u(p_1)\,, \tag{2.33}$$

where Γ contains the information of the vertex and of the decay kinematics. Inspecting

also the phase space in the p_1-collinear limit,

$$\begin{aligned}\mathrm{d}\Phi &= \mathrm{d}\Phi_X \frac{\mathrm{d}^4k}{(2\pi)^4}\,(2\pi)\,\delta(k^2)\,\theta(k^0)\,(2\pi)^4\,\delta^{(4)}(p_1+p_2-k-p_X)\\ &\approx \mathrm{d}\Phi_X\,(2\pi)^4\delta^{(4)}(zp_1+p_2-p_X)\times\frac{\mathrm{d}^4k}{(2\pi)^4}\,(2\pi)\,\delta(k^2)\,\theta(k^0)\,. \end{aligned} \tag{2.34}$$

Squaring eq. (2.33), summing and averaging over polarizations and color and integrating over the phase space eq. (2.34), the real emission partonic cross section at NLO reads [36]

$$\hat{\sigma}^{(1)}_{c_1} = C_F\frac{\alpha_s}{2\pi}\int_0^{\hat{s}}\frac{\mathrm{d}k_T^2}{k_T^2}\int_0^1\mathrm{d}z\,\frac{1+z^2}{1-z}\hat{\sigma}^{(0)}_{q\bar{q}}(zp_1,p_2)\,, \tag{2.35}$$

where $\hat{\sigma}^{(0)}_{q\bar{q}}$ is the Born cross section,

$$\hat{\sigma}^{(0)}_{q\bar{q}}(p_1,p_2) = \frac{1}{2\hat{s}}\int\mathrm{d}\Phi_X\sum_{\text{col.pol.}}\left|\mathrm{i}\mathcal{M}_{\text{Born}}\right|^2(2\pi)^4\delta^{(4)}(p_1+p_2-p_X)\,, \tag{2.36}$$

and $\hat{s}=(p_1+p_2)^2$ is the partonic COM energy. Note that the k_T^2 integral in eq. (2.35) has necessarily an upper bound since the collinear approximation is valid only up to the hard scale of the process $\sim\sqrt{\hat{s}}$.

Analogously to the example in the previous paragraph, we see that eq. (2.35) exhibits a double divergence when $k_T\to 0$ and $z\to 1$, or a single one for the limiting case of either variable. Physically, $k_T\to 0$ corresponds to a collinear divergence since the momenta of the emitted gluon become almost aligned to those of the parent quark, whereas $z\to 1$ corresponds to a soft singularity since the momenta carried away by the gluon are almost zero. It comes as no surprise that the soft divergence is canceled when including the virtual correction to the cross section, right panel of figure 2.2,

$$\hat{\sigma}^{(1)}_{c_1} = C_F\frac{\alpha_s}{2\pi}\int_0^{\hat{s}}\frac{\mathrm{d}k_T^2}{k_T^2}\int_0^1\mathrm{d}z\,\frac{1+z^2}{1-z}\left[\hat{\sigma}^{(0)}_{q\bar{q}}(zp_1,p_2)-\hat{\sigma}^{(0)}_{q\bar{q}}(p_1,p_2)\right] \tag{2.37}$$

$$\equiv \frac{\alpha_s}{4\pi}\int_0^{\hat{s}}\frac{\mathrm{d}k_T^2}{k_T^2}\int_0^1\mathrm{d}z\,P^{(0)}_{qq}(z)\,\sigma^{(0)}_{q\bar{q}}(zp_1,p_2)\,, \tag{2.38}$$

where in the second line we defined the $q\to q$ splitting function as

$$P^{(0)}_{qq}(z) = 2C_F\left[\frac{1+z^2}{1-z}\right]_+, \tag{2.39}$$

and introduced the *plus distribution* which is defined as follows. For a function $f(z)$ that is non-integrable in $z\to 1$ and does not diverge worse than $1/(1-z)$, the corresponding plus distribution $[f(z)]_+$ is defined by its action on a test function $g(z)$ as

$$\int_0^1\mathrm{d}z\big[f(z)\big]_+\,g(z) = \int_0^1\mathrm{d}z\,f(z)\big[g(z)-g(1)\big]\,, \tag{2.40}$$

where the term in the square brackets regulates the $z=1$ singularity of $f(z)$.

Elaborating a bit more on eq. (2.38), we stress that while the virtual contribution remedied the soft divergence, the collinear singularity $k_T \to 0$ is still present and uncancelled. The crucial observation here is that in the soft singular limit $z \to 1$, both real and virtual contributions of the cross section share the same initial state kinematics since the same momenta are flowing into the hard vertex. On the other hand, in the collinear limit, $k_T \to 0$ but $z \not\to 1$ and thus the term in the square brackets of eq. (2.37) does not vanish.

To proceed and regulate the divergent k_T integral in eq. (2.38), we use dimensional regularization by extending the dimensions of k_T from $4-2 \mapsto d-2 = 2-2\epsilon$. Including the $\overline{\text{MS}}$ factor, the result of the integral reads

$$\Big(\frac{\mu^2 e^{\gamma_E}}{4\pi}\Big)^{\epsilon} \frac{\Omega_{2-2\epsilon}}{(2\pi)^{1-2\epsilon}} \int_0^{\hat{s}} \frac{\mathrm{d}k_T^2}{k_T^{2+2\epsilon}} = -\frac{1}{\epsilon} - \ln\Big(\frac{\mu^2}{\hat{s}}\Big) + \mathcal{O}(\epsilon)\,, \tag{2.41}$$

where $\Omega_d = 2\pi^{d/2}/\Gamma(d/2)$ is the d-dimensional solid angle. The appearance of the collinear singularity as an explicit pole in ϵ would herald fundamental problems for QCD had it not been for the following two important points. Firstly, concerning the universality of the collinear singularity, i.e. that it emerges independently from the details of the underlying hard scattering process and therefore it is a feature that all partonic cross sections share. Secondly, concerning the fact that it is the *hadronic cross section* σ that is a *physical observable* and should be a finite and not the partonic $\hat{\sigma}_{q\bar{q}}$. Substituting eq. (2.41) to eq. (2.38), the hadronic cross section up to $\mathcal{O}(\alpha_s)$ is given by

$$\begin{aligned}\sigma(pp \to X) = \int_0^1 \mathrm{d}x_1 \mathrm{d}x_2\, f_{\bar{q}}(x_2) \Big[& f_q(x_1) \hat{\sigma}^{(0)}_{q\bar{q}}(x_1 p_1, x_2 p_2) \\ & - f_q(x_1) \frac{1}{\epsilon} \frac{\alpha_s}{4\pi} \int_0^1 \mathrm{d}z\, P^{(0)}_{qq}(z) \hat{\sigma}^{(0)}_{q\bar{q}}(z x_1 p_1, x_2 p_2) \\ & - f_q(x_1) \frac{\alpha_s}{4\pi} \ln\Big(\frac{\mu^2}{\hat{s}}\Big) \int_0^1 \mathrm{d}z\, P^{(0)}_{qq}(z) \hat{\sigma}^{(0)}_{q\bar{q}}(z x_1 p_1, x_2 p_2) \\ & + f_q(x_1) \hat{\sigma}^{(1)}_{q\bar{q}}(x_1 p_1, x_2 p_2) + \ldots \Big]\,, \end{aligned} \tag{2.42}$$

where $\hat{\sigma}^{(1)}_{q\bar{q}}$ denotes the $\mathcal{O}(\alpha_s)$ corrections to the partonic cross section stemming from phase space regions that the momenta are neither soft nor collinear. The dots in eq. (2.42) capture the fact that we have not yet considered all $\mathcal{O}(\alpha_s)$ corrections to σ; while we examined only the collinear splitting $q \to qg$, the $g \to q\bar{q}$ with the quark q participating in the hard scattering may also occur. Considering this case changes nothing in the main steps of the previous derivation apart from the emerging splitting kernel that is different

$$P^{(0)}_{qg}(z) = 2T_F[(1-z^2) + z^2]\,. \tag{2.43}$$

In light of the previous arguments and in the spirit of renormalization, we can treat the PDFs appearing eq. (2.42) as bare quantities and absorb the $1/\epsilon$ divergence in them,

$$f_q(x,\mu) = f_q^{\text{bare}}(x) - \frac{1}{\epsilon} \frac{\alpha_s}{4\pi} \int_z^1 \frac{\mathrm{d}z}{z} \Big[P^{(0)}_{qq}(z)\, f_q\Big(\frac{x}{z}\Big) + P^{(0)}_{qg}(z)\, f_g\Big(\frac{x}{z}\Big) \Big]\,, \tag{2.44}$$

resulting into a finite partonic cross section in eq. (2.42).

Note though that the renormalized PDF in eq. (2.44) acquired an explicit scale dependence. Taking the derivative with respect to μ while being careful about the scale dependence of the strong coupling constant in d-dimensions, eq. (2.17), we obtain

$$\mu\frac{\mathrm{d}}{\mathrm{d}\mu}f_q(x,\mu) = \frac{\alpha_s}{4\pi}\int_z^1 \frac{\mathrm{d}z}{z}\left[2P_{qq}^{(0)}(z)\, f_q\Big(\frac{x}{z}\Big) + 2P_{qg}^{(0)}(z)\, f_g\Big(\frac{x}{z}\Big)\right]. \tag{2.45}$$

This is the famous Dokshitzer-Gribov-Lipatov-Altarelli-Parisi (DGLAP) equation [41–43] at NLO that captures the logarithmic dependence of the quark PDF with respect to the *factorization scale* μ. Analogous integro-differential equations up to different splitting kernels $P_{ij}(z)$ are also be obtained for the antiquark $f_{\bar{q}}(x)$ and gluon $f_g(x)$ PDFs by considering the collinear limits where correspondingly a $\bar{q}$ or a g undergoes collinear splittings.

IR safety and Sudakov double logarithms. So far in our discussions we focused on total cross sections, but these are not the only measurable quantities that provide information about the rich QCD dynamics. Differential cross sections in some resolution variable τ are a prime example that have been and are extensively investigated in collider experiments. Contributions to a differential cross section $\mathrm{d}\sigma/\mathrm{d}\tau$ from different parts of the τ spectrum not only can provide stringent tests to perturbative QCD and help to establish particle properties within the Standard Model (SM), but they may also be sensitive to physics Beyond the Standard Model (BSM) and therefore shed light to long standing and open questions. All of the above motivate for a proper definition of observables that are free of IR divergences such that a *meaningful* comparison between theory and experiment is feasible. To this end, a resolution variable τ is defined to be *Infrared-Collinear* (IRC) *safe* if it is insensitive to both soft and collinear singular limits. More precisely, if τ depends on the momenta of $n+1$ emissions it has to satisfy

$$\text{soft}: \quad \tau(p_1,\ldots,p_n,p_{n+1}) = \tau(p_1,\ldots,p_n)\,, \qquad p_{n+1}\to 0\,, \tag{2.46}$$

$$\text{collinear}: \quad \tau(p_1,\ldots,p_n,(1-\kappa)p_{n+1},\kappa p_{n+1}) = \tau(p_1,\ldots,p_{n+1})\,, \qquad \kappa\to 1\,. \tag{2.47}$$

It should be noted that even though experiments may perform measurements of variables that do not satisfy eqs. (2.46) and (2.47), it is *only* with IRC safe resolution variables that a comparison with theory is plausible.

While the KLN theorem guarantees that real and virtual contributions in differential cross sections of an IRC safe resolution variable τ yield IR finite results, it is known that this cancellation is incomplete. The reason for this can be traced on the measurement of τ, which contrary to total inclusive cross sections, it upsets the exact cancellation between real and virtual contributions; it imposes restrictions on the real radiation phase space while the virtual contributions are unconstrained, resulting into a leftover logarithmic imprint. Resolution variables that are sensitive to soft and collinear emissions exhibit a characteristic logarithmic dependence which is known as *Sudakov double logarithms*, a name that stems from the relative power of said logarithms that appear at each order in perturbation theory.

Assuming that τ is a dimensionless variable sensitive to soft and collinear emissions, we can schematically express the perturbative expansion of a differential cross section

$$\frac{\mathrm{d}\sigma}{\mathrm{d}\tau} \sim \delta(\tau) + \sum_{n=1}^{\infty}\sum_{m=0}^{2n-1} \alpha_s^n \Big(\delta(\tau) + c_{n,m}(\tau)\Big[\frac{\ln^m \tau}{\tau}\Big]_+\Big)\,, \tag{2.48}$$

where $c_{n,m}(\tau)$ denote some coefficients that do not bare any logarithmic dependent on τ. Eq. (2.48) has a well behaved and convergent perturbative expansion when $\tau \sim 1$ but in corners of the phase space where $\tau \ll 1$, the existence of the Sudakov double logarithms $\alpha_s^n \ln^m \tau/\tau$ result into its deterioration by overcoming the strong coupling suppression. In this part of the spectrum the expansion invalidated and necessitates a reorganization such that the highest-power logarithms are *resummed* to all orders. As a matter of fact, we have already come across the effect of leftover logarithms and their resummation in the example $pp \to X$. There, the cross section is sensitive only to collinear emissions which give rise to the single logarithm. These are resummed to all orders by evaluating the hadronic cross section at $\mu \sim \sqrt{\hat{s}}$, such that logarithms are minimized, and using the DGLAP equations the PDFs are *evolved* from $\mu \sim \sqrt{\hat{s}}$ to the scale that is used as a boundary condition in solving eq. (2.45).

In this thesis we will be taking the point of view of performing resummation via effective field theories (EFT) and specifically using Soft-Collinear Effective theory (SCET) [44–46], which we present in section 2.3. Though we mention that other formalisms for performing resummation exist as well, e.g. see refs. [47, 48]. In SCET, differential cross sections are systematically expanded in the limit of small-τ,

$$\frac{\mathrm{d}\sigma}{\mathrm{d}\tau} \sim \quad \frac{\mathrm{d}\sigma^{(0)}}{\mathrm{d}\tau} \quad + \quad \frac{\mathrm{d}\sigma^{(1)}}{\mathrm{d}\tau} \quad + \quad \frac{\mathrm{d}\sigma^{(2)}}{\mathrm{d}\tau} \quad + \quad \dots \tag{2.49}$$

$$\sim \frac{1}{\tau}\Big[\ \mathcal{O}(1) \quad + \quad \mathcal{O}(\tau) \quad + \quad \mathcal{O}(\tau^2) \quad + \quad \dots\ \Big]\,, \tag{2.50}$$

where the first addend corresponds to the *leading power* (LP) cross section and contains the most singular terms $\delta(\tau)$ and $[\ln^m \tau/\tau]_+$, while the rest are suppressed by at least one power of τ and they are called *power corrections*. Roughly speaking, in SCET the LP cross section $\mathrm{d}\sigma^{(0)}/\mathrm{d}\tau$ obtains a factorized form with each function capturing physics at a different scale while satisfying its own RGE. Solving these RGEs, each function is evolved from its natural scale that is free of large logarithms, to a common (arbitrary) scale and Sudakov double logarithms are resummed to all orders in perturbation theory, resulting to a physical spectrum for all values of τ. In chapter 3 we review the factorization of the transverse momentum (q_T) distribution for a color-singlet production in SCET and discuss the resummation of Sudakov double logarithms that results from the solutions of the RGEs.

We conclude this section by showing in figure 2.3 an illustrative example for the Drell-Yan (left panel) and Higgs (right panel) q_T spectrum. In both plots the blue dashed curve shows the NLO fixed-order (FO) result that diverges as $q_T \to 0$ due to Sudakov double logarithms, whereas the red solid curve shows the resummed result at next-to-leading-logarithmic (NLL) accuracy, which is well behaved and exhibits the so-called *Sudakov peak* at $q_T \sim 7 - 10\,\mathrm{GeV}$.

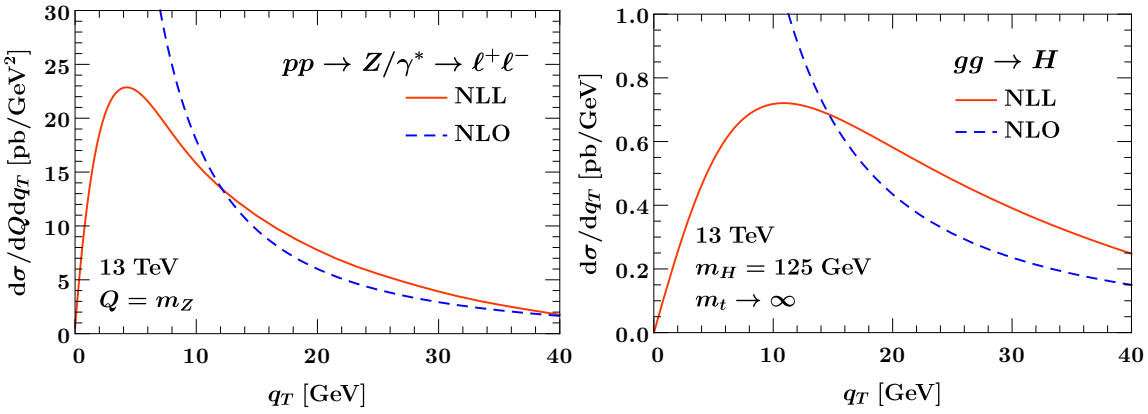

Figure 2.3: The resummed (solid red) and fixed-order (dashed blue) inclusive transverse momentum spectrum for the Drell-Yan (left) and Higgs (right) processes. Both results are obtained from `SCETlib` [49].

2.3 Soft-Collinear Effective Theory (SCET)

Soft-Collinear Effective Theory [44–46] is an EFT that captures the IR limits of QCD. It corresponds to a systematic expansion of the QCD Lagrangian in the soft-collinear limits and describes the propagation and interaction of soft and collinear modes under the presence of a hard interaction. Since soft and collinear modes live deep into the IR region, they are characterized by invariant masses parametrically much smaller than those appearing in the hard scattering which leads to the emergence of multiple, widely separated scales. Thus, it comes as no surprise that an EFT is the right tool in order to disentangle physics sensitive to each scale and to obtain insight and physical information about the hard process.

SCET corresponds to a *top-down* EFT since the full theory Lagrangian $\mathcal{L}_{\mathrm{QCD}}$, eq. (2.15), is known. As we show in section 2.3.3, it is constructed by 'integrating out' of the theory hard modes that we do not wish to describe, while the remaining ones (soft and collinear) constitute the dynamical part of the EFT. Note that this is a characteristic difference of SCET compared to other EFTs, since momentum regions of particles are integrated out rather than entire degrees of freedom. As a final remark, we mention that SCET is not the only way to address such physical settings. For example, in the diagrammatic method [35, 40, 50] a the straightforward expansion of Feynman integrals in different momentum regions is considered by assigning a power counting parameter and determining the degree of their IR divergence. In contrast to the diagrammatic method, SCET provides a natural language for the incorporation of the universal IR limits of QCD in the fundamental quantity that captures its dynamics, namely the Lagrangian. This way, gauge invariance is manifest and allows for a systematic way to calculate power suppressed contributions while factorization and resummation of large logarithms come out naturally.

In the following review of SCET we mainly follow ref. [51], while additional material from cited references have also been added.

2.3.1 Basics of SCET

Lightcone coordinates. Since we are interested in describing modes that propagate and fluctuate around a specific direction n_i^μ, we have to pick a parametrization that makes their momentum scaling explicit. These are the lightcone coordinates. To be able to decompose any four-vector with respect to the lightcone direction n_i^μ, we define in addition an auxiliary vector $\bar{n}_i^\mu$ such that,

$$n_i^2 = \bar{n}_i^2 = 0\,, \qquad n_i \cdot \bar{n}_i = 2\,. \tag{2.51}$$

This allows to decompose an arbitrary four-vector p^μ in this coordinate basis as

$$p^\mu = p_i^- \frac{n_i^\mu}{2} + p_i^+ \frac{\bar{n}_i^\mu}{2} + p_{\perp i}^\mu \equiv (p_i^-, p_i^+, \vec{p}_{\perp i})\,, \tag{2.52}$$

with each component is defined as

$$p_i^- = \bar{n}_i \cdot p\,, \qquad p_i^+ = n_i \cdot p\,, \qquad n_i \cdot p_{\perp i} = \bar{n}_i \cdot p_{\perp i} = 0\,. \tag{2.53}$$

It is understood that $p_{\perp i}^\mu$ are the projections of p^μ in the perpendicular plane that $n_i^\mu, \bar{n}_i^\mu$ define. We stress that although n_i^μ does have a physical interpretation — it is after all the lightcone direction of the (collinear) particle's momenta that we wish to parametrize — $\bar{n}_i^\mu$ has none whatsoever. It is only introduced to allow for a complete decomposition of p^μ as done in eq. (2.52). Further below in section 2.3.2, we see how this arbitrariness in choosing $\bar{n}_i^\mu$ translates into a symmetry of SCET.

At the LHC the protons move along the beam direction[4] and therefore the natural choice for the lightcone vectors is

$$n_a^\mu \equiv n^\mu = (1,0,0,1)\,, \qquad n_b^\mu \equiv \bar{n}^\mu = (1,0,0,-1)\,, \tag{2.54}$$

where now

$$p^- = p^0 + p^3\,, \qquad p^+ = p^0 - p^3\,, \qquad p_\perp^\mu = (0, p^1, p^2, 0)\,. \tag{2.55}$$

The invariant product is then given by,

$$p^2 = p^- p^+ + p_\perp^2 = p^- p^+ - p_T^2\,, \tag{2.56}$$

and $\vec{p}_T$ are the corresponding Euclidian transverse components, $p_T^2 \equiv \vec{p}_T^{\,2} = -p_\perp^2$.

Throughout this thesis we are mostly concerned with the environment of LHC and therefore we predominantly use the lightcone vectors in eq. (2.54) unless stated otherwise.

[4] Throughout this thesis, we assume a right-handed coordinate system where the z-axis is along the beam pipe of LHC and the x-axis is pointing to the center of the LHC ring.

Modes in SCET. In order to construct the SCET Lagrangian, the contributing modes for the physical process in question have to be deduced. Doing so, allows to disentangle physics that happens at widely separated scales. The cornerstone of this procedure is understanding the constraints imposed by the measurement that is performed. Depending on the resolution variable, two types of soft modes can contribute which in turn define two distinct SCET classes, based on which numerous physical processes can be described. These classes are referred to as SCET_I and SCET_II and we present their basic features with two specific examples.

Consider the process $e^+e^- \to \gamma^* \to 2\,\text{jets}$ where the invariant mass $m_J, m_{\bar{J}}$ of each jet is measured. Working at the COM frame, the momenta carried by the vector boson are $q^\mu = (Q, \vec{0})$ where Q sets the hard scale, and from momentum conservation the two jets will be in a back-to-back configuration each carrying momenta $\sim Q$. Aligning the two jet axes with lightcone vectors n^μ, $\bar{n}^\mu$ and inspecting the momentum components for the jet in the n-direction, we find them scaling as

$$p_n \sim \left(Q, \frac{p_\perp^2}{Q}, p_\perp\right) \sim Q(1, \lambda^2, \lambda)\,, \tag{2.57}$$

where we introduced the dimensionless book-keeping parameter $\lambda = p_\perp/Q \ll 1$. It serves for power counting purposes and will be proven to be extremely useful when we consider the construction of the SCET Lagrangian in section 2.3.3. Here, $p^- \sim Q$ and $p_\perp \ll Q$ in order to comply with the definition of a jet,[5] while from the on-shell condition $p^-p^+ \sim p_\perp^2$ we have that $p^+ \sim p_\perp^2/Q$. Looking at the relative scaling of the jet's momentum components in eq. (2.57) we find,

$$p^- \gg p_\perp \gg p^+\,. \tag{2.58}$$

From now on, momenta that adhere to the hierarchy of eq. (2.58) or equivalently have the scaling of eq. (2.57) will be referred to as *n-collinear momenta*. At this point we can appreciate the benefits of the decomposition in lightcone coordinates, eq. (2.55), since they successfully expose the large (p^-) and small ($p^+, p_\perp$) momentum components, allowing for definite statements with respect to their scaling.

The invariant mass of the jet is formally defined by considering the $x-y$ plane partitioning the space into two hemispheres a, b and assigning all particle momenta in each hemisphere to the corresponding jet. For the jet in hemisphere a

$$m_J = \left(\sum_{i\in a} p_i^\mu\right)^2, \tag{2.59}$$

where the sum i runs over all particles in hemisphere a. Based on this definition, we may ask what information we can extract for the scaling of the ultrasoft[6] momenta, p_{us}^μ, by

[5] Among many, a definition of a jet is that of an energetic parton that due to QCD radiation undergoes multiple splittings enhanced by collinear singularities that result into a collection of collimated hadrons and other particles that move preferentially in a specific direction.

[6] While the name 'ultrasoft' appears arbitrary at the moment, it becomes clear further below that it is chosen such that we distinguish them from the parametrically larger soft modes that appear in SCET_II.

considering their clustering with a collinear particle,

$$m_J \sim (p_n + p_{us})^2 \sim p_n^2 + 2\, p_n \cdot p_{us} + p_{us}^2 \sim Q^2\lambda^2 \ll Q^2\,, \tag{2.60}$$

where the scaling of m_J is dictated by $p_n^2 \sim Q^2\lambda^2$, eq. (2.57). Looking at the second addend,

$$p_n \cdot p_{us} \sim p^- p_{us}^+ + \ldots \sim Q^2\lambda^2\,, \tag{2.61}$$

where we drop terms that are further λ-suppressed. Since $p^- \sim Q$ this forces $p_{us}^+ \sim Q\lambda^2$ at most and following from the isotropy of the ultrasoft modes we find,

$$p_{us} \sim Q(\lambda^2, \lambda^2, \lambda^2)\,, \qquad p_{us}^2 \sim Q^2\lambda^4\,. \tag{2.62}$$

Repeating the previous analysis for the jet $\bar{J}$ in the $\bar{n}$-direction is trivial upon realizing that it simply amounts to the change $n^\mu \leftrightarrow \bar{n}^\mu$ and thus its momentum components can be obtained by those of J under $+ \leftrightarrow -$. Summarizing the results for the $n, \bar{n}$-collinear and ultrasoft momenta,

$$p_n \sim Q(1, \lambda^2, \lambda)\,, \qquad p_n^2 \sim Q^2\lambda^2\,, \tag{2.63}$$

$$p_{\bar{n}} \sim Q(\lambda^2, 1, \lambda)\,, \qquad p_{\bar{n}}^2 \sim Q^2\lambda^2\,, \tag{2.64}$$

$$p_{us} \sim Q(\lambda^2, \lambda^2, \lambda^2)\,, \qquad p_{us}^2 \sim Q^2\lambda^4\,, \tag{2.65}$$

where we see that the virtualities between collinear and ultrasofts are parametrically different and this defines an SCET_I setting. A convenient way to depict the modes is that in the left panel of figure 2.4 where only the $p^\pm$ components are shown.[7] From there, it is clear that the $n, \bar{n}$-collinear (green) and ultrasoft (orange) modes live in different invariant mass hyperbolas. All modes with $p^2 \gg Q^2\lambda^2$, such as the hard modes (blue), are not part of the EFT and they are integrated out, whereas those with $p^2 \lesssim Q^2\lambda^2$ (green and orange) constitute its dynamical part and they are represented by degrees of freedom in SCET.

Now consider the measurement of the transverse momenta q_T of a color-singlet particle produced at the LHC via the process $p_n p_{\bar{n}} \to LX$. Here, $p_n(p_{\bar{n}})$ is the incoming proton in the $n\,(\bar{n})$-direction, L is the produced color-singlet with invariant mass Q that sets the hard scale, and X denotes the total hadronic radiation. Focusing on the kinematic regime $\lambda \equiv q_T/Q \ll 1$, the dominant contributions to q_T come either from collinear emissions or from homogeneous modes which we call soft, and they are both constrained by the measurement of q_T. From eqs. (2.63) and (2.64) the collinear modes have $p_{\perp n} \sim p_{\perp \bar{n}} \sim Q\lambda$ which in turn restricts the perpendicular component of the contributing soft modes to be $p_{\perp s} \sim Q\lambda$. Evoking once more the isotropy of the soft modes, we have

$$p_s \sim Q(\lambda, \lambda, \lambda)\,, \qquad p_s^2 \sim Q^2\lambda^2\,. \tag{2.66}$$

As before, in the right panel of figure 2.4 we show the $p^\pm$ components for the collinear and soft modes where they now lie on the same invariant mass hyperbola. This defines an SCET_II

[7] The $p_\perp$ component can always be deduced by the on-shell condition $p^- p^+ \sim p_\perp^2$.

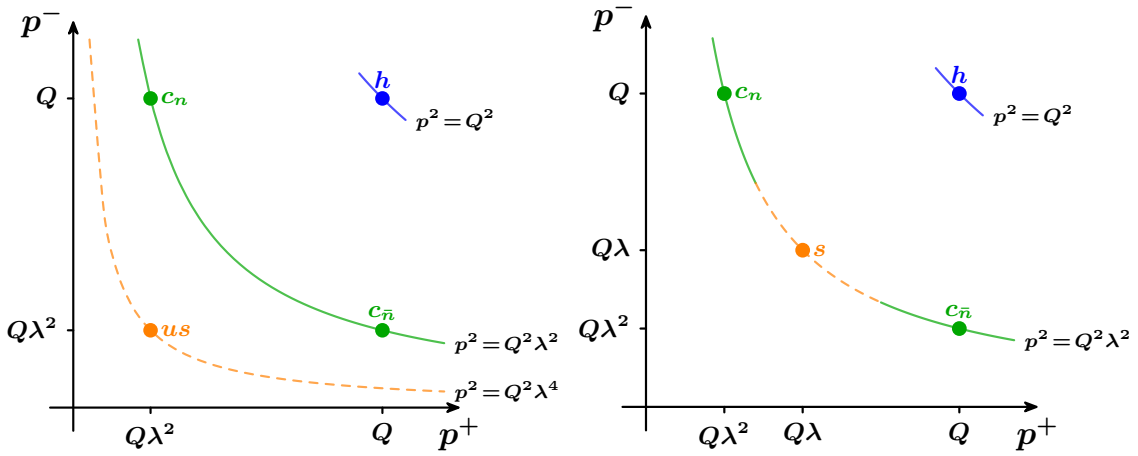

Figure 2.4: Illustration of the $p^{\pm}$ momentum scaling for the hard (blue), the collinear (green) and the soft/ultrasoft (orange) momentum modes. Left (right) panel corresponds to an SCET_I (SCET_II) setting where dynamical degrees of freedom are the collinear and ultrasoft (soft) modes.

setting [52]. A crucial consequence of this observation is that the distinction between the two modes can no longer happen solely on their invariant mass since, $p_n^2 \sim p_{\bar{n}}^2 \sim p_s^2 \sim Q^2\lambda^2$, but their rapidity, $e^{2y} = p^-/p^+$, is necessary as an additional variable to completely separate them. Furthermore, it should be noted that collinear-soft interactions result into off-shell configurations, and therefore they require special treatment. We come back to that in section 2.3.5.

Before concluding a comment is in line with respect to the *Glauber modes*. These correspond to off-shell soft modes with scaling $p_G \sim Q(\lambda^a, \lambda^b, \lambda)$ where $a + b > 2$. Since their perpendicular component has the same parametric scaling as that of the collinear modes, the Glaubers induce nontrivial cross-talk between collinear modes from different directions prohibiting the soft-collinear factorization[8] and therefore resulting into factorization breaking effects. They are described by the Glauber Lagrangian [53] and their effects will not be considered in this thesis as a proper treatment thereof lies outside of its scope. Note though that for the factorization of transverse momentum distribution in the Drell-Yan process it has been proven that they cancel [35, 40, 54].

According to the previous analysis, we saw that depending on the resolution variable and along with the collinear modes, two type of homogeneous modes can emerge: *ultrasofts* (SCET_I) and *softs* (SCET_II). In the following sections and for definiteness, we restrict our discussions to a single quark flavor and to one collinear direction, the n^μ. All derivations apply equally well for the $\bar{n}$-direction or any direction n_i^μ around which we wish to describe (ultra)soft and collinear fluctuations while the rest of the quark flavors can be trivially reinstated at the very end. Furthermore, we consider only ultrasoft modes (i.e. an SCET_I

[8] Soft-collinear factorization refers to the process of eliminating all soft-collinear interactions at LP SCET Lagrangian via field redefinitions. It is presented and discussed in section 2.3.3.

setting) but we come back to the treatment of soft modes and how they can be properly incorporated in SCET in section 2.3.5.

Degrees of freedom in SCET$_\mathrm{I}$. The relevant degrees of freedom (d.o.f.) in SCET$_\mathrm{I}$ are massless quarks and gluons whose momenta have either n-collinear $\sim (1, \lambda^2, \lambda)$ or ultrasoft scaling $\sim (\lambda^2, \lambda^2, \lambda^2)$.[9] Since we will be eventually expanding $\mathcal{L}_{\mathrm{QCD}}$ about the soft and collinear limit, the analysis with respect to the power counting parameter λ will proven to be crucial in determining the relevance of different operators. To this end, in this paragraph we determine the scaling of collinear quarks $\hat{\xi}_n$ and gluons $\hat{A}_n^\mu \equiv \hat{A}_n^{a\,\mu} T^a$, as well as that of ultrasoft quarks ψ_{us} and gluons $A_{us}^\mu \equiv A_{us}^{a\,\mu} T^a$.

We start by considering the LP term from the expansion of the QCD propagator in the n-collinear limit

$$\frac{\mathrm{i}\not{p}}{p^2 + \mathrm{i}\epsilon} \xrightarrow{p \to p_n} \frac{\mathrm{i}\not{n}/2}{p^+ + \frac{p_\perp^2}{p^-} + \mathrm{i}\epsilon\,\mathrm{sgn}\,p^-} = \int \mathrm{d}^4x\, e^{\mathrm{i}k\cdot x}\, \langle 0|\mathrm{T}[\bar{\hat{\xi}}_n(x)\hat{\xi}_n(0)]|0\rangle\,, \tag{2.67}$$

where the equality states that the LP propagator is given by the time-ordered product of two collinear quark fields. From power counting analysis, the expanded propagator scales $\sim \lambda^{-2}$, whereas on the RHS of the equality the measure scales $\mathrm{d}^4x \sim \lambda^{-4}$. This implies that

$$\hat{\xi}_n \sim \lambda\,. \tag{2.68}$$

Notice that the scaling of the collinear quark is *not* the same as its mass dimension which are still those of a fermion field $[\hat{\xi}_n] = 3/2$.

Working along the same lines by analyzing the n-collinear limit of the gluon propagator, we find for $\hat{A}_n^\mu$,

$$\hat{A}_n^\mu \sim (1, \lambda^2, \lambda)\,. \tag{2.69}$$

Notice that it scales exactly like the n-collinear momenta. This comes as no surprise since gauge invariance dictates that ∂^μ and A^μ will always appear together, thus, if ∂^μ has collinear scaling so must the n-collinear limit of A^μ.

Now turning to the ultrasoft fields, the scaling of ψ_{us} can be determined as before by working out the ultrasoft limit of the quark propagator. On the other hand, for A_{us}^μ we can exploit the previous argument on gauge invariance and immediately infer that the scaling of A_{us}^μ must match that of the derivative operator $\partial^\mu \sim (\lambda^2, \lambda^2, \lambda^2)$ which leads to,

$$\psi_{us} \sim \lambda^3\,, \qquad A_{us}^\mu \sim (\lambda^2, \lambda^2, \lambda^2)\,. \tag{2.70}$$

[9] Whereas in the previous paragraph we already saw some examples where λ had an explicit definition, in what follows we will not be giving any, but only assume that $\lambda \ll 1$. Its precise definition is irrelevant as it only serves the purpose of determining the relative scaling of momenta, fields, operators, etc. Furthermore, in the rest of the thesis and for brevity, we drop the overall Q in the scaling relations as it can be always be reintroduced by dimensional analysis.

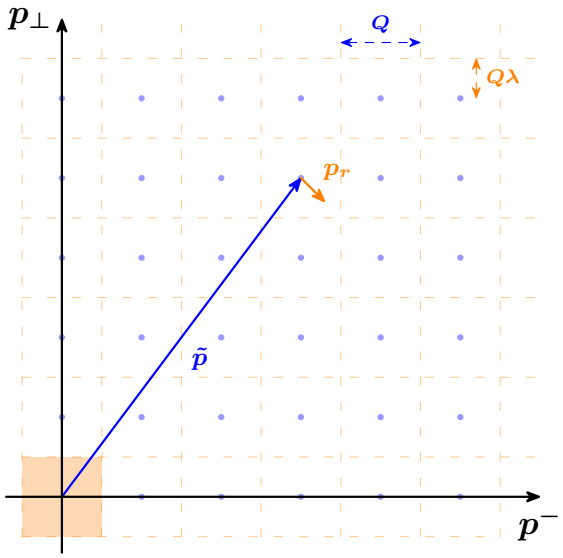

Figure 2.5: Illustration of the collinear momentum decomposition $p^\mu = \tilde{p}^\mu + p_r^\mu$. The label component $\tilde{p}^\mu \sim (1, 0, \lambda)$ is understood to take discrete values at each grid point (blue dots), whereas the residual component $p_r^\mu \sim (\lambda^2, \lambda^2, \lambda^2)$ takes continuous values which are restricted by the surrounding orange boxes. The orange box at the origin of the axes corresponds to the purely residual zero-bin $\tilde{p} = 0$.

2.3.2 Symmetries of SCET

Label and residual momenta. Given the different scaling of the momenta between collinear and ultrasoft modes, it will proven to be beneficial if we provide with a transparent way for their distinction. To achieve this, we define the separation of the collinear momenta into *label* $\tilde{p}^\mu$ and *residual* p_r^μ components

$$p^\mu = \tilde{p}^\mu + p_r^\mu \,, \tag{2.71}$$

each scaling as

$$\tilde{p}^\mu \sim Q(1, 0, \lambda) \,, \qquad p_r^\mu \sim Q(\lambda^2, \lambda^2, \lambda^2) \,. \tag{2.72}$$

Figure 2.5 provides a convenient way to visualize such decomposition, where the label components of p^μ are shown in the x- and y-axis. The label component, $\tilde{p}^\mu$, is considered to be discretized with each value corresponding to a grid point (blue dots), whereas the residual momenta, p_r^μ, are considered to be continuous and take values within the surrounding boxes (orange dashed). The distances between grid points are considered to be large such that no addition of residual momenta can change a label value by moving it from one box and into the neighboring. Even though figure 2.5 might be deceptive as it captures the momentum decomposition into two continuous spaces $(\tilde{p}^\mu, p_r^\mu) \in \mathbb{R}^3 \times \mathbb{R}^4/\mathcal{I}$, with $\mathcal{I}$ specified by the redundancy of the splitting in eq. (2.71), it proves to be useful in formulating a set of rules for fields and derivatives while exploiting the relative scaling of $\tilde{p}^\mu$ and p_r^μ.

With the decomposition of eq. (2.71) we can write the Fourier Transform (FT) of the particle piece for a collinear quark separately over $\tilde{p}$ and p_r,

$$\hat{\xi}^{+}_{n}(x) = \int \frac{\mathrm{d}^4 p}{(2\pi)^4}\, e^{-\mathrm{i}p\cdot x} \tilde{\hat{\xi}}^{+}_{n}(p) = \sum_{\tilde{p}\neq 0} \int \frac{\mathrm{d}^4 p_r}{(2\pi)^4}\, e^{-\mathrm{i}(\tilde{p}+p_r)\cdot x} \tilde{\hat{\xi}}^{+}_{n,\tilde{p}}(p_r) = \sum_{\tilde{p}\neq 0} e^{-\mathrm{i}\tilde{p}\cdot x} \hat{\xi}^{+}_{n,\tilde{p}}(x)\,, \quad (2.73)$$

where $\tilde{\hat{\xi}}^{+}_{n,\tilde{p}}(p_r)$ is expressed in *both label and residual* momentum space whereas $\hat{\xi}^{+}_{n,\tilde{p}}(x)$ is written in label momentum and residual position space. Note that the sum over $\tilde{p}$ excludes $\tilde{p}=0$ since in this bin the momenta of $\tilde{\hat{\xi}}^{+}_{n}$ cease to be collinear as they acquire a purely residual scaling.[10] To proceed, we introduce the *label momentum operator* $\mathcal{P}^\mu$ [56]

$$\mathcal{P}^\mu \hat{\xi}^{+}_{n,\tilde{p}}(x) = \tilde{p}^\mu \hat{\xi}^{+}_{n,\tilde{p}}(x)\,, \quad (2.74)$$

where its action results in picking the label momenta carried by the field. Since all the previous manipulations go through in exact same way also for the antiparticle piece $\xi^{-}_{n}(x)$, we find it convenient to combine them into a single field $\xi_{n,\tilde{p}}(x) \equiv \hat{\xi}^{+}_{n,\tilde{p}}(x) + \hat{\xi}^{-}_{n,-\tilde{p}}(x)$ where $\xi_{n,\tilde{p}}$ ($\bar{\xi}_{n,\tilde{p}}$) annihilates (creates) a particle for $\bar{n}\cdot\tilde{p} > 0$, whereas $\bar{\xi}_{n,\tilde{p}}$ ($\xi_{n,\tilde{p}}$) annihilates (creates) an anti-particle for $\bar{n}\cdot\tilde{p} < 0$. Same manipulations apply also for the collinear gluon $\hat{A}^\mu_n$ with the same convention as above for the creation and destruction of a gluon.

The above lead to the FT of the collinear fields expressed as

$$\hat{\xi}_n(x) = \sum_{\tilde{p}\neq 0} e^{-\mathrm{i}\tilde{p}\cdot x} \xi_{n,\tilde{p}}(x) \;\equiv e^{-\mathrm{i}\mathcal{P}\cdot x} \xi_n(x)\,, \quad (2.75)$$

$$\hat{A}^\mu_n(x) = \sum_{\tilde{p}\neq 0} e^{-\mathrm{i}\tilde{p}\cdot x} A^\mu_{n,\tilde{p}}(x) \equiv e^{-\mathrm{i}\mathcal{P}\cdot x} A^\mu_n(x)\,, \quad (2.76)$$

where in the last equality we define $\xi_n(x) = \sum_{\tilde{p}\neq 0} \xi_{n,\tilde{p}}(x)$ and similarly for A^μ_n, with their spacetime dependence x being conjugate to residual momenta. Based on the previous manipulations we are lead to the following substitution for the derivative operator acting on collinear fields,

$$\mathrm{i}\partial^\mu \mapsto (\mathcal{P}^\mu + \mathrm{i}\partial^\mu) \quad \text{with} \quad \mathcal{P}^\mu \sim Q(1,0,\lambda)\,, \qquad \mathrm{i}\partial^\mu \sim Q(\lambda^2,\lambda^2,\lambda^2)\,, \quad (2.77)$$

where now the scaling of the derivative operator has become explicit.

Important consequence of eq. (2.71) is the existence of *separate* momentum conservation laws for $\tilde{p}$ and p_r,

$$\int \mathrm{d}^4 x\, e^{\mathrm{i}(p-q)\cdot x} = \int \mathrm{d}^4 x\, e^{\mathrm{i}(\tilde{p}-\tilde{q})\cdot x}\, e^{\mathrm{i}(p_r-q_r)\cdot x} = (2\pi)^4\, \delta_{\tilde{p},\tilde{q}}\, \delta(p_r - q_r)\,. \quad (2.78)$$

Note that this implies a different way of viewing momentum flow in Feynman diagrams involving collinear particles. Since they carry both $(\tilde{p}, p_r)$, collinear-ultrasoft particle interactions will change only their residual component, whereas collinear-collinear particle interactions will change both.

[10] In practical calculations involving collinear loop integrals, a naive result is obtained by including the zero bin ($\tilde{p}=0$) since it allows the recombination of $\tilde{p}+p_r$ back to continuous momenta p^μ and thus the use of dimensional regularization as (the preferred) regulator. To make up for the — otherwise wrongly — included $\tilde{p}=0$ region, a procedure known as *zero bin subtraction* [55] is employed, where the collinear integral expanded in the ultrasoft limit is subtracted from the naive result, thus removing the $\tilde{p}=0$ bin.

Gauge symmetry. Important part of SCET are the set of symmetries that satisfies since they dictate the interactions among the fields and set constraints on operators. In eqs. (2.2) and (2.3) we saw how the QCD fields transform under a generic $\mathrm{SU}(3)_c$ gauge transformation $U(x) = e^{\mathrm{i}\alpha(x)^a T^a}$. Turning to SCET, we must be cautious that such transformations do not take collinear or ultrasoft fields off their mass-shell by injecting them large momenta. This would happen for example if,

$$\mathrm{i}\partial^\mu \alpha^a(x) \sim Q(1,1,1)\alpha^a(x)\,. \tag{2.79}$$

Therefore it is mandatory to define the allowed *collinear* and *ultrasoft gauge transformations* [45, 46, 57, 58] as those that have support over momentum regions that keep the momentum scaling of the transformed fields unaltered,

$$\text{collinear} \quad U_n(x): \quad \mathrm{i}\partial^\mu U_n(x) \sim (1,\lambda^2,\lambda)U_n(x)\,, \tag{2.80}$$

$$\text{ultrasoft} \quad U_{us}(x): \quad \mathrm{i}\partial^\mu U_{us}(x) \sim (\lambda^2,\lambda^2,\lambda^2)U_{us}(x)\,. \tag{2.81}$$

The action of $U_n(x)$ on any of the collinear fields with definite label momenta is written as a convolution, e.g. $\xi_{n,\tilde{p}}(x) \mapsto (\hat{U}_n)_{\tilde{p},\tilde{q}}\,\xi_{n,\tilde{q}}(x)$, where $(\hat{U}_n)_{\tilde{p},\tilde{q}} \equiv (U_n)_{\tilde{p}-\tilde{q}}(x)$ is understood to be in label-momentum residual-position space with an implicit summation over repeated indices. Since the label momenta (conceptually) are considered to be discrete-valued, we may regard $(\hat{U}_n)_{\tilde{p},\tilde{q}}$ as a matrix in label momentum space. Based on this definition we fix the boundary condition

$$U_n(n\cdot x = -\infty) = 1 \qquad \Rightarrow \qquad (\hat{U}_n)_{\tilde{p},0} = \delta_{\tilde{p},0}\,, \tag{2.82}$$

which captures the statement that in the zero-bin ($\tilde{q} = 0$) the collinear fields do not transform under collinear gauge transformations since their momenta have ultrasoft scaling and they would result into an off-shell configuration.

The *collinear gauge transformations* for both quark and gluon fields read [45, 46, 57, 58]

$$\xi_{n,\tilde{p}}(x) \mapsto (\hat{U}_n)_{\tilde{p},\tilde{q}}(x)\,\xi_{n,\tilde{q}}(x)\,, \tag{2.83}$$

$$A^\mu_{n,\tilde{p}}(x) \mapsto (\hat{U}_n)_{\tilde{p},\tilde{q}}(x)\left(A^\mu_{n,\tilde{q}-\tilde{k}}(x) + \delta_{\tilde{q},\tilde{k}}\frac{1}{g}\mathrm{i}\mathcal{D}^\mu_{us}\right)(\hat{U}^\dagger_n)_{\tilde{k}}(x)\,, \tag{2.84}$$

$$\psi_{us}(x) \mapsto \psi_{us}(x)\,, \tag{2.85}$$

$$A^\mu_{us}(x) \mapsto A^\mu_{us}(x)\,. \tag{2.86}$$

Notice in eq. (2.84) the appearance of[11] $\mathrm{i}\mathcal{D}^\mu_{us} = \mathcal{P}^\mu + \mathrm{i}n\cdot\partial + g\frac{\bar{n}^\mu}{2}n\cdot A_{us}$ which is covariant under ultrasoft transformations. This can be understood by realizing that the rapid variation of A^μ_n results into seeing A^μ_{us} as classical background field, thus allowing to consider A^μ_n as a quantum field in a background gauge.

[11] The derivative has been expanded appropriately in the n-collinear limit and the appearance of $n\cdot A_{us}$ stems from power counting arguments since only $n\cdot A_{us} \sim n\cdot A_n \sim \lambda^2$.

The *ultrasoft gauge transformations* of the fields read [45, 46, 57, 58]

$$\xi_{n,\tilde{p}}(x) \mapsto U_{us}(x)\xi_{n,\tilde{p}}(x)\,, \tag{2.87}$$

$$A^{\mu}_{n,\tilde{p}}(x) \mapsto U_{us}(x)A^{\mu}_{n,\tilde{p}}U^{\dagger}_{us}(x)\,, \tag{2.88}$$

$$\psi_{us}(x) \mapsto U_{us}(x)\psi_{us}(x)\,, \tag{2.89}$$

$$A^{\mu}_{us}(x) \mapsto U_{us}(x)\left(A^{\mu}_{us}(x) + \frac{1}{g}\mathrm{i}\partial^{\mu}\right)U^{\dagger}_{us}(x)\,. \tag{2.90}$$

where we see in eqs. (2.87) and (2.88) that ξ_n, A^{μ}_n transform as quantum fields under a background gauge transformation in the appropriate representation [36]. Notice that $U_{us}(x)$ transformations do not change the label momenta of the collinear fields. This implies that for the spacetime components conjugate to label momenta, $U_{us}(x)$ transformations are similar to a global color rotation, whereas for those conjugate to residual momenta they are local and heralds interactions between ξ_n, A^{μ}_n and $n \cdot A_{us}$. As a final comment we note that since two different gauge transformations were introduced, it is expected that collinear and ultrasoft fields will have *different* gauge fixing terms.

Reparametrization invariance. The description of a collinear field inevitably involves the choice of a reference vector. It is therefore expected that upon formulating SCET, the Lorentz symmetry of the underlying theory is broken by specifying the collinear direction n^{μ}. So far in our derivations we have been working for concreteness with the lightcone vectors in eq. (2.54), but any choice that satisfies eq. (2.51) is equally valid. This is reflected by the existence of a set of transformations that relate different choices for n^{μ} and $\bar{n}^{\mu}$. These transformations correspond to an invariance of SCET that it is realized at each order in the power counting parameter λ and it is referred to as *reparametrization invariance* (RPI) [59],

I	**II**	**III**
$n^{\mu} \mapsto n^{\mu} + \Delta^{\mu}_{\perp}$	$n^{\mu} \mapsto n^{\mu}$	$n^{\mu} \mapsto e^{\alpha} n^{\mu}$
$\bar{n}^{\mu} \mapsto \bar{n}^{\mu}$	$\bar{n}^{\mu} \mapsto \bar{n}^{\mu} + \epsilon^{\mu}_{\perp}$	$\bar{n}^{\mu} \mapsto e^{-\alpha} \bar{n}^{\mu}$
$\Delta^{\mu}_{\perp} \sim \lambda$	$\epsilon^{\mu}_{\perp} \sim \lambda^0$	$\alpha \sim \lambda^0$

Each transformation acts solely on n^{μ} and $\bar{n}^{\mu}$ changing them by an amount such that the collinear momentum scaling is preserved, a constraint that fixes uniquely the maximum scaling of the parameters $\Delta^{\mu}_{\perp}, \epsilon^{\mu}_{\perp}$ and α. RPI-I captures that the physical direction n^{μ} is allowed to be boosted and rotated by $\sim \mathcal{O}(\lambda)$ without changing the physics, whereas $\bar{n}^{\mu}$ under RPI-II may have $\sim \mathcal{O}(1)$ change without any effect, reflecting its auxiliary nature. Invariance under RPI-III has the most interesting consequences since it imposes that n^{μ} and $\bar{n}^{\mu}$ should always appear in the following forms

$$(n \cdot a)(\bar{n} \cdot b)\,, \qquad \frac{n \cdot a}{n \cdot b}\,, \qquad \frac{\bar{n} \cdot a}{\bar{n} \cdot b}\,, \tag{2.91}$$

where a^μ, b^μ are arbitrary four-vectors.

In addition, part of our manipulations involved in eq. (2.71) the separation of collinear momenta into a label and a residual piece. In principle this corresponds to an arbitrary splitting since we can always move small, residual momenta $p_\epsilon^\mu \sim \lambda^2$ between $\tilde{p}^\mu$ and p_r^μ without changing their scaling,

$$p^\mu = \underbrace{(\tilde{p}^\mu + p_\epsilon^\mu)}_{\sim(1,0,\lambda)} + \underbrace{(p_r^\mu - p_\epsilon^\mu)}_{\sim(\lambda^2,\lambda^2,\lambda^2)} . \tag{2.92}$$

This invariance implies that the differential operators $\mathcal{P}^\mu$ and $\mathrm{i}\partial^\mu$ should be always grouped together as $\mathcal{P}^\mu + \mathrm{i}\partial^\mu$ [59].

As a closing and crucial remark, we note that RPI-II and RPI-III relate LP with power suppressed operators as well as those that appear at the same order in λ, whereas RPI-I and the invariance in eq. (2.92) connect only operators at different orders in λ. These transformations, together with collinear and ultrasoft gauge invariance place constraints or rule out operators and lead to the unique determination of the LP $\mathrm{SCET_I}$ Lagrangian [57].

2.3.3 $\mathrm{SCET_I}$

In this section we discuss the derivation of the LP $\mathrm{SCET_I}$ Lagrangian which includes terms for the collinear and ultrasoft quarks and gluons,

$$\mathcal{L}^{(0)}_{\mathrm{SCET_I}} = \sum_{n_i} \Big(\mathcal{L}^{(0)}_{n_i\xi} + \mathcal{L}^{(0)}_{n_i g} \Big) + \mathcal{L}^{(0)}_{us} \,, \tag{2.93}$$

and we consider as part of $\mathcal{L}^{(0)}_{n_i g}$ and $\mathcal{L}^{(0)}_{us}$ the corresponding gauge fixing and ghost Lagrangian terms. In full generality the sum runs over all possible n_i-collinear directions, although as we mentioned, we restrict our derivation to the n-collinear case with the extension to an arbitrary n_i-direction being straightforward. On the way deriving each term in eq. (2.93), we introduce all the relevant ingredients required, including the collinear Wilson line and the factorization of ultrasoft-collinear interactions via field redefinitions.

Collinear quark Lagrangian. Before we dive into the expansion of $\mathcal{L}_{\mathrm{QCD}}$, it is beneficial to understand the scaling of the quark and antiquark spinors in the collinear limit. We start by introducing the projector operators,

$$P_n = \frac{\not{n}\bar{\not{n}}}{4} \,, \qquad P_{\bar{n}} = \frac{\bar{\not{n}}\not{n}}{4} \,, \qquad \text{with} \qquad P_n + P_{\bar{n}} = \mathbf{1}_{4\times 4} \,, \tag{2.94}$$

where their action on the QCD quark fields defines the $\hat{\xi}_n$ and $\varphi_{\bar{n}}$ fields

$$\hat{\xi}_n(x) = P_n \psi(x) \,, \qquad \varphi_{\bar{n}}(x) = P_{\bar{n}} \psi(x) \,. \tag{2.95}$$

Inspecting the effect of the projectors on the scaling of the unexpanded quark spinor $u(p)$ we get,

$$u_n(p) = P_n u(p) = \frac{1}{2\sqrt{p^0}} \begin{pmatrix} \big[p^- + \mathrm{i}(\vec{p_T} \times \vec{\sigma}) \cdot \hat{z}\big]\mathcal{U} \\ \sigma_3 \big[p^- + \mathrm{i}(\vec{p_T} \times \vec{\sigma}) \cdot \hat{z}\big]\,\mathcal{U} \end{pmatrix} , \tag{2.96}$$

$$u_{\bar{n}}(p) = P_{\bar{n}} u(p) = \frac{1}{2\sqrt{p^0}} \begin{pmatrix} \big[p^+ - \mathrm{i}(\vec{p_T} \times \vec{\sigma}) \cdot \hat{z}\big]\mathcal{U} \\ \sigma_3 \big[p^+ - \mathrm{i}(\vec{p_T} \times \vec{\sigma}) \cdot \hat{z}\big]\,\mathcal{U} \end{pmatrix} , \tag{2.97}$$

where the appearance of $p^- \sim \lambda^0$ in $u_n(p)$ compared to $p_T \sim \lambda$ in $u_{\bar{n}}(p)$ implies that the latter is suppressed in the n-collinear limit. One can show that similar relations hold for the antiquark spinors $v(p)$, with $v_n(p) \sim \lambda^0$ whereas $v_{\bar{n}}(p)$ is suppressed by at least one power of λ. Therefore, in the n-collinear limit the relevant degrees of freedom are quarks and antiquarks of *both spins*.

Now starting from the (massless) quark term of $\mathcal{L}_{\mathrm{QCD}}$ in eq. (2.15), we express it in terms of the $\hat{\xi}_n, \varphi_{\bar{n}}$ fields

$$\begin{aligned} \mathcal{L} = \bar{\psi} \mathrm{i}\not{D} \psi &= (\bar{\hat{\xi}}_n + \bar{\varphi}_{\bar{n}}) \bigg(\frac{\not{n}}{2} \mathrm{i}\bar{n} \cdot D + \frac{\not{\bar{n}}}{2} \mathrm{i}n \cdot D + \mathrm{i}\not{D}_\perp \bigg) (\hat{\xi}_n + \varphi_{\bar{n}}) \\ &= \bar{\hat{\xi}}_n \frac{\not{\bar{n}}}{2} \mathrm{i}n \cdot D \hat{\xi}_n + \bar{\varphi}_{\bar{n}} \frac{\not{n}}{2} \mathrm{i}\bar{n} \cdot D \varphi_{\bar{n}} + \bar{\varphi}_{\bar{n}} \mathrm{i}\not{D}_\perp \hat{\xi}_n + \bar{\hat{\xi}}_n \mathrm{i}\not{D}_\perp \varphi_{\bar{n}} \,. \end{aligned} \tag{2.98}$$

To get to the second line we make use of spinor identities such as $\not{n}\hat{\xi}_n = \not{\bar{n}}\varphi_{\bar{n}} = 0$ and $\bar{\hat{\xi}}_n P_n = \bar{\varphi}_{\bar{n}} P_{\bar{n}} = 0$ that result from the projector defining properties in eq. (2.94). The field $\varphi_{\bar{n}}$ carries $u_{\bar{n}}, v_{\bar{n}}$ and as we saw it will not be contributing at LP, so it can be integrated out by shifting $\varphi_{\bar{n}}$ and completing the square in eq. (2.98),

$$\begin{aligned} &\varphi_{\bar{n}} \mapsto \varphi_{\bar{n}} - \frac{\not{\bar{n}}}{2} \frac{1}{\mathrm{i}\bar{n} \cdot D} \mathrm{i}\not{D}_\perp \hat{\xi}_n \,, \\ &\mathcal{L} \mapsto \bar{\hat{\xi}}_n \bigg(\mathrm{i}n \cdot D + \mathrm{i}\not{D}_\perp \frac{1}{\mathrm{i}\bar{n} \cdot D} \mathrm{i}\not{D}_\perp \bigg) \frac{\not{\bar{n}}}{2} \hat{\xi}_n + \bar{\varphi}_{\bar{n}} \frac{\not{n}}{2} \mathrm{i}\bar{n} \cdot D \varphi_{\bar{n}} \,. \end{aligned} \tag{2.99}$$

Since $\varphi_{\bar{n}}$ is a Grassmann field, integrating it out yields the determinant $\det\big(\frac{\not{n}}{2}\mathrm{i}\bar{n} \cdot D\big)$ which at first sight appears to be gauge field dependent. The easiest way to see that it will not be contributing, is realizing its independence under gauge transformations and that in lightcone gauge $\bar{n} \cdot A = 0$. This implies that the determinant is independent of $\bar{n} \cdot A$ in any gauge and results to an overall trivial factor [60].[12] The Lagrangian for the $\hat{\xi}_n$ field then reads

$$\mathcal{L} = \bar{\hat{\xi}}_n \bigg(\mathrm{i}n \cdot D + \mathrm{i}\not{D}_\perp \frac{1}{\mathrm{i}\bar{n} \cdot D} \mathrm{i}\not{D}_\perp \bigg) \frac{\not{\bar{n}}}{2} \hat{\xi}_n \,. \tag{2.100}$$

[12] Equivalently, one can consider closed loop Feynman diagrams of $\varphi_{\bar{n}}$ where only $\bar{n} \cdot A$ fields appear as external legs. In these, all fermion propagators have the same $+\mathrm{i}\epsilon$ prescription and thus lie at the same side of the complex plane, allowing to close the integration contour on the opposite side and pick none of the poles.

Note that we have not yet expanded in the strict n-collinear limit since the covariant derivatives still contain the *full* gauge field A^μ as well as power suppressed terms from the action of ∂^μ on the fields. We start by disentangling the collinear and ultrasoft scaling of A^μ by expanding it as

$$A^\mu = \hat{A}_n^\mu + A_{us}^\mu + \dots \,, \tag{2.101}$$

where we drop any power suppressed terms that are irrelevant for the LP Lagrangian. Note that eq. (2.101) is on par with the picture presented in section 2.3.1, where the $\hat{A}_n^\mu$ is considered as a quantum field and A_{us}^μ is the corresponding classical background field. To separate momentum contributions of different scaling, we perform the label-residual decomposition which amounts to the replacement of $\mathrm{i}\partial^\mu \mapsto \mathcal{P}^\mu + \mathrm{i}\partial^\mu$ and the substitutions $\hat{\xi}_n \mapsto \xi_n$, $\hat{A}_n^\mu \mapsto A_n^\mu$ as defined in eqs. (2.75) and (2.76). The last step involves the expansion of the covariant derivatives in eq. (2.100) using the scaling of the fields in eqs. (2.69) and (2.70) and of the differential operators in eq. (2.77),

$$\mathrm{i}n\cdot D = \mathrm{i}n\cdot\partial + gn\cdot A_n + gn\cdot A_{us} + \mathcal{O}(\lambda^3)\,, \tag{2.102}$$

$$\mathrm{i}\bar{n}\cdot D = \bar{n}\cdot\mathcal{P} + g\bar{n}\cdot A_n \qquad\qquad + \mathcal{O}(\lambda^2)\,, \tag{2.103}$$

$$\mathrm{i}D_\perp^\mu = \mathcal{P}_\perp^\mu \quad + gA_{n\perp}^\mu \qquad\qquad + \mathcal{O}(\lambda^2)\,. \tag{2.104}$$

Taking into account all of the above leads to the LP Lagrangian for the n-collinear quark field,

$$\mathcal{L}_{n\xi}^{(0)} = e^{-\mathrm{i}\mathcal{P}\cdot x}\bar{\xi}_n\left(\mathrm{i}n\cdot D + \mathrm{i}\not{D}_{n\perp}\frac{1}{\mathrm{i}\bar{n}\cdot D_n}\mathrm{i}\not{D}_{n\perp}\right)\frac{\not{\bar{n}}}{2}\xi_n\,. \tag{2.105}$$

where we defined

$$\mathrm{i}\bar{n}\cdot D_n \equiv \bar{n}\cdot\mathcal{P} + g\bar{n}\cdot A_n\,, \qquad \mathrm{i}D_{n\perp}^\mu \equiv \mathcal{P}_\perp^\mu + gA_{n\perp}^\mu\,. \tag{2.106}$$

To proceed and bring eq. (2.105) to its final form we have to discuss first two important emerging quantities in SCET, the collinear and ultrasoft Wilson lines, which are the topics of the next two paragraphs.

Collinear Wilson line. In eq. (2.69) we saw that $\bar{n}\cdot A_n \sim \mathcal{O}(1)$, a result that went rather unappreciated. In practical terms, this implies that we can have an arbitrary number of $\bar{n}\cdot A_n$ gluon insertions in an operator, at any order in the power expansion, without inducing any λ suppression to it. The implications of this observation are far reaching and already affect eq. (2.105): were we to expand the $1/(\mathrm{i}\bar{n}\cdot D_n)$ with respect to $g\bar{n}\cdot A_n$, we would find that already at LP an infinite number of such gluon insertions are contributing and thus no closed form expression of the Lagrangian would be possible to be formulated [46]. Therefore, it is convenient to capture their effect in terms of the *collinear Wilson line* [58],

$$\begin{aligned} W_n \equiv W_n(x) &= \mathrm{P}\exp\left[\mathrm{i}g\int_{-\infty}^0 \mathrm{d}s\,\bar{n}\cdot A_n(x+\bar{n}s)\right] \\ &= \sum_{\text{perm}} \exp\left[\frac{-g}{\bar{n}\cdot\mathcal{P}}\bar{n}\cdot A_n(x)\right], \end{aligned} \tag{2.107}$$

where 'P' denotes the necessary path ordering for non-abelian fields. In the second line we performed the FT with respect to the label momenta, such that now the x spacetime dependence that $\bar{n}\cdot A_n$ carries is only with respect to residual momenta.

Under a gauge transformation a (full theory) QCD Wilson line $W(x,y)$ transforms as $W(x,y) \overset{U}{\mapsto} U(x)W(x,y)U^\dagger(y)$ [36], which implies the following collinear and ultrasoft gauge transformations for W_n,

$$\text{collinear}: \qquad W_n(x) \overset{\hat{U}_n}{\longmapsto} \hat{U}_n W_n(x) \tag{2.108}$$

$$\text{ultrasoft}: \qquad W_n(x) \overset{U_{us}}{\longmapsto} U_{us}(x)W_n(x)U_{us}^\dagger(x)\,. \tag{2.109}$$

Note that under $\hat{U}_n$ transformations, $W_n(x)$ transforms only with respect to the upper integration bound since for the lower $U_n^\dagger(n\cdot x=-\infty)=1$ which corresponds to the position space analog of the boundary condition that we imposed in eq. (2.82). On the other hand, ultrasoft transformations amount to local transformations since $W_n(x)$ is a local operator in the conjugate space of residual momenta as all collinear fields $\bar{n}\cdot A_n$ are localized at x.

Expressed in label momentum space, the collinear Wilson line satisfies the equations

$$W_n^\dagger W_n = 1\,, \qquad \mathrm{i}\bar{n}\cdot D_n W_n = 0\,, \tag{2.110}$$

with the covariant derivative defined in eq. (2.106). From these it is straightforward to show that

$$f(\mathrm{i}\bar{n}\cdot D_n) = W_n f(\bar{n}\cdot\mathcal{P})W_n^\dagger\,, \tag{2.111}$$

for any function f. In order to fully exploit eq. (2.111), we observe that collinear gauge invariance imposes that $\bar{n}\cdot\mathcal{P}$ and $\bar{n}\cdot A_n$ appear always together, something that allows the effective substitution of $\bar{n}\cdot A_n \leftrightarrow \bar{n}\cdot\mathcal{P}$ via

$$\frac{1}{\mathrm{i}\bar{n}\cdot D_n} = W_n \frac{1}{\bar{n}\cdot\mathcal{P}} W_n^\dagger\,. \tag{2.112}$$

Ultrasoft Wilson line. Inspecting the field content of the collinear quark Lagrangian in eq. (2.105),

$$\mathcal{L}_{n\xi}^{(0)} \equiv \mathcal{L}_{n\xi}^{(0)}\big(\xi_n, A_n^\mu, n\cdot A_{us}\big)\,, \tag{2.113}$$

we see interaction terms between ξ_n and all components of the collinear gluon field A_n^μ as well as with $n\cdot A_{us}$ ultrasoft gauge field, both of which are dictated by gauge invariance and power counting. The attentive reader may have noticed that using eq. (2.112) we can swap in eq. (2.105) the $\mathrm{i}\bar{n}\cdot D_n$ for ordinary derivatives at the expense of introducing (some) Wilson lines. Having this in mind and aiming for a factorization between modes of different scaling, it is natural to ask whether the same can be achieved for the ultrasoft gauge field $n\cdot A_{us}$ appearing in $\mathcal{L}_{n\xi}^{(0)}$? While the answer is positive, what is more surprising is that it can be shown that *all* collinear-ultrasoft interactions can be completely eliminated from the LP collinear Lagrangian [58]. To show this, we make the following two considerations.

First, we introduce the *ultrasoft Wilson line* which in the fundamental representation reads,

$$Y_n \equiv Y_n(x) = \mathrm{P}\exp\left[\mathrm{i}g\int_{-\infty}^{0}\mathrm{d}s\, n\cdot A^{\mu}_{us}(x+ns)\right], \tag{2.114}$$

and it is understood that the corresponding ultrasoft Wilson line in the adjoint representation $\mathcal{Y}_n(x)$ is obtained from eq. (2.114) upon $T^a \mapsto -\mathrm{i}f^{abc}$. Now, Y_n satisfies the usual defining equation of Wilson lines,

$$Y_n^{\dagger}Y_n = 1\,, \qquad \mathrm{i}n\cdot D_{us}Y_n = 0\,, \tag{2.115}$$

where $\mathrm{i}n\cdot D_{us} \equiv \mathrm{i}n\cdot\partial + gn\cdot A_{us}$. Same as we did for W_n, using eq. (2.115) it is easy to show that

$$Y_n^{\dagger}\mathrm{i}n\cdot D_{us}Y_n = \mathrm{i}n\cdot\partial\,, \tag{2.116}$$

which achieves the first goal, namely to exchange covariant derivatives $\mathrm{i}n\cdot D_{us}$ for Wilson lines Y_n and ordinary partial derivatives $\mathrm{i}n\cdot\partial$.

Secondly, we employ a *field redefinition* in order to simplify the collinear Lagrangian by using the equations of motion (EoM) and replace redundant terms that give identical contributions to the S matrix elements [61]. Specifically for SCET, these redefinitions go by the name *Bauer-Pirjol-Stewart (BPS) field redefinitions* [58] which for the collinear quark, gluon and ghost fields amount to

$$\xi_{n,\tilde{p}}(x) = Y_n\,\xi^{(0)}_{n,\tilde{p}}(x)\,, \qquad A^{\mu}_{n,\tilde{p}}(x) = Y_n\,A^{\mu(0)}_{n,\tilde{p}}(x)\,Y_n^{\dagger}\,, \qquad c_{n,\tilde{p}}(x) = Y_n c^{(0)}_{n,\tilde{p}}(x)Y_n^{\dagger}\,. \tag{2.117}$$

Here, the superscript '(0)' is used to denote the BPS-transformed fields and we introduced the ghost fields $c_{n,\tilde{p}}$ which are relevant in any general covariant gauge. The transformation of $A^{\mu}_{n,\tilde{p}}$ is according to the adjoint representation and from the definition of W_n in eq. (2.107), together with the fact that the label momentum operator $\mathcal{P}^{\mu}$ commutes[13] with Y_n, the collinear Wilson line also transforms the same,

$$W_n = Y_n\,W_n^{(0)}\,Y_n^{\dagger}\,. \tag{2.118}$$

Collinear quark Lagrangian (continued). At this point we are in position bring $\mathcal{L}^{(0)}_{n\xi}$ to its final form by using the results of the two previous paragraphs. We start by employing eq. (2.112) in eq. (2.105) to replace any occurrence of $\mathrm{i}\bar{n}\cdot D_n$,

$$\mathcal{L}^{(0)}_{n\xi} = e^{-\mathrm{i}\mathcal{P}\cdot x}\bar{\xi}_n\left(\mathrm{i}n\cdot D + \mathrm{i}\not{D}_{n\perp}W_n\frac{1}{\bar{n}\cdot\mathcal{P}}W_n^{\dagger}\mathrm{i}\not{D}_{n\perp}\right)\frac{\not{\bar{n}}}{2}\xi_n\,, \tag{2.119}$$

[13]The ultrasoft Wilson line is composed out of ultrasoft fields A^{μ}_{us} which carry only residual momenta and therefore $\mathcal{P}^{\mu}$ does not act on them.

where the entire effect of the $\bar{n}\cdot A_n \sim \mathcal{O}(1)$ fields is now encoded in the collinear Wilson lines W_n. Next, using eq. (2.116) and performing the BPS field redefinitions, eqs. (2.117) and (2.118), we have

$$\begin{aligned}
\mathcal{L}^{(0)}_{n\xi}\Big(\xi_n, A^\mu_n, n\cdot A_{us}\Big) &\xmapsto{\text{BPS}} \mathcal{L}^{(0)}_{n\xi}\Big(\xi^{(0)}_n, A^{\mu(0)}_n, n\cdot A_{us}\Big) = \\
&= e^{-\mathrm{i}\mathcal{P}\cdot x}\bar{\xi}^{(0)}_n\left(Y^\dagger_n \mathrm{i}n\cdot D_{us} Y_n + gn\cdot A^{(0)}_n + \mathrm{i}\not{D}^{(0)}_{n\perp} W^{(0)}_n \frac{1}{\bar{n}\cdot\mathcal{P}} W^{\dagger(0)}_n \mathrm{i}\not{D}^{(0)}_{n\perp}\right)\frac{\not{\bar{n}}}{2}\xi^{(0)}_n \\
&= e^{-\mathrm{i}\mathcal{P}\cdot x}\bar{\xi}^{(0)}_n\left(\mathrm{i}n\cdot\partial + gn\cdot A^{(0)}_n + \mathrm{i}\not{D}^{(0)}_{n\perp} W^{(0)}_n \frac{1}{\bar{n}\cdot\mathcal{P}} W^{\dagger(0)}_n \mathrm{i}\not{D}^{(0)}_{n\perp}\right)\frac{\not{\bar{n}}}{2}\xi^{(0)}_n \qquad (2.120)\\
&\equiv \mathcal{L}^{(0)}_{n\xi}\Big(\xi^{(0)}_n, A^{\mu(0)}_n, 0\Big)\,,
\end{aligned}$$

where $\mathrm{i}\not{D}^{(0)}_{n\perp} = \not{\mathcal{P}}_\perp + g\not{A}^{(0)}_{n\perp}$ denotes the covariant derivative with respect to the BPS-transformed gluon field. Eq. (2.120) is the final form of the n-collinear quark Lagrangian and as it is explicitly shown, the BPS field redefinitions along with eq. (2.116) have allowed for the complete elimination of the $n\cdot A_{us}$ gauge field from $\mathcal{L}^{(0)}_{n\xi}$. This translates to the absence of any collinear-ultrasoft interactions between the fields. It is important to state though that ultrasoft interactions *did not* completely *disappear*; a consistent treatment of the BPS redefinitions requires the redefinition of the fields in any of their occurrences, thus moving collinear-ultrasoft interactions out of the Lagrangian and into operators. This result is quite remarkable as it corresponds to the first instance of *factorization* between fields that capture different modes.

The BPS redefinitions are instrumental in proving factorization theorems and we explicitly employ them in section 3.2 where we show the factorization of the transverse momentum distribution for the process $p_n p_{\bar{n}} \to Z \to \nu_\ell \bar{\nu}_\ell$ in SCET. Finally, we remark that the elimination of ultrasoft modes via BPS field redefinitions is plausible only for the LP SCET Lagrangian $\mathcal{L}^{(0)}_{\text{SCET}_\text{I}}$, since at subleading orders in λ, ultrasoft-collinear interactions do appear in $\mathcal{L}^{(n>0)}_{\text{SCET}_\text{I}}$ in a from that cannot be reproduced entirely from ultrasoft Wilson lines Y_n.

Collinear gluon Lagrangian. Having developed all the tools needed in the previous sections, the construction of the LP collinear gluon Lagrangian $\mathcal{L}^{(0)}_{ng}$ is now straightforward except for one subtle point that needs extra care.

We start from the definition of the QCD field strength tensor in eq. (2.11) and expand the covariant derivative in the n-collinear limit. This was already performed in eqs. (2.102), (2.103), and (2.104) which allows us to isolate the strict LP terms

$$\mathrm{i}D^\mu = \mathrm{i}\mathcal{D}^\mu + \dots\,, \qquad \text{where} \qquad \mathrm{i}\mathcal{D}^\mu = \frac{n^\mu}{2}\mathrm{i}\bar{n}\cdot D_n + \frac{\bar{n}^\mu}{2}\mathrm{i}n\cdot D + D^\mu_{n\perp}\,, \qquad (2.121)$$

and the neglected terms correspond to power suppressed contributions that are irrelevant at LP.

To proceed, we remind the analogy that we made between the collinear A^μ_n and ultrasoft A^μ_{us} fields, namely that we shall consider the former as a quantum field and the latter as

a classical field in a background gauge. This implies that both the gauge fixing and the collinear ghost Lagrangian terms[14] should be *covariant* with respect to A^μ_{us}. Another way to view it, is by recalling that collinear and ultrasoft gauge transformations have support over different momentum scalings and thus the collinear gauge fixing term should only break the invariance of collinear gauge transformations while being completely covariant with respect to the ultrasoft. Given these observations, we replace all partial derivatives appearing in eqs. (2.12) and (2.13) with ultrasoft covariant derivatives, which at LP it amounts to the substitution

$$\mathrm{i}\partial^\mu \mapsto \mathrm{i}\mathcal{D}^\mu_{us} = \mathcal{P}^\mu + \frac{\bar{n}^\mu}{2}\big(\mathrm{i}n\cdot\partial + gn\cdot A_{us}\big)\,, \tag{2.122}$$

where only the $n\cdot A_{us}$ component appears due to power counting. Thus, the LP collinear gluon Lagrangian reads

$$\begin{aligned}\mathcal{L}^{(0)}_{ng} =& e^{-\mathrm{i}\mathcal{P}\cdot x}\frac{1}{2g^2}\,\mathrm{Tr}\left\{([\mathrm{i}\mathcal{D}^\mu,\mathrm{i}\mathcal{D}^\nu])^2\right\} + e^{-\mathrm{i}\mathcal{P}\cdot x}\frac{1}{\tau_n}\,\mathrm{Tr}\left\{([\mathrm{i}\mathcal{D}^{us}_\mu, A^\mu_n])^2\right\}\\ &+ e^{-\mathrm{i}\mathcal{P}\cdot x}\,2\,\mathrm{Tr}\left\{\bar{c}_n\big[\mathrm{i}\mathcal{D}^{us}_\mu,[\mathrm{i}\mathcal{D}^\mu,c_n]\big]\right\}.\end{aligned} \tag{2.123}$$

where τ_n is the gauge fixing parameter for the collinear gluon fields and the traces are understood to be over color indices.

Closing, we mention that although so far we included the ultrasoft gauge field $n\cdot A_{us}$ in the derivation of $\mathcal{L}^{(0)}_{ng}$, resulting into interaction terms between A^μ_n, c^a_n and $n\cdot A_{us}$, it can be shown that all occurrences of $n\cdot A_{us}$ can be completely eliminated from $\mathcal{L}^{(0)}_{ng}$ by employing the BPS field redefintions same way as it happened for the collinear quark Lagrangian $\mathcal{L}^{(0)}_{n\xi}$. This results into the decoupling collinear-ultrasoft interactions from the LP gluon Lagrangian.

Ultrasoft Lagrangian. In eq. (2.70) we derived the scaling for the ultrasoft gluons where we crucially found that $A^\mu_{us}\sim(\lambda^2,\lambda^2,\lambda^2)$, i.e. all of its components have the same scaling. This result, in addition to the ultrasoft momenta being homogeneous and isotropic, $p_{us}\sim(\lambda^2,\lambda^2,\lambda^2)$, imply that the ultrasoft Lagrangian for both quarks and gluons will be a mere copy of $\mathcal{L}_{\mathrm{QCD}}$. One thing that we should be cautious about is that τ_n in eq. (2.123) does not fix the gauge of A^μ_{us} and therefore a *separate* gauge fixing term τ_{us} has to be introduced. This reflects once more the fact that collinear and ultrasoft gauge transformations are different and realized separately. Therefore, the full LP ultrasoft Lagrangian reads,

$$\mathcal{L}^{(0)}_{us} = \bar{\psi}_{us}\mathrm{i}\not{D}_{us}\psi_{us} - \frac{1}{2}\,\mathrm{Tr}\,F^{\mu\nu}_{us}F^{us}_{\mu\nu} + \frac{1}{\tau_{us}}\,\mathrm{Tr}\left\{(\mathrm{i}\partial_\mu A^\mu_{us})^2\right\} + 2\,\mathrm{Tr}\left\{\bar{c}_{us}\mathrm{i}\partial_\mu \mathrm{i}D^\mu_{us}c_{us}\right\}, \tag{2.124}$$

where now we defined the covariant derivative $\mathrm{i}D^\mu_{us} = \mathrm{i}\partial^\mu + gA^\mu_{us}$ and c_{us} are the corresponding ultrasoft ghost fields.

[14] We remind the reader that $\mathcal{L}^{(0)}_{ng}$ is defined to contain both the gauge fixing and the collinear ghost Lagrangian terms.

2.3.4 Hard-collinear factorization and operator building blocks

Our discussion in section 2.3.3 focused only on the dynamical d.o.f. of SCET, namely the collinear and ultrasoft modes. Goal of this section is to describe how modes with momenta $p^\mu \sim Q$, where Q some characteristic hard scale of the physical process, are integrated out and consistently included in SCET.

Wilson coefficients. Not only particular to SCET, but ubiquitous in EFTs is the inclusion of the high-energy effects through a matching procedure between the full theory and the corresponding EFT operators. The necessity for such procedure stems from the observation that EFTs are constructed to capture (certain part of) the IR physics, thus being completely agnostic about the UV region of the underlying theory. It is also understood from the fact that the hard modes are not part of the EFT's propagating d.o.f and therefore the mismatch between full theory and EFT must be properly accounted for via a (matching) coefficient, the so-called *Wilson coefficient*. While in EFTs such as Fermi's theory of EW interactions, the matching procedure has a simple multiplicative form, this is not the case in SCET since operators and Wilson coefficient share the same (hard) scale.

To better illustrate the procedure and discuss some features of the Wilson coefficient which are particular in SCET, we consider the matching for $e^+e^- \to \gamma^* \to 2\,\text{jets}$ [62, 63]. The gauge invariant QCD hadronic current reads,

$$J^\mu_{\text{QCD}} = \bar{\psi}\gamma^\mu\psi\,. \tag{2.125}$$

Turning to the corresponding SCET operator, naively we would think that the current that mediates this process is composed only out of two collinear quark fields, one in each lightcone direction n_1^μ, n_2^μ of the (hard) partons that emerge out of the hard scatter. The naive SCET current then reads [64],

$$J^\mu_{\text{SCET}} = \bar{\xi}_{n_1,\tilde{p}}\gamma^\mu\xi_{n_2,\tilde{q}}\,. \tag{2.126}$$

To see why J^μ_{SCET} in eq. (2.126) is referred to as 'naive', consider its collinear gauge transformation given by eq. (2.83),

$$J^\mu_{\text{SCET}} \overset{\hat{U}_n}{\longmapsto} J^{\mu\prime}_{\text{SCET}} = \bar{\xi}_{n_1,\tilde{p}}\hat{U}^\dagger_{n_1}\gamma^\mu\hat{U}_{n_2}\xi_{n_2,\tilde{q}} \neq J^\mu_{\text{SCET}}\,, \tag{2.127}$$

where we see that the current J^μ_{SCET} is not collinear gauge invariant. To remedy this, we must include as part of the SCET current the collinear Wilson lines W_{n_i}, one for each direction [64]

$$J^\mu_{\text{SCET}} = \bar{\xi}_{n_1,\tilde{p}}W_{n_1}\gamma^\mu W^\dagger_{n_2}\xi_{n_2,\tilde{q}}\,, \tag{2.128}$$

where now the transformation of $W_{n_i} \overset{\hat{U}_{n_i}}{\longmapsto} U_{n_i}W_n$ compensates that of the fields $\bar{\xi}_{n_i}$ (same for $W^\dagger_{n_2}$ and ξ_{n_2}) and ensures collinear gauge invariance of the current in eq. (2.128). Of course and as it should, the current in eq. (2.128) is also invariant under ultrasoft gauge transformations as defined in eqs. (2.87) and (2.109).

Having discussed the form of the SCET current, we would be ready to perform the matching procedure had it not been for a delicate point that we have to consider. The Wilson coefficient in full generality depends on the hard scale of the process, which corresponds to the large label momenta that are *also* carried by the collinear fields. Thus, in place of a multiplicative matching there is instead a *convolution* between the Wilson coefficient and the SCET current in the label momenta. This is best implemented using the label momentum operator $\mathcal{P}^\mu$ [64],

$$\begin{aligned} J^\mu_{\text{QCD}} &= [\bar{\xi}_{n_1,\tilde{p}} W_{n_1}] \gamma^\mu C(\bar{n}_1 \cdot \mathcal{P}^\dagger, \bar{n}_2 \cdot \mathcal{P}) [W^\dagger_{n_2} \xi_{n_2,\tilde{q}}] \\ &= \int \mathrm{d}\omega_1 \mathrm{d}\omega_2 \; C(\omega_1, \omega_2) \; [\bar{\xi}_{n_1,\tilde{p}} W_{n_1} \, \delta(\omega_1 - \bar{n}_1 \cdot \mathcal{P}^\dagger)] \gamma^\mu [\delta(\omega_2 - \bar{n}_2 \cdot \mathcal{P}) \, W^\dagger_{n_2} \xi_{n_2,\tilde{q}}] \\ &\equiv \int \mathrm{d}\omega_1 \mathrm{d}\omega_2 \; C(\omega_1, \omega_2) \, O(\omega_1, \omega_2) \,, \end{aligned} \tag{2.129}$$

where in the first line it is understood that the Wilson coefficient $C(\bar{n}_1 \cdot \mathcal{P}^\dagger, \bar{n}_2 \cdot \mathcal{P})$ acts as an operator by picking the label momenta of collinear gauge invariant products of fields, here grouped in square brackets. In the second line we trade $C(\bar{n}_1 \cdot \mathcal{P}^\dagger, \bar{n}_2 \cdot \mathcal{P})$ for delta functions that act as operators on fields and Wilson lines within the square brackets. This allows us to rewrite the expression as a convolution between a real-valued function $C(\omega_1, \omega_2)$ and a SCET operator $O(\omega_1, \omega_2)$ of definite label momenta ω_1, ω_2. Note that since $\mathcal{P}^\mu$ commutes with the ultrasoft Wilson lines Y_n, we can perform the BPS field redefinitions of eq. (2.117) at any point without affecting the form of the Wilson coefficient. Eq. (2.129) holds a remarkable result as it encodes the factorization of the hard dynamics captured by $C(\omega_1, \omega_2)$, from the ultrasoft and collinear dynamics encoded in the SCET operator $O(\omega_1, \omega_2)$.

Operator building blocks. Taking into consideration the requirement of collinear and ultrasoft gauge invariance that SCET operators must fulfill, we are motivated to define and work with fields that comply with such restrictions. To this end, we introduce the fields [65, 66]

$$\chi_{n,\omega}(x) = \left[\delta(\omega - \bar{n} \cdot \mathcal{P}) W^\dagger_n(x) \xi_n(x)\right] , \tag{2.130}$$

$$\mathcal{B}^\mu_{n\perp,\omega}(x) = \frac{1}{g}\left[\delta(\omega + \bar{n} \cdot \mathcal{P}) W^\dagger_n(x) \mathrm{i} D^\mu_{n\perp} W_n(x)\right] , \tag{2.131}$$

where $\chi_{n,\omega}$ is the corresponding n-collinear gauge invariant quark building block and $\mathcal{B}^\mu_{n\perp,\omega}$ is the analogous one for the gluon. For the latter, its two components can be taken as its physical polarizations. Both fields carry definite continuous label momenta, ω, that are set by the delta functions $\delta(\omega \pm \bar{n} \cdot \mathcal{P})$. Notation-wise, it is understood and used throughout in this thesis, that both the label momentum operator and the derivative operators that appear in square brackets, act only on the fields *inside the square brackets*. It is easy to show that under the BPS field redefinitions ultrasoft interactions can be completely factored

out of eqs. (2.130) and (2.131) and captured by ultrasoft Wilson lines Y_n,

$$\chi_{n,\omega}(x) = Y_n^\dagger(x)\chi^{(0)}_{n,\omega}(x)\,, \tag{2.132}$$

$$\mathcal{B}^\mu_{n\perp,\omega}(x) = Y_n^\dagger(x)\mathcal{B}^{\mu(0)}_{n\perp,\omega}(x)Y_n(x)\,. \tag{2.133}$$

As a final comment, we mention that the operators

$$\chi_{n,\omega}(x)\,, \qquad \mathcal{B}^\mu_{n\perp,\omega}(x)\,, \qquad \mathcal{P}^\mu_\perp\,, \qquad \bar{n}\cdot\mathcal{P}\,, \tag{2.134}$$

form a complete basis, i.e. all other collinear operators can be reduced such that they contain only the *basic building blocks* of eq. (2.134) [66].

2.3.5 $\mathrm{SCET_{II}}$

As we mentioned in section 2.3.1, measurements that restrict the transverse momenta of the contributing modes, e.g. the q_T of a color-singlet probe $(H, Z, W^\pm, \ldots)$ or jet broadening [67], cannot be described by $\mathrm{SCET_I}$. This can understood from the fact that for the ultrasoft modes $p_{\perp us} \sim \lambda^2$ which is parametrically suppressed compared to the corresponding component of the collinear modes $p_{\perp n} \sim \lambda$. Instead, the correct homogeneous modes that contribute to such measurements are the *soft modes*

$$p_s \sim Q(\lambda,\lambda,\lambda)\,, \qquad p_s^2 \sim Q^2\lambda^2\,, \tag{2.135}$$

and the LP Lagrangian $\mathcal{L}_s^{(0)}$ that captures their dynamics is just a copy of the QCD Lagrangian. Thus, $\mathrm{SCET_{II}}$ is the EFT that describes interactions between soft and collinear modes in the presence of a hard interaction.

One of the crucial differences between $\mathrm{SCET_I}$ and $\mathrm{SCET_{II}}$ is that while the scaling of the ultrasoft modes allows for interactions with the collinears, this is not the case when we consider soft-collinear interactions. A simple power counting argument is enough to convince that the resulting momenta of such interaction is that of an off-shell mode,

$$k_n = p_n + p_s \sim Q(1,\lambda,\lambda)\,, \qquad k_n^2 \sim Q^2\lambda\,, \tag{2.136}$$

where we see that the resulting mode's virtuality is no longer that of a collinear $\sim (Q\lambda)^2$. Therefore, in contrast to the ultrasofts that explicitly appear in $\mathcal{L}^{(0)}_{n\xi}$ and $\mathcal{L}^{(0)}_{ng}$ as interaction terms, the softs do not, and since they lead to off-shell configurations they have to be integrated out of SCET. This is achieved via a matching procedure and gives rise to the *soft Wilson line* [58] which in the fundamental representation reads,

$$S_n(x) = \mathrm{P}\exp\left[\mathrm{i}g\int_{-\infty}^0 \mathrm{d}s\; n\cdot A_s(x+ns)\right] \tag{2.137}$$

$$= \sum_{\mathrm{perm}} \exp\left[\frac{-g}{n\cdot\mathcal{P}} n\cdot A_s(x)\right], \tag{2.138}$$

and the corresponding soft Wilson line in the adjoint representation $\mathcal{S}_n(x)$ can be obtained from eq. (2.137) by $T^a \mapsto -\mathrm{i}f^{abc}$.

In ref. [58] it is proven using the auxiliary field method that integrating out off-shell soft-collinear interactions builds up $S_n(x)$ and in ref. [64] a proof is given for the case involving two collinear directions. Another way to understand the necessity for the emergence of $S_n(x)$ is that the SCET currents must also be invariant under soft gauge transformations, something that places stringent restrictions on the way that soft Wilson lines appear in operators. Thus, much like the collinear Wilson line $W_n(x)$ which ensures collinear gauge invariance, $S_n(x)$ should be regarded as a fundamental object in SCET.

In order to construct SCET_{II}, a stepped procedure was proposed in refs. [58, 68], with the subsequent matchings defined as follows:

1. Match from QCD to SCET_{I} with n-collinear modes scaling $\sim Q(1, \lambda, \sqrt{\lambda})$ and ultrasoft modes scaling $\sim Q(\lambda, \lambda, \lambda)$. Note that although the scaling of the ultrasofts is what we call soft modes, the virtuality of the collinears is $p_n^2 \sim Q^2\lambda$ and this effectively corresponds to a SCET_{I} setting.

2. Perform the BPS field redefintion as defined in eq. (2.117). That way the ultrasoft-collinear interactions are completely eliminated in the SCET Lagrangian and moved into the currents in terms of ultrasoft Wilson lines $Y_n(x)$.

3. Lower the virtuality of the collinear modes $\lambda \mapsto \lambda^2$ such that they now scale $p_n \sim Q(1, \lambda^2, \lambda)$, have the correct virtuality $p_n^2 \sim (Q\lambda)^2$, and do not induce a nontrivial Wilson coefficient. Since the scaling of the ultrasoft modes remained the same in the previous step, set $Y_n(x) \mapsto S_n(x)$ to obtain an explicit dependence on soft Wilson lines in the currents.

The second crucial difference between SCET_{I} and SCET_{II} is the emergence of a certain type of divergences that appear only in the latter and they cannot be treated by dimensional regularization. These divergences go by the name of *rapidity divergences* [69–72]. Their nature is neither UV nor IR as they don't exist in the underlying full theory and they result as a product of the power expansion of QCD in λ. Specifically, their appearance can be traced in that soft and collinear modes share the same virtuality $p_s^2 \sim p_n^2 \sim (Q\lambda)^2$ while their rapidities are distinct, $p_s^-/p_s^+ \sim \mathcal{O}(1)$ whereas $p_n^-/p_n^+ \sim \mathcal{O}(\lambda^{-2})$. This can be seen in the right panel of figure 2.4. The intuitive picture is that since soft modes (orange) live on the same mass hyperbola as the collinear modes (green), a longitudinal boost can slide them towards either collinear direction, thus obtaining a collinear scaling. Analogously, the same boost applied to collinear modes can turn them to soft. This implies that such divergences will manifest themselves in both soft and collinear (factorized) matrix elements in SCET, but cancel when both sectors are combined. In order to address this issue, the limits between soft and collinear modes have to be clearly separated, that is to say, invariance under boosts has to be broken.

Throughout the literature various rapidity regulators have been proposed and employed [73–76] and one of them is the η regulator [69, 70] which is very much in spirit of dimensional regularization. In that, boost invariance is explicitly broken by regulating

the lightcone and longitudinal momenta upon introducing the following modifications in the collinear and soft Wilson lines of eqs. (2.107) and (2.138) [69, 70]

$$W_n(x) = \sum_{\text{perm}} \exp\left[-gw^2 \frac{|\bar{n}\cdot\mathcal{P}_g|^{-\eta}}{\nu^{-\eta}} \frac{\bar{n}\cdot A_n(x)}{\bar{n}\cdot\mathcal{P}}\right], \tag{2.139}$$

$$S_n(x) = \sum_{\text{perm}} \exp\left[-gw \frac{|2\mathcal{P}_g^3|^{-\eta/2}}{\nu^{-\eta/2}} \frac{n\cdot A_s(x)}{n\cdot\mathcal{P}}\right]. \tag{2.140}$$

where ν is a dimensionful parameter such that the exponent remains dimensionless. In eq. (2.107) the label momentum operator $\mathcal{P}_g$ picks the group momenta of a connected web (c-web) and w is a bookkeeping parameter that satisfies

$$\nu \frac{\mathrm{d}w}{\mathrm{d}\nu} = -\frac{\eta}{2} w\,, \tag{2.141}$$

so that the bare matrix elements are ν-independent and at the end of each calculation it is set $w = 1$. With the η regulator rapidity divergences in the soft and collinear matrix elements appear as poles in η, for $\eta \to 0$, and they are renormalized along the UV-originating ϵ-poles in the $\overline{\text{MS}}$ scheme. Note that the order of taking the zero limit of the regulators is important, as the $\eta \to 0$ has to happen while the modes lie on the same invariant mass hyperbola, which implies that the correct way is *first* taking $\eta \to 0$ and *then* $\epsilon \to 0$. In close analogy to μ-independence, bare matrix elements also have to be ν-independent something that yields their corresponding *rapidity anomalous dimensions* and gives rise to the corresponding *rapidity renormalization group equations (RRGEs)*. The latter are solved in order to evolve functions that live in distinct rapidities to a common, arbitrary one and effectively resum all (large) rapidity logarithms. In section 3.2 we see the form of the RRGEs in the context of q_T factorization, and in section 4.3 we solve them for the transverse momentum dependent beam and soft functions in order to predict their ν-dependent FO structure up to $\mathcal{O}(\alpha_s^3)$.

Chapter 3

Resummation in the presence of multiple gauge interactions

In this chapter we consider the higher-order resummation of Sudakov double logarithms in the presence of multiple coupled gauge interactions. The associated evolution equations depend on the coupled β-functions of two (or more) coupling constants α_a and α_b, as well as on anomalous dimensions that have joint perturbative series in α_a and α_b. We discuss possible strategies for solving the system of evolution equations that arises. As an example, we obtain the complete three-loop (NNLL) QCD⊗QED Sudakov evolution factor. As part of our analysis we also revisit the case of a single gauge interaction (pure QCD), and study the numerical differences and reliability of various methods for evaluating the Sudakov evolution factor at higher orders. We find that the approximations involved in deriving commonly used analytic expressions for the evolution kernel can induce noticeable numerical differences, exceeding the perturbative precision at $\mathrm{N^3LL}$ and in some cases even at NNLL.

This chapter is based on ref. [1] while section 3.2 has been added.

3.1 Introduction

Despite their smaller couplings in the SM, corrections from the emission of EW bosons can be comparable to those of QCD calculated at NNLO (cf. $\alpha_e \sim \alpha_s^2$). The exchange of massive virtual EW bosons in high-energy processes can generate EW Sudakov logarithms, which can cause sizeable EW corrections. The resummation of EW Sudakov logarithms has been studied for many years, albeit typically at lower orders than in QCD, see e.g. refs. [77–90]. As a result, achieving sufficiently precise predictions for many collider observables requires considering them in a joint QCD⊗EW environment to fully capture all relevant effects. This is of course true when considering an extremely high energy future collider [91], where EW corrections can be $\mathcal{O}(1)$, but also for measurements at the LHC reaching percent-level precision, the prime example being the high-precision measurements of W and Z production [92–97]. The literature reflects this: The impact of EW and mixed QCD⊗EW corrections on the W-mass measurement have received much attention (see e.g. refs. [98–101] and references therein). QED corrections to the evolution of PDFs have also been obtained, see e.g. refs. [102–107]. The full NNLO $\mathcal{O}(\alpha_e\alpha_s)$ mixed QCD⊗QED corrections and $\mathcal{O}(\alpha_e^2)$

QED corrections for on-shell Z production were calculated recently in ref. [108] and for Higgs production in bottom-quark annihilation in ref. [109]. The one-loop QED corrections to the Sudakov resummation were included in the high-precision analysis of thrust in e^+e^- collisions [110]. The resummed p_T spectrum of Z-boson production including QED corrections was obtained in ref. [111], capturing the pure QED logarithmic contributions at NLL and the mixed QCD⊗QED contributions at LL. Closely related, the QED corrections to the two-loop anomalous dimensions of p_T-dependent distributions were obtained in ref. [112] and of the quark form factors in ref. [109].

In light of the above and in an effort to match the ever increasing experimental precision, it is therefore timely to perform a thorough study on the methods for performing higher-order Sudakov resummation in the presence of multiple gauge interactions. To motivate for the emerging structure in such cases, we begin this chapter with a review on the transverse momentum (q_T) factorization in QCD⊗QED. Specifically, we consider the production in hadronic collisions of a color-singlet at small $q_T \ll Q$, with Q its invariant mass, when *only* QED initial state radiation (ISR) effects are accounted for. We work in SCET, following closely the corresponding derivation of the pure QCD factorization [71, 113, 114] and discuss the appropriate the modifications for the inclusion of QED radiation. While it has been shown that these effects can be straightforwardly incorporated [112], going through the factorization serves well for motivating its RGE structure, discuss the strategy for the extraction of higher-order QCD⊗QED perturbative ingredients, and provides a stepping stone for the rest of the chapter.

In the second part, we step back and reevaluate some of the technical aspects of Sudakov resummation when the interactions of two gauge symmetries $G_a \otimes G_b$ are involved, staying agnostic as to the precise resummation formalism utilized. In particular, we analyze the integrand structure of the Sudakov evolution factor

$$U(\mu_0, \mu) = \exp\left\{ \int_{\mu_0}^{\mu} \frac{d\mu'}{\mu'} \Gamma_{\text{cusp}}[\alpha_a(\mu'), \alpha_b(\mu')] \ln \frac{Q}{\mu'} + \gamma[\alpha_a(\mu'), \alpha_b(\mu')] \right\}. \tag{3.1}$$

An evolution factor of this form necessarily appears in all formulations of higher-order Sudakov resummation. It implicitly depends on the β-functions controlling the renormalization group evolution of both gauge coupling constants $\alpha_a(\mu)$ and $\alpha_b(\mu)$, which in general are a coupled system of differential equations, as well as on anomalous dimensions $(\Gamma_{\text{cusp}}, \gamma)$ whose perturbative expansions are themselves joint series in $\alpha_{a,b}$. We attempt to be as generic as possible in our discussion and therefore do not immediately specify $G_{a,b}$. To draw some phenomenological conclusions we eventually consider the example of QCD⊗QED, i.e. $G_a \equiv \text{SU}(3)_c$ and $G_b \equiv \text{U}(1)_{\text{em}}$, for which we obtain the complete three-loop (NNLL) Sudakov evolution factor.

Interestingly, we also find that the approximations made in obtaining closed-form analytic expressions for eq. (3.1) that are commonly used in the literature can lead to nonnegligible numerical differences. When evolving to low scales, where the resummation becomes most important, the resulting effects can reach several percent or more. In other words, the use of different strategies for evaluating eq. (3.1) can be a source of nontrivial systematic

differences between different resummation implementations that can potentially exceed the perturbative precision one is aiming for.

Since these issues already appear for a single gauge interaction we devote a substantial fraction of this chapter in exploring them for this simpler case, using pure QCD as test case. Ultimately, we are forced to conclude that the commonly used approximate analytic expressions for eq. (3.1) are not sufficiently reliable when aiming for percent-level precision. We find that a seminumerical approach, where the μ-integration in the exponent of eq. (3.1) is carried out numerically while using an approximate analytic solution for the running of the coupling, provides a good compromise, which also straightforwardly generalizes to multiple gauge interactions.

The structure of the chapter is as follows. In section 3.2 we go through the extension of QCD q_T factorization when QED ISR effects are included. We discuss the resulting RGE structure and comment on the method for extracting pure QED and mixed QCD⊗QED perturbative ingredients. In section 3.3, we discuss the coupled β-functions for $\alpha_{a,b}$. We first review the standard approximate analytic solutions for α in the one-dimensional case, and then derive corresponding approximate analytic solutions for the coupled system up to three-loop (NNLO) running. In section 3.4, we move to analyzing the Sudakov evolution kernel for the one-dimensional case, discussing several methods for evaluating it and studying their numerical performance up to N^{3}LL. In section 3.5 we then apply the lessons learned to the case of two coupled gauge interactions. We conclude in section 3.6.

3.2 QCD⊗QED transverse momentum factorization

We consider the production of a Z boson in hadronic collisions and its subsequent decay to neutrinos

$$p_n(P_n)p_{\bar{n}}(P_{\bar{n}}) \to Z(q)X(p_X) \to \nu_\ell(p_1)\bar{\nu}_\ell(p_2)X(p_X)\,, \tag{3.2}$$

where the incoming protons $p_n, p_{\bar{n}}$ carry momenta $P_n^\mu = (E_{\rm cm}/2)n^\mu$ and $P_{\bar{n}}^\mu = (E_{\rm cm}/2)\bar{n}^\mu$. We denote the four-momenta of the vector boson by q^μ and X is any hadronic or electromagnetic radiation with momentum p_X^μ upon which we are inclusive. Since our focus is the investigation of QCD and QED ISR effects and their impact on transverse momentum factorization, we conveniently choose the decay $Z \to \nu_\ell\bar{\nu}_\ell$ which is neither charged under SU(3)$_c$ nor under U(1)$_{\rm em}$. This implies the absence of final state (FSR) and initial-final state (IFI) QED radiation effects that would otherwise impose further conceptual and practical difficulties to the derivation of the factorization.

We measure the invariant mass Q^2 and the rapidity Y of the vector boson

$$Q^2 = q^2\,, \qquad Y = \frac{1}{2}\ln\frac{q^-}{q^+}\,, \quad \text{with} \quad q^\pm = e^{\mp Y}\sqrt{Q^2+q_T^2}\,, \tag{3.3}$$

as well as the transverse momentum $\vec{p}_{T_X}$ of all the hadronic and electromagnetic radiation, which as we show, it is eventually identified with the Z boson's transverse momenta. The

differential, full theory cross section reads

$$\frac{\mathrm{d}\sigma}{\mathrm{d}Q^2\mathrm{d}Y\,\mathrm{d}^2\vec{p}_T} = \frac{1}{4E_{\mathrm{cm}}^2}\int\frac{\mathrm{d}^2\vec{q}_T}{(2\pi)^4}\int \mathrm{d}\Phi_L(q)\;(2\pi)^4\delta^{(4)}(P_n+P_{\bar{n}}-p_X-q)\,\delta^{(2)}(\vec{p}_T-\vec{p}_{T_X}) \sum\!\!\!\!\!\!\int_X \left|\mathcal{M}(p_np_{\bar{n}}\to\nu_\ell\bar{\nu}_\ell X)\right|^2, \tag{3.4}$$

where we keep the average and sum over color/polarizations implicit while the summation over X is understood to include the corresponding phase space integrals (denoted with the superimposed integral). Here, $\mathrm{d}\Phi_L(q)$ is the Lorentz invariant (massless) two-body phase space

$$\mathrm{d}\Phi_L(q) = \prod_{i=1,2}\left[\frac{\mathrm{d}^4p_i}{(2\pi)^4}(2\pi)\delta(p_i^2)\theta(p_i^0)\right](2\pi)^4\delta^{(4)}(q-p_1-p_2)\,. \tag{3.5}$$

Since the final state is electromagnetically and color neutral, we can separately treat production from decay. The squared matrix element can then be written into the form

$$\left|\mathcal{M}(p_np_{\bar{n}}\to\nu_\ell\bar{\nu}_\ell X)\right|^2 = L^{\mu\dagger}L^\nu\langle p_np_{\bar{n}}|J_\mu^\dagger(0)|X\rangle\langle X|J_\nu(0)|p_np_{\bar{n}}\rangle\,, \tag{3.6}$$

and $J^\mu\equiv J_Z^\mu$ is the EW current that couples quarks of flavor q to the Z boson

$$J_Z^\mu = -|e|\sum_q \bar{\psi}_q\gamma^\mu(v_q-a_q\gamma_5)\psi_q\,, \tag{3.7}$$

where v_q, a_q are the vector and axial-vector couplings respectively. In eq. (3.6) L^μ is the amplitude for the propagation and decay of $Z\to\nu_\ell\bar{\nu}_\ell$. In order to make the production-decay factorization explicit, we cast the cross into the form

$$\frac{\mathrm{d}\sigma}{\mathrm{d}Q^2\mathrm{d}Y\,\mathrm{d}^2\vec{p}_T} = \frac{1}{4E_{\mathrm{cm}}^2}\int\frac{\mathrm{d}^2\vec{q}_T}{(2\pi)^4}W_{\mu\nu}(q,\vec{p}_T)L^{\mu\nu}(q)\,, \tag{3.8}$$

where we defined

$$W_{\mu\nu}(q,\vec{p}_T) = \sum\!\!\!\!\!\!\int_X \langle p_np_{\bar{n}}|J_\mu^\dagger(0)|X\rangle\langle X|J_\nu(0)|p_np_{\bar{n}}\rangle \times(2\pi)^4\delta^{(4)}(P_n+P_{\bar{n}}-p_X-q)\,\delta^{(2)}(\vec{p}_T-\vec{p}_{T_X})\,, \tag{3.9}$$

$$L^{\mu\nu}(q) = \int\mathrm{d}\Phi_L(q)\;L^{\mu\dagger}L^\nu \equiv \left(g^{\mu\nu}-\frac{q^\mu q^\nu}{q^2}\right)L(Q^2)\,. \tag{3.10}$$

Here, $L^{\mu\nu}$ is the leptonic tensor and going from the first to the second equality in eq. (3.10) we made use of the leptonic current conservation and that in the SM the neutrino masses $m_{\nu_\ell}=0$. In eq. (3.9) we defined the hadronic tensor $W^{\mu\nu}$ which crucially captures all QCD *and* QED dynamics.

At this point, standard manipulations involve promoting $\vec{p}_{T_X}$ to an operator $\vec{p}_{T_X}\mapsto\hat{\vec{p}}_{T_X}$ that acts upon the states X picking their transverse momenta and express the momentum conserving delta function in eq. (3.9) as an exponential. The current in the conjugate

matrix element of eq. (3.9) can then be translated, something that allows to perform the summation over the states X and write

$$W_{\mu\nu}(q,\vec{p}_T) = \int \mathrm{d}^4x\; e^{-\mathrm{i}q\cdot x}\; \big\langle p_n p_{\bar{n}}\big| J^\dagger_\mu(x)\delta^{(2)}(\vec{p}_T - \hat{\vec{p}}_{T_X}) J_\nu(0)\big| p_n p_{\bar{n}}\big\rangle\,. \tag{3.11}$$

We are interested in expanding the cross section in the limit $q_T \equiv |\vec{q}_T| \ll Q$ and to this end we define the dimensionless power counting parameter

$$\lambda = \frac{q_T}{Q} \ll 1\,, \tag{3.12}$$

with respect to which the expansion will take place. As discussed in section 2.3.1, in this limit the dominant modes contributing to the measurement of $\vec{p}_{T_X}$ will be either soft or collinear with their momenta scaling as

$$n\text{-collinear:} \qquad k_n \sim (1,\lambda^2,\lambda)\,, \tag{3.13}$$

$$\bar{n}\text{-collinear:} \qquad k_{\bar{n}} \sim (\lambda^2,1,\lambda)\,, \tag{3.14}$$

$$\text{soft:} \qquad k_s \sim (\lambda,\lambda,\lambda)\,. \tag{3.15}$$

To achieve the expansion of the cross section in λ we work in SCET. Notice that based on the scaling of the soft modes in eq. (3.15) we are in a $\mathrm{SCET_{II}}$ setting [68] (see section 2.3.5). We start by matching the full theory currents $J^\mu(x)$ onto the LP SCET currents $J^\mu(x) \mapsto J^\mu_{\mathrm{SCET}}(x)$ with

$$J^\mu_{\mathrm{SCET}}(x) = \sum_{n_1,n_2}\int \mathrm{d}\omega_1\mathrm{d}\omega_2\mathrm{d}^2\vec{p}_{T_1}\mathrm{d}^2\vec{p}_{T_2}\mathrm{d}^4\tilde{p}_s\; e^{-\mathrm{i}(\tilde{p}_1+\tilde{p}_2+\tilde{p}_s)\cdot x}\sum_q C^\mu_{q\bar{q}}(\omega_1,\omega_2)\mathcal{O}_{q\bar{q}}(\tilde{p}_1,\tilde{p}_2,\tilde{p}_s;x)\,. \tag{3.16}$$

Here, $C^\mu_{q\bar{q}}$ is the quark Wilson coefficient that captures all the dynamics at the hard scale $\sim Q$, whereas $\mathcal{O}_{q\bar{q}}$ is the quark SCET operator that captures all the soft and collinear dynamics. It is understood to be manifestly expressed in label momentum and residual position space with its field content being,

$$\mathcal{O}_{q\bar{q}}(\tilde{p}_1,\tilde{p}_2,\tilde{p}_s;x) = \bar{\chi}^{(0)}_{n_1,-\tilde{p}_1}(x)\,\mathrm{T}\big[\delta^{(4)}(\tilde{p}_s-\mathcal{P}_s)\mathbb{S}^\dagger_{n_1}\mathbb{S}_{n_2}(x)\big]\chi^{(0)}_{n_2,\tilde{p}_2}(x)\,. \tag{3.17}$$

Here, $\chi^{(0)}_{n_i,\tilde{p}_i} \equiv \chi^{(0)}_{q\,n_i,\tilde{p}_i}$ are BPS [58] transformed n_i-collinear quark fields of flavor q and definite label momentum

$$\chi^{(0)}_{n_i,\tilde{p}_i}(x) = \big[\delta(\omega_i - \bar{n}_i\cdot\mathcal{P})\delta^{(2)}(\vec{p}_{T_i}-\mathcal{P}_{\perp n_i})\mathbb{W}^{(0)\dagger}_{n_i}\xi^{(0)}_{n_i}(x)\big]\,, \tag{3.18}$$

$$\tilde{p}^\mu_i = \omega_i\frac{n^\mu_i}{2} + p^\mu_{\perp i}\,, \tag{3.19}$$

and $\mathcal{P}^\mu$ is the label momentum operator, see eq. (2.74). Note that we follow the convention of including the appropriate sign in the label momenta of the fields in eq. (3.17) such that incoming particles have $\omega_i > 0$. For ease of notation we have suppressed the spinor and

color indices in $C^{\mu}_{q\bar{q}}$ and $\mathcal{O}_{q\bar{q}}$. From now on we also drop the superscript '(0)' where all fields are understood to be BPS transformed.

At this point we come across the first difference to the pure QCD factorization since quarks carry electromagnetic charge and they transform under $\mathrm{U}(1)_{\mathrm{em}}$ on top of the usual $\mathrm{SU}(3)_c$. This necessitates the emergence of soft and collinear Wilson lines that account for quark-photon interactions and render the SCET operator $\mathcal{O}_{q\bar{q}}$ in eq. (3.17) invariant also under $\mathrm{U}(1)_{\mathrm{em}}$ collinear and soft gauge transformations. This is accomplished by identifying in eq. (3.18) [112],

$$\mathbb{W}_{n_i}(x) \equiv W_{n_i}(x) W^e_{n_i}(x)\,, \tag{3.20}$$

$$W^e_{n_i}(x) = \exp\left[\mathrm{i}eQ_q \int_{-\infty}^{0} \mathrm{d}s\ \bar{n}_i \cdot B_{n_i}(x + \bar{n}_i s)\right], \tag{3.21}$$

where Q_q is the charge of the collinear quark $\xi_{n_i}(x)$ and $B^{\mu}_{n_i}(x)$ is the n_i-collinear photon field. $W^e_{n_i}(x)$ is the *collinear photon Wilson line* that captures the effect of $\bar{n}_i \cdot B_{n_i} \sim \mathcal{O}(\lambda^0)$ collinear photon field, in direct analogy to the collinear gluon Wilson line $W_{n_i}(x)$ that we defined in eq. (2.107). Similar considerations apply also for the soft Wilson lines in eq. (3.17) which are defined as [112],

$$\mathbb{S}_{n_i}(x) \equiv S_{n_i}(x) S^e_{n_i}(x)\,, \tag{3.22}$$

$$S^e_{n_i}(x) = \exp\left[\mathrm{i}eQ_q \int_{-\infty}^{0} \mathrm{d}s\ n_i \cdot B_s(x + n_i s)\right], \tag{3.23}$$

with B^{μ}_s the soft photon field and accordingly $S^e_{n_i}(x)$ the *soft photon Wilson line*. $S_{n_i}(x)$ is the soft gluon Wilson line, defined in eq. (2.137). Note in both eqs. (3.21) and (3.23) the absence of path ordering as is appropriate for an abelian field.

At this point some comments are in line with respect to the Lagrangians that govern the dynamics and interactions of the introduced soft and collinear photon fields. For the soft photon field B^{μ}_s, the situation is exactly the same as that for the soft gluon fields. Its Lagrangian is given by an exact (soft) copy of the full theory Maxwell Lagrangian with the corresponding soft gauge fixing term, while its coupling to soft quark fields is obtained by properly extending the covariant derivative of the latter. Accordingly, the Lagrangian for B^{μ}_n follows as an abelian analogue of the collinear gluon Lagrangian in eq. (2.123). Note though, that due to the abelian nature of the photon field, the soft and collinear ghost Lagrangian terms are absent. Finally, to make the BPS transformed collinear quark Lagrangian in eq. (2.120) manifestly invariant under collinear $\mathrm{U}(1)_{\mathrm{em}}$, it suffices to extend the covariant derivatives with the coupling to B^{μ}_n and account for the emergence of the QED collinear Wilson line, W^e_n, by substituting $W^{(0)}_n(x) \mapsto \mathbb{W}^{(0)}_n(x)$.

Coming back to factorization, we proceed to obtain the LP hadronic tensor $W^{(0)}_{\mu\nu} \sim \mathcal{O}(\lambda^0)$,

by substituting eq. (3.16) in eq. (3.11)

$$
\begin{aligned}
W^{(0)}_{\mu\nu}(q,\vec{p}_{T_X}) = \sum_q \sum_{n_1,n_2,n_1',n_2'} \prod_{i=1,2} \int \mathrm{d}\omega_i \mathrm{d}^2\vec{p}_{T_i} \mathrm{d}^4\tilde{p}_s \int \mathrm{d}\omega_i' \mathrm{d}^2\vec{p}_{T_i}' \mathrm{d}^4\tilde{p}_s' \int \mathrm{d}^4x \\
\times e^{\mathrm{i}(\tilde{p}_1'+\tilde{p}_2'+\tilde{p}_s'-q)\cdot x}\ \bar{C}_{q\bar{q}\,\mu}(\omega_1',\omega_2') C_{q\bar{q}\,\nu}(\omega_1,\omega_2) \qquad (3.24)\\
\times \big\langle p_n p_{\bar{n}} \big| \mathcal{O}^\dagger_{q\bar{q}}(\tilde{p}_1',\tilde{p}_2',\tilde{p}_s';x) \delta^{(2)}(\vec{p}_T - \hat{\vec{p}}_{T_X}) \mathcal{O}_{q\bar{q}}(\tilde{p}_1,\tilde{p}_2,\tilde{p}_s;0) \big| p_n p_{\bar{n}} \big\rangle \,.
\end{aligned}
$$

where the conjugate Wilson line is defined as $\bar{C}_{q\bar{q}\,\mu} = \gamma^0 C^\dagger_{q\bar{q}\,\mu}\gamma^0$. Note that here we have exploited that flavor number conservation forces $q = q'$ in the product $(\sum_q \mathcal{O}^\dagger_{q\bar{q}})(\sum_{q'} \mathcal{O}_{q'\bar{q}'})$ [65]. Since at LP there are no interactions between collinear and soft fields, the Fock space factorizes $|p_n p_{\bar{n}}\rangle = |p_n\rangle|p_{\bar{n}}\rangle|0\rangle$ and we can consider soft and collinear contributions separately to $\vec{p}_{T_X}$ by expressing the measurement delta function as

$$
\begin{aligned}
\delta^{(2)}(\vec{p}_T - \hat{\vec{p}}_{T_X}) = \int \mathrm{d}^2\vec{k}_n \mathrm{d}^2\vec{k}_{\bar{n}} \mathrm{d}^2\vec{k}_s\ \delta^{(2)}(\vec{p}_T - \vec{k}_n - \vec{k}_{\bar{n}} - \vec{k}_s) \qquad (3.25)\\
\times \delta^{(2)}(\vec{k}_n - \mathcal{P}_{\perp n}) \delta^{(2)}(\vec{k}_{\bar{n}} - \mathcal{P}_{\perp \bar{n}}) \delta^{(2)}(\vec{k}_s - \mathcal{P}_{\perp s}) \,,
\end{aligned}
$$

This allows us to express $W^{(0)}_{\mu\nu}$ in a manifestly factorized form,

$$
\begin{aligned}
W^{(0)}_{\mu\nu}(q,\vec{p}_T) = \sum_q \sum_{n_1,n_2,n_1',n_2'} \prod_{i=1,2} \int \mathrm{d}\omega_i \mathrm{d}^2\vec{p}_{T_i} \mathrm{d}^4\tilde{p}_s \int \mathrm{d}\omega_i' \mathrm{d}^2\vec{p}_{T_i}' \mathrm{d}^4\tilde{p}_s' \int \mathrm{d}^2\vec{k}_n \mathrm{d}^2\vec{k}_{\bar{n}} \mathrm{d}^2\vec{k}_s \int \mathrm{d}^4x \\
\times \delta^{(2)}(\vec{p}_T - \vec{k}_n - \vec{k}_{\bar{n}} - \vec{k}_s)\ e^{\mathrm{i}(\tilde{p}_1'+\tilde{p}_2'+\tilde{p}_s'-q)\cdot x}\ \bar{C}_{q\bar{q}\,\mu}(\omega_1',\omega_2') C_{q\bar{q}\,\nu}(\omega_1,\omega_2) \\
\times \big\langle 0 \big| \bar{\mathrm{T}}\big[\delta^{(4)}(\tilde{p}_s' - \mathcal{P}_s) \mathbb{S}^\dagger_{n_2} \mathbb{S}_{n_1}(x)\big] \delta^{(2)}(\vec{k}_s - \mathcal{P}_{\perp s})\, \mathrm{T}\big[\delta^{(4)}(\tilde{p}_s - \mathcal{P}_s) \mathbb{S}^\dagger_{n_1} \mathbb{S}_{n_2}(x)\big] \big| 0 \big\rangle \\
\times \theta(\omega_2)\theta(\omega_2') \big\langle p_n \big| \bar{\chi}_{n_2',-\tilde{p}_2'}(x) \delta^{(2)}(\vec{k}_n - \mathcal{P}_{\perp n}) \chi_{n_2,\tilde{p}_2}(0) \big| p_n \big\rangle \\
\times \theta(\omega_1)\theta(\omega_1') \big\langle p_{\bar{n}} \big| \chi_{n_1',\tilde{p}_1'}(x) \delta^{(2)}(\vec{k}_{\bar{n}} - \mathcal{P}_{\perp \bar{n}}) \bar{\chi}_{n_1,-\tilde{p}_1}(0) \big| p_{\bar{n}} \big\rangle \ + \ \ldots \,, \qquad (3.26)
\end{aligned}
$$

where the '…' denote contributions with different arrangements of the collinear fields χ_{n_i} in the proton matrix elements. In order to proceed, we exploit that fields with positive (negative) label momenta annihilate incoming (outgoing) proton states. This sets the $n^{(\prime)}_{1,2}$ directions to those of the external states $n, \bar{n}$, up to an overall multiplicative factor which results from all possible ways of matching [65]. Furthermore, we impose label momentum conservation in each matrix element of eq. (3.26) which sets $\tilde{p}_{1,2} = \tilde{p}_{1,2}'$, $\tilde{p}_s = \tilde{p}_s'$ and allows us to perform all the primed integrals using the delta functions that are part of the definition of the collinear fields (see eq. (3.18)). The resulting expression for $W^{(0)}_{\mu\nu}$ reads,

$$
\begin{aligned}
W^{(0)}_{\mu\nu}(q,\vec{p}_T) = 2 \sum_q \prod_{i=1,2} \int \mathrm{d}\omega_i \mathrm{d}^2\vec{p}_{T_i} \mathrm{d}^4\tilde{p}_s \int \mathrm{d}^2\vec{k}_n \mathrm{d}^2\vec{k}_{\bar{n}} \mathrm{d}^2\vec{k}_s \int \mathrm{d}^4x \\
\times \delta^{(2)}(\vec{p}_T - \vec{k}_n - \vec{k}_{\bar{n}} - \vec{k}_s)\ e^{\mathrm{i}(\tilde{p}_1+\tilde{p}_2+\tilde{p}_s-q)\cdot x}\ \bar{C}_{q\bar{q}\,\mu}(\omega_1,\omega_2) C_{q\bar{q}\,\nu}(\omega_1,\omega_2) \\
\times \big\langle 0 \big| \bar{\mathrm{T}}\big[\mathbb{S}^\dagger_n \mathbb{S}_{\bar{n}}(x)\big] \delta^{(2)}(\vec{k}_s - \mathcal{P}_{\perp s})\, \mathrm{T}\big[\delta^{(4)}(\tilde{p}_s - \mathcal{P}_s) \mathbb{S}^\dagger_{\bar{n}} \mathbb{S}_n(0)\big] \big| 0 \big\rangle \\
\times \theta(\omega_2) \big\langle p_n \big| \bar{\chi}_n(x) \delta^{(2)}(\vec{k}_n - \mathcal{P}_{\perp n}) [\delta^{(2)}(\vec{p}_{T_2} - \mathcal{P}_{\perp n}) \delta(\omega_2 - \bar{n}\cdot\mathcal{P}) \chi_n(0)] \big| p_n \big\rangle \\
\times \theta(\omega_1) \big\langle p_{\bar{n}} \big| \chi_{\bar{n}}(x) \delta^{(2)}(\vec{k}_{\bar{n}} - \mathcal{P}_{\perp \bar{n}}) [\delta^{(2)}(\vec{p}_{T_1} - \mathcal{P}_{\perp \bar{n}}) \delta(\omega_1 - n\cdot\mathcal{P}) \bar{\chi}_{\bar{n}}(0)] \big| p_{\bar{n}} \big\rangle \\
+ (q \leftrightarrow \bar{q}) \,. \qquad (3.27)
\end{aligned}
$$

The matrix elements in eq. (3.27) are still dependent in residual momenta via the spacetime dependence of the fields. Although so far we found it conceptually easier to treat the label momenta $\tilde{p}_i$ as continuous, formally they are discrete and they have to be recombined with their residual components in order to be made manifestly continuous. To see how this would happen, consider the soft matrix element in eq. (3.27), which we abbreviate as $\mathcal{M}_s$

$$\begin{aligned}\sum_{\tilde{p}_s} e^{\mathrm{i}\tilde{p}_s\cdot x}\mathcal{M}_s(\vec{k}_s,\tilde{p}_s;x) &= \sum_{\tilde{p}_s}\int \mathrm{d}^4p_r\; e^{\mathrm{i}(\tilde{p}_s+p_r)\cdot x}\;\mathcal{M}_s(\vec{k}_s,\tilde{p}_s,p_r)\\ &= \sum_{\tilde{p}_s}\int \mathrm{d}^4p_r\; e^{\mathrm{i}(\tilde{p}_s+p_r)\cdot x}\;\mathcal{M}_s(\vec{k}_s,\tilde{p}_s+p_r;0)\\ &\equiv \int \mathrm{d}^4p_s\; e^{\mathrm{i}p_s\cdot x}\mathcal{M}_s(\vec{k}_s,p_s;0)\,. \end{aligned} \tag{3.28}$$

In the second equality we made use of the RPI [59] which dictates that label and residual momenta can only appear as a sum, $p_s = \tilde{p}_s + p_r$, and recombined their components to form continuous momenta p_s. This effectively localizes $\mathcal{M}_s$ at $x = 0$.

Similar manipulations also apply to the $n,\bar{n}$-collinear proton matrix elements in eq. (3.27), although in this case not all of their spacetime dependence is absorbed. This is due to the fact that the (e.g.) n-collinear matrix element carries label momenta only with respect to the x^+ and $x_\perp$ directions but not with respect to the x^-. The latter component corresponds to purely residual momenta and thus leaves a leftover spacetime dependence. Same considerations also apply for the $\bar{n}$-collinear matrix element upon $x^\pm \mapsto x^\mp$. Since the leftover spacetime dependence corresponds to residual momenta it can be multipole expanded, and to see this we Fourier transform both collinear matrix elements (which we abbreviate as $\mathcal{M}_{n,\bar{n}}$) explicitly in momentum space,

$$\mathcal{M}_n(\vec{k}_n,\tilde{p}_2;x^-) = \int\frac{\mathrm{d}k^+}{2\pi}\; e^{\mathrm{i}k^+x^-/2}\tilde{\mathcal{M}}_n(\vec{k}_n,\tilde{p}_2,k^+)\,, \tag{3.29}$$

$$\mathcal{M}_{\bar{n}}(\vec{k}_{\bar{n}},\tilde{p}_1;x^+) = \int\frac{\mathrm{d}k^-}{2\pi}\; e^{\mathrm{i}k^-x^+/2}\tilde{\mathcal{M}}_{\bar{n}}(\vec{k}_{\bar{n}},\tilde{p}_1,k^-)\,. \tag{3.30}$$

Substituting eqs. (3.28), (3.29), and (3.30) in eq. (3.27) we obtain,

$$\begin{aligned}W^{(0)}_{\mu\nu}(q,\vec{p}_T) = 2\sum_q\int \mathrm{d}^4x\prod_{i=1,2}\int \mathrm{d}\omega_i\mathrm{d}^2\vec{p}_{T_i}\mathrm{d}^4p_s\int \mathrm{d}^2\vec{k}_n\mathrm{d}^2\vec{k}_{\bar{n}}\mathrm{d}^2\vec{k}_s\;\delta^{(2)}(\vec{p}_T-\vec{k}_n-\vec{k}_{\bar{n}}-\vec{k}_s)\\ \times\int\frac{\mathrm{d}k^+}{2\pi}\frac{\mathrm{d}k^-}{2\pi}\; e^{\mathrm{i}(\tilde{p}_1+\tilde{p}_2+p_s-q+k^+\bar{n}/2+k^-n/2)\cdot x}\;\bar{C}_{q\bar{q}\,\mu}(\omega_1,\omega_2)C_{q\bar{q}\,\nu}(\omega_1,\omega_2)\\ \times\;\mathcal{M}_s(\vec{k}_s,p_s;0)\,\tilde{\mathcal{M}}_n(\vec{k}_n,\tilde{p}_2,k^+)\,\tilde{\mathcal{M}}_{\bar{n}}(\vec{k}_{\bar{n}},\tilde{p}_1,k^-)+(q\leftrightarrow\bar{q})\,,\end{aligned} \tag{3.31}$$

where now all the spacetime dependence has moved from the matrix elements into a phase

and therefore we are in position to perform the x integration. It yields the delta function,

$$\begin{aligned}\int \mathrm{d}^4x\; e^{\mathrm{i}(\tilde{p}_1+\tilde{p}_2+p_s-q+k^+\bar{n}/2+k^-n/2)\cdot x}&\\ &= (2\pi)^4\delta^{(4)}(\tilde{p}_1+\tilde{p}_2+p_s+k^+\bar{n}/2+k^-n/2-q)\\ &= 2(2\pi)^4\delta(\omega_1-q^+)\delta(\omega_2-q^-)\delta^{(2)}(\vec{q}_T-\vec{p}_{T_1}-\vec{p}_{T_2}-\vec{p}_{T_s})\times[1+\mathcal{O}(\lambda)]\,, \quad (3.32)\end{aligned}$$

and to go from the second to third line we expanded away the $p_s^\pm \sim \mathcal{O}(\lambda)$ and $k^\pm \sim \mathcal{O}(\lambda^2)$. Thus, we can perform the $k^\pm$ integrals that correspond to a Fourier transform of $\mathcal{M}_{n,\bar{n}}$ at $x^\mp = 0$, as well as the $p_s^\pm$ integrals since these components do not contribute to the measurement of $\vec{p}_T$. Writing explicitly the matrix elements,

$$\begin{aligned}W^{(0)}_{\mu\nu}(q,\vec{p}_T) = 4(2\pi)^4\sum_q\prod_{i=1,2}\int \mathrm{d}\omega_i\mathrm{d}^2\vec{p}_{T_i}\mathrm{d}^2\vec{p}_{T_s}\int \mathrm{d}^2\vec{k}_n\mathrm{d}^2\vec{k}_{\bar{n}}\mathrm{d}^2\vec{k}_s\;\bar{C}_{q\bar{q}\,\mu}(\omega_1,\omega_2)C_{q\bar{q}\,\nu}(\omega_1,\omega_2)&\\ \times\delta^{(2)}(\vec{p}_T-\vec{k}_n-\vec{k}_{\bar{n}}-\vec{k}_s)\,\delta(\omega_1-q^+)\delta(\omega_2-q^-)&\\ \times\delta^{(2)}(\vec{q}_T-\vec{p}_{T_1}-\vec{p}_{T_2}-\vec{p}_{T_s})\,\delta^{(2)}(\vec{p}_{T_1}-\vec{k}_{\bar{n}})\,\delta^{(2)}(\vec{p}_{T_2}-\vec{k}_n)\,\delta^{(2)}(\vec{p}_{T_s}-\vec{k}_s)&\\ \times\big\langle 0\big|\bar{\mathrm{T}}\big[\mathbb{S}_n^\dagger\mathbb{S}_{\bar{n}}(0)\big]\delta^{(2)}(\vec{k}_s-\mathcal{P}_{\perp s})\,\mathrm{T}\big[\mathbb{S}_{\bar{n}}^\dagger\mathbb{S}_n(0)\big]\big|0\big\rangle \quad (3.33)&\\ \times\theta(\omega_2)\big\langle p_n\big|\bar{\chi}_n(0)[\delta^{(2)}(\vec{k}_n-\mathcal{P}_{\perp n})\delta(\omega_2-\bar{n}\cdot\mathcal{P})\chi_n(0)]\big|p_n\big\rangle&\\ \times\theta(\omega_1)\big\langle p_{\bar{n}}\big|\chi_{\bar{n}}(0)[\delta^{(2)}(\vec{k}_{\bar{n}}-\mathcal{P}_{\perp\bar{n}})\delta(\omega_1-n\cdot\mathcal{P})\bar{\chi}_{\bar{n}}(0)]\big|p_{\bar{n}}\big\rangle+(q\leftrightarrow\bar{q})\,,&\end{aligned}$$

where it is evident from the arguments of the delta functions that they set $\vec{q}_T = \vec{p}_T$. This is in accord with our expectation that hadronic and electromagnetic radiation sets the transverse momentum of the vector boson. The rest of the delta functions set lightcone momenta

$$\omega_1 = q^+ = e^{-Y}Q\times[1+\mathcal{O}(\lambda^2)]\,,\qquad \omega_2 = q^- = e^{+Y}Q\times[1+\mathcal{O}(\lambda^2)]\,. \quad (3.34)$$

where we expanded the definition of $q^\pm$ in eq. (3.3) for $\lambda \ll 1$.

To bring the LP hadronic tensor into its final form we define the quark *hard*, *soft* and *beam functions*

$$H_q(Q^2)\equiv H_{q\bar{q}}(q^+,q^-) = \frac{\big(g^{\mu\nu}-q^\mu q^\nu/q^2\big)}{4E_{\mathrm{cm}}^2N_c}\,\mathrm{Tr}\Big(\frac{\not{n}}{2}\bar{C}_{q\bar{q}\,\mu}(q^-,q^+)\frac{\not{\bar{n}}}{2}C_{q\bar{q}\,\nu}(q^-,q^+)\Big)\,, \quad (3.35)$$

$$S_q(\vec{p}_T) = \frac{1}{N_c}\,\mathrm{Tr}\big\langle 0\big|\bar{\mathrm{T}}\big[\mathbb{S}_n^\dagger\mathbb{S}_{\bar{n}}(0)\big]\delta^{(2)}(\vec{p}_T-\mathcal{P}_{\perp s})\,\mathrm{T}\big[\mathbb{S}_{\bar{n}}^\dagger\mathbb{S}_n(0)\big]\big|0\big\rangle\,, \quad (3.36)$$

$$B_{q\,n}(\omega,\vec{p}_T) = \theta(\omega)\big\langle p_n\big|\bar{\chi}_n(0)[\delta^{(2)}(\vec{p}_T-\mathcal{P}_{\perp n})\delta(\omega-\bar{n}\cdot\mathcal{P})\frac{\not{\bar{n}}}{2}\chi_n(0)]\big|p_n\big\rangle\,. \quad (3.37)$$

In eq. (3.35) the trace of the Wilson coefficients is understood to be over both color and spin whereas in eq. (3.36) it is only over color. Here, we exploited that RPI-III [59] dictates that the hard function H_q can only depend on the product $q^+q^- = Q^2\,[1+\mathcal{O}(\lambda^2)]$. Analogously for the quark beam function $B_{q\,n}(\omega,\vec{p}_T)$, besides $\vec{p}_T$, it can only depend on $x = \omega/P_n^- = (Q/E_{\mathrm{cm}})e^Y$ with x the momentum fraction of the proton carried by the quark

that participates in the hard scatter. Similarly, the antiquark beam function $B_{\bar{q}\,\bar{n}}(\omega, \vec{p}_T)$ depends on $x = (Q/E_{\rm cm})e^{-Y}$.

Finally, the factorized LP cross section can be written as,

$$\frac{\mathrm{d}\sigma}{\mathrm{d}Q^2\mathrm{d}Y\mathrm{d}^2\vec{q}_T} = W^{(0)}(Q^2, Y, \vec{q}_T)L(Q^2) \times \Big[1 + \mathcal{O}\Big(\frac{q_T^2}{Q^2}\Big)\Big]\,, \tag{3.38}$$

with $W^{(0)}$ given by

$$\begin{aligned} W^{(0)}(Q^2, Y, \vec{q}_T) &= \sum_q \int \mathrm{d}^2\vec{k}_n \mathrm{d}^2\vec{k}_{\bar{n}} \mathrm{d}^2\vec{k}_s\ \delta^{(2)}(\vec{q}_T - \vec{k}_n - \vec{k}_{\bar{n}} - \vec{k}_s) \\ &\qquad \times H_q(Q^2) S_q(\vec{k}_s) B_{q\,n}(x_2, \vec{k}_n) B_{\bar{q}\,\bar{n}}(x_1, \vec{k}_{\bar{n}}) + (q \leftrightarrow \bar{q}) \\ &\equiv \sum_q H_q(Q^2) \left[S_q(\vec{q}_T) \otimes_{\vec{q}_T} B_{q\,n}(x_2, \vec{q}_T) \otimes_{\vec{q}_T} B_{\bar{q}\,\bar{n}}(x_1, \vec{q}_T)\right] + (q \leftrightarrow \bar{q})\,, \end{aligned} \tag{3.39}$$

where the symbol '$\otimes$' denotes the convolution with respect to the variable $\vec{q}_T$, see eq. (A.13). The hard function H_q corresponds to (the square of) the IR finite part of the Z boson quark form factor which is calculated by matching the full theory current onto SCET. The beam functions $B_{q\,n}, B_{\bar{q}\,\bar{n}}$ describe collinear radiation with total transverse momentum $\vec{k}_{n,\bar{n}}$ and longitudinal momentum fractions $x_{1,2} = (Q/E_{\rm cm})e^{\mp Y}$, while the soft function S_q describes wide angle, soft radiation with total transverse momentum $\vec{k}_s$.

Contrasting eq. (3.39) to the pure QCD transverse momentum factorization, e.g. in refs. [69, 71, 113, 114], allows us to assert that the inclusion of *only* QED ISR radiation corresponds to a straightforward extension of the former. The factorized structure is not altered in the sense that the LP spectrum is still given in terms of the same hard, soft and beam functions and we can retrieve the pure QCD factorization by simply setting $W^e_{n_i} \mapsto 1$ and $S^e_{n_i} \mapsto 1$ in $W^{(0)}$. The only difference in field theoretical level involves the inclusion of QED collinear and soft Wilson lines such that the newly introduced collinear and soft $\mathrm{U}(1)_{\rm em}$ gauge invariance is satisfied. It is precisely the presence of these Wilson lines that give rise to pure QED and mixed QCD-QED higher order effects that appear as perturbative corrections in the soft and beam functions. In addition, the hard function also receives pure QED and mixed QCD-QED radiative corrections from its matching to the full theory current, calculated now in mixed QCD-QED perturbation theory. All the above imply that a simultaneous expansion in both the strong coupling α_s and the electromagnetic coupling $\alpha_e = e^2/(4\pi)$ is in now appropriate for $W^{(0)}$,[1]

$$B_q(x, \vec{q}_T) = \sum_{n,m=0} B_q^{(n,m)}(x, \vec{q}_T)\Big(\frac{\alpha_s}{4\pi}\Big)^n\Big(\frac{\alpha_e}{4\pi}\Big)^m\,, \tag{3.40}$$

$$S_q(\vec{q}_T) = \sum_{n,m=0} S_q^{(n,m)}(\vec{q}_T)\Big(\frac{\alpha_s}{4\pi}\Big)^n\Big(\frac{\alpha_e}{4\pi}\Big)^m\,, \tag{3.41}$$

$$H_q(Q) = \sum_{n,m=0} H_q^{(n,m)}(Q)\Big(\frac{\alpha_s}{4\pi}\Big)^n\Big(\frac{\alpha_e}{4\pi}\Big)^m\,. \tag{3.42}$$

[1] From now we drop the subscript of the collinear direction in the beam function as it does not affect the discussion that follows.

Renormalization Group. The matrix elements that enter eq. (3.39) are bare quantities and at higher orders in perturbation theory suffer from UV divergences which are addressed by renormalization. As discussed in section 2.3.5, the measurement of q_T corresponds to a $\mathrm{SCET_{II}}$ problem, thus the soft and beam functions also exhibit rapidity divergences which have to be regularized and renormalized.[2]

The renormalization follows the standard steps with the exception that for the soft and beam functions it has a convolutional form due to their $\vec{q}_T$ dependence,

$$B_q^{\mathrm{bare}}(x,\vec{q}_T) = Z_B(\omega,\vec{q}_T,\mu,\nu) \otimes_{\vec{q}_T} B_q(x,\vec{q}_T,\mu,\nu)\,, \tag{3.43}$$

$$S_q^{\mathrm{bare}}(\vec{q}_T) = Z_S(\vec{q}_T,\mu,\nu) \otimes_{\vec{q}_T} S_q(\vec{q}_T,\mu,\nu)\,, \tag{3.44}$$

$$H_q^{\mathrm{bare}}(Q) = Z_H(Q,\mu) \times H_q(Q,\mu)\,, \tag{3.45}$$

where μ denotes the standard renormalization scale and ν is the rapidity scale emerging from the regulated rapidity divergences. Exploiting that bare quantities do not depend on either scale we can derive their μ-RGE equations,

$$\mu\frac{\mathrm{d}}{\mathrm{d}\mu} B_q(x,\vec{q}_T,\mu,\nu) = \tilde{\gamma}_B^q(\mu,\nu/\omega)\, B_q(x,\vec{q}_T,\mu,\nu)\,, \tag{3.46}$$

$$\mu\frac{\mathrm{d}}{\mathrm{d}\mu} S_q(\vec{q}_T,\mu,\nu) = \tilde{\gamma}_S^q(\mu,\nu)\, S_q(\vec{q}_T,\mu,\nu)\,, \tag{3.47}$$

$$\mu\frac{\mathrm{d}}{\mathrm{d}\mu} H_q(Q,\mu) = \gamma_H^q(Q,\mu)\, H_q(Q,\mu)\,, \tag{3.48}$$

and accordingly their ν-RGE equations,

$$\nu\frac{\mathrm{d}}{\mathrm{d}\nu} B_q(x,\vec{q}_T,\mu,\nu) = \tilde{\gamma}_{\nu,B}^q(\vec{q}_T,\mu) \otimes_{\vec{q}_T} B_q(x,\vec{q}_T,\mu,\nu)\,, \tag{3.49}$$

$$\nu\frac{\mathrm{d}}{\mathrm{d}\nu} S_q(\vec{q}_T,\mu,\nu) = \tilde{\gamma}_{\nu,S}^q(\vec{q}_T,\mu) \otimes_{\vec{q}_T} S_q(\vec{q}_T,\mu,\nu)\,. \tag{3.50}$$

The $\tilde{\gamma}_{B,S}^q, \gamma_H^q$ are the quark μ anomalous dimensions and $\tilde{\gamma}_{\nu,S}^q, \tilde{\gamma}_{\nu,B}^q$ are the quark rapidity anomalous dimensions. They are defined as

$$\tilde{\gamma}_B^q(\mu,\nu/\omega)\,\delta^{(2)}(\vec{q}_T) = -Z_B^{-1}(\omega,\vec{q}_T,\mu,\nu) \otimes_{\vec{q}_T} \frac{\mathrm{d}}{\mathrm{d}\ln\mu} Z_B(\omega,\vec{q}_T,\mu,\nu)\,, \tag{3.51}$$

$$\tilde{\gamma}_S^q(\mu,\nu)\,\delta^{(2)}(\vec{q}_T) = -Z_S^{-1}(\vec{q}_T,\mu,\nu) \otimes_{\vec{q}_T} \frac{\mathrm{d}}{\mathrm{d}\ln\mu} Z_S(\vec{q}_T,\mu,\nu)\,, \tag{3.52}$$

$$\gamma_H^q(Q,\mu) = -Z_H^{-1}(Q,\mu) \times \frac{\mathrm{d}}{\mathrm{d}\ln\mu} Z_H(Q,\mu)\,, \tag{3.53}$$

$$\tilde{\gamma}_{\nu,B}^q(\vec{q}_T,\mu) = -Z_B^{-1}(\omega,\vec{q}_T,\mu,\nu) \otimes_{\vec{q}_T} \frac{\mathrm{d}}{\mathrm{d}\ln\nu} Z_B(\omega,\vec{q}_T,\mu,\nu)\,, \tag{3.54}$$

$$\tilde{\gamma}_{\nu,S}^q(\vec{q}_T,\mu) = -Z_S^{-1}(\vec{q}_T,\mu,\nu) \otimes_{\vec{q}_T} \frac{\mathrm{d}}{\mathrm{d}\ln\nu} Z_S(\vec{q}_T,\mu,\nu)\,. \tag{3.55}$$

[2] Here we implicitly assume that the rapidity divergences are regularized with the η regulator [69, 70], see section 2.3.5 for relevant discussion.

The μ anomalous dimensions have the all order structure,

$$\tilde{\gamma}_B^q(\mu,\nu/\omega) = 2\Gamma^q_{\rm cusp}[\alpha_s,\alpha_e]\ln\frac{\nu}{\omega} + \tilde{\gamma}_B^q[\alpha_s,\alpha_e]\,, \tag{3.56}$$

$$\tilde{\gamma}_S^q(\mu,\nu) = 4\Gamma^q_{\rm cusp}[\alpha_s,\alpha_e]\ln\frac{\mu}{\nu} + \tilde{\gamma}_S^q[\alpha_s,\alpha_e]\,, \tag{3.57}$$

$$\gamma_H^q(Q,\mu) = 4\Gamma^q_{\rm cusp}[\alpha_s,\alpha_e]\ln\frac{Q}{\mu} + 2\gamma_H^q[\alpha_s,\alpha_e] \tag{3.58}$$

where $\Gamma^q_{\rm cusp}$ are the quark cusp anomalous dimension, $\tilde{\gamma}^q_{B,S}, \gamma^q_H$ the quark noncusp anomalous dimensions and admit a perturbative expansion in both α_s, α_e. Note that we have left implicit the μ-dependence of both couplings $\alpha_s \equiv \alpha_s(\mu), \alpha_e \equiv \alpha_e(\mu)$.

The μ-independence of the cross section in eq. (3.38) dictates that the QCD⊗QED factorization satisfies the consistency relation,

$$\tilde{\gamma}_B^q(\mu,\nu/\omega) + \tilde{\gamma}_B^{\bar{q}}(\mu,\nu/\omega) + \tilde{\gamma}_S^q(\mu,\nu) + \gamma_H^q(Q,\mu) = 0 \tag{3.59}$$

$$\Rightarrow \qquad 2\tilde{\gamma}_B^q[\alpha_s,\alpha_e] + \tilde{\gamma}_S^q[\alpha_s,\alpha_e] + 2\gamma_H^q[\alpha_s,\alpha_e] = 0\,, \tag{3.60}$$

where between the first and the second line all cusp terms canceled, resulting to an all-order relation for the noncusp anomalous dimensions.

Accordingly, the ν-independence of the cross section implies the relation between the beam and soft rapidity anomalous dimensions,

$$\tilde{\gamma}^q_{\nu,S}(\vec{q}_T,\mu) + \tilde{\gamma}^q_{\nu,B}(\vec{q}_T,\mu) + \tilde{\gamma}^{\bar{q}}_{\nu,B}(\vec{q}_T,\mu) = 0\,, \tag{3.61}$$

$$\tilde{\gamma}^q_{\nu}(\vec{q}_T,\mu) \equiv \tilde{\gamma}^q_{\nu,S}(\vec{q}_T,\mu) = -2\tilde{\gamma}^q_{\nu,B}(\vec{q}_T,\mu)\,. \tag{3.62}$$

An important relation can be derived by noticing that the (μ,ν) path independence for the beam (or equivalently the soft) function,

$$\Big[\mu\frac{\mathrm{d}}{\mathrm{d}\mu}, \nu\frac{\mathrm{d}}{\mathrm{d}\nu}\Big] B_q(x,\vec{q}_T,\mu,\nu) = 0\,, \tag{3.63}$$

implies that the rapidity anomalous dimension satisfies the RGE,

$$\frac{\mathrm{d}}{\mathrm{d}\ln\mu}\tilde{\gamma}^q_{\nu}(\vec{q}_T,\mu) = -4\Gamma^q_{\rm cusp}[\alpha_s,\alpha_e]\,\delta^{(2)}(\vec{q}_T)\,. \tag{3.64}$$

The resummation of large double logarithms induced by soft and collinear *gluon and photon* emissions follows from the solution of the μ,ν-RGEs in eqs. (3.46)–(3.50). It effectively involves the evaluation of each function at its natural (*canonical*) scale where it is free of large logarithms and its evolution at an (arbitrary) common point in the (μ,ν) plane via the *Sudakov evolution kernel*. To illustrate the procedure, consider the solution of the hard function RGE, eq. (3.48),

$$H_q(Q,\mu) = H_q(Q,\mu_H)\,U^q(\mu_H,\mu)\,, \tag{3.65}$$

$$U^q(\mu_H,\mu) = \exp\bigg\{\int_{\mu_H}^{\mu}\frac{\mathrm{d}\mu'}{\mu'}4\Gamma^q_{\rm cusp}[\alpha_s(\mu'),\alpha_e(\mu')]\ln\frac{Q}{\mu'} + 2\gamma_H^q[\alpha_s(\mu'),\alpha_e(\mu')]\bigg\}\,. \tag{3.66}$$

On the RHS of eq. (3.65) the hard function is evaluated at its canonical scale μ_H and subsequently evolved at an arbitrary scale μ via the Sudakov evolution kernel $U^q(\mu_H, \mu)$. As it can be understood, of central importance for the resummation is the evaluation of the evolution kernel in eq. (3.66) and the perturbative ingredients (cusp and noncusp anomalous dimensions) that enter the RGE equations.

Concerning the former, an important observation is that the evolution kernel implicitly depends on the QCD and QED β-functions that control the renormalization group evolution of both couplings α_s, α_e which now are a *coupled system* of differential equations. This results into nontrivial implications for the evaluation of the evolution kernel that are not present in pure QCD. Therefore, in section 3.3.2 we discuss and provide with an analytic solution for such coupled β-functions which serves as an important input when in section 3.5 we study the evaluation of the Sudakov evolution kernel in the presence of multiple gauge interactions as that of QCD⊗QED.

Turning now to the perturbative ingredients, and for the pure QCD case, all the noncusp [2, 115–118] and rapidity anomalous dimensions [115, 119, 120] are known to three loops with the exception of Γ_{cusp} [121–130] and the QCD β-function [131–134] which are known to four loops. The entire fixed order μ, ν-dependence of $B_q, S_q, H_q, \tilde{\gamma}_\nu^q$ is dictated by their RGEs in eqs. (3.46)–(3.50) and eq. (3.64) which in section 4.3 we solve and derive their structure up to three loops $\mathcal{O}(\alpha_s^3)$.[3] For all functions, the boundary (μ, ν-independent) terms are also known at $\mathcal{O}(\alpha_s^3)$, see refs. [2, 115, 119, 135–140].

For the pure QED and mixed QCD-QED perturbative ingredients a procedure known as 'abelianization' was proposed in ref. [106, 108] for extracting them. It corresponds into taking the abelian limit of pure QCD coefficients while using a simple set of replacement rules between the $\text{SU}(3)_c$ Casimirs and the electromagnetic charges in QED. The very essence of this method lies in identifying the relevant QCD Feynman diagrams that contribute to the perturbative coefficient in question and replacing the gluons (one at a time) with photons while properly accounting for (i) the change of the gauge group's generators (ii) the multiplicity factors resulting from $g \mapsto \gamma$ replacement (iii) the extension of matter fields to both quarks and leptons when they couple only to photons. Although this method is particularly useful and straightforward at lower orders, it gets quickly cumbersome (and full of caveats) at higher orders as it requires to have a complete handle over the basic topologies of the contributing Feynman diagrams. In ref. [141] it was shown that certain color factors appearing in three loop (pure) QCD Feynman diagrams do not have an unambiguous mapping to mixed QCD-QED, which implies that there is a natural limitation to this procedure, at least in full generality.[4] Using the 'abelianization' procedure we have extracted all the pure QED and mixed QCD-QED ingredients relevant for QCD⊗QED q_T-resummation at NNLL order. These include the three-loop cusp, the two-loop hard, soft, beam noncusp and rapidity anomalous dimensions as well as their one-loop boundary terms. Together with the corresponding pure QED and mixed QCD-QED β-function coefficients,

[3] For the three loop μ-dependent structure of the hard function H_q, see ref. [135].

[4] As the authors of ref. [141] also mention, it may happen that certain color factors do not appear in higher order pure QCD coefficients and therefore their 'abelianization' is unambiguous.

they are collected in appendix B.2.

Concluding, we comment that since the inclusion of QED ISR effects involves a straightforward generalization of the soft and collinear Wilson lines such that the corresponding photon interactions are taken into account, it is expected that a similar QCD⊗QED factorization is also valid for a variety of other resolution variables. One of them is 0-jettinness ($\mathcal{T}_0$) [65, 142] although a formal derivation of its factorization differs from the one presented in this section since it is a $\mathrm{SCET_I}$ observable.

3.3 Iterative solutions to β-function RGEs

Before discussing the evaluation of the Sudakov evolution kernel, it is important to analyze one of its key ingredients, namely the solution of the β-function RGE of the coupling constant. In section 3.3.1, we review the well-known case of a single gauge theory, with particular attention given to the numerical accuracy of different approximate analytic RGE solutions. In section 3.3.2 we then discuss the solution of the coupled RGE system for the coupling constants of two gauge theories.

3.3.1 Single gauge theory

We start from the well-known β-function RGE for the coupling constant $\alpha(\mu)$ of a generic gauge theory,

$$\begin{aligned}\frac{\mathrm{d}\alpha(\mu)}{\mathrm{d}\ln\mu} \equiv \beta[\alpha(\mu)] &= -2\alpha(\mu)\sum_{n=0}^{\infty}\epsilon^n\beta_n\Big[\frac{\alpha(\mu)}{4\pi}\Big]^{n+1}\\ &= -2\beta_0\,\frac{\alpha(\mu)^2}{4\pi}\left[1+\epsilon\,\frac{\alpha(\mu)}{4\pi}\,b_1+\epsilon^2\,\frac{\alpha(\mu)^2}{(4\pi)^2}\,b_2+\mathcal{O}(\epsilon^3)\right],\end{aligned} \tag{3.67}$$

where we introduced a formal expansion parameter $\epsilon \equiv 1$, which we use to keep track of the evolution order. The perturbative coefficients b_n in the second line are defined by the ratio

$$b_n = \frac{\beta_n}{\beta_0}\,. \tag{3.68}$$

We take the viewpoint that eq. (3.67) *defines* the running order of the RGE. That is, keeping the terms up to $\mathcal{O}(\epsilon^k)$ in eq. (3.67) defines the $\mathrm{N^kLO}$ or $(k+1)$-loop running of $\alpha(\mu)$. At leading order, $\mathcal{O}(\epsilon^0)$, eq. (3.67) has the well-known exact analytic solution,

$$\alpha(\mu) = \frac{\alpha(\mu_0)}{X}\,, \qquad X \equiv X(\mu_0,\mu) = 1+\frac{\alpha(\mu_0)}{2\pi}\,\beta_0\,\ln\frac{\mu}{\mu_0}\,, \tag{3.69}$$

where $\alpha(\mu_0)$ is a boundary condition for the coupling constant.

As is well known, eq. (3.67) does not admit an exact analytic solution at NLO and beyond.[5] While the exact solution can be easily obtained numerically using standard

[5] More precisely, eq. (3.67) can still be integrated analytically at NLO and even NNLO. The resulting expressions, however, cannot be analytically solved for $\alpha(\mu)$ in terms of $\alpha(\mu_0)$ anymore.

numerical differential-equation solvers, in practice it is often more convenient to have an approximate analytic solution that can be evaluated much faster than the numerical solution, which becomes important when the scale μ is not fixed but dynamical. This is precisely the case for the Sudakov evolution kernel, for which we will need to integrate $\alpha(\mu)$ over μ.

First we review an iterative method to obtain an approximate analytic solution for eq. (3.67). At NLO, $\mathcal{O}(\epsilon)$, the β-function RGE reads

$$\begin{aligned}\frac{\mathrm{d}\alpha(\mu)}{\mathrm{d}\ln\mu} &= -2\beta_0\frac{\alpha(\mu)^2}{4\pi}\left[1+\epsilon\,\frac{\alpha(\mu)}{4\pi}\,b_1\right]\\ &= -2\beta_0\frac{\alpha(\mu)^2}{4\pi}\left[1+\epsilon\,\frac{\alpha(\mu_0)}{4\pi}\,\frac{b_1}{X(\mu_0,\mu)}+\mathcal{O}(\epsilon^2)\right].\end{aligned} \tag{3.70}$$

In the second line we substituted the LO solution in eq. (3.69) for the μ dependence of $\alpha(\mu)$ in the $\mathcal{O}(\epsilon)$ term. This induces an $\mathcal{O}(\epsilon^2)$ error, since the difference between the LO and NLO μ dependence will itself be of $\mathcal{O}(\epsilon)$. Since the μ dependence in the term in square brackets is now explicit, it can be easily integrated, yielding the NLO solution

$$\begin{aligned}&\frac{1}{\alpha(\mu)} = \frac{X}{\alpha(\mu_0)}+\epsilon\,\frac{b_1}{4\pi}\,\ln X\,,\\ \Rightarrow\qquad &\alpha(\mu) = \alpha(\mu_0)\left[X+\epsilon\,\frac{\alpha(\mu_0)}{4\pi}\,b_1\ln X\right]^{-1}.\end{aligned} \tag{3.71}$$

We refer to this (and its higher-order analogues) as the "iterative" solution for $\alpha(\mu)$. We can also expand the inverse in eq. (3.71) in ϵ to obtain

$$\alpha(\mu) = \frac{\alpha(\mu_0)}{X}\left[1-\epsilon\,\frac{\alpha(\mu_0)}{4\pi}\,b_1\,\frac{\ln X}{X}+\mathcal{O}(\epsilon^2)\right]. \tag{3.72}$$

We will refer to eq. (3.72) (and its higher-order analogues) as the "expanded" solution.

One might wonder whether the iterative or expanded solution provides a better approximation to the exact solution, and to this end it is instructive to see to what extent they satisfy the original β-function RGE. For the iterative solution in eq. (3.71), it is trivial to verify that upon differentiation with respect to $\ln\mu$ it reproduces the RGE as given in the second line of eq. (3.70). On the other hand, taking the $\ln\mu$ derivative of the expanded NLO solution in eq. (3.72) yields

$$\begin{aligned}\frac{\mathrm{d}\alpha(\mu)}{\mathrm{d}\ln\mu} &= -2\beta_0\,\frac{\alpha(\mu_0)^2}{4\pi}\,\frac{1}{X^2}\left[1+\epsilon\,\frac{\alpha(\mu_0)}{4\pi}\,b_1\,\frac{1-2\ln X}{X}\right]\\ &= -2\beta_0\,\frac{\alpha(\mu_0)^2}{4\pi}\,\frac{1}{X^2}\left\{\left[1-2\epsilon\,\frac{\alpha(\mu_0)}{4\pi}\,b_1\,\frac{\ln X}{X}\right]+\epsilon\,\frac{\alpha(\mu_0)}{4\pi}\,\frac{b_1}{X}\right\}.\end{aligned} \tag{3.73}$$

Comparing this with eqs. (3.70) and (3.72), we see that the term in square brackets corresponds to expanding the overall $\alpha(\mu)^2$ in the β-function to $\mathcal{O}(\epsilon)$. This clearly amounts to a further approximation, so we can expect the expanded solution in general to provide a worse approximation, which is indeed what we find numerically below.

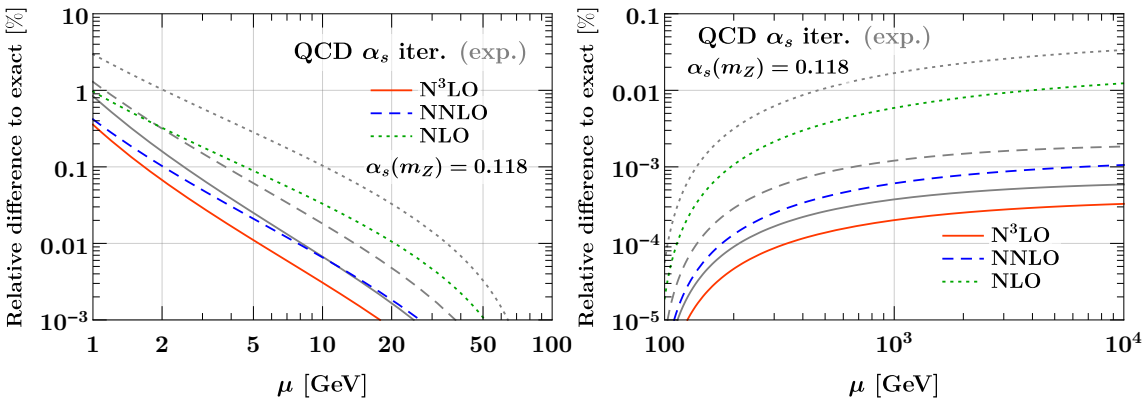

Figure 3.1: Relative deviation of the iterative (colored) and expanded solutions (gray) from the exact solution for the running of $\alpha_s(\mu)$ at NLO (dotted), NNLO (dashed), and N^{3}LO (solid).

The iterative solution at NNLO, $\mathcal{O}(\epsilon^2)$, follows analogously. Starting from the exact NNLO RGE, we substitute the (expanded) NLO and LO solutions, eqs. (3.72) and (3.69), in the $\mathcal{O}(\epsilon)$ and $\mathcal{O}(\epsilon^2)$ terms, keeping all terms up to $\mathcal{O}(\epsilon^2)$ as well as the overall $\alpha(\mu)^2$,

$$\begin{aligned}\frac{\mathrm{d}\alpha(\mu)}{\mathrm{d}\ln\mu} &= -2\beta_0\frac{\alpha(\mu)^2}{4\pi}\left[1+\epsilon\,\frac{\alpha(\mu)}{4\pi}\,b_1+\epsilon^2\frac{\alpha(\mu)^2}{(4\pi)^2}\,b_2\right]\\ &= -2\beta_0\frac{\alpha(\mu)^2}{4\pi}\left[1+\epsilon\,\frac{\alpha(\mu_0)}{4\pi}\,\frac{b_1}{X}+\epsilon^2\,\frac{\alpha(\mu_0)^2}{(4\pi)^2}\,\frac{b_2-b_1^2\,\ln X}{X^2}+\mathcal{O}(\epsilon^3)\right].\end{aligned} \tag{3.74}$$

The μ-dependence in the square brackets on the second line, encoded in $X \equiv X(\mu_0,\mu)$, is again simple enough to be integrated analytically.[6] This yields the NNLO iterative solution

$$\alpha(\mu) = \alpha(\mu_0)\left\{X+\epsilon\,\frac{\alpha(\mu_0)}{4\pi}\,b_1\ln X+\epsilon^2\,\frac{\alpha(\mu_0)^2}{(4\pi)^2}\left(b_2\,\frac{X-1}{X}+b_1^2\,\frac{1-X+\ln X}{X}\right)\right\}^{-1}. \tag{3.75}$$

Expanding the inverse in eq. (3.75) in ϵ, we obtain the expanded NNLO solution,

$$\begin{aligned}\alpha(\mu) = \frac{\alpha(\mu_0)}{X}\Bigg\{&1-\epsilon\,\frac{\alpha(\mu_0)}{4\pi}\,b_1\,\frac{\ln X}{X}\\ &+\epsilon^2\,\frac{\alpha(\mu_0)^2}{(4\pi)^2}\,\frac{1}{X^2}\Big[b_2(1-X)+b_1^2\,(\ln^2 X-\ln X-1+X)\Big]+\mathcal{O}(\epsilon^3)\Bigg\}.\end{aligned} \tag{3.76}$$

It is straightforward to extend the iterative solution to higher orders. To obtain the N^{k}LO solution, one simply inserts the N^{k-1}LO solution for $\alpha(\mu)$ into the N^{k}LO β-function and expands it to $\mathcal{O}(\epsilon^k)$, while keeping the overall $\alpha(\mu)^2$ exact. The N^{3}LO solution is given in appendix B.5.

To illustrate the numerical precision of the approximate analytic solutions, we take the QCD coupling constant $\alpha_s(\mu)$ as an example, using $m_Z = 91.1876\,\mathrm{GeV}$ and $\alpha_s(m_Z) = 0.118$

[6] This would not be the case had we used the unexpanded NLO solution from eq. (3.71) in the $\mathcal{O}(\epsilon)$ term.

as our boundary condition. The β-function coefficients are given in appendix B.1. As we are primarily interested in the numerical precision of the solution, we always use $n_f = 5$ massless flavors and do not consider any flavor thresholds. The difference of the iterative and expanded solutions to the exact[7] numerical solution, which we refer to as the approximation error, is shown in figure 3.1 for different running orders.

The approximation error decreases as the order increases, as expected. The approximation error is largest for running from m_Z down to lower scales, since here the running increases the coupling. The iterative solution still provides an excellent approximation, with the error at NNLO and beyond reaching at most 0.1% when running down to $\mu = 2\,\text{GeV}$, and at most 0.3% at $\mu = 1\,\text{GeV}$. For running above m_Z, the approximation error is much smaller due to asymptotic freedom. Beyond the highest scale shown, $\mu = 10^4\,\text{GeV}$, the error stops growing and at some point starts decreasing again. We also observe that the approximation error for the expanded solution (gray lines) is always 2-3 times larger than for the iterative solution.

3.3.2 Two coupled gauge theories

We now consider the case of two gauge theories. Their β-functions become coupled as soon as there are matter fields that are charged under both gauge interactions, since loops of matter particles can exchange the gauge bosons from both theories. The example we will eventually consider is the mixed QCD⊗QED running. For now, we keep the discussion general and consider the following set of coupled β-function RGEs for two gauge couplings $\alpha_a(\mu)$ and $\alpha_b(\mu)$,

$$\begin{aligned}
\frac{\mathrm{d}\alpha_a(\mu)}{\mathrm{d}\ln\mu} &\equiv \beta^a[\alpha_a(\mu),\alpha_b(\mu)] = -2\alpha_a(\mu)\sum_{n,k=0}^{\infty}\epsilon_a^n\epsilon_b^k\,\beta^a_{nk}\left[\frac{\alpha_a(\mu)}{4\pi}\right]^{n+1}\left[\frac{\alpha_b(\mu)}{4\pi}\right]^{k},\\
\frac{\mathrm{d}\alpha_b(\mu)}{\mathrm{d}\ln\mu} &\equiv \beta^b[\alpha_b(\mu),\alpha_a(\mu)] = -2\alpha_b(\mu)\sum_{n,k=0}^{\infty}\epsilon_b^n\epsilon_a^k\,\beta^b_{nk}\left[\frac{\alpha_b(\mu)}{4\pi}\right]^{n+1}\left[\frac{\alpha_a(\mu)}{4\pi}\right]^{k}.
\end{aligned}\tag{3.77}$$

We have again introduced formal expansion parameters $\epsilon_{a,b} \equiv 1$ to easily keep track of the evolution order. For future convenience, we also define the rescaled coefficients

$$b^a_{nk} = \frac{\beta^a_{nk}}{\beta^a_{00}}\,,\qquad b^b_{nk} = \frac{\beta^b_{nk}}{\beta^b_{00}}\,,\qquad\text{and}\qquad b^a_0 = \frac{\beta^a_{00}}{\beta^b_{00}}\,,\qquad b^b_0 = \frac{\beta^b_{00}}{\beta^a_{00}}\,.\tag{3.78}$$

Note that by definition $\beta^x_{n0} \equiv \beta_n$ and $b^x_{n0} \equiv b_n$ are the coefficients of the individual gauge theories in the absence of the second.

As before, the order in $\epsilon_{a,b}$ to which eq. (3.77) is expanded is what defines the running order of the couplings. Generically, we consider $\epsilon_{a,b}$ on equal footing and define the N^{n}LO evolution by including in eq. (3.77) all terms of $\mathcal{O}(\epsilon_a^k\epsilon_b^{n-k})$ with $0 \le k \le n$. Note that this also makes it easy to have well-defined mixed orders, e.g., when there is a hierarchy between

[7] We always perform the numerical solution with sufficiently high numerical precision such that the numerical error is completely negligible for our purposes.

the two couplings, as is the case for QCD and QED. For this purpose, one can simply specify the explicit combinations of powers of ϵ_a and ϵ_b that are included in eq. (3.77).

As in the single gauge scenario, an exact solution to the coupled system of differential equations can be obtained straightforwardly at any given order by solving it numerically. Our goal is to derive an approximate analytic solution for the coupled β-function RGE system by extending the iterative method in section 3.3.1. The key property of eq. (3.77) that allows us to do so is that, at leading order, $\mathcal{O}(\epsilon_a^0, \epsilon_b^0)$, the RGE system decouples, yielding exact LO solutions:

$$\begin{aligned} \alpha_a(\mu) &= \frac{\alpha_a(\mu_0)}{X_a}\,, \qquad X_a \equiv X_a(\mu_0,\mu) = 1 + \frac{\alpha_a(\mu_0)}{2\pi}\,\beta_{00}^a\,\ln\frac{\mu}{\mu_0}\,, \\ \alpha_b(\mu) &= \frac{\alpha_b(\mu_0)}{X_b}\,, \qquad X_b \equiv X_b(\mu_0,\mu) = 1 + \frac{\alpha_b(\mu_0)}{2\pi}\,\beta_{00}^b\,\ln\frac{\mu}{\mu_0}\,. \end{aligned} \tag{3.79}$$

To obtain an approximate NLO solution, it then suffices to substitute the above LO solutions into the $\mathcal{O}(\epsilon_a)$ and $\mathcal{O}(\epsilon_b)$ terms of the NLO RGE system, which induces $\mathcal{O}(\epsilon_a^2, \epsilon_a\epsilon_b, \epsilon_b^2)$ errors,

$$\begin{aligned} \frac{\mathrm{d}\alpha_a(\mu)}{\mathrm{d}\ln\mu} &= -2\beta_{00}^a\frac{\alpha_a(\mu)^2}{4\pi}\left[1 + \epsilon_a\,\frac{\alpha_a(\mu)}{4\pi}\,b_{10}^a + \epsilon_b\,\frac{\alpha_b(\mu)}{4\pi}\,b_{01}^a\right] \\ &= -2\beta_{00}^a\frac{\alpha_a(\mu)^2}{4\pi}\left[1 + \epsilon_a\,\frac{\alpha_a(\mu_0)}{4\pi}\,\frac{b_{10}^a}{X_a(\mu_0,\mu)} + \epsilon_b\,\frac{\alpha_b(\mu_0)}{4\pi}\,\frac{b_{01}^a}{X_b(\mu_0,\mu)} + \mathcal{O}(\epsilon_a^2, \epsilon_a\epsilon_b, \epsilon_b^2)\right]. \end{aligned} \tag{3.80}$$

The terms in square brackets can now be explicitly integrated over $\ln\mu$ to obtain the iterative NLO solution

$$\alpha_a(\mu) = \alpha_a(\mu_0)\left[X_a + \frac{\alpha_a(\mu_0)}{4\pi}\Big(\epsilon_a\,b_{10}^a\,\ln X_a + \epsilon_b\,b_0^a\,b_{01}^a\,\ln X_b\Big)\right]^{-1}. \tag{3.81}$$

The solution for $\alpha_b(\mu)$ is given by replacing $a \leftrightarrow b$ everywhere.

Note that in eq. (3.81) the utility of the $\epsilon_{a,b}$ counting parameters becomes evident. Naively, one might have expected that the $\mathcal{O}(\epsilon_a)$ and $\mathcal{O}(\epsilon_b)$ terms will be proportional to $\alpha_a(\mu_0)$ and $\alpha_b(\mu_0)$ respectively, which however is not the case, as both are proportional to $\alpha_a(\mu_0)$. Instead, the $\epsilon_{a,b}$ actually keep track of the fact that the $\ln X_{a,b}$ factors respectively resum a series of $\alpha_{a,b}^n \ln^n(\mu/\mu_0)$ terms.

The iterative NNLO solution is obtained by substituting the NLO solutions into the β-function RGE system and expanding it to $\mathcal{O}(\epsilon_a^2, \epsilon_a\epsilon_b, \epsilon_b^2)$, while keeping the overall $\alpha_{a,b}(\mu)^2$ exact. We find

$$\begin{aligned} \frac{\alpha_a(\mu_0)}{\alpha_a(\mu)} &= X_a + \epsilon_a\,\frac{\alpha_a(\mu_0)}{4\pi}\,b_{10}^a\ln X_a + \epsilon_a^2\,\frac{\alpha_a(\mu_0)^2}{(4\pi)^2}\left(b_{20}^a\,\frac{X_a-1}{X_a} + (b_{10}^a)^2\frac{1-X_a+\ln X_a}{X_a}\right) \\ &\quad + \epsilon_b\frac{\alpha_a(\mu_0)}{4\pi}\,b_0^a\,b_{01}^a\ln X_b + \epsilon_b^2\frac{\alpha_a(\mu_0)\alpha_b(\mu_0)}{(4\pi)^2}b_0^a\left(b_{02}^a\frac{X_b-1}{X_b} + b_{01}^a b_{10}^b\frac{1-X_b+\ln X_b}{X_b}\right) \\ &\quad + \epsilon_a\epsilon_b\,\frac{\alpha_a(\mu_0)}{b_0^a\,\alpha_a(\mu_0) - \alpha_b(\mu_0)}\left[\frac{\alpha_a^2(\mu_0)}{(4\pi)^2}(b_0^a)^2 b_{10}^a b_{01}^a\left(\frac{X_b}{X_a}\ln X_b - \frac{1-X_b}{1-X_a}\ln X_a\right)\right. \\ &\quad \left. - \frac{\alpha_b^2(\mu_0)}{(4\pi)^2}\,b_{01}^a b_{01}^b\left(\frac{X_a}{X_b}\ln X_a - \frac{1-X_a}{1-X_b}\ln X_b\right) + \frac{\alpha_a(\mu_0)\alpha_b(\mu_0)}{(4\pi)^2}b_0^a\,b_{11}^a\ln\frac{X_a}{X_b}\right]. \end{aligned} \tag{3.82}$$

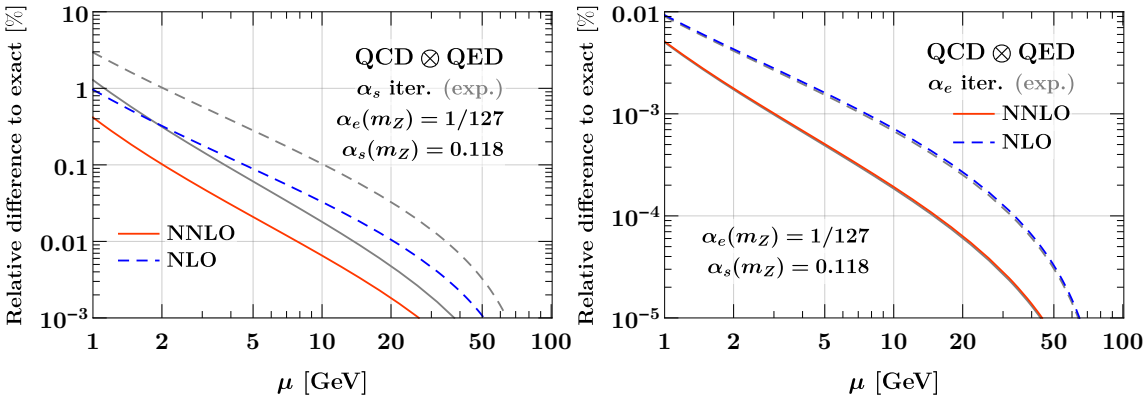

Figure 3.2: Relative deviation from the exact solution for the running of the QCD (left) and QED (right) coupling constants in QCD⊗QED for the iterative (colored) and expanded (gray) solutions.

As before, the solution for $\alpha_b(\mu)$ is obtained by replacing $a \leftrightarrow b$. The terms in the first line correspond to the NNLO solution of α_a in the absence of α_b, while the remaining ones are the mixing contributions involving at least one power of ϵ_b. The corresponding expanded solution is obtained by inverting eq. (3.82) and expanding it in ϵ_i. Note that when doing so, it becomes essential to expand in terms of ϵ_i and not $\alpha_i(\mu_0)$. The necessity of using ϵ_i as expansion parameter is also evident in the mixed $\mathcal{O}(\epsilon_a\epsilon_b)$ term in square brackets, which involves a nontrivial rational function of both couplings. The iterative NNLO solution in eq. (3.82) constitutes a central ingredient for the seminumerical evaluation of the Sudakov evolution factor in section 3.5.

To illustrate the approximation error for the two analytic solutions, we consider the case of QCD⊗QED. The relevant coefficients for the coupled β-function RGE to NNLO are given in appendices B.1 and B.2. Curiously, we were not able to find explicit expressions in the literature for the mixed three-loop QED coefficient β^e_{11}. We therefore performed an explicit extraction of all mixed three-loop coefficients from the general results for a generic product group given in ref. [143], as discussed in more detail in appendix C.

For the numerical results, we use $m_Z = 91.1876\,\text{GeV}$ with $\alpha_s(m_Z) = 0.118$, $\alpha_e(m_Z) = 1/127$ as boundary conditions, $n_f = 5$ for the number of active quark flavors, and $n_\ell = 3$ for the number of active charged leptons. As before we do not consider any flavor thresholds.

The approximation error of the iterative (expanded) solution relative to the exact numerical solution is shown in figure 3.2 by the colored (gray) lines at NLO (dashed) and NNLO (solid). For the strong coupling constant (left panel), the approximation error for the iterative solution does not exceed 1%, and it is again 2-3 times larger for the expanded solution. For the QED coupling constant (right panel), the approximation error is much smaller owing to the fact that α_e is much smaller, and therefore both the iterative and expanded solutions yield equally good approximations. It is interesting to see the individual effects of various terms in the coupled β-function. In figures 3.3 and 3.4 we show them for the case of QCD⊗QED as well as for a toy QCD⊗QED′ for which we set the boundary condition to $\alpha'_e(m_Z) = 1/10$. In figure 3.3, as expected, the QED corrections $\sim \mathcal{O}(\epsilon_s^0, \epsilon_e^1)$

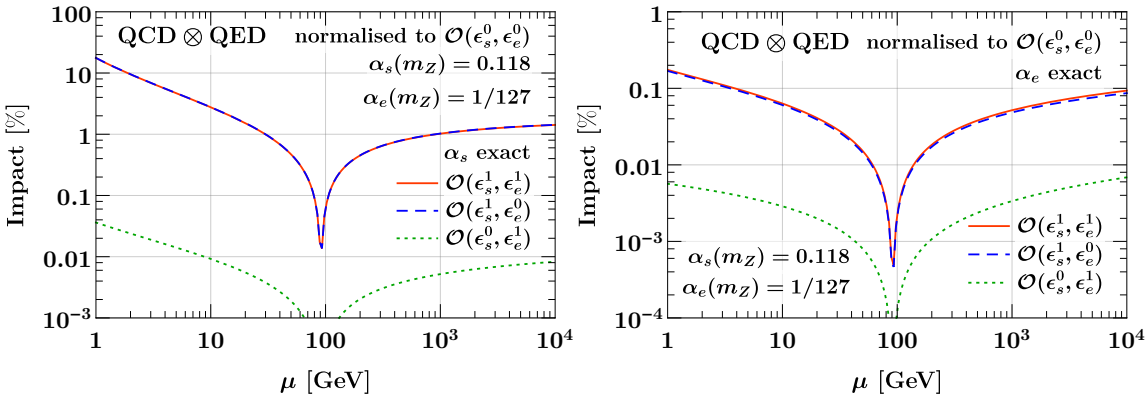

Figure 3.3: Impact of different higher-order terms on the running of the QCD (left) and QED (right) couplings. Shown are the relative differences to the LO running $\sim \mathcal{O}(\epsilon_s^0, \epsilon_e^0)$.

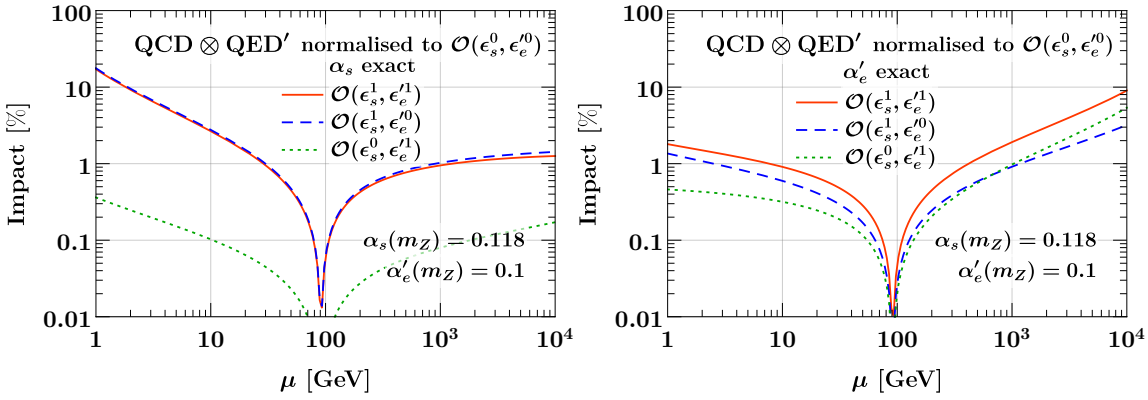

Figure 3.4: Same as figure 3.3 but for QCD⊗QED′, where QED′ is a toy theory with a modified boundary condition of $\alpha_e'(m_Z) = 0.1$.

have almost negligible effect on α_s, with only the higher order QCD corrections $\sim \mathcal{O}(\epsilon_s^1, \epsilon_e^0)$ being relevant. This is also the case for the QED coupling constant, whose evolution is almost entirely dictated by the QCD corrections. But this is not the case for the toy QCD⊗QED′ scenario shown in figure 3.4. The fact that the QCD coupling constant is still almost unaffected by the QED′ corrections is somewhat accidental and due to the fact that the β-function coefficients β_{10}^s and β_{01}^s differ numerically by an order of magnitude. On the other hand, the QED′ coupling constant now has comparable higher-order QCD and QED′ corrections since here both β-function coefficients are of similar numerical size.

3.4 Sudakov evolution kernels with a single gauge interaction

In this section, we examine different strategies for evaluating the Sudakov evolution kernel for the case of a single gauge interaction, with particular emphasis on their numerical accuracy and reliability. This will then serve as a guide when considering the two-dimensional case in section 3.5. In section 3.4.1, we start with a general discussion and give an overview of the different methods we study for evaluating the Sudakov evolution factor, which are then elaborated on in section 3.4.2 to section 3.4.5. We then provide a detailed numerical comparison in section 3.4.6.

3.4.1 General overview

All ingredients of a factorized cross section obey RGEs of the form

$$\frac{\mathrm{d}F(\mu)}{\mathrm{d}\ln\mu} = \gamma_F(\mu) \otimes F(\mu)\,, \tag{3.83}$$

as we explicitly saw in section 3.2 in the context of q_T factorization. Here, the function $F(\mu)$ can be any of the factorized ingredients (e.g. H_q, B_q or S_q) and $\gamma_F(\mu)$ is the corresponding anomalous dimension. In general, $\gamma_F(\mu)$ and $F(\mu)$ both depend on an additional external kinematic quantity (which appears as part of the argument of the Sudakov logarithms in the cross section). The $\otimes$ denotes the fact that γ_F and F are not necessarily multiplied but could be convolved in said kinematic variable (e.g. see eqs. (3.49) and (3.50)). It is worth noting that the convolution structure can play a significant role in the solution of eq. (3.83) and for a detailed discussion see ref. [144]. However, it does not play any role for the purpose of our discussion, so we consider only the simplest multiplicative case. In case of a convolution, one can always transform to a suitable conjugate space (e.g. Fourier or Laplace space), where the convolution turns into a simple product.[8] The Sudakov evolution factor in that conjugate space then has the same general form we discuss here and all our conclusions apply equally.

The all-order expansion of the anomalous dimension is given by

$$\gamma_F(\mu) = \frac{1}{\epsilon}\,\Gamma_{\mathrm{cusp}}[\alpha(\mu)]\ln\frac{Q}{\mu} + \gamma[\alpha(\mu)]\,, \tag{3.84}$$

where Q denotes the above-mentioned kinematic quantity, Γ_{cusp} is (proportional to) the cusp anomalous dimension, and γ is the noncusp anomalous dimension. They obey the perturbative expansions

$$\Gamma_{\mathrm{cusp}}(\alpha) = \sum_{n=0}^{\infty} \epsilon^{n+1}\,\Gamma_n \left(\frac{\alpha}{4\pi}\right)^{n+1}, \qquad \gamma(\alpha) = \sum_{n=0}^{\infty} \epsilon^{n+1}\,\gamma_n \left(\frac{\alpha}{4\pi}\right)^{n+1}. \tag{3.85}$$

[8] In fact, this is the most common way of performing q_T resummation and we explicitly employ it in chapter 5 for the phenomenological study on the Higgs transverse momentum spectrum.

Order	Γ_{cusp}	γ	β
LL	1-loop	-	1-loop
NLL	2-loop	1-loop	2-loop
NNLL	3-loop	2-loop	3-loop
N^3LL	4-loop	3-loop	4-loop

Table 3.1: The necessary perturbative coefficients for the Sudakov evolution factor at each resummation order. Γ_{cusp} is the cusp anomalous dimension, γ is the noncusp anomalous dimensions and β is the beta function for the running of the coupling.

We have again introduced the formal expansion parameter $\epsilon \equiv 1$, which we use to define the resummation order. Since the μ dependence of $\gamma_F(\mu)$ primarily enters via the coupling constant's μ dependence, the β-RGE for $\alpha(\mu)$ in eq. (3.67) is an integral part of the full RGE system to be solved. In particular, the ϵ parameter in eqs. (3.84) and (3.85) is the same that appears in eq. (3.67).

As for the case of the coupling constant before, the truncation of eq. (3.84) together with eq. (3.67) to a certain order in ϵ fundamentally *defines* the resummation order. That is, keeping terms up to $\mathcal{O}(\epsilon^k)$ defines the Sudakov evolution at N^kLL order. The explicit $1/\epsilon$ factor for the cusp term accounts for the fact that it comes with an additional explicit logarithm relative to the noncusp term. As a result, the noncusp term always enters at one lower order in perturbation theory than the cusp term. And since the β-function in eq. (3.67) starts at $\mathcal{O}(\epsilon^0)$, it enters at the same loop order as the cusp anomalous dimension. So at N^kLL order we require the $k+1$-loop cusp and beta function coefficients and the k-loop noncusp coefficients.

Solving the RGE in eq. (3.83), one finds

$$F(\mu) = F(\mu_0)U(\mu_0,\mu)\,, \tag{3.86}$$

where $U(\mu_0,\mu)$ is the Sudakov evolution factor given by

$$U(\mu_0,\mu) = \exp\left\{\int_{\mu_0}^{\mu}\frac{\mathrm{d}\mu'}{\mu'}\gamma_F(\mu')\right\} = \exp\left\{\int_{\mu_0}^{\mu}\frac{\mathrm{d}\mu'}{\mu'}\,\frac{1}{\epsilon}\,\Gamma_{\text{cusp}}[\alpha(\mu')]\ln\frac{Q}{\mu'} + \gamma[\alpha(\mu')]\right\}. \tag{3.87}$$

It resums the Sudakov logarithms appearing in the perturbative series of $F(\mu)/F(\mu_0)$. One can easily check that counting powers of ϵ in the anomalous dimension is equivalent to counting powers of logarithms in the Sudakov exponent, simply because the entire structure of $U(\mu_0,\mu)$ is fully encoded by the anomalous dimension. This can be easily seen by considering for example the case $\mu_0 = Q$ in eq. (3.86), which up to $\mathcal{O}(\epsilon)$ reads

$$\frac{F(\mu)}{F(Q)} = \exp\left\{\int_{Q}^{\mu}\frac{\mathrm{d}\mu'}{\mu'}\left[\Gamma_0\ln\frac{Q}{\mu'}a + \epsilon(\Gamma_1\ln\frac{Q}{\mu'}a^2 + \gamma_0 a) + \mathcal{O}(\epsilon^2)\right]\right\}, \tag{3.88}$$

where $a \equiv \alpha/(4\pi)$. Now taking also into account the running of the coupling α, we can perform the integration and cast the exponent into the form

$$\frac{F(\mu)}{F(Q)} = \exp\Big\{ \quad \epsilon^0\Big[-\frac{1}{2}\Gamma_0\, aL^2 - \frac{2}{3}\beta_0\Gamma_0\, a^2L^3 \qquad\qquad + \mathcal{O}(a^nL^{n+1})\Big] \\ +\epsilon\Big[-\frac{1}{2}\Gamma_1\, a^2L^2 - \gamma_0\, a\, L - \frac{2}{3}\Gamma_0\beta_1 a^3L^3 + \mathcal{O}(a^nL^n)\Big] \quad + \quad \mathcal{O}(\epsilon^2)\Big\}, \quad (3.89)$$

where we abbreviated the (potentially large) logarithm $L \equiv \ln(Q/\mu)$. Thus, we see that the exponent sums an infinite tower of logarithms $a^nL^{n+1} \sim \mathcal{O}(\epsilon^0)$ which corresponds to LL accuracy, $a^nL^n \sim \mathcal{O}(\epsilon^1)$ which corresponds to NLL accuracy, and so on. In table 3.1 we summarize the perturbative coefficients necessary to achieve certain logarithmic accuracy for the Sudakov evolution factor.

In the final resummed cross section, where $F(\mu)$ is combined with other ingredients, $U(\mu_0, \mu)$ eventually appears with both scales μ and μ_0 corresponding to two different kinematic quantities such that $U(\mu_0, \mu)$ resums (part of) the Sudakov logarithms of the ratio of these quantities.

We stress that while we obtained eq. (3.87) starting from the RGE in eq. (3.83), a Sudakov evolution factor of the same structure (necessarily) appears in all the various approaches for performing Sudakov resummation that exist in the literature. This includes EFT-based and non-EFT-based approaches, and both analytic as well as numerical Monte-Carlo techniques such as parton showers.

On the other hand, different implementations tend to follow different strategies for evaluating the integral in the Sudakov exponent. In the following sections we investigate several methods for doing so, paying close attention to where additional assumptions and/or approximations are made. As we show, additional approximations that may appear mathematically justified can still conspire to yield results for eq. (3.87) that exhibit nontrivial numerical differences. We investigate the following methods in the sections that follow:

- **Numerical:** In this method, both the β-function RGE eq. (3.67) and the evolution kernel eq. (3.87) are evaluated fully numerically (with sufficiently high numerical precision that numerical integration errors are negligible). This provides the exact solution of the complete Sudakov RGE system at a given resummation order as defined above, and we use it as the benchmark to compare the other methods against. As this method can be computationally expensive, it is often not very suitable for practical purposes.

- **Seminumerical:** One option to speed up the fully numerical method is to employ an approximate analytic solution to the β-function RGE, but to perform the kernel integration numerically. In other words, we numerically integrate eq. (3.87) but with the iterative analytic solution for $\alpha(\mu)$ used in the perturbative expansion of the anomalous dimensions. This is described along with the fully numerical method in section 3.4.2.

- **Unexpanded analytic:** Approximate but fully analytic, closed-form expressions for eq. (3.87) can be obtained. One way to achieve this is to exploit the β-function to turn the μ integration into an integration over α, which can be performed analytically after some expansion in ϵ. This is combined with the analytic iterative solution for $\alpha(\mu)$ as input. We give details of the derivation and the resulting forms explicitly in section 3.4.3.

- **Expanded analytic:** Another way to obtain an approximate closed-form result for eq. (3.87) is to insert the analytic solution for $\alpha(\mu)$ in eq. (3.76) in the perturbative expansions of $\Gamma(\alpha)$ and $\gamma(\alpha)$ and fully expand the integrand in ϵ. The integration can then be performed directly in terms of μ. This method is described in more detail in section 3.4.4.

- **Reexpanded analytic:** Finally, to connect to some of the available literature, we elaborate another analytic approach where, upon achieving the expanded analytic evolution kernels, one further expands $\alpha(\mu_0)$ in terms of $\alpha(\mu_R)$ at a different reference scale μ_R, assuming that $\mu_0 \sim \mu_R$, i.e., that there is no hierarchy between them. This method is discussed in more detail in section 3.4.5.

Given these five methods of integration, we probe their reliability in two different ways in section 3.4.6: *closure tests* and *approximation errors*. The latter simply tests the absolute difference between any one method and the numerically exact method described above. The closure test provides a test of the mathematical consistency of the evolution factor. That is, it should satisfy the renormalization group property

$$U(\mu_0, \mu_1)\, U(\mu_1, \mu_2) = U(\mu_0, \mu_2)\,, \tag{3.90}$$

which is obvious from its definition in eq. (3.87). A simple way to test that eq. (3.90) is satisfied is to consider the special case of $\mu_2 = \mu_0$, which yields

$$U(\mu_0, \mu)\, U(\mu, \mu_0) = 1\,, \tag{3.91}$$

and simply expresses the fact that the RG evolution should close on itself. Since the intermediate scale here is completely arbitrary, this property should be satisfied exactly at any given order. However, deviations from unity can arise due to simplifying assumptions or approximations made in evaluating the integral in the exponent.

3.4.2 Numerical and seminumerical methods

The most accurate method of integration is to perform the integration fully numerically. The error introduced by the numerical integration routine can be made arbitrarily small at the expense of computing time. We always use a sufficiently high integration precision such that the numerical integration error is completely negligible.

Our strategy in the numerical and seminumerical approaches is summarized schematically as

$$U(\mu_0,\mu) = \exp\Bigg\{\underbrace{\int_{\mu_0}^{\mu}\frac{\mathrm{d}\mu'}{\mu'}}_{\text{numerical}}\sum_{n=0}^{\infty}\Bigg[\epsilon^n\Gamma_n\overbrace{\left(\frac{\alpha(\mu')}{4\pi}\right)^{n+1}}^{\text{numerical / eq. (3.75)}}\ln\frac{Q}{\mu'}+\epsilon^{n+1}\gamma_n\overbrace{\left(\frac{\alpha(\mu')}{4\pi}\right)^{n+1}}^{\text{numerical / eq. (3.75)}}\Bigg]\Bigg\}, \tag{3.92}$$

where we have written the generic evolution kernel $U(\mu_0,\mu)$ explicitly in terms of the perturbative series of the anomalous dimensions from eq. (3.85). In both the numerical and seminumerical methods we truncate the series in square brackets at the desired order in ϵ, and evaluate the overall μ-integration numerically.

For the numerical method, we use the exact numerical result for the solution of the running coupling $\alpha(\mu')$, as indicated in red in eq. (3.92). For the seminumerical method we instead insert the iterative solution for the running of the coupling, eq. (3.75). In both cases, the running of the coupling is truncated at the appropriate order in ϵ.

The seminumerical method turns out to provide a very good approximation of the integral, since as we have seen in section 3.3, the iterative solution for the running coupling provides a very accurate solution. At the same time, it is much faster than the fully numerical method because it avoids calling the computationally costly numerical solution for the running coupling in each integrand call.

3.4.3 Unexpanded analytic method

We start from eq. (3.84) and split the logarithm at μ_0,

$$\gamma_F(\mu) = \frac{1}{\epsilon}\,\Gamma_{\text{cusp}}[\alpha(\mu)]\left(\ln\frac{\mu_0}{\mu}+\ln\frac{Q}{\mu_0}\right)+\gamma[\alpha(\mu)]\,. \tag{3.93}$$

To integrate it over μ we use the standard method of exploiting the β-function for α,

$$\mathrm{d}\ln\mu = \frac{\mathrm{d}\alpha(\mu)}{\beta[\alpha(\mu)]}\,, \tag{3.94}$$

to change the integration variable from μ to α. To replace the explicit logarithm of μ in eq. (3.93), we integrate eq. (3.94) once to obtain

$$\ln\frac{\mu_0}{\mu} = \int_{\alpha(\mu)}^{\alpha(\mu_0)}\frac{\mathrm{d}\alpha}{\beta(\alpha)}\,. \tag{3.95}$$

The evolution kernel in eq. (3.87) then takes the form

$$U(\mu_0,\mu) = \exp\Big\{-K_\Gamma(\mu_0,\mu)+\eta_\Gamma(\mu_0,\mu)\ln\frac{Q}{\mu_0}+K_\gamma(\mu_0,\mu)\Big\}\,, \tag{3.96}$$

where the individual functions are defined as

$$K_\Gamma(\mu_0,\mu) = \frac{1}{\epsilon}\int_{\alpha(\mu_0)}^{\alpha(\mu)} \frac{\mathrm{d}\alpha}{\beta(\alpha)}\,\Gamma_{\mathrm{cusp}}(\alpha) \int_{\alpha(\mu_0)}^{\alpha} \frac{\mathrm{d}\alpha'}{\beta(\alpha')}\,, \tag{3.97}$$

$$\eta_\Gamma(\mu_0,\mu) = \frac{1}{\epsilon}\int_{\alpha(\mu_0)}^{\alpha(\mu)} \frac{\mathrm{d}\alpha}{\beta(\alpha)}\,\Gamma_{\mathrm{cusp}}(\alpha)\,, \tag{3.98}$$

$$K_\gamma(\mu_0,\mu) = \int_{\alpha(\mu_0)}^{\alpha(\mu)} \frac{\mathrm{d}\alpha}{\beta(\alpha)}\,\gamma(\alpha)\,. \tag{3.99}$$

The integrals in eqs. (3.97), (3.98), and (3.99) yield an evolution kernel which manifestly depends on μ and μ_0 only via $\alpha(\mu)$ and $\alpha(\mu_0)$. To illustrate this, for K_Γ at LL order, $\sim \mathcal{O}(\epsilon^0)$, we have

$$K_\Gamma(\mu_0,\mu) = \frac{\Gamma_0}{4\beta_0^2}\int_{a(\mu_0)}^{a(\mu)} \frac{\mathrm{d}a}{a}\int_{a(\mu_0)}^{a} \frac{\mathrm{d}a'}{a'^2}\,, \qquad a(\mu) \equiv \frac{\alpha(\mu)}{4\pi}\,. \tag{3.100}$$

The integrations can be carried out easily to yield

$$K_\Gamma(\mu_0,\mu) = -\frac{\Gamma_0}{4\beta_0^2}\,\frac{4\pi}{\alpha(\mu_0)}\Big(1-\frac{1}{r}-\ln r\Big)\,, \qquad r = \frac{\alpha(\mu)}{\alpha(\mu_0)}\,. \tag{3.101}$$

At NLL, $\mathcal{O}(\epsilon)$, we have

$$K_\Gamma(\mu_0,\mu) = \frac{\Gamma_0}{4\beta_0^2}\int_{a(\mu_0)}^{a(\mu)} \frac{\mathrm{d}a}{a}\,\frac{1+\epsilon\,\hat\Gamma_1 a}{1+\epsilon\,b_1 a}\int_{a(\mu_0)}^{a} \frac{\mathrm{d}a'}{a'^2}\,\frac{1}{1+\epsilon\,b_1 a'}\,, \qquad \hat\Gamma_n = \frac{\Gamma_n}{\Gamma_0}\,. \tag{3.102}$$

The approach followed in the unexpanded analytic method is to expand the denominators in ϵ keeping terms up to the $\mathcal{O}(\epsilon)$, which induces an approximation error of $\mathcal{O}(\epsilon^2)$, but in turn allows to easily perform the integration,

$$\begin{aligned} K_\Gamma(\mu_0,\mu) &= \frac{\Gamma_0}{4\beta_0^2}\bigg\{\int_{a(\mu_0)}^{a(\mu)}\frac{\mathrm{d}a}{a}\Big[1+\epsilon(\hat\Gamma_1-b_1)a\Big]\int_{a(\mu_0)}^{a}\frac{\mathrm{d}a'}{a'^2} - \epsilon\,b_1\int_{a(\mu_0)}^{a(\mu)}\frac{\mathrm{d}a}{a}\int_{a(\mu_0)}^{a}\frac{\mathrm{d}a'}{a'} + \mathcal{O}(\epsilon^2)\bigg\} \\ &= -\frac{\Gamma_0}{4\beta_0^2}\bigg\{\frac{4\pi}{\alpha(\mu_0)}\Big(1-\frac{1}{r}-\ln r\Big) + \epsilon\Big[(\hat\Gamma_1-b_1)(1-r+\ln r)+\frac{b_1}{2}\ln^2 r\Big]\bigg\}\,. \end{aligned} \tag{3.103}$$

The other two integrals, η_Γ and K_γ, are obtained in a completely analogous fashion. At NLL, for η_Γ we find

$$\begin{aligned} \eta_\Gamma(\mu_0,\mu) &= -\frac{\Gamma_0}{2\beta_0}\int_{a(\mu_0)}^{a(\mu)}\frac{\mathrm{d}a}{a}\big[1+\epsilon\,(\hat\Gamma_1-b_1)a+\mathcal{O}(\epsilon^2)\big] \\ &= -\frac{\Gamma_0}{2\beta_0}\Big[\ln r + \epsilon\,\frac{\alpha(\mu_0)}{4\pi}(\hat\Gamma_1-b_1)(r-1)\Big]\,. \end{aligned} \tag{3.104}$$

We stress, that in this method the anomalous dimensions in η_Γ are kept to the same loop order as in K_Γ, despite the fact that η_Γ has an additional power of $\alpha(\mu_0)$ compared to K_Γ at each order in ϵ. From the above derivation it should be clear that the separation

of the cusp term into K_Γ and η_Γ is arbitrary and merely a technical tool to perform the integration. In other words, the fact that we used μ_0 on the right-hand side of eq. (3.93) was merely for convenience and we could have used any other arbitrary scale. Dropping the highest term in η_Γ (as is sometimes done) amounts to multiplying the $\ln(Q/\mu_0)$ in eq. (3.93) by ϵ, which introduces an artificial dependence on μ_0 into γ_F. In particular, doing so would lead to an explicit violation of the RGE consistency in eq. (3.90).

From the expressions in eqs. (3.98) and (3.99) it is clear that K_γ can be obtained from η_Γ by replacing $\Gamma_n \mapsto \gamma_n$ and multiplying by an overall ϵ. Hence, it does not contribute at LL, and at NLL we have

$$K_\gamma(\mu_0, \mu) = -\frac{\gamma_0}{2\beta_0}\,\epsilon\,\ln r\,. \tag{3.105}$$

The calculation at higher orders proceeds in exactly the same fashion. The results up to $\mathrm{N^3LL}$ are given in appendix B.5 in eqs. (B.33), (B.34), and (B.35).

To fully specify the method, we also have to specify how to obtain the integration limits $\alpha(\mu)$ and $\alpha(\mu_0)$. To be consistent, we have to use a solution for the β-RGE to the same order in ϵ to which we performed the integration. To render the method fully analytic, we use the unexpanded iterative solution to the corresponding order.

The Sudakov evolution factor expressed in terms of K_Γ, η_Γ, K_γ obtained as described above and combined with the iterative solution for α, is precisely the form that is commonly used to perform Sudakov resummation in QCD in much of the SCET literature; a few examples from a variety of applications include e.g. refs. [110, 135, 142, 145–155].

3.4.4 Expanded analytic method

If, instead of changing integration variables from μ to α via eq. (3.94), the expanded solution eq. (3.76) for $\alpha(\mu)$ is inserted into the integrand of the evolution kernel eq. (3.87) and expanded in ϵ, the resulting integral exhibits an explicit μ dependence which can be integrated analytically.

Equivalently, the same result is obtained by starting from the unexpanded analytic integrals of the previous subsection (see eqs. (B.33), (B.34), and (B.35)), substituting the expanded solution eq. (3.76) for $\alpha(\mu)$ in terms of $\alpha(\mu_0)$ and expanding everywhere in ϵ. We therefore refer to these kernels as "expanded analytic" as they involve a further expansion in ϵ compared to the unexpanded ones of the previous subsection.

The expanded analytic evolution kernels to NNLL, $\mathcal{O}(\epsilon^2)$, are given by

$$\begin{aligned}
\eta_\Gamma(\mu_0, \mu) = -\frac{\Gamma_0}{2\beta_0}\Bigg\{&\ln\frac{1}{X} - \epsilon\,\frac{\alpha(\mu_0)}{4\pi} b_1 \frac{\ln X}{X} + \epsilon^2\,\frac{\alpha(\mu_0)^2}{(4\pi)^2}\left[\frac{b_1^2}{2}\frac{\ln^2 X}{X^2} - \frac{b_2}{X}\Big(1-\frac{1}{X}\Big)\right.\\
&\left. - \frac{b_1^2}{X}\Big(\frac{\ln X}{X} + \frac{1}{X} - 1\Big)\right]\\
&+ \epsilon\,\frac{\alpha(\mu_0)}{4\pi}(\hat\Gamma_1 - b_1)\left[\frac{1-X}{X} - \epsilon\frac{\alpha(\mu_0)}{4\pi} b_1 \frac{\ln X}{X^2}\right]\\
&+ \epsilon^2\,\frac{\alpha(\mu_0)^2}{(4\pi)^2}(\hat\Gamma_2 - b_1\hat\Gamma_1 + b_1^2 - b_2)\frac{1-X^2}{2X^2}\Bigg\}\,,
\end{aligned} \tag{3.106}$$

and

$$
\begin{aligned}
K_\Gamma(\mu_0,\mu) = -\frac{\Gamma_0}{(2\beta_0)^2}\Bigg\{ & \frac{4\pi}{\alpha(\mu_0)}\Bigg[(1-X+\ln X) + \epsilon\,\frac{\alpha(\mu_0)}{4\pi}\,b_1\frac{1-X}{X}\ln X \\
& + \epsilon^2\,\frac{\alpha(\mu_0)^2}{(4\pi)^2}\frac{1}{X^2}\Big[b_1^2\Big((1-X)^2+(1-X)\ln X - \frac{1}{2}\ln^2 X\Big) - b_2(1-X)^2\Big]\Bigg] \\
& + \epsilon\,(\hat\Gamma_1 - b_1)\Bigg[1-\frac{1}{X}-\ln X + \epsilon\frac{\alpha(\mu_0)}{4\pi}b_1\frac{1-X}{X^2}\ln X\Bigg] \\
& + \epsilon\,b_1\Bigg[\frac{1}{2}\ln^2 X + \epsilon\,\frac{\alpha(\mu_0)}{4\pi}\,b_1\frac{\ln^2 X}{X}\Bigg] \\
& + \epsilon^2\,\frac{\alpha(\mu_0)}{4\pi}\Bigg[(b_1^2-b_2)\Big(\frac{X^2-1}{2X^2}-\ln X\Big) + (b_1\hat\Gamma_1 - b_1^2)\frac{X-1-\ln X}{X} \\
& - (\hat\Gamma_2 - b_1\hat\Gamma_1)\frac{(X-1)^2}{2X^2}\Bigg]\Bigg\}\,,
\end{aligned}
\tag{3.107}
$$

where as before $b_i = \beta_i/\beta_0$, $\hat\Gamma_i = \Gamma_i/\Gamma_0$, and $X \equiv X(\mu_0,\mu) = 1 + \frac{\alpha(\mu_0)}{2\pi}\beta_0 \ln\frac{\mu}{\mu_0}$. For illustration, we kept explicit the additional terms compared to the unexpanded results that correspond to the expansion of $r = \alpha(\mu)/\alpha(\mu_0)$ in terms of ϵ. The K_γ kernel is again obtained from η_Γ in eq. (3.106) by replacing $\Gamma_n \mapsto \gamma_n$ and multiplying by an overall ϵ. The N^{3}LL results are obtained analogously. Since they are rather lengthy and not very illuminating we do not give them explicitly here.

As it can be seen, in this method the dependence on the two scales appears explicitly in the argument of the logarithm in $X(\mu_0,\mu)$. One can still choose how to obtain the value for $\alpha(\mu_0)$, for which we use by default the expanded solution as it is closer in spirit to this method. In our numerical results we also show the effect of using the iterative solution for $\alpha(\mu_0)$.

3.4.5 Reexpanded analytic method

This method is related to the expanded analytic method of the previous subsection but uses a different treatment for the remaining dependence on α. That is, starting from the expanded results of the previous subsection, all powers of $\alpha(\mu_0)$ are reexpanded in terms of $\alpha(\mu_R)$ evaluated at a reference scale μ_R, which is typically chosen equal or proportional to the (hard) kinematic variable Q.[9]

To illustrate this for the simplest case, we start from the LL expanded analytic result, which written out explicitly is given by

$$
K_\Gamma = -\frac{\Gamma_0}{(2\beta_0)^2}\frac{4\pi}{\alpha(\mu_0)}\Bigg[\alpha(\mu_0)\frac{\beta_0}{2\pi}\ln\frac{\mu_0}{\mu} + \ln\Big(1-\alpha(\mu_0)\frac{\beta_0}{2\pi}\ln\frac{\mu_0}{\mu}\Big)\Bigg]\,. \tag{3.108}
$$

[9] In our notation, taking Drell-Yan as an example, the kinematic variable Q would be equivalent to the Z-boson or dilepton invariant mass. It should not be confused with what is sometimes called the resummation scale and also denoted as $Q \equiv Q_{\rm res}$, and which is the same as our μ_0, i.e. $\mu_0 \equiv Q_{\rm res}$.

To proceed, we reexpand $\alpha(\mu_0)$ in terms of $\alpha(\mu_R)$ using its fixed-order expansion

$$\alpha(\mu_0) = \alpha(\mu_R)\Big[1 - \epsilon\,\alpha(\mu_R)\frac{\beta_0}{2\pi}\ln\frac{\mu_0}{\mu_R} + \mathcal{O}(\epsilon^2)\Big]\,. \tag{3.109}$$

In doing so, it is assumed that $\mu_0 \sim \mu_R$ or, more precisely, it is chosen explicitly that the logarithms of μ_0/μ_R are *not resummed* via the evolution of α but are instead *treated at fixed order*. Formally, this is implemented by multiplying any $\ln(\mu_0/\mu_R)$ in the relation between $\alpha(\mu_0)$ in terms of $\alpha(\mu_R)$ by ϵ as in eq. (3.109) and expanding in ϵ. Substituting eq. (3.109) into eq. (3.108) and reexpanding to $\mathcal{O}(\epsilon^0)$, we obtain the "reexpanded analytic" result at LL,

$$K_\Gamma = -\frac{\Gamma_0}{2\beta_0}\,\frac{\lambda + \ln(1-\lambda)}{\lambda}\,L\,, \qquad \lambda \equiv \alpha(\mu_R)\,\frac{\beta_0}{2\pi}\,L\,, \qquad L \equiv \ln\frac{\mu_0}{\mu}. \tag{3.110}$$

At this order, the result only involves the resummed logarithms $\ln(\mu_0/\mu)$. The results at higher orders also contain explicit fixed-order logarithms $\ln(\mu_0/\mu_R)$ induced by the fixed-order expansion of $\alpha(\mu_0)$ in terms of $\alpha(\mu_R)$. Since the higher-order results are very lengthy we do not give them here. Their calculation is discussed for example in appendix C of ref. [156]. The LL result for K_Γ in eq. (3.110) is equivalent to the $Lg^{(1)}(\alpha L)$ term in the notation there, and we also explicitly verified that we reproduce the NLL $g^{(2)}(\alpha L)$ term. The N^{3}LL expressions are taken from ref. [157] translated to our conventions.

Another important difference in this method is the treatment of the η_Γ term,

$$\eta_\Gamma(\mu_0, \mu)\,\ln\frac{Q}{\mu_0}\,, \tag{3.111}$$

in the Sudakov exponent. Since μ_R and Q are either identified or considered of similar size, the explicit $\ln(Q/\mu_0)$ here is treated analogously to the $\ln(\mu_0/\mu_R)$ in eq. (3.109) and multiplied by ϵ, such that the η_Γ term is treated like the noncusp term and included at one order lower than K_Γ. This is typically achieved by absorbing it into the noncusp term as

$$\overline{\gamma}(\alpha) = \gamma(\alpha) + \Gamma_{\text{cusp}}(\alpha)\ln\frac{Q}{\mu_0}\,. \tag{3.112}$$

For the specific choice $\mu_0 = \mu_R = Q$, this method reduces to the expanded analytic method, since all logarithms that are treated differently vanish exactly. However, as soon as these scales are chosen not to coincide, the different treatment of the μ_0 dependence can have a sizeable numerical effect on the evolution kernel, as we show in section 3.4.6. It is also important to note that since the first and second arguments of $U(\mu_0, \mu)$ are explicitly treated differently, and μ_0 is assumed to be of order Q, the group property in eq. (3.90) is lost, and similarly the closure condition in eq. (3.91) becomes meaningless. In other words, with the above modifications the evolution factor explicitly targets a *specific situation* and *cannot* (and is not meant to) be used to evolve between two arbitrary scales.

This reexpanded analytic expression for the Sudakov evolution factor is also commonly used, in particular in the formalism of refs. [156, 158–160] and (presumably most) implementations following it, and also in the formalism of refs. [157, 161, 162].

3.4.6 Numerical analysis of the evolution kernel

Having elaborated various methods for evaluating the Sudakov evolution factor, we now study their numerical behaviour. We consider the relative deviation from the exact closure condition in eq. (3.91) as well as the approximation error as given by the relative difference of each method to the exact numerical method.

In general, the Sudakov evolution factor depends on the process and observable under consideration, so we have to specify a concrete example. Here, we consider the hard evolution for two colored partons in QCD, namely the $q\bar{q}$ vector current (corresponding to Drell-Yan production or $e^+e^- \to$ dijets) and the gg scalar current (corresponding to $gg \to H$ production). The relevant hard evolution kernel is given by

$$\begin{aligned} U^i(\mu_0,\mu) &= \exp\left\{\int_{\mu_0}^{\mu}\frac{\mathrm{d}\mu'}{\mu'}\,4\Gamma^i_{\mathrm{cusp}}[\alpha_s(\mu')]\ln\frac{Q}{\mu'}\right\}\times\exp\left\{\int_{\mu_0}^{\mu}\frac{\mathrm{d}\mu'}{\mu'}\gamma^i_H[\alpha_s(\mu')]\right\} \\ &\equiv U^i_\Gamma(\mu_0,\mu)\times U^i_\gamma(\mu_0,\mu)\,, \end{aligned} \tag{3.113}$$

where $i = q, g$ denotes the quark and gluon cases, and we have separately defined the cusp U^i_Γ and noncusp U^i_γ evolution factors. All relevant anomalous dimension coefficients are given in appendix B.1.

In this case, the kinematic quantity Q appearing in eq. (3.113) is the invariant mass $Q = \sqrt{q^2}$ of the momentum q flowing through the current, which we take to be $Q = 100\,\mathrm{GeV}$ (i.e. typical of Drell-Yan production). We consider the case of evolving from $\mu_0 \sim Q$ to an arbitrary scale μ over two decades above and below. As before, we use $n_f = 5$, $m_Z = 91.1876\,\mathrm{GeV}$ with $\alpha_s(m_Z) = 0.118$ and ignore any flavor thresholds.

Of course, the takeaway message of our analysis would be the same if we were to use anomalous dimension coefficients associated with soft or collinear quantities. The advantage of considering the hard evolution is that it is multiplicative and independent of the low-energy observable, so it provides a simple and generic use case, while the only process dependence of the evolution is via the color channel. Furthermore, the hard evolution factor $U^i(\mu_0,\mu)$ in this scenario has a direct correspondence in various resummation formalisms. In the formalisms of refs. [156, 158–160] and refs. [157, 161, 162] it corresponds to the Sudakov form factor or the Sudakov radiator with $\mu_0 \equiv Q_{\mathrm{res}}$ being the resummation scale. In the context of SCET, it constitutes the evolution factor for the $q\bar{q}$ and gg hard functions with $\mu_0 \equiv \mu_H$ being the renormalization scale of the hard function. In all cases, μ would then be associated with an appropriate low-energy quantity, e.g. $\mu \sim b_0/b_T \sim q_T$ in the case of q_T resummation.[10]

Closure tests

By construction, the seminumerical and numerical methods satisfy the closure condition exactly, since they treat the integral and integration limits exactly. As already mentioned

[10] Here b_T is the Fourier-conjugate variable to q_T and it emerges when performing q_T resummation in the Fourier-conjugate b_T-space. For more see section 4.3.1.

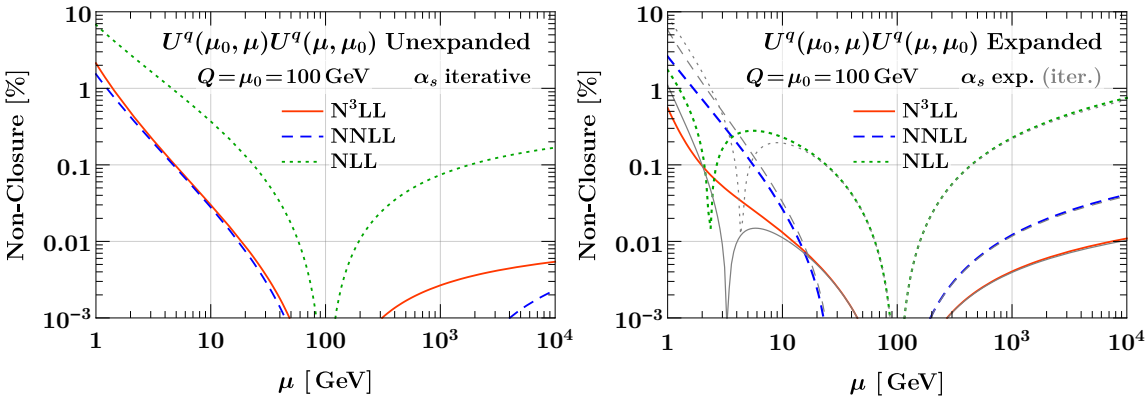

Figure 3.5: Deviation from the closure condition $U^q(\mu_0,\mu)U^q(\mu,\mu_0) = 1$ for the quark evolution kernels from NLL to N^{3}LL for the unexpanded method (left) and expanded method (right). For the expanded method, the colored (gray) lines show the result of using the expanded (iterative) $\alpha_s(\mu_0)$.

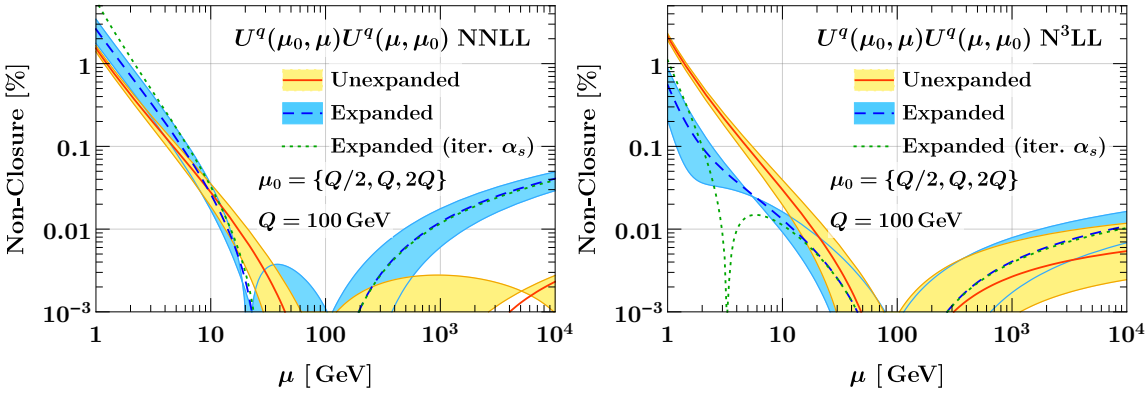

Figure 3.6: Deviation from the closure condition $U^q(\mu_0,\mu)U^q(\mu,\mu_0) = 1$ at NNLL (left) and N^{3}LL (right) for the unexpanded method (solid) and expanded method (dashed). The central lines are for $\mu_0 = Q$, while the bands show the variation when changing μ_0 to $Q/2$ and $2Q$. The green dotted line shows the result of using the iterative $\alpha_s(\mu_0)$ in the expanded kernels (for $\mu_0 = Q$ only).

in section 3.4.5, the closure condition cannot be applied to the reexpanded method. We therefore only consider the unexpanded and expanded methods here. The reason these methods do not satisfy the closure condition exactly is due to the expansions in the integrand after the variable transformation from μ to α, which means that the change of variables in the integration limits and the integrand are not in exact correspondence.[11]

In figure 3.5, we compare the non-closure for the full quark evolution factor at different orders for the unexpanded (left panel) and expanded (right panel) methods. At LL, the integrals are trivially exact and satisfy exact closure, so we do not show them. At NLL (dotted green), the non-closure can be quite sizeable, exceeding $\gtrsim 5\%$ when running to low scales. For the expanded kernels it even reaches $\sim 1\%$ when running to high scales. While

[11] Note that in ref. [153] modified unexpanded kernels were constructed that restore exact closure.

the non-closure effect is reduced at higher orders, it can still reach $1-2\%$ at the lowest scales, and for the unexpanded kernels it does not reduce from NNLL (dashed blue) to N^{3}LL (solid orange). For the expanded kernels, the non-closure reduces to below 1% at N^{3}LL, but this is likely accidental, since the expanded kernels are very sensitive to numerical cancellations when evolving to scales $\mu \lesssim 10\,\text{GeV}$. This is evident when comparing the effect of using the iterative instead of the expanded solution for $\alpha_s(\mu_0)$: Even a small change in $\alpha_s(\mu_0)$ causes large changes in the observed level of non-closure.

In figure 3.6, we compare the unexpanded and expanded methods to each other at NNLL (left panel) and N^{3}LL (right panel). In addition we vary μ_0 away from Q to $Q/2$ and $2Q$, as it is done in practical applications to estimate a resummation uncertainty. Here, this should however not be considered as an uncertainty estimate on the non-closure. Rather, it illustrates the effect of η_Γ, which contributes when $\mu_0 \neq Q$, and the level at which the non-closure may influence such uncertainty estimates. The (non-)closure of the unexpanded kernels tends to be less sensitive to the choice of μ_0 than the expanded ones.

Overall, we might say that the unexpanded kernels show a somewhat better closure behaviour. However, considering that at N^{3}LL the aim for a perturbative precision is in the several percent range, their non-closure at this order is uncomfortably large.

For brevity we have only shown results for the quark evolution kernels here. The gluon evolution kernels have the same qualitative behaviour. The only difference is that the overall non-closure effect is about a factor of two larger for gluons than for quarks, corresponding to their larger color factor.

Approximation errors

We now study the approximation errors of all four approximate methods relative to the exact numerical method. The results for the quark cusp contribution, U_Γ^q, are shown in figure 3.7, and for the quark and gluon noncusp contributions, $U_\gamma^{q,g}$, in figures 3.8 and 3.9. In all cases, we show the results at NNLL (top rows) and N^{3}LL (bottom rows), and at $\mu_0 = Q$ (left panels) and $\mu_0 = Q/2$ (right panels).

At NNLL, we see a clear hierarchy, with the seminumerical method having the smallest approximation errors, followed by the unexpanded, and then the expanded methods, which is as expected, given the increasing level of approximation involved in each method. At N^{3}LL, the seminumerical method again performs best. The unexpanded and expanded kernels have similar errors for the cusp term, while the unexpanded ones fare better for the noncusp terms. The approximation error for the cusp term is always much larger than for the noncusp term, which is not surprising due to the additional $\ln(\mu)$ in its integrand. The errors for the gluon cusp contribution are about a factor of two larger than for quarks.

We find, somewhat surprisingly, that at NNLL the approximation error for the expanded kernels can exceed several percent when evolving to low scales, while at N^{3}LL it still exceeds the percent level for both the unexpanded and expanded kernels alike. Overall, the picture is quantitatively quite similar to what we observed with the closure test.

We stress that the systematic differences we observe are solely due to the method of

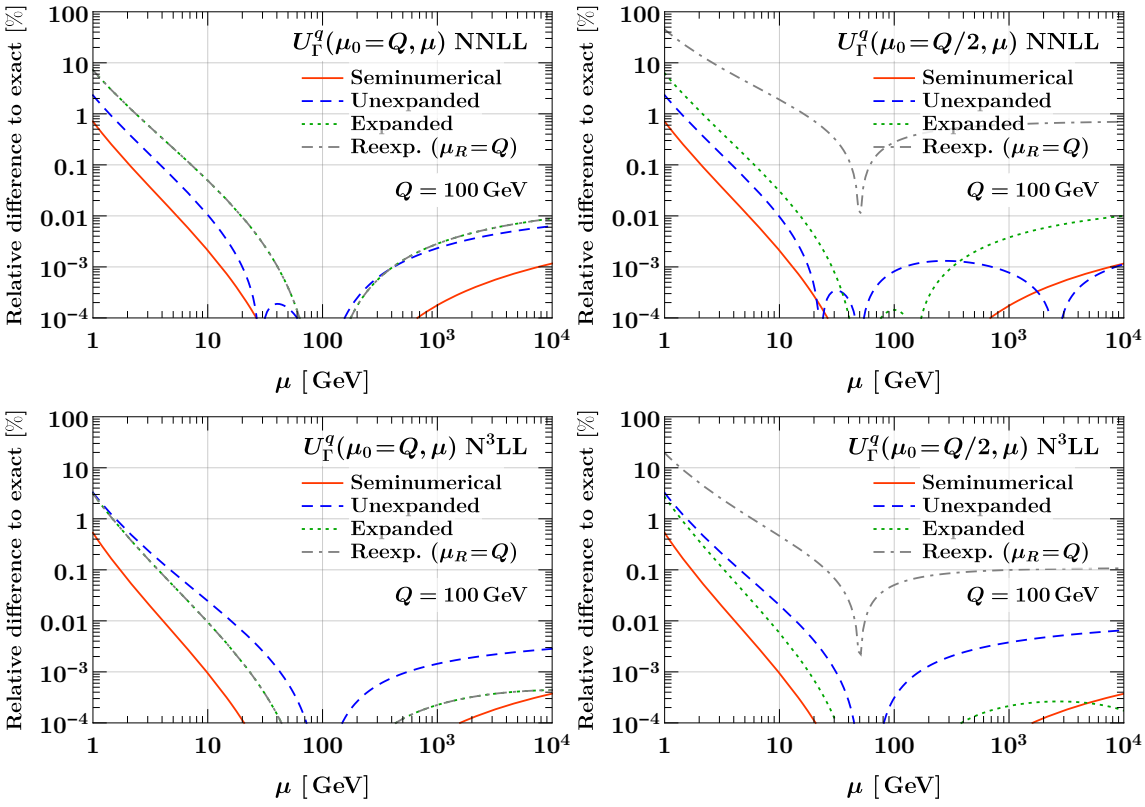

Figure 3.7: Deviation from the exact result for the quark cusp evolution kernel at NNLL (top) and N^{3}LL (bottom) for all four approximate integration methods. On the left we use $\mu_0 = Q$, for which the expanded and reexpanded kernels are equivalent. On the right we use $\mu_0 = Q/2$, with $\mu_R = Q$ for the reexpanded method.

integrating the RGE for identical perturbative inputs. Typically, we would want such systematic effects to be much smaller than the perturbative precision we are aiming at, as was the case for the running of the coupling. In other words, we clearly want to avoid the method of integration to bias the result in any way. This is clearly not the case here, since at NNLL and N^{3}LL one would typically aim at a perturbative precision of order several to few percent.

For $\mu_0 = \mu_R = Q$, the reexpanded and expanded kernels are still equivalent. In the right panels, we therefore also show the results when reducing the hard scale of the evolution to $\mu_0 = Q/2$. This has essentially no effect on the approximation error of the seminumerical, unexpanded, and expanded kernels. For the reexpanded kernels, we keep $\mu_R = Q$, which is a commonly used choice in resummation applications. The impact of treating the logarithms of μ_0/μ_R and Q/μ_0 at fixed-order in the reexpanded kernels compared to the expanded ones now becomes visible and turns out to be very large, which is quite unexpected. It easily exceeds the percent level even at N^{3}LL, and not just for the cusp but even the noncusp contributions. For the cusp term, it exceeds $\gtrsim 10\%$ at the lowest scales. Note that roughly half of the observed difference is due to the reexpansion around $\alpha(\mu_R)$ and half is due to

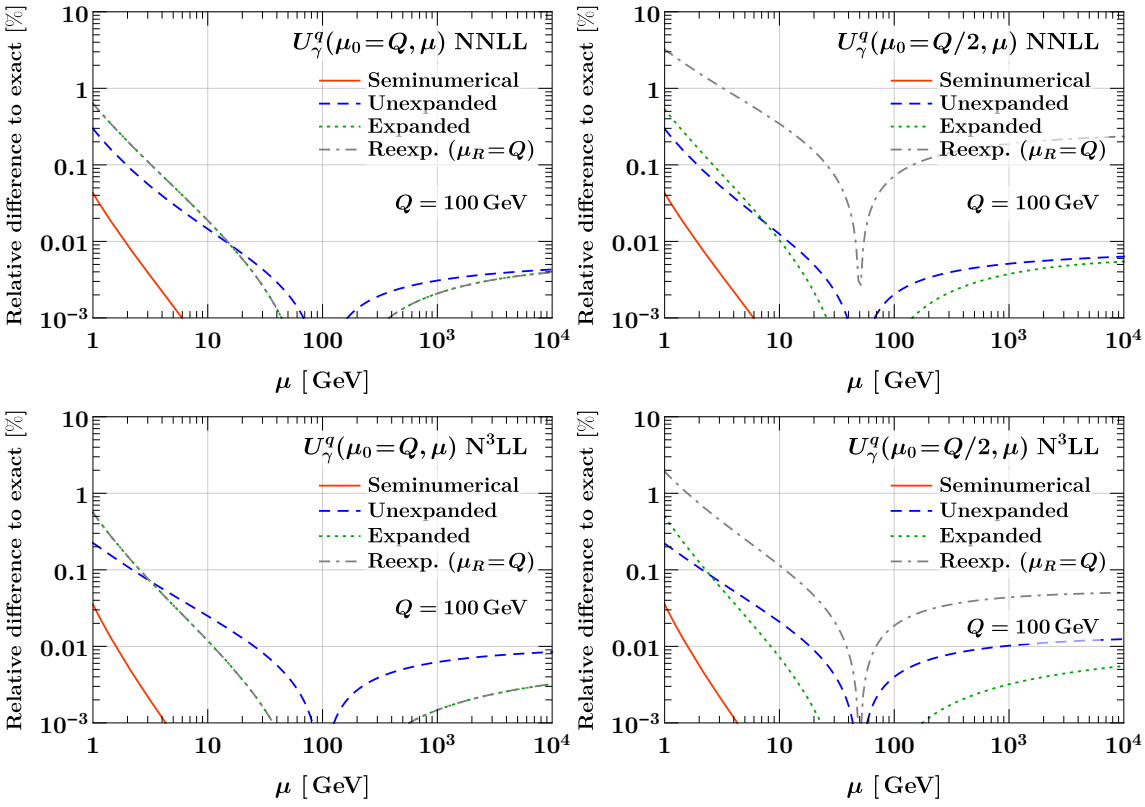

Figure 3.8: Deviation from the exact result for the quark noncusp evolution kernel at NNLL (top) and N^{3}LL (bottom) for all four approximate integration methods. On the left we use $\mu_0 = Q$, for which the expanded and reexpanded kernels are equivalent. On the right we use $\mu_0 = Q/2$, with $\mu_R = Q$ for the reexpanded method.

the lower-order treatment of the η_Γ term. This effect is not just due to the reduced amount of evolution from $Q/2$ to μ, as that is present for all methods including the exact numerical result. Given the large numerical impact it has, it might be worthwhile to reconsider the reasons for performing this additional reexpansion around $\alpha(\mu_R)$. Certainly, from the point of view of the evolution, the appropriate scale for α when starting the evolution from μ_0 is μ_0.

Of course, the differences due to the various approximations involved in all methods, including the reexpanded method, might be considered as higher-order effects. Nevertheless, given that they are not negligible or even exceed the perturbative precision, they have to be addressed and accounted for. One option would be to include them as an additional systematic uncertainty in the theoretical uncertainty estimate. On the other hand, there is no fundamental theoretical reason for using any specific approximate solution. Hence, the best option would be to avoid incurring this additional uncertainty by using the unique exact solution of the defining RGE system resulting from the truncation of the perturbative series of the anomalous dimensions. If that is computationally prohibitive (or technically inconvenient), the seminumerical method offers a good compromise, since its approximation

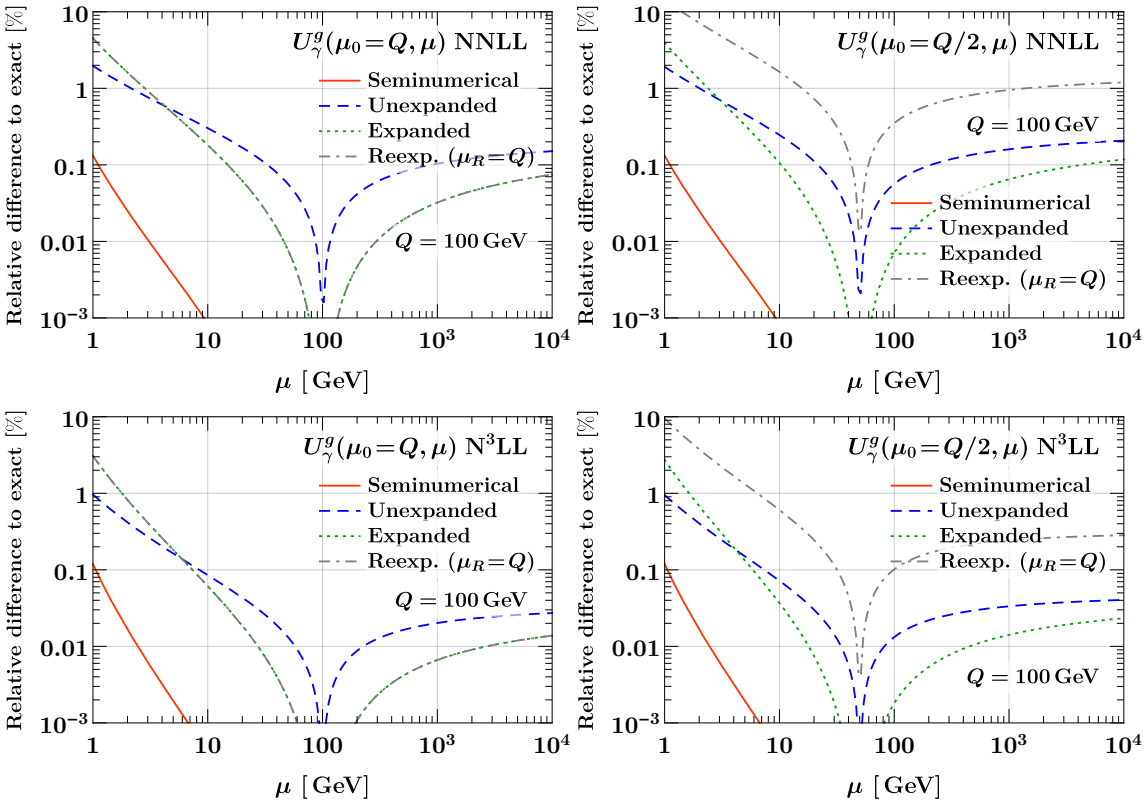

Figure 3.9: Deviation from the exact result for the gluon noncusp evolution kernel at NNLL (top) and N^{3}LL (bottom) for all four approximate integration methods. On the left we use $\mu_0 = Q$, for which the expanded and reexpanded kernels are equivalent. On the right we use $\mu_0 = Q/2$, with $\mu_R = Q$ for the reexpanded method.

error is always well below the percent level, and so it is sufficiently accurate even for high-precision predictions.

3.5 Sudakov evolution kernels with two gauge interactions

Having investigated the integration of the one-dimensional kernels, we now consider the extension to two gauge interactions, in which case also mixed effects involving both (generic) gauge couplings $\alpha_{a,b}$ require resummation. In section 3.5.1, we review the general analytic structure for this case and the methods for evaluating them, based on what we learned from our exhaustive analysis of the one-dimensional case. We then present numerical results for the case of QCD⊗QED in section 3.5.2.

3.5.1 Structure of the two-dimensional evolution kernel

We consider the Sudakov resummation for the direct product of two generic gauge groups $G_a \otimes G_b$. The extension to more groups is then straightforward. One key difference from

the one-dimensional case is that the β-functions that govern the evolution of the couplings α_a and α_b now become a set of nonlinear coupled differential equations, as discussed in section 3.3.2.

The generic Sudakov RGE structure remains the same as in eq. (3.83), except that the perturbative expansions for all quantities now involve a double series in α_a and α_b, including mixed terms corresponding to the emissions of two distinct gauge bosons. Hence, the all-order structure of the anomalous dimension is now given by[12]

$$\gamma_F(\mu) = \frac{1}{\epsilon}\,\Gamma_{\text{cusp}}[\alpha_a(\mu), \alpha_b(\mu)] \ln\frac{Q}{\mu} + \gamma[\alpha_a(\mu), \alpha_b(\mu)]\,, \tag{3.114}$$

with

$$\Gamma_{\text{cusp}}(\alpha_a, \alpha_b) \equiv \sum_{\substack{n,m \\ n+m\geq 1}} \epsilon_a^n \epsilon_b^n\, \Gamma_{(n,m)} \left(\frac{\alpha_a}{4\pi}\right)^n \left(\frac{\alpha_b}{4\pi}\right)^m, \tag{3.115}$$

$$\gamma(\alpha_a, \alpha_b) \equiv \sum_{\substack{n,m \\ n+m\geq 1}} \epsilon_a^n \epsilon_b^m\, \gamma_{(n,m)} \left(\frac{\alpha_a}{4\pi}\right)^n \left(\frac{\alpha_b}{4\pi}\right)^m. \tag{3.116}$$

The bookkeeping parameters $\epsilon_{a,b} \equiv 1$ are the same as in the β-functions in eq. (3.77), and $\epsilon \sim \epsilon_a \sim \epsilon_b$, i.e. we make no assumption about the relative hierarchy of the two coupling constants. It is also important to note the correspondence to the typical notation for a single gauge theory G_a,[13]

$$\Gamma_n \equiv \Gamma_{(n+1,0)}\,, \qquad \gamma_n \equiv \gamma_{(n+1,0)} \tag{3.117}$$

The Sudakov evolution kernel is given by the two-dimensional analogue of eq. (3.87),

$$U(\mu_0, \mu) = \exp\left\{\int_{\mu_0}^{\mu} \frac{\mathrm{d}\mu'}{\mu'} \frac{1}{\epsilon}\,\Gamma_{\text{cusp}}[\alpha_a(\mu'), \alpha_b(\mu')] \ln\frac{Q}{\mu'} + \gamma[\alpha_a(\mu'), \alpha_b(\mu')]\right\}. \tag{3.118}$$

It is clear from eqs. (3.115) and (3.116) that the sums implicit in eq. (3.118) include pure G_a terms $\mathcal{O}(\epsilon_a^n)$, pure G_b terms $\mathcal{O}(\epsilon_b^m)$ terms, and mixed terms $\mathcal{O}(\epsilon_a^n \epsilon_b^m)$.

3.5.2 Evaluation of the two-dimensional evolution kernel

Evaluating eq. (3.118) does not correspond to a simple extension of the single gauge interaction scenario, since mixed terms $\sim \mathcal{O}(\alpha_a \alpha_b)$ appear in conjunction with the coupled β-functions.

The fully numerical method is of course still applicable, although it is even more computationally demanding now, since multiple coupled differential equations for $\alpha_{a,b}$ must be

[12] For the general EW case, the complete factorized structure of the cross section can become more involved, because the masses of the EW gauge bosons introduce an additional scale. The generic Sudakov RGE however still has the form of eq. (3.114) with at most a single logarithm $\ln(\mu)$ [82].

[13] In contrast to the β-functions, α_a and α_b appear on equal footing in eqs. (3.115) and (3.116), so we have no choice but to increment the meaning of n in the subscript compared to the one-dimensional case.

solved. As before, we use the fully numerical method to provide the exact reference result to which other methods are compared.

The unexpanded analytic method is not easily extendable, since the coupled β-functions do not allow an analogous change of variables along the lines of $\mathrm{d}\ln\mu \to \mathrm{d}\alpha_a/\beta^a(\alpha_a, \alpha_b)$, because of the dependence on the second coupling. Doing so would require to express the μ dependence of α_b in terms of α_a, which in turn requires that one treats α_b as in the expanded analytic method, at which point the advantage of the unexpanded method is lost. In principle, this could still be an option for cases where there is a clear hierarchy between two couplings to justify treating them on unequal footing, as would be the case for QCD⊗QED. However, we do not pursue this option further here for the reasons given below.

The expanded analytic method can still be applied to evaluate eq. (3.118). This is achieved by using the expanded solution of the coupled β-RGE for α_a and α_b obtained from eq. (3.82), substituting it into the perturbative expansions of the anomalous dimensions, and then explicitly performing the integration in terms of $\ln\mu$. This was done in ref. [111].

In either case, the obtained analytic kernels will inevitably suffer from the same-sized approximation errors already seen in the pure QCD case in section 3.4.6. The generalization to the product group $G_a \otimes G_b$ does not alter the ultimate source, which are the additional approximation(s) made in the integrand. By including EW or QED corrections, we are essentially aiming for percent-level effects, and based on our findings and discussion in the previous section, the analytic methods do not appear to provide sufficient numerical accuracy.[14]

We therefore take the seminumerical method as our method of choice for evaluating the two-dimensional evolution kernels. As already seen in section 3.4.6, it features exact closure and very small approximation errors (well below the percent-level at NNLL), at a reasonable computational cost. The extension to the two-dimensional case eq. (3.118) only requires two steps:

1. We solve the coupled β-functions in eq. (3.77) via the iterative method, up to the required order in ϵ, which yields the closed-form analytic expressions for $\alpha_a(\mu)$ and $\alpha_b(\mu)$ in eq. (3.82).

2. We then evaluate the evolution kernel $U(\mu, \mu_0)$ by employing a numerical integration routine in eq. (3.118), using the analytic expressions for $\alpha_{a,b}(\mu)$ obtained in step 1 in the integrand.

[14] It is possible to consider using a more accurate (semi)numerical method for the dominant QCD contributions, while including the smaller mixed and pure EW corrections via an analytic approximation. However, we do not see any gain in doing so compared to e.g. using the seminumerical method everywhere.

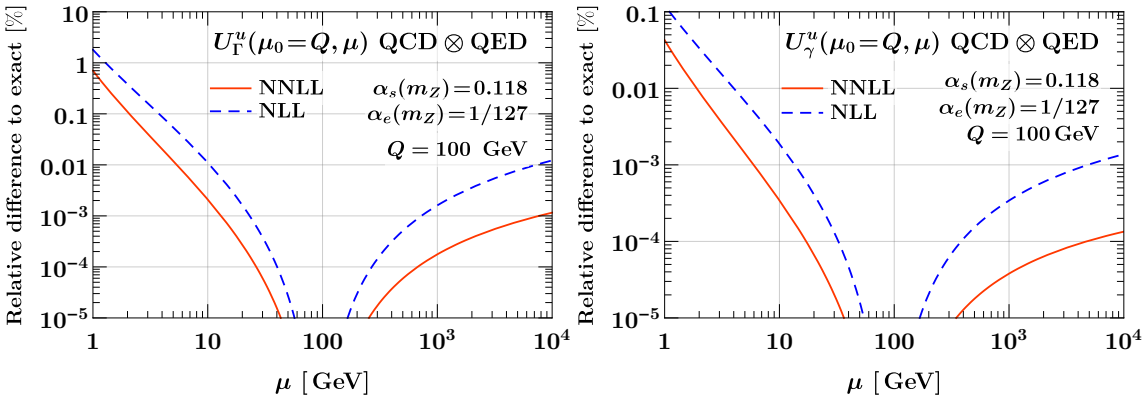

Figure 3.10: Deviation of the seminumerical kernels from the exact result for the joint QCD⊗QED u-quark evolution kernel at NLL (dashed blue) and NNLL (solid orange). The cusp contribution is shown on the left and the noncusp contribution on the right.

Schematically, this procedure is illustrated by

$$U(\mu_0,\mu)=\exp\Bigg\{\underbrace{\int_{\mu_0}^{\mu}\frac{\mathrm{d}\mu'}{\mu'}}_{\text{numerical}}\sum_{\substack{n,m\\ n+m\geq 1}}\Bigg[\frac{\epsilon_a^n\epsilon_b^m}{\epsilon}\Gamma_{(n,m)}\overbrace{\left(\frac{\alpha_a(\mu')}{4\pi}\right)^n\left(\frac{\alpha_b(\mu')}{4\pi}\right)^m}^{\text{eq. (3.82)}}\ln\frac{Q}{\mu'}$$
$$+\epsilon_a^n\epsilon_b^m\gamma_{(n,m)}\underbrace{\left(\frac{\alpha_a(\mu')}{4\pi}\right)^n\left(\frac{\alpha_b(\mu')}{4\pi}\right)^m}_{\text{eq. (3.82)}}\Bigg]\Bigg\}. \tag{3.119}$$

In what follows, we apply this method to the mixed gauge QCD⊗QED scenario. We consider the $u\bar{u}$ hard function as a concrete example and the numerical inputs are the same as in section 3.3.2. The relevant coefficients up to three loops can be found in appendices B.1 and B.2, allowing us to obtain the complete NNLL joint QCD⊗QED Sudakov evolution.

In figure 3.10, we show the approximation errors for the seminumerical method at NLL and NNLL for the cusp (left panel) and noncusp (right panel) contributions. As for the pure QCD case, the former has a larger approximation error, while overall it remains well below 1% everywhere (except at NLL for the cusp term at the very lowest μ values).

In figure 3.11, we show the relative impact of the QED corrections by comparing the full QCD⊗QED to the pure QCD resummation kernels at each order. For the cusp piece (left panel) the impact reaches $4-5\%$ over two decades of evolution, while for the noncusp piece (right panel) it reaches close to 1%. The overall effect for QED is expectedly small due to the smallness of the electromagnetic coupling. Considering a toy QCD⊗QED′ model with $\alpha'_e(m_Z)=0.1$ in figure 3.12, the corrections become much larger, $30-50\%$ for the cusp piece and $5-15\%$ for the noncusp piece. Note that the impact is driven not only by pure QED and mixed corrections in the expansion of the anomalous dimensions, but also by the effects induced by the mixed β-functions in the coupling evolution. Note also that the impact for the cusp term is practically identical at NLL and NNLL even for QED′.

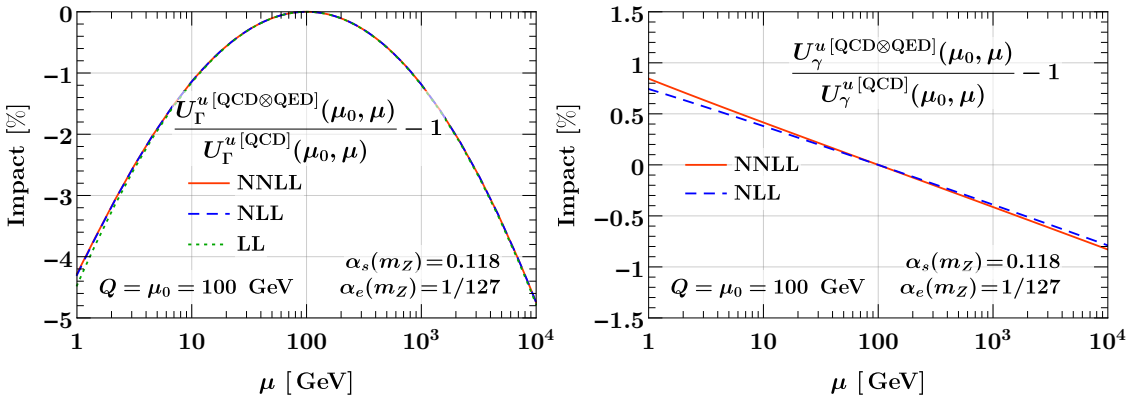

Figure 3.11: Impact of the QED corrections on the u-quark Sudakov evolution kernel at LL, NLL, and NNLL for the cusp (left panel) and noncusp (right panel) contributions. We show the relative difference of the full QCD⊗QED evolution to the pure QCD case at the corresponding order.

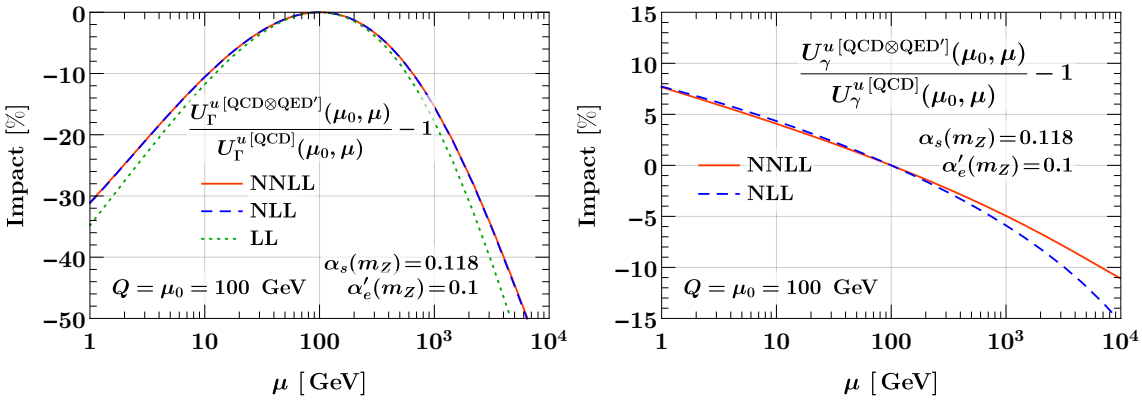

Figure 3.12: Impact of the toy QED′ corrections on the u-quark Sudakov evolution kernel at LL, NLL, and NNLL for the cusp (left panel) and noncusp (right panel) contributions. We show the relative difference of the full QCD⊗QED′ evolution to the pure QCD case at the corresponding order.

This is somewhat accidental and due to the fact that the cusp anomalous dimension does not yet receive any mixed contributions at three loops [83] while its pure QCD and QED three-loop coefficients happen to be very small.

3.6 Summary

In this chapter we studied the technical aspects of achieving joint resummation at higher orders in generic coupled gauge environments. In particular, at the level of the Sudakov evolution kernel appearing in any resummation formalism, we showed that the commonly used methods of evaluating the associated integrals in the Sudakov exponent via analytic approximations can cause numerical differences of the same size as the contributions coming from moving to a higher logarithmic accuracy or including EW radiation. In other

words, systematic integration errors that are typically assumed to be subleading cannot be overlooked when attempting percent-level precision.

To show this, we first reviewed a central ingredient of the Sudakov evolution kernel, the β-function. For the case of a single gauge interaction, we explored its possible approximate analytic solutions and we demonstrated that the iterative method, which results from the minimum amount of expansions, induces smaller relative errors compared to the expanded method. Subsequently we moved to the scenario of two coupled gauge theories for which we solved the coupled β-functions based on the iterative method, providing analytic solutions for the running of both couplings at NNLO order, exemplifying them for the case of QCD$\otimes$QED.

Then we turned to the investigation of the Sudakov evolution kernel in the presence of a single gauge interaction where we studied five methods for integrating the kernel: numerical, seminumerical, unexpanded analytic, expanded analytic, and reexpanded analytic. Their main difference lies in the treatment of the μ dependence of $\alpha(\mu)$ that one has to integrate over. Although all methods employ a priori justifiable assumptions, we showed that the latter three analytic methods can introduce errors at and above the percent-level compared to the exact result (obtained via a fully numerical treatment at a sufficiently high numerical precision). One should therefore be cautious in using them, since their approximation errors can be nonnegligible compared to the perturbative precision one is aiming for. The reexpanded kernels, which are often used in the literature, are particularly notable; differences greater than 10% are possible over only two decades of evolution.

On the other hand, we found that a seminumerical method, which combines an accurate analytic approximation for the running of the couplings (iterative method) with a numerical integration, yielded minimal errors (typically $\leq 0.1\%$), while still maintaining reasonable computing times. As an example, we used it to obtain the complete NNLL QCD$\otimes$QED Sudakov evolution factor.

Chapter 4

Subtractions at N^{3}LO

In this chapter we derive the leading-power singular terms at three loops for both q_T and 0-jettiness ($\mathcal{T}_0$) resolution variables for generic color-singlet processes. Our results provide the complete set of differential subtraction terms for q_T and $\mathcal{T}_0$ subtractions at N^{3}LO, which are an important ingredient for matching N^{3}LO calculations with PS, and they are necessary ingredients in the context of q_T and $\mathcal{T}_0$ resummation at N^{3}LL$'$ and N^{4}LL order. Furthermore, we employ consistency relations between different factorization limits and derive results for the q_T and $\mathcal{T}_0$ beam function boundary coefficients at N^{3}LO in the $z \to 1$ threshold limit. These correspond to genuine predictions and we use them to build ansätze that are valid beyond threshold. Finally, exploiting the analytic structure of kernels such as the q_T beam function boundary coefficients, we present a cost-optimal and precision-driven method for their numerical implementation.

This chapter is based on ref. [2] while numerical results in sections 4.2.3, 4.2.5, 4.3.4 and 4.3.6 have been updated and section 4.5 has been added. Parts of this work have also appeared in ref. [163] as a result of a close collaboration with the author.

4.1 Introduction

Color-singlet processes play a central role in the LHC physics program. The $pp \to Z, W$ Drell-Yan processes are key benchmark processes that have been measured at the percent level and below [94, 164–166], while precise measurements of Higgs and diboson processes provide strong sensitivity to possible contributions beyond the Standard Model [167–172].

The inclusion of higher-order QCD corrections is crucial to obtain reliable predictions. Depending on the specific process and phase-space region, reducing the current theoretical uncertainties requires the calculation of the full corrections at the next order in α_s and/or the resummation of the dominant higher-order terms to all orders in α_s. For color-singlet processes, theory predictions are being pushed to the third order in the fixed-order expansion [173–185] as well as in resummed perturbation theory [3, 110, 135, 151, 186–192].

A key requirement in both cases is to understand the infrared singular structure of QCD at N^{3}LO. For fixed-order calculations this is crucial for the cancellation of infrared divergences between real and virtual emissions, as evidenced by the variety of methods that have been developed by now at NNLO [193–208]. Resummed predictions are intimately linked to the singular limit, and the N^{3}LO singular structure is a key ingredient to extend

the resummation to the full three-loop level.

One way to study the infrared singular limit of QCD is to consider a suitable resolution variable τ, whose differential cross section $\mathrm{d}\sigma/\mathrm{d}\tau$ can be factorized in the singular limit $\tau \to 0$. In this chapter we consider the production of a generic color-singlet final state L in hadronic collisions. In the singular limit, the only hard interaction process that contributes is the Born process, which we denote as

$$\kappa_a(q_a)\,\kappa_b(q_b) \to L(q) \quad \text{with} \quad q_a^\mu + q_b^\mu = q^\mu\,. \tag{4.1}$$

We always use the indices a and b to label the initial states, and $\kappa_i \in \{g, u, \bar{u}, d, \bar{d}, s, \ldots\}$ denotes the parton type and flavor. When there is no ambiguity we simply identify $\kappa_i \equiv i$, e.g., we just write $ab \to L$. The $q_{a,b}^\mu$ are lightlike Born reference (label) momenta given by

$$q_{a,b}^\mu = \omega_{a,b}\frac{n_{a,b}^\mu}{2}\,, \qquad x_{a,b} = \frac{\omega_{a,b}}{E_{\mathrm{cm}}} = \frac{Q}{E_{\mathrm{cm}}}e^{\pm Y}\,, \tag{4.2}$$

with $n_a^\mu = (1, \hat{z})$ and $n_b^\mu = (1, -\hat{z})$. The precise definition of the Born momentum fractions $x_{a,b}$ and the associated $\omega_{a,b} = x_{a,b}E_{\mathrm{cm}}$ depends on how we choose to parametrize the Born phase space in terms of physical observables. For definiteness, in eq. (4.2) we have chosen the total invariant mass $Q = \sqrt{q^2}$ and rapidity Y of the color singlet. Other choices are possible as well, e.g., $\omega_{a,b} = q^\mp \equiv e^{\pm Y}\sqrt{Q^2 + q_T^2}$. In the singular limit, all possible choices are equivalent and yield the same factorized cross section. The specific choice affects the nonsingular power-suppressed corrections.

The entire τ dependence in the factorized cross section is encoded by the beam and soft functions (e.g. see eq. (3.39) in the context of q_T factorization). The beam functions $B_{a,b}$ describe collinear emissions from the incoming partons a and b, while the soft function S_c encodes soft radiation between them. The beam function B_i only depends on the type of its incoming parton $i \equiv \kappa_i$, while S_c only depends on the color channel of the Born process. In our case, the only possible color channels are $c = \{q\bar{q}, gg\}$, which are equivalent to the color representation of the incoming partons, so we simply label it by $c \equiv i = \{q, g\}$. Both B_i and S_c are universal objects that do not depend on the details of the hard process. The process dependence is carried by the hard function H_{ab} which describes the Born process $ab \to L$. At higher orders, it encodes finite virtual corrections to the Born process and thus can be obtained from the corresponding quark or gluon form factors. The hard function also encodes any additional cuts or measurements on the constituents of L, which we keep implicit.[1] Results for H_{ab} at three loops are known for $gg \to H$ in the $m_t \to \infty$ limit, $b\bar{b} \to H$, and Drell-Yan production [116, 136–138, 209–218]. Explicit expressions in our notation can be found in ref. [135].

Two resolution variables that probe the IR limits of QCD are 0-jettiness, $\mathcal{T}_0$, and the total color-singlet transverse momentum q_T. In this chapter we derive their singular

[1] In this chapter and for convenience, we consider as part of the hard function *also* the decay of the color-singlet. This is common practice, especially for inclusive factorized cross sections in SCET, e.g. see [65]. In section 3.2 and in chapter 5 we consider the leptonic function, which captures the decay of the color-singlet, and the hard function separately.

structure to N^{3}LO. Specifically, we derive the analytic structure of the $\mathcal{T}_0$ and q_T beam and soft functions at three loops from their known RGEs. The beam and soft functions relevant for $\mathcal{T}_0$ and q_T are the most basic of their type, measuring the small light-cone momentum or the total transverse momentum of the inclusive sum of all collinear and soft emissions, respectively. For this reason, they are important objects in their own right, encoding fundamental properties of the singular structure of QCD, and also appear in a variety of other contexts. In particular, they often serve as building blocks for constructing the beam and soft functions necessary for more complicated scenarios or observables, see e.g. refs. [147, 155, 219–229].

The nonlogarithmic boundary coefficients for both B_i, S_c are not predicted by the RGE and require an explicit three-loop calculation. The most complicated are the beam function boundary coefficients, because they are nontrivial functions of a partonic momentum fraction z. However, they drastically simplify in the limit $z \to 1$. In this limit, the energy of collinear emissions is constrained to be small which means their interactions with the primary collinear parton can be described in the eikonal approximation where they only resolve its color charge and direction. Here, we exploit this to obtain the three-loop beam function coefficients in the $z \to 1$ limit for both $\mathcal{T}_0$ and q_T by relating them via appropriate consistency relations to known soft matrix elements. We give their detailed derivation and show explicitly that they hold to all orders, allowing one to obtain the $z \to 1$ limits of the beam functions also to higher orders once the relevant soft matrix elements are known. We also employ the obtained eikonal terms of the beam function coefficients to construct ansätze for the next-to-eikonal coefficients. At the time of their construction [2], the exact N^{3}LO beam boundary coefficients were not known. Since by now they have become available [139, 230, 231], we perform an explicit comparison to our proposed ansätze.

Another aspect that brings to the surface the complexity of the beam function boundary coefficients is related to their numerical evaluation. While their straightforward implementation based on current codes is possible, their long and complicated functional form disallows for an accurate numerical evaluation, thus hindering their use in high-precision phenomenological analyses. In light of this, we provide a method for an improved approximation of kernels that bear such functional signature, by exploiting their analytic structure to achieve a high-precision and cost-optimal numerical implementation.

The chapter is organized as follows. The three-loop structure of the beam and soft functions and the eikonal limit of the beam functions are derived for $\mathcal{T}_0$ in section 4.2 and for q_T in section 4.3. The application to $\mathcal{T}_0$ and q_T subtractions at N^{3}LO is reviewed in section 4.4. In section 4.5 we discuss the strategy for an improved kernel approximation. We conclude in section 4.6.

4.2 $\mathcal{T}_0$ factorization to three loops

In this section we study the singular structure of the $\mathcal{T}_0$ soft and beam functions. In section 4.2.1 we review key concepts of the $\mathcal{T}_0$ factorization, in sections 4.2.2 and 4.2.3 we calculate soft and beam functions to $\mathrm{N^3LO}$ by solving their RGEs and study the numerical impact of the newly calculated terms. In section 4.2.4 we discuss the extraction of the beam function coefficients the eikonal limit and finally in section 4.2.5 we provide an ansatz that is valid beyond the $z \to 1$ limit.

4.2.1 Overview of $\mathcal{T}_0$ factorization

The factorization for N-jettiness, $\mathcal{T}_N$, has been derived using SCET in refs. [65, 219, 232]. Here we focus on 0-jettiness, $\mathcal{T}_0$, which is relevant for color-singlet production and coincides with beam thrust [65, 142]. It can be defined in terms of generic measures as [219, 232]

$$\mathcal{T}_0 = \sum_i \min\Big\{\frac{2q_a \cdot k_i}{Q_a}, \frac{2q_b \cdot k_i}{Q_b}\Big\}\,, \tag{4.3}$$

where the sum runs over the momenta k_i of all final-state particles excluding L and any of its constituents. The measures $Q_{a,b}$ determine different definitions of 0-jettiness. Two possible choices, corresponding to the original definitions in refs. [65, 142], are

$$\begin{aligned}
&\text{leptonic:} \qquad Q_a = Q_b = \sqrt{\omega_a \omega_b} = Q\,, \qquad \mathcal{T}_0^{\text{lep}} = \sum_i \min\Big\{e^{Y} n_a \cdot k_i\,,\, e^{-Y} n_b \cdot k_i\Big\} \\
&\text{hadronic:} \qquad Q_{a,b} = \omega_{a,b} = Q\, e^{\pm Y}\,, \qquad \mathcal{T}_0^{\text{cm}} = \sum_i \min\Big\{n_a \cdot k_i\,,\, n_b \cdot k_i\Big\}\,.
\end{aligned} \tag{4.4}$$

The choice between the two measures is related to the process $pp \to L$ and practical experimental limitations. For example, in the charged Drell-Yan process, $pp \to W^{\pm} \to \ell\nu_\ell$, due to the presence of the neutrino the rapidity Y of the vector boson is not known and therefore the hadronic definition in eq. (4.4) must be used. For our present purposes, the precise choice of the Q_i is not important, so we will simply use the symbol $\mathcal{T}_0$.

The factorization for $\mathcal{T}_0$ is given by [65]

$$\begin{aligned}
\frac{\mathrm{d}\sigma}{\mathrm{d}Q^2 \mathrm{d}Y \mathrm{d}\mathcal{T}_0} =& \sum_{a,b} H_{ab}(Q^2,\mu) \int \mathrm{d}t_a\, \mathrm{d}t_b\, B_a(t_a, x_a, \mu)\, B_b(t_b, x_b, \mu)\, S_i\Big(\mathcal{T}_0 - \frac{t_a}{Q_a} - \frac{t_b}{Q_b}, \mu\Big) \\
&\times \Big[1 + \mathcal{O}\Big(\frac{\mathcal{T}_0}{Q}\Big)\Big]\,.
\end{aligned} \tag{4.5}$$

The factorization receives power corrections suppressed by $\mathcal{T}_0/Q$, while starting at $\mathrm{N^4LO}$ it also receives contributions from perturbative Glauber-gluon exchanges, which are not captured by eq. (4.5) [233, 234].

4.2.2 $\mathcal{T}_0$ soft function

In SCET the quark ($i = q$) and gluon ($i = g$) bare $\mathcal{T}_0$ soft function corresponds to the hemisphere soft function. It is given by the vacuum expectation value (VEV) of incoming

ultrasoft Wilson lines with a measurement in the *small* lightcone momenta [65]

$$S_i(k) = \int \mathrm{d}k_a^+ \mathrm{d}k_b^+ \, S_i(k_a^+, k_b^+) \, \delta(k - k_a^+ - k_b^+) \,, \tag{4.6}$$

$$S_q(k_a^+, k_b^+) = \frac{1}{N_c} \langle 0 | \mathrm{Tr}\big\{ \bar{\mathrm{T}}[Y_{n_a}^\dagger Y_{n_b}(0)] \delta(k_a^+ - \hat{p}_a^+) \delta(k_b^+ - \hat{p}_b^+) \, \mathrm{T}[Y_{n_b}^\dagger Y_{n_a}(0)] \big\} | 0 \rangle \,, \tag{4.7}$$

$$S_g(k_a^+, k_b^+) = \frac{1}{N_c^2 - 1} \langle 0 | \mathrm{Tr}\big\{ \bar{\mathrm{T}}[\mathcal{Y}_{n_a}^\dagger \mathcal{Y}_{n_b}(0)] \delta(k_a^+ - \hat{p}_a^+) \delta(k_b^+ - \hat{p}_b^+) \, \mathrm{T}[\mathcal{Y}_{n_b}^\dagger \mathcal{Y}_{n_a}(0)] \big\} | 0 \rangle \,, \tag{4.8}$$

where $Y_{n_i}, \mathcal{Y}_{n_i}$ are ultrasoft Wilson lines in the fundamental and adjoint representation respectively (see eq. (2.114)) and the trace is over color. In eqs. (4.6), (4.7), and (4.8) we use the abbreviation $\ell_{a,b}^+ \equiv n_{a,b} \cdot \ell$ for arbitrary ℓ^μ and $\hat{p}^\mu$ is the residual momentum operator that picks up soft momenta in the corresponding hemisphere, as defined by $n_{a,b}^\mu$. The $\mathcal{T}_0$ soft function is closely related to the hemisphere soft function for $e^+e^- \to$ jets, which is known to NNLO [145, 235–238]. They have the same anomalous dimensions to all orders [65, 118], and are equal to NNLO [65, 239]. interestingly, it is still an open question whether they remain equivalent at higher fixed orders.

The beam thrust soft function satisfies the all-order RGE [65, 118]

$$\begin{aligned} \mu \frac{\mathrm{d}}{\mathrm{d}\mu} S_i(k, \mu) &= \int \mathrm{d}k' \gamma_S^i(k - k', \mu) \, S_i(k', \mu) \equiv (\gamma_S^i \, S_i)(k, \mu) \,, \\ \gamma_S^i(k, \mu) &= 4\Gamma_{\mathrm{cusp}}^i[\alpha_s(\mu)] \, \mathcal{L}_0(k, \mu) + \gamma_S^i[\alpha_s(\mu)] \delta(k) \,, \end{aligned} \tag{4.9}$$

which fully predicts the structure of $S_i(k, \mu)$ in k and μ to all orders in perturbation theory. By solving it recursively order by order in α_s, we can derive this structure at any given fixed order. Expanding both sides of eq. (4.9) to fixed order in $\alpha_s(\mu)$ and accounting for the running of $\alpha_s(\mu)$, we obtain a relation for the $(n+1)$-loop coefficient in terms of the coefficients up to n loops,

$$\mu \frac{\mathrm{d}}{\mathrm{d}\mu} S_i^{(n+1)}(k, \mu) = \sum_{m=0}^{n} \Big[4\Gamma_{n-m}^i \big(\mathcal{L}_0 S_i^{(m)} \big)(k, \mu) + \big(2m\beta_{n-m} + \gamma_{S\,n-m}^i \big) S_i^{(m)}(k, \mu) \Big], \tag{4.10}$$

where we used the short-hand notation in eq. (A.11) for the convolution in k. This can be integrated to give

$$\begin{aligned} S_i^{(n+1)}(k, \mu) = \int_{k|_+}^{\mu} \frac{\mathrm{d}\mu'}{\mu'} \sum_{m=0}^{n} \Big[4\Gamma_{n-m}^i \big(\mathcal{L}_0 S_i^{(m)} \big)(k, \mu') + \big(2m\beta_{n-m} + \gamma_{S\,n-m}^i \big) S_i^{(m)}(k, \mu') \Big] \\ + \delta(k) \, s_i^{(n+1)} \,, \end{aligned} \tag{4.11}$$

where the soft function boundary coefficients are defined by

$$S_i^{(n)}(k, \mu = k|_+) = \delta(k) \, s_i^{(n)} \qquad \text{with} \qquad s_i^{(0)} = 1 \,. \tag{4.12}$$

Here, we have used distributional scale setting $\mu_0 = k|_+$ [144], which is defined such that it effectively allows us to treat the μ dependence of the logarithmic distributions like ordinary

logarithms. In particular, it satisfies [144]

$$\begin{aligned}
\mathcal{L}_n(k,\mu_0 = k|_+) &= 0\,,\\
\delta(k)\ln^{n+1}\frac{\mu_0}{\mu}\bigg|_{\mu_0=k|_+} &= (n+1)\mathcal{L}_n(k,\mu)\,,\\
\int_{\mu_0=k|_+}^{\mu}\frac{\mathrm{d}\mu'}{\mu'}\,\mathcal{L}_n(k,\mu') &= -\frac{1}{n+1}\mathcal{L}_{n+1}(k,\mu)\,.
\end{aligned} \tag{4.13}$$

The first relation is used in eq. (4.12) to define the boundary coefficients as the coefficients of the $\delta(k)$ by setting all logarithmic distributions in $S_i^{(n)}(k,\mu)$ to zero. The other two relations allow us to easily perform the μ' integral in eq. (4.11), essentially turning a $\delta(k)$ into a $\mathcal{L}_0(k)$ and a $\mathcal{L}_n(k)$ into a $\mathcal{L}_{n+1}(k)$. In addition, to evaluate the cross terms for $m \geq 1$ in eq. (4.11), we need the convolutions [146]

$$\begin{aligned}
(\mathcal{L}_0\mathcal{L}_0)(k,\mu) &= 2\mathcal{L}_1(k,\mu) - \zeta_2\,\delta(k)\,,\\
(\mathcal{L}_0\mathcal{L}_1)(k,\mu) &= \frac{3}{2}\mathcal{L}_2(k,\mu) - \zeta_2\mathcal{L}_0(k,\mu) + \zeta_3\,\delta(k)\,,\\
(\mathcal{L}_0\mathcal{L}_2)(k,\mu) &= \frac{4}{3}\mathcal{L}_3(k,\mu) - 2\zeta_2\mathcal{L}_1(k,\mu) + 2\zeta_3\mathcal{L}_0(k,\mu) - 2\zeta_4\,\delta(k)\,,\\
(\mathcal{L}_0\mathcal{L}_3)(k,\mu) &= \frac{5}{4}\mathcal{L}_4(k,\mu) - 3\zeta_2\mathcal{L}_2(k,\mu) + 6\zeta_3\mathcal{L}_1(k,\mu) - 6\zeta_4\mathcal{L}_0(k,\mu) + 6\zeta_5\,\delta(k)\,.
\end{aligned} \tag{4.14}$$

Starting from the LO result, $s_i^{(0)} = 1$, eq. (4.11) yields up to two loops

$$\begin{aligned}
S_i^{(0)}(k,\mu) &= \delta(k)\,,\\
S_i^{(1)}(k,\mu) &= -\mathcal{L}_1(k,\mu)\,4\Gamma_0^i - \mathcal{L}_0(k,\mu)\,\gamma_{S\,0}^i + \delta(k)\,s_i^{(1)}\,,\\
S_i^{(2)}(k,\mu) &= \mathcal{L}_3(k,\mu)\,8(\Gamma_0^i)^2 + \mathcal{L}_2(k,\mu)\,2\Gamma_0^i(2\beta_0 + 3\gamma_{S\,0}^i)\\
&\quad + \mathcal{L}_1(k,\mu)\Big[-16\zeta_2(\Gamma_0^i)^2 + (2\beta_0 + \gamma_{S\,0}^i)\gamma_{S\,0}^i - 4\Gamma_1^i - 4\Gamma_0^i\,s_i^{(1)}\Big]\\
&\quad + \mathcal{L}_0(k,\mu)\Big[4\Gamma_0^i(4\zeta_3\Gamma_0^i - \zeta_2\gamma_{S\,0}^i) - \gamma_{S\,1}^i - (2\beta_0 + \gamma_{S\,0}^i)\,s_i^{(1)}\Big] + \delta(k)\,s_i^{(2)}\,,
\end{aligned} \tag{4.15}$$

which agrees with ref. [202]. Evaluating eq. (4.11) at the next order, we obtain the three-loop result,

$$S^{(3)}(k,\mu) = \delta(k)\,s_i^{(3)} + \sum_{\ell=0}^{5} S_{i,\ell}^{(3)}\,\mathcal{L}_\ell(k,\mu)\,, \tag{4.16}$$

with the coefficients of the logarithmic distributions given by

$$\begin{aligned}
S_{i,5}^{(3)} &= -8(\Gamma_0^i)^3\\
S_{i,4}^{(3)} &= -\frac{10}{3}(\Gamma_0^i)^2\,(4\beta_0 + 3\gamma_{S\,0}^i)\\
S_{i,3}^{(3)} &= 4\Gamma_0^i\Big[16\zeta_2(\Gamma_0^i)^2 - \frac{4}{3}\beta_0^2 - \Big(\frac{10}{3}\beta_0 + \gamma_{S\,0}^i\Big)\gamma_{S\,0}^i + 4\Gamma_1^i + 2\Gamma_0^i\,s_i^{(1)}\Big]
\end{aligned}$$

$$
\begin{aligned}
S_{i,2}^{(3)} &= 16(\Gamma_0^i)^2\big[-10\zeta_3\Gamma_0^i + 3\zeta_2(\beta_0+\gamma_{S\,0}^i)\big] + (4\beta_0+3\gamma_{S\,0}^i)(-\beta_0\gamma_{S\,0}^i+2\Gamma_1^i) - \frac{(\gamma_{S\,0}^i)^3}{2} \\
&\quad + 2\Gamma_0^i\Big[2\beta_1 + 3\gamma_{S\,1}^i + (8\beta_0+3\gamma_{S\,0}^i)s_i^{(1)}\Big] \\
S_{i,1}^{(3)} &= 32(\Gamma_0^i)^2\big[\zeta_4\Gamma_0^i - \zeta_3(3\beta_0+2\gamma_{S\,0}^i)\big] + 8\zeta_2\Gamma_0^i\big[(3\beta_0+\gamma_{S\,0}^i)\gamma_{S\,0}^i - 4\Gamma_1^i\big] \\
&\quad + 4\beta_0\gamma_{S\,1}^i + 2\gamma_{S\,0}^i(\beta_1+\gamma_{S\,1}^i) + \big[-16\zeta_2(\Gamma_0^i)^2 + 8\beta_0^2 + (6\beta_0+\gamma_{S\,0}^i)\gamma_{S\,0}^i - 4\Gamma_1^i\big]s_i^{(1)} \\
&\quad - 4\Gamma_2^i - 4\Gamma_0^i\, s_i^{(2)} \\
S_{i,0}^{(3)} &= 16(\Gamma_0^i)^2\Big[4\Gamma_0^i(2\zeta_2\zeta_3-3\zeta_5) + \zeta_4\Big(2\beta_0+\frac{\gamma_{S\,0}^i}{2}\Big)\Big] - 4\zeta_3\Gamma_0^i\big[(2\beta_0+\gamma_{S\,0}^i)\gamma_{S\,0}^i - 8\Gamma_1^i\big] \\
&\quad - 4\zeta_2\big(\gamma_{S\,0}^i\Gamma_1^i + \Gamma_0^i\gamma_{S\,1}^i\big) + \Big\{4\Gamma_0^i\big[4\zeta_3\Gamma_0^i - \zeta_2(2\beta_0+\gamma_{S\,0}^i)\big] - (2\beta_1+\gamma_{S\,1}^i)\Big\}s_i^{(1)} \\
&\quad - \gamma_{S\,2}^i - (4\beta_0+\gamma_{S\,0}^i)s_i^{(2)}\,.
\end{aligned}
\tag{4.17}
$$

This agrees with a corresponding numerical expression in ref. [110]. The required anomalous dimension coefficients up to three loops and boundary coefficients up to two loops are given in appendix B.

Numerical impact. The soft function $S_i(k,\mu)$ has an explicit dependence on μ, which cancels against that of the hard and beam functions in eq. (4.5). Therefore, simply varying the scale μ is not very meaningful for illustrating the numerical impact of the μ-dependent three-loop terms. Instead, we consider the resummed soft function which results from the solution of the RGE in eq. (4.9)

$$
S_i(k,\mu) = \int \mathrm{d}k'\, S_i(k',\mu_S)\, U_S^i(k-k',\mu_S,\mu)\,,
\tag{4.18}
$$

where the evolution kernel U_S^i evolves the soft function between the scales μ_S and μ while it satisfies $U_S^i(k,\mu_S,\mu_S)=\delta(k)$. Its closed form solution reads [118, 142]

$$
U_S^i(k,\mu_S,\mu) = \frac{e^{K_S^i-\gamma_E\,\eta_S^i}}{\Gamma(1+\eta_S^i)}\left[\frac{\eta_S^i}{\mu_S}\mathcal{L}^{\eta_S^i}\Big(\frac{k}{\mu_S}\Big)+\delta(k)\right],
\tag{4.19}
$$

$$
K_S^i \equiv K_S^i(\mu_S,\mu) = -4K_\Gamma^i(\mu_S,\mu) + K_{\gamma_S^i}(\mu_S,\mu)\,, \qquad \eta_S^i \equiv \eta_S^i(\mu_S,\mu) = 4\eta_\Gamma^i(\mu_S,\mu)\,,
\tag{4.20}
$$

where the definition of the plus distributions $\mathcal{L}^a(x)$ is given in appendix A.2.1 and the functional form of K_S^i, η_S^i in appendix B.5. A detailed solution of RGEs as that of eq. (4.9) that involve anomalous dimensions with plus and delta functions, is given in appendix D of ref. [63].

Formally, the μ_S dependence on the right-hand side of eq. (4.18) cancels, but when the starting condition $S_i(k,\mu_S)$ is evaluated at fixed order, it only cancels up to higher-order terms. For ease of presentation, we consider the cumulant of the soft function

$$
(S_i\otimes U_S^i)_{\mathrm{cut}}(\mathcal{T}_{\mathrm{cut}},\mu) = \int^{\mathcal{T}_{\mathrm{cut}}}\mathrm{d}k \int \mathrm{d}k'\, S_i(k',\mu_S)\, U_S^i(k-k',\mu_S,\mu)\,,
\tag{4.21}
$$

for which the distributions turn into ordinary logarithms of $\mathcal{T}_{\mathrm{cut}}$.

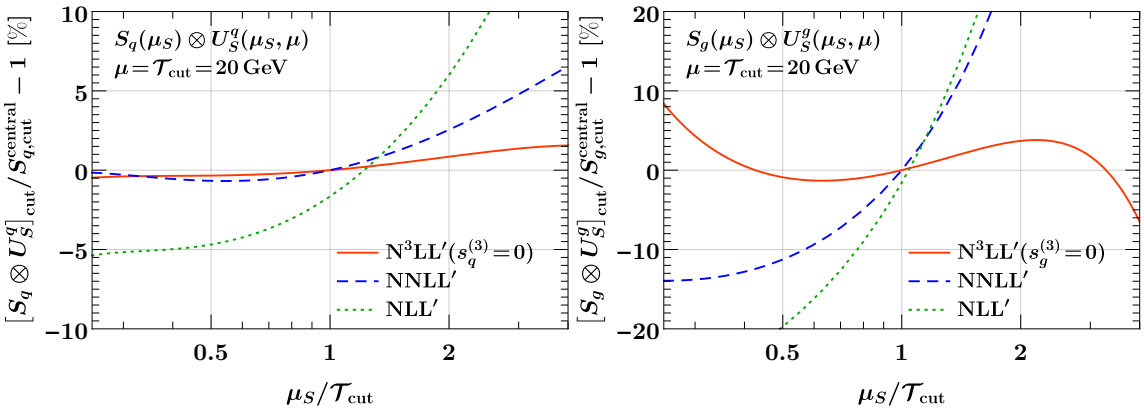

Figure 4.1: Residual scale dependence of the integrated resummed $\mathcal{T}_0$ soft function for $i = q$ (left) and $i = g$ (right). Shown are the relative deviations from the NNLL′ result $S_{i,\rm cut}^{\rm central}$ at the central scale $\mu_S = \mathcal{T}_{\rm cut}$.

In figure 4.1, we take as an example $\mathcal{T}_{\rm cut} = \mu = 20\,\text{GeV}$ and show the residual μ_S dependence of the resummed soft function when varying μ_S around the canonical central value $\mu_S = \mathcal{T}_{\rm cut}$ at NLL′ (dotted green), NNLL′ (dashed blue), and N^{3}LL′ (solid orange). For the latter we set the currently unknown three-loop constant term $s_i^{(3)} = 0$. In all cases, we show the relative difference to the central value at NNLL′. For simplicity we always use the same four-loop (N^{3}LL) running for α_s (see appendix B.5), which formally amounts to a higher-order effect at (N)NLL′. For the quark soft function (left panel), the μ_S dependence is more than halved going from NLL′ to NNLL′, and roughly halved again at N^{3}LL′. In the gluon case (right panel), the μ_S dependence is noticeably larger, but also reduces significantly at each order as it should. Note that the missing three-loop constant term will add an additional source of μ_S dependence due to its $\alpha_s^3(\mu_S)$ prefactor, which however should not change the general picture.

We stress that the residual μ_S dependence in the resummed soft function by itself is not necessarily a good indicator of the perturbative uncertainty. Nevertheless, the reduction in the scale dependence still provides a useful cross check and an indication of the typical reduction of perturbative uncertainties one might expect at each order. We also emphasize that the size of the variations in figure 4.1 does not necessarily reflect the variations one should expect in the resummed cross section, where the evolution of the soft function happens in conjunction with the beam and hard functions.

4.2.3 $\mathcal{T}_0$ beam function

In SCET the quark ($i = q$) and gluon ($i = g$) bare $\mathcal{T}_0$ beam functions correspond to the inclusive virtuality-dependent (SCET$_{\rm I}$) beam functions. They are defined as forward matrix elements of proton states with lightlike momenta $P_a^\mu = E_{\rm cm} n_a^\mu / 2$ and n_a-collinear quarks

χ_{n_a} and gluons $\mathcal{B}_{n_a\perp}$ [118]

$$B_q(t_a, x_a) = \theta(\omega_a)\langle p_{n_a}|\bar{\chi}_{n_a}(0)\delta(t_a - \omega_a\hat{p}_a^+)[\delta(\omega_a - \bar{n}_a\cdot\mathcal{P})\frac{\bar{\not{n}}_a}{2}\chi_{n_a}(0)]|p_{n_a}\rangle\,, \tag{4.22}$$

$$B_g(t_a, x_a) = \theta(\omega_a)\omega_a\langle p_{n_a}|\mathcal{B}^\mu_{n_a\perp}(0)\delta(t_a - \omega_a\hat{p}_a^+)[\delta(\omega_a - \bar{n}_a\cdot\mathcal{P})\mathcal{B}_{n_a\perp\mu}(0)]|p_{n_a}\rangle\,, \tag{4.23}$$

where the matrix elements are implicitly averaged over proton spin. The n_b-collinear beam functions are analogously defined. As before, $\hat{p}^\mu$ is the residual momentum operator with $\hat{p}_a^+ \equiv n_a\cdot\hat{p}$ and $\mathcal{P}^\mu$ is the label momentum operator. The $\delta(t_a - \omega_a\hat{p}_a^+)$ measures the total (small) plus momentum of all initial-state collinear radiation with t_a denoting the transverse virtuality of the beam function, whereas $\delta(\omega_a - \bar{n}_a\cdot\mathcal{P})$ measures the large lightcone momenta of the parton that participates in the hard interaction. In what follows, we suppress the indices a, b that differentiate between $n_{a,b}$-beam functions as it is irrelevant for our derivations and only keep the index $i = q, g$.

The $\mathcal{T}_0$ beam function appears in the N-jettiness factorization for any N [232], including deep-inelastic scattering [240]. It has been shown that it also arises in generalized threshold factorization theorems for inclusive color-singlet production in hadronic collisions [241]. The virtuality-dependent quark and gluon beam functions are known to NNLO [118, 142, 242, 243] and they were recently calculated at N^{3}LO [244].

The beam function $B_i(t, x, \mu)$ obeys the all-order RGE [65, 118]

$$\mu\frac{\mathrm{d}}{\mathrm{d}\mu}B_i(t, x, \mu) = \int \mathrm{d}t'\,\gamma_B^i(t - t', \mu)\,B_i(t', x, \mu)\,,$$
$$\gamma_B^i(t, \mu) = -2\Gamma^i_{\mathrm{cusp}}[\alpha_s(\mu)]\,\mathcal{L}_0(t, \mu^2) + \gamma_B^i[\alpha_s(\mu)]\,\delta(t)\,. \tag{4.24}$$

For $t \gg \Lambda_{\mathrm{QCD}}$, the beam function satisfies an operator product expansion (OPE) in terms of standard PDFs [65, 118]

$$B_i(t, x, \mu) = \sum_j \int\frac{\mathrm{d}z}{z}\,\mathcal{I}_{ij}(t, z, \mu)\,f_j\Big(\frac{x}{z}, \mu\Big)\left[1 + \mathcal{O}\Big(\frac{\Lambda^2_{\mathrm{QCD}}}{t}\Big)\right], \tag{4.25}$$

where the $\mathcal{I}_{ij}(t, z, \mu)$ are perturbatively calculable matching coefficients. Taking into account the evolution of the PDFs (see eq. (A.32)), they obey the RGE [118]

$$\mu\frac{\mathrm{d}}{\mathrm{d}\mu}\mathcal{I}_{ij}(t, z, \mu) = \sum_k \int \mathrm{d}t'\,\frac{\mathrm{d}z'}{z'}\,\mathcal{I}_{ik}\Big(t - t', \frac{z}{z'}, \mu\Big)\Big[\gamma_B^i(t', \mu)\,\mathbf{1}_{kj}(z') - \delta(t')\,2P_{kj}(z', \mu)\Big], \tag{4.26}$$

where $\mathbf{1}_{ij}(z) \equiv \delta_{ij}\,\delta(1 - z)$ and $2P_{ij}(z, \mu)$ are the PDF anomalous dimensions.

By solving the RGE in eq. (4.26) recursively order by order, we can derive the complete structure of $\mathcal{I}_{ij}(t, z, \mu)$ at any given fixed order, as was done in refs. [142, 242] to NNLO. Following the same procedure as in section 4.2.2, keeping track of the flavor indices and Mellin convolutions, the $(n + 1)$-loop term is determined from the up to n-loop terms as

$$\mathcal{I}_{ij}^{(n+1)}(t, z, \mu^2) = \delta(t)\,I_{ij}^{(n+1)}(z) + \int_{t|_+}^{\mu^2}\frac{\mathrm{d}\tilde{\mu}^2}{\tilde{\mu}^2}\sum_{m=0}^{n}\Big\{-\Gamma^i_{n-m}\big[\mathcal{L}_0\mathcal{I}_{ij}^{(m)}(z)\big](t, \tilde{\mu}^2) \tag{4.27}$$
$$+ \Big(m\beta_{n-m} + \frac{\gamma^i_{B\,n-m}}{2}\Big)\mathcal{I}_{ij}^{(m)}(t, z, \tilde{\mu}^2) - \big[\mathcal{I}^{(m)}(t, \tilde{\mu}^2)P^{(n-m)}\big]_{ij}(z)\Big\}\,,$$

where the μ-independent boundary coefficients are defined as

$$\mathcal{I}_{ij}^{(n)}(t,z,\mu^2=t|_+) = \delta(t)\, I_{ij}^{(n)}(z)\,. \tag{4.28}$$

Starting from the LO result, $I_{ij}^{(0)}(z) = \mathbf{1}_{ij}(z) \equiv \delta_{ij}\,\delta(1-z)$, we obtain up to two loops

$$\begin{aligned}
\mathcal{I}_{ij}^{(0)}(t,z,\mu^2) &= \delta(t)\,\mathbf{1}_{ij}(z)\,,\\
\mathcal{I}_{ij}^{(1)}(t,z,\mu^2) &= \mathcal{L}_1(t,\mu^2)\,\Gamma_0^i\,\mathbf{1}_{ij}(z) + \mathcal{L}_0(t,\mu^2)\Big[-\frac{\gamma_{B\,0}^i}{2}\,\mathbf{1}_{ij}(z) + P_{ij}^{(0)}(z)\Big] + \delta(t)\,I_{ij}^{(1)}(z)\,,\\
\mathcal{I}_{ij}^{(2)}(t,z,\mu^2) &= \mathcal{L}_3(t,\mu^2)\,\frac{(\Gamma_0^i)^2}{2}\,\mathbf{1}_{ij}(z)\\
&\quad + \mathcal{L}_2(t,\mu^2)\,\frac{\Gamma_0^i}{2}\Big[-\Big(\beta_0+\frac{3}{2}\gamma_{B\,0}^i\Big)\mathbf{1}_{ij}(z) + 3P_{ij}^{(0)}(z)\Big]\\
&\quad + \mathcal{L}_1(t,\mu^2)\Big\{\Big[-\zeta_2(\Gamma_0^i)^2 + \Big(\beta_0+\frac{\gamma_{B\,0}^i}{2}\Big)\frac{\gamma_{B\,0}^i}{2} + \Gamma_1^i\Big]\mathbf{1}_{ij}(z)\\
&\qquad\qquad - (\beta_0+\gamma_{B\,0}^i)P_{ij}^{(0)}(z) + (P^{(0)}P^{(0)})_{ij}(z) + \Gamma_0^i\,I_{ij}^{(1)}(z)\Big\}\\
&\quad + \mathcal{L}_0(t,\mu^2)\Big\{\Big[\Gamma_0^i\Big(\zeta_3\Gamma_0^i + \zeta_2\frac{\gamma_{B\,0}^i}{2}\Big) - \frac{\gamma_{B\,1}^i}{2}\Big]\mathbf{1}_{ij}(z) - \zeta_2\Gamma_0^i\,P_{ij}^{(0)}(z)\\
&\qquad\qquad + P_{ij}^{(1)}(z) - \Big(\beta_0+\frac{\gamma_{B\,0}^i}{2}\Big)I_{ij}^{(1)}(z) + (I^{(1)}P^{(0)})_{ij}(z)\Big\}\\
&\quad + \delta(t)\,I_{ij}^{(2)}(z)\,,
\end{aligned} \tag{4.29}$$

which agrees with refs. [142, 202, 242]. The NLO and NNLO boundary coefficients $I_{ij}^{(1,2)}(z)$ together with the required Mellin convolutions $(P^{(0)}P^{(0)})_{ij}(z)$ and $(I^{(1)}P^{(0)})_{ij}(z)$ can be found in refs. [242, 243].[2]

Plugging eq. (4.29) back into eq. (4.27), we obtain the N^{3}LO result

$$\mathcal{I}_{ij}^{(3)}(t,z,\mu^2) = \delta(t)\,I_{ij}^{(3)}(z) + \sum_{\ell=0}^{5}\mathcal{I}_{ij,\ell}^{(3)}(z)\,\mathcal{L}_\ell(t,\mu^2)\,, \tag{4.30}$$

with the coefficients

$$\begin{aligned}
\mathcal{I}_{ij,5}^{(3)}(z) &= \frac{(\Gamma_0^i)^3}{8}\mathbf{1}_{ij}(z)\\
\mathcal{I}_{ij,4}^{(3)}(z) &= \frac{5}{8}(\Gamma_0^i)^2\Big[-\Big(\frac{2}{3}\beta_0+\frac{\gamma_{B\,0}^i}{2}\Big)\mathbf{1}_{ij}(z) + P_{ij}^{(0)}\Big]\\
\mathcal{I}_{ij,3}^{(3)}(z) &= \Gamma_0^i\Big\{\Big[-\zeta_2(\Gamma_0^i)^2 + \frac{\beta_0^2}{3} + \Big(\frac{5}{3}\beta_0+\frac{\gamma_{B\,0}^i}{2}\Big)\frac{\gamma_{B\,0}^i}{2} + \Gamma_1^i\Big]\mathbf{1}_{ij}(z)\\
&\quad - \Big(\frac{5}{3}\beta_0+\gamma_{B\,0}^i\Big)P_{ij}^{(0)}(z) + (P^{(0)}P^{(0)})_{ij}(z) + \frac{\Gamma_0^i}{2}I_{ij}^{(1)}(z)\Big\}
\end{aligned}$$

[2] We caution that the functions $P_{ij}(z)$ and $I_{ij}(z)$ in refs. [202, 242, 243] are expanded in powers of $\alpha_s/(2\pi)$ while here we expand them in powers of $\alpha_s/(4\pi)$.

$$
\begin{aligned}
\mathcal{I}^{(3)}_{ij,2}(z) &= \Big\{(\Gamma^i_0)^2\Big[\frac{5}{2}\zeta_3\Gamma^i_0 + \frac{3}{2}\zeta_2(\beta_0+\gamma^i_{B\,0})\Big] - \Big(\beta_0+\frac{3}{4}\gamma^i_{B\,0}\Big)\Big(\beta_0\frac{\gamma^i_{B\,0}}{2}+\Gamma^i_1\Big) - \frac{(\gamma^i_{B\,0})^3}{16} \\
&\quad - \frac{\Gamma^i_0}{2}\Big(\beta_1+\frac{3}{2}\gamma^i_{B\,1}\Big)\Big\}\mathbf{1}_{ij}(z) + 3\Big[-\zeta_2(\Gamma^i_0)^2 + \frac{\beta_0^2}{3} + \Big(\beta_0+\frac{\gamma^i_{B\,0}}{4}\Big)\frac{\gamma^i_{B\,0}}{2} + \frac{\Gamma^i_1}{2}\Big]P^{(0)}_{ij}(z) \\
&\quad - \frac{3}{2}\Big(\beta_0+\frac{\gamma^i_{B\,0}}{2}\Big)(P^{(0)}P^{(0)})_{ij}(z) + \frac{1}{2}(P^{(0)}P^{(0)}P^{(0)})_{ij}(z) \\
&\quad + \frac{3}{2}\Gamma^i_0\Big[P^{(1)}_{ij}(z) - \Big(\frac{4}{3}\beta_0+\frac{\gamma^i_{B\,0}}{2}\Big)I^{(1)}_{ij}(z) + (I^{(1)}P^{(0)})_{ij}(z)\Big] \\
\mathcal{I}^{(3)}_{ij,1}(z) &= \Big\{-(\Gamma^i_0)^2\Big[\frac{\zeta_4}{2}\Gamma^i_0 + \zeta_3(3\beta_0+2\gamma^i_{B\,0})\Big] - \zeta_2\Gamma^i_0\Big[(3\beta_0+\gamma^i_{B\,0})\frac{\gamma^i_{B\,0}}{2} + 2\Gamma^i_1\Big] \\
&\quad + \beta_0\gamma^i_{B\,1} + \frac{\gamma^i_{B\,0}}{2}(\beta_1+\gamma^i_{B\,1}) + \Gamma^i_2\Big\}\mathbf{1}_{ij}(z) + \Big\{\Gamma^i_0\big[4\zeta_3\Gamma^i_0 + \zeta_2(3\beta_0+2\gamma^i_{B\,0})\big] \\
&\quad - (\beta_1+\gamma^i_{B\,1})\Big\}P^{(0)}_{ij}(z) - 2\zeta_2\Gamma^i_0(P^{(0)}P^{(0)})_{ij}(z) - (2\beta_0+\gamma^i_{B\,0})P^{(1)}_{ij}(z) \\
&\quad + (P^{(0)}P^{(1)}+P^{(1)}P^{(0)})_{ij}(z) + \Big[-\zeta_2(\Gamma^i_0)^2 + 2\beta_0^2 + \Big(3\beta_0+\frac{\gamma^i_{B\,0}}{2}\Big)\frac{\gamma^i_{B\,0}}{2} + \Gamma^i_1\Big]I^{(1)}_{ij}(z) \\
&\quad - (3\beta_0+\gamma^i_{B\,0})(I^{(1)}P^{(0)})_{ij}(z) + (I^{(1)}P^{(0)}P^{(0)})_{ij}(z) + \Gamma^i_0\, I^{(2)}_{ij}(z) \\
\mathcal{I}^{(3)}_{ij,0}(z) &= \Big\{(\Gamma^i_0)^2\Big[-\Gamma^i_0(2\zeta_2\zeta_3-3\zeta_5) + \zeta_4\Big(\beta_0+\frac{\gamma^i_{B\,0}}{4}\Big)\Big] + \zeta_3\Gamma^i_0\Big[\Big(\beta_0+\frac{\gamma^i_{B\,0}}{2}\Big)\frac{\gamma^i_{B\,0}}{2} + 2\Gamma^i_1\Big] \\
&\quad + \frac{\zeta_2}{2}\big(\gamma^i_{B\,0}\Gamma^i_1 + \Gamma^i_0\gamma^i_{B\,1}\big) - \frac{\gamma^i_{B\,2}}{2}\Big\}\mathbf{1}_{ij}(z) - \Big\{\Gamma^i_0\Big[\frac{\zeta_4}{2}\Gamma^i_0 + \zeta_3(\beta_0+\gamma^i_{B\,0})\Big] \\
&\quad + \zeta_2\Gamma^i_1\Big\}P^{(0)}_{ij}(z) + \Gamma^i_0\big[\zeta_3(P^{(0)}P^{(0)})_{ij}(z) - \zeta_2 P^{(1)}_{ij}(z)\big] + P^{(2)}_{ij}(z) \\
&\quad + \Big\{\Gamma^i_0\Big[\zeta_3\Gamma^i_0 + \zeta_2\Big(\beta_0+\frac{\gamma^i_{B\,0}}{2}\Big)\Big] - \Big(\beta_1+\frac{\gamma^i_{B\,1}}{2}\Big)\Big\}I^{(1)}_{ij}(z) - \Gamma^i_0\zeta_2(I^{(1)}P^{(0)})_{ij}(z) \\
&\quad + (I^{(1)}P^{(1)})_{ij}(z) - \Big(2\beta_0+\frac{\gamma^i_{B\,0}}{2}\Big)I^{(2)}_{ij}(z) + (I^{(2)}P^{(0)})_{ij}(z)\,. \qquad (4.31)
\end{aligned}
$$

The required anomalous dimensions and splitting functions up to three loops are given in appendices B and A.3 respectively. We have evaluated all Mellin convolutions appearing in eq. (4.31) using the `MT` package [245]. The calculation of $(I^{(2)}P^{(0)})_{ij}(z)$ required the use of the identity

$$
\mathrm{Li}_3\Big(\frac{1}{1+z}\Big)+\mathrm{Li}_3(-z)+\mathrm{Li}_3\Big(\frac{z}{1+z}\Big) = \zeta_3-\zeta_2\ln(1+z)-\frac{1}{2}\ln^2(1+z)\ln z+\frac{1}{3}\ln^3(1+z)\,. \quad (4.32)
$$

Numerical impact. To illustrate the numerical impact of the three-loop corrections, we consider the resummed beam function which results from the solution of the RGE in eq. (4.24)

$$
B_i(t,x,\mu) = \int \mathrm{d}t'\, B_i(t',x,\mu_B)\, U^i_B(t-t',\mu_B,\mu)\,, \qquad (4.33)
$$

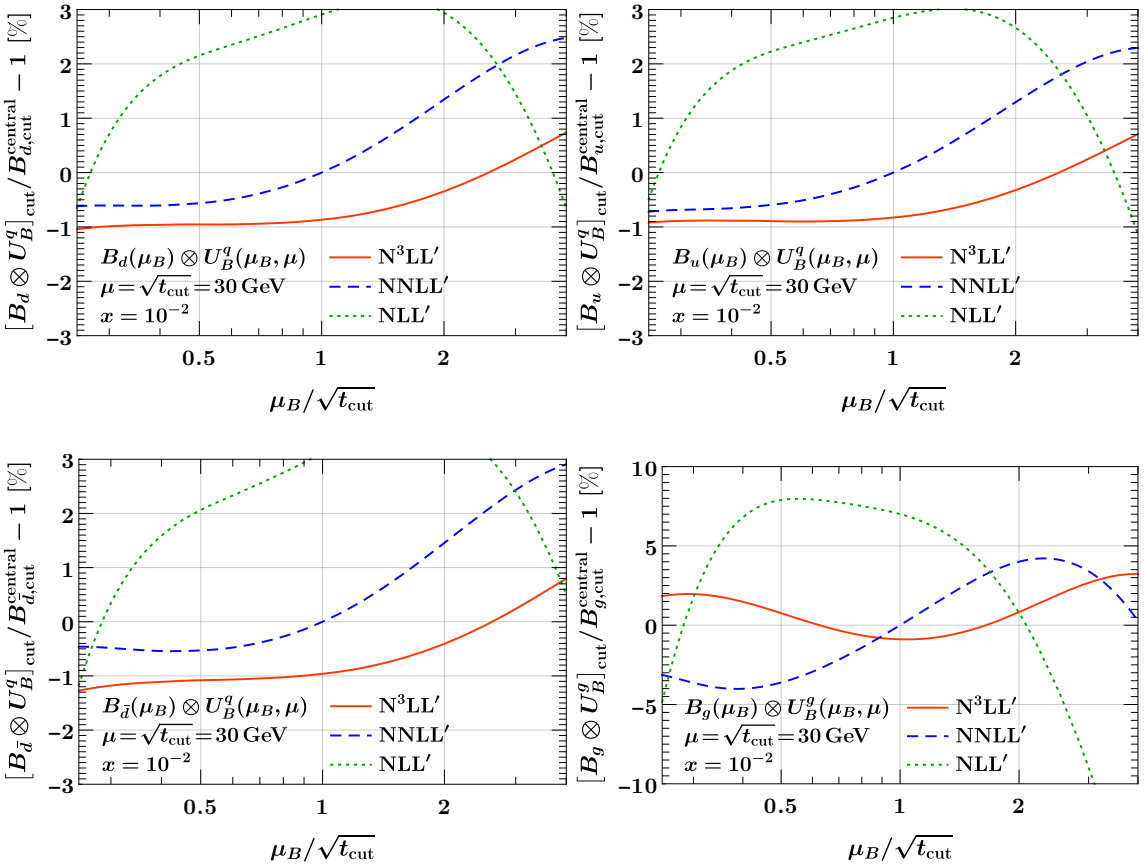

Figure 4.2: Residual scale dependence of the resummed integrated $\mathcal{T}_N$ beam function for $i = d$ (top left), u (top right), $\bar{d}$ (bottom left), and g (bottom right). Shown are the relative deviations from the NNLL′ result $B_{i,\rm cut}^{\rm central}$ at the central scale $\mu_B = \sqrt{t_{\rm cut}}$.

where U_B^i is the beam function evolution kernel that evolves B_i between the scales μ_B and μ while it satisfies $U_B^i(t, \mu_B, \mu_B) = \delta(t)$. Its closed form solution reads [118, 142]

$$U_B^i(t,\mu_B,\mu) = \frac{e^{K_B^i - \gamma_E\,\eta_B^i}}{\Gamma(1+\eta_B^i)} \left[\frac{\eta_B^i}{\mu_B^2}\,\mathcal{L}^{\eta_B^i}\!\left(\frac{t}{\mu_B^2}\right) + \delta(t)\right], \tag{4.34}$$

$$K_B^i \equiv K_B^i(\mu_B,\mu) = 4K_\Gamma^i(\mu_B,\mu) + K_{\gamma_B^i}(\mu_B,\mu)\,, \quad \eta_B^i \equiv \eta_B^i(\mu_B,\mu) = -2\eta_\Gamma^i(\mu_B,\mu)\,, \tag{4.35}$$

where the definition of the plus distributions $\mathcal{L}^a(x)$ given in appendix A.2.1 and the functional form of K_B^i, η_B^i in appendix B.5.

Similar to the soft function above, the μ_B dependence on the right-hand side of eq. (4.33) formally cancels, but since $B_i(t, x, \mu_B)$ is only evaluated at fixed order, this cancellation is satisfied up to higher order terms in its perturbative expansion. For ease of presentation, we show results for the cumulant of the resummed beam function

$$(B_i \otimes U_B^i)_{\rm cut}(t_{\rm cut}, x, \mu) = \int^{t_{\rm cut}} {\rm d}t \int {\rm d}t'\, B_i(t', x, \mu_B)\, U_B^i(t - t', \mu_B, \mu)\,. \tag{4.36}$$

In figure 4.2, we show the residual μ_B dependence of the resummed integrated beam function at fixed representative values of $x = 10^{-2}$ and $\sqrt{t_{\rm cut}} = \mu = 30\,\text{GeV}$. We again show the relative difference to the NNLL′ central result at $\mu_B = \sqrt{t_{\rm cut}}$ at NLL′ (dotted green), NNLL′ (dashed blue), and N^{3}LL′ (solid orange).[3] We use the `MMHT2014nnlo68cl` [246] NNLO PDFs and four-loop running of α_s everywhere. These evolution orders are sufficient to ensure the formal cancellation of the μ_B dependence at N^{3}LL′, while at lower orders they amount to a higher-order effect. Numerical results to N^{3}LL with PDFs and α_s evolution at corresponding lower orders can be found in ref. [243]. While for the gluon case (bottom right panel) the residual μ_B dependence is noticeably reduced about a factor of two between N^{3}LL′ and NNLL′, the same doesn't (entirely) happen for the quark cases (top row and bottom left panels). In these, while the up variation shows a significant reduction of more than a factor of two, for the down variation this is not the case. We stress once more that as for the soft function, the residual μ_B dependence of the resummed B_i by itself is not necessarily a good indicator of the perturbative uncertainty. Finally, we note that the depicted shifts $\sim \mathcal{O}(\%)$ of the N^{3}LL′ quark beam function at the central scale $\mu_B = \sqrt{t_{\rm cut}}$, implies that the $\mathcal{O}(\alpha_s^3)$ corrections are important. It will be interesting to see whether they impact the $\mathcal{T}_0$ spectrum in a nontrivial way, once the N^{3}LO corrections to the beam thrust soft function are available.

4.2.4 Beam function coefficients in the eikonal limit

We now obtain the beam function coefficients $I_{ij}^{(n)}(z)$ in the $z \to 1$ limit. As was already pointed out and exploited in the NNLO calculation in refs. [242, 243], the beam function in this limit is effectively determined by a matrix element of eikonal Wilson lines. Here, we exploit a recently derived consistency relation [241] that explicitly relates the $I_{ij}^{(n)}(z \to 1)$ to the threshold soft function to all orders in α_s. Consistency relations of this kind generically arise from different factorization theorems that apply in different limits of the same multi-differential cross section. In particular, a soft or collinear matrix element of several arguments will refactorize into a product (or convolution) of simpler pieces of fewer arguments by taking a stronger limit.

We start by defining the color-singlet lightcone momenta $q^\mp$ and corresponding momentum fractions $x_\mp$,

$$q^- \equiv \bar{n}\cdot q = \sqrt{Q^2+q_T^2}\,e^{+Y}\,, \qquad q^+ \equiv n\cdot q = \sqrt{Q^2+q_T^2}\,e^{-Y}\,, \qquad x_\mp = \frac{q^\mp}{E_{\rm cm}}\,. \tag{4.37}$$

As recently shown in ref. [241], in the generalized threshold limit $x_- \to 1$ but generic x_+, the inclusive color-singlet cross section differential in $q^\pm$ factorizes as

$$\frac{\mathrm{d}\sigma}{\mathrm{d}q^-\mathrm{d}q^+} = \sum_{a,b} H_{ab}(q^+q^-,\mu) \int \mathrm{d}t\, f_a^{\rm thr}\Big[x_-\Big(1+\frac{t}{q^+q^-}\Big),\mu\Big] B_b(t,x_+,\mu)\,\big[1+\mathcal{O}(1-x_-)\big]\,. \tag{4.38}$$

[3] Note that in comparison to ref. [2], figure 4.2 has been updated to include the N^{3}LO boundary coefficient $I_{ij}^{(3)}(z)$, hence the complete N^{3}LL′ beam functions are shown.

Here, H_{ab} is the same hard function as in eq. (4.5), and B_b is the same inclusive beam function as in eq. (4.5). The threshold PDF $f_a^{\text{thr}}(x)$ encodes the extraction of parton a from the proton for $x \to 1$.

On the other hand, in the well-known and stronger soft threshold limit, where both $x_- \to 1$ and $x_+ \to 1$, the cross section factorizes as [247–251]

$$\frac{\mathrm{d}\sigma}{\mathrm{d}q^-\mathrm{d}q^+} = \sum_{a,b} H_{ab}(q^+q^-,\mu) \int \mathrm{d}k^-\mathrm{d}k^+ \, f_a^{\text{thr}}\Big[x_-\Big(1+\frac{k^-}{q^-}\Big),\mu\Big] \, f_b^{\text{thr}}\Big[x_+\Big(1+\frac{k^+}{q^+}\Big),\mu\Big] \\ \times S_i^{\text{thr}}(k^-,k^+,\mu)\,\big[1+\mathcal{O}(1-x_-,1-x_+)\big]\,. \tag{4.39}$$

The new ingredient is the threshold soft function $S_i^{\text{thr}}(k^-,k^+,\mu)$. It describes the process-independent contribution of soft emissions with total lightcone momenta $k^+ = n\cdot k$ and $k^- = \bar{n}\cdot k$. It also only depends on the color representation $c \equiv i = \{q,g\}$ of the incoming partons.

The threshold soft function is defined as a vacuum matrix element of Wilson lines that are invariant under longitudinal boosts, and therefore satisfies the rescaling property

$$S_i^{\text{thr}}(k^-,k^+,\mu) = S_i^{\text{thr}}(e^{+y}k^-,e^{-y}k^+,\mu)\,. \tag{4.40}$$

More specifically, in the context of SCET, the soft function is invariant under RPI-III transformations [66, 252]. Exploiting this property, the soft function can be extracted [76, 119, 176, 181, 248] from the soft-virtual limit of the total color-singlet production cross section $\mathrm{d}\sigma/\mathrm{d}Q^2$, which is known to $\mathcal{O}(\alpha_s^3)$ [173, 174]. In appendix D.1, we review this procedure and give explicit results for $S_i^{\text{thr}}(k^-,k^+,\mu)$ to three loops.

The factorization theorems in eqs. (4.38) and (4.39) describe the same cross section and share a number of common ingredients. In particular, only the beam function depends on x_+ in eq. (4.38). Further expanding eq. (4.38) in the limit $x = x_+ \to 1$, it must reproduce eq. (4.39). As a result, the eikonal $x \to 1$ limit of the beam function must coincide with the threshold soft function [241],

$$B_i(t,x,\mu) = \int \frac{\mathrm{d}k}{\omega}\, S_i^{\text{thr}}\Big(\frac{t}{\omega},k,\mu\Big)\, f_i^{\text{thr}}\Big[x\Big(1+\frac{k}{\omega}\Big),\mu\Big]\,\big[1+\mathcal{O}(1-x)\big]\,. \tag{4.41}$$

Replacing $f_i^{\text{thr}}[x(1+1-z)]$ by $f_i(x/z)/z$, which is justified at leading power in $1-z$, yields the corresponding relation for the matching coefficients [241],

$$\mathcal{I}_{ij}(t,z,\mu) = \delta_{ij}\, S_i^{\text{thr}}\Big[\frac{t}{\omega},\omega(1-z),\mu\Big]\,\big[1+\mathcal{O}(1-z)\big]\,. \tag{4.42}$$

This relation captures all terms in $\mathcal{I}_{ij}(t,z,\mu)$ that are singular for $z \to 1$, while power corrections have at most an integrable singularity for $z \to 1$. Notably, the beam function becomes flavor diagonal as $z \to 1$, while offdiagonal channels are $\mathcal{O}(1-z)$ suppressed. By eq. (4.42), the matching coefficients also inherit the rescaling property in eq. (4.40), i.e., in the limit $z \to 1$, they become invariant under a simultaneous rescaling $t \mapsto e^{+y}t$ and $1-z \mapsto e^{-y}(1-z)$. In other words, they are symmetric in t/ω and $\omega(1-z)$ such that the dependence on ω cancels on the right-hand side.

In ref. [241], eq. (4.42) was explicitly confirmed at two loops by comparison to refs. [242, 243]. We now use it to predict the beam function coefficients in the eikonal limit at three loops. They are given by the coefficient of $\delta(k^-)$ in the threshold soft function upon identifying $\delta(k^+) \mapsto \delta(1-z)$ and $\mathcal{L}_n(k^+,\mu) \mapsto \mathcal{L}_n(1-z)$. Including the one-loop and two-loop results for reference, we find

$$
\begin{aligned}
I_{ij}^{(1)}(z) &= \delta_{ij}\Big[\mathcal{L}_1(1-z)\,\Gamma_0^i + \delta(1-z)\,s_i^{\mathrm{thr}(1)}\Big] + \mathcal{O}\big[(1-z)^0\big]\,,\\
I_{ij}^{(2)}(z) &= \delta_{ij}\bigg\{\mathcal{L}_3(1-z)\,\frac{(\Gamma_0^i)^2}{2} - \mathcal{L}_2(1-z)\,\frac{\Gamma_0^i}{2}\beta_0 + \mathcal{L}_1(1-z)\Big[-2\zeta_2(\Gamma_0^i)^2 + \Gamma_1^i + \Gamma_0^i\,s_i^{\mathrm{thr}(1)}\Big]\\
&\qquad + \mathcal{L}_0(1-z)\Big[2\zeta_3(\Gamma_0^i)^2 + \frac{\gamma_{S\,1}^i}{2} - \beta_0\,s_i^{\mathrm{thr}(1)}\Big] + \delta(1-z)\,s_i^{\mathrm{thr}(2)}\bigg\} + \mathcal{O}\big[(1-z)^0\big]\,,\\
I_{ij}^{(3)}(z) &= \delta_{ij}\bigg\{\mathcal{L}_5(1-z)\,\frac{(\Gamma_0^i)^3}{8} - \mathcal{L}_4(1-z)\,\frac{5}{12}(\Gamma_0^i)^2\beta_0\\
&\qquad + \mathcal{L}_3(1-z)\,\Gamma_0^i\Big[-2\zeta_2(\Gamma_0^i)^2 + \frac{\beta_0^2}{3} + \Gamma_1^i + \frac{\Gamma_0^i}{2}s_i^{\mathrm{thr}(1)}\Big]\\
&\qquad + \mathcal{L}_2(1-z)\,\Big[(\Gamma_0^i)^2(5\zeta_3\Gamma_0^i + 3\zeta_2\beta_0) - \beta_0\Gamma_1^i - \frac{\Gamma_0^i}{2}\Big(\beta_1 - \frac{3}{2}\gamma_{S\,1}^i + 4\beta_0\,s_i^{\mathrm{thr}(1)}\Big)\Big]\\
&\qquad + \mathcal{L}_1(1-z)\,\Big[(\Gamma_0^i)^2(4\zeta_4\Gamma_0^i - 6\zeta_3\beta_0) - 4\zeta_2\Gamma_0^i\Gamma_1^i - \beta_0\gamma_{S\,1}^i + \Gamma_2^i\\
&\qquad\qquad + \big(-2\zeta_2(\Gamma_0^i)^2 + 2\beta_0^2 + \Gamma_1^i\big)s_i^{\mathrm{thr}(1)} + \Gamma_0^i\,s_i^{\mathrm{thr}(2)}\Big]\\
&\qquad + \mathcal{L}_0(1-z)\,\Big[(\Gamma_0^i)^2\big(-\Gamma_0^i(8\zeta_2\zeta_3 - 6\zeta_5) + 2\zeta_4\beta_0\big) + \Gamma_0^i(4\zeta_3\Gamma_1^i - \zeta_2\gamma_{S\,1}^i) + \frac{\gamma_{S\,2}^i}{2}\\
&\qquad\qquad + \Big((\Gamma_0^i)^2 2\zeta_3 + \Gamma_0^i 2\zeta_2\beta_0 - \beta_1 + \frac{\gamma_{S\,1}^i}{2}\Big)s_i^{\mathrm{thr}(1)} - 2\beta_0\,s_i^{\mathrm{thr}(2)}\Big]\\
&\qquad + \delta(1-z)\,s_i^{\mathrm{thr}(3)}\bigg\} + \mathcal{O}\big[(1-z)^0\big]\,.
\end{aligned}
\tag{4.43}
$$

The boundary coefficients $s_i^{\mathrm{thr}(n)}$ of the threshold soft function are given in eq. (D.7). We have exploited that the noncusp anomalous dimension of the threshold soft function is given by $-\gamma_S^i(\alpha_s)$, see appendix D.1.2. For brevity, we also used that $\gamma_{S\,0}^i = 0$. The result for generic $\gamma_{S\,0}^i$ can be read off from the full expression for the threshold soft function in eq. (D.4).

The three-loop result in eq. (4.43) is a genuine prediction of the consistency relation in eq. (4.42). We stress that the information provided by it goes beyond the RGE-predicted three-loop structure in eq. (4.31). The fact that the leading $z \to 1$ terms must be symmetric in t/ω and $\omega(1-z)$ allows one to directly determine (or check) the $\delta(t)\mathcal{L}_n(1-z)$ terms from the RGE-predicted $\mathcal{L}_n(t)\delta(1-z)$ terms, which was already noted in refs. [242, 253]. However, the $\delta(t)\delta(1-z)$ coefficient cannot be predicted in this way, and eq. (4.42) explicitly identifies it with the threshold soft function coefficients $s_i^{\mathrm{thr}(3)}$. The coefficient $I_{ij}^{(3)}(z)$ in eq. (4.43) has been confirmed in ref. [244] by an explicit computation of the exact N^{3}LO beam function boundary term.

As was shown in ref. [241], a factorization theorem analogous to eq. (4.38) also holds for the inclusive cross section differential in Q and Y, with B_i replaced by a closely related,

modified beam function $\tilde{B}_i(t, x, \mu)$.[4] Note that here, the difference between the cross sections differential in $q^\pm$ and (Q, Y) matters. The RGE for $\tilde{B}_i(t, x, \mu)$ is the same as for $B_i(t, x, \mu)$ in eq. (4.24), and hence eq. (4.31) also holds for $\tilde{B}_i$ just with different boundary coefficients $\tilde{I}_{ij}^{(n)}(z)$. In the limit $z \to 1$, the difference between B_i and $\tilde{B}_i$ becomes power suppressed in $1 - z$. As a result, the $z \to 1$ limit of the modified $\tilde{I}_{ij}^{(n)}(z)$ is also given by eq. (4.43).

4.2.5 Estimating beam function coefficients beyond the eikonal limit

We now wish to study to what extent the eikonal limit of the beam function coefficients can be used to approximate the full result and/or estimate the uncertainty of terms beyond the eikonal limit.

In figure 4.3, we compare the full $\mathcal{T}_0$ beam function coefficient (solid) to its eikonal (LP dotted green) and next-to-eikonal (NLP dashed blue) expansions at NLO and NNLO for the u quark and gluon channels. We always show the convolution $(I_{ij} \otimes f_j)(x)/f_i(x)$ with the appropriate PDF f_j and normalize to the PDF $f_i(x)$, corresponding to the LO result, where $i = u$ for the u-quark case and $i = g$ for the gluon case. With this normalization, the shape gives an indication of the rapidity dependence of the beam function coefficient relative to the LO rapidity dependence induced by the shape of the PDFs. We also include the appropriate powers of $\alpha_s/(4\pi)$ at each order, so the overall normalization shows the percent impact relative to the LO result. For definiteness, we choose $\mu = 30$ GeV for the scale entering the PDFs and α_s.

The eikonal approximation reproduces the correct divergent behavior of the full flavor-diagonal contributions, denoted as[5] qqV and gg, toward large x but is off away from large x. On the other hand, including the next-to-eikonal terms yields an excellent approximation for all x, particularly for the quark beam function. The rise at very small x for the gluon, which is not reproduced at NLP, is due to the $z \to 0$ divergent behavior in the gluon coefficient, which is not reproduced by its $z \to 1$ expansion. If desired, it can be captured by including the leading $z \to 0$ behavior of the coefficients, which for simplicity we refrain from doing here. For illustration, we also show the total contribution from all other corresponding nondiagonal channels (gray dot-dashed). In each case, they are numerically subdominant to the flavor-diagonal channel and also much flatter in x, since they only start at NLP.

The fact that the NLP result reproduces the full result very well, motivates the construction of the following ansatz for the beam function coefficients

$$I_{ij,\text{approx}}^{(n)}(z) = I_{ij}^{\text{LP}(n)}(z) + I_{ij,\text{approx}}^{\text{NLP}(n)}(z) + X_2\,(1-z) I_{ij,\text{approx}}^{\text{NLP}(n)}(z)\,, \tag{4.44}$$

where the NLP coefficient itself is approximated as

$$I_{ij,\text{approx}}^{\text{NLP}(n)}(z) = -(1-z) I_{ij}^{\text{LP}(n)}(z) + X_1\,(1-z) \frac{\mathrm{d}}{\mathrm{d}(1-z)} \Big[(1-z) I_{ij}^{\text{LP}(n)}(z)\Big]\,, \tag{4.45}$$

[4] Not to be confused with the q_T beam function $\tilde{B}_i(x, \vec{b}_T, \mu, \nu)$ in the following section.
[5] See appendix A.3 for our conventions on the flavor decomposition of Mellin kernels.

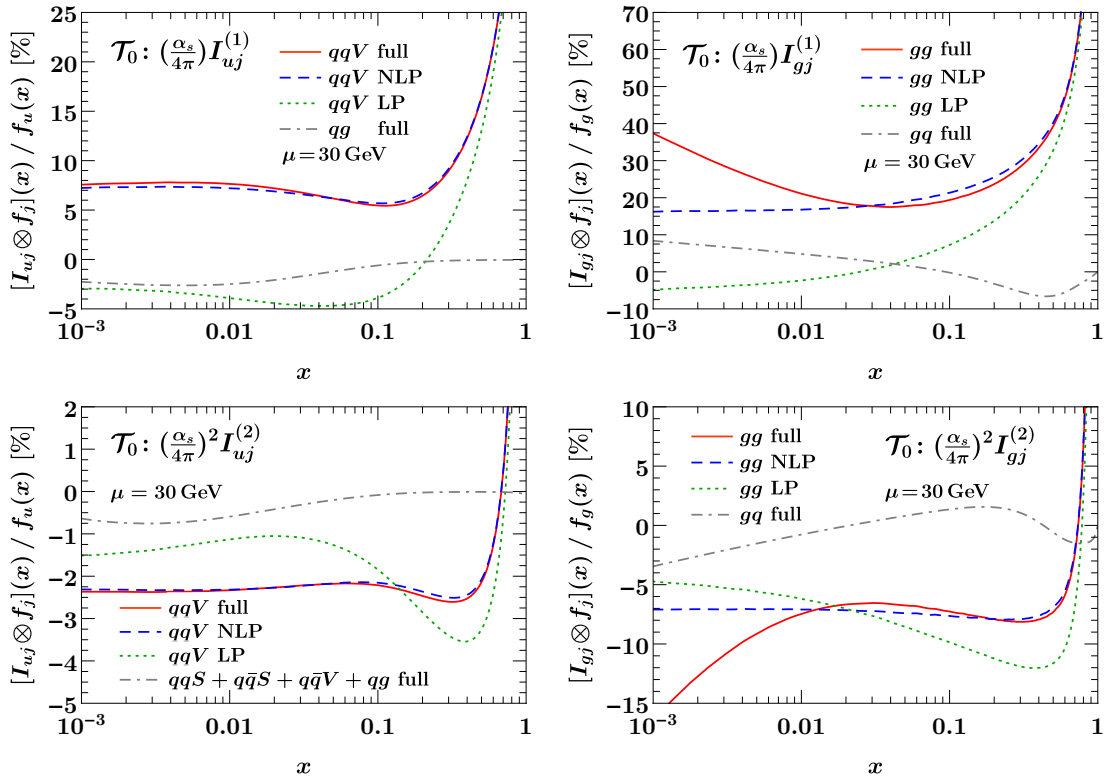

Figure 4.3: Comparison of the full beam function coefficients to their leading eikonal (LP) and next-to-eikonal (NLP) expansion at NLO (top) and NNLO (bottom). The u-quark channel is shown on the left and the gluon channel on the right. In each case we also show the sum of all nondiagonal partonic channels for comparison.

and X_1 and X_2 are free parameters that can be varied to estimate residual uncertainties. This ansatz is motivated by the known general logarithmic structure at NLP

$$I_{ij}^{\mathrm{NLP}(n)}(z) = \sum_{k=0}^{2n-1} c_{n,k}^{\mathrm{NLP}} \ln^k(1-z)\,. \tag{4.46}$$

By multiplying the LP term by $(1-z)$ in eq. (4.45), we generate the appropriate logarithmic structure at NLP. The first term in eq. (4.45) reproduces the correct NLO and NNLO coefficients for the leading logarithm at NLP $c_{1,1}^{\mathrm{NLP}} = -4C_i$ and $c_{2,3}^{\mathrm{NLP}} = -8C_i^2$ for both quarks ($C_q \equiv C_F$) and gluons ($C_g \equiv C_A$). Here, the additional double logarithm is determined by the same power of $(\Gamma_0^i)^n$ as at LP, and this pattern can be expected to hold at higher orders. The second term in eq. (4.45) generates a next-to-leading logarithmic NLP series. We fix the central value for $X_1 = 1$ to reproduce the NLL constant term at NLO $c_{1,0} = 4C_i$. Interestingly, we find that this choice also reproduces all NNLO coefficients $c_{2,k}$ very well, typically to within 10%, for both quarks and gluons and also independently of the choice of n_f. This provides a very nontrivial check and so we expect that eq. (4.45) provides a very good model of the true NLP structure also at higher orders ($n \geq 4$). To

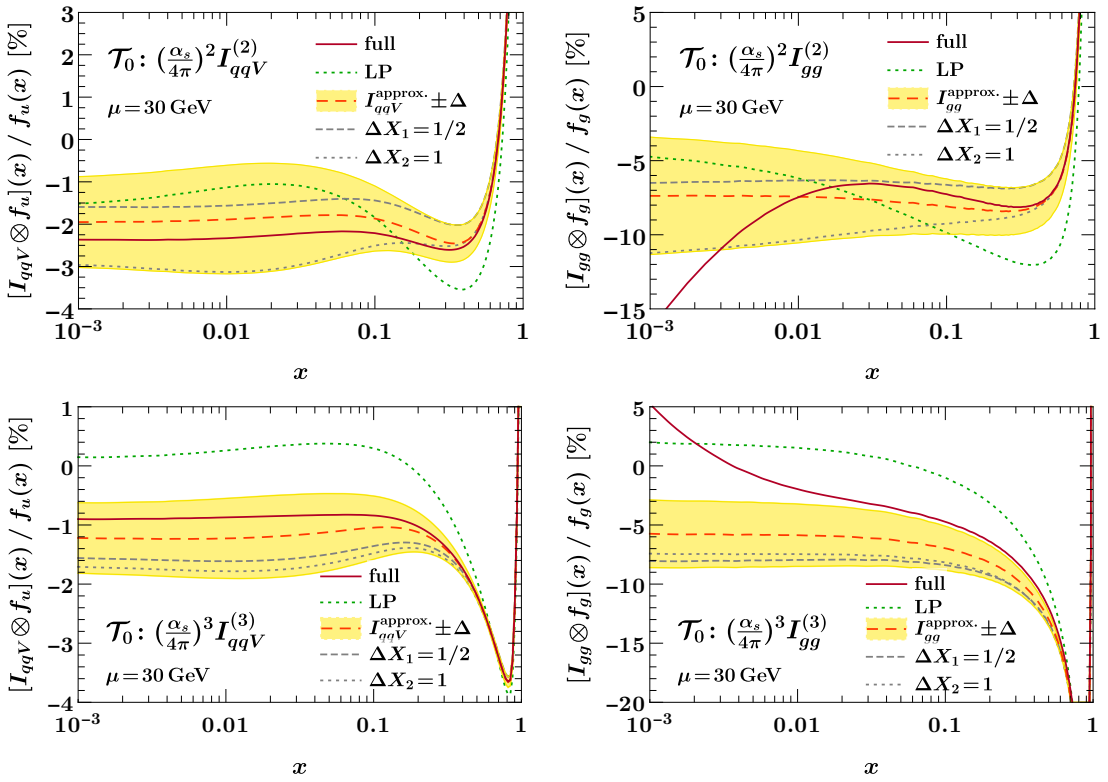

Figure 4.4: Approximate ansätze for the NNLO (top) and N^{3}LO (bottom) kernels, in the u-quark (left) and gluon (right) channels. The central curve of the ansätze corresponds to the orange dashed curves and the yellow bands are the estimated uncertainty. The exact kernels are shown in solid red.

estimate the uncertainties, we vary X_1 by ± 0.5, which effectively varies the coefficients of the subleading terms. At NNLO, this variation covers the exact value for all coefficients. In addition, the last term in eq. (4.44) estimates the possible effect of terms beyond NLP. Here, we simply take the central value $X_2 = 0$ and vary it by ± 1.

Since X_i probe independent structures, we can consider them as uncorrelated. Hence, we add the impacts Δ_i on the final result of their variation in quadrature

$$\Delta = \Delta_1 \oplus \Delta_2 = \sqrt{\Delta_1^2 + \Delta_2^2}\,. \tag{4.47}$$

In figure 4.4, we show the approximate kernel at NNLO (top) and N^{3}LO (bottom) for the u-quark (left) and gluon (right) channels. The dashed orange line shows the central result from our ansatz and the yellow band its estimated uncertainty. The gray lines show the impact of the individual variations of the X_i as indicated. The full results at NNLO (top) and N^{3}LO (bottom)[6] are shown as red solid curves. At NNLO, it shows that the

[6]Note that in comparison to ref. [2], the bottom panels of figure 4.4 have been updated to include the recently computed exact $I^{(3)}_{qqV}(z)$ and $I^{(3)}_{gg}(z)$ kernels [244] (solid red), allowing for a direct comparison between our ansatz in eq. (4.44) and the exact kernels.

ansatz including uncertainties approximates the true result very well, except for the gluon at very small x where we do not expect it to hold.

At N^{3}LO, we see that the ansatz gives rise to a sizable shift from the pure eikonal limit, which is crucial in order approximate the relative size of the true kernels. A direct comparison for both quark and gluon cases, shows our ansatz to (almost) perfectly capture the relative rapidity dependence of the exact kernels within uncertainties, except for the small x region of the gluon kernel whose behavior is inherent to $1/z$ terms. Interestingly, the exact three-loop coefficients have one to few percent impact, something already hinted from the resummed beam function (see section 4.2.3) and therefore we expect them to have a nontrivial impact in the $\mathcal{T}_0$ spectrum.

4.3 q_T factorization to three loops

In this section we study the singular structure of the q_T soft and beam functions. We start with section 4.3.1 where we review key concepts of the q_T factorization. In sections 4.3.2, 4.3.3, and 4.3.4 we calculate the rapidity anomalous dimension, the soft and beam functions to N^{3}LO by solving their RGEs and study the numerical impact of the newly calculated corrections for the latter two. In section 4.3.5 we discuss the extraction of the beam function coefficients the eikonal limit and finally in section 4.3.6 we construct an ansatz that is valid beyond the $z \to 1$ limit.

4.3.1 Overview of q_T factorization

The factorization of the q_T distribution in QCD for the limit $q_T \ll Q$ was first established by Collins, Soper, and Sterman (CSS) [54, 254, 255], and was later elaborated on in refs. [158, 256–258]. The factorization for q_T was also shown within the framework of SCET in refs. [71, 76, 259, 260]. We write the factorized cross section as

$$\begin{aligned}\frac{\mathrm{d}\sigma}{\mathrm{d}Q^2\mathrm{d}Y\,\mathrm{d}^2\vec{q}_T} &= \frac{\mathrm{d}\sigma^{(0)}}{\mathrm{d}Q^2\mathrm{d}Y\,\mathrm{d}^2\vec{q}_T}\Big[1+\mathcal{O}\Big(\frac{q_T^2}{Q^2}\Big)\Big] \\ &= \int \mathrm{d}^2\vec{b}_T\, e^{\mathrm{i}\,\vec{q}_T\cdot\vec{b}_T}\, W^{(0)}(Q^2,Y,\vec{b}_T)\Big[1+\mathcal{O}\Big(\frac{q_T^2}{Q^2}\Big)\Big]\,, \\ W^{(0)}(Q^2,Y,\vec{b}_T) &= \sum_{a,b} H_{ab}(Q^2,\mu)\tilde{B}_a(x_a,\vec{b}_T,\mu,\nu)\,\tilde{B}_b(x_b,\vec{b}_T,\mu,\nu)\,\tilde{S}_i(b_T,\mu,\nu)\,. \end{aligned} \tag{4.48}$$

As indicated, it receives quadratic power corrections $\sim \mathcal{O}(q_T^2/Q^2)$.[7] As is common, we consider the factorized singular cross section in Fourier-conjugate $\vec{b}_T$-space, where convolutions in $\vec{q}_T$ space turn into simple products. In particular, Fourier transforming the $\vec{q}_T$-dependent plus distributions $\mathcal{L}_n(\vec{q}_T,\mu)$ turns them into powers of the canonical $\vec{b}_T$-space logarithms,

[7] When additional cuts or measurements are applied on the decay products of the color singlet L, the factorization in eq. (4.48) receives enhanced linear power corrections $\sim \mathcal{O}(q_T/Q)$ [261, 262]. We discuss this case in chapter 5 for the Higgs boson fiducial q_T spectrum at the LHC.

which we denote as

$$L_b = \ln \frac{b_T^2 \mu^2}{b_0^2}\,, \qquad b_0 = 2e^{-\gamma_E}\,. \tag{4.49}$$

More details on their Fourier transformation are given in appendix A.2.2.

For the rapidity divergences that q_T factorization is affected (see section 2.3.5), we use the exponential regulator of ref. [76], which up to two loops gives results equivalent to the η regulator of refs. [260, 263].

The beam function appearing in eq. (4.48) is the inclusive transverse-momentum dependent (SCET_{II}) beam function, which also appears in the q_T factorization of $Z + j$ and $\gamma + j$ [264, 265]. The q_T-dependent soft function in eq. (4.48) is the renormalized vacuum matrix element of two incoming soft Wilson lines. Note that for simplicity, we generically refer to them as q_T or transverse momentum dependent (TMD) beam and soft functions, even though we mostly consider their b_T-dependent Fourier conjugates. The q_T beam and soft functions are known at two loops for several regulators [115, 266–272]. The beam function have been recently calculated at three loops [139, 140, 231] and the soft function is known at three loops using the exponential regulator [119].

We also note that one can equivalently define ν-independent transverse momentum dependent PDFs (TMDPDFs) as

$$\tilde{f}_i(x, \vec{b}_T, \mu, \zeta) = \tilde{B}_i(x, \vec{b}_T, \mu, \nu) \sqrt{\tilde{S}_i(b_T, \mu, \nu)}\,, \qquad \zeta = \omega^2 = (x E_{\text{cm}})^2\,, \tag{4.50}$$

as is done e.g. in refs. [54, 71, 158, 256–259]. Here, the Collins-Soper scale $\zeta = \omega^2$ [254, 255] is given in terms of the lightcone momentum $\omega = xP^-$ carried by the struck parton.

4.3.2 Rapidity anomalous dimension

The ν dependence of the beam and soft functions is encoded in their rapidity RGEs [260], which in $\vec{b}_T$-space assumes a multiplicative form (see eqs. (3.49) and (3.50) for the equivalent form in $\vec{q}_T$-space)

$$\begin{aligned} \nu \frac{\mathrm{d}}{\mathrm{d}\nu} \tilde{B}_i(x, \vec{b}_T, \mu, \nu) &= -\frac{1}{2} \tilde{\gamma}_\nu^i(b_T, \mu)\, \tilde{B}_i(x, \vec{b}_T, \mu, \nu)\,, \\ \nu \frac{\mathrm{d}}{\mathrm{d}\nu} \tilde{S}_i(b_T, \mu, \nu) &= \tilde{\gamma}_\nu^i(b_T, \mu)\, \tilde{S}_i(b_T, \mu, \nu)\,, \end{aligned} \tag{4.51}$$

where $\tilde{\gamma}_\nu^i$ are the rapidity anomalous dimensions, which are closely related to the Collins-Soper kernel [254, 255]. We remind that the ν-independence of the cross section relates the soft and beam rapidity anomalous dimension via eq. (3.62), which allows us to use the same $\tilde{\gamma}_\nu^i(b_T, \mu)$ (up to a factor) for both $\tilde{B}_i$ and $\tilde{S}_i$.

An important property of $\tilde{\gamma}_\nu^i(b_T, \mu)$ in QCD is that like the soft function it only depends on the color representation $i = \{q, g\}$ but not on the specific massless quark flavor.[8] While

[8] This should be contrasted to the QCD⊗QED q_T factorization in section 3.2, where the pure QED and the mixed QCD-QED anomalous dimensions are aware of the quark flavor via its charge, e.g. see eq. (B.15) for the $\mathcal{O}(\alpha_e^2)$ coefficient of the quark rapidity anomalous dimensions.

we only need its fixed-order expansion, we note that it becomes genuinely nonperturbative for $b_T^{-1} \lesssim \Lambda_{\rm QCD}$, and recently a proposal was made to calculate it nonperturbatively using lattice QCD [273, 274].

The rapidity anomalous dimension itself satisfies an RGE in μ,

$$\mu \frac{\mathrm{d}}{\mathrm{d}\mu} \tilde{\gamma}_\nu^i(b_T, \mu) = -4\Gamma^i_{\rm cusp}[\alpha_s(\mu)]\,, \tag{4.52}$$

which predicts its all-order structure in b_T and μ. Similar to the $\mathcal{T}_0$ soft function in section 4.2.2, it can be solved recursively order by order in α_s. Expanding both sides of eq. (4.52) to fixed order in $\alpha_s(\mu)$ and accounting for the running of $\alpha_s(\mu)$, the $(n+1)$-loop term is related to the lower-order terms by

$$\tilde{\gamma}_\nu^{i\,(n+1)}(b_T, \mu) = -2\Gamma^i_{n+1} L_b + \sum_{m=0}^{n} 2(m+1)\,\beta_{n-m} \int_{b_0/b_T}^{\mu} \frac{\mathrm{d}\mu'}{\mu'}\, \tilde{\gamma}_\nu^{i\,(m)}(b_T, \mu') + \tilde{\gamma}^i_{\nu\,n+1}\,, \tag{4.53}$$

where the nonlogarithmic boundary coefficients are defined as

$$\tilde{\gamma}^i_{\nu\,n} = \tilde{\gamma}_\nu^{i\,(n)}(b_T, \mu = b_0/b_T)\,. \tag{4.54}$$

The result up to three loops is

$$\begin{aligned}
\tilde{\gamma}_\nu^{i\,(0)}(b_T, \mu) &= -L_b\, 2\Gamma^i_0 + \tilde{\gamma}^i_{\nu\,0}\,, \\
\tilde{\gamma}_\nu^{i\,(1)}(b_T, \mu) &= -L_b^2\, \Gamma^i_0 \beta_0 + L_b\big(\beta_0 \tilde{\gamma}^i_{\nu\,0} - 2\Gamma^i_1\big) + \tilde{\gamma}^i_{\nu\,1}\,, \\
\tilde{\gamma}_\nu^{i\,(2)}(b_T, \mu) &= -L_b^3\, \frac{2}{3}\Gamma^i_0 \beta_0^2 + L_b^2\big(\beta_0^2 \tilde{\gamma}^i_{\nu\,0} - 2\Gamma^i_1 \beta_0 - \Gamma^i_0 \beta_1\big) + L_b\big(2\beta_0 \tilde{\gamma}^i_{\nu\,1} + \beta_1 \tilde{\gamma}^i_{\nu\,0} - 2\Gamma^i_2\big) \\
&\quad + \tilde{\gamma}^i_{\nu\,2}\,.
\end{aligned} \tag{4.55}$$

The boundary coefficients $\tilde{\gamma}^i_{\nu\,n}$ are known up to three loops [115, 119, 120] and are summarized in eq. (B.26).

4.3.3 q_T soft function

In SCET the quark ($i = q$) and gluon ($i = g$) bare q_T soft functions in distribution space are given as the vacuum matrix elements of time ordered soft Wilson lines. The gluon soft function reads

$$S_g(\vec{k}_s) = \frac{1}{N_c^2 - 1} \big\langle 0 \big| \mathrm{Tr}\big\{ \bar{\mathrm{T}}\big[\mathcal{S}^\dagger_{n_a} \mathcal{S}_{n_b}(0)\big] \delta^{(2)}(\vec{k}_s - \mathcal{P}_\perp)\, \mathrm{T}\big[\mathcal{S}^\dagger_{n_b} \mathcal{S}_{n_a}(0)\big] \big\} \big| 0 \big\rangle\,, \tag{4.56}$$

and the quark soft function S_q is given in eq. (3.36) upon setting $\mathbb{S}_{n_i} \mapsto S_{n_i}$. The $S_{n_i}, \mathcal{S}_{n_i}$ correspond to soft Wilson lines in the fundamental and adjoint representation respectively, and the trace in soft function matrix elements is over color. $\mathcal{P}_\perp$ is the label momentum operator that measures the perpendicular (label) momentum components of real soft emissions. The equivalent $\vec{b}_T$-space expressions follow trivially from their Fourier transform.

The soft function is explicitly known to three loops [119]. For completeness, we explicitly derive its fixed-order structure to illustrate the joint solution of its μ and ν RGEs, which in $\vec{b}_T$-space read

$$\begin{aligned}\mu\frac{\mathrm{d}}{\mathrm{d}\mu}\tilde{S}_i(b_T,\mu,\nu) &= \tilde{\gamma}^i_S(\mu,\nu)\,\tilde{S}_i(b_T,\mu,\nu)\,,\\ \nu\frac{\mathrm{d}}{\mathrm{d}\nu}\tilde{S}_i(b_T,\mu,\nu) &= \tilde{\gamma}^i_\nu(b_T,\mu)\,\tilde{S}_i(b_T,\mu,\nu)\,.\end{aligned} \tag{4.57}$$

The perturbative structure of γ^i_ν is discussed in section 4.3.2 above. The μ anomalous dimension has the all-order structure,

$$\tilde{\gamma}^i_S(\mu,\nu) = 4\Gamma^i_{\mathrm{cusp}}[\alpha_s(\mu)]\ln\frac{\mu}{\nu} + \tilde{\gamma}^i_S[\alpha_s(\mu)]\,. \tag{4.58}$$

Expanding both sides of eq. (4.57) order by order in α_s, we obtain the coupled RGEs

$$\begin{aligned}\mu\frac{\mathrm{d}}{\mathrm{d}\mu}\tilde{S}_i^{(n+1)}(b_T,\mu,\nu) &= \sum_{m=0}^{n}\Big(4\Gamma^i_{n-m}\ln\frac{\mu}{\nu} + 2m\beta_{n-m} + \tilde{\gamma}^i_{S\,n-m}\Big)\tilde{S}_i^{(m)}(b_T,\mu,\nu)\,,\\ \nu\frac{\mathrm{d}}{\mathrm{d}\nu}\tilde{S}_i^{(n+1)}(b_T,\mu,\nu) &= \sum_{m=0}^{n}\tilde{\gamma}_\nu^{i\,(n-m)}(b_T,\mu)\,\tilde{S}_i^{(m)}(b_T,\mu,\nu)\,.\end{aligned} \tag{4.59}$$

These are easily integrated to give

$$\begin{aligned}\tilde{S}_i^{(n+1)}(b_T,\mu,\nu) = \sum_{m=0}^{n}\Bigg[&\int_{b_0/b_T}^{\mu}\frac{\mathrm{d}\mu'}{\mu'}\Big(4\Gamma^i_{n-m}\ln\frac{\mu'}{\nu} + 2m\beta_{n-m} + \tilde{\gamma}^i_{S\,n-m}\Big)\tilde{S}_i^{(m)}(b_T,\mu',\nu)\\ &+\int_{b_0/b_T}^{\nu}\frac{\mathrm{d}\nu'}{\nu'}\,\tilde{\gamma}^i_{\nu\,n-m}\,\tilde{S}_i^{(m)}(b_T,b_0/b_T,\nu')\Bigg] + \tilde{s}_i^{(n+1)}\,,\end{aligned} \tag{4.60}$$

where we first integrated the ν RGE at fixed $\mu = b_0/b_T$ and then the μ RGE at arbitrary ν. In this way, the rapidity anomalous dimension reduces to its boundary coefficients $\gamma^i_{\nu\,n}$. The soft boundary coefficients in eq. (4.60) are defined as

$$\tilde{s}_i^{(n)} = \tilde{S}_i^{(n)}(b_T,\mu = b_0/b_T,\nu = b_0/b_T)\,. \tag{4.61}$$

Starting from the LO result, $\tilde{s}_i^{(0)} = 1$, and expressing the results in terms of

$$L_b = \ln\frac{b_T^2\mu^2}{b_0^2}\,,\quad b_0 = 2e^{-\gamma_E}\,,\qquad L_\nu = \ln\frac{\mu}{\nu}\,, \tag{4.62}$$

eq. (4.60) yields up to two loops

$$\begin{aligned}&\tilde{S}_i^{(0)}(b_T,\mu,\nu) = 1\,,\\ &\tilde{S}_i^{(1)}(b_T,\mu,\nu) = -L_b^2\,\frac{\Gamma^i_0}{2} + L_b\Big(L_\nu\,2\Gamma^i_0 + \frac{\tilde{\gamma}^i_{S\,0}}{2} + \frac{\tilde{\gamma}^i_{\nu\,0}}{2}\Big) - L_\nu\tilde{\gamma}^i_{\nu\,0} + \tilde{s}_i^{(1)}\,,\end{aligned}$$

$$
\begin{aligned}
\tilde{S}_i^{(2)}(b_T,\mu,\nu) = {}& L_b^4\,\frac{(\Gamma_0^i)^2}{8} - L_b^3\,\Gamma_0^i\Big(L_\nu\Gamma_0^i + \frac{\beta_0}{3} + \frac{\tilde\gamma_{S\,0}^i}{4} + \frac{\tilde\gamma_{\nu\,0}^i}{4}\Big) \\
& + L_b^2\bigg[L_\nu^2\,2(\Gamma_0^i)^2 + L_\nu\Gamma_0^i\Big(\beta_0 + \tilde\gamma_{S\,0}^i + \frac{3}{2}\tilde\gamma_{\nu\,0}^i\Big) \\
& \qquad + \beta_0\Big(\frac{\tilde\gamma_{S\,0}^i}{4} + \frac{\tilde\gamma_{\nu\,0}^i}{2}\Big) + \frac{1}{8}(\tilde\gamma_{S\,0}^i + \tilde\gamma_{\nu\,0}^i)^2 - \frac{\Gamma_1^i}{2} - \frac{\Gamma_0^i}{2}\,\tilde s_i^{(1)}\bigg] \\
& + L_b\bigg\{-L_\nu^2\,2\Gamma_0^i\tilde\gamma_{\nu\,0}^i + L_\nu\Big[-\Big(\beta_0 + \frac{\tilde\gamma_{S\,0}^i}{2} + \frac{\tilde\gamma_{\nu\,0}^i}{2}\Big)\tilde\gamma_{\nu\,0}^i + 2\Gamma_1^i + 2\Gamma_0^i\,\tilde s_i^{(1)}\Big] \\
& \qquad + \frac{\tilde\gamma_{S\,1}^i}{2} + \frac{\tilde\gamma_{\nu\,1}^i}{2} + \Big(\beta_0 + \frac{\tilde\gamma_{S\,0}^i}{2} + \frac{\tilde\gamma_{\nu\,0}^i}{2}\Big)\tilde s_i^{(1)}\bigg\} \\
& + L_\nu^2\,\frac{(\tilde\gamma_{\nu\,0}^i)^2}{2} - L_\nu\big(\tilde\gamma_{\nu\,1}^i + \tilde\gamma_{\nu\,0}^i\,\tilde s_i^{(1)}\big) + \tilde s_i^{(2)}\,. \qquad (4.63)
\end{aligned}
$$

At three loops, we write the result as

$$
\tilde{S}_i^{(3)}(b_T,\mu,\nu) = \sum_{\ell=0}^{6} \tilde{S}_{i,\ell}^{(3)}(L_\nu)\,L_b^\ell\,, \qquad (4.64)
$$

where the $\tilde{S}_{i,k}^{(3)}$ coefficients themselves are polynomials in L_ν. Inserting $\tilde\gamma_{S\,0}^i = \tilde\gamma_{\nu\,0}^i = 0$ for brevity, they are given by

$$
\begin{aligned}
\tilde{S}_{i,6}^{(3)}(L_\nu) &= -\frac{(\Gamma_0^i)^3}{48}\,, \\
\tilde{S}_{i,5}^{(3)}(L_\nu) &= L_\nu\,\frac{(\Gamma_0^i)^3}{4} + \frac{(\Gamma_0^i)^2}{6}\beta_0\,, \\
\tilde{S}_{i,4}^{(3)}(L_\nu) &= -L_\nu^2\,(\Gamma_0^i)^3 - L_\nu\,\frac{7}{6}(\Gamma_0^i)^2\beta_0 + \frac{\Gamma_0^i}{4}\Big(-\beta_0^2 + \Gamma_1^i + \frac{\Gamma_0^i}{2}\,\tilde s_i^{(1)}\Big)\,, \\
\tilde{S}_{i,3}^{(3)}(L_\nu) &= L_\nu^3\,\frac{4}{3}(\Gamma_0^i)^3 + L_\nu^2\,2(\Gamma_0^i)^2\beta_0 + L_\nu\Gamma_0^i\Big(\frac{2}{3}\beta_0^2 - 2\Gamma_1^i - \Gamma_0^i\,\tilde s_i^{(1)}\Big) \\
&\quad - \frac{2}{3}\Gamma_1^i\beta_0 - \Gamma_0^i\Big(\frac{\beta_1}{3} + \frac{\tilde\gamma_{S\,1}^i}{4} + \frac{\tilde\gamma_{\nu\,1}^i}{4} + \frac{5}{6}\beta_0\,\tilde s_i^{(1)}\Big)\,, \\
\tilde{S}_{i,2}^{(3)}(L_\nu) &= L_\nu^2\,\Gamma_0^i\big(4\Gamma_1^i + 2\Gamma_0^i\,\tilde s_i^{(1)}\big) + L_\nu\Big[2\Gamma_1^i\beta_0 + \Gamma_0^i\Big(\beta_1 + \tilde\gamma_{S\,1}^i + \frac{3}{2}\tilde\gamma_{\nu\,1}^i + 3\beta_0\,\tilde s_i^{(1)}\Big)\Big] \\
&\quad + \beta_0\Big(\frac{\tilde\gamma_{S\,1}^i}{2} + \tilde\gamma_{\nu\,1}^i\Big) - \frac{\Gamma_2^i}{2} + \Big(\beta_0^2 - \frac{\Gamma_1^i}{2}\Big)\tilde s_i^{(1)} - \frac{\Gamma_0^i}{2}\,\tilde s_i^{(2)}\,, \\
\tilde{S}_{i,1}^{(3)}(L_\nu) &= -L_\nu^2\,2\Gamma_0^i\tilde\gamma_{\nu\,1}^i + L_\nu\,2\big(-\beta_0\tilde\gamma_{\nu\,1}^i + \Gamma_2^i + \Gamma_1^i\,\tilde s_i^{(1)} + \Gamma_0^i\,\tilde s_i^{(2)}\big) \\
&\quad + \frac{\tilde\gamma_{S\,2}^i}{2} + \frac{\tilde\gamma_{\nu\,2}^i}{2} + \Big(\beta_1 + \frac{\tilde\gamma_{S\,1}^i}{2} + \frac{\tilde\gamma_{\nu\,1}^i}{2}\Big)\tilde s_i^{(1)} + 2\beta_0\,\tilde s_i^{(2)}\,, \\
\tilde{S}_{i,0}^{(3)}(L_\nu) &= -L_\nu\big(\tilde\gamma_{\nu\,2}^i + \tilde\gamma_{\nu\,1}^i\,\tilde s_i^{(1)}\big) + \tilde s_i^{(3)}\,. \qquad (4.65)
\end{aligned}
$$

Eqs. (4.63) and (4.65) agree with refs. [115, 119]. The required anomalous dimension and boundary coefficients up to three loops are given in appendix B.4.

Numerical impact. The soft function $\tilde{S}_i(b_T,\mu,\nu)$ has an explicit dependence on the scales μ and ν that cancel against that of the hard and beam functions in eq. (4.48).

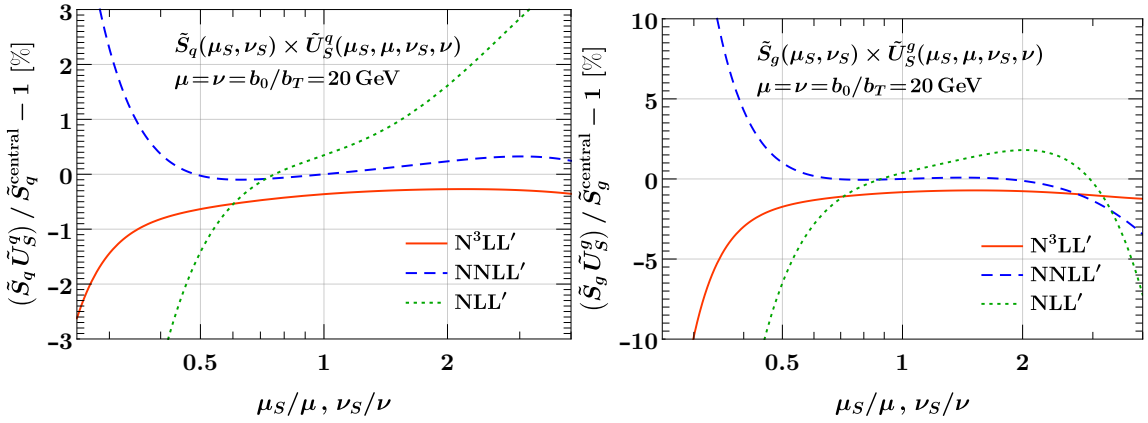

Figure 4.5: Residual scale dependence of the resummed q_T soft function in Fourier space for $i=q$ (left) and $i=g$ (right). Shown are the relative deviations from the NNLL′ result $\tilde{S}_i^{\mathrm{central}}$ at the central scales $(\mu_S,\nu_S)=(\mu,\nu)=(b_0/b_T,b_0/b_T)$.

Therefore, varying μ and ν is not very meaningful for illustrating the numerical impact of the scale-dependent three-loop terms. Instead, we consider the resummed soft function which results from the solution of the coupled RGEs in eq. (4.57),

$$\begin{aligned}
\tilde{S}_i(b_T,\mu,\nu) &= \tilde{S}_i(b_T,\mu_S,\nu_S)\,\tilde{U}_S^i(b_T,\mu_S,\mu,\nu_S,\nu)\,,\\
\tilde{U}_S^i(b_T,\mu_S,\mu,\nu_S,\nu) &= \exp\biggl[\int_{\mu_S}^{\mu}\frac{\mathrm{d}\mu'}{\mu'}\,\tilde{\gamma}_S^i(\mu',\nu)\biggr]\exp\biggl[\ln\frac{\nu}{\nu_S}\,\tilde{\gamma}_\nu^i(b_T,\mu_S)\biggr]\\
&= \exp\biggl[4K_\Gamma^i(\mu_S,\mu)+4\eta_\Gamma^i(\mu_S,\mu)\ln\frac{\mu_S}{\nu}+K_{\tilde{\gamma}_S^i}(\mu_S,\mu)\biggr]\\
&\quad\times\exp\biggl[\ln\frac{\nu}{\nu_S}\,\tilde{\gamma}_\nu^i(b_T,\mu_S)\biggr]\,,
\end{aligned}\tag{4.66}$$

where $\tilde{U}_S^i$ is the soft function evolution kernel that evolves $\tilde{S}_i$ between the scales (μ_S,ν_S) and (μ,ν), and we have chosen to first evolve in ν and then in μ. Note that we use the unexpanded analytic evolution kernels (see section 3.4), and explicit expressions of the $K_\Gamma^i,\eta_\Gamma^i,K_\gamma$ are given in appendix B.5.

To probe the full set of terms in the fixed-order expansion of $\tilde{S}_i(b_T,\mu_S,\nu_S)$, we consider simultaneous variations of (μ_S,ν_S) around the canonical central scales $\mu_S=\nu_S=\mu=\nu=b_0/b_T$. In figure 4.5 we show the residual scale dependence of the resummed soft function at the representative value $b_0/b_T=20\,\mathrm{GeV}$ at NLL′ (dotted green), NNLL′ (dashed blue), and N^{3}LL′ (solid orange), normalized to the NNLL′ result at the central scale. The three-loop finite term is included in figure 4.5, so the NNLL′ and N^{3}LL′ results do not coincide at the central scales. We use four-loop running of α_s throughout, which formally amounts to a higher-order effect at (N)NLL′. As expected, the scale dependence reduces from NLL′ to NNLL′, where it is already quite small. At N^{3}LL′, it further stabilizes over a wider range of scales. As in section 4.2.2, we stress that the residual scale dependence in the resummed soft function by itself is not necessarily a good indicator of the perturbative uncertainty,

but gives an indication of the typical reduction of perturbative uncertainties one might expect at each order.

4.3.4 q_T beam function

In SCET the quark ($i = q$) and gluon ($i = g$) bare q_T beam functions in distribution space are defined as forward matrix elements of proton states with lightlike momenta $P_a^\mu = E_{\rm cm} n_a^\mu/2$ and n_a-collinear quark χ_{n_a} and gluon $\mathcal{B}_{n_a\perp}$ fields. The gluon beam function reads

$$B_g^{\mu\nu}(x_a, \vec{k}_a) = \theta(\omega_a)\omega_a \big\langle p_{n_a}\big| \mathcal{B}^\mu_{n_a\perp}(0)[\delta^{(2)}(\vec{k}_a - \mathcal{P}_\perp)\delta(\omega_a - \bar{n}_a\cdot\mathcal{P})\mathcal{B}^\nu_{n_a\perp}(0)]\big|p_{n_a}\big\rangle\,, \quad (4.67)$$

and the quark beam function is given in eq. (3.37) upon setting $\mathbb{W}_{n_i} \mapsto W_{n_i}$. The matrix elements are implicitly averaged over proton spin and the n_b-collinear beam functions are analogously defined. Their equivalent formulation in $\vec{b}_T$-space follows trivially from their Fourier transform. As before, $\mathcal{P}_\perp$ is understood to measure the perpendicular (label) momentum components of real collinear radiation for the fields inside the square brackets whereas $\delta(\omega_a - \bar{n}_a\cdot\mathcal{P})$ sets the lightcone momenta of the parton that participates in the hard interaction. In what follows, we continue to suppress the indices a, b that differentiate between the $n_{a,b}$-beam functions as it is irrelevant for our derivations and only keep the index $i = q, g$.

In $\vec{b}_T$-space the beam function obeys the multiplicative coupled RGEs

$$\begin{aligned}
\mu\frac{\mathrm{d}}{\mathrm{d}\mu}\tilde{B}_i(x,\vec{b}_T,\mu,\nu) &= \tilde{\gamma}_B^i(\mu,\nu/\omega)\,\tilde{B}_i(x,\vec{b}_T,\mu,\nu)\,,\\
\nu\frac{\mathrm{d}}{\mathrm{d}\nu}\tilde{B}_i(x,\vec{b}_T,\mu,\nu) &= -\frac{1}{2}\tilde{\gamma}_\nu^i(b_T,\mu)\,\tilde{B}_i(x,\vec{b}_T,\mu,\nu)\,,
\end{aligned} \quad (4.68)$$

where the ν anomalous dimension was discussed in section 4.3.2, and the μ anomalous dimension has the all-order form

$$\tilde{\gamma}_B^i(\mu,\nu/\omega) = 2\Gamma^i_{\rm cusp}[\alpha_s(\mu)]\ln\frac{\nu}{\omega} + \tilde{\gamma}_B^i[\alpha_s(\mu)]\,. \quad (4.69)$$

For perturbative $b_0/b_T \gg \Lambda_{\rm QCD}$, the TMD beam function satisfies an OPE in terms of standard PDFs [54],

$$\begin{aligned}
\tilde{B}_q(x,b_T,\mu,\nu) &= \sum_j \int\frac{\mathrm{d}z}{z}\,\tilde{\mathcal{I}}_{qj}(z,b_T,\mu,\nu/\omega) f_j\Big(\frac{x}{z},\mu\Big)\big[1+\mathcal{O}(b_T\Lambda_{\rm QCD})\big]\,,\\
\tilde{B}_g^{\rho\lambda}(x,\vec{b}_T,\mu,\nu) &= \sum_j \int\frac{\mathrm{d}z}{z}\bigg[\frac{g_\perp^{\rho\lambda}}{2}\,\tilde{\mathcal{I}}_{gj}(z,b_T,\mu,\nu/\omega) + \bigg(\frac{g_\perp^{\rho\lambda}}{2} - \frac{b_\perp^\rho b_\perp^\lambda}{b_\perp^2}\bigg)\tilde{\mathcal{J}}_{gj}(z,b_T,\mu,\nu/\omega)\bigg]\\
&\qquad\times f_j\Big(\frac{x}{z},\mu\Big)\big[1+\mathcal{O}(b_T\Lambda_{\rm QCD})\big]\,.
\end{aligned} \quad (4.70)$$

For the gluon beam function, we have made its dependence on the gluon helicity explicit, and decomposed it into two orthogonal structures, namely the polarization-independent

piece $\tilde{\mathcal{I}}_{gj}$ and the polarization-dependent piece $\tilde{\mathcal{J}}_{gj}$, where $g_\perp^{\rho\lambda} = g^{\rho\lambda} - (n_a^\rho n_b^\lambda + n_b^\rho n_a^\lambda)/2$ is the transverse metric and $b_\perp^\rho$ is the transverse four vector with $b_\perp^2 = -\vec{b}_T^2$. Due to the multiplicative structure of eq. (4.68), both $\tilde{\mathcal{I}}_{gj}$ and $\tilde{\mathcal{J}}_{gj}$ obey the same RGE, and in the following we will only consider the RGEs for $\tilde{\mathcal{I}}_{ij}$.

The $\tilde{\mathcal{I}}_{ij}$ are perturbatively calculable matching coefficients, whose RGEs follow from eq. (4.68) by taking the evolution of the PDFs into account (see eq. (A.32)),

$$\begin{aligned}
\mu\frac{\mathrm{d}}{\mathrm{d}\mu}\tilde{\mathcal{I}}_{ij}(z,b_T,\mu,\nu/\omega) &= \sum_k \int\frac{\mathrm{d}z'}{z'}\,\tilde{\mathcal{I}}_{ik}\Big(\frac{z}{z'},b_T,\mu,\nu/\omega\Big)\big[\tilde{\gamma}_B^i(\mu,\nu/\omega)\mathbf{1}_{kj}(z') - 2P_{kj}(z',\mu)\big]\,,\\
\nu\frac{\mathrm{d}}{\mathrm{d}\nu}\tilde{\mathcal{I}}_{ij}(z,b_T,\mu,\nu/\omega) &= -\frac{1}{2}\tilde{\gamma}_\nu^i(b_T,\mu)\,\tilde{\mathcal{I}}_{ij}(z,b_T,\mu,\nu/\omega)\,.
\end{aligned}\tag{4.71}$$

Similar to the soft function, these coupled RGEs can be solved recursively as

$$\begin{aligned}
\tilde{\mathcal{I}}_{ij}^{(n+1)}(z,b_T,\mu,\nu/\omega) = \sum_{m=0}^{n}\Bigg[&\int_{b_0/b_T}^{\mu}\frac{\mathrm{d}\mu'}{\mu'}\Big(2\Gamma^i_{n-m}\ln\frac{\nu}{\omega} + \tilde{\gamma}^i_{B\,n-m} + 2m\beta_{n-m}\Big)\tilde{\mathcal{I}}_{ij}^{(m)}(z,b_T,\mu',\nu/\omega)\\
&- 2\int_{b_0/b_T}^{\mu}\frac{\mathrm{d}\mu'}{\mu'}\,\big[\tilde{\mathcal{I}}^{(m)}(b_T,\mu',\nu/\omega)P^{(n-m)}\big]_{ij}(z)\\
&- \int_{\omega}^{\nu}\frac{\mathrm{d}\nu'}{\nu'}\,\frac{\tilde{\gamma}^i_{\nu\,n-m}}{2}\,\tilde{\mathcal{I}}_{ij}^{(m)}(z,b_T,b_0/b_T,\nu'/\omega)\Bigg] + \tilde{I}_{ij}^{(n+1)}(z)\,,
\end{aligned}\tag{4.72}$$

where the nonlogarithmic boundary coefficients are defined as

$$\tilde{I}_{ij}^{(n+1)}(z) = \tilde{\mathcal{I}}_{ij}^{(n+1)}(z,b_T,\mu=b_0/b_T,\nu/\omega=1)\,.\tag{4.73}$$

Starting from the LO result, $\tilde{I}_{ij}^{(0)}(z) = \mathbf{1}_{ij}(z) \equiv \delta_{ij}\,\delta(1-z)$, we obtain up to two loops

$$\begin{aligned}
\tilde{\mathcal{I}}_{ij}^{(0)}(z,b_T,\mu,\nu/\omega) &= \mathbf{1}_{ij}(z)\,,\\
\tilde{\mathcal{I}}_{ij}^{(1)}(z,b_T,\mu,\nu/\omega) &= L_b\Big[\Big(L_\omega\Gamma_0^i + \frac{\tilde{\gamma}^i_{B\,0}}{2}\Big)\mathbf{1}_{ij}(z) - P_{ij}^{(0)}(z)\Big] - L_\omega\frac{\tilde{\gamma}^i_{\nu\,0}}{2}\,\mathbf{1}_{ij}(z) + \tilde{I}_{ij}^{(1)}(z)\,,\\
\tilde{\mathcal{I}}_{ij}^{(2)}(z,b_T,\mu,\nu/\omega) &= L_b^2\Bigg\{\Big[L_\omega^2\,\frac{(\Gamma_0^i)^2}{2} + L_\omega\,\frac{\Gamma_0^i}{2}(\beta_0+\tilde{\gamma}^i_{B\,0}) + \Big(\beta_0+\frac{\tilde{\gamma}^i_{B\,0}}{2}\Big)\frac{\tilde{\gamma}^i_{B\,0}}{4}\Big]\mathbf{1}_{ij}(z)\\
&\qquad - \Big(L_\omega\Gamma_0^i + \frac{\beta_0}{2} + \frac{\tilde{\gamma}^i_{B\,0}}{2}\Big)P_{ij}^{(0)}(z) + \frac{1}{2}(P^{(0)}P^{(0)})_{ij}(z)\Bigg\}\\
&\quad + L_b\Bigg\{\Big[-L_\omega^2\,\Gamma_0^i\frac{\tilde{\gamma}^i_{\nu\,0}}{2} + L_\omega\Big[-\Big(\beta_0+\frac{\tilde{\gamma}^i_{B\,0}}{2}\Big)\frac{\tilde{\gamma}^i_{\nu\,0}}{2} + \Gamma_1^i\Big] + \frac{\tilde{\gamma}^i_{B\,1}}{2}\Big]\mathbf{1}_{ij}(z)\\
&\qquad + L_\omega\,\frac{\tilde{\gamma}^i_{\nu\,0}}{2}\,P_{ij}^{(0)}(z) - P_{ij}^{(1)}(z)\\
&\qquad + \Big(L_\omega\Gamma_0^i + \beta_0 + \frac{\tilde{\gamma}^i_{B\,0}}{2}\Big)\tilde{I}_{ij}^{(1)}(z) - (\tilde{I}^{(1)}P^{(0)})_{ij}(z)\Bigg\}\\
&\quad + \Big[L_\omega^2\,\frac{(\tilde{\gamma}^i_{\nu\,0})^2}{8} - L_\omega\,\frac{\tilde{\gamma}^i_{\nu\,1}}{2}\Big]\mathbf{1}_{ij}(z) - L_\omega\,\frac{\tilde{\gamma}^i_{\nu\,0}}{2}\,\tilde{I}_{ij}^{(1)}(z) + \tilde{I}_{ij}^{(2)}(z)\,,
\end{aligned}\tag{4.74}$$

where we abbreviated

$$L_b = \ln\frac{b_T^2\mu^2}{b_0^2}\,,\quad b_0 = 2e^{-\gamma_E}\,,\qquad L_\omega = \ln\frac{\nu}{\omega}\,.\tag{4.75}$$

Note that L_ω differs from the characteristic logarithm of the q_T soft function, eq. (4.62). This is equivalent to the statement that the beam function lives at large rapidities $\nu \sim \omega$ whereas the soft function lives at small rapidities $\nu \sim b_0/b_T$. The $\tilde{I}_{ij}^{(n)}(z)$ are given in ref. [115] for quark and gluon beam functions in terms of the results of ref. [269], and were directly calculated at NNLO using the exponential regulator for the quark case in ref. [272].

At three loops we write

$$\tilde{\mathcal{I}}_{ij}^{(3)}(z, b_T, \mu, \nu/\omega) = \sum_{\ell=0}^{3} \tilde{\mathcal{I}}_{ij,\ell}^{(3)}(z, L_\omega)\, L_b^\ell\,, \tag{4.76}$$

and using $\tilde{\gamma}_{\nu\,0}^i = 0$ for brevity, the coefficients are

$$\begin{aligned}
\tilde{\mathcal{I}}_{ij,3}^{(3)}(z, L_\omega) = {}& \Big\{ L_\omega^3\, \frac{(\Gamma_0^i)^3}{6} + L_\omega^2\, \frac{(\Gamma_0^i)^2}{2} \Big(\beta_0 + \frac{\tilde{\gamma}_{B\,0}^i}{2}\Big) + L_\omega \Gamma_0^i \Big[\frac{\beta_0^2}{3} + \Big(\beta_0 + \frac{\tilde{\gamma}_{B\,0}^i}{4}\Big) \frac{\tilde{\gamma}_{B\,0}^i}{2} \Big] \\
& + \Big(\beta_0 + \frac{\tilde{\gamma}_{B\,0}^i}{2}\Big) \Big(\beta_0 + \frac{\tilde{\gamma}_{B\,0}^i}{4}\Big) \frac{\tilde{\gamma}_{B\,0}^i}{6} \Big\} \mathbf{1}_{ij}(z) \\
& - \Big[L_\omega^2\, \frac{(\Gamma_0^i)^2}{2} + L_\omega \Gamma_0^i \Big(\beta_0 + \frac{\tilde{\gamma}_{B\,0}^i}{2}\Big) + \frac{\beta_0^2}{3} + \Big(\beta_0 + \frac{\tilde{\gamma}_{B\,0}^i}{4}\Big) \frac{\tilde{\gamma}_{B\,0}^i}{2} \Big] P_{ij}^{(0)}(z) \\
& + \Big(L_\omega\, \frac{\Gamma_0^i}{2} + \frac{\beta_0}{2} + \frac{\tilde{\gamma}_{B\,0}^i}{4} \Big) (P^{(0)} P^{(0)})_{ij}(z) - \frac{1}{6} (P^{(0)} P^{(0)} P^{(0)})_{ij}(z)\,, \\
\tilde{\mathcal{I}}_{ij,2}^{(3)}(z, L_\omega) = {}& \Big\{ L_\omega^2\, \Gamma_0^i \Gamma_1^i + L_\omega \Big[\Gamma_1^i \Big(\beta_0 + \frac{\tilde{\gamma}_{B\,0}^i}{2}\Big) + \frac{\Gamma_0^i}{2} (\beta_1 + \tilde{\gamma}_{B\,1}^i) \Big] \\
& + \beta_0 \frac{\tilde{\gamma}_{B\,1}^i}{2} + \frac{\tilde{\gamma}_{B\,0}^i}{4} (\beta_1 + \tilde{\gamma}_{B\,1}^i) \Big\} \mathbf{1}_{ij}(z) - \Big(L_\omega \Gamma_1^i + \frac{\beta_1}{2} + \frac{\tilde{\gamma}_{B\,1}^i}{2} \Big) P_{ij}^{(0)}(z) \\
& - \Big(L_\omega \Gamma_0^i + \beta_0 + \frac{\tilde{\gamma}_{B\,0}^i}{2} \Big) P_{ij}^{(1)}(z) + \frac{1}{2} (P^{(0)} P^{(1)} + P^{(1)} P^{(0)})_{ij}(z) \\
& + \Big[L_\omega^2\, \frac{(\Gamma_0^i)^2}{2} + L_\omega\, \frac{\Gamma_0^i}{2} (3\beta_0 + \tilde{\gamma}_{B\,0}^i) + \Big(\beta_0 + \frac{\tilde{\gamma}_{B\,0}^i}{2}\Big) \Big(\beta_0 + \frac{\tilde{\gamma}_{B\,0}^i}{4}\Big) \Big] \tilde{I}_{ij}^{(1)}(z) \\
& - \Big(L_\omega \Gamma_0^i + \frac{3}{2} \beta_0 + \frac{\tilde{\gamma}_{B\,0}^i}{2} \Big) (\tilde{I}^{(1)} P^{(0)})_{ij}(z) + \frac{1}{2} (\tilde{I}^{(1)} P^{(0)} P^{(0)})_{ij}(z)\,, \\
\tilde{\mathcal{I}}_{ij,1}^{(3)}(z, L_\omega) = {}& \Big\{ -L_\omega^2\, \Gamma_0^i \frac{\tilde{\gamma}_{\nu\,1}^i}{2} + L_\omega \Big[-\Big(\beta_0 + \frac{\tilde{\gamma}_{B\,0}^i}{4}\Big) \tilde{\gamma}_{\nu\,1}^i + \Gamma_2^i \Big] + \frac{\tilde{\gamma}_{B\,2}^i}{2} \Big\} \mathbf{1}_{ij}(z) \\
& + L_\omega \frac{\tilde{\gamma}_{\nu\,1}^i}{2} P_{ij}^{(0)}(z) - P_{ij}^{(2)}(z) + \Big(L_\omega \Gamma_1^i + \beta_1 + \frac{\tilde{\gamma}_{B\,1}^i}{2} \Big) \tilde{I}_{ij}^{(1)}(z) - (\tilde{I}^{(1)} P^{(1)})_{ij}(z) \\
& + \Big(L_\omega \Gamma_0^i + 2\beta_0 + \frac{\tilde{\gamma}_{B\,0}^i}{2} \Big) \tilde{I}_{ij}^{(2)}(z) - (\tilde{I}^{(2)} P^{(0)})_{ij}(z)\,, \\
\tilde{\mathcal{I}}_{ij,0}^{(3)}(z, L_\omega) = {}& -L_\omega\, \frac{\tilde{\gamma}_{\nu\,2}^i}{2}\, \mathbf{1}_{ij}(z) - L_\omega\, \frac{\tilde{\gamma}_{\nu\,1}^i}{2}\, \tilde{I}_{ij}^{(1)}(z) + \tilde{I}_{ij}^{(3)}(z)\,,
\end{aligned} \tag{4.77}$$

where the three-loop boundary coefficients $\tilde{I}_{ij}^{(3)}(z)$ were recently calculated in refs. [139, 140, 231]. We have evaluated all Mellin convolutions appearing in eqs. (4.74) and (4.77) with the help of the `MT` package [245]. In contrast to ref. [180], we were able to perform all required convolutions in terms of standard harmonic polylogarithms without encountering multiple polylogarithms, after using the identity in eq. (4.32) to simplify some of the inputs.

The polarization-dependent kernels $\tilde{\mathcal{J}}_{gj}$ in eq. (4.70) have a simpler structure than the $\tilde{\mathcal{I}}_{ij}$ since at LO, the beam functions must collapse into the usual collinear PDFs and therefore $\tilde{\mathcal{J}}^{(0)}_{gj}$ vanishes. For unpolarized gluon-fusion processes, the accompanying tensor structures are only contracted with each other, and hence we only require their NNLO expressions for the N^{3}LO cross section. They are given by

$$\begin{aligned}
\tilde{\mathcal{J}}^{(0)}_{gj}(z, b_T, \mu, \nu/\omega) &= 0\,, \\
\tilde{\mathcal{J}}^{(1)}_{gj}(z, b_T, \mu, \nu/\omega) &= \tilde{J}^{(1)}_{gj}(z) = 4C_j\,\frac{1-z}{z}\,, \\
\tilde{\mathcal{J}}^{(2)}_{gj}(z, b_T, \mu, \nu/\omega) &= L_b\Big[\Big(L_\omega\Gamma^g_0 + \beta_0 + \frac{\tilde{\gamma}^g_{B\,0}}{2}\Big)\tilde{J}^{(1)}_{gj}(z) - (\tilde{J}^{(1)}P^{(0)})_{gj}(z)\Big] \\
&\quad - L_\omega\,\frac{\tilde{\gamma}^g_{\nu\,0}}{2}\,\tilde{J}^{(1)}_{gj}(z) + \tilde{J}^{(2)}_{gj}(z)\,.
\end{aligned} \tag{4.78}$$

The two-loop terms $\tilde{J}^{(2)}_{gj}$ have recently been calculated in ref. [275] using the exponential regulator and in ref. [276] using the δ regulator. They can be converted to our convention via the relation

$$\begin{aligned}
\tilde{J}^{(2)}_{gj}(z) &= I'^{(2)}_{gi}(z) \\
&= -\delta^L C^{(2;0,0)}_{g\leftarrow j}(z) - \frac{1}{2}\tilde{s}^{(1)}_g\tilde{J}^{(1)}_{gj}(z)\,.
\end{aligned} \tag{4.79}$$

In the first line of eq. (4.79), $I'^{(2)}_{gi}(z)$ is the two-loop boundary term as given in ref. [275]. In the second line of eq. (4.79), $\tilde{s}^{(1)}_g = -2C_A\zeta_2$ is the soft function constant at one loop and $\delta^L C^{(2;,0,0)}_{g\leftarrow j}(z)$ is the two-loop finite piece of the TMDPDF given in ref. [276].

Numerical impact. As for the soft function above, we illustrate the numerical impact of the three-loop corrections for the resummed beam function that results from the solution of the coupled RGEs in eq. (4.68)

$$\begin{aligned}
\tilde{B}_i(x, \vec{b}_T, \mu, \nu) &= \tilde{B}_i(x, \vec{b}_T, \mu_B, \nu_B)\,\tilde{U}^i_B(\omega, b_T, \mu_B, \mu, \nu_B, \nu)\,, \\
\tilde{U}^i_B(\omega, b_T, \mu_B, \mu, \nu_B, \nu) &= \exp\left[\int_{\mu_B}^{\mu}\frac{\mathrm{d}\mu'}{\mu'}\tilde{\gamma}^i_B(\mu', \nu/\omega)\right]\exp\left[-\frac{1}{2}\ln\frac{\nu}{\nu_B}\tilde{\gamma}^i_\nu(b_T, \mu_B)\right] \\
&= \exp\left[2\eta^i_\Gamma(\mu_B, \mu)\ln\frac{\nu}{\omega} + K_{\tilde{\gamma}^i_B}(\mu_B, \mu)\right] \\
&\quad \times \exp\left[-\frac{1}{2}\ln\frac{\nu}{\nu_B}\tilde{\gamma}^i_\nu(b_T, \mu_B)\right].
\end{aligned} \tag{4.80}$$

where $\tilde{U}^i_B$ is the beam function evolution kernel that evolves $\tilde{B}_i$ between the scales (μ_B, ν_B) and (μ, ν). Here we have chosen to first evolve in ν and then in μ. Note that in eq. (4.80) we use the unexpanded analytic evolution kernels (see section 3.4) and explicit expressions for η^i_Γ, K_γ are given in appendix B.5. For $i = g$, we restrict to the polarization-independent piece $\tilde{\mathcal{I}}_{gj}$ and write $\tilde{B}_g \equiv -g_{\perp,\rho\lambda}\tilde{B}^{\rho\lambda}_g$ for short. As for the soft function, we restrict to simultaneous variations of μ_B and ν_B.

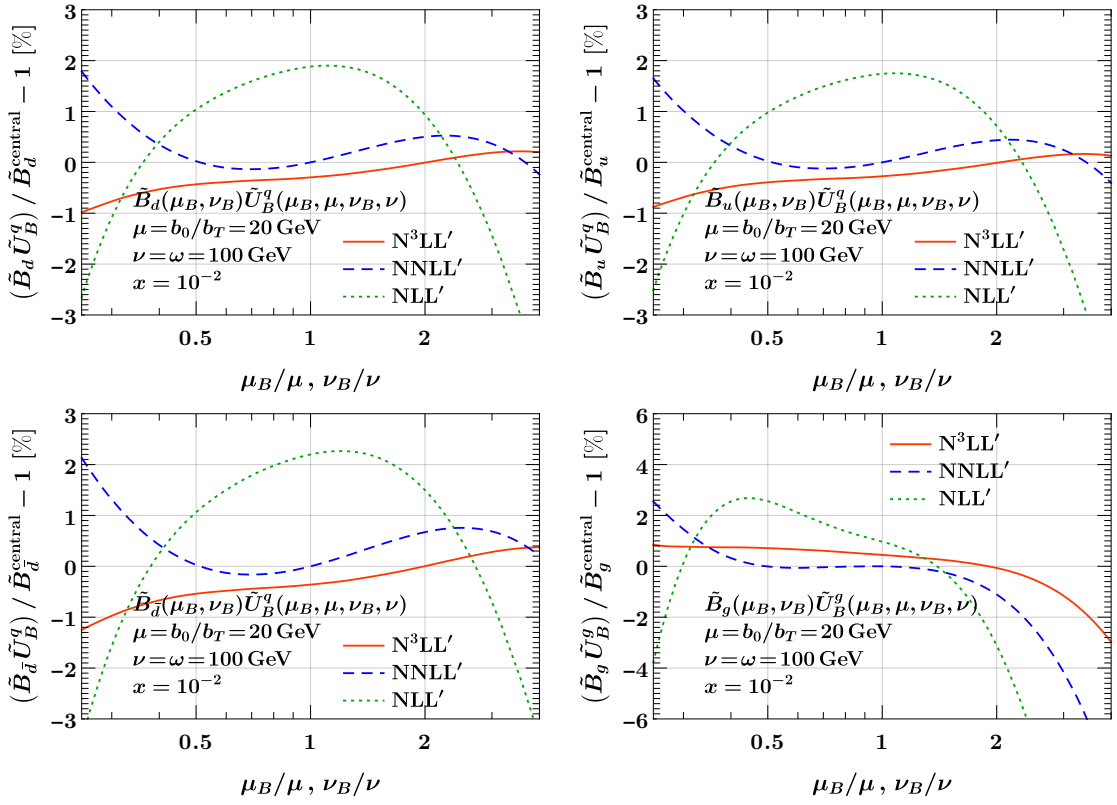

Figure 4.6: Residual scale dependence of the resummed q_T beam function in Fourier-space for $i = d$ (top left), u (top right), $\bar{d}$ (bottom left), and g (bottom right). Shown are the relative deviations from the NNLL′ result $\tilde{B}_i^{\rm central}$ at the central scales $(\mu_B, \nu_B) = (\mu, \nu) = (b_0/b_T, \omega)$.

In figure 4.6, we show the residual dependence on (μ_B, ν_B) at NLL′ (dotted green), NNLL′ (dashed blue), and N^{3}LL′ (solid orange)[9] as the relative difference to the central NNLL′ result at $(\mu_B, \nu_B) = (\mu, \nu) = (b_0/b_T, \omega)$ for $b_0/b_T = 20\,\text{GeV}$ and $\omega = 100\,\text{GeV}$. As for $\mathcal{T}_0$, we use four-loop running of α_s and `MMHT2014nnlo68cl` [246] NNLO PDFs throughout. In all cases we find the scale dependence to be substantially reduced at each order.

4.3.5 Beam function coefficients in the eikonal limit

We now proceed to extract the three-loop beam function coefficients in the $z \to 1$ limit from consistency relations with known soft matrix elements. For the q_T beam function, these consistency relations arise from factorization theorems for the triple-differential cross section $\mathrm{d}\sigma_{pp\to L}/\mathrm{d}Q^2\mathrm{d}Y\mathrm{d}q_T$ that enable the joint q_T and soft threshold resummation [277–280]. In terms of the momentum fractions $x_{a,b}$ defined in eq. (4.2), the soft threshold limit is equivalent to taking both $x_a \to 1$ and $x_b \to 1$. As $x_{a,b} \to 1$, initial state radiation is

[9] Note that in comparison to ref. [2], figure 4.6 has been updated to include the N^{3}LO boundary coefficient $\tilde{I}^{(3)}_{ij}(z)$, hence the complete N^{3}LL′ beam functions are shown.

constrained to have energy $\lesssim \lambda_-\lambda_+ Q$, where

$$\lambda_-^2 \sim 1 - x_a \qquad \text{and} \qquad \lambda_+^2 \sim 1 - x_b \tag{4.81}$$

are power-counting parameters that encode the distance from the kinematic endpoint.

The all-order factorization relevant for different hierarchies in q_T/Q and the threshold constraint $\lambda_-\lambda_+$ was derived in refs. [76, 281]. Some consequences of the resulting consistency relations have already been explored in refs. [76, 281]. In fact, the exponential regulator is *defined* by its action on the refactorized pieces in these consistency relations. In the following, we briefly review the relevant factorization theorems and derive the all-order structure that arises for the q_T beam function in the eikonal limit.

$\boldsymbol{q_T/Q \ll \lambda_-\lambda_+ \sim 1}$ In this regime, initial-state radiation is not yet subject to the threshold constraint, and the standard q_T factorization theorem eq. (4.48) holds. It receives power corrections $\mathcal{O}(q_T^2/Q^2)$, but captures the exact dependence on $x_{a,b}$ via the beam functions.

$\boldsymbol{q_T/Q \ll \lambda_-\lambda_+ \ll 1}$ For this hierarchy, the factorization takes a form similar to eq. (4.48), but real collinear radiation into the final state is constrained in energy by $1 - x_{a,b} \ll 1$. The leftover radiation in this limit is described by intermediate collinear-soft modes [224, 282] in terms of $n_{a,b}$-collinear-soft functions $\tilde{\mathcal{S}}_i(k, b_T, \mu, \nu)$. They are matrix elements of collinear-soft Wilson lines and depend on the small additional momentum $k = k^\mp$ available from either one of the (threshold) PDFs and on the color charge of the colliding partons. The factorization theorem in this regime reads [76, 281]

$$\begin{aligned}
\frac{\mathrm{d}\sigma^{(0)}}{\mathrm{d}Q^2\,\mathrm{d}Y\,\mathrm{d}^2\vec{q}_T} = \sum_{a,b} \int \mathrm{d}^2\vec{b}_T\, e^{\mathrm{i}\vec{q}_T\cdot\vec{b}_T}\, H_{ab}(Q^2,\mu) \\
&\times \int \mathrm{d}k^-\, \tilde{\mathcal{S}}_i(k^-, b_T, \mu, \nu)\, f_a^{\mathrm{thr}}\Big[x_a\Big(1 + \frac{k^-}{\omega_a}\Big), \mu\Big] \\
&\times \int \mathrm{d}k^+\, \tilde{\mathcal{S}}_i(k^+, b_T, \mu, \nu)\, f_b^{\mathrm{thr}}\Big[x_b\Big(1 + \frac{k^+}{\omega_b}\Big), \mu\Big]\, \tilde{S}_i(b_T, \mu, \nu) \\
&\times \Big[1 + \mathcal{O}\Big(\frac{1}{b_T^2\lambda_-^2\lambda_+^2 Q^2}, \lambda_-^2, \lambda_+^2\Big)\Big]\,.
\end{aligned} \tag{4.82}$$

Collinear-soft emissions do not contribute angular momentum, so the polarization indices for gluon-induced processes become trivial in this limit and we suppress them in the following.

$\boldsymbol{q_T/Q \sim \lambda_-\lambda_+ \ll 1}$ In this regime, the threshold constraint dominates and all radiation is forced to be soft. The recoil against soft radiation with transverse momentum $\vec{k}_T = -\vec{q}_T$ is encoded in the fully-differential threshold soft function $S_i^{\mathrm{thr}}(k^-, k^+, \vec{k}_T)$. The factorization

theorem in this regime reads

$$\begin{aligned}\frac{\mathrm{d}\sigma^{(0)}}{\mathrm{d}Q^2\,\mathrm{d}Y\,\mathrm{d}^2\vec{q}_T} &= \sum_{a,b}\int \mathrm{d}^2\vec{b}_T\, e^{\mathrm{i}\vec{q}_T\cdot\vec{b}_T}\, H_{ab}(Q^2,\mu) \\ &\quad\times \int \mathrm{d}k^-\mathrm{d}k^+ f_a^{\mathrm{thr}}\Big[x_a\Big(1+\frac{k^-}{\omega_a}\Big),\mu\Big] f_b^{\mathrm{thr}}\Big[x_b\Big(1+\frac{k^+}{\omega_b}\Big),\mu\Big] \\ &\quad\times \tilde{S}_i^{\mathrm{thr}}(k^-,k^+,b_T,\mu)\,\big[1+\mathcal{O}(\lambda_-^2,\lambda_+^2)\big]\,. \end{aligned} \tag{4.83}$$

Notably, the fully-differential threshold soft function is free of rapidity divergences because they are regulated by the threshold constraint. (This is the starting point of the exponential regularization procedure.) The fully-differential soft function was calculated to $\mathcal{O}(\alpha_s^2)$ in ref. [283], albeit in a different context, and to $\mathcal{O}(\alpha_s^3)$ in ref. [119]. By construction, it satisfies

$$\int \mathrm{d}^2\vec{k}_T\, S_i^{\mathrm{thr}}(k^-,k^+,\vec{k}_T,\mu) = \tilde{S}_i^{\mathrm{thr}}(k^-,k^+,b_T=0,\mu) = S_i^{\mathrm{thr}}(k^-,k^+,\mu)\,, \tag{4.84}$$

where $S_i^{\mathrm{thr}}(k^-,k^+,\mu)$ is the double-differential threshold soft function appearing in eq. (4.39).

Consistency relations. Consistency between eqs. (4.48) and (4.82) implies that the $x\to 1$ limit of the q_T beam function is captured by the collinear-soft function [76, 281],

$$\tilde{B}_i(x,\vec{b}_T,\mu,\nu) = \int \mathrm{d}k\,\tilde{\mathcal{S}}_i(k,b_T,\mu,\nu)\, f_i^{\mathrm{thr}}\Big[x\Big(1+\frac{k}{\omega}\Big),\mu\Big]\,\big[1+\mathcal{O}(1-x)\big]\,. \tag{4.85}$$

This is the analog of eq. (4.41) for q_T, but this time relates the eikonal limit of the beam function to an exclusive collinear-soft matrix element instead of the inclusive threshold soft function. At the partonic level, eq. (4.85) implies [76, 281]

$$\tilde{\mathcal{I}}_{ij}(z,b_T,\mu,\nu/\omega) = \delta_{ij}\,\omega\,\tilde{\mathcal{S}}_i\big[\omega(1-z),b_T,\mu,\nu\big]\,\big[1+\mathcal{O}(1-z)\big]\,. \tag{4.86}$$

Note that eq. (4.86) is true for any rapidity regulator as long as the same regulator is used on both sides. The consistency between eqs. (4.82) and (4.83) implies [76, 281]

$$\tilde{S}_i^{\mathrm{thr}}(k^-,k^+,b_T,\mu) = \tilde{\mathcal{S}}_i(k^-,b_T,\mu,\nu)\,\tilde{\mathcal{S}}_i(k^+,b_T,\mu,\nu)\,\tilde{S}_i(b_T,\mu,\nu)\,\Big[1+\mathcal{O}\Big(\frac{1}{b_T^2k^-k^+}\Big)\Big]\,, \tag{4.87}$$

which again holds for any choice of rapidity regulator. In particular, the left-hand side has no rapidity divergences, so the dependence on the rapidity regulator cancels between the terms on the right-hand side. Together, eqs. (4.85) and (4.87) uniquely determine the eikonal limit of the beam function in any given rapidity regulator scheme in terms of the fully-differential soft function (which is independent of the scheme) and the q_T soft function $\tilde{S}_i(b_T,\mu,\nu)$ (which determines the scheme). Furthermore, the scheme ambiguity amounts to moving terms from the soft function boundary coefficients into the coefficient of $\delta(1-z)$ in the beam function coefficients. Since $\delta(1-z)$ is a leading-power contribution as $z\to 1$, it follows that up to lower-order cross terms, all scheme-dependent terms in the beam function are contained in the leading eikonal terms predicted by eq. (4.86).

Extraction of the finite terms. For the exponential regulator, the relation between the fully-differential and standard TMD soft function is particularly simple, leading to an all-order result for the collinear-soft function in terms of the rapidity anomalous dimension, see appendix D.2. Inserting this result into eq. (4.86), we find for the eikonal limit of the b_T-space beam function matching coefficient $\tilde{\mathcal{I}}_{ij}$ in the exponential regulator scheme,

$$\tilde{\mathcal{I}}_{ij}(z, b_T, \mu, \nu/\omega) = \delta_{ij}\,\frac{\omega}{\nu}\mathcal{V}_{\tilde{\gamma}^i_\nu(b_T,\mu)/2}\Big[\frac{\omega}{\nu}(1-z)\Big]\,\big[1+\mathcal{O}(1-z)\big]\,, \tag{4.88}$$

where the plus distribution $\mathcal{V}_a(x)$ is defined in eq. (A.19). The simplicity of this result is a direct consequence of the specific rapidity regulator, i.e., one may equally well have imposed this form of the eikonal limit as the renormalization condition. Nonetheless, when combined with the soft function to a given order, the scheme dependence cancels and leaves behind a unique set of terms that capture the threshold limit of the singular cross section in eq. (4.48). We note that a close relation between the rapidity anomalous dimension and the eikonal limit of the beam function is a scheme-independent feature [281], and was also conjectured for the δ-regulator in ref. [271].

It is straightforward to expand eq. (4.88) in α_s to obtain the finite terms in the matching coefficient at any given fixed order using eqs. (4.55) and (A.22). Up to two loops we have

$$\begin{aligned}
\tilde{I}^{(1)}_{ij}(z) &= \mathcal{O}\big[(1-z)^0\big]\,,\\
\tilde{I}^{(2)}_{ij}(z) &= \delta_{ij}\,\frac{\tilde{\gamma}^i_{\nu\,1}}{2}\,\mathcal{L}_0(1-z) + \mathcal{O}\big[(1-z)^0\big]\,,
\end{aligned} \tag{4.89}$$

in agreement with the full two-loop result [115], and where we have used that $\tilde{\gamma}^i_{\nu\,0} = 0$. Including terms up to six loops for illustration, we find

$$\begin{aligned}
\tilde{I}^{(3)}_{ij}(z) &= \delta_{ij}\,\frac{\tilde{\gamma}^i_{\nu\,2}}{2}\,\mathcal{L}_0(1-z) + \mathcal{O}\big[(1-z)^0\big]\,,\\
\tilde{I}^{(4)}_{ij}(z) &= \delta_{ij}\,\frac{\tilde{\gamma}^i_{\nu\,3}}{2}\,\mathcal{L}_0(1-z) + \frac{(\tilde{\gamma}^i_{\nu\,1})^2}{4}\Big[\mathcal{L}_1(1-z) - \frac{\zeta_2}{2}\delta(1-z)\Big] + \mathcal{O}\big[(1-z)^0\big]\,,\\
\tilde{I}^{(5)}_{ij}(z) &= \delta_{ij}\,\frac{\tilde{\gamma}^i_{\nu\,4}}{2}\,\mathcal{L}_0(1-z) + \frac{\tilde{\gamma}^i_{\nu\,1}\tilde{\gamma}^i_{\nu\,2}}{2}\Big[\mathcal{L}_1(1-z) - \frac{\zeta_2}{2}\delta(1-z)\Big] + \mathcal{O}\big[(1-z)^0\big]\,,\\
\tilde{I}^{(6)}_{ij}(z) &= \delta_{ij}\,\frac{\tilde{\gamma}^i_{\nu\,5}}{2}\,\mathcal{L}_0(1-z) + \frac{(\tilde{\gamma}^i_{\nu\,2})^2 + 2\tilde{\gamma}^i_{\nu\,1}\tilde{\gamma}^i_{\nu\,3}}{4}\Big[\mathcal{L}_1(1-z) - \frac{\zeta_2}{2}\delta(1-z)\Big]\\
&\quad + \frac{(\tilde{\gamma}^i_{\nu\,1})^3}{8}\Big[\frac{\mathcal{L}_2(1-z)}{2} - \frac{\zeta_2}{2}\mathcal{L}_0(1-z) + \frac{\zeta_3}{3}\delta(1-z)\Big] + \mathcal{O}\big[(1-z)^0\big]\,.
\end{aligned} \tag{4.90}$$

We again stress that these expressions are a direct consequence of the renormalization condition in the exponential regulator scheme and must be combined with the soft function in the same scheme to obtain a scheme-independent result. It is interesting to note that starting at four loops, eq. (4.88) does in fact predict a term proportional to $\delta(1-z)$ in the beam function matching coefficient due to the inverse Fourier transform to $k^\pm$ back from the conjugate $b^\pm$ space, where the regularization procedure is applied. Concluding, we note that the $\tilde{I}^{(3)}_{ij}(z)$ prediction in eq. (4.90) was confirmed by recent, explicit three-loop calculation of the exact q_T beam function boundary coefficients in refs. [139, 140, 231].

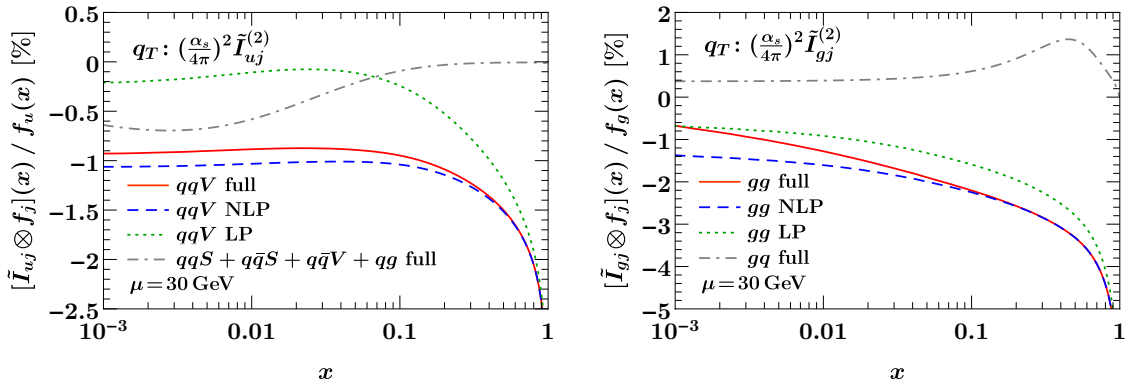

Figure 4.7: Comparison of the full beam function coefficients to their leading eikonal (LP) and next-to-eikonal (NLP) expansion at NNLO. The u-quark channel is shown on the left and the gluon channel on the right. In both cases we also show the sum of all nondiagonal partonic channels for comparison.

4.3.6 Estimating beam function coefficients beyond the eikonal limit

As in section 4.2.5, we can use the eikonal limit of the beam function coefficients and study to what extent it can be employed to approximate the full result and/or estimate the uncertainty of terms beyond the eikonal limit.

In figure 4.7, we compare the full q_T beam function coefficient (solid) to its eikonal (LP dotted green) and next-to-eikonal (NLP dashed blue) expansions at NNLO for the u-quark and gluon channels. Since the NLO coefficients are not singular, we do not show the corresponding NLO results. We always show the convolution $(I_{ij} \otimes f_j)(x)/f_i(x)$ with the appropriate PDF f_j and normalize to the PDF $f_i(x)$, corresponding to the LO result, where $i = u$ for the u-quark case and $i = g$ for the gluon case. With this normalization, the shape gives an indication of the rapidity dependence of the beam function coefficient relative to the LO rapidity dependence induced by the shape of the PDFs. We also include the appropriate powers of $\alpha_s/(4\pi)$ at each order, so the overall normalization shows the percent impact relative to the LO result. For definiteness, the renormalization scale entering the PDFs is chosen as $\mu = 30$ GeV.

In both flavor-diagonal contributions, denoted as[10] qqV and gg, the eikonal limit correctly reproduces the divergent behavior as $x \to 1$, but is off away from very large x. Including the next-to-eikonal terms yields a sizable shift from the eikonal limit, and provides a very good approximation in the shown x region. In the gluon channel, one can see a rise of the full kernel towards small x, arising from an overall $1/z$ divergence in the coefficient $\tilde{I}^{(2)}_{gg}(z)$, which is not captured by the expansion around $z \to 1$. If desired, one could also include the leading $z \to 0$ behavior of the coefficients, which for simplicity is not done here. For illustration, we also show the total contribution from all other corresponding nondiagonal channels (gray dot-dashed). In both cases, they are numerically subdominant

[10] See appendix A.3 for our conventions on the flavor decomposition of Mellin kernels.

to the flavor-diagonal channel and also much flatter in x, since they only start at NLP.

Similar to the $\mathcal{T}_0$ coefficients in section 4.2.5, we now wish to make an ansatz for the three-loop NLP terms. A peculiar feature of the q_T coefficients is that up to three loops, its eikonal limit contains no logarithmic distributions $\mathcal{L}_n(1-z)$ with $n > 0$, but only $\mathcal{L}_0(1-z)$. In contrast, the NLP NNLO coefficient does contain a double logarithm $\ln^2(1-z)$. Based on this observation, we make the following ansatz for the N^{n}LO beam coefficient,

$$\tilde{I}^{(n)}_{ij,\text{approx}}(z) = \tilde{I}^{(n)\,\text{LP}}_{ij}(z) + \Big[X_1\Gamma^i_0 \ln^2(1-z) + X_2\gamma^i_X \ln(1-z)\Big]\tilde{I}^{(n-1)}_{ij,\text{reg}}(z) - X_3(1-z)\tilde{I}^{(n)\,\text{LP}}_{ij}(z)\,. \tag{4.91}$$

Here, $\tilde{I}^{(n)}_{ij,\text{reg}}$ refers to the full regular (non-eikonal) piece of the beam coefficient at $\mathcal{O}(\alpha_s^n)$. At NLO, there is no NLP term, so at this order we simply define the regular piece to be the appropriate color factor. More explicitly, we use

$$\tilde{I}^{(1)}_{ij,\text{reg}}(z) = -\delta_{ij}C_i\,, \qquad \tilde{I}^{(2)}_{ij,\text{reg}}(z) = \tilde{I}^{(2)}_{ij}(z) - \delta_{ij}\frac{\tilde{\gamma}^i_{\nu\,1}}{2}\mathcal{L}_0(1-z)\,, \tag{4.92}$$

where $C_i = C_F\,(C_A)$ for $i = q\,(g)$. The ansatz in eq. (4.91) dresses the lower-order regular kernel with two additional logarithms $\ln(1-z)$. The coefficients of these logarithms are chosen such that at the central choices $X_1 = X_2 = 1$, they reproduce the known double and single logarithms at NNLO. The effective noncusp anomalous dimension γ^i_X needed to achieve this is given by

$$\gamma^g_X = 3C_A - \beta_0\,, \qquad \gamma^q_X = 10(C_F - C_A)\,. \tag{4.93}$$

The size of these additional logarithms can be probed by varying the coefficients $X_{1,2}$ by ± 1 around the central choice. Furthermore, we add the eikonal limit $\tilde{I}^{(n)\,\text{LP}}_{ij}$ suppressed by one power of $(1-z)$ to estimate the pure NLP constant. Its coefficient X_3 is varied by ± 1 around the central choice $X_3 = 0$.

Since the X_i probe independent structures, we can consider them as uncorrelated. Hence, we add the impacts Δ_i on the final result of their variation in quadrature

$$\Delta = \Delta_1 \oplus \Delta_2 \oplus \Delta_3 = \sqrt{\Delta_1^2 + \Delta_2^2 + \Delta_3^2}\,. \tag{4.94}$$

In figure 4.8, we show the approximate kernel at NNLO (top) and N^{3}LO (bottom) for the u-quark (left) and gluon (right) channels. The dashed orange line shows the central result from our ansatz and the yellow band its estimated uncertainty. The gray lines show the impact of the individual variations of the X_i as indicated. The full results are shown as solid dark red curves in all cases. At NNLO (top panel) we see that the ansatz including uncertainties approximates the true result relatively well, even for the gluon case in the shown x region. In particular, the rather large shift from LP to the approximate NLP result is needed to correctly capture the full result within uncertainties.

At N^{3}LO (bottom panel)[11], we see again that the approximate result gives rise to a sizable shift from the pure eikonal limit, which by itself is a very small correction. This

[11] Note that in comparison to ref. [2], the bottom panel of figure 4.8 has been updated to include the recently computed $\tilde{I}^{(3)}_{qqV}(z)$ and $\tilde{I}^{(3)}_{gg}(z)$ kernels [139, 140, 231] (solid dark red), allowing for a direct comparison between our ansatz in eq. (4.91) and the exact kernels.

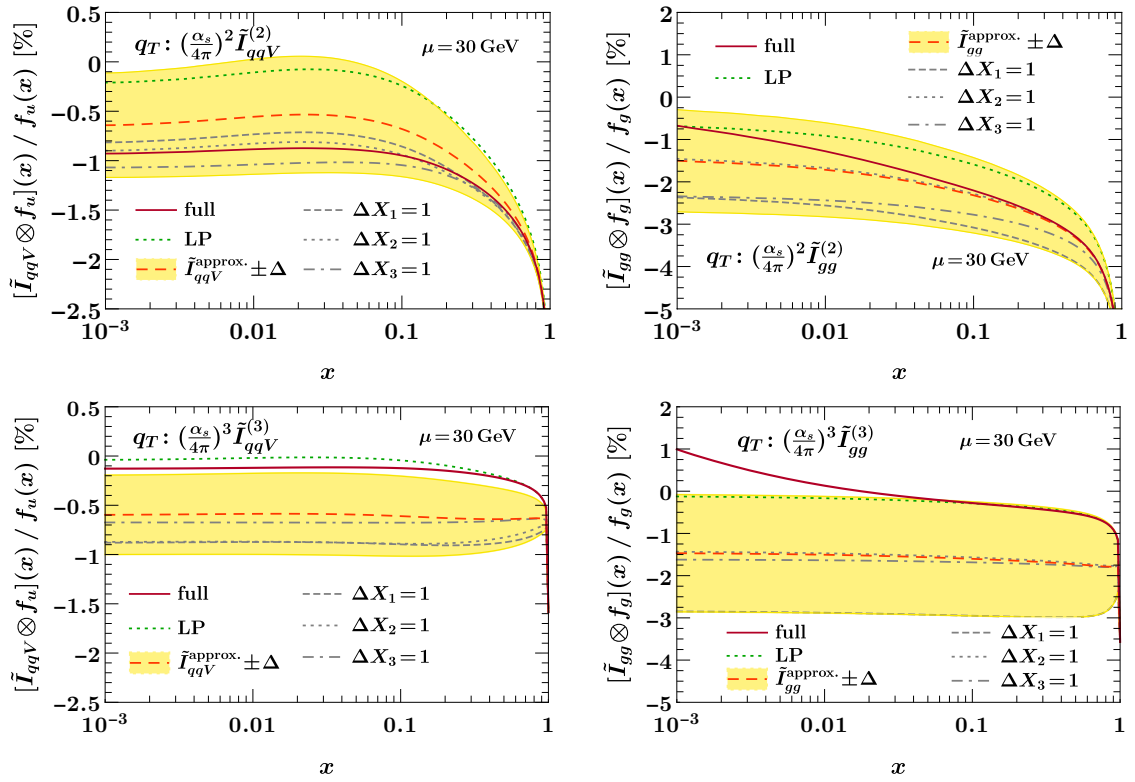

Figure 4.8: Approximate ansätze (dashed orange) for the NNLO (top) and N^{3}LO (bottom) kernels, in the u-quark (left) and gluon (right) channels. The yellow bands correspond to their estimated uncertainties resulting from variations of the $X_{1,2,3}$ coefficients. The eikonal limit and the full kernel correspond to the dotted green and solid dark red curves respectively.

large shift arises on the one hand because the LP limit only contains $\mathcal{L}_0(1-z)$ with a rather small coefficient $\gamma^i_{\nu\,2}$, while the NLP now contains up to $\ln^4(1-z)$. Surprisingly and in contrast to the NNLO kernel, the full N^{3}LO coefficients are well approximated by their eikonal limit, except for the gluon case at small x which is attributed to $1/z$ divergent terms that are not part of our ansatz. Nevertheless, it is clear that our ansätze successfully provide reliable approximate kernels within uncertainties. Thus, we expect their analytic form in eq. (4.91) to be a useful parametrization for kernels beyond the eikonal limit at higher orders in perturbation theory.

Finally, we briefly comment on the treatment of the three-loop beam function coefficients in ref. [180], where the q_T-slicing method was first applied at N^{3}LO for Higgs production and at that time the $\tilde{I}^{(3)}_{ij}(z)$ were unknown. There, the employed approximation was $\tilde{I}^{(3)}_{gg}(z) = \tilde{C}_{N3}\,\delta(1-z)$, with $\tilde{C}_{N3}$ fixed such that the inclusive cross section is correctly reproduced. This effectively absorbs the averaged effect of the actual z dependence into an effective $\delta(1-z)$ coefficient which does not accurately capture its LP rapidity dependence since already from our results (and by now from the recently calculated, exact $\tilde{I}^{(3)}_{gg}(z)$) we know the exact $\delta(1-z)$ coefficient.

4.4 N^{3}LO subtractions

The factorization theorems in eqs. (4.5) and (4.48) fully describe the limit $q_T \to 0$, $\mathcal{T}_0 \to 0$ and thus they capture the singular structure of QCD in this limit. Hence, they can be used to construct a subtraction method for fixed-order calculations. In principle, this works for any resolution variable τ and any process for which a corresponding factorization is known [198, 201, 202, 284–289]. In order to make our discussion as general as possible, from now on we consider τ as the (generic) resolution variable and only specify it when necessary. The subtractions can be formulated differential in τ or as a global τ slicing, both of which we review in the following and for an extensive discussion see ref. [202].

Our starting point is to write the cross section as the integral over the differential cross section in τ,

$$\sigma(X) = \int \mathrm{d}\tau \, \frac{\mathrm{d}\sigma(X)}{\mathrm{d}\tau} \,, \qquad \sigma(X, \tau_{\mathrm{cut}}) = \int^{\tau_{\mathrm{cut}}} \mathrm{d}\tau \, \frac{\mathrm{d}\sigma(X)}{\mathrm{d}\tau} \,, \tag{4.95}$$

where the second relation defines the cumulant in τ_{cut}. Here, X denotes any measurements performed, which can include Q and Y of the color singlet L but also additional measurements or cuts on its constituents. For $\tau \to 0$, the cross sections scales like $\sim 1/\tau$, so performing the τ integral requires knowing the full analytic distributional structure involving $\delta(\tau)$ and $\mathcal{L}_n(\tau)$, which encodes the cancellation of real and virtual IR divergences. To separate out the singular structure in τ, we introduce a subtraction term,

$$\sigma(X) = \sigma^{\mathrm{sub}}(X, \tau_{\mathrm{off}}) + \int \mathrm{d}\tau \left[\frac{\mathrm{d}\sigma(X)}{\mathrm{d}\tau} - \frac{\mathrm{d}\sigma^{\mathrm{sub}}(X)}{\mathrm{d}\tau} \theta(\tau < \tau_{\mathrm{off}}) \right] , \tag{4.96}$$

where $\mathrm{d}\sigma^{\mathrm{sub}}(X)/\mathrm{d}\tau$ captures at least all singularities for $\tau \to 0$,

$$\frac{\mathrm{d}\sigma(X)}{\mathrm{d}\tau} = \frac{\mathrm{d}\sigma^{(0)}(X)}{\mathrm{d}\tau} \left[1 + \mathcal{O}(\tau)\right] , \qquad \frac{\mathrm{d}\sigma^{\mathrm{sub}}(X)}{\mathrm{d}\tau} = \frac{\mathrm{d}\sigma^{(0)}(X)}{\mathrm{d}\tau} \left[1 + \mathcal{O}(\tau)\right] , \tag{4.97}$$

with the singular cross section

$$\frac{\mathrm{d}\sigma^{(0)}(X)}{\mathrm{d}\tau} \sim \frac{1}{\tau} \,, \tag{4.98}$$

and $\sigma^{\mathrm{sub}}(X, \tau_{\mathrm{off}})$ is the integrated subtraction term,

$$\sigma^{\mathrm{sub}}(X, \tau_{\mathrm{off}}) = \int \mathrm{d}\tau \, \frac{\mathrm{d}\sigma^{\mathrm{sub}}(X)}{\mathrm{d}\tau} \theta(\tau < \tau_{\mathrm{off}}) \,. \tag{4.99}$$

By construction, the integrand in square brackets in eq. (4.96) contains at most integrable singularities for $\tau \to 0$ and so the integral can be performed numerically. Hence, the full cross section $\mathrm{d}\sigma(X)/\mathrm{d}\tau$ is only ever evaluated at finite $\tau > 0$, which means it can be obtained from a calculation of the corresponding $ab \to L + 1$-parton process at one lower order. In practice, one always has a small IR cutoff δ on the τ integral,

$$\sigma(X) = \sigma^{\mathrm{sub}}(X, \tau_{\mathrm{off}}) + \int_{\delta} \mathrm{d}\tau \left[\frac{\mathrm{d}\sigma(X)}{\mathrm{d}\tau} - \frac{\mathrm{d}\sigma^{\mathrm{sub}}(X)}{\mathrm{d}\tau} \theta(\tau < \tau_{\mathrm{off}}) \right] + \Delta\sigma(X, \delta) \,, \tag{4.100}$$

where the last term contains the integral over $\tau \leq \delta$,

$$\Delta\sigma(X,\delta) = \sigma(X,\delta) - \sigma^{\text{sub}}(X,\delta) \sim \mathcal{O}(\delta)\,, \tag{4.101}$$

and it is neglected for $\delta \to 0$.

The above is a *differential* τ-subtraction scheme, where the parameter $\tau_{\text{off}} \sim \mathcal{O}(1)$ determines the range over which the subtraction acts. The key advantage of formulating the subtractions in terms of a physical resolution variable τ, is that the subtraction terms are given by the singular limit of a physical cross section $\mathrm{d}\sigma^{(0)}/\mathrm{d}\tau$. Hence, they are precisely given by the factorization formula for $\tau \to 0$, which is also the basis for the resummation in τ. In fact, this form of the subtraction is routinely used when the resummed and fixed-order results are combined via an additive matching, which we employ in chapter 5 for an application on the Higgs fiducial q_T spectrum and total fiducial cross section. In eq. (4.96), τ_{off} corresponds to the point where the τ resummation is turned off, and the term in square brackets in is the nonsingular cross section that is added to the pure resummed result. Differential $\mathcal{T}_0$ subtractions are used in this way in the `Geneva` Monte Carlo to combine the fully-differential NNLO calculation together with the NNLL$'$ $\mathcal{T}_0$ resummation with a parton shower [290–292]. The differential subtractions at N^{3}LO are a key ingredient for using this method to combine N^{3}LO calculations with parton showers.

In contrast to a fully local subtraction scheme, all singularities are projected onto the resolution variable τ, so the subtractions are local in τ but nonlocal in the additional radiation phase space that is integrated over. As discussed in ref. [202], the subtractions can be made more local by considering a factorization theorem that is differential in more variables. For example, the combined q_T and $\mathcal{T}_0$ resummation [155, 224] offers the possibility to construct double-differential $q_T - \mathcal{T}_0$ subtractions.

The key point of the differential subtraction is that δ can in principle be made arbitrarily small, because the integrand of the τ integral is nonsingular, which also means that the numerically expensive small τ region does not need to be sampled with weight $1/\tau$. On the other hand, by letting $\delta = \tau_{\text{cut}}$ be a small but finite cutoff and setting $\tau_{\text{off}} = \tau_{\text{cut}}$, eq. (4.100) turns into a global τ subtraction or *slicing*,

$$\sigma(X) = \sigma^{\text{sub}}(X,\tau_{\text{cut}}) + \int_{\tau_{\text{cut}}} \mathrm{d}\tau\, \frac{\mathrm{d}\sigma(X)}{\mathrm{d}\tau} + \Delta\sigma(X,\tau_{\text{cut}})\,. \tag{4.102}$$

The practical advantage of the slicing method is that since $\tau_{\text{cut}} > 0$, the integrand of the second addend in eq. (4.102) corresponds to a $L+1$-jet cross section and thus allows one to readily turn an existing N^{n-1}LO calculation into a N^{n}LO calculation for L, and so most implementations use this approach [180, 201, 293–299]. The main disadvantage is that the cancellation of the divergences now only happens after the integration over τ. This makes the $L+1$-jet calculation very demanding, both in terms of computational expense and numerical stability, because the $1/\tau$-divergent integral of $\mathrm{d}\sigma(X)/\mathrm{d}\tau$ must be computed with sufficient accuracy down to sufficiently small τ_{cut}, which in practice limits how small one can take τ_{cut}. Since the integral is divergent, one cannot let $\tau_{\text{cut}} \to 0$ even in principle,

so one always has a leftover systematic uncertainty from the neglected power corrections $\Delta\sigma(X, \tau_{\text{cut}})$.

The numerical efficiency of the subtractions can be improved by including the power corrections in the subtractions for both $\mathcal{T}_0$ [300–305] and q_T [306, 307]. The size of the missing power corrections also strongly depends on the precise definition of $\mathcal{T}_0$ [300–302]. The hadronic definition in eq. (4.4) exhibits power corrections that grow like $e^{|Y|}$ at large Y, which is not the case for the leptonic definition. The power corrections also depend on the Born measurement X. In particular, additional selection or isolation cuts on the color-singlet constituents typically enhance the power corrections from $\mathcal{O}(\tau)$ to $\mathcal{O}(\sqrt{\tau})$ [261, 262], which renders them numerically important and (if possible) they have to be included in the subtraction terms. In chapter 5, where we study the fiducial q_T spectrum and total cross section of the Higgs boson, we come across such enhanced power corrections that result from experimental selection cuts and which we address by explicitly considering them as part of the subtraction term $\mathrm{d}\sigma^{\text{sub}}(X)/\mathrm{d}\tau$.

Subtraction terms. The singular terms needed for the subtractions only depend on the Born phase space, so we can write them as

$$\frac{\mathrm{d}\sigma^{(0)}(X)}{\mathrm{d}\tau} = \int \mathrm{d}\Phi_0 \, \frac{\mathrm{d}\sigma^{(0)}(\Phi_0)}{\mathrm{d}\tau} \, X(\Phi_0) \,, \tag{4.103}$$

where $\Phi_0 \equiv \Phi_0(\kappa_a, \kappa_b, \omega_a, \omega_b)$ denotes the full Born phase space, including the parton labels $\kappa_{a,b}$, the total color-singlet momentum q^μ parametrized in terms of $\omega_{a,b}$ as in eqs. (4.1) and (4.2) as well as the internal phase space of L. The $X(\Phi_0)$ denotes the measurement function that implements the measurement X (e.g. fiducial cuts) on a Born configuration.

The singular terms are defined such that their τ dependence is minimal and given by

$$\begin{aligned}
\frac{\mathrm{d}\sigma^{(0)}(\Phi_0)}{\mathrm{d}\tau} &= \mathcal{C}_{-1}(\Phi_0)\,\delta(\tau) + \sum_{n\geq 0} \mathcal{C}_n(\Phi_0)\,\mathcal{L}_n(\tau) \\
&= \sum_{m\geq 0} \left[\mathcal{C}_{-1}^{(m)}(\Phi_0)\,\delta(\tau) + \sum_{n=0}^{2m-1} \mathcal{C}_n^{(m)}(\Phi_0) \mathcal{L}_n(\tau) \right] \left(\frac{\alpha_s}{4\pi}\right)^m .
\end{aligned} \tag{4.104}$$

Their integral over $\tau \leq \tau_{\text{cut}}$ immediately follows as

$$\begin{aligned}
\sigma^{(0)}(\Phi_0, \tau_{\text{cut}}) &= \mathcal{C}_{-1}(\Phi_0) + \sum_{n\geq 0} \mathcal{C}_n(\Phi_0)\,\frac{\ln^{n+1}\tau_{\text{cut}}}{n+1} \\
&= \sum_{m\geq 0} \left[\mathcal{C}_{-1}^{(m)}(\Phi_0) + \sum_{n=0}^{2m-1} \mathcal{C}_n^{(m)}(\Phi_0) \frac{\ln^{n+1}\tau_{\text{cut}}}{n+1} \right] \left(\frac{\alpha_s}{4\pi}\right)^m .
\end{aligned} \tag{4.105}$$

The differential subtractions are given by using eq. (4.104) for $\tau > 0$, which amounts to dropping the $\mathcal{C}_{-1}(\Phi_0)\delta(\tau)$ term and using $\mathcal{L}_n(\tau > 0) = \ln^n(\tau)/\tau$. The integrated subtractions are directly given by eq. (4.105).

The precise definition of the $\mathcal{C}_n(\Phi_0)$ coefficients depends on the normalization of the dimensionless variable τ or equivalently on the boundary condition of the $\mathcal{L}_n(\tau)$. Rescaling $\tau \to \lambda\tau$ moves contributions from $\mathcal{C}_n(\Phi_0)$ to $\mathcal{C}_{m<n}(\Phi_0)$. This freedom was used in ref. [202] to absorb all terms with $n \geq 0$ in eq. (4.105) into a $\mathcal{C}_{-1}(\Phi_0, \mathcal{T}_{\text{off}})$ by taking $\tau \equiv \mathcal{T}_0/\mathcal{T}_{\text{off}}$. Here, we prefer to keep the cutoff dependence explicit as in eq. (4.105) and take

$$\tau \equiv \frac{\mathcal{T}_0}{Q} \qquad (\text{for } \mathcal{T}_0)\,, \qquad \tau \equiv \frac{q_T^2}{Q^2} \qquad (\text{for } q_T)\,. \tag{4.106}$$

The m-loop subtraction coefficients $\mathcal{C}_n^{(m)}(\Phi_0)$ directly follow from expanding eq. (4.5) for $\mathcal{T}_0$ or eq. (4.48) for q_T to mth order in α_s. For the three-loop coefficients this yields

$$\begin{aligned}
\mathcal{C}_{-1}^{(3)}(\Phi_0) &= H^{(3)}(\Phi_0)\, f_a(x_a)\, f_b(x_b) + \sum_{m=1}^{3} H^{(3-m)}(\Phi_0)\, \big[B_a(x_a) B_b(x_b) S\big]_{-1}^{(m)}\,, \\
\mathcal{C}_{n\geq 0}^{(3)}(\Phi_0) &= \sum_{k=1}^{3} H^{(3-k)}(\Phi_0)\, \big[B_a(x_a) B_b(x_b) S\big]_{n}^{(k)}\,,
\end{aligned} \tag{4.107}$$

where for simplicity we have suppressed the dependence on μ and the distinction of the $\mathcal{T}_0$ vs. q_T beam and soft functions. The virtual three-loop corrections to the Born process are contained in $H^{(3)}(\Phi_0)$, which only enters in $\mathcal{C}_{-1}^{(3)}$. The m-loop soft/collinear contribution $[BBS]_n^{(m)}$ follows from inserting the fixed-order expansions of the respective beam and soft function, reexpanding their product to mth order and picking out the coefficients of $\delta(\tau)$ and $\mathcal{L}_n(\tau)$. The three-loop boundary coefficients of the beam and soft functions only enter in $\mathcal{C}_{-1}^{(3)}$ and thus are needed for the integrated subtraction terms but not the differential ones. Note also that most of the process and Φ_0 dependence resides in the hard coefficients, while the soft/collinear contributions only depend on $x_{a,b}$ and the parton types,

$$\big[B_a(x_a) B_b(x_b) S\big]_n^{(m)} = \int \frac{\mathrm{d}z_a}{z_a} \frac{\mathrm{d}z_b}{z_b} \sum_{i,j} \big[\mathcal{I}_{ai}(z_a) \mathcal{I}_{bi}(z_b) S\big]_n^{(m)} f_i\Big(\frac{x_a}{z_a}\Big) f_j\Big(\frac{x_b}{z_b}\Big)\,. \tag{4.108}$$

We have implemented the results for the subtraction coefficients $\mathcal{C}_n(\Phi_0)$ in eq. (4.107) up to three loops for both $\mathcal{T}_0$ and q_T in the C++ library `SCETlib` [49]. The latter are required for the phenomenological study of the Higgs boson q_T spectrum and total fiducial cross section that we perform in chapter 5.

Note that evaluating eq. (4.107) for $\mathcal{T}_0$ requires rescaling and convolving the plus distributions in the beam and soft functions, as discussed in ref. [202]. For q_T, expanding the $\vec{b}_T$-space result of $W^{(0)}(Q^2, Y, \vec{b}_T)$ (see eq. (4.48)) yields powers of the $\vec{b}_T$-space logarithm L_b^n up to $n \leq 6$. Their Fourier transform, given in table A.1 in appendix A.2.2, yields simple $\delta(\vec{q}_T)$ and $\mathcal{L}_n(\vec{q}_T, \mu)$, which are easily rescaled to $\delta(\tau)$ and $\mathcal{L}_n(\tau)$.

Finally, we comment on the original q_T subtraction method in ref. [198] that was based on the q_T resummation framework of ref. [159], where the canonical $\vec{b}_T$-space logarithms are replaced by

$$L_b \to \tilde{L}_b \equiv \ln\Big(\frac{b_T^2 \mu^2}{b_0^2} + 1\Big)\,. \tag{4.109}$$

This form is also used e.g. in refs. [180, 295]. While using $\tilde{L}_b$ has certain advantages in the context of q_T resummation, it is unnecessary for the purpose of q_T subtractions, since L_b and $\tilde{L}_b$ yield the same singular terms and only differ by power corrections. A drawback of using $\tilde{L}_b$ here is that the Fourier transform of $\tilde{L}_b^n$ yields complicated expressions in q_T space, see appendix B in ref. [159], whose cumulants are not known analytically and must be performed numerically.

4.5 Aspects of numerical implementation

The boundary coefficients of the singular differential cross section in eq. (4.104) are not predicted by their corresponding RGEs and they have to be explicitly calculated. For the soft and beam functions and up to two loops, all of them were known for some time[12] while recently, the full three-loop coefficients have become available.[13] Specifically, results for the three-loop $\mathcal{T}_0$ quark beam function in the generalized large-N_c approximation have appeared in ref. [308] and the complete result was calculated in ref. [230]. For the three-loop q_T beam function the complete result was recently calculated in refs. [139, 140, 231]. From a phenomenological point of view, they are of great significance as they correspond (in part) to the $\mathcal{O}(\alpha_s^3)$ corrections of the singular cross section which dominates the region where the differential cross section peaks. Consequently, in order to asses their impact in theoretical predictions, it is of central importance that a numerical implementation thereof meets certain stability and precision-goal criteria. While for the soft and hard function these terms are mere constants and do not admit a special treatment, for the beam function this is not the case; for both q_T and $\mathcal{T}_0$ they bear dependence in a momentum fraction z and they are convolved against PDFs, something that renders their numerical implementation nontrivial.

Although at one-loop the beam boundary coefficients have a simple dependence in z, starting at two loops rational polynomials along with harmonic polylogarithms (HPLs) [309] emerge, culminating at three loops, where they assume the greatest complexity both in functional form and size. This is not unique to the beam function kernels, since a similar form is also met at the NNLO splitting functions, $P_{ij}^{(2)}(z)$, which are also part of the beam function matching coefficients. Even though numerical implementations of HPLs are in abundance [310–316] and achieve excellent approximations for *individual* HPLs, they appear to be insufficient in meeting the desired precision-goal for the aforementioned kernels. Culprit for that can be traced in the high degree polynomials intertwined with HPLs of large weight that appear as part of the kernels. These allow for intricate numerical (catastrophic) cancellations, prohibiting a high-precision phenomenological study or even worse, threatening the genuine $\mathrm{N^3LO}$ terms to be buried in numerical noise. In light of the above, it is imperative that an alternative method is employed for their numerical implementation which in addition, it is endowed with desirable features such as stability

[12] With the exception of the q_T soft function which was known to three-loops [119].
[13] Besides those of the $\mathcal{T}_0$ soft function which are still unknown.

and optimized computation time. This naturally leads to a custom treatment of kernels with such functional signature.

Here, we focus on deriving an improved approximation for kernels that have a functional form similar to that of the q_T beam boundary terms, $\tilde{I}_{ij}^{(n)}(z)$, and the NNLO splitting functions, $P_{ij}^{(2)}(z)$. Our interest lies primarily in these since they are an indispensable ingredient for the phenomenological study of the Higgs boson q_T spectrum that we perform in chapter 5. We note though, that the approximation methods presented in sections 4.5.2 and 4.5.3 partially apply also for the $\mathcal{T}_0$ kernels, but further investigation is necessary since they involve a class of functions (Goncharov Polylogarithms [317]) that is absent in both $\tilde{I}_{ij}^{(n)}(z)$ and $P_{ij}^{(2)}(z)$, thus prohibiting a straightforward application of our method.

Understanding the manipulations for an improved kernel approximation necessitates that their basic building blocks, the HPLs, are studied. This is the topic of section 4.5.1, where we introduce and discuss all of their properties required for a kernel expansion in the phenomenologically relevant limits $z \to 0$ and $z \to 1$. In sections 4.5.2 and 4.5.3, we exploit the analytic structure of HPLs and present an algorithm that generates cost-optimal and precise approximations *at the level of the kernels*, in both aforementioned limits. Finally, in section 4.5.4 we show representative results of our method.

4.5.1 Harmonic Polylogarithms (HPLs)

The HPLs correspond to a natural generalization of the logarithm and the dilogarithm, $\mathrm{Li}_2(z)$, and they are the simplest class of special functions that are ubiquitous in multiloop calculations of Feynman diagrams. Naturally, they also appear as basic building blocks in the q_T beam boundary terms and the NNLO splitting functions $P_{ij}^{(2)}(z)$. It is thus crucial that their analytic and algebraic properties are understood before we proceed and investigate an improved kernel approximation. In the following review of HPLs we mainly follow ref. [309].

Definition. HPLs [309] are defined as functions of a variable z and they are classified by a weight vector $\vec{w} = \{w_n, \ldots, w_1\}$. We refer to the w_i as *letters* while the number of letters carried by an HPL specifies its *weight* w. The functional form of HPLs results form the iterative procedure

$$H_{\vec{w}}(z) \equiv H_{w_n,\ldots,w_1}(z) = \int_0^z \mathrm{d}x\, f_{w_n}(x)\, H_{w_{n-1},\ldots,w_1}(x)\,, \qquad w_i \in \{-1, 0, 1\}\,, \tag{4.110}$$

and it follows from their definition that

$$\frac{\mathrm{d}}{\mathrm{d}z} H_{w_n,\ldots,w_1}(z) = f_{w_n}(z)\, H_{w_{n-1},\ldots,w_1}(z)\,. \tag{4.111}$$

For each letter $w_i \in \{-1, 0, 1\}$ the functions $f_{w_i}(x)$ are defined as

$$f_{-1}(x) = \frac{1}{1+x}\,, \qquad f_0(x) = \frac{1}{x}\,, \qquad f_1(x) = \frac{1}{1-x}\,, \tag{4.112}$$

and the lowest weight or *weight 1* HPLs read

$$H_0(z) = \ln z\,, \qquad H_{-1}(z) = \ln(1+z)\,, \qquad H_1(z) = -\ln(1-z)\,. \tag{4.113}$$

Special case are the HPLs with a weight vector that has throughout the same n entries, for which we use the compact notation $\vec{w} = \{\underbrace{w, w, \ldots, w}_{n}\} \equiv \vec{w}_n$,

$$H_{\vec{0}_n}(z) = \frac{1}{n!}\ln^n z\,, \qquad H_{-\vec{1}_n}(z) = \frac{1}{n!}\ln^n(1+z)\,, \qquad H_{\vec{1}_n}(z) = \frac{(-1)^n}{n!}\ln^n(1-z)\,. \tag{4.114}$$

At each weight w there are 3^w linearly independent HPLs and which at $w = 1$ they are plain logarithmic functions, see eq. (4.113). Once identifying that $\mathrm{Li}_2(z) = H_{0,1}(z)$, it can be easily worked out that HPLs of $w = 2$ can be written as linear combinations of the dilogarithm and logarithms. Following the same pattern, HPLs of $w = 3$ can be expressed in terms of Nielsen's polylogarithm [318] $S_{n,p}(z) = H_{\vec{0}_n,\vec{1}_p}(z)$. On the other hand, starting at $w = 4$ it is no longer feasible to express the HPLs in terms of $S_{n,p}(z)$, which implies that $H_{\vec{w}}(z)$ constitute a bigger set of functions.

HPL identities. HPLs satisfy an important set of identities, that of *integration by parts (IBP)* and the *product algebra* [309].

Consider an HPL with weight vector $\vec{w} = \{w_n, \ldots, w_1\}$. The IBP relations read

$$\begin{aligned} H_{w_n,\ldots,w_1}(z) = {} & H_{w_n}(z)H_{w_{n-1},\ldots,w_1}(z) - H_{w_{n-1},w_n}(z)H_{w_{n-2},\ldots,w_1}(z) \\ & + H_{w_{n-2},w_{n-1},w_n}(z)H_{w_{n-3},\ldots,w_1}(z) - \ldots - (-1)^{n-3}H_{w_1,\ldots,w_n}(z)\,, \end{aligned} \tag{4.115}$$

where it implies that if $\vec{w}$ is symmetric and n is even, then $H_{\vec{w}}(z)$ is given by a product of HPLs of lower weight. For example at $w = 2$, eq. (4.115) yields $H_{w_i,w_i}(z) = \frac{1}{2}[H_{w_i}(z)]^2$ for any $w_i \in \{-1, 0, 1\}$.

Now consider two HPLs of different weights w_i, w_j and with weight vectors $\vec{w}_i, \vec{w}_j$ respectively. The product algebra identity dictates that their product can be expressed as a linear combination of HPLs with total weight $w_k = w_i + w_j$,

$$H_{\vec{w}_i}(z)H_{\vec{w}_j}(z) = \sum_{\vec{w}_k = \vec{w}_i \uplus \vec{w}_j} H_{\vec{w}_k}(z)\,. \tag{4.116}$$

Here, $\vec{w}_k = \vec{w}_i \uplus \vec{w}_j$ denotes the weight vectors $\vec{w}_k$ that result from all possible letter ordering combinations of $\{\vec{w}_i, \vec{w}_j\}$ such that the original ordering of $\vec{w}_i$ and $\vec{w}_j$ is preserved. To be more precise through an example, consider two HPLs with weight vectors $\vec{w}_a = \{w_1, w_2\}$, $\vec{w}_b = \{w_3, w_4\}$, then

$$\begin{aligned} H_{\vec{w}_a}(z)H_{\vec{w}_b}(z) = {} & H_{w_1,w_2,w_3,w_4}(z) + H_{w_1,w_3,w_2,w_4}(z) + H_{w_1,w_3,w_4,w_2}(z) \\ & + H_{w_3,w_1,w_2,w_4}(z) + H_{w_3,w_1,w_4,w_2}(z) + H_{w_3,w_4,w_1,w_2}(z)\,. \end{aligned} \tag{4.117}$$

At this point, a comment is in line with respect to the singular behavior of the HPLs. It can be shown that HPLs whose m-rightmost vector indices are zero, $\vec{0}_m$, have logarithmic singularities at $z = 0$ [309]

$$H_{\ldots,\vec{0}_m}(z) \sim \ln^m z\,, \tag{4.118}$$

and similarly HPLs that carry m-leftmost vector indices $\pm\vec{1}_m$ have logarithmic singularities at $z = \pm 1$ [309]

$$H_{\pm\vec{1}_m,\ldots}(z) \sim \ln^m(1 \mp z)\,, \tag{4.119}$$

where in both eqs. (4.118) and (4.119) the '...' denote an arbitrary number of any letters. An important observation is that eq. (4.116) can be exploited in order to *isolate the singularity* of an HPL by writing it as a linear combination of explicitly singular and nonsingular terms. Take for example $H_{w_i,w_j,0}(z)$ and assume that $w_{i,j} \neq 0$. Using eq. (4.116) we can write,

$$H_{w_i,w_j,0}(z) = H_{w_i,w_j}(z)H_0(z) - H_{w_i,0,w_j}(z) - H_{0,w_i,w_j}(z)\,, \tag{4.120}$$

where in the first term the logarithmic singularity $H_0(z) \equiv \ln z$ is explicitly isolated, whereas the rest of the HPLs are well defined in the limit $z \to 0$. This is a particularly useful property of the product algebra that we heavily employ for the approximation of the kernels in $z \to 0$ and $z \to 1$ in sections 4.5.2 and 4.5.3 respectively.

Analytic properties. For the lowest weight HPLs in eq. (4.113) we can already read off their branch cut structure

$$H_0(z):\ \ (-\infty, 0]\,, \quad H_{-1}(z):\ \ (-\infty, -1]\,, \quad H_1(z):\ \ [1, \infty)\,. \tag{4.121}$$

We refer to the branch cut of $H_{-1}(z)$ as "negative" cut and to the branch cut of $H_1(z)$ as a "positive" cut. Since at higher weights the letters mix, it is beneficial to understand what kind of branch cuts the HPLs of $w > 1$ can develop. We work as a concrete example the HPLs of $w = 2$ and disregard the case that the rightmost letter is 0.[14] Consider for example the $H_{w_i,1}(z)$. If $w_i = 1$,

$$H_{1,1}(z) = \int_0^z \frac{\mathrm{d}x}{1-x} \ln(1-x) \equiv \frac{1}{2}\ln^2(1-x)\,, \tag{4.122}$$

where it is obvious that $H_{1,1}(z)$ and $H_1(z)$ share the same positive branch cut. Now if $w_i = 0$,

$$H_{0,1}(z) = \int_0^z \frac{\mathrm{d}x}{x} \ln(1-x)\,. \tag{4.123}$$

[14] As mentioned in the previous paragraph, we can always use eq. (4.116) to isolate this logarithmic singularity, which effectively allows to consider HPLs without rightmost 0-letter. This procedure is not constrained to HPLs of a particular weight, as its iterative application isolates any number of logarithmic singularities that appear as rightmost 0-letters.

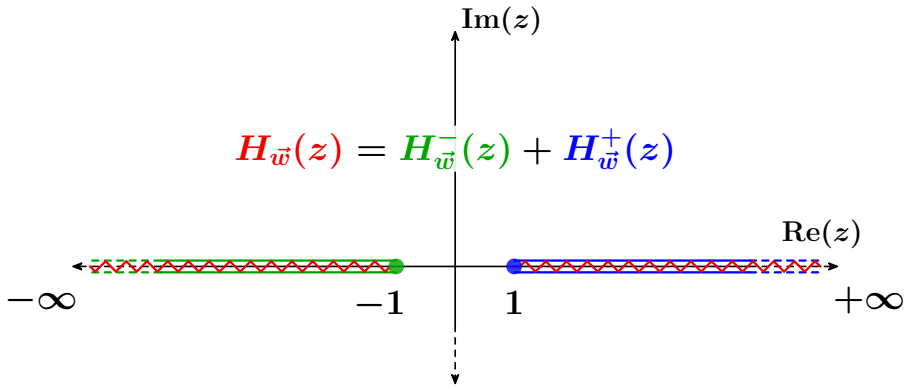

Figure 4.9: Analytic structure of an HPL with arbitrary weight vector $\vec{w}$ that contains (at least) both $w_i = \pm 1$ letters. The $H_{\vec{w}}(z)$ (red) has branch cuts in $(-\infty, -1]$ and $[1, \infty)$ and it is split into $H^{+}_{\vec{w}}(z)$ (blue) that has only the $[1, \infty)$ cut and into $H^{-}_{\vec{w}}(z)$ (green) that has only $(-\infty, -1]$ cut.

While the primitive $1/x$ could imply that $H_{0,1}(z)$ develops in addition to $[1, \infty)$ a branch cut starting at $z = 0$, the expansion of $\ln(1 - x)$ at $x \to 0$ is of $\mathcal{O}(x)$ and therefore $H_{0,1}(z)$ results in having the same branch cut as $H_1(z)$. The last case is for $w_i = -1$ and the situation is different since,

$$H_{-1,1}(z) = \int_0^z \frac{\mathrm{d}x}{1+x} \ln(1-x)\,, \tag{4.124}$$

where the $1/(1+x)$ primitive now induces a negative cut with the resulting HPL exhibiting *both* branch cuts.

Analogously, working out the case of $H_{w_i,-1}(z)$, $w_i = \{-1, 0, 1\}$, we find that $H_{-1,-1}(z)$ and $H_{0,-1}(z)$ share the same branch cut structure as $H_{-1}(z)$ whereas $H_{1,-1}(z)$ develops both branch cuts.

While the previous discussion was based only on HPLs of $w = 2$, already at this point we can draw some powerful conclusions concerning the analytic structure of higher weight HPLs. Considering an HPL of arbitrary weight $\vec{w}$, without trailing 0's while having only a positive (negative) branch cut, then increasing $\vec{w}$ with the letter $w_i = 1$ ($w_i = -1$) or $w_i = 0$ leaves its analytic structure intact, whereas increasing it with $w_i = -1$ ($w_i = 1$) induces to the resulting HPL both branch cuts. Based on these observations it is useful to define an HPL as a sum of terms with *separated branch cuts*. This is achieved by defining the split of an HPL [310] with weight vector $\vec{w}$ as

$$H_{\vec{w}}(z) = H^{+}_{\vec{w}}(z) + H^{-}_{\vec{w}}(z)\,, \tag{4.125}$$

where '+' ('−') superscript denotes that the term carries only a positive (negative) branch cut. In figure 4.9 we show an illustration with the branch cut structure of $H_{\vec{w}}(z)$ and $H^{\pm}_{\vec{w}}(z)$ that results from eq. (4.125).

At $w = 1$ it follows immediately from their definition in eq. (4.113) that

$$H_1(z) \equiv H^{+}_1(z)\,, \qquad H_{-1}(z) \equiv H^{-}_{-1}(z)\,. \tag{4.126}$$

The construction of '+/−' higher weight HPLs proceeds in an iterative manner, exploiting the previous observations regarding the addition of a letter w_i to their existing weight $\vec{w}$. If $w_i = 1$, we have

$$H^{+}_{1,\vec{w}}(z) = \int_0^z \frac{\mathrm{d}x}{1-x}\left[H^{+}_{\vec{w}}(x) + H^{-}_{\vec{w}}(1)\right], \tag{4.127}$$

$$H^{-}_{1,\vec{w}}(z) = \int_0^z \frac{\mathrm{d}x}{1-x}\left[H^{-}_{\vec{w}}(x) - H^{-}_{\vec{w}}(1)\right]. \tag{4.128}$$

In eq. (4.128) the $H^{-}_{\vec{w}}(z)$ by definition has only a negative cut but the primitive $1/(1-x)$ induces a positive cut, which is prevented by subtracting the HPL evaluated at $x = 1$. Finally, the mismatch of this subtraction is added to the '+' term in eq. (4.127), for which it is innocuous since it doesn't alter its analytic structure. Note that adding eqs. (4.127) and (4.128) we retrieve the full $H_{1,\vec{w}}(z)$, as dictated by eq. (4.125).

Following the same train of thought, the case for the addition of the letter $w_i = -1$ can be similarly worked out,

$$H^{+}_{-1,\vec{w}}(z) = \int_0^z \frac{\mathrm{d}x}{1+x}\left[H^{+}_{\vec{w}}(x) - H^{+}_{\vec{w}}(-1)\right], \tag{4.129}$$

$$H^{-}_{-1,\vec{w}}(z) = \int_0^z \frac{\mathrm{d}x}{1+x}\left[H^{-}_{\vec{w}}(x) + H^{+}_{\vec{w}}(-1)\right]. \tag{4.130}$$

Finally, for the case $w_i = 0$ and based on the fact that any number of such letter additions do not change the branch cut structure of an HPL allows to write,

$$H^{\pm}_{0,\vec{w}}(z) = \int_0^z \frac{\mathrm{d}x}{x}\, H^{\pm}_{\vec{w}}(x). \tag{4.131}$$

4.5.2 Kernel approximation: limit $z \to 0$

Having explored in section 4.5.1 the analytic properties as well as the algebraic identities of the HPLs, we are now in position to describe our kernel approximation method. We denote the kernel whose approximation we investigate by $K(z)$, and having in mind the most general functional form that $\tilde{I}^{(3)}_{ij}(z)$ and $P^{(2)}_{ij}(z)$ assume, we decompose it as

$$K(z) = \sum_i \left[\frac{F_i(z)}{R_i(z)} + \frac{G_i(z)}{Q_i(z)} H_{\vec{w}_i}(z)\right], \tag{4.132}$$

where $F_i(z), R_i(z), G_i(z), Q_i(z)$ are polynomials in z. The subscript i serves for indexing purposes and the summation runs over all terms that are part of $K(z)$.

We begin by examining the best possible approximation that can be achieved for the most basic building block of $K(z)$, namely the HPLs $H_{\vec{w}_i}(z)$. We assume that the $H_{\vec{w}_i}(z)$ appearing in eq. (4.132) do not have any rightmost 0-letters as they correspond to logarithmic singularities $\ln z$ and inhibit their $z \to 0$ expansion. In case that HPLs of the form $H_{\vec{w}_j,\vec{0}_n}(z)$, with arbitrary $\vec{w}_j$, are part of the kernel, we use the product algebra identity in

eq. (4.116) to explicitly isolate them and proceed with the steps described bellow for the rest of the HPLs.

In full generality and as shown in section 4.5.1, HPLs can have both positive and negative branch cuts. Therefore, a straightforward expansion of $H_{\vec{w}_n}(z)$ as a power series in z has a constrained radius of convergence $|z| < 1$, and for achieving a relative error $\sim \mathcal{O}(10^{-15})$ it requires the truncation of the series at $\sim \mathcal{O}(z^{35})$. To address this issue, we first separate the branch cut structure of the HPLs according to eq. (4.125), and then perform the Bernoulli change of variables [319] in each of the terms with a single branch cut [310]

$$H_{\vec{w}_i}(z) = H^+_{\vec{w}_i}(z) + H^-_{\vec{w}_i}(z)\,, \tag{4.133}$$

$$H^+_{\vec{w}_i}(z): \qquad z \mapsto 1 - e^{-u}\,, \tag{4.134}$$

$$H^-_{\vec{w}_i}(z): \qquad z \mapsto e^{v} - 1\,. \tag{4.135}$$

The final step involves the expansion in the limit $u, v \to 0$, which results to a polynomial in u, v for $H^+_{\vec{w}_i}$ and $H^-_{\vec{w}_i}$ respectively. The Bernoulli change of variables in eq. (4.134) (eq. (4.135)) maps the $z = +1$ (-1) branch point to $+\infty$ $(-\infty)$, and the resulting u (v) series has an extended radius of convergence 2π. The necessity for the branch cut separation stems from the observation that if we allow HPLs to carry both cuts, then none of the above transformations will be of any help; the $z \mapsto 1 - e^{-u}$ moves the $z = -1$ branch point to $z = -\ln 2 \approx -0.693$ and similarly the $z \mapsto e^{v} - 1$ moves the $z = 1$ branch point to $z = +\ln 2 \approx 0.693$, both of which end up reducing the radius of convergence, even compared to a standard z-series. Employing the Bernoulli transformations allows for the truncation of the u, v-series at $\mathcal{O}(16)$ with a relative error $\sim \mathcal{O}(10^{-16})$ [310]. Note though that in our case, even with this improved approximation for the HPLs, achieving such a small relative error *at the level of* $K(z)$ corresponds to an overly optimistic estimation, since numerical cancellations between HPLs in $K(z)$ are quite strong.

On the other hand, the method described above for the HPLs provides an important hint on how similar results can be pursued at the level of the entire kernel. Therefore, we treat $K(z)$ as *one entity* whose series expansion results from that of its individual pieces. This allows at intermediate steps for arbitrary precision calculations between the terms appearing in eq. (4.132) and results to a controlled loss of precision. To achieve this, we first separate the positive and negative branch cuts of the kernel $K(z)$, then we perform the Bernoulli transformations, and finally we expand in the limit $u, v \to 0$,

$$K(z) = K^+(z) + K^-(z)\,, \tag{4.136}$$

$$K^+(z): \qquad z \mapsto 1 - e^{-u}\,, \tag{4.137}$$

$$K^-(z): \qquad z \mapsto e^{v} - 1\,. \tag{4.138}$$

A caveat to this simplified approach is the presence of rational polynomials $G_i(z)/Q_i(z)$ in eq. (4.132), which as we show below, they can change the analytic structure of the HPLs. This is equivalent to the statement that the separation in $K^{\pm}(z)$ *is not equivalent* to the separation in $H^{\pm}_{\vec{w}_i}(z)$. Before we proceed to examine the effect for each primitive factor

separately, we note that presence of $G_i(z)$ in $G_i(z)/Q_i(z)$ admits no special treatment. Since $G_i(z)$ are a polynomials in z of integer powers, they do not introduce any new branch cuts and therefore we gain nothing from the Bernoulli transformations. Consequently, there is no preferred variable between u or v for their expansion, and $G_i(z)$ inherit the Bernoulli transformation of the accompanying '+' or '−' term, together with which they are expanded.

Now consider the case of $G_i(z)/Q_i(z) \equiv c/z$, where c is a constant. As already mentioned in section 4.5.1, any number of extra $w_i = 0$ letters on an HPL do not alter its branch cut structure. Therefore, neither will the $1/z$ primitive, since we can think of it as an effective extra weight on the HPL, $\frac{1}{z}H_{\vec{w}_i}(z) \equiv \frac{\mathrm{d}}{\mathrm{d}z}H_{0,\vec{w}_i}(z)$. Thus, the '+' and '−' separation is trivial for such terms,

$$\left[\frac{1}{z}H_{\vec{w}_i}(z)\right]_+ = \frac{1}{z}H^+_{\vec{w}_i}(z)\,, \tag{4.139}$$

$$\left[\frac{1}{z}H_{\vec{w}_i}(z)\right]_- = \frac{1}{z}H^-_{\vec{w}_i}(z)\,, \tag{4.140}$$

where the term in the square brackets with '+' ('−') subscript denotes that it has only a positive (negative) branch cut. Given eqs. (4.139) and (4.140), in what follows we suppress the overall multiplicative z-terms in the functional form of $Q_i(z)$ as they have no impact on the analytic structure of the HPLs.

Turning to more complicated $Q_i(z)$ makes the situation slightly more involved. To examine it, we restrict our discussion to the specific cases of $Q_i(z) \in \{(1-z)^n, (1+z)^n\}$ where $n > 0$. Considering only these cases is motivated by the primitives that are met in $\tilde{I}^{(3)}_{ij}(z), P^{(2)}_{ij}(z)$ kernels.[15] For such terms, a straightforward separation of the branch cuts in *just* the HPLs leads to wrong results. To see this, consider the simple case

$$\frac{1}{1\pm z}H_{\vec{w}_i}(z) = \frac{1}{1\pm z}\left[H^+_{\vec{w}_i}(z) + H^-_{\vec{w}_i}(z)\right]. \tag{4.141}$$

The presence of $1/(1+z)$ develops a negative cut to $H^+_{\vec{w}_i}(z)$ and the resulting $H^+_{\vec{w}_i}(z)/(1+z)$ has both cuts, thus prohibiting its (improved) expansion in terms of the Bernoulli variable u. Note though, that $1/(1+z)$ is harmless for $H^-_{\vec{w}_i}(z)$ as it leaves its analytic structure intact, i.e. $H^-_{\vec{w}_i}(z)/(1+z)$ still has only a negative cut. Analogous considerations apply for the effect of $1/(1-z)$ on $H^{\mp}_{\vec{w}_i}(z)$. One way to regard the above, is realizing that the presence of the $1/(1\pm z)$ primitive practically induces an *extra weight* in the multiplying HPL since

$$\frac{1}{1\pm z}H_{\vec{w}_i}(z) \equiv \frac{\mathrm{d}}{\mathrm{d}z}H_{\mp 1,\vec{w}_i}(z)\,, \tag{4.142}$$

[15] We note that different functional forms of $Q_i(z)$ may be part of the kernel, e.g. $1-z^2$, but they can be easily worked out and converted into $\{(1-z)^n, (1+z)^n\}, n > 0$. In both $\tilde{I}^{(3)}_{ij}(z), P^{(2)}_{ij}(z)$ we were unable to find a primitive that under elementary algebraic manipulations could not be reduced into either of the aforementioned forms.

where crucially, the '+' and '−' terms of $H_{\mp 1,\vec{w}_i}(z)$ differ from those of $H_{\vec{w}_i}(z)$. Therefore, and for terms like these, we modify the definition for the branch cut separation such that the accompanying primitives are properly taken into account

$$\frac{H_{\vec{w}_i}(z)}{(1+z)^n} = \left[\frac{H^+_{\vec{w}_i}(z)}{(1+z)^n}\right]_+ + \left[\frac{H^-_{\vec{w}_i}(z)}{(1+z)^n}\right]_- , \tag{4.143}$$

$$\left[\frac{H^+_{\vec{w}_i}(z)}{(1+z)^n}\right]_+ = \frac{H^+_{\vec{w}_i}(z)}{(1+z)^n} - \sum_{k=0}^{n-1}(1+z)^{k-n}\frac{1}{k!}\frac{\mathrm{d}^k}{\mathrm{d}z^k}H^+_{\vec{w}_i}(z)\bigg|_{z=-1} , \tag{4.144}$$

$$\left[\frac{H^-_{\vec{w}_i}(z)}{(1+z)^n}\right]_- = \frac{H^-_{\vec{w}_i}(z)}{(1+z)^n} + \sum_{k=0}^{n-1}(1+z)^{k-n}\frac{1}{k!}\frac{\mathrm{d}^k}{\mathrm{d}z^k}H^+_{\vec{w}_i}(z)\bigg|_{z=-1} , \tag{4.145}$$

where eq. (4.144) (eq. (4.145)) corresponds to the term with only a positive (negative) branch cut. The subtrahend in eq. (4.144) serves the purpose of eliminating the cut developed at $z=-1$ by the primitive factor(s), with the resulting term maintaining its analytic structure of a single positive cut. Finally, the subtracted term is added to the piece with the opposite branch cut in eq. (4.145), for which it does not alter its analytic structure. Contrasting eqs. (4.144) and (4.145) to eqs. (4.127) and (4.128), it is understood that the former method of separating the branch cuts corresponds to an adequate extension of the latter, with the $Q_i(z)$ treated as effective extra weights on HPLs. Under similar considerations for the $1/(1-z)$ primitive, we define the corresponding '+' and '−' separation to be

$$\left[\frac{H^+_{\vec{w}_i}(z)}{(1-z)^n}\right]_+ = \frac{H^+_{\vec{w}_i}(z)}{(1-z)^n} + \sum_{k=0}^{n-1}(1-z)^{k-n}\frac{1}{k!}\frac{\mathrm{d}^k}{\mathrm{d}z^k}H^-_{\vec{w}_i}(z)\bigg|_{z=1} , \tag{4.146}$$

$$\left[\frac{H^-_{\vec{w}_i}(z)}{(1-z)^n}\right]_- = \frac{H^-_{\vec{w}_i}(z)}{(1-z)^n} - \sum_{k=0}^{n-1}(1-z)^{k-n}\frac{1}{k!}\frac{\mathrm{d}^k}{\mathrm{d}z^k}H^-_{\vec{w}_i}(z)\bigg|_{z=1} . \tag{4.147}$$

where now the subtraction takes place for $H^-_{\vec{w}_i}(z)$ since $1/(1-z)$ causes a positive branch cut to develop.

We now turn to the terms $F_i(z)/R_i(z)$ in eq. (4.132) that are independent of HPLs. As before, we restrict to the specific cases $R_i(z) \in \{(1-z)^n, (1+z)^n\}$, where $n>0$. From the previous analysis it should be clear that $1/(1+z)^n$ terms can be treated as (effectively) having only a negative branch cut, whereas the $1/(1-z)^n$ terms as (effectively) having only a positive branch cut. Therefore, an improved series expansion is achieved under

$$R_i(z) = (1-z)^n : \qquad z \mapsto 1-e^{-u} , \tag{4.148}$$

$$R_i(z) = (1+z)^n : \qquad z \mapsto e^{v}-1 , \tag{4.149}$$

and the polynomial $F_i(z)$ inherits the variable transformation of the accompanying $R_i(z)$.

Finally, we comment on the terms $\propto \ln^n z/z$, $n \geq 0$ which appear in the gluon kernels and emerge from either addends in eq. (4.132). Although in principle they can be expanded opting for either Bernoulli change of variables, here we choose not to do so, since they induce

terms $\propto \ln^n u/u$ or $\propto \ln^n v/v$ which obstruct the possibility for a Chebyshev acceleration of the resulting series.

The above considerations conclude the algorithm for an improved approximation of $K(z)$ in the limit $z \to 0$. Summarizing all the steps in a schematic sequence,

$$\begin{aligned} K(z) &= \sum_i \left[\frac{F_i(z)}{R_i(z)} + \frac{G_i(z)}{Q_i(z)} H_{\vec{w}_i}(z)\right] \\ &= \sum_{n=0}^{w_{\max}} d_n \frac{H_0^n(z)}{z} + \sum_{n=0}^{w_{\max}} C_n(z) H_0^n(z) \\ &= \sum_{n=0}^{w_{\max}} d_n \frac{H_0^n(z)}{z} + \sum_{n=0}^{w_{\max}} \Big[C_n^+(z) + C_n^-(z)\Big] H_0^n(z) \\ &= \sum_{n=0}^{w_{\max}} d_n \frac{\ln^n z}{z} + \sum_{n=0}^{w_{\max}} \sum_{m=0}^{\ell} \Big[c_{n,m}^+ u^m + c_{n,m}^- v^m\Big] \ln^n z + \mathcal{O}\big(u^{\ell+1}\big) + \mathcal{O}\big(v^{\ell+1}\big)\,, \end{aligned} \tag{4.150}$$

where $d_n, c_{n,m}^{\pm}$ are constants, $u = -\ln(1-z)$, $v = \ln(1+z)$ and the sum over n is bounded by the maximum weight $w_{\max}$ of the HPLs present in $K(z)$. In the second line we isolate the logarithmic singularities $H_0(z) \equiv \ln z$ of the HPLs using eq. (4.116) and separate the terms $\propto \ln^n z/z$ that we do not expand. The coefficients $C_n(z)$ have a functional form that falls under one of the cases that we considered in this section, i.e. they are composed out of rational polynomials and HPLs without rightmost 0-letters. Thus, to obtain an improved expansion for these, in the third line we split their positive and negative branch cuts while properly accounting for the primitive factors, and we perform the Bernoulli change of variables in eqs. (4.137) and (4.138). Finally, we expand in $u, v \to 0$, resulting to the polynomial form in eq. (4.150).

4.5.3 Kernel approximation: limit $z \to 1$

Turning now to the opposite limit, $z \to 1$, the most natural question that should be posed is how many of the tools developed in the previous paragraph for the $z \to 0$ approximation apply also in this case? Unfortunately, the answer is few and the reason twofold. On the one hand and in terms of numerical implementation, the most convenient way to express the kernel in this limit is by the change of variables

$$z \mapsto 1 - y\,, \tag{4.151}$$

where now $z \to 1$ is realized for $y \to 0$. The reason that this transformation is preferred, is related to numerical precision arguments relevant for the dominant, singular terms of the kernel $\propto \ln^n(1-z)/(1-z) \mapsto \ln^n y/y$, $n \geq 0$. On the other hand and looking at how the $w = 1$ HPLs transform under eq. (4.151), we have

$$H_0(z) \mapsto -H_1(y)\,, \qquad H_1(z) \mapsto -H_0(y)\,, \qquad H_{-1}(z) \mapsto \int_0^y \frac{\mathrm{d}x}{x-2} + \ln 2\,. \tag{4.152}$$

Notably, while $H_0(z), H_1(z)$ still map to the HPL class of functions (although of different weight), this is not the case for $H_{-1}(z)$ where its analytic form changed entirely. Formally, under $z \mapsto 1-y$ the full basis of HPLs[16] maps to a wider set of functions known as Multiple Polylogarithms (MPLs) [320].

MPLs can be regarded as a class of functions with one possible definition via iterative integrals, same as that of the HPLs in eq. (4.110). An important difference between the two is that the weights w_i of MPLs are not restricted to the values $\{-1, 0, 1\}$, as they can be any complex variable. For example, the transformation of $H_{-1}(z)$ in terms of MPLs reads

$$H_{-1}(z) \xrightarrow{z\mapsto 1-y} G_2(y) + \ln 2\,, \tag{4.153}$$

where $G_{\vec{w}}(y)$ is an MPL of weight vector $\vec{w} = \{w_n, \ldots, w_1\}$ and weight w. Furthermore, MPLs satisfy the so-called *shuffle algebra* [320] which is analogous to the product algebra of HPLs in eq. (4.116). This is an important property that we harvest — in complete analogy to the $z \to 0$ limit — in order to isolate the logarithmic singularities $\sim \ln y$ that manifest as rightmost 0-letters in MPLs.

Looking back at eq. (4.152), a direct consequence of the y-transformed HPLs is that they cease to have a negative branch cut at $(-\infty, -1]$. The same also applies when considering the induced branch cuts emerging from the transformation of primitive factors $1/(1+z) \mapsto 1/(2-y)$ present in the kernel $K(z)$. Therefore, the Bernoulli transformation in eq. (4.135) does not provide an improvement for a series expansion and in contrast to the limit $z \to 0$, a positive and negative branch cut separation of the kernel is no longer justified.

In light of the above, we address the kernel approximation of $K(z)$ in eq. (4.132) in the limit $z \to 1$ as follows: we first map $K(z) \xrightarrow{z\mapsto 1-y} \tilde{K}(y)$ where we stress that under this transformation $\tilde{K}(y)$ depends on both HPLs and MPLs. We then separate the terms $\propto \ln^n y/y$, which same as in section 4.5.2, we leave unexpanded. Subsequently, we isolate the logarithmic singularities $\propto \ln^n y$ that manifest as rightmost 0-letters in HPLs and MPLs using the product and shuffle algebra respectively. Finally, we apply the transformation $y \mapsto 1 - e^{-r}$ in the coefficients of $\ln^n y$ and expand them in the limit $r \to 0$. Putting the previous steps into math,

$$\begin{aligned} K(z) \xrightarrow{z\mapsto 1-y} \tilde{K}(y) &= \sum_{n=0}^{w_{\max}} d_n \frac{\ln^n y}{y} + \sum_{n=0}^{w_{\max}} C_n(y) \ln^n y \\ &= \sum_{n=0}^{w_{\max}} d_n \frac{\ln^n y}{y} + \sum_{n=0}^{w_{\max}} \sum_{m=0}^{\ell} c_{n,m} r^m \ln^n y + \mathcal{O}(r^{\ell+1})\,, \end{aligned} \tag{4.154}$$

where d_n, $c_{n,m}$ are constants and $r = -\ln(1-y)$. The coefficients $C_n(y)$ are composed out of rational polynomials, HPLs and MPLs free of logarithmic singularities and the sum over n is bounded by the maximum weight $w_{\max}$ of the HPLs present in $K(z)$.

[16] As it can be understood from eq. (4.152), only HPLs that carry the letter(s) $w_i = -1$ map to MPLs, while those that do not, still transform to linear combinations of HPLs under $z \mapsto 1-y$.

The transformation $y \mapsto 1 - e^{-r} \Rightarrow z \mapsto e^{-r}$ addresses successfully the expansion of $H_{\vec{w}}(z)$ that carry only the letters $w_i = 0$ and/or $w_i = 1$, as well as of the primitive factors $1/z$. It is analogous to the Bernoulli transformation that we performed in eq. (4.137), and as expected, it results to an improvement in the convergence of such terms, hence (partially) to that of the kernel. Conversely, it does not address adequately the expansion of $H_{\vec{w}}(z)$ that carry the letter(s) $w_i = -1$ or the primitive factors $\propto 1/(1+z)$, for which we are (potentially) forced to truncate the y-series at higher orders in order to meet a certain precision goal. It should be noted though, that this is correlated to the analytic structure of the kernel, in the sense of how strong it is the presence of such primitives and HPLs.

Concluding, we stress that while this choice for expanding $K(z)$ corresponds to a compromise, since not all terms are optimally approximated, it still amounts to an amelioration compared to a standard y-series. This is due to the fact that the y-series has inherently a restricted radius of convergence $|y| < 1$ due to the branch cuts of the HPLs.

4.5.4 Representative results

Having presented in sections 4.5.2 and 4.5.3 an improved approximation method for kernels with the functional form of eq. (4.132), in this section we exemplify this improvement. We show representative results for the splitting functions[17] $P^{(2)}_{qqS}(z), P^{(2)}_{qq\Delta S}(z)$ and the N^{3}LO gluon beam function kernels $\tilde{I}^{(3)}_{gg}(z)$, $\tilde{I}^{(3)}_{gq}(z)$, with the latter being directly relevant for the phenomenological study that takes place in chapter 5. In order to be fully exhaustive in our comparison, we contrast our approximation method against a plain polynomial expansion for $\tilde{I}^{(3)}_{gg}, \tilde{I}^{(3)}_{gq}$ and with respect to a code implementation for $P^{(2)}_{qqS}(z), P^{(2)}_{qq\Delta S}(z)$.

All kernels — irrespectively of how (and if) they are approximated — are compared to their 'exact' counterpart. We obtain these from the evaluation of the full, unexpanded kernels that carry the exact z and HPL dependence. Specifically, we use a `Mathematica` [321] implementation together with the `HPL` [314] program which explicitly allows for the evaluation of the HPLs and the kernels at arbitrary precision.

For the kernels that are approximated based on the method developed in sections 4.5.2 and 4.5.3, we use our own implementation in `SCETlib` [49].

For the plain polynomial expansion of $\tilde{I}^{(3)}_{gg}(z)$, $\tilde{I}^{(3)}_{gq}(z)$, we use results provided by the authors of ref. [139], which correspond to power series in z (limit $z \to 0$) and in $1 - z$ (limit $z \to 1$). While the authors of ref. [139] provide the expansions to very high order, here, the truncation of the series is chosen to be the same as that in the improved approximation since the latter always allow for lower order polynomials.

For $P^{(2)}_{qqS}(z), P^{(2)}_{qq\Delta S}(z)$ we use our own code implementation. Specifically, these kernels are *unexpanded*, i.e. they carry the exact z and HPL dependence, and we obtain numerical values for the HPLs using the program `hplog` [310].

Figure 4.10 shows for $\tilde{I}^{(3)}_{gq}(z)$ (top panel), $\tilde{I}^{(3)}_{gg}(z)$ (bottom panel) the relative difference between the 'exact' and the approximate kernels in units of machine epsilon ϵ. The left column shows the standard z expansion whereas the right column shows the improved

[17] See appendix A.3 for our conventions on the flavor decomposition of a generic Mellin-convolution kernel.

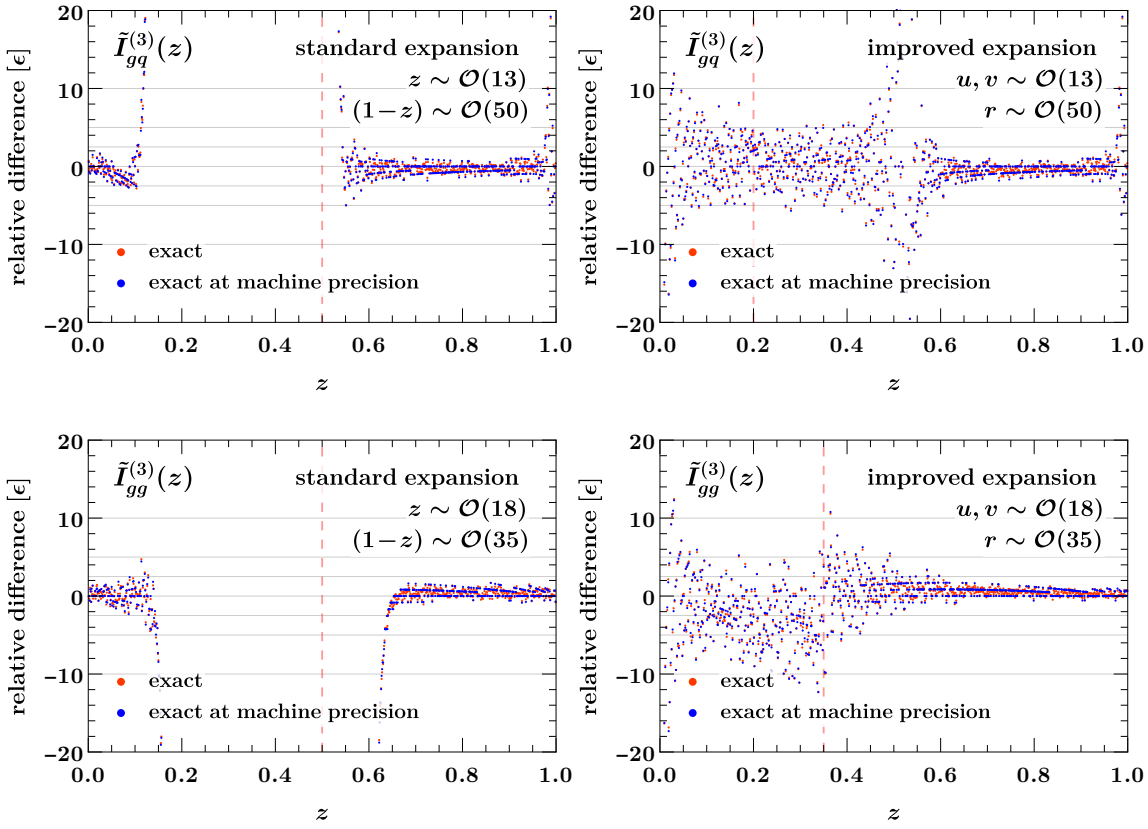

Figure 4.10: Relative difference of the N^{3}LO gluon beam boundary coefficients in units of machine epsilon ϵ between the 'exact' and the approximated kernels either employing the standard series expansion (left panels) or the improved method (right panels). A detailed explanation of the plots is given in the text.

expansion. In all cases, the kernels are evaluated at binary exact z values in order to avoid any numerical noise stemming from standard approximations of non-binary exact z values. The red data points correspond to the relative difference where the 'exact' kernel is allowed to return values beyond machine precision and therefore a scattering around $\pm\epsilon/2$ indicates that the approximate kernels are correct to machine precision. The blue data points show the same as the red, but now the 'exact' kernels are truncated to machine precision, therefore the relative difference is expected to be exactly 0 if the expanded kernels yield the best possible double precision approximation. The dashed red vertical line shows the point in z where we switch between expansions. Overall, and for both flavor channels, it is clear that the improved method corresponds to a better approximation, especially in the limit $z \to 0$. It is evident that the standard expansion results in high relative error in the range $0.2 \lesssim z \lesssim 0.6$, which constitutes a clear indication that the power series should be truncated at a higher order; in fact we have checked that their relative error improves when the standard series are truncated $\sim \mathcal{O}(50)$. Although at first sight this might appear as a (viable) choice, its ramifications are rather important. In the beam functions, both

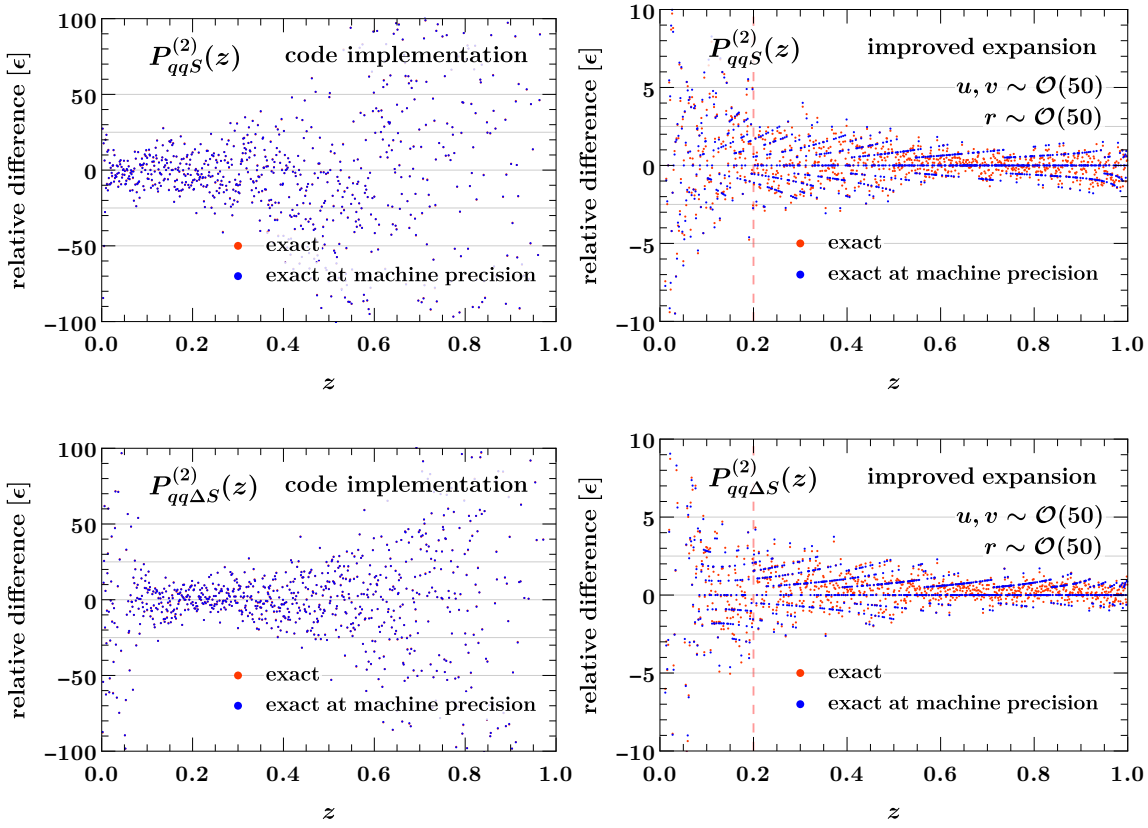

Figure 4.11: Relative difference of the NNLO splitting functions in units of machine epsilon ϵ between the 'exact' and an implementation either via a numerical code (left panels) or via the improved approximation method (right panels). A detailed explanation of the plots is given in the text.

$\tilde{I}^{(3)}_{gq}(z)$, $\tilde{I}^{(3)}_{gg}(z)$ are convolved against PDFs and inevitably involves 'calling' them several thousand of times, resulting in a significant slower evaluation of the beam functions as the expansion order increases.

Figure 4.11 shows the same plots as before, only now for $P^{(2)}_{qqS}(z)$ (top panels) and $P^{(2)}_{qq\Delta S}(z)$ (bottom panels), either using a code implementation for the unexpanded kernels (left column) or using the improved approximation method (right column). In this case, the results are more dramatic. The relative difference of the code implementation is (more) than one order of magnitude away from that of the improved expansion, exceeding $100\,\epsilon$ when the latter are less than $10\,\epsilon$. This is due to catastrophic numerical cancellations that take place within the *exact and unexpanded* kernel, inherent to their size and complicated functional form. Thus we see, that even though a code implementation may achieve excellent results for the evaluation of *individual* HPLs, it fails to address the precision requirements at the level of such complicated kernels.

4.6 Summary

In this chapter we studied the three-loop structure of beam and soft functions for both 0-jettiness, $\mathcal{T}_0$, and transverse momentum q_T resolution variables. These functions are defined as collinear proton matrix elements and soft vacuum matrix element, measuring the small light-cone momentum (for $\mathcal{T}_0$) or total transverse momentum (for q_T) of all soft and collinear emissions, and thus are universal objects probing the infrared structure of QCD. Exploiting that the all-order singular structure of the beam and soft functions is governed by their RGEs, we derived results up to $\mathcal{O}(\alpha_s^3)$. Subsequently, we performed a numerical study on the residual scale dependence of the resummed soft and beam functions for both q_T and $\mathcal{T}_0$, where we found that at N^{3}LL$'$ and in almost all cases it is substantially reduced. Exception to that was the down variation of the $\mathcal{T}_0$ quark beam function between the two highest orders, NNLL$'$ and N^{3}LL$'$, although we stress once more that the residual scale dependence of just the resummed beam function may not be representative of the perturbative uncertainty one might expect at the cross section level.

Furthermore, for the scale-independent boundary coefficients $I_{ij}^{(3)}(z)$ of the N^{3}LO beam functions, we exploited relations between different factorization limits to derive the leading eikonal limit $I_{ij}^{(3)}(z \to 1)$, i.e. the full singular limit of the beam functions as $z \to 1$. These correspond to genuine predictions that provided nontrivial cross checks and the only ones at N^{3}LO, for the authors of refs. [139, 140, 231, 244] that performed the calculation of the exact $\mathcal{T}_0$ and q_T beam boundary coefficients at $\mathcal{O}(\alpha_s^3)$. We then studied the extent to which the eikonal limit of the beam boundary terms can provide a good approximation to the exact kernels, and based on our findings at lower orders, we constructed ansätze for both $\mathcal{T}_0$ and q_T. Since the N^{3}LO exact kernels were made (long after) available, we directly compared them to our ansätze, finding very good agreement always within the uncertainty estimate of the latter.

Finally, motivated by the importance of the N^{3}LO beam boundary terms and their nontrivial functional form, we presented an improved method for the approximation of kernels that bear such functional signature, in the phenomenologically relevant limits $z \to 0$ and $z \to 1$. To achieve this, we exploited the analytic and algebraic properties of the most basic building block, the HPLs, while properly taking into account the effects of primitive functions on their analyticity. Crucial points in obtaining an improved approximation was the treatment of the kernels as one entity and the Bernoulli change of variables. In addition, we illustrated the improvement by examining the relative error for the gluon beam function kernels $\tilde{I}_{gg}^{(3)}(z)$, $\tilde{I}_{gq}^{(3)}(z)$ and the splitting functions $P_{qqS}^{(2)}(z)$, $P_{qq\Delta S}^{(2)}(z)$ as approximated by our method, and contrasted either to a standard series expansion (gluon kernels) or to a code implementation (splitting functions). While for the former kernels we saw that the improved method allows for a significantly lower truncation order of the series while achieving very good precision, for the latter the findings were more compelling. The relative difference for the code implementation of the exact kernels exceeded $100\,\epsilon$, when their corresponding improved approximation was below $10\,\epsilon$. In light of these, we concluded on the evident advantages of the improved approximation.

Chapter 5

Higgs physics

In this chapter we present predictions for the gluon-fusion Higgs boson q_T spectrum at N^{3}LL$'$+N^{3}LO both inclusively and with fiducial cuts as required by experimental measurements at the LHC. By integrating the fiducial q_T spectrum, we predict the total fiducial cross section to third order (N^{3}LO) and improved by timelike and transverse momentum resummation. We find that the N^{3}LO correction is enhanced by cut-induced logarithmic effects and it is not reproduced by the inclusive N^{3}LO correction times a lower-order acceptance factor.

This chapter is based on ref. [3] while discussions have been extended appropriately both in depth and in order to cover the necessary background material. Sections 5.3 and 5.4.1 have been added.

5.1 Introduction

Fiducial and differential cross section measurements of the discovered Higgs boson [4, 5] provide the most model-independent way to study Higgs production at the LHC. They are thus central to its physics program [31, 322–333] and will remain so in the future [334].

It is well known that theoretical predictions for the dominant gluon-fusion ($gg \to H$) Higgs production mode suffer from large perturbative corrections. This has led to the calculation of the total inclusive production cross section to N^{3}LO [179, 335–342], which is made possible by treating the decay of the Higgs boson fully inclusively. Unfortunately, this also makes it a primarily theoretical quantity; one that cannot be measured in experiment. The experimental measurements necessarily involve kinematic selection and acceptance cuts on the Higgs decay products, which reduce the cross section by an $\mathcal{O}(1)$ amount. Therefore, any comparison of theory and experiment always involves a prediction of the *fiducial* cross section, i.e., the cross section within the experimental acceptance. Up to now, the fiducial cross section for $gg \to H$ was only known to NNLO and a key theoretical challenge was to calculate it at N^{3}LO, which we do in this chapter.

Arguably, the most important differential cross section of the Higgs boson is its transverse-momentum (q_T) distribution, serving as a benchmark spectrum in many experimental analyses. At finite q_T, it is known to NNLO$_1$ [299, 343–351], i.e., from calculating $H+1$ parton to NNLO, including fiducial cuts, which is an important ingredient for our results. For $q_T \ll m_H$, the q_T spectrum contains large Sudakov logarithms of q_T/m_H, which deteriorate

the perturbative expansion, and they must be resummed to all orders in perturbation theory in order to obtain precise and reliable theoretical predictions. So far, q_T resummation has been achieved to NNLL′ and N^{3}LL [151, 157, 159, 191, 276, 352–354], which capture in particular all $\mathcal{O}(\alpha_s^2)$ contributions that are singular for $q_T \to 0$. In this chapter, we obtain the resummed q_T spectrum at N^{3}LL′+N^{3}LO, both inclusively and with fiducial cuts. Compared to N^{3}LL, the resummation at N^{3}LL′ incorporates the complete $\mathcal{O}(\alpha_s^3)$ singular structure for $q_T \to 0$, i.e. all three-loop virtual and corresponding real corrections, allowing us to consistently match to N^{3}LO and obtain $\mathcal{O}(\alpha_s^3)$ accuracy throughout the q_T spectrum. For the fiducial cross section, we incorporate the experimental cuts in the resummed q_T spectrum following the recent analysis in ref. [262]. This allows us to also resum large, so-called fiducial power corrections induced by the fiducial cuts [261, 262], and eventually to predict the total fiducial cross section at N^{3}LO from the integral of the resummed fiducial q_T spectrum. This constitutes the first complete application of differential q_T subtractions at this order. (For earlier results and discussions see refs. [2, 180] and for a recent application in the context of q_T-slicing method see ref. [355])

The structure of the chapter is as follows. In section 5.2 we review the theoretical framework that the present analysis is based on. In section 5.3 we discuss the method for extracting power suppressed contributions of the q_T spectrum. In section 5.4 we present predictions both for the inclusive and the fiducial transverse momentum spectrum, and discuss in each case the impact of the ensuing theoretical uncertainties. In section 5.5 we calculate the total fiducial cross section and investigate potential pitfalls that the q_T-slicing method involves. We conclude in section 5.6.

5.2 Framework

This section is devoted to providing the necessary background material that the present phenomenological study is based on. In section 5.2.1 we review important theoretical considerations regarding Higgs boson production in the gluon fusion channel, while in section 5.2.2 the nontrivial effects of the fiducial cuts on the q_T spectrum are discussed. In sections 5.2.3, 5.2.4, and 5.2.5 we present the method to achieve both q_T and timelike resummation, the matching to the FO cross section and our setup for estimating theoretical uncertainties. Section 5.2.6 collects all numerical inputs relevant to our predictions.

5.2.1 Higgs production

We consider Higgs production at the LHC in the diphoton decay channel,

$$p(P_a)\, p(P_b) \to H(q) + X(p_X) \to \gamma(p_1)\, \gamma(p_2) + X(p_X)\,, \tag{5.1}$$

where $P_{a,b}^\mu = E_{\rm cm} n_{a,b}^\mu/2$ are the momenta of the incoming protons and $n_a^\mu = (1, \hat{z})$, $n_b^\mu = (1, -\hat{z})$. We denote the Higgs boson momentum by q^μ and we are inclusive over any additional hadronic radiation X with momentum p_X^μ. We are interested in the dominant gluon-fusion production channel, $gg \to H$, which is a loop induced process with a top

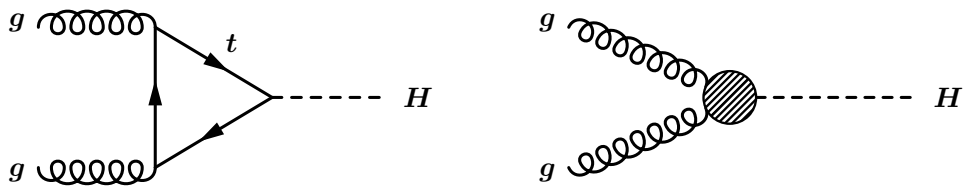

Figure 5.1: Leading order Feynman diagrams for Higgs production in the gluon fusion process with the exact m_t dependence (left) and in the limit $m_t \to \infty$ (right) where the top quark is integrated out.

quark in the loop mediating the effective coupling between the Higgs and the gluons. In general, analytical expressions for the amplitudes contributing to the gluon-fusion process are quite complicated due to the presence of multiple mass scales, m_H and m_t. Fortunately, the hierarchy that m_H and m_t exhibit can be exploited by working in the so-called infinite top mass limit, $m_t \to \infty$, where the top quark is integrated out and an effective theory with $n_f = 5$ massless quarks is defined. In figure 5.1 we show LO Feynman diagrams for the process $gg \to H$ with the exact m_t dependence (left) and in the limit $m_t \to \infty$ where the top quark is integrated out (right). In that limit the EFT current reads [356–358]

$$J_{gg} = \frac{\alpha_s(\mu_t)}{12\pi v} C_t(m_t, \mu_t) F^a_{\mu\nu} F^{\mu\nu\, a}\,, \tag{5.2}$$

where $v = (\sqrt{2}G_F)^{-1/2} = 246\,\text{GeV}$ is the Higgs VEV while $C_t(m_t, \mu_t) = 1 + \mathcal{O}(\alpha_s)$ is a Wilson coefficient that stems from integrating out the top quark and carries all the m_t dependence. It is known to up to N^{4}LO [359–361] and satisfies the RGE

$$\mu \frac{\mathrm{d}}{\mathrm{d}\mu} C_t(m_t, \mu) = \gamma_t[\alpha_s(\mu)]\, C_t(m_t, \mu)\,, \tag{5.3}$$

$$\gamma_t[\alpha_s] = \alpha_s^2 \frac{\mathrm{d}}{\mathrm{d}\alpha_s} \frac{\beta[\alpha_s]}{\alpha_s^2}\,, \tag{5.4}$$

with $\gamma_t[\alpha_s]$ its anomalous dimension. It is common to rescale the current in eq. (5.2) with the exact LO m_t dependence [362],

$$F_0(\rho) = \frac{3}{2\rho} - \frac{3}{2\rho}\left|1 - \frac{1}{\rho}\right| \arcsin^2(\sqrt{\rho})\,, \qquad \rho = \frac{m_H^2}{4m_t^2} < 1\,, \tag{5.5}$$

which defines the *rescaled EFT* (rEFT) [362] and the corresponding current is given by

$$J_{\text{rEFT}} = F_0(\rho) \frac{\alpha_s(\mu_t)}{12\pi v} C_t(m_t, \mu_t) F^a_{\mu\nu} F^{\mu\nu\, a}\,. \tag{5.6}$$

It should be noted that rescaling J_{gg} with $F_0(\rho)$ provides a good approximation of the exact m_t dependence at NLO and therefore it is believed to be also useful at higher orders [363–366, 366–369].

Working in the limit $m_t \to \infty$ and neglecting the proton masses, we write the cross section for the process in eq. (5.1) differential in the Higgs four-momentum

$$\frac{\mathrm{d}\sigma}{\mathrm{d}^4 q} = \frac{1}{2E_{\mathrm{cm}}^2}\mathcal{W}(q, P_a, P_b) L(q, \Theta)\,. \tag{5.7}$$

Here, the scalar hadronic structure function $\mathcal{W}(q, P_a, P_b)$ encodes all the QCD dynamics of the production process $gg \to H$ and it is defined as

$$\mathcal{W}(q, P_a, P_b) = \sum\!\!\!\!\!\!\int_X \langle pp|J^\dagger_{\mathrm{rEFT}}|X\rangle\langle X|J_{\mathrm{rEFT}}|pp\rangle\, \delta^{(4)}(P_a + P_b - p_X - q)\,, \tag{5.8}$$

where we keep implicit the average over spin and color while the sum over X includes all possible intermediate states with the corresponding phase space integrals. Since $\mathcal{W}$ is a Lorentz scalar and inclusive over the hadronic final state X, it can only depend on the Higgs momentum q^μ and the proton momenta $P^\mu_{a,b}$ via q^2 and $2q\cdot P_{a,b} = E_{\mathrm{cm}}\sqrt{q^2 + \vec{q}_T^{\,2}}e^{\mp Y}$, where q^2, Y and $\vec{q}_T$ are the Higgs virtuality, rapidity and transverse momentum, respectively.

In eq. (5.7) the leptonic function $L(q, \Theta)$ captures the propagation and the decay of the Higgs boson and it is defined as

$$L\big(q, \Theta\big) = \int \mathrm{d}\Phi_{\gamma\gamma}(q)\, \big|\mathcal{M}_{H\to\gamma\gamma}\big|^2\, \Theta(\Phi_{\gamma\gamma})\,, \tag{5.9}$$

$$\text{with}\quad \mathrm{d}\Phi_{\gamma\gamma}(q) = \left[\prod_{i=1}^{2} \frac{\mathrm{d}^4 p_i}{(2\pi)^4}(2\pi)\delta(p_i^2)\,\theta(p_i^0)\right](2\pi)^4\delta^{(4)}(q - p_1 - p_2)\,, \tag{5.10}$$

where $\mathcal{M}_{H\to\gamma\gamma}$ is the matrix element for the propagation and the decay of the Higgs boson while $\mathrm{d}\Phi_{\gamma\gamma}(q)$ is the differential diphoton phase space. In eq. (5.9) the function $\Theta(\Phi_{\gamma\gamma})$ is responsible for implementing all the fiducial cuts and in general, it can be regarded as a collection of θ-functions that impose restrictions on the diphoton phase space. As we will see, a common example would be a cut on the photon momenta and/or their rapidities.

Owing to the SM prediction for the Higgs total decay width, $\Gamma_H \approx 4\,\mathrm{MeV} \ll m_H$ [15], it is justifiable to make use of the narrow width approximation (NWA) and further simplify the calculational complexity of the cross section by factorizing the production and decay subprocesses. This amounts to the limiting case $\Gamma_H/m_H \to 0$ for the (squared) Higgs propagator

$$\left|\frac{\mathrm{i}}{q^2 - m_H^2 + \mathrm{i}m_H\Gamma_H}\right|^2 \xrightarrow{\frac{\Gamma_H}{m_H}\to 0} \frac{\pi}{m_H\Gamma_H}\,\delta(q^2 - m_H^2)\,, \tag{5.11}$$

under which the leptonic function $L(q, \Theta)$ can be recast into the form

$$\begin{aligned} L(q,\Theta) \xrightarrow{\frac{\Gamma_H}{m_H}\to 0} L(q,\Theta) &= 2\pi\delta(q^2 - m_H^2)\frac{1}{2m_H\Gamma_H}\int \mathrm{d}\Phi_{\gamma\gamma}(q)\, \big|\mathcal{M}^{\mathrm{NWA}}_{H\to\gamma\gamma}\big|^2\Theta(\Phi_{\gamma\gamma}) \\ &= 2\pi\delta(q^2 - m_H^2)\,\mathcal{B}_{\gamma\gamma}\,A(q;\Theta)\,. \end{aligned} \tag{5.12}$$

Here, $\mathcal{M}^{\text{NWA}}_{H\to\gamma\gamma}$ is the matrix element capturing only the decay of the Higgs boson, i.e. stripping off the squared propagator, and $\mathcal{B}_{\gamma\gamma}$ is the branching ratio of the Higgs to decay into two photons,

$$\mathcal{B}_{\gamma\gamma} = \frac{1}{2m_H\Gamma_H}\int \mathrm{d}\Phi_{\gamma\gamma}(q)\ \left|\mathcal{M}^{\text{NWA}}_{H\to\gamma\gamma}\right|^2 . \tag{5.13}$$

In eq. (5.12) we introduced the *acceptance function* $A(q;\Theta)$ which is defined as

$$A(q;\Theta) = 8\pi\int \mathrm{d}\Phi_{\gamma\gamma}(q)\ \Theta(\Phi_{\gamma\gamma}) . \tag{5.14}$$

Going from the first to the second line of eq. (5.12), we exploited the fact that since the Higgs is a scalar particle the squared matrix element $\left|\mathcal{M}^{\text{NWA}}_{H\to\gamma\gamma}\right|^2$ depends only on $(p_1+p_2)^2 = q^2 = m_H^2$, which allows us in NWA to explicitly pull it out of the phase space integral and express the leptonic function $L(q,\Theta)$ as a product of $\mathcal{B}_{\gamma\gamma}$ and $A(q;\Theta)$.

Turning back to the acceptance function $A(q;\Theta)$, in full generality it depends on $q_T = |\vec{q}_T|$ and Y, both induced by the fiducial cuts that are imposed on the diphoton phase space. In eq. (5.14) we follow the normalization convention that in the inclusive case, which is defined as the absence of any cuts, $\Theta(\Phi_{\gamma\gamma}) = 1$, the acceptance evaluates to

$$A_{\text{incl}} \equiv A(q_T, Y; 1) = 1 , \qquad \Theta(\Phi_{\gamma\gamma}) = 1 . \tag{5.15}$$

We proceed by decomposing the differential measure $\mathrm{d}^4q = (\pi/2)\mathrm{d}q^2\mathrm{d}Y\mathrm{d}q_T^2$ and set $q^2 = m_H^2$ using the delta function in eq. (5.12). This allows us to write the cross section in eq. (5.7) differential in the Higgs transverse momentum as

$$\frac{\mathrm{d}\sigma}{\mathrm{d}q_T^2} = \mathcal{B}_{\gamma\gamma}\int \mathrm{d}Y\ W(q_T,Y)A(q_T,Y;\Theta) , \tag{5.16}$$

where we defined $W(q_T,Y) = \pi^2\mathcal{W}(q,P_a,P_b)/(2E_{\text{cm}}^2)$. In the discussions that follow, we drop the $\mathcal{B}_{\gamma\gamma}$ from $\mathrm{d}\sigma/\mathrm{d}q_T^2$ since we eventually only show results normalized to $\mathcal{B}_{\gamma\gamma}$.

5.2.2 Fiducial power corrections

Expanding in eq. (5.16) both the acceptance and the hadronic structure function in the limit $q_T/m_H \ll 1$, the q_T spectrum can be written as

$$\begin{aligned}\frac{\mathrm{d}\sigma}{\mathrm{d}q_T^2} &= \frac{\mathrm{d}\sigma^{(0)}}{\mathrm{d}q_T^2} + \frac{\mathrm{d}\sigma^{(1)}}{\mathrm{d}q_T^2} + \frac{\mathrm{d}\sigma^{(2)}}{\mathrm{d}q_T^2} + \cdots \\ &\sim \frac{1}{q_T^2}\left[\ \mathcal{O}(1) + \mathcal{O}\Big(\frac{q_T}{m_H}\Big) + \mathcal{O}\Big(\frac{q_T^2}{m_H^2}\Big) + \cdots\right] .\end{aligned} \tag{5.17}$$

The singular, leading-power term $\mathrm{d}\sigma^{(0)}/\mathrm{d}q_T^2$ scales as $1/q_T^2$ and dominates for $q_T \ll m_H$. It contains $\delta(q_T)$ and $[\ln^n(q_T/m_H)/q_T]_+$ distributions encoding the cancellation of real and virtual infrared singularities at $q_T = 0$. The $\mathrm{d}\sigma^{(n\geq 1)}/\mathrm{d}q_T^2$ are power corrections and *formally* subleading in this limit as they are weighted by at least one power of q_T/m_H.

Due to azimuthal symmetry, $W(q_T, Y)$ receives only quadratic power corrections [262, 306],

$$W(q_T, Y) = W^{(0)}(q_T, Y) + W^{(2)}(q_T, Y) + \dots \,, \tag{5.18}$$

where $W^{(0)} \sim 1/q_T^2$ contains the singular terms. On the other hand, the acceptance corrections are finite at $q_T = 0$, but the fiducial cuts Θ generically break azimuthal symmetry and thus it receives linear power corrections [261, 262] (see also refs. [370, 371]),

$$A(q_T, Y; \Theta) = A(0, Y; \Theta)\Big[1 + \mathcal{O}\Big(\frac{q_T}{m_H}\Big)\Big] \,. \tag{5.19}$$

To better understand the origin of such linear power corrections, we consider the prototypical example [261, 262, 370] of imposing a minimum cut on the transverse momenta of each photon $p_{T_{1,2}} \geq p_T^{\min}$. In this case, a particularly useful parametrization for q^μ and $p_{1,2}^\mu$ is that in the hadronic COM frame,

$$q^\mu = \Big(\sqrt{m_H^2 + q_T^2}\cosh Y, q_T, 0, \sqrt{m_H^2 + q_T^2}\sinh Y\Big) \,, \tag{5.20}$$

$$p_1^\mu = p_{T_1}(\cosh\eta_1, \cos\phi, \sin\phi, \sinh\eta_1) \,, \tag{5.21}$$

$$p_2^\mu = q^\mu - p_1^\mu \,, \tag{5.22}$$

where we made use of the overall azimuthal symmetry to align the Higgs transverse momentum q_T with the x-axis. The azimuthal angle ϕ of the photon is defined as that between $\vec{q}_T$ and its transverse momentum $\vec{p}_{T_1}$, whereas η_1 denotes its rapidity. Using eq. (5.22) and the fact that the photons are on-shell, we solve for p_{T_1} and p_{T_2},

$$p_{T_1} = \frac{m_H^2/2}{\sqrt{m_H^2 + q_T^2}\cosh(Y - \eta_1) - q_T\cos\phi} \,, \tag{5.23}$$

$$p_{T_2} = \sqrt{p_{T_1}^2 + q_T^2 - 2q_T p_{T_1}\cos\phi} \,. \tag{5.24}$$

The acceptance A in eq. (5.14), with a set of theta functions encoding the case of a cut in the photon transverse momenta, is written in this frame as

$$\begin{aligned} A(q;\Theta) &= 8\pi \int \mathrm{d}\Phi_{\gamma\gamma}(q)\, \theta\big(p_{T_1}^2 - p_T^{\min 2}\big)\theta\big(p_{T_2}^2 - p_T^{\min 2}\big) \\ &= \frac{4}{\pi}\int_0^\pi \mathrm{d}\phi \int_0^\infty \mathrm{d}\Delta\eta\, \frac{p_{T_1}^2}{m_H^2}\, \theta\big(p_{T_1}^2 - p_T^{\min 2}\big)\, \theta\big(p_{T_1}^2 - p_T^{\min 2} - 2p_{T_1} q_T\cos\phi + q_T^2\big) \,, \end{aligned} \tag{5.25}$$

where we expressed the diphoton phase space in terms of the azimuthal angle ϕ and the rapidity difference $\Delta\eta = \eta_1 - Y$. Notably, the q_T dependence of A comes either from quadratic $\propto q_T^2$ or linear terms $\propto q_T\cos\phi$, and upon expanding in the small-q_T limit it would be tempting to conclude that all linear terms average out under the ϕ integral. A careful investigation though, renders this statement false since the $p_T^{\min}$ condition imposed by both θ-functions has nontrivial consequences. This can be understood by inspecting

the different domains in ϕ that each θ-function prevails. A straightforward analysis yields that for $\phi \in [0, \pi/2]$ the second θ-function in eq. (5.25) is the relevant one, whereas for $\phi \in (\pi/2, \pi]$ the opposite happens. To see this,

$$\begin{aligned} &\theta\big(p_{T_1}^2 - p_T^{\min 2}\big)\,\theta\big(p_{T_1}^2 - p_T^{\min 2} - 2q_T p_{T_1}\cos\phi\big) \times [1 + \mathcal{O}(q_T^2)] \\ &= \begin{cases} \theta\big(p_{T_1}^2 - p_T^{\min 2}\big) & \cos\phi < 0\,, \\ \theta\big(p_{T_1}^2 - p_T^{\min 2} - 2q_T p_{T_1}\cos\phi\big) & \cos\phi \geq 0\,. \end{cases} \end{aligned} \tag{5.26}$$

This observation points to the fact that linear terms no longer vanish upon ϕ integration and therefore *linear (fiducial) power corrections* emerge. Thus, we see that the presence of the fiducial cuts explicitly breaks azimuthal symmetry whereas in the inclusive case, where no restriction is imposed on the decay phase space, azimuthal symmetry is manifest. Finally note that while for this example the specific set of cuts induced no dependence on Y, in general this is not the case, e.g., when additional cuts on the rapidities of the photons are imposed.

Coming back to our discussion, it will be beneficial for what follows to define the *strict leading-power* spectrum,

$$\frac{\mathrm{d}\sigma^{(0)}}{\mathrm{d}q_T^2} = \int \mathrm{d}Y\, A(0, Y; \Theta)\, W^{(0)}(q_T, Y)\,, \tag{5.27}$$

and the *fiducial power corrections* as

$$\frac{\mathrm{d}\sigma^{\mathrm{fpc}}}{\mathrm{d}q_T^2} = \int \mathrm{d}Y \Big[A(q_T, Y; \Theta) - A(0, Y; \Theta)\Big] W^{(0)}(q_T, Y)\,. \tag{5.28}$$

The latter were analyzed in refs. [261, 262] and include all linear power corrections $\mathrm{d}\sigma^{(1)}/\mathrm{d}q_T^2$, which are absent in the inclusive spectrum. These are quite subtle, and can be further enhanced to $\mathcal{O}(q_T/p_L)$, where p_L is an effective kinematic scale set by the fiducial cuts with typically $p_L \ll m_H$. This prohibits the expansion of $A(q_T, Y; \Theta)$ even for $q_T \ll m_H$, since in the phase space region where $q_T \sim p_L$, the acceptance receives uncontrolled $\mathcal{O}(q_T/p_L) \sim \mathcal{O}(1)$ power corrections. For example, the $p_T^{\min}$ cut that we saw before sets the scale $p_L \sim m_H - 2p_{T\min}$. It is thus critical to use the *exact* q_T-dependent acceptance and take

$$\frac{\mathrm{d}\sigma^{\mathrm{sing}}}{\mathrm{d}q_T^2} = \int \mathrm{d}Y\, A(q_T, Y; \Theta)\, W^{(0)}(q_T, Y) \tag{5.29}$$

as the leading "singular" contribution at small q_T, which corresponds to the sum of eqs. (5.27) and (5.28). The remaining "nonsingular" contributions then read

$$\frac{\mathrm{d}\sigma^{\mathrm{nons}}}{\mathrm{d}q_T^2} = \int \mathrm{d}Y\, A(q_T, Y; \Theta) \Big[W^{(2)}(q_T, Y) + \cdots\Big] \tag{5.30}$$

and they are quadratically suppressed $\sim \mathcal{O}(q_T^2/m_H^2)$.

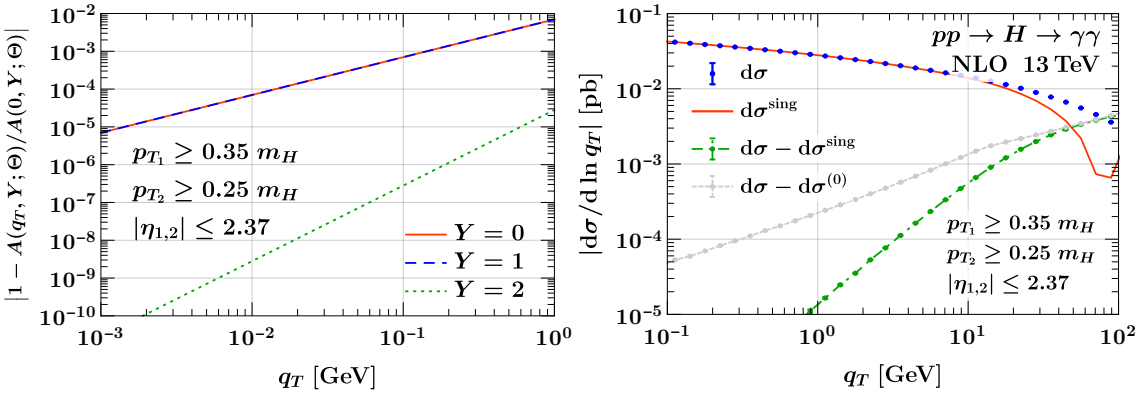

Figure 5.2: Left: Relative difference of the exact acceptance function $A(q_T, Y; \Theta)$ to its leading power approximation $A(0, Y; \Theta)$. Right: Numerical illustration of the power corrections for the Higgs transverse momentum spectrum at NLO.

In figure 5.2 we exemplify the presence of fiducial power corrections. We impose the asymmetric cuts $p_{T_1} \geq 0.35\, m_H$ and $p_{T_2} \geq 0.25\, m_H$ on the transverse momenta of the photons and a rapidity cut $|\eta_{1,2}| \leq 2.37$ using $m_H = 125\,\mathrm{GeV}$ for the Higgs mass. The left panel shows the exact acceptance relative to its LP ($q_T = 0$) approximation for various rapidity values Y. At $Y = 0$ (solid orange) and $Y = 1$ (dashed blue) the p_T-cuts dominate and result in linear power corrections to A, which can be seen from the slope of the curves. As discussed in ref. [262], the $Y = 2$ case (dotted green) is close to the edge of the fiducial region and the cut on $\eta_{1,2}$ dominates over the ones on the photon transverse momenta, resulting in quadratic power corrections to A. Turning to the right panel, we show the q_T spectrum of the Higgs in the diphoton decay channel at NLO for the same set of fiducial cuts. The blue points show the full cross section $\mathrm{d}\sigma$ whereas the solid orange line captures the singular contribution $\mathrm{d}\sigma^{\mathrm{sing}}$, which as expected dominates in the small q_T region.[1] As is clearly illustrated by the slope of the curves, the strict leading-power spectrum $\mathrm{d}\sigma^{(0)}$ receives linear and parametrically enhanced power corrections (dotted gray) compared to those received by the singular spectrum $\mathrm{d}\sigma^{\mathrm{sing}}$ that follow a quadratic trend (dashed green).

5.2.3 Resummation and nonperturbative treatment

Resummation. In order to calculate the singular spectrum, the hadronic structure function W must be expanded in the limit $q_T \ll m_H$. To do so, we work in the SCET framework [45, 58, 64, 373, 374] with rapidity renormalization [260, 263] using the exponential regulator [76], where the LP hadronic function assumes the following factorized form

[1] The full cross section $\mathrm{d}\sigma$ is obtained from `MCFM-8.0` [372] whereas the strict leading power $\mathrm{d}\sigma^{(0)}$ and the singular $\mathrm{d}\sigma^{\mathrm{sing}}$ spectrum are obtained from `SCETlib` [49]. A description of the numerical inputs is given in section 5.2.6.

in distribution space

$$W^{(0)}(q_T, Y) = \sigma_B H_{gg}^t(m_H^2, \mu) \int \mathrm{d}^2\vec{k}_a\, \mathrm{d}^2\vec{k}_b\, \mathrm{d}^2\vec{k}_s\; \delta\big(q_T^2 - |\vec{k}_a - \vec{k}_b - \vec{k}_s|^2\big) \tag{5.31}$$
$$\times\, B_g^{\mu\nu}(x_a, \vec{k}_a, \mu, \nu)\, B_{g\,\mu\nu}(x_b, \vec{k}_b, \mu, \nu)\, S_g(\vec{k}_s, \mu, \nu) \left[1 + \mathcal{O}\Big(\frac{\Lambda_{\mathrm{QCD}}^2}{m_H^2}\Big)\right],$$

with

$$x_a = \frac{m_H}{E_{\mathrm{cm}}} e^Y\,, \qquad x_b = \frac{m_H}{E_{\mathrm{cm}}} e^{-Y}\,, \qquad \sigma_B = \frac{\sqrt{2} G_F m_H^2}{576\pi E_{\mathrm{cm}}^2}\,, \tag{5.32}$$

where σ_B is the Born cross section for $gg \to H$. It is straightforward to relate $W^{(0)}$ with the expression given in eq. (4.48), by setting $Q^2 = m_H^2$ (and resolving the differential in Q^2). In our own implementation we work in the Fourier conjugate space, where the $\vec{b}_T$-space expression for $W^{(0)}$ is given in eq. (4.48), and we can immediately make use of the results of section 4.3. We stress that while working in b_T space further simplifies the resummation of $W^{(0)}$, methods to achieve resummation directly in distribution space also exist by now [144, 375].

In eq. (5.31) the hard function H_{gg}^t describes the hard interaction for producing a Higgs boson and captures the virtual corrections of the $gg \to H$ Born process. It is defined as[2]

$$H_{gg}^t(m_H^2, \mu) = \big|C_{gg}^t(m_H^2, \mu)\big|^2 \equiv \big|F_0(\rho)\alpha_s(\mu) C_t(m_t, \mu) C_{gg}(m_H^2, \mu)\big|^2\,, \tag{5.33}$$

where the hard matching coefficient $C_{gg}(m_H^2, \mu)$ corresponds to the IR finite part of the timelike gluon form factor. It is calculated by matching the gluon field strength tensors in the rEFT current eq. (5.6), onto SCET [135, 376]

$$F_{\mu\nu}^a F^{\mu\nu\,a} \mapsto m_H^2 C_{gg}(m_H, \mu) \mathcal{B}_{n_a\perp}^{\mu} \mathcal{B}_{\mu\, n_b\perp}\,, \tag{5.34}$$

where $\mathcal{B}_{n_i\perp}^{\mu}$ are n_i-collinear gluon fields. It has been calculated up to N^{3}LO in the limit $m_t \to \infty$ [377–382]. Note that here we opt for a two-step matching, where we first integrate out the top quark at the scale $\mu_t \sim m_t$, giving rise to the effective current in eq. (5.2), and subsequently we match it to SCET at the scale $\mu \sim m_H$ via eq. (5.34). In principle, this allows to sum logarithms of m_H/m_t by evolving C_t between the scales μ_t and $\mu \sim m_H$, although in the present analysis we choose not to do so and therefore we have already set $\mu_t \equiv \mu$ in eq. (5.33). As a final comment, we mention that a one-step matching is also feasible, as performed in ref. [376].

In eq. (5.31) the gluon beam functions $B_g^{\mu\nu}$ describe collinear radiation with total transverse momentum $\vec{k}_{a,b}$ and longitudinal momentum fractions $x_{a,b}$, while the soft function S_g describes soft isotropic radiation with total transverse momentum $\vec{k}_s$. They were discussed and calculated, including their dominant contributions at N^{3}LO, in sections 4.3.3 and 4.3.4 by solving their corresponding coupled RGEs in $\vec{b}_T$-space. We stress once more that for the unpolarized gluon-fusion process that we consider here, only the NNLO expressions of

[2]Note that for simplicity we suppress the m_t dependence in the arguments of H_{gg}^t and C_{gg}^t.

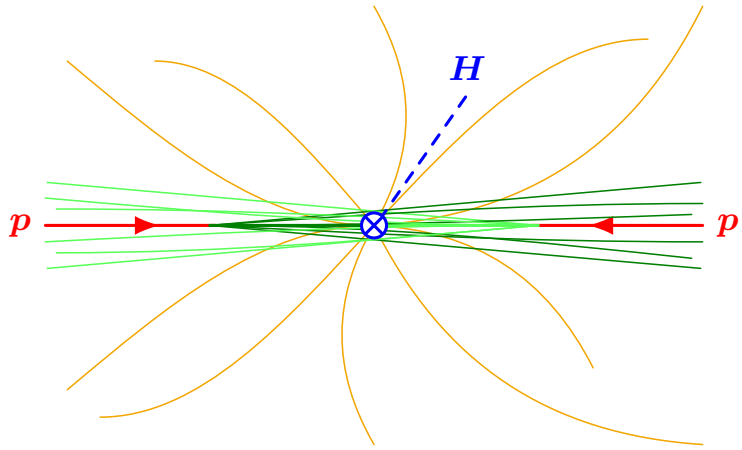

Figure 5.3: Graphical illustration of the Higgs boson production at small transverse momentum at the LHC. The collinear modes (green) and initial state protons (red) are captured by the beam functions, the soft modes (orange) are captured by the soft function and the hard virtual modes (blue vertex) are captured by the hard function.

the polarized kernels in eq. (4.78) are necessary for $W^{(0)}$ at N^{3}LO order. In figure 5.3 we show an illustration of the different modes that each function in $W^{(0)}$ captures.

As already mentioned in section 5.2.2, $W^{(0)}$ contains all the singular terms that have to be resummed to all orders in perturbation theory in order to restore the validity of the spectrum at small-q_T. Crucially, the acceptance function A does not contain large logarithms and therefore resumming $W^{(0)}$ in eq. (5.29) correctly *resums also the fiducial power corrections* to the *same order*. This was also explicitly shown for the Drell-Yan process in ref. [262]. Naturally, the resummation of $W^{(0)}$ is equivalent to that of the leading-power inclusive spectrum. An indispensable part for it is the resummation of both S_g and $B_g^{\mu\nu}$ by solving their coupled RGEs in eqs. (4.57) and (4.68), with the corresponding solutions given in eqs. (4.66) and (4.80). Analogously, for the resummation of the hard function the corresponding RGE that the Wilson coefficient C_{gg}^t satisfies must be solved. Its RGE reads

$$\mu \frac{\mathrm{d}}{\mathrm{d}\mu} C_{gg}^t(m_H^2, \mu) = \gamma_{gg}^t(m_H, \mu) C_{gg}^t(m_H^2, \mu)\,, \tag{5.35}$$

with $\gamma_{gg}^t(m_H, \mu)$ its anomalous dimension [135],

$$\gamma_{gg}^t(m_H, \mu) = 2\Gamma_{\text{cusp}}^g[\alpha_s(\mu)] \ln\Big(\frac{-\mathrm{i}m_H}{\mu}\Big) + \gamma_H^g[\alpha_s(\mu)]\,, \tag{5.36}$$

where the cusp Γ_{cusp}^g and noncusp γ_H^g anomalous dimensions are given in appendix B.1. The matching coefficient C_{gg}^t up to three loops and in our notation is given in ref. [135]. Solving eq. (5.35) we find for the hard function

$$H_{gg}^t(m_H^2, \mu) = H_{gg}^t(m_H^2, \mu_H) U_H^g(m_H, \mu_H, \mu)\,, \tag{5.37}$$

$$U_H^g(m_H,\mu_H,\mu) = \left|\exp\left[\int_{\mu_H}^{\mu}\frac{\mathrm{d}\mu'}{\mu'}\gamma_{gg}^t(m_H,\mu')\right]\right|^2 \tag{5.38}$$

$$= \left|\exp\left[-2K_\Gamma^g(\mu_H,\mu)+2\eta_\Gamma^g(\mu_H,\mu)\ln\Big(\frac{-\mathrm{i}m_H}{\mu_H}\Big)+K_{\gamma_H^g}(\mu_H,\mu)\right]\right|^2, \tag{5.39}$$

where the definitions of $K_\Gamma^g, \eta_\Gamma^g$ and $K_{\gamma_H^g}$ are given in appendix B.5.

The all-order resummation of $H_{gg}^t, B_g^{\mu\nu}$ and S_g is achieved by evaluating them at their own *canonical scale(s)* $\mu_{H,B,S}$, $\nu_{B,S}$ and subsequently evolving them to a common arbitrary point (μ,ν), where all large logarithms are resummed through the evolution kernels $\tilde{U}_{B,S}^g, U_H^g$, as given in eqs. (4.66), (4.80), and (5.38) respectively. Formally, both μ,ν scales cancel exactly in the resummed cross section, but as we saw in section 3.4, it is strongly dependent on the implementation of $\tilde{U}_{B,S}^g, U_H^g$ and there can be small residual leftover dependence in these scales. Here, we employ the unexpanded analytic evolution kernels [1] which we discussed in section 3.4.3. The canonical scales are defined by the requirement that the fixed order expansion of $H_{gg}^t, B_g^{\mu\nu}$ and S_g is free of large logarithms. For $B_g^{\mu\nu}$ and S_g the scales $\mu_{B,S}, \nu_{B,S}$ can be directly read off from the logarithmic dependence of their perturbative expansion at any nontrivial order, e.g. from eqs. (4.65), (4.77), and (4.78). Turning to the hard function, and for timelike processes such as $gg \to H$, it is well known that it contains timelike logarithms $\ln^2[(-m_H^2-\mathrm{i}0)/\mu^2]$ [383]. If the spacelike $\mu_H = m_H$ is chosen as the canonical scale of H_{gg}^t, then terms $\ln^2(-1-\mathrm{i}0) = -\pi^2$ appear, which are anything but innocuous since they give rise to large corrections in the hard function at each perturbative order. This is easily addressed by using an imaginary boundary scale $\mu_H = m_H e^{-\mathrm{i}\pi/2} \equiv -\mathrm{i}m_H$ and resumming all such π^2-terms by evolving H_{gg}^t from μ_H to $\mu_{\mathrm{FO}} = m_H$. The timelike scale choice $\mu_H = -\mathrm{i}m_H$ significantly improves the perturbative convergence in contrast to the spacelike choice $\mu_H = m_H$ [384–388]. In fact, it is advantageous to apply this timelike resummation not just to $W^{(0)}$, which contains H_{gg}^t naturally, but also to the full $W(q_T,Y)$, as demonstrated for the rapidity spectrum in ref. [135], or equivalently the nonsingular corrections [142, 147]. To do so, we take [135]

$$W(q_T,Y) = H_{gg}^t(m_H^2,\mu_{\mathrm{FO}})\left[\frac{W(q_T,Y)}{H_{gg}^t(m_H^2,\mu_{\mathrm{FO}})}\right]_{\mathrm{FO}}, \tag{5.40}$$

and analogously for $\mathrm{d}\sigma^{\mathrm{nons}}$. The ratio in square brackets is expanded to fixed order in $\alpha_s(\mu_{\mathrm{FO}})$, while $H_{gg}^t(m_H^2,\mu_{\mathrm{FO}})$ in front is evolved from $\mu_H = -\mathrm{i}m_H$ to $\mu_{\mathrm{FO}} = m_H$ at the same order as S_g and $B_g^{\mu\nu}$ in eq. (5.31). This yields substantial improvements for the spectrum up to $q_T \sim 200$ GeV, which is not unexpected, as $W^{(2)}$ will contain H_{gg}^t in parts of its factorization. Beyond $q_T \gtrsim 200$ GeV, a dynamic hard scale $\sim q_T$ becomes more appropriate and the heavy top ($m_t \to \infty$) limit breaks down, indicating that the hard interaction has become completely unrelated to the $H+0$-parton process.

Summarizing, the canonical scales in conjugate space for each function in eq. (5.31) read

$$\mu_H \sim -\mathrm{i}m_H\,, \quad \mu_B \sim b_0/b_T\,, \quad \mu_S \sim b_0/b_T\,, \tag{5.41}$$

$$\nu_B \sim m_H\,, \qquad \nu_S \sim b_0/b_T\,. \tag{5.42}$$

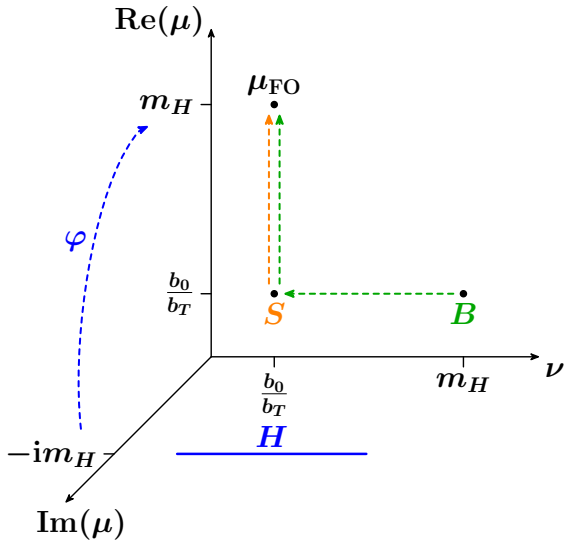

Figure 5.4: Illustration for the renormalization group evolution of the hard $H \equiv H_{gg}^{t}$, soft $S \equiv S_g$ and the beam function $B \equiv B_g^{\mu\nu}$ in the (μ, ν) space.

In figure 5.4 we show an illustration for the resummation of $W^{(0)}$ that results from the evolution of each function in the three-dimensional (μ, ν) space. We first evolve the beam functions that live at large rapidities $\nu_B \sim m_H$ down to small rapidities $\nu_S \sim b_0/b_T$ and in conjunction with the soft function, we perform a μ-evolution from the low scale $\mu_B \sim \mu_S \sim b_0/b_T$ up to $\mu_{\text{FO}} = m_H$. On the other hand, the hard function is evolved in the complex μ-plane from $\mu_H = m_H e^{-\mathrm{i}\pi/2}$ to $\mu_{\text{FO}} = m_H$, which corresponds to a rotation parametrized by the angle φ, and successfully resums all timelike logarithms.

For the phenomenological predictions of the q_T spectrum that we present in section 5.4, all necessary perturbative ingredients are known. Specifically, at N^{3}LL$'$ (N^{3}LL) we require the N^{3}LO (NNLO) boundary conditions for the hard [135–138, 212], beam and soft functions [2, 115, 119, 139, 140, 275], the 3-loop noncusp anomalous dimensions [2, 115, 119, 120, 142, 215, 389], and the 4-loop β-function [131–134] and gluon cusp anomalous dimension [121, 123–128]. At NNLL, all ingredients enter at one order lower than at N^{3}LL.

Nonperturbative treatment. An important aspect of q_T resummation is the treatment of the nonperturbative regime. At very large $b_T \gtrsim 1/\Lambda_{\text{QCD}}$ (equivalently at very small q_T) the $B_g^{\mu\nu}, S_g$ as well as the rapidity anomalous dimension $\tilde{\gamma}_\nu^g$ start to get affected by nonperturbative effects and are bound to hit the Landau pole. A plethora of prescriptions to avoid the Landau pole exist in the literature, see e.g. refs. [155, 254, 255]. In this analysis, and since the impact of nonperturbative effects is not of primary concern, we employ a simpler prescription. Following the method described in ref. [262], we perform a freeze out of both the running coupling and the PDFs by the replacement

$$\alpha_s(\mu) \mapsto \alpha_s^{\text{fr}}(\mu) \equiv \alpha_s\big[\mu_{\text{fr}}(\mu)\big]\,, \qquad f_i(\mu) \mapsto f_i^{\text{fr}}(\mu) \equiv f_i[\mu_{\text{fr}}(\mu)\big]\,, \tag{5.43}$$

with the function $\mu_{\rm fr}(\mu)$ that dictates the freeze-out defined as

$$\mu_{\rm fr}(\mu) = \begin{cases} \Lambda_{\rm fr} + \frac{\mu^2}{4\Lambda_{\rm fr}} & \mu \leq 2\Lambda_{\rm fr}\,, \\ \mu & \mu > 2\Lambda_{\rm fr}\,. \end{cases} \tag{5.44}$$

We use $\Lambda_{\rm fr} = 1\,\text{GeV}$ as our central value. Different prescriptions are equivalent up to power suppressed terms $\sim \Lambda_{\rm QCD}/q_T$, and to be on par with this choice, we furthermore neglect nonperturbative power suppressed contributions $\sim \mathcal{O}(b_T\Lambda_{\rm QCD})$ in both S_g and those resulting from the OPE matching of $B_g^{\mu\nu}$ (see eq. (4.70)).

5.2.4 Fixed-order matching and profile scales

Fixed-order matching. In the small-q_T region the full cross section $\mathrm{d}\sigma$ is given by the singular cross section $\mathrm{d}\sigma^{\rm sing}$ up to quadratic power corrections $\mathrm{d}\sigma^{\rm nons} \sim \mathcal{O}(q_T^2/m_H^2)$. Given that $\mathrm{d}\sigma^{\rm sing}$ is predicted by SCET, we incorporate the power suppressed contributions and extend the spectrum towards large values of $q_T \sim m_H$ using an additive matching

$$\mathrm{d}\sigma = \mathrm{d}\sigma^{\rm sing}(\mu_{\rm res}) + \underbrace{\left[\mathrm{d}\sigma_{\rm FO_1}(\mu_{\rm FO}) - \mathrm{d}\sigma^{\rm sing}(\mu_{\rm FO})\right]}_{\mathrm{d}\sigma^{\rm nons}}\,, \tag{5.45}$$

where the first addend is evaluated at the (schematically denoted) resummation scales $\mu_{\rm res}$, constructed according to the hybrid profile scales that we discuss in the next paragraph. The term in the square brackets corresponds to a differential subtraction term between the full cross section at fixed-order $\mathrm{d}\sigma_{\rm FO_1}$ (which amounts to a Higgs+1 parton configuration as it is evaluated for $q_T > 0$) and the singular cross section expanded at fixed-order. The result of the subtraction is what we previously defined as nonsingular cross section and it suffices to be evaluated at the scale $\mu_{\rm FO} = m_H$ since it is power suppressed. At $\mathrm{N}^n\mathrm{LO}$, or $\mathcal{O}(\alpha_s^n)$ relative to the LO Born cross section, we need the full spectrum at one order lower $\mathrm{N}^{n-1}\mathrm{LO}_1$. Therefore, we refer to the result of the fixed-order matching in eq. (5.45) as $\mathrm{N}^n\mathrm{LL}'+\mathrm{N}^n\mathrm{LO}$ when the singular cross section is resummed (together with the fiducial power corrections) at $\mathrm{N}^n\mathrm{LL}$ order including the $\mathcal{O}(\alpha_s^n)$ boundary terms, and matched to the $\mathrm{N}^{n-1}\mathrm{LO}_1$ full spectrum. The unprimed counting convention involves using the boundary terms at one order lower compared to that of the resummation. In table 5.1 we summarize the resummed and resummed + matched order counting along with the perturbative ingredients necessary for claiming certain accuracy.

Profile scales. While for $q_T \ll m_H$, the singular and nonsingular contributions can be considered separately, this separation becomes meaningless for $q_T \sim m_H$. To obtain a valid prediction there, the q_T resummation is switched off and only the timelike resummation is kept, such that singular and nonsingular terms in eq. (5.45) exactly recombine at fixed order into the full cross section. To achieve this, we use the hybrid profile scales [147, 155, 262] which enforce the correct q_T resummation for $q_T \ll m_H$ and smoothly turn it off towards $q_T \sim m_H$. The hybrid profile scales effectively induce the asymptotic behavior

$$\mu_{B,S}(q_T, b_T),\, \nu_{B,S}(q_T, b_T) \to \mu_{\rm FO} = \mathrm{i}\mu_H \quad \text{as} \quad q_T \to m_H\,. \tag{5.46}$$

Order	$\Gamma^g_{\rm cusp}$	$\gamma^g_{H,B,S}$	γ^g_ν	β	boundary terms	nonsingular
LL	1-loop	-	-	1-loop	-	-
NLL	2-loop	1-loop	1-loop	2-loop	-	-
NNLL	3-loop	2-loop	2-loop	3-loop	1-loop	-
N^{3}LL	4-loop	3-loop	3-loop	4-loop	2-loop	-
NLL′+NLO	2-loop	1-loop	1-loop	2-loop	1-loop	1-loop
NNLL+NLO	3-loop	2-loop	2-loop	3-loop	1-loop	1-loop
NNLL′+NNLO	3-loop	2-loop	2-loop	3-loop	2-loop	2-loop
N^{3}LL+NNLO	4-loop	3-loop	3-loop	4-loop	2-loop	2-loop
N^{3}LL′+ N^{3}LO	4-loop	3-loop	3-loop	4-loop	3-loop	3-loop

Table 5.1: The resummed (upper part) and resummed + matched (lower part) orders together with the necessary perturbative ingredients at each order of accuracy. $\Gamma^g_{\rm cusp}, \gamma^g_{H,B,S}$ are the gluon cusp and noncusp anomalous dimensions for the hard, beam and soft functions respectively. By γ^g_ν we denote the gluon rapidity anomalous dimensions and β is the QCD beta function. The boundary terms capture the fixed order expansion of $H^t_{gg}, B^{\mu\nu}_g, S_g$ at canonical scales and by nonsingular we denote the order for the fixed-order matching in eq. (5.45).

The choice of the boundary scales reads

$$\mathrm{i}\mu_H = \nu_B = \mu_{\rm FO} \equiv m_H\,, \qquad \mu_{B,S} = \nu_S = \mu_{\rm FO}\, f_{\rm run}\Big(\frac{q_T}{m_H}, \frac{b_0}{b_T\, m_H}\Big)\,, \tag{5.47}$$

with the hybrid profile function defined as

$$f_{\rm run}(x,y) = 1 + g_{\rm run}(x)(y-1)\,. \tag{5.48}$$

The function $f_{\rm run}(x,y)$ governs the amount by which the hard, beam and soft functions are evolved in (μ,ν) by modulating the slope of the scales in b_T-space for a specific target value of q_T/m_H through the function

$$g_{\rm run}(x) = \begin{cases} 1 & 0 < x \le x_1\,, \\ 1 - \frac{(x-x_1)^2}{(x_2-x_1)(x_3-x_1)} & x_1 < x \le x_2\,, \\ \frac{(x-x_3)^2}{(x_3-x_1)(x_3-x_2)} & x_2 < x \le x_3\,, \\ 0 & x_3 \le x\,. \end{cases} \tag{5.49}$$

For $q_T \le x_1 m_H$, resummation is fully turned on, whereas it's fully turned off for $q_T \ge x_3 m_H$. The functional form that $g_{\rm run}(x)$ assumes for the in-between range $x_1 < x \le x_3$ provides a smooth connection of the aforementioned cases as both resummation effects and the nonsingular contribution are important in this range. For our central results we use the transition points $(x_1, x_2, x_3) = (0.2, 0.5, 0.8)$, which for $m_H = 125\,\mathrm{GeV}$ translate to

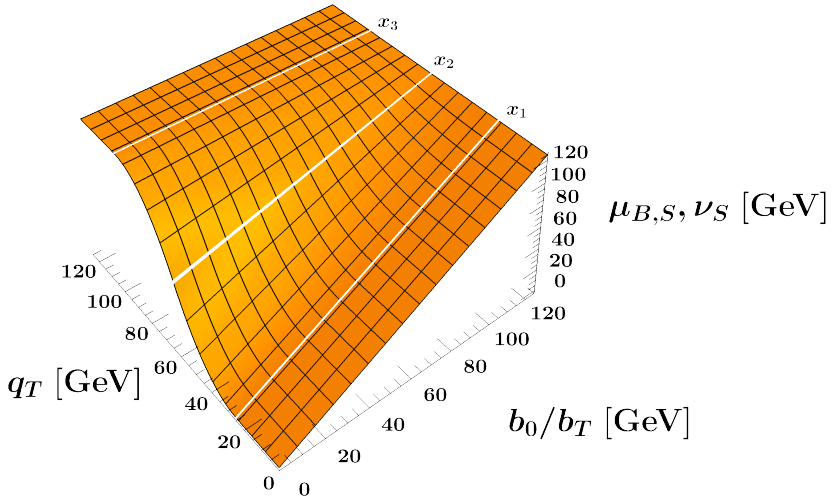

Figure 5.5: Illustration of the $(q_T, b_0/b_T)$ functional dependence for the μ_B, μ_S, ν_S profile scales in eq. (5.47). The white lines of constant q_T capture the different transition points $(x_1, x_2, x_3) = (25, 62.5, 100)\,\text{GeV}$, where $g_{\text{run}}(x)$ assumes different functional form.

$(x_1, x_2, x_3) = (25, 62.5, 100)\,\text{GeV}$. In figure 5.5 we show the hybrid profile scales μ_B, μ_S and ν_B as a function of both q_T and b_0/b_T. The white lines of constant q_T correspond to our central choice for the transition points (x_1, x_2, x_3) where $g_{\text{run}}(x)$ changes its functional form. Contrasting to the Drell-Yan case in ref. [262], turning off the resummation slightly earlier is motivated by the faster onset of the quadratic fixed-order power corrections.

5.2.5 Estimation of uncertainties

An indispensable part of every theoretical prediction is a reliable uncertainty estimation by a thorough exploration of the space of all possible scale variations. Variations of the unphysical scales provide a way to estimate missing higher-order terms in the perturbative expansion of the cross section.[3] To this end, we identify several sources of perturbative uncertainties: the fixed-order (Δ_{FO}), the q_T-resummation (Δ_{q_T}), the timelike-resummation (Δ_φ), and the matching (Δ_{match}). They are estimated via appropriate scale variations which we review in what follows, and a detailed description thereof can be found in refs. [135, 262]. For each source $X = \{\text{FO}, q_T, \varphi, \text{match}\}$, we identify the corresponding uncertainty as the maximum deviation from the central prediction that results out of all scale variations v_i that are part of X's total set of variations V_X

$$\Delta_X = \max_{\text{v}_i \in \text{V}_X} \left| \text{d}\sigma^{\text{v}_i} - \text{d}\sigma^{\text{central}} \right|, \qquad X = \{\text{FO}, q_T, \varphi, \text{match}\}\,. \tag{5.50}$$

[3] However, scale variations should be cautiously regarded as the 'true' uncertainty, since they are not able to probe new color structures that might appear at higher-order terms and/or they can be accidentally small due to, e.g., coincidentally small coefficients at a certain perturbative order.

In addition, each X is regarded as an independent source and they are added in quadrature in order to obtain the total uncertainty yield,

$$\Delta_{\rm total} = \Delta_{\rm FO} \oplus \Delta_{q_T} \oplus \Delta_{\varphi} \oplus \Delta_{\rm match} = \sqrt{\Delta^2_{\rm FO} + \Delta^2_{q_T} + \Delta^2_{\varphi} + \Delta^2_{\rm match}}\,. \tag{5.51}$$

The fixed-order uncertainty $\Delta_{\rm FO}$ is estimated from an up and down variation of the $\mu_{\rm FO}$ scale by a conventional factor of two, i.e. $\mu_{\rm FO}/2, 2\mu_{\rm FO}$.[4] Since all the resummed logarithms contain ratios of the scales in eq. (5.47), $\mu_H/\mu_B, \mu_H/\mu_S, \nu_B/\nu_S$, varying only $\mu_{\rm FO}$ effectively leaves intact all resummed logarithms while it probes the fixed order expansion of $H^t_{gg}, B^{\mu\nu}_g, S_g$ and that of the nonsingular cross section. Note that in the fixed order region $q_T \sim m_H$, this variation reduces to the usual up/down variation in the fixed-order cross section.

The q_T-resummation uncertainty Δ_{q_T} is estimated from variations of the hybrid profile scales [147]. While the ensuing variations of the resummed logarithms formally cancel against that of the boundary terms, as we saw in sections 4.3.3 and 4.3.4 for the soft and beam functions, in practice there is some residual scale dependence from the truncation of $H^t_{gg}, B^{\mu\nu}_g, S_g$ at fixed-order. Therefore, varying the hybrid profile scales provides an estimation of the resummation uncertainty Δ_{q_T}. The hybrid profile scale variations are realized via the following modifications in the scale definitions

$$\begin{aligned}
\mu_B &= \mu_{\rm FO}\left[f_{\rm vary}\Big(\frac{q_T}{m_H}\Big)\right]^{v_{\mu_B}} \; f_{\rm run}\Big(\frac{q_T}{m_H}, \frac{b_0}{b_T m_H}\Big)\,,\\
\mu_S &= \mu_{\rm FO}\left[f_{\rm vary}\Big(\frac{q_T}{m_H}\Big)\right]^{v_{\mu_S}} \; f_{\rm run}\Big(\frac{q_T}{m_H}, \frac{b_0}{b_T m_H}\Big)\,,\\
\nu_S &= \mu_{\rm FO}\left[f_{\rm vary}\Big(\frac{q_T}{m_H}\Big)\right]^{v_{\nu_S}} \; f_{\rm run}\Big(\frac{q_T}{m_H}, \frac{b_0}{b_T m_H}\Big)\,,\\
\nu_B &= \mu_{\rm FO}\left[f_{\rm vary}\Big(\frac{q_T}{m_H}\Big)\right]^{v_{\nu_B}}\,.
\end{aligned} \tag{5.52}$$

The central choice of the exponents is given by $(v_{\mu_B}, v_{\mu_S}, v_{\nu_S}, v_{\nu_B}) = (0,0,0,0)$ which is in accord with the definitions of the central scales in eq. (5.47). The variations are given for $v_i = \{-1, 0, +1\}$ and we explicitly exclude all those that result in variation by a factor larger than two in the arguments of the resummed logarithms [147]. The functional form of $f_{\rm vary}(x)$ reads

$$f_{\rm vary}(x) = \begin{cases} 2(1 - x^2/x_3^2) & 0 \le x < x_3/2\,,\\ 1 + 2(1 - x/x_3)^2 & x_3/2 \le x < x_3\,,\\ 1 & x_3 \le x\,. \end{cases} \tag{5.53}$$

[4] In practice, we only vary the renormalization scale μ_R whose dependency is carried by α_s, while we keep the factorization scale μ_F in the PDFs fixed. Varying μ_R while keeping μ_F fixed, is compensated by fixed-order logarithms of μ_R/μ_F that we have implemented in the singular cross section, alternatively these logarithms are predicted by a reexpansion of $\alpha_s(\mu_F)$ in terms of $\alpha_s(\mu_R)$, and performing this reexpansion we also obtain the full (and nonsingular) cross section at $\mu_R \neq \mu_F$ starting from available results at the central $\mu_R = \mu_F = m_H$. This variation justified since it is the μ_R dependency of the overall α_s^2 in the Born cross section that drives the 7-point variation (μ_R, μ_F), as evidenced in ref. [135]. We have explicitly checked that this holds at NLO, NNLO and N^{3}LO.

The two extreme cases correspond to either completely turning off profile scale variations in the fixed-order region $q_T \geq x_3\, m_H$, where resummation is by construction turned off, or inducing a factor of 2 variation as $q_T \to 0$. Note that independent variations of μ_H are not contained in Δ_{q_T}, as the corresponding variation of the resummed logarithms is already covered by those in eq. (5.52).

We separately probe the perturbative uncertainty associated with the resummation of timelike logarithms in the gluon form factor. To achieve so, we parameterize the hard scale as [135]

$$\mu_H = \mu_{\rm FO} \exp(-\mathrm{i}\varphi)\,, \tag{5.54}$$

and vary the phase $\varphi \in [\pi/4, 3\pi/4]$ around the central choice $\varphi = \pi/2$, which amounts to the usual factor of 2 variation since $\pi/4 \simeq \ln 2$. The resulting maximum deviation yields the timelike-resummation uncertainty Δ_φ.

In the matching that we perform via eq. (5.45), the resummation and fixed-order regions are separated via profile scales that govern the transition based on the parameters (x_1, x_2, x_3). To account for the ambiguity in the explicit choice of their values, we perform a four-point variation around the central choice

$$(x_1, x_2, x_3)_{\rm central} = (0.2, 0.5, 0.8)\,, \tag{5.55}$$

$$(x_1, x_2, x_3) \qquad = \big\{(0.3, 0.65, 1),\, (0.1, 0.35, 0.6),\, (0.3, 0.45, 0.65),\, (0.1, 0.55, 1)\big\}\,, \tag{5.56}$$

which yield the $\Delta_{\rm match}$ uncertainty of the matching procedure.

Finally, a rough uncertainty estimate for the nonperturbative prescription in eq. (5.43) can be obtained in similar fashion to the rest of the sources, by varying the freezeout model parameter around our central choice $\Lambda_{\rm fr} = 1\,\text{GeV}$. While we explicitly performed such variations we found them to be negligible compared to the rest of the sources and therefore we do not include it as part of our uncertainty estimate.

5.2.6 Computational setup

In this paragraph we summarize all the computational settings and numerical inputs relevant for the phenomenological analysis of the q_T spectrum and total cross section that we present in sections 5.4 and 5.5.

We consider the LHC at $E_{\rm cm} = 13\,\text{TeV}$ with the fiducial cuts used by the ATLAS collaboration [31, 32]

$$\begin{aligned} p_{T_1} \geq 0.35\, m_H\,, \qquad p_{T_2} \geq 0.25\, m_H\,, \\ |\eta_{1,2}| \leq 1.37 \quad \text{or} \quad 1.52 \leq |\eta_{1,2}| \leq 2.37\,. \end{aligned} \tag{5.57}$$

where $p_{T_{1,2}}, \eta_{1,2}$ are the transverse momenta and rapidities of the two photons that the Higgs boson decays. For all different perturbative orders that we present, we use both the same PDF set, PDF4LHC15 NNLO PDFs [390], and the 'iterative' solution (see section 3.3.1) of

the four-loop running[5] of $\alpha_s(\mu)$ given in appendix B.5. The input constants in our analysis are

$$m_Z = 91.1876 \text{ GeV}\,, \qquad m_t = 172.5 \text{ GeV}\,, \qquad m_H = 125 \text{ GeV}\,, \tag{5.58}$$

$$\alpha_s(m_Z) = 0.118\,, \qquad G_F = 1.1663787 \times 10^{-5} \text{ GeV}^{-2}\,. \tag{5.59}$$

The singular cross section, both inclusive and fiducial, is obtained from the C++ library `SCETlib` [49]. This includes the LP hadronic structure function $W^{(0)}(q_T, Y)$ both at fixed order and resummed (up to N^{3}LO and N^{3}LL$'$ respectively), as well as the evaluation of the acceptance function $A(q_T, Y; \Theta)$. For the latter, we follow a semi-analytical method for solving the two-body decay phase space in the Higgs rest frame, where both fiducial cuts and phase space are parametrized in terms of the Collins-Soper angles [391], for more details see ref. [262]. A crucial part of the numerical setup is a cost-optimal and precise evaluation of the N^{3}LO beam function boundary terms and the NNLO QCD splitting functions. We implement both in `SCETlib` as a series expansion based on the methods developed in sections 4.5.2 and 4.5.3. For the inverse Fourier transform in eq. (4.48), we use a double-exponential method for oscillatory integrals [392–394], while the q_T and Y integrals are performed with the help of `Cuba-4.2.1` library [395, 396]. We have explicitly checked that uncertainty resulting from all aforementioned numerical integrations is entirely negligible compared to the perturbative uncertainties presented in section 5.2.5, and thus we do not consider it.

For the fixed-order cross section at LO$_1$ and NLO$_1$, we use our own analytic implementation of $W(q_T, Y)$, which for the fiducial case we integrate against $A(q_T, Y; \Theta)$. Specifically for the NLO$_1$, we implement results from ref. [397] after performing the necessary renormalization, and which we checked against the numerical code from ref. [345]. At NNLO$_1$, we use existing results [151, 191] from `NNLOjet` [346, 350] for both the inclusive and fiducial cases.

5.3 Extraction of the nonsingular cross section

An imperative requirement in order to match to the total fixed-order cross section is the calculation of the nonsingular contribution. Elaborating on its definition in eq. (5.45), we may explicitly write it as

$$\frac{\mathrm{d}\sigma^{\text{nons}}}{\mathrm{d}q_T^2} = \frac{\mathrm{d}\sigma_{\text{FO}_1}}{\mathrm{d}q_T^2} - \frac{\mathrm{d}\sigma^{\text{sing}}}{\mathrm{d}q_T^2} = \int \mathrm{d}Y\, A(q_T, Y; \Theta)\Big[W(q_T, Y) - W^{(0)}(q_T, Y)\Big]\,. \tag{5.60}$$

Here, we give the expression for the fiducial case and it is understood that the inclusive follows trivially from setting $A(q_T, Y; 1) \equiv A_{\text{incl}} = 1$ under the rapidity integral. Although with the inputs specified in section 5.2.6, we are in possession of all the required ingredients to calculate $\mathrm{d}\sigma^{\text{nons}}$, we come across a rather common obstacle: obtaining *stable* and *precise*

[5] We have explicitly checked that numerical differences stemming from a consistent α_s running at each order are entirely negligible.

numerical data of $\mathrm{d}\sigma_{\mathrm{FO}_1}$ for $q_T \to 0$ is a quite hard endeavour, especially at higher orders in perturbation theory. A way around this issue would be to neglect the nonsingular contributions in the spectrum below some value q_T^{cut}, where q_T^{cut} is chosen based on power-counting arguments for the relevance of $\mathrm{d}\sigma^{\mathrm{nons}}$ and the target precision of the phenomenological analysis. This defines the q_T-slicing method. As we show in section 5.5 and for the present case, *dropping the nonsingular* below (some value of) q_T^{cut} *is not a viable option* since none of the aforementioned arguments are met.

Instead, we take another way of addressing this obstacle by exploiting our knowledge on the cross section's analytical structure at subleading powers. Specifically, we parametrize each coefficient of the nonsingular cross section's perturbative expansion as

$$q_T^2 \frac{\mathrm{d}\sigma^{\mathrm{nons}}}{\mathrm{d}q_T^2}\bigg|_{\mathcal{O}(\alpha_s^n)} = \frac{q_T^2}{m_H^2} \sum_{k=0}^{2n-1} \left(a_k + b_k \frac{q_T}{m_H} + c_k \frac{q_T^2}{m_H^2} + \dots \right) \ln^k \frac{q_T^2}{m_H^2}\,, \tag{5.61}$$

and perform a standard χ^2 fit to the inclusive and fiducial nonsingular data to determine the corresponding parameters $(a_k^{\mathrm{incl}}, c_k^{\mathrm{incl}}, \dots)$ and $(a_k^{\mathrm{fid}}, b_k^{\mathrm{fid}}, \dots)$. This method has been extensively used and tested for the similar needs of extracting nonsingular cross sections in the context of N-jettiness subtractions, and for a detailed description see refs. [300, 301]. Here we review the most important points of this procedure.

Two aspects of the fitting procedure necessitate caution, with the first revolving around the number of fitted parameters. While we are interested in extracting the leading quadratic power suppressed coefficients a_k, part of $\mathrm{d}\sigma^{\mathrm{nons}}$ is the whole "tower of power corrections" $\sim \mathcal{O}(q_T^{n+2}/m_H^{n+2})\,,\ n \geq 0$. Therefore, a fit that focuses on extracting just the a_k and disregards the power suppressed parameters $(b_k, c_k, \dots)$ amounts in absorbing their effect as part of a_k. Thus, it is crucial that we include $b_k, c_k, \dots$ as additional nuisance parameters that quantify the theoretical uncertainty of the fitted a_k. Note, that the relevance of the former parameters is not to be judged according to their size, but rather in comparison to the statistical uncertainties of the generated data; to put it another way, the more precise the data set is, the more nuisance parameters we are able to, and must include in the fit.

The second aspect is with respect to the effective q_T-range in which the fit is performed. Ideally, the fitting procedure should take place in the low-q_T region, but as already mentioned, this can be a difficult task to achieve due to imprecision of the data and large numerical cancellations taking place between the fixed-order and the singular cross sections. On the other hand, increasing the range towards larger q_T values implies data of better quality, but at this point we run the risk of overfitting. To avoid this, we include data towards larger q_T until the standard p-value of the fit decreases, which constitutes a clear indication that the fit starts to become biased. In order to check that the choice of the final q_T window is the appropriate one, we add an extra parameter expecting the p-value to not increase.

For the $\mathcal{O}(\alpha_s)$ (NLO) and $\mathcal{O}(\alpha_s^2)$ (NNLO) nonsingular coefficients we generate data using our own analytical implementation of $W(q_T, Y)$ (see section 5.2.6) which permits in particular to obtain the fixed-order cross section to excellent precision; notably, we are

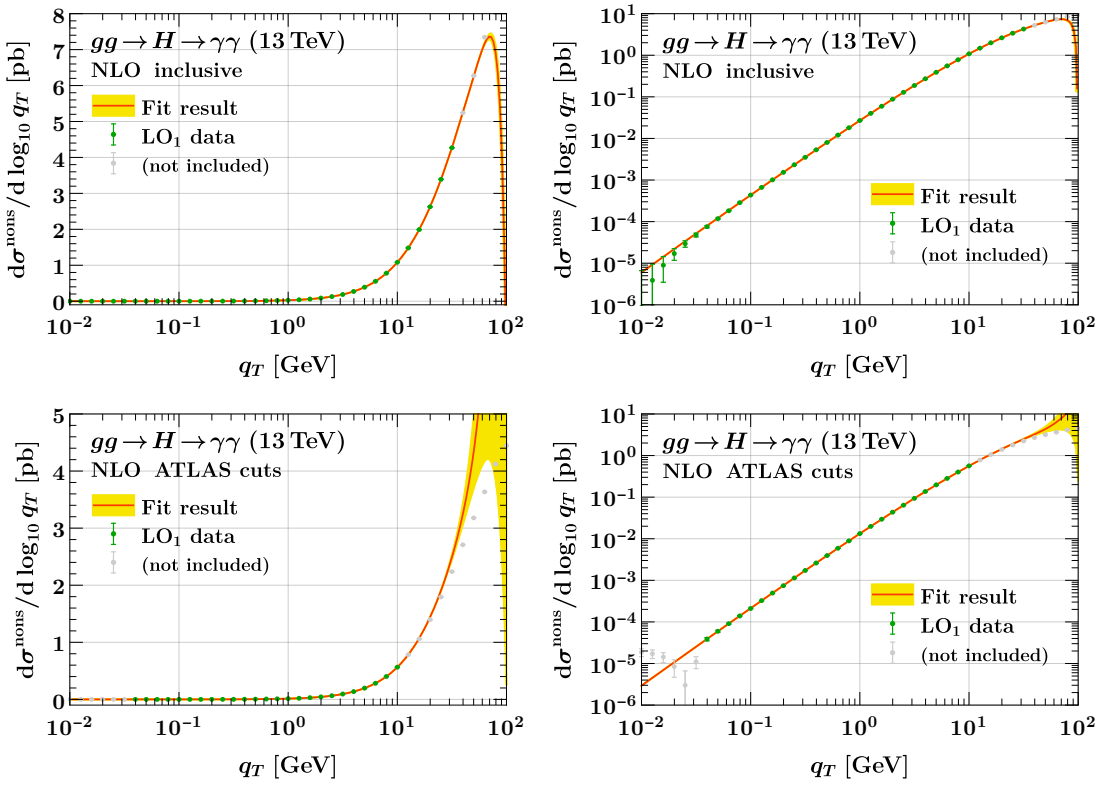

Figure 5.6: Results for the fit of the $\mathcal{O}(\alpha_s)$ (NLO) inclusive (top panel) and fiducial (bottom panel) nonsingular coefficients. Left and right columns show the same result, with the latter in absolute logarithmic scale. The dark orange line is the central value of the fit whereas the yellow band captures its resulting uncertainty. The green (gray) data points correspond to the nonsingular data that are included (excluded) in the fit along with their statistical uncertainties. The precise definition of the ATLAS fiducial cuts is given in eq. (5.57). Note that for the fiducial case, the fit-data comparison serves for illustrative purposes only since the resulting fit is subject to an additional constraint, as explained in the text.

able to reach 10^{-4} relative precision down to $q_T = 0.1\,\mathrm{GeV}$ (fiducial case). We perform a separate fit to the inclusive and fiducial data, where in the latter case all b_k^{fid} coefficients are included. Specifically for the fiducial case, we make use of the observation that not only eq. (5.60) determines the quadratic a_k^{fid}, but also the (otherwise unphysical) expression

$$q_T^2 \int \mathrm{d}Y\, A(0,Y;\Theta)\big[W(q_T,Y) - W^{(0)}(q_T,Y)\big] \equiv \frac{q_T^2}{m_H^2} \sum_{k=0}^{2n-1} \left(a_k^{\mathrm{fid}} + \tilde{c}_k^{\mathrm{fid}} \frac{q_T^2}{m_H^2} + \dots\right) \ln^k \frac{q_T^2}{m_H^2}\,, \tag{5.62}$$

which we exploit to extract the a_k^{fid}. Using the fitted values of a_k^{fid} (while taking into account their uncertainties parametrized by $\tilde{c}_k^{\mathrm{fid}}$), we extract the b_k^{fid} from eq. (5.60). As a benchmark for our fitting procedure, we correctly reproduce the $\mathcal{O}(\alpha_s)$ and $\mathcal{O}(\alpha_s^2)$ coefficients of the total inclusive cross section to better than 10^{-5} and 10^{-4} relative precision respectively.

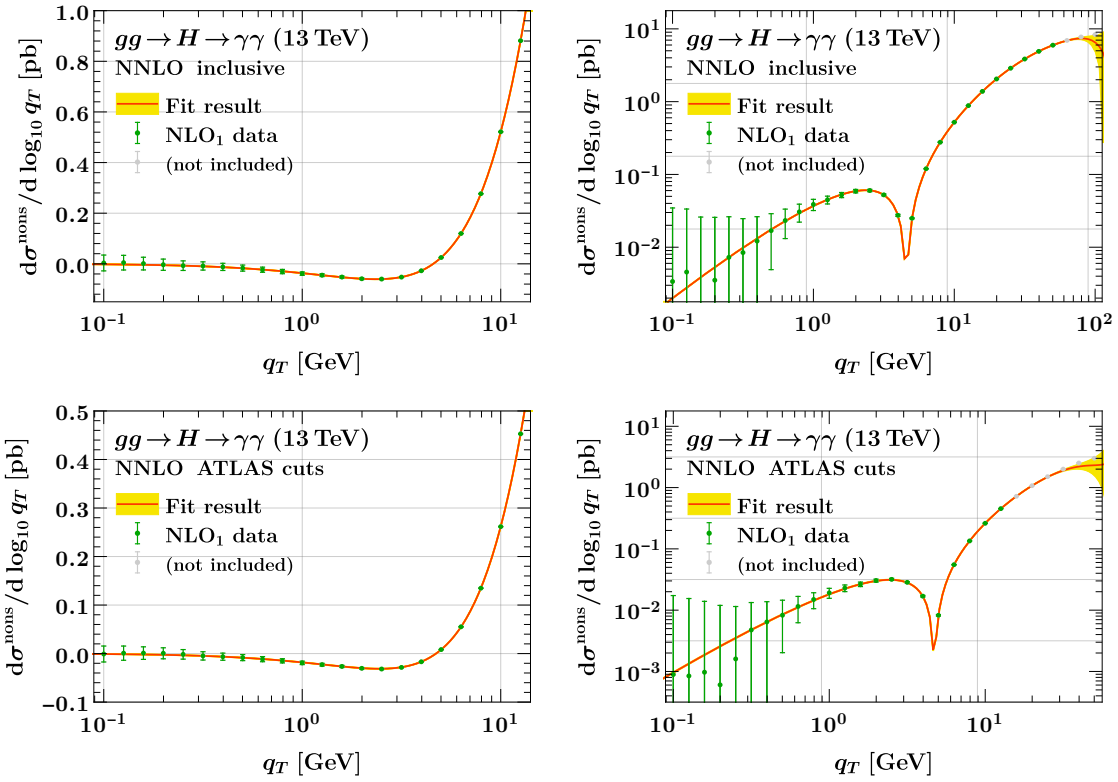

Figure 5.7: Results for the fit of the $\mathcal{O}(\alpha_s^2)$ (NNLO) inclusive (top panel) and fiducial (bottom panel) nonsingular coefficients. Left and right columns show the same result, with the latter in absolute logarithmic scale. The dark orange line is the central value of the fit whereas the yellow band captures its resulting uncertainty. The green (gray) data points correspond to the nonsingular data that are included (excluded) in the fit along with their statistical uncertainties. The precise definition of the ATLAS fiducial cuts is given in eq. (5.57). Note that for the fiducial case, the fit-data comparison serves for illustrative purposes only since the resulting fit is subject to an additional constraint, as explained in the text.

In figures 5.6 and 5.7 we show the results of our fits for the NLO and NNLO inclusive (top panel) and fiducial (bottom panel) nonsingular coefficients. Left and right columns show the same results, with the left column capturing the overall shape of the coefficient while the right column depicts it in absolute logarithmic scale and shows its magnitude towards small q_T. The orange line is the central value of the fit whereas the yellow band is the corresponding uncertainty. The nonsingular data that are included (excluded) during the fitting procedure are shown as green (gray) data points. It is clear from the excellent statistical uncertainties of the data that we are able to fit a_k^{incl} and a_k^{fid} at high precision, something that in turn results in a negligible uncertainty of the fit, which only becomes important outside its range of validity.

For the $\mathcal{O}(\alpha_s^3)$ (N^{3}LO) coefficient we use existing `NNLOjet` results [151, 191] to get nonsingular data. While these are not yet precise enough towards small q_T to give a stable fit on

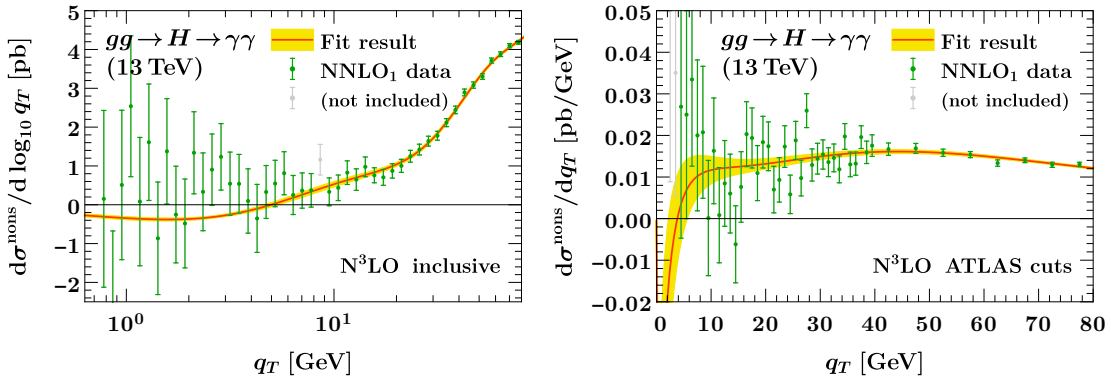

Figure 5.8: Results for the fit of the $\mathcal{O}(\alpha_s^3)$ (N^{3}LO) inclusive (left panel) and fiducial (right panel) nonsingular coefficients. The dark orange line is the central value of the fit whereas the yellow band captures its resulting uncertainty. The green (gray) data points correspond to the nonsingular data that are included (excluded) in the fit along with their statistical uncertainties. The definition of the ATLAS fiducial cuts is given in eq. (5.57). Note that the fit-data comparison serves for illustrative purposes only since both inclusive and fiducial fits are subject to further constraints, as explained in the text.

their own, we exploit that in the inclusive case, the known $\mathcal{O}(\alpha_s^3)$ coefficient of the total inclusive cross section [179, 398] provides a sufficiently strong additional constraint to obtain a reliable fit. In the fiducial case, we exploit that a_k^{incl} stem from $q_T^2 \int \mathrm{d}Y\, W^{(2)}(q_T, Y)$ whereas a_k^{fid} stem (also) from $q_T^2 \int \mathrm{d}Y\, A(0, Y; \Theta) W^{(2)}(q_T, Y)$, and thus are related since they arise from the same Y-dependent coefficient functions $W^{(2)}(q_T, Y)$ which solely governs their q_T dependence, whereas the presence/absence of the LP acceptance factor merely affects the Y integral bounds. At NLO and NNLO, we empirically find their ratios $0.4 \leq a_k^{\mathrm{fid}}/a_k^{\mathrm{incl}} \leq 0.55$. At N^{3}LO, we thus perform a simultaneous fit to inclusive and fiducial data, using 12 fiducial (all a_k^{fid} and b_k^{fid}) and 8 inclusive parameters (all six a_k^{incl} and the leading two c_k^{incl} at $\mathcal{O}(q_T^4/m_H^4)$, as the b_k^{incl} are absent in the inclusive case), with a loose 1σ constraint on the fiducial parameters $0.4\, a_k^{\mathrm{incl}} \leq a_k^{\mathrm{fid}} \leq 0.55\, a_k^{\mathrm{incl}}$ (the $b_k^{\mathrm{fid}}, \ldots$ parameters are unrelated and unconstrained). We stress that this does not amount to rescaling any part of the fiducial NNLO cross section with an inclusive N^{3}LO K factor. It merely tells the fit to only consider a_k^{fid} of roughly the right expected size. This is sufficient to break the degeneracies and yields a stable fit.

In figure 5.8 we show our results for the fit of the N^{3}LO inclusive (left panel) and fiducial (right panel) nonsingular coefficient. The dark orange line shows the central value of the fit whereas the yellow band captures its resulting uncertainty. The nonsingular data that were included (excluded) in the fitting procedure are shown as green (gray) data points along with their statistical uncertainties. At this order, the inclusion of the subleading parameters $b_k^{\mathrm{fid}}, c_k^{\mathrm{incl}}$ is crucial, since they effectively allow the extension of the fitting range to fairly large values of q_T, which results in a determination of both inclusive and fiducial a_k with a reasonable uncertainty estimate.

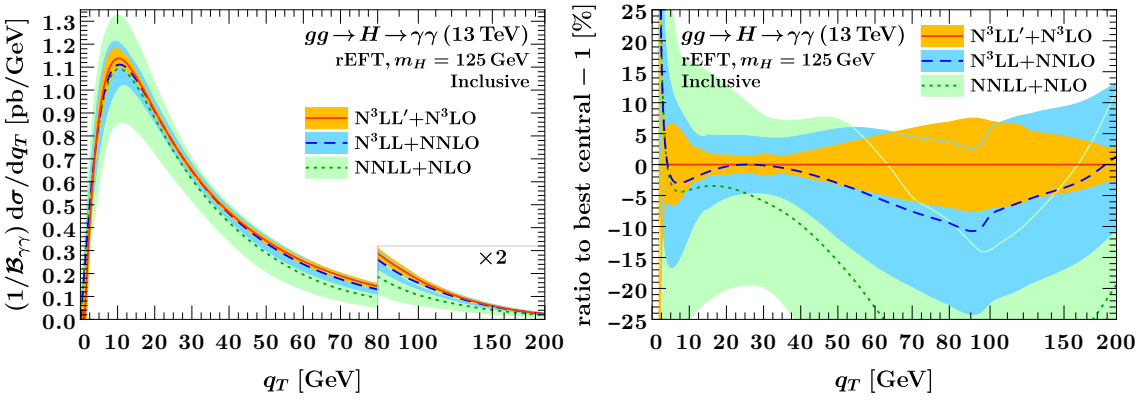

Figure 5.9: Left panel: Prediction for the Higgs inclusive transverse momentum spectrum at the LHC 13 TeV. Right panel: Percent relative error to the N^{3}LL′+N^{3}LO central prediction.

On the other hand and in comparison to NLO and NNLO, it is clear from figure 5.8 that the uncertainty of the fit can no longer be neglected. Thus, for the results in sections 5.4 and 5.5 that include the $\mathcal{O}(\alpha_s^3)$ nonsingular coefficient, we identify as an *additional source of uncertainty* that of the fit, which we denote as Δ_{nons}. Since it is unrelated to the rest of the uncertainty sources in eq. (5.51), it is added to Δ_{total} in quadrature.

5.4 Transverse momentum spectrum

In this section we present predictions for the Higgs transverse momentum spectrum in the gluon-fusion production and diphoton decay channel, $gg \to H \to \gamma\gamma$, at the LHC. In section 5.4.1 we consider the inclusive spectrum and in section 5.4.2 the fiducial one. Both cases are compared to lower orders and we inspect separately all various sources of uncertainty that impact the spectrum.

5.4.1 Inclusive spectrum

The inclusive transverse momentum spectrum is defined as that in absence of any set of fiducial cuts applied on diphoton phase space, i.e. $\Theta(\Phi_{\gamma\gamma}) \equiv 1$, such that the acceptance function in eq. (5.14) evaluates to $A(q_T, Y; 1) = A_{\text{incl}} = 1$.

In the left panel of figure 5.9 we show results at NNLL+NLO (dotted green), at N^{3}LL+NNLO (dashed blue), and for our new prediction at N^{3}LL′+N^{3}LO (solid dark orange). The bands correspond to the total uncertainty Δ_{total} at each order, as defined in eq. (5.51) and whose estimation is described in detail in section 5.2.5. Note that the N^{3}LL′+N^{3}LO prediction includes Δ_{nons} as an additional source of uncertainty that results from the fit of the nonsingular $\mathcal{O}(\alpha_s^3)$ coefficient, as described in section 5.3. In the right panel we show for the same results the relative error to the highest-order prediction. Throughout the spectrum we observe excellent perturbative convergence, especially for the central predictions at the two highest orders. Focusing on the resummation re-

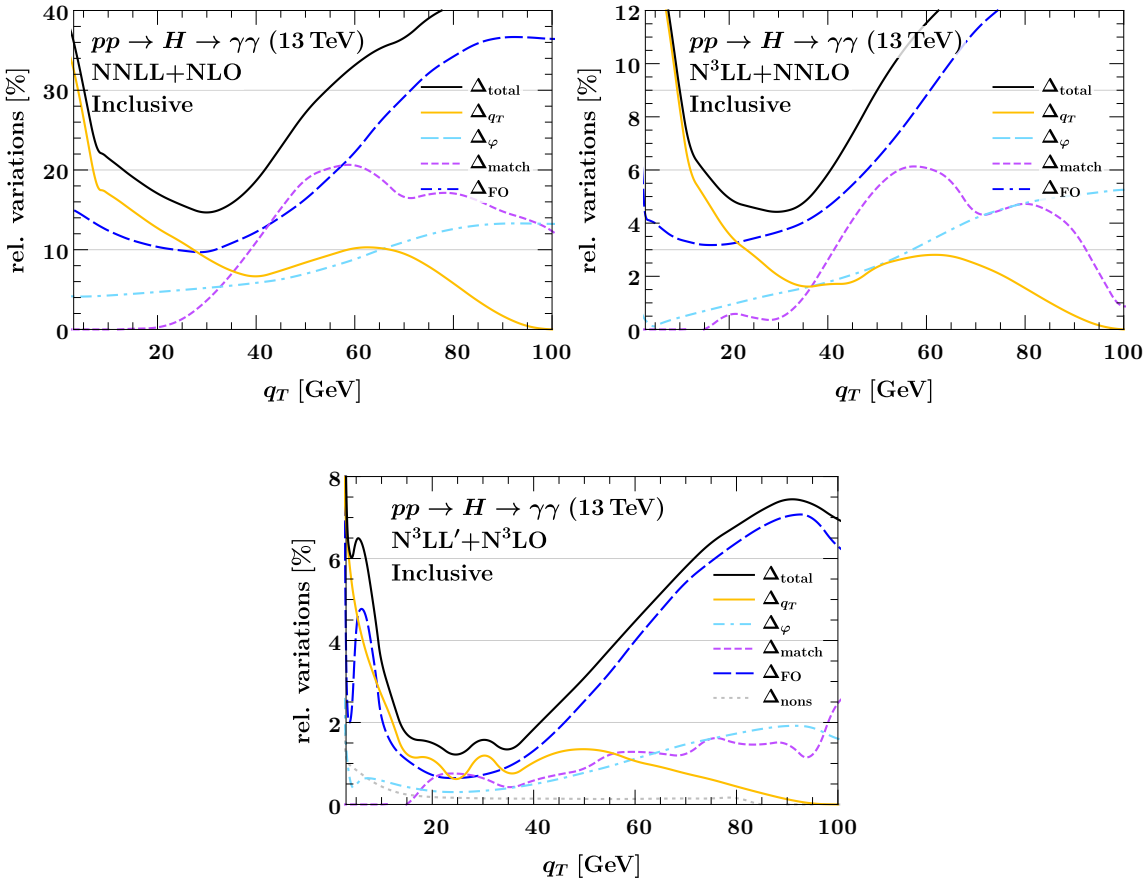

Figure 5.10: Total uncertainty decomposition for the inclusive transverse momentum spectrum in terms of the percent impact of each individual contributing source. For the two lowest orders the nonsingular fit uncertainty Δ_{nons} is found to be negligible and thus neglected.

gion ($q_T \lesssim 40\,\text{GeV}$) where the singular cross section dominates, the mild deviation of the N^{3}LL′+N^{3}LO central curve from the N^{3}LL+NNLO implies that the inclusion of the three loop boundary terms has a nontrivial impact on the spectrum. For $q_T \lesssim 2-3\,\text{GeV}$, the increase in the uncertainty bands is due to the spectrum approaching $q_T \to 0$, where the unresummed quadratic nonsingular contributions become significant. Furthermore, from both panels it is clear that the estimated uncertainties are substantially reduced at each consecutive order and remarkably, at N^{3}LL′+N^{3}LO, they are found to be below $5-7\%$.

In figure 5.10 we show for each order a complete decomposition of Δ_{total} (solid black) in terms of each individual uncertainty source that impacts the spectrum. We restrict the range up to $q_T = 100\,\text{GeV}$ since above that only the timelike Δ_{φ} (dot-dashed light blue) and the fixed-order Δ_{FO} (dashed blue) uncertainties contribute (q_T resummation is turned off there), with Δ_{FO} dominating at all three orders.[6] As expected, for $q_T \lesssim 40\,\text{GeV}$ where

[6] We remind the reader that timelike resummation is applied not only to the singular cross section, but also to the full hadronic structure function W. See section 5.2.3 for relevant discussion.

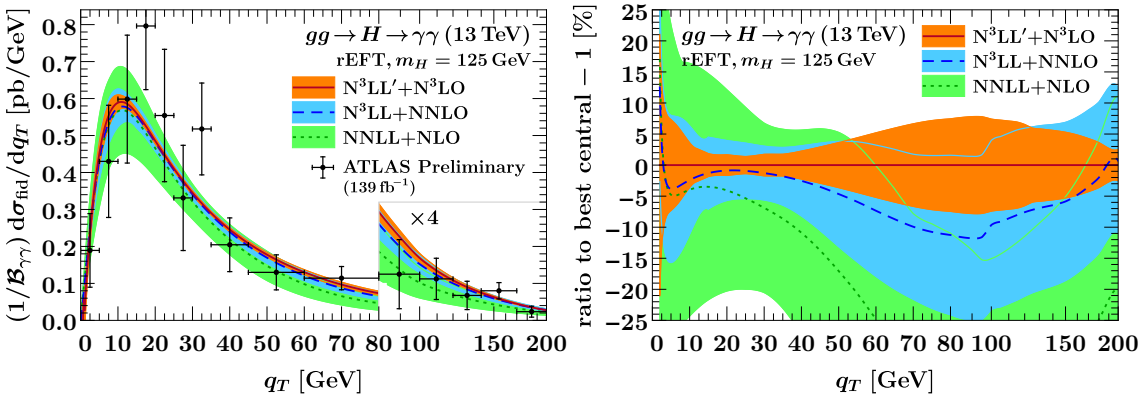

Figure 5.11: Left panel: Prediction for the Higgs fiducial transverse momentum spectrum and comparison to ATLAS 13 TeV preliminary data [32]. Right panel: Percent relative error to the N^{3}LL′+N^{3}LO central prediction.

resummation is turned on, Δ_{q_T} (solid light orange) is the most relevant source along with Δ_{FO}. While at the two lowest orders and for $q_T \lesssim 30\,\mathrm{GeV}$, Δ_{q_T} has the largest impact, at N^{3}LL′+N^{3}LO they are brought on equal footing, which illustrates the importance of the $\mathcal{O}(\alpha_s^3)$ boundary terms in the singular cross section. The fit uncertainty Δ_{nons} (dotted gray) is almost negligible ($\lesssim 0.5\%$) throughout the spectrum. As an overall impression, we comment that all sources of uncertainty have evidently decreased, especially between the two highest orders, where at N^{3}LL′+N^{3}LO we observe almost $\sim 50\%$ reduction.

5.4.2 Fiducial spectrum

The fiducial differential cross section is defined in eq. (5.16) and in contrast to the inclusive case, the q_T dependence of the acceptance function A has a nontrivial effect on the spectrum. For the comparison to ATLAS preliminary data [32] we have corrected them for the photon isolation efficiency [31], subtracted all other Higgs production processes which are denoted as XH in ref. [32], and divided out the branching ratio $\mathcal{B}_{\gamma\gamma}$.

In figure 5.11 we present results at NNLL+NLO (dotted green), at N^{3}LL+NNLO (dashed blue) and for our new prediction at N^{3}LL′+N^{3}LO (solid dark red). Their uncertainty bands represent Δ_{total} and the N^{3}LL′+N^{3}LO prediction includes Δ_{nons} as an additional source of uncertainty that stems from the fit of the nonsingular $\mathcal{O}(\alpha_s^3)$ coefficient. In the right panel we show the same results but normalized to the highest-order prediction. Overall, similar to the inclusive case, we observe excellent perturbative convergence at each successive order, evident from uncertainty bands and the central curves. The uncertainty band at N^{3}LL′+N^{3}LO corresponds to a significant improvement since it has been reduced throughout the spectrum to below $\sim 8\%$. Especially in the Sudakov region ($q_T \lesssim 30\,\mathrm{GeV}$) where the bulk of the cross section is, we notice a $\sim 40\% - 50\%$ decrease from the previous order. It is worth mentioning once more that the moderate difference in the resummation region of the central predictions between the two highest orders, points to the fact that the N^{3}LO boundary terms influence the spectrum nontrivially. Finally, the observed inflation

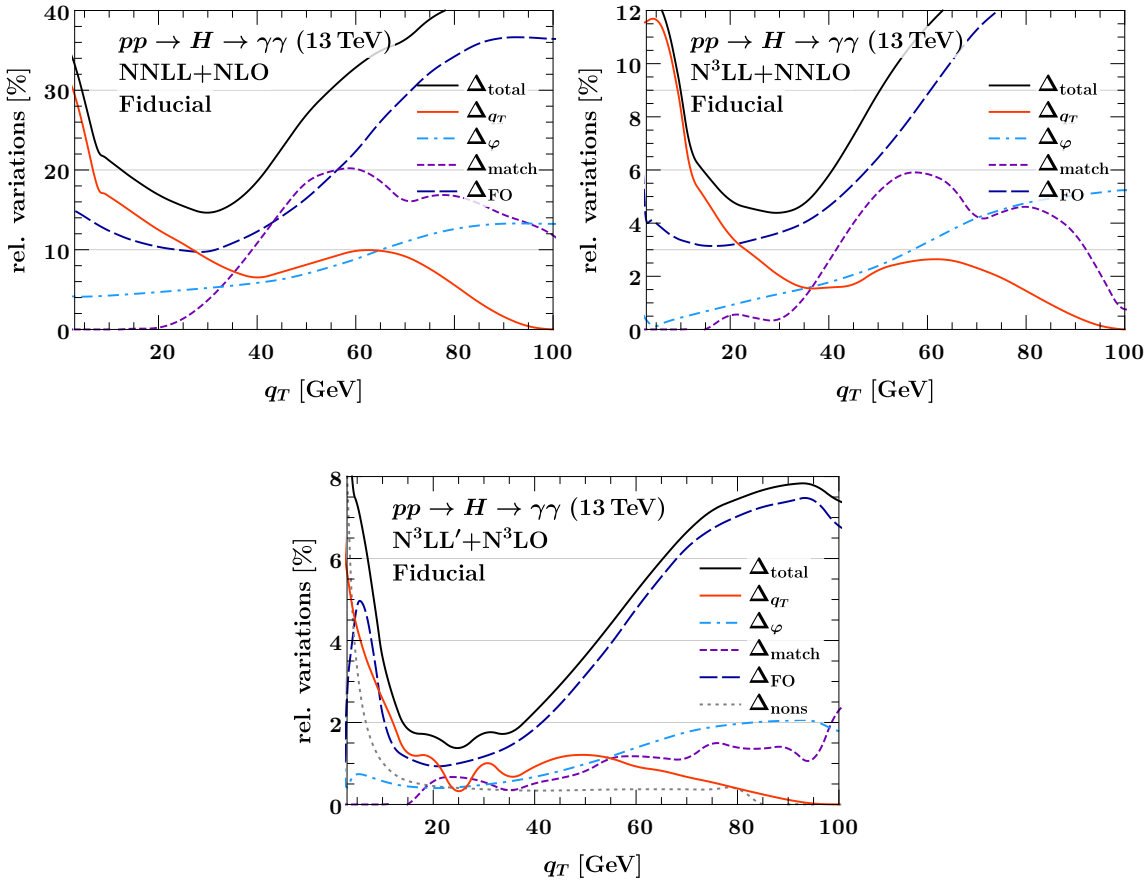

Figure 5.12: Total uncertainty decomposition for the fiducial transverse momentum spectrum in terms of the percent impact of each individual contributing source. For the two lowest orders the nonsingular fit uncertainty Δ_{nons} is found to be negligible and thus neglected.

of the uncertainties at $q_T \lesssim 2-3\,\text{GeV}$ is a direct consequence of the spectrum approaching $q_T \to 0$, where the unresummed quadratic nonsingular contributions become significant. Turning to the comparison with the ATLAS preliminary data, it is quite pleasing to notice such good agreement, both in the Sudakov peak and in the tail region. The data are well described, although the significant experimental uncertainties prohibit definite statements on whether the higher-order prediction(s) are favored over the lower order ones.

In figure 5.12 we show a breakdown of Δ_{total} (solid black) in terms of each individual uncertainty source that impacts the spectrum. As in the inclusive case, we restrict to $q_T \leq 100\,\text{GeV}$ since above that range only Δ_{FO} (dashed dark blue) and Δ_{φ} (dot-dashed blue) contribute, with the former dominating throughout. The qualitative picture is not changed compared to the inclusive case. In the resummation region $q_T \lesssim 40\,\text{GeV}$, Δ_{q_T} (solid orange) and Δ_{FO} contribute the most to Δ_{total}, whereas it is apparent that at N^{3}LL′+N^{3}LO, Δ_{q_T} is tamed with a reduced and similar impact as Δ_{FO}, something that can be attributed to the newly included $\mathcal{O}(\alpha_s^3)$ boundary terms in the singular cross section. The Δ_{nons}

(dotted gray) has a fairly small contribution ($\sim 0.5\%$) on the highest order prediction, although in comparison to the inclusive case it is marginally larger, which is expected based on the discussion in section 5.3 for the assigned uncertainty on the extraction of the nonsingular $\mathcal{O}(\alpha_s^3)$ coefficient.

5.5 Total fiducial cross section

If (and only if) the singular distributional structure of the q_T spectrum is known analytically, then the transverse momentum distribution can be integrated to obtain the total cross section $\sigma \equiv \sigma_{\rm fid}/\mathcal{B}_{\gamma\gamma}$,

$$\sigma = \int \mathrm{d}q_T \frac{\mathrm{d}\sigma}{\mathrm{d}q_T} = \sigma^{\rm sub}(q_T^{\rm off}) + \int \mathrm{d}q_T \left[\frac{\mathrm{d}\sigma}{\mathrm{d}q_T} - \frac{\mathrm{d}\sigma^{\rm sub}}{\mathrm{d}q_T}\theta(q_T \leq q_T^{\rm off})\right]. \tag{5.63}$$

This is the basis of differential q_T subtractions [198] that we discussed in section 4.4. Here, $q_T^{\rm off}$ is the range over which the differential subtractions act and it cancels exactly between all terms. The subtraction term $\mathrm{d}\sigma^{\rm sub}$ contains *at least* all the singular terms, with $\sigma^{\rm sub}(q_T^{\rm off})$ corresponding to its distributional integral over $q_T \leq q_T^{\rm off}$, while the term in brackets is numerically integrable. In practical calculations, an IR cutoff $q_T^{\rm cut}$ is introduced in eq. (5.63), which then takes the form

$$\sigma = \sigma^{\rm sub}(q_T^{\rm off}) + \int_{q_T^{\rm cut}} \mathrm{d}q_T \left[\frac{\mathrm{d}\sigma}{\mathrm{d}q_T} - \frac{\mathrm{d}\sigma^{\rm sub}}{\mathrm{d}q_T}\theta(q_T \leq q_T^{\rm off})\right] + \Delta\sigma(q_T^{\rm cut})\,, \tag{5.64}$$

with

$$\Delta\sigma(q_T^{\rm cut}) = \int^{q_T^{\rm cut}} \mathrm{d}q_T \left[\frac{\mathrm{d}\sigma}{\mathrm{d}q_T} - \frac{\mathrm{d}\sigma^{\rm sub}}{\mathrm{d}q_T}\right], \tag{5.65}$$

where it is understood that $q_T^{\rm cut} \ll q_T^{\rm off}$. Now taking $\mathrm{d}\sigma^{\rm sub} \equiv \mathrm{d}\sigma^{\rm sing}$ as given in eq. (5.29), we write eq. (5.64) as

$$\sigma = \sigma^{\rm sing}(q_T^{\rm off}) + \sigma^{\rm nons}(q_T^{\rm cut}) + \int_{q_T^{\rm cut}}^{q_T^{\rm off}} \mathrm{d}q_T \, \frac{\mathrm{d}\sigma^{\rm nons}}{\mathrm{d}q_T} + \int_{q_T^{\rm off}} \mathrm{d}q_T \, \frac{\mathrm{d}\sigma}{\mathrm{d}q_T}\,, \tag{5.66}$$

with $\mathrm{d}\sigma^{\rm nons}$ given in eq. (5.30). Eq. (5.66) is our master formula both for the evaluation of the total cross section and the discussion that follows.

We proceed and evaluate the total cross section σ by taking $q_T^{\rm cut} = 0$ in eq. (5.66), where the nonsingular cumulant identically vanishes

$$\sigma = \sigma^{\rm sing}(q_T^{\rm off}) + \int_0^{q_T^{\rm off}} \mathrm{d}q_T \, \frac{\mathrm{d}\sigma^{\rm nons}}{\mathrm{d}q_T} + \int_{q_T^{\rm off}} \mathrm{d}q_T \, \frac{\mathrm{d}\sigma}{\mathrm{d}q_T}\,. \tag{5.67}$$

A crucial point here that allows us to integrate the nonsingular cross section *explicitly down to* $q_T^{\rm cut} = 0$, is that we are in possession of its analytic form, eq. (5.61), which results from the fitting procedure of the nonsingular coefficients in section 5.3.

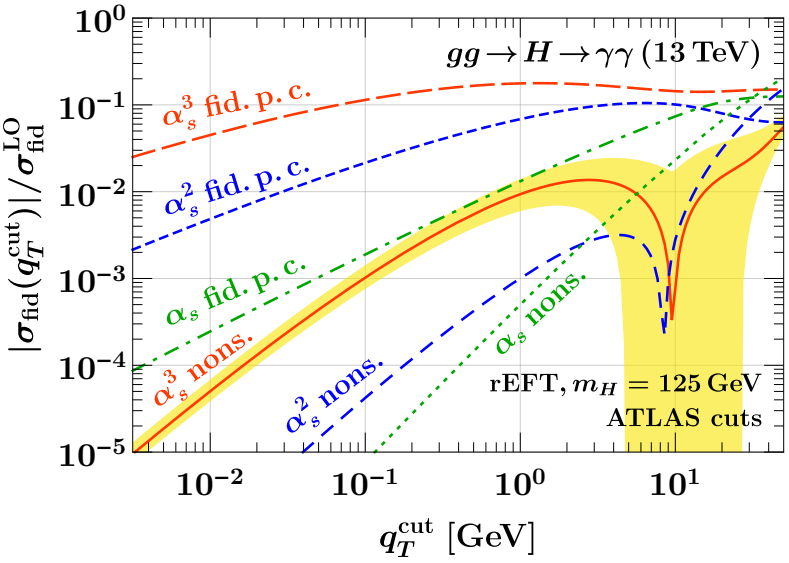

Figure 5.13: Cumulant of the fiducial and nonsingular power corrections as a function of $q_T^{\rm cut}$ and normalized to the Born fiducial cross section $\sigma_{\rm fid}^{\rm LO}$. The yellow band captures the nonsingular uncertainty $\Delta_{\rm nons}$ of the fit.

If on the other hand such analytic form of the nonsingular cross section is not available (which is usually the case), then the q_T-slicing method is employed. This amounts to setting $q_T^{\rm off} \to q_T^{\rm cut} \sim 1\,\text{GeV}$ in eq. (5.66) and simply *dropping* the nonsingular cumulant below $q_T^{\rm cut}$

$$\sigma = \sigma^{\rm sing}(q_T^{\rm cut}) + \int_{q_T^{\rm cut}} \mathrm{d}q_T \, \frac{\mathrm{d}\sigma}{\mathrm{d}q_T} + \mathcal{O}\Big(\frac{{q_T^{\rm cut}}^2}{m_H^2}\Big)\,. \tag{5.68}$$

As we discuss in section 5.2.2, the power corrections in eq. (5.68) that stem from neglecting the below $q_T^{\rm cut}$ nonsingular contribution, $\sigma^{\rm nons}(q_T^{\rm cut}) \sim \mathcal{O}({q_T^{\rm cut}}^2/m_H^2)$, follow a quadratic power law *only because* we treat the acceptance function exactly. To put it in other words, it is due to the fact that we consider as part of the singular cross section all the *linear*, cut-induced power corrections by choosing $\mathrm{d}\sigma^{\rm sub} \equiv \mathrm{d}\sigma^{\rm sing} = \mathrm{d}\sigma^{(0)} + \mathrm{d}\sigma^{\rm fpc}$. If on the other hand we took $\mathrm{d}\sigma^{\rm sub} = \mathrm{d}\sigma^{(0)}$, then the resulting power corrections in eq. (5.68) would be linearly enhanced $\sigma^{\rm fpc}(q_T^{\rm cut}) \sim \mathcal{O}(q_T^{\rm cut}/m_H)$, deteriorating severely the validity of the q_T-slicing method. This was also observed in ref. [261] and further refined in refs. [262, 370].

To better illustrate the previous arguments, in figure 5.13 we show the nonsingular (nons.) and fiducial power corrections (fid. p. c.) as a function of $q_T^{\rm cut}$, and normalized to the Born fiducial cross section $\sigma_{\rm fid}^{\rm LO}$. As expected, the nonsingular power corrections follow the correct quadratic power law in contrast to the linear enhancement that the fiducial ones are subject to. We observe that the latter contributions are huge at α_s^3 (dashed red), and even at α_s^2 (short-dashed blue) only become negligible below $q_T^{\rm cut} \lesssim 10^{-2}$ GeV. Conversely, the nonsingular power corrections are significantly better behaved and smaller even at relatively high values of $q_T^{\rm cut}$, although growing larger order by order in perturbation theory. Specifically, the α_s^3 (solid red) are about ten times larger than at α_s^2 (dashed blue), and at

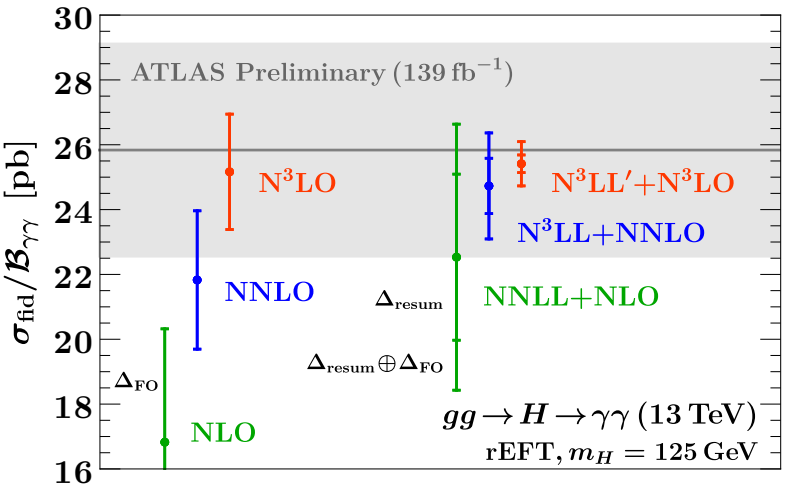

Figure 5.14: Total fiducial $gg \to H \to \gamma\gamma$ cross section at fixed N^{3}LO order and including resummation, where $\Delta_{\rm resum} \equiv \Delta_{q_T} \oplus \Delta_\varphi \oplus \Delta_{\rm match}$, compared to preliminary ATLAS measurements [32].

$q_T^{\rm cut} = 1 - 5$ GeV still contribute $5 - 10\%$ of the total α_s^3 coefficient. The underlying reason for that can be understood from the analytic form of the cross section at subleading powers in eq. (5.61). Even though *both* fiducial and nonsingular contributions are *formally* power suppressed, they do come with explicit logarithms of q_T/m_H, whose power increases at each perturbative order. This partially compensates their power suppression at higher orders in perturbation theory, rendering them numerically more and more relevant. For this reason it is imperative to *include and resum* the linearly enhanced fiducial power corrections in the subtractions. Finally, it is interesting to notice the plateau that the α_s^3 nonsingular power corrections exhibit at $q_T^{\rm cut} \sim 1 - 5\,\text{GeV}$, which upon variation of $q_T^{\rm cut}$ would give the impression of a stability for the slicing method while at the same time such a huge contribution would be neglected.

Coming back to eq. (5.67), it can be evaluated strictly at fixed order or including resummation. Aiming for a direct comparison, we proceed in both ways with our final results for the total fiducial cross section presented in figure 5.14. The results on the left correspond to the evaluation of eq. (5.67) at fixed order with the uncertainty bands resulting only from fixed-order variations ($\Delta_{\rm FO}$). The results on the right correspond to the evaluation of eq. (5.67) including both q_T and timelike resummation. The inner uncertainty band captures $\Delta_{\rm resum} \equiv \Delta_{q_T} \oplus \Delta_\varphi \oplus \Delta_{\rm match} \oplus \Delta_{\rm nons}$ and the outer band $\Delta_{\rm total} = \Delta_{\rm resum} \oplus \Delta_{\rm FO}$. The apparent poor convergence at fixed order is largely due to the fiducial power corrections. To see this,

$$\begin{aligned} \sigma_{\rm incl}^{\rm FO} &= 13.80\,[1 + 1.291 + 0.783 + 0.299]\ \text{pb}\,, \\ \sigma_{\rm fid}^{\rm FO}/\mathcal{B}_{\gamma\gamma} &= 6.928\,[1 + (1.300 + 0.129_{\rm fpc}) \\ &\qquad + (0.784 - 0.061_{\rm fpc}) \\ &\qquad + (0.331 + 0.150_{\rm fpc})]\ \text{pb}\,. \end{aligned} \tag{5.69}$$

where the successive terms denote the contributions from each order in α_s. The numbers with "fpc" subscript are the contributions of the fiducial power corrections in eq. (5.28) integrated over $q_T \leq 130$ GeV. Note that the corrections without them are almost identical to the inclusive case. It is precisely the presence of the fiducial power corrections that breaks this would-be universal acceptance effect, causing a 10% correction at NLO and NNLO and a 50% correction at N^{3}LO, while it shows no perturbative convergence.

Integrating the inclusive spectrum over q_T, all q_T logarithms and resummation effects formally have to cancel, though numerically it strongly depends on the specific implementation of resummation and matching.[7] For the fiducial power corrections on the other hand, the nontrivial q_T-dependence of the acceptance spoils this cancellation; it acts as a weight under the q_T integral and induces residual logarithmic dependence in the scale ratio p_L/m_H. This causes the large corrections in eq. (5.69), which get resummed using the resummed σ^{sing} in eq. (5.67). In light of the above, we can assert that the *fiducial q_T spectrum* is the more *fundamental quantity*, while the *total fiducial cross section* becomes a *derived quantity*.

Together with timelike resummation, this leads to the excellent convergence of the resummed results in figure 5.14, very similar to the inclusive case [135],

$$\begin{aligned}\sigma_{\text{incl}} &= 24.16\,[1 + 0.756 + 0.207 + 0.024]\ \text{pb}\,,\\ \sigma_{\text{fid}}/\mathcal{B}_{\gamma\gamma} &= 12.89\,[1 + 0.749 + 0.171 + 0.053]\ \text{pb}\,.\end{aligned} \tag{5.70}$$

At this point it should be stressed that q_T and timelike resummation are two orthogonal procedures, both necessary to restore a well behaved perturbative convergence of the cross section; q_T resummation addresses the leading and subleading power effects in the small-q_T region whereas timelike resummation remedies the timelike logarithms induced by the hard process throughout the spectrum.

To conclude, our best prediction for the Higgs fiducial cross section at N^{3}LL$'$+N^{3}LO for the cuts in eq. (5.57), reads

$$\begin{aligned}\sigma_{\text{fid}}/\mathcal{B}_{\gamma\gamma} &= (25.41 \pm 0.59_{\text{FO}} \pm 0.21_{q_T} \pm 0.17_{\varphi} \pm 0.06_{\text{match}} \pm 0.20_{\text{nons}})\ \text{pb}\\ &= (25.41 \pm 0.68_{\text{pert}})\ \text{pb}\,,\end{aligned} \tag{5.71}$$

where in the first line we explicitly give the uncertainty from each source and in the second line we add them in quadrature to obtain the total perturbative uncertainty. Multiplying by $\mathcal{B}_{\gamma\gamma} = (2.270 \pm 0.047) \times 10^{-3}$ [399–401], we find

$$\boxed{\sigma_{\text{fid}} = 57.69\,(1 \pm 2.7\%_{\text{pert}} \pm 2.1\%_{\mathcal{B}_{\gamma\gamma}} \pm 3.2\%_{\text{PDF}+\alpha_s} \pm 2\%_{\text{EW}} \pm 2\%_{t,b,c})\ \text{fb}} \tag{5.72}$$

where we also included approximations of additional uncertainties. The PDF+α_s uncertainty is taken from the inclusive case [342, 401]. For the inclusive cross section, NLO electroweak effects give a +5% correction [402], while the net effect of finite top-mass, bottom, and charm contributions is −5% (in the pole scheme we use). We can expect roughly similar acceptance corrections for both, and therefore keep the central result unchanged but include a conservative 2% uncertainty (40% of the expected correction) for each effect.

[7] In our approach we have verified explicitly that this is well satisfied.

5.6 Summary

In this chapter we performed a phenomenological study for the process $gg \to H \to \gamma\gamma$ at the LHC, providing predictions both for the inclusive and fiducial transverse momentum spectrum at N^{3}LL$'$+N^{3}LO. In addition, by integrating the fiducial q_T spectrum we obtained the total fiducial cross section at N^{3}LO, and improved by q_T and timelike resummation. Both results correspond to the highest-order predictions to date for the dominant gluon-fusion Higgs boson production channel at the LHC.

Our starting point was a review of the framework that our analysis was based on. Specifically, we presented our theoretical considerations which involved us working in NWA and in an EFT where the top quark is integrated out ($m_t \to \infty$) while the cross section is rescaled to incorporate the exact LO m_t dependence (rEFT). Furthermore, we introduced one of the central ingredients of this chapter, the acceptance function A, which incorporates all the fiducial cuts applied on the Higgs decay products.

Next, we discussed the limit $q_T \to 0$ of the transverse momentum spectrum, which we obtained by matching the rEFT onto SCET. We saw that while the inclusive spectrum receives quadratic power corrections $\sim \mathcal{O}(q_T^2/m_H^2)$, this is no longer true in the presence of fiducial cuts. In this case, linearly enhanced (fiducial) power corrections $\sim \mathcal{O}(q_T/m_H)$ appear. Their origin can be traced to the broken azimuthal symmetry of the diphoton phase space due to experimental cuts, and which emerge solely from the $q_T \to 0$ expansion of A. Crucially, said power corrections are predicted by q_T factorization and can be resummed at the same order as the LP hadronic structure function (inclusive spectrum) by keeping the exact q_T dependence on A.

Subsequently, we reviewed our resummation and fixed-order matching framework, part of which was addressing the large timelike logarithms present in the $gg \to H$ form factor via resummation of the full hadronic structure function. For the extraction of the nonsingular cross section, we exploited our knowledge of the analytic structure of the q_T spectrum at subleading powers and performed a fit of the nonsingular inclusive and fiducial data. This explicitly allowed us to obtain an analytic handle on the quadratically power suppressed (nonsingular) spectrum which proved to be instrumental for the calculation of the total fiducial cross section.

Then we presented predictions for the inclusive and fiducial q_T spectrum. In both cases we found excellent perturbative convergence with the ensuing uncertainties having significantly reduced at N^{3}LL$'$+N^{3}LO below $5-7\%$ for the inclusive and $7-8\%$ for the fiducial spectrum. For the latter, we performed a comparison to ATLAS preliminary data with evident agreement both in the peak and in the tail region.

Finally, employing differential q_T subtractions we integrated the fiducial q_T spectrum and obtained the total fiducial cross section, with our best prediction at N^{3}LL$'$+N^{3}LO. We investigated both a pure fixed-order calculation and one including resummation (q_T and timelike), where we saw a poor perturbative convergence for the former and an excellent one for the latter. This is attributed to the acceptance function whose nontrivial q_T dependence induces leftover logarithms of p_L/m_H ($p_L \approx m_H - 2p_T^{\text{cut}}$ being a kinematic scale set by

the fiducial cuts) which in turn can be resummed together with the LP hadronic structure function. Contrary to the inclusive case, this allowed us to identify the fiducial q_T spectrum as the fundamental quantity and the total fiducial cross section as a derived quantity. Finally, we explored the caveats that the slicing method entails when the nonsingular or the fiducial power corrections are neglected below q_T^{cut}. For commonly employed values of $q_T^{\text{cut}} \sim 1\,\text{GeV}$ and at $\mathcal{O}(\alpha_s^3)$, we found that dropping the nonsingular contribution can have $\sim \mathcal{O}(\%)$ effects relative to the Born cross section, whereas neglecting the fiducial power corrections would be catastrophic as they induce $\gtrsim 10\%$ effects.

Chapter 6

Conclusion and outlook

The extensive study of differential distributions lies at the core of the LHC precision frontier. They play a central role for the measurement of various SM parameters as well as in BSM searches, the effects of which might manifest only as small deviations from the SM-predicted spectra. Of fundamental importance are theoretical predictions that match the experimental precision so that even the most subtle deviations can be established. Differential cross sections of resolution variables that are sensitive to soft and collinear emissions are known to develop a distinctive perturbative structure, characterized by the presence of Sudakov double logarithms. In corners of the phase space where these logarithms grow large, the perturbative expansion is invalidated and necessitates resummation, a process that restores convergence in the singular limit.

In this thesis, working in the framework of SCET, we studied technical aspects for improving the resummation precision and accuracy and provided with higher-order phenomenological predictions relevant for the LHC. Concretely, the basic lines of research involved the extension of the resummation framework to a multi-gauge interaction environment, the study of the three-loop singular structure for two resolution variables $(q_T, \mathcal{T}_0)$, and higher-order phenomenological predictions for the Higgs boson in the gluon-fusion production channel. In the following, we provide a detailed overview and conclusions of the aforementioned research topics of this thesis.

Resummation in the presence of multiple gauge interactions. In chapter 3 we studied the technical aspects of performing higher order Sudakov resummation when multiple gauge interactions are involved. Our main focus was the numerical accuracy of various methods for the evaluation of the Sudakov evolution kernel, which constitutes a central ingredient in every resummation framework. Phenomenologically, this is of particular importance since resummation applications of immediate interest involve considering QCD together with QED/EW, where the effects of the latter are expected to be $\sim \mathcal{O}(\%)$. Therefore, it is crucial that a theoretical treatment of the Sudakov evolution kernel does not bias the expected precision of such predictions.

We embarked on our analysis focusing on a key ingredient for the evolution kernel, the solution of β-function RGE. First, we reviewed approximate analytic solutions for the running of a coupling in a single gauge interaction scenario and which are based on an iterative method. We saw, using α_s as a test case, that the method with the least amount of approximations yielded results of highest numerical accuracy. Then we moved

on to consider solutions for the β-functions of two gauge groups. Although in this case the β-functions are a set of coupled differential equations, at lowest order they decouple. This allowed us to extend the most optimal iterative method used in the single coupling case, and provide a solution for the coupled system which applies at arbitrary orders. We explicitly obtained solutions for the running of two generic couplings at three loops and exemplified their numerical robustness by considering the running of α_s, α_e in QCD⊗QED, where their difference relative to a high-precision numerical solution was at the sub-percent level.

Then we turned our attention to the possible ways of evaluating the Sudakov evolution kernel. As before, we first focused on the single gauge interaction case (pure QCD). We extensively analyzed various approximate analytic methods that are of common use in the literature and the (amount of) approximations that underlie the evolution kernel calculation. Specifically, we studied the unexpanded, expanded and reexpanded analytic methods along with our own proposal, the seminumerical. The latter method is based on a numerical treatment for the integral of the kernel while employing the approximate analytic solution for the running of the coupling, a way that addresses both precision requirements and a cost-optimal evaluation of the kernel. We compared all methods by probing their difference relative to an 'exact' (high-accuracy, fully-numerical) evaluation of the evolution factor as well as via the renormalization group consistency property (closure) that the kernels must satisfy. We found that all approximate analytic methods are prone to relative errors that can reach the percent level and above, even at high logarithmic accuracy ($\mathrm{N^3LL}$), while the seminumerical stayed at the sub-percent level.

Finally, we discussed the structure of the Sudakov kernel in generic coupled gauge environments. In this case, an approximate analytic method is not easily extendable and one would have to resolve into (further) approximations for its solution. In addition, given the high precision requirements that this case necessitates and in light of our findings in the single gauge interaction picture, we concluded that approximate analytic methods do not fit for the purpose of its evaluation. In turn, the seminumerical method provides an excellent candidate, combining both high-accuracy and reasonable computing times. We applied the seminumerical method to the NNLL Sudakov evolution kernel for the mixed QCD⊗QED scenario, where its relative difference to the 'exact' kernel did fall into our expectations of having sub-percent relative errors, even when running at the lowest scales.

Subtractions at $\mathbf{N^3LO}$. In chapter 4 we studied the singular structure of both q_T and $\mathcal{T}_0$ beam and soft functions. Specifically, by exploiting that their all-order logarithmic structure is predicted by the RGEs they satisfy, we derived the $\mathcal{O}(\alpha_s^3)$ coefficients. We then performed a numerical analysis on the newly calculated terms by inspecting the residual scale dependence that the resummed beam and soft functions exhibit, finding in (almost) all cases significant reduction at the $\mathrm{N^3LL'}$ order. These results are necessary ingredients for the resummation at $\mathrm{N^3LL'}$ and $\mathrm{N^4LL}$ orders, for q_T and $\mathcal{T}_0$ subtractions at $\mathrm{N^3LO}$ and for the extension to $\mathrm{N^3LO{+}PS}$.

In addition, we extracted the eikonal terms ($z \to 1$) for both q_T and $\mathcal{T}_0$ beam function

boundary coefficients at N^{3}LO, by relating them to soft matrix elements in different factorization limits. These correspond to genuine predictions that provided nontrivial cross checks to the authors that performed the exact calculations after our work had appeared. The derived relations hold at all orders in perturbation theory, and therefore they are a useful tool for the extraction of the eikonal terms of even higher order beam functions, once the relevant soft matrix elements are known. Notably, the knowledge of the beam function singular terms can also simplify their full calculation since it allows for their calculation at $z < 1$, reducing their degree of divergence.

Exploiting the predicted eikonal terms of the beam boundary coefficients, we constructed ansätze that are valid beyond the limit $z \to 1$ by utilizing their known analytic form at subleading powers. Since the exact kernels were made available some time after our ansätze construction, we were able to perform a direct comparison, finding in all cases very good agreement, always within the uncertainties of the latter. We are confident that our ansätze, given that they are tested at two nontrivial orders (NNLO and N^{3}LO), will be useful, providing reliable approximations for (incomplete) beam function boundary terms beyond the eikonal limit.

In the last part, we proposed a method for an improved approximation of kernels that bear a complicated dependence on HPLs and rational functions. Our motivation lies in that implementing such kernels in terms of available numerical codes does not address sufficiently the requirements for high-precision phenomenological analyses since catastrophic cancellations can occur. Our strategy is based on exploiting the analytic structure of the kernels and the Bernoulli transformations. The latter result in an increased radius of convergence, allowing for a lower truncation order compared to a plain series expansion, and therefore a low computational cost. To further stress the gains of our method, we compared results of our approach both to a plain series expansion and to an available numerical code. While in both cases the improvements of our method were evident, the latter clearly demonstrated its inadequacy for high-precision applications by exhibiting relative errors larger than an order of magnitude. Given the ubiquitous presence of HPLs and the complexity of results in higher-loop calculations, we expect that our method will provide an improved way for a precise numerical implementation.

Higgs physics. In chapter 5 we presented predictions for the Higgs transverse momentum (q_T) spectrum in the channel $gg \to H \to \gamma\gamma$ at N^{3}LL$'$+N^{3}LO at the LHC. We studied both the inclusive and the fiducial spectrum, where for the latter we saw that in the limit $q_T \to 0$, it receives linearly enhanced (fiducial) power corrections arising solely from the experimental cuts applied on the diphoton phase space. Crucially, said power corrections can be uniquely predicted by q_T factorization and resummed, together with the kinematically induced timelike logarithms, at the same order as the inclusive spectrum. For the fiducial spectrum we saw a significant improvement compared to previous orders. The excellent perturbative convergence was evident and the included $\mathcal{O}(\alpha_s^3)$ coefficients resulted in reducing the theoretical uncertainties 50% compared to the previous order (N^{3}LL+NNLO). In addition, we performed a comparison to ATLAS preliminary data where we found a very

good agreement, both in the resummation and in the tail region.

Employing differential q_T subtractions, we then integrated the fiducial q_T spectrum and predicted the total fiducial cross section at N^{3}LO order. We investigated both cases of integrating the q_T spectrum with or without resummation, and for the latter case a poor convergence was observed. This is attributed to the fiducial cuts, that impact the cross section's perturbative expansion via leftover logarithms of p_L/m_H, with $p_L \ll m_H$ a kinematic scale specific to the fiducial cuts. We addressed them by considering the fiducial power corrections as part of the leading singular cross section and resumming them. Including both q_T and timelike resummation, it lead to an excellent convergence of the fiducial cross section, with our best prediction at N^{3}LL$'$+N^{3}LO given by

$$\sigma_{\text{fid}} = 57.69\,(1 \pm 2.7\%_{\text{pert}} \pm 2.1\%_{\mathcal{B}_{\gamma\gamma}} \pm 3.2\%_{\text{PDF}+\alpha_s} \pm 2\%_{\text{EW}} \pm 2\%_{t,b,c})\ \text{fb}\,.$$

For both the q_T spectrum and the total fiducial cross section, central ingredients were the quadratically power suppressed (nonsingular) contributions. For these, a dedicated extraction took place by exploiting the known analytic form of the cross section at subleading powers, which allowed us to perform a fit for all coefficients up to $\mathcal{O}(\alpha_s^3)$. Having these at our disposal, we were able to explicitly perform differential q_T subtractions for the calculation of the total cross section and avoid the q_T-slicing method. For the latter method, we showed that at three-loop order and for commonly used values of q_T^{cut}, it can have severe effects on the precision of the results, especially if the fiducial power corrections are included at fixed order and they are not resummed.

Possible future avenues involve a more thorough uncertainty estimate of PDFs and α_s, the exploration of electroweak effects as well as finite $m_{t,b,c}$ contributions. For the latter and based on their impact on the inclusive cross section, they are expected to be nonnegligible at this order. Their inclusion however requires their proper incorporation into the resummation framework which we plan to address in the future.

With the LHC Run 2 data still to be fully explored and the upcoming HL-LHC era, a precision-driven physics program will play a central role in shedding light on the SM itself but perhaps also to the questions that it has left unanswered. This thesis constitutes part of an effort to improve theoretical precision by providing higher-order perturbative ingredients, tools and predictions for differential distributions in order to keep up with the remarkable experimental efforts.

Appendix A

Notation and conventions

A.1 General notation

Throughout this thesis we use the lightcone coordinates

$$n_a^\mu \equiv n^\mu = (1,0,0,1)\,, \qquad n_b^\mu \equiv \bar{n}^\mu = (1,0,0,-1)\,, \tag{A.1}$$

and in this basis we decompose an arbitrary four-vector p^μ as

$$p^\mu = \bar{n}\cdot p\frac{n^\mu}{2} + n\cdot p\frac{\bar{n}^\mu}{2} + p_\perp^\mu = (\bar{n}\cdot p, n\cdot p, \vec{p}_\perp) \equiv (p^-, p^+, \vec{p}_\perp)\,. \tag{A.2}$$

We denote the perturbative expansion of any function $F(\mu)$ as

$$F(\mu) = \sum_{n,m=0}^{\infty} F^{(n,m)}(\mu)\left[\frac{\alpha_s(\mu)}{4\pi}\right]^n\left[\frac{\alpha_e(\mu)}{4\pi}\right]^m. \tag{A.3}$$

and in the pure QCD case we use the abbreviated form

$$F^{(n)}(\mu) \equiv F^{(n,0)}(\mu)\,. \tag{A.4}$$

All QCD anomalous dimensions $\gamma_x^i(\alpha_s)$ and the QCD splitting functions are expanded as

$$\gamma_x^i(\alpha_s) = \sum_{n=0}^{\infty}\gamma_{x\,n}^i\left(\frac{\alpha_s}{4\pi}\right)^{n+1}, \qquad P_{ij}(z,\mu) = \sum_{n=0}^{\infty}P_{ij}^{(n)}(z)\left[\frac{\alpha_s(\mu)}{4\pi}\right]^{n+1}. \tag{A.5}$$

In QCD⊗QED the cusp and noncusp anomalous dimensions are expanded as

$$\Gamma_{\text{cusp}}^i(\alpha_s,\alpha_e) = \sum_{\substack{n,m\\ n+m\geq 1}}\Gamma_{(n,m)}^i\Big(\frac{\alpha_s}{4\pi}\Big)^n\Big(\frac{\alpha_e}{4\pi}\Big)^m, \tag{A.6}$$

$$\gamma_x^i(\alpha_s,\alpha_e) = \sum_{\substack{n,m\\ n+m\geq 1}}\gamma_{x\,(n,m)}^i\Big(\frac{\alpha_s}{4\pi}\Big)^n\Big(\frac{\alpha_e}{4\pi}\Big)^m, \tag{A.7}$$

and in the pure QCD case we use the abbreviated form

$$\Gamma_n^i \equiv \Gamma_{(n+1,0)}^i\,, \qquad \gamma_{x\,n}^i \equiv \gamma_{x\,(n+1,0)}^i\,. \tag{A.8}$$

We use the following notation to abbreviate Mellin convolutions and flavor sums

$$(I^{(m)}P^{(n)})_{ij}(z) \equiv \sum_k \int \frac{\mathrm{d}z'}{z'}\, I^{(m)}_{ik}\Big(\frac{z}{z'}\Big) P^{(n)}_{kj}(z')\,,$$
$$[\mathcal{I}(t,\mu)P^{(n)}]_{ij}(z) \equiv \sum_k \int \frac{\mathrm{d}z'}{z'}\, \mathcal{I}_{ik}\Big(t, \frac{z}{z'}, \mu\Big) P^{(n)}_{kj}(z')\,, \tag{A.9}$$

where $i,j,k \in \{g, u, \bar{u}, d, \bar{d}, s, \ldots\}$ label parton type and flavor. We also define a corresponding identity operator as

$$\mathbf{1}_{ij}(z) \equiv \delta_{ij}\,\delta(1-z) \quad \text{with} \quad (\mathbf{1}P)_{ij}(z) = P_{ij}(z)\,. \tag{A.10}$$

For Fourier-type convolutions, we use the notation

$$(FG)(k,\mu) \equiv \int \mathrm{d}k'\, F(k-k',\mu)\, G(k',\mu)\,,$$
$$\big[F\,\mathcal{I}_{ij}(z)\big](t,\mu^2) \equiv \int \mathrm{d}t'\, F(t-t',\mu^2)\, \mathcal{I}_{ij}(t',z,\mu^2)\,. \tag{A.11}$$

and the corresponding identity elements are simply $\delta(k)$ or $\delta(t)$.

Two-dimensional convolutions are defined as

$$F(\vec{q}_T,\ldots) \otimes_{\vec{q}_T} G(\vec{q}_T,\ldots) = \int \mathrm{d}^2\vec{k}_1 \int \mathrm{d}^2\vec{k}_2\; F(\vec{k}_1,\ldots)\, G(\vec{k}_2,\ldots)\, \delta^{(2)}(\vec{q}_T - \vec{k}_1 - \vec{k}_2)\,. \tag{A.12}$$

where now the identity element is $\delta^{(2)}(\vec{k}_2)$. The case of multiple convolutions corresponds to a straightforward extension,

$$F_1(\vec{q}_T,\ldots) \otimes_{\vec{q}_T} \ldots \otimes_{\vec{q}_T} F_n(\vec{q}_T,\ldots)$$
$$= \int \mathrm{d}^2\vec{k}_1 \ldots \int \mathrm{d}^2\vec{k}_n\; F_1(\vec{k}_1,\ldots)\ldots F_n(\vec{k}_n,\ldots)\, \delta^{(2)}(\vec{q}_T - \vec{k}_1 \ldots - \vec{k}_n)\,. \tag{A.13}$$

We denote logarithmic plus distributions as

$$\mathcal{L}_n(x) = \bigg[\frac{\theta(x)\ln^n x}{x}\bigg]_+ \qquad \text{with} \qquad \int_0^1 \mathrm{d}x\, \mathcal{L}_n(x) = 0\,. \tag{A.14}$$

For dimensionful arguments, we define

$$\mathcal{L}_n(k,\mu) = \frac{1}{\mu}\mathcal{L}_n\Big(\frac{k}{\mu}\Big)\,, \quad \mathcal{L}_n(t,\mu^2) = \frac{1}{\mu^2}\mathcal{L}_n\Big(\frac{t}{\mu^2}\Big)\,, \quad \mathcal{L}_n(\vec{q}_T,\mu) = \frac{1}{\pi\mu^2}\mathcal{L}_n\bigg(\frac{q_T^2}{\mu^2}\bigg)\,. \tag{A.15}$$

More details are given in appendix A.2.

A.2 Plus distributions and Fourier transforms

A.2.1 One-dimensional plus distributions

Following ref. [146], we denote plus distributions as

$$\mathcal{L}_n(x) = \bigg[\frac{\theta(x)\ln^n x}{x}\bigg]_+ = \lim_{\epsilon\to 0}\frac{\mathrm{d}}{\mathrm{d}x}\bigg[\theta(x-\epsilon)\frac{\ln^{n+1} x}{n+1}\bigg]\,,$$
$$\mathcal{L}^a(x) = \bigg[\frac{\theta(x)}{x^{1-a}}\bigg]_+ = \lim_{\epsilon\to 0}\frac{\mathrm{d}}{\mathrm{d}x}\bigg[\theta(x-\epsilon)\frac{x^a-1}{a}\bigg]\,, \tag{A.16}$$

such that

$$\mathcal{L}_n(x>0)=\frac{\ln^n x}{x}\,,\quad \mathcal{L}^a(x>0)=\frac{1}{x^{1-a}}\,,\qquad \int_0^1 \mathrm{d}x\,\mathcal{L}_n(x)=\int_0^1 \mathrm{d}x\,\mathcal{L}^a(x)=0\,. \tag{A.17}$$

For distributions with dimensionful arguments we define

$$\mathcal{L}_n(k,\mu)=\frac{1}{\mu}\mathcal{L}_n\Big(\frac{k}{\mu}\Big)\,,\qquad \mathcal{L}_n(t,\mu^2)=\frac{1}{\mu^2}\mathcal{L}_n\Big(\frac{t}{\mu^2}\Big)\,. \tag{A.18}$$

Using $\mathcal{L}^a(x)$ we further define the distribution

$$\mathcal{V}_a(x)=\frac{e^{-\gamma_E a}}{\Gamma(1+a)}\big[a\mathcal{L}^a(x)+\delta(x)\big]\,,\qquad \mathcal{V}_a(k,\mu)=\frac{1}{\mu}\mathcal{V}_a\Big(\frac{k}{\mu}\Big)\,, \tag{A.19}$$

which satisfies the group property

$$(\mathcal{V}_a\mathcal{V}_b)(k,\mu)=\int \mathrm{d}k'\,\mathcal{V}_a(k-k',\mu)\,\mathcal{V}_b(k',\mu)=\mathcal{V}_{a+b}(k,\mu)\,,\qquad \mathcal{V}_0(k,\mu)=\delta(k)\,. \tag{A.20}$$

The μ dependence of $\mathcal{V}_a(k,\mu)$ is given by

$$\mathcal{V}_a(k,\mu)=\Big(\frac{\mu'}{\mu}\Big)^a\,\mathcal{V}_a(k,\mu')\,,\qquad \mu\frac{\mathrm{d}}{\mathrm{d}\mu}\mathcal{V}_a(k,\mu)=-a\mathcal{V}_a(k,\mu)\,. \tag{A.21}$$

Expanding $\mathcal{V}_a(k,\mu)$ in powers of a we find

$$\begin{aligned}\mathcal{V}_a(k,\mu)=\delta(k)+a\,\mathcal{L}_0(k,\mu)+\frac{a^2}{2!}\big[2\mathcal{L}_1(k,\mu)-\zeta_2\delta(k)\big]\\ +\frac{a^3}{3!}\big[3\mathcal{L}_2(k,\mu)-3\zeta_2\mathcal{L}_0(k,\mu)+2\zeta_3\delta(k)\big]+\mathcal{O}(a^4)\,.\end{aligned} \tag{A.22}$$

The Fourier transformation of $\mathcal{V}_a(k,\mu)$ is given by

$$\int \mathrm{d}k\,e^{-\mathrm{i}ky}\,\mathcal{V}_a(k,\mu)=e^{-aL_y}\,,\quad \int\frac{\mathrm{d}y}{2\pi}\,e^{\mathrm{i}ky}\,e^{-aL_y}=\mathcal{V}_a(k,\mu)\,,\quad L_y=\ln(\mathrm{i}y\mu e^{\gamma_E})\,. \tag{A.23}$$

A.2.2 Two-dimensional plus distributions for $\vec{q}_T$

Following ref. [144], we define two-dimensional plus distributions in $\vec{q}_T$ as

$$\mathcal{L}_n(\vec{q}_T,\mu)=\frac{1}{\pi\mu^2}\mathcal{L}_n\left(\frac{q_T^2}{\mu^2}\right)\,, \tag{A.24}$$

where $\mathcal{L}_n(x)$ is defined as above in eq. (A.16), such that

$$\int_{|\vec{q}_T|\le\mu}\mathrm{d}^2\vec{q}_T\,\mathcal{L}_n(\vec{q}_T,\mu)=\pi\int_0^{\mu^2}\mathrm{d}q_T^2\,\frac{1}{\pi\mu^2}\mathcal{L}_n\left(\frac{q_T^2}{\mu^2}\right)=0\,. \tag{A.25}$$

The cumulant for a generic cut $|\vec{q}_T|\le q_T^{\mathrm{cut}}$ follows to be

$$\int_{|\vec{q}_T|\le q_T^{\mathrm{cut}}}\mathrm{d}^2\vec{q}_T\,\mathcal{L}_n(\vec{q}_T,\mu)=\frac{\theta(q_T^{\mathrm{cut}})}{n+1}\ln^{n+1}\frac{(q_T^{\mathrm{cut}})^2}{\mu^2}\,. \tag{A.26}$$

L_b^n	$\mathrm{FT}^{-1}[L_b^n]$
1	$\delta^{(2)}(\vec{q}_T)$
L_b	$-\mathcal{L}_0(\vec{q}_T,\mu)$
L_b^2	$+2\mathcal{L}_1(\vec{q}_T,\mu)$
L_b^3	$-3\mathcal{L}_2(\vec{q}_T,\mu)-4\zeta_3\delta^{(2)}(\vec{q}_T)$
L_b^4	$+4\mathcal{L}_3(\vec{q}_T,\mu)+16\zeta_3\mathcal{L}_0(\vec{q}_T,\mu)$
L_b^5	$-5\mathcal{L}_4(\vec{q}_T,\mu)-80\zeta_3\mathcal{L}_1(\vec{q}_T,\mu)-48\zeta_5\delta^{(2)}(\vec{q}_T)$
L_b^6	$+6\mathcal{L}_5(\vec{q}_T,\mu)+240\zeta_3\mathcal{L}_2(\vec{q}_T,\mu)+288\zeta_5\mathcal{L}_0(\vec{q}_T,\mu)+160\zeta_3^2\delta^{(2)}(\vec{q}_T)$

Table A.1: Fourier transform of $L_b^n=\ln^n(b_T^2\mu^2/b_0^2)$ to $\vec{q}_T$ space for $n\leq 6$, as given by eq. (A.27).

The Fourier transformation of $\mathcal{L}_n(\vec{q}_T,\mu)$ and its inverse are [144]

$$\int \mathrm{d}^2\vec{q}_T\, e^{-i\vec{q}_T\cdot\vec{b}_T}\mathcal{L}_n(\vec{q}_T,\mu)=\frac{1}{n+1}\sum_{k=0}^{n+1}(-1)^k\binom{n+1}{k}R_2^{(n+1-k)}L_b^k\,, \tag{A.27}$$

$$\int\frac{\mathrm{d}^2\vec{b}_T}{(2\pi)^2}\,e^{i\vec{q}_T\cdot\vec{b}_T}L_b^n=\sum_{k=0}^{n-1}(-1)^{k+1}n\binom{n-1}{k}R_2^{(n-k-1)}\mathcal{L}_k(\vec{q}_T,\mu)+R_2^{(n)}\delta^{(2)}(\vec{q}_T)\,,$$

where L_b is the usual logarithm in Fourier space

$$L_b=\ln(b_T^2\mu^2/b_0^2)\,,\qquad b_0=2e^{-\gamma_E}\,, \tag{A.28}$$

and the coefficients $R_2^{(n)}$ in eq. (A.27) are given by

$$R_2^{(n)}=\frac{\mathrm{d}^n}{\mathrm{d}a^n}\,e^{2\gamma_E a}\,\frac{\Gamma(1+a)}{\Gamma(1-a)}\bigg|_{a=0}\,. \tag{A.29}$$

For the analysis that takes place in sections 4.3 and 5.4 up to N^{3}LO, we require the Fourier transforms of L_b^n with $n\leq 6$, which are summarized in table A.1.

A.3 Mellin kernels and splitting functions in QCD

In QCD we decompose the flavor dependence of a generic Mellin-convolution kernel $K_{ij}(z)$ as

$$\begin{aligned}
K_{q_iq_j}(z)=K_{\bar{q}_i\bar{q}_j}(z)&=\delta_{ij}K_{qqV}(z)+K_{qqS}(z)+K_{qq\Delta S}(z)\,,\\
K_{q_i\bar{q}_j}(z)=K_{\bar{q}_iq_j}(z)&=\delta_{ij}K_{q\bar{q}V}(z)+K_{qqS}(z)-K_{qq\Delta S}(z)\,,\\
K_{q_ig}(z)=K_{\bar{q}_ig}(z)&=K_{qg}(z)\,,\\
K_{gg}(z)&=K_{gg}(z)\,,\\
K_{gq_i}(z)=K_{g\bar{q}_i}(z)&=K_{gq}(z)\,.
\end{aligned} \tag{A.30}$$

This decomposition is sufficient and unique to all orders by the flavor and charge symmetries of QCD. The K_{qqV} and K_{gg} contributions are already present at tree level, the K_{qg} and K_{gq} channels start at one loop, the K_{qqS} and $K_{q\bar{q}V}$ channels open up at two loops, and the $K_{qq\Delta S}$ channel only receives contributions from topologies at three loops and beyond. This decomposition also makes it straightforward to evaluate and iterate sums over intermediate partons. For example, for the convolution of two generic kernels $(KK')_{ij}(z)$, we have

$$\begin{aligned}
(KK')_{gg}(z) &= (K_{gg}K'_{gg})(z) + 2n_f(K_{gq}K'_{qg})(z)\,,\\
(KK')_{qg}(z) &= \big[\big(K_{qqV} + K_{q\bar{q}V} + 2n_f K_{qqS}\big)K'_{qg}\big](z) + (K_{qg}\,K'_{gg})(z)\,,\\
(KK')_{gq}(z) &= \big[K_{gq}\big(K'_{qqV} + K'_{q\bar{q}V} + 2n_f K'_{qqS}\big)\big](z) + (K_{gg}\,K'_{gq})(z)\,,\\
(KK')_{qqV}(z) &= (K_{qqV}K'_{qqV})(z) + (K_{q\bar{q}V}K'_{q\bar{q}V})(z)\,,\\
(KK')_{q\bar{q}V}(z) &= (K_{qqV}K'_{q\bar{q}V})(z) + (K_{q\bar{q}V}K'_{qqV})(z)\,,\\
(KK')_{qqS}(z) &= \big[K_{qqS}\big(K'_{qqV} + K'_{q\bar{q}V}\big)\big](z) + \big[\big(K_{qqV} + K_{q\bar{q}V}\big)K'_{qqS}\big](z)\\
&\quad + 2n_f\big(K_{qqS}\,K'_{qqS}\big)(z) + \big(K_{qg}\,K'_{gq}\big)(z)\,,\\
(KK')_{qq\Delta S}(z) &= \big[K_{qq\Delta S}(K'_{qqV} - K'_{q\bar{q}V})\big](z) + \big[(K_{qqV} - K_{q\bar{q}V})K'_{qq\Delta S}\big](z)\\
&\quad + 2n_f\big(K_{qq\Delta S}K'_{qq\Delta S}\big)(z)\,,
\end{aligned} \tag{A.31}$$

where n_f is the number of active flavors, and the outer brackets on the right-hand side indicate Mellin convolutions *without* flavor sums.

The DGLAP splitting functions are defined as the anomalous dimension of the PDFs,

$$\mu\frac{\mathrm{d}}{\mathrm{d}\mu}f_i(x,\mu) = 2\sum_j \int\frac{\mathrm{d}z}{z}\,P_{ij}(z,\mu)\,f_j\Big(\frac{x}{z},\mu\Big)\,. \tag{A.32}$$

We perturbatively expand them in powers of $\alpha_s/4\pi$, see eq. (A.5), and decompose their flavor dependence as in eq. (A.30). The DGLAP kernels have been calculated at three loops in refs. [128, 129]. Denoting the results of refs. [128, 129] by a calligraphic $\mathcal{P}$ to distinguish them from our $P_{ij}^{(n)}$, we can relate the two notations by

$$\begin{aligned}
P^{(n)}_{qqV}(z) &= \frac{1}{2}\Big[\mathcal{P}^{(n)+}_{ns}(z) + \mathcal{P}^{(n)-}_{ns}(z)\Big]\,, & P^{(n)}_{gg}(z) &= \mathcal{P}^{(n)}_{gg}(z)\,,\\
P^{(n)}_{q\bar{q}V}(z) &= \frac{1}{2}\Big[\mathcal{P}^{(n)+}_{ns}(z) - \mathcal{P}^{(n)-}_{ns}(z)\Big]\,, & P^{(n)}_{gq}(z) &= \mathcal{P}^{(n)}_{gq}(z)\,,\\
P^{(n)}_{qqS}(z) &= \frac{1}{2n_f}\mathcal{P}^{(n)}_{ps}(z)\,, & P^{(n)}_{qg}(z) &= \frac{1}{2n_f}\mathcal{P}^{(n)}_{qg}(z)\,,\\
P^{(n)}_{qq\Delta S}(z) &= \frac{1}{2n_f}\mathcal{P}^{(n)s}_{ns}(z)\,.
\end{aligned} \tag{A.33}$$

Appendix B

Perturbative ingredients

In this section we collect all relevant perturbative ingredients that were used in chapters 3, 4, and 5. For clarity, we use wherever it is relevant both the usual notation found in much of the QCD and SCET literature, as well as the two-dimensional notation that we introduced in chapter 3 (see also appendix A.1).

B.1 QCD ingredients

We expand the QCD β-function according to eq. (3.67) (see eq. (3.77) for the two-dimensional notation). The coefficients in the $\overline{\text{MS}}$ scheme up to 4 loops read [131–134]

$$\begin{aligned}
\beta_0 &\equiv \beta^s_{00} = \frac{11}{3}\,C_A - \frac{4}{3}\,T_F\,n_f\,,\\
\beta_1 &\equiv \beta^s_{10} = \frac{34}{3}\,C_A^2 - 2T_F\,n_f\Big(\frac{10}{3}\,C_A + 2C_F\Big)\,,\\
\beta_2 &\equiv \beta^s_{20} = \frac{2857}{54}C_A^3 + 2T_F\,n_f\Big(-\frac{1415}{54}C_A^2 - \frac{205}{18}C_F C_A + C_F^2\Big) + 4T_F^2\,n_f^2\Big(\frac{79}{54}C_A + \frac{11}{9}C_F\Big)\,,\\
\beta_3 &\equiv \beta^s_{30} = \Big(\frac{149753}{6} + 3564\zeta_3\Big) - \Big(\frac{1078361}{162} + \frac{6508}{27}\zeta_3\Big)n_f + \Big(\frac{50065}{162} + \frac{6472}{81}\zeta_3\Big)n_f^2 + \frac{1093}{729}n_f^3.
\end{aligned} \tag{B.1}$$

where for a more compact result we specified $N_c = 3$ for the four-loop coefficient β_3.

The $\overline{\text{MS}}$ cusp anomalous dimension coefficients up to three loops are [121, 128, 129]

$$\begin{aligned}
\Gamma^i_0 &\equiv \Gamma^i_{(1,0)} = 4C_i\,,\\
\Gamma^i_1 &\equiv \Gamma^i_{(2,0)} = 4C_i\bigg[C_A\Big(\frac{67}{9} - \frac{\pi^2}{3}\Big) - \frac{20}{9}\,T_F\,n_f\bigg]\,,\\
\Gamma^i_2 &\equiv \Gamma^i_{(3,0)} = 4C_i\bigg\{C_A^2\Big(\frac{245}{6} - \frac{134\pi^2}{27} + \frac{11\pi^4}{45} + \frac{22\zeta_3}{3}\Big)\\
&\qquad + 2T_F\,n_f\bigg[C_A\Big(-\frac{209}{27} + \frac{20\pi^2}{27} - \frac{28\zeta_3}{3}\Big) + C_F\Big(-\frac{55}{6} + 8\zeta_3\Big)\bigg] - \frac{16}{27}\,T_F^2\,n_f^2\bigg\}.
\end{aligned} \tag{B.2}$$

where $C_i = C_F$ for $i = q$ and $C_i = C_A$ for $i = g$. The four-loop coefficient entering at N^{3}LL has become available during recent years, see e.g. refs. [123–125, 130, 403, 404]. In chapter 3 we use the numerical result for $N_c = 3$ and $n_f = 5$ obtained from ref. [125],

$$\Gamma^q_3 \equiv \Gamma^q_{(4,0)} = 104.93\,C_F\,, \tag{B.3}$$

whereas in chapters 4 and 5 we use the exact Γ^i_3 given in ref. [404].

The $\overline{\text{MS}}$ quark and gluon noncusp anomalous dimension coefficients for the hard function are known up to three loops [116, 209–212, 214, 215, 379, 405, 406]. For the quark read

$$\begin{aligned}
\gamma^q_{H\,0} &\equiv \gamma^q_{H\,(1,0)} = -6C_F\,,\\
\gamma^q_{H\,1} &\equiv \gamma^q_{H\,(2,0)} = -2C_F\Big[C_A\Big(\frac{41}{9}-26\zeta_3\Big)+C_F\Big(\frac{3}{2}-2\pi^2+24\zeta_3\Big)+\beta_0\Big(\frac{65}{18}+\frac{\pi^2}{2}\Big)\Big]\,,\\
\gamma^q_{H\,2} &\equiv \gamma^q_{H\,(3,0)} = -2C_F\Big[C_A^2\Big(\frac{66167}{324}-\frac{686\pi^2}{81}-\frac{302\pi^4}{135}-\frac{782\zeta_3}{9}+\frac{44\pi^2\zeta_3}{9}+136\zeta_5\Big)\\
&\qquad + C_FC_A\Big(\frac{151}{4}-\frac{205\pi^2}{9}-\frac{247\pi^4}{135}+\frac{844\zeta_3}{3}+\frac{8\pi^2\zeta_3}{3}+120\zeta_5\Big)\\
&\qquad + C_F^2\Big(\frac{29}{2}+3\pi^2+\frac{8\pi^4}{5}+68\zeta_3-\frac{16\pi^2\zeta_3}{3}-240\zeta_5\Big)\\
&\qquad + C_A\beta_0\Big(-\frac{10781}{108}+\frac{446\pi^2}{81}+\frac{449\pi^4}{270}-\frac{1166\zeta_3}{9}\Big)\\
&\qquad + \beta_1\Big(\frac{2953}{108}-\frac{13\pi^2}{18}-\frac{7\pi^4}{27}+\frac{128\zeta_3}{9}\Big)+\beta_0^2\Big(-\frac{2417}{324}+\frac{5\pi^2}{6}+\frac{2\zeta_3}{3}\Big)\Big]\,.
\end{aligned}\tag{B.4}$$

and the corresponding ones for the gluon are

$$\begin{aligned}
\gamma^g_{H\,0} &= -2\beta_0\,,\\
\gamma^g_{H\,1} &= 2C_A\Big[C_A\Big(-\frac{59}{9}+2\zeta_3\Big)+\beta_0\Big(-\frac{19}{9}+\frac{\pi^2}{6}\Big)\Big]-2\beta_1\,,\\
\gamma^g_{H\,2} &= C_A\Big[C_A^2\Big(-\frac{60875}{162}+\frac{634\pi^2}{81}+\frac{8\pi^4}{5}+\frac{1972\zeta_3}{9}-\frac{40\pi^2\zeta_3}{9}-32\zeta_5\Big)\\
&\qquad + C_A\beta_0\Big(\frac{7649}{54}+\frac{134\pi^2}{81}-\frac{61\pi^4}{45}-\frac{500\zeta_3}{9}\Big)+\beta_0^2\Big(\frac{466}{81}+\frac{5\pi^2}{9}-\frac{28\zeta_3}{3}\Big)\\
&\qquad + \beta_1\Big(-\frac{1819}{54}+\frac{\pi^2}{3}+\frac{4\pi^4}{45}+\frac{152\zeta_3}{9}\Big)\Big]-2\beta_2\,.
\end{aligned}\tag{B.5}$$

B.2 QED and mixed QCD⊗QED ingredients

Here we collect various pure QED and mixed QCD⊗QED perturbative ingredients, part of which enter in the numerical results in sections 3.3.2 and 3.5.

We expand the coupled β-functions for α_s and α_e according to eq. (3.77). The mixed QCD β-function coefficients to three loops are

$$\begin{aligned}
\beta^s_{01} &= -4T_F\,\overline{Q^2}\,,\\
\beta^s_{02} &= \frac{44}{9}\,T_F\,\overline{Q^2}\big(N_c\,\overline{Q^2}+n_\ell\,Q_\ell^2\big)+2T_F\,\overline{Q^4}\,,\\
\beta^s_{11} &= (4C_F-8C_A)\,T_F\,\overline{Q^2}\,,
\end{aligned}\tag{B.6}$$

while the pure and mixed QED β-function coefficients up to three loops are

$$\begin{aligned}
\beta^e_{00} &= \frac{4}{3}\big(N_c\,\overline{Q^2} + n_\ell\,Q_\ell^2\big)\,,\\
\beta^e_{10} &= 4\big(N_c\,\overline{Q^4} + n_\ell\,Q_\ell^4\big)\,,\\
\beta^e_{20} &= -\frac{44}{9}\big(N_c\,\overline{Q^4} + n_\ell\,Q_\ell^4\big)\big(N_c\,\overline{Q^2} + n_\ell\,Q_\ell^2\big) - 2\big(N_c\,\overline{Q^6} + n_\ell\,Q_\ell^6\big)\,,
\end{aligned} \tag{B.7}$$

$$\begin{aligned}
\beta^e_{01} &= 4C_F\,N_c\,\overline{Q^2}\,,\\
\beta^e_{02} &= \Big(\frac{133}{18}C_A - C_F\Big)2C_F\,N_c\,\overline{Q^2} - \frac{44}{9}\,C_F\,T_F\,n_f\,N_c\,\overline{Q^2}\,,\\
\beta^e_{11} &= -4\,C_F\,N_c\,\overline{Q^4}\,.
\end{aligned} \tag{B.8}$$

Here we defined

$$\overline{Q^n} = \sum_q Q_q^n\,, \tag{B.9}$$

where the sum runs over the active quark flavors with $Q_{u,c} = 2/3$ and $Q_{d,s,b} = -1/3$ the quark charges, $N_c = 3$ the number of colors, $Q_\ell = -1$ the lepton charge, and $n_\ell = 3$ the number of charged leptons. The extraction of the three-loop mixed coefficients is discussed in appendix C.

The QED coefficients for the cusp anomalous dimension are obtained straightforwardly by taking the abelian QED limit of eq. (B.2) following the abelianization procedure in ref. [108],

$$\begin{aligned}
\Gamma^q_{(0,1)} &= 4Q_q^2\,,\\
\Gamma^q_{(0,2)} &= 4Q_q^2\Big[-\frac{20}{9}\big(N_c\,\overline{Q^2} + n_\ell\,Q_\ell^2\big)\Big]\,,\\
\Gamma^q_{(0,3)} &= 4Q_q^2\bigg[Q_q^2\big(N_c\,\overline{Q^2} + n_\ell\,Q_\ell^2\big)\Big(-\frac{55}{3} + 16\zeta_3\Big) - \frac{16}{27}\big(N_c\,\overline{Q^2} + n_\ell\,Q_\ell^2\big)^2\bigg]\,.
\end{aligned} \tag{B.10}$$

Up to three loops, the mixed coefficients vanish, as was noted in ref. [83],

$$\Gamma^q_{(1,1)} = \Gamma^q_{(1,2)} = \Gamma^q_{(2,1)} = 0\,. \tag{B.11}$$

A nonzero mixed contribution is expected to first appear at four loops.

The quark noncusp anomalous dimension for the hard function are

$$\begin{aligned}
\gamma^q_{H\,(0,1)} &= -6Q_q^2\,,\\
\gamma^q_{H\,(0,2)} &= Q_q^2\bigg[Q_q^2(-3 + 24\zeta_2 - 48\zeta_3) - 2\beta^e_{00}\Big(\frac{65}{18} + 3\zeta_2\Big)\bigg]\,,\\
\gamma^q_{H(1,1)} &= -2Q_q^2\,C_F\,(3 - 24\zeta_2 + 48\zeta_3)\,.
\end{aligned} \tag{B.12}$$

For completeness, we also give all relevant ingredients for the QCD⊗QED q_T resummation at NNLL for the process $q\bar{q} \to ZX$, where only ISR QED effects are considered. The

quark noncusp anomalous dimension for the q_T beam function are

$$\begin{aligned}
\tilde{\gamma}^q_{B(0,1)} &= 6Q_q^2\,,\\
\tilde{\gamma}^q_{B(0,2)} &= Q_q^2\big[Q_q^2(3-24\zeta_2+48\zeta_3)+\beta^e_{00}(1+8\zeta_2)\big]\,,\\
\tilde{\gamma}^q_{B(1,1)} &= 2Q_q^2C_F(3-24\zeta_2+48\zeta_3)\,,
\end{aligned} \tag{B.13}$$

and for the q_T soft function are

$$\begin{aligned}
\tilde{\gamma}^q_{S(0,1)} &= 0\,,\\
\tilde{\gamma}^q_{S(0,2)} &= 2Q_q^2\beta^e_{00}\Big(\frac{56}{9}-2\zeta_2\Big)\,,\\
\tilde{\gamma}^q_{S(1,1)} &= 0\,.
\end{aligned} \tag{B.14}$$

The quark rapidity anomalous dimension boundary coefficients are given by

$$\begin{aligned}
\tilde{\gamma}^q_{\nu(0,1)} &= 0\,,\\
\tilde{\gamma}^q_{\nu(0,2)} &= -Q_q^2\beta^e_{00}\frac{112}{9}\,,\\
\tilde{\gamma}^q_{\nu(1,1)} &= 0\,.
\end{aligned} \tag{B.15}$$

To obtain the coefficients we take the abelian limit of the corresponding coefficients in pure QCD, following the abelianization procedure in ref. [108]. They agree with those given in refs. [112, 141].

The one-loop pure QED boundary terms read,

$$\tilde{I}^{(0,1)}_{qi}(z) = \tilde{I}^{(0,1)}_{qqV}(z)\,\delta_{iq} + \tilde{I}^{(0,1)}_{q\gamma}(z)\,\delta_{i\gamma}\,, \tag{B.16}$$

$$\tilde{I}^{(0,1)}_{qqV}(z) = 2Q_q^2(1-z)\,, \tag{B.17}$$

$$\tilde{I}^{(0,1)}_{q\gamma}(z) = 4Q_q^2z(1-z)\,, \tag{B.18}$$

$$s^{(0,1)} = 2Q_q^2\zeta_2\,, \tag{B.19}$$

$$C^{V(0,1)}_{qq} = Q_q^2(-8+\zeta_2)\,. \tag{B.20}$$

where $\tilde{I}^{(0,1)}_{qi}(z)$ and $s^{(0,1)}_q$ correspond to the q_T beam and q_T soft function respectively, whereas $C^{V(0,1)}_{qq}$ corresponds to the Wilson coefficient that enters the hard function. The one loop QED corrections to the splitting functions which are required for the quark beam function are given in, e.g., refs. [105, 106].

B.3 Ingredients for $\mathcal{T}_0$

The quark beam function noncusp anomalous dimension coefficients to three loops are [118]

$$\begin{aligned}
\gamma^q_{B\,0} &= 6C_F\,,\\
\gamma^q_{B\,1} &= 2C_F\Big[C_A\Big(\frac{73}{9}-40\zeta_3\Big)+C_F\Big(\frac{3}{2}-12\zeta_2+24\zeta_3\Big)+\beta_0\Big(\frac{121}{18}+2\zeta_2\Big)\Big]\,,\\
\gamma^q_{B\,2} &= 2C_F\Big[C_A^2\Big(\frac{52019}{162}-\frac{1682}{27}\zeta_2-\frac{2056}{9}\zeta_3-\frac{820}{3}\zeta_4+\frac{176}{3}\zeta_2\zeta_3+232\zeta_5\Big)\\
&\quad + C_AC_F\Big(\frac{151}{4}-\frac{410}{3}\zeta_2+\frac{844}{3}\zeta_3-\frac{494}{3}\zeta_4+16\zeta_2\zeta_3+120\zeta_5\Big)\\
&\quad + C_F^2\Big(\frac{29}{2}+18\zeta_2+68\zeta_3+144\zeta_4-32\zeta_2\zeta_3-240\zeta_5\Big)\\
&\quad + C_A\beta_0\Big(-\frac{7739}{54}+\frac{650}{27}\zeta_2-\frac{1276}{9}\zeta_3+\frac{617}{3}\zeta_4\Big)\\
&\quad + \beta_0^2\Big(-\frac{3457}{324}+\frac{10}{3}\zeta_2+\frac{16}{3}\zeta_3\Big)+\beta_1\Big(\frac{1166}{27}-\frac{16}{3}\zeta_2+\frac{52}{9}\zeta_3-\frac{82}{3}\zeta_4\Big)\Big]\,. \qquad \text{(B.21)}
\end{aligned}$$

They have been confirmed recently by an explicit three-loop calculation of the jet function [407], see also ref. [408].

The gluon beam function noncusp anomalous dimension coefficients to three loops are [142]

$$\begin{aligned}
\gamma^g_{B\,0} &= 2\beta_0\,,\\
\gamma^g_{B\,1} &= 2C_A\Big[C_A\Big(\frac{91}{9}-16\zeta_3\Big)+\beta_0\Big(\frac{47}{9}-2\zeta_2\Big)\Big]+2\beta_1\,,\\
\gamma^g_{B\,2} &= 2C_A\Big[C_A^2\Big(\frac{49373}{162}-\frac{944}{27}\zeta_2-\frac{2260}{9}\zeta_3-144\zeta_4+\frac{128}{3}\zeta_2\zeta_3+112\zeta_5\Big)\\
&\quad + C_A\,\beta_0\Big(-\frac{6173}{54}-\frac{376}{27}\zeta_2+\frac{140}{9}\zeta_3+117\zeta_4\Big)+\beta_0^2\Big(-\frac{493}{81}-\frac{10}{3}\zeta_2+\frac{28}{3}\zeta_3\Big)\\
&\quad + \beta_1\Big(\frac{1765}{54}-2\zeta_2-\frac{152}{9}\zeta_3-8\zeta_4\Big)\Big]+2\beta_2\,. \qquad \text{(B.22)}
\end{aligned}$$

The soft noncusp anomalous dimension coefficients to three loops follow from consistency by $\gamma^i_S(\alpha_s) = -2\gamma^i_B(\alpha_s) - 2\gamma^i_H(\alpha_s)$, where the $\gamma^i_H(\alpha_s)$ are given in eqs. (B.4) and (B.5). We obtain,

$$\begin{aligned}
\gamma^i_{S\,0} &= 0\,,\\
\gamma^i_{S\,1} &= 2C_i\Big[C_A\Big(-\frac{64}{9}+28\zeta_3\Big)+\beta_0\Big(-\frac{56}{9}+2\zeta_2\Big)\Big]\,,\\
\gamma^i_{S\,2} &= 2C_i\Big[C_A^2\Big(-\frac{37871}{162}+\frac{620}{27}\zeta_2+\frac{2548}{9}\zeta_3+144\zeta_4-\frac{176}{3}\zeta_2\zeta_3-192\zeta_5\Big)\\
&\quad + C_A\,\beta_0\Big(\frac{4697}{54}+\frac{484}{27}\zeta_2+\frac{220}{9}\zeta_3-112\zeta_4\Big)+\beta_0^2\Big(\frac{520}{81}+\frac{10}{3}\zeta_2-\frac{28}{3}\zeta_3\Big)\\
&\quad + \beta_1\Big(-\frac{1711}{54}+2\zeta_2+\frac{152}{9}\zeta_3+8\zeta_4\Big)\Big]\,. \qquad \text{(B.23)}
\end{aligned}$$

Finally, the soft function coefficients to two loops are [65, 236–239]

$$
\begin{aligned}
s_i^{(0)} &= 1\,, \\
s_i^{(1)} &= C_i\, 2\zeta_2\,, \\
s_i^{(2)} &= C_i\Big[-C_i\, 27\zeta_4 + C_A\Big(-\frac{640}{27} + 8\zeta_2 + 44\zeta_4\Big) + \beta_0\Big(-\frac{20}{27} - \frac{37}{3}\zeta_2 + \frac{58}{3}\zeta_3\Big)\Big]\,.
\end{aligned}
\tag{B.24}
$$

where $C_i = C_F$ for $i = q$ and $C_i = C_A$ for $i = g$. The three-loop coefficient is still unknown.

B.4 Ingredients for q_T

In the exponential regulator, the noncusp anomalous dimension $\tilde{\gamma}_S^i(\alpha_s)$ of the q_T soft function is equal to that of the threshold soft function $\gamma_{\rm thr}^i(\alpha_s)$, which in turn is the negative of the $\mathcal{T}_0$ soft anomalous dimension $\gamma_S^i(\alpha_s)$. As a result, we have

$$
\begin{aligned}
\tilde{\gamma}_S^i(\alpha_s) &= \gamma_{\rm thr}^i(\alpha_s) = -\gamma_S^i(\alpha_s)\,, & \tilde{\gamma}_{S\,n}^i &= -\gamma_{S\,n}^i\,, \\
\tilde{\gamma}_B^i(\alpha_s) &= \gamma_B^i(\alpha_s) + \gamma_S^i(\alpha_s)\,, & \tilde{\gamma}_{B\,n}^i &= \gamma_{B\,n}^i + \gamma_{S\,n}^i\,.
\end{aligned}
\tag{B.25}
$$

The result for $\tilde{\gamma}_B^i(\alpha_s)$ follows from RG consistency and the fact that the hard anomalous dimension is the same for q_T and $\mathcal{T}_0$. The $\gamma_{S\,n}^i$ and $\gamma_{B\,n}^i$ coefficients are given in eqs. (B.21), (B.22), and (B.23) above.

The rapidity anomalous dimensions coefficients, which enter the fixed-order expansion of $\tilde{\gamma}_\nu^i$ in eq. (4.55), are known up to three loops [115, 119, 120]. They are given by

$$
\begin{aligned}
\tilde{\gamma}_{\nu\,0}^i \equiv \tilde{\gamma}_{\nu\,(1,0)}^i &= 0\,, \\
\tilde{\gamma}_{\nu\,1}^i \equiv \tilde{\gamma}_{\nu\,(2,0)}^i &= 2C_i\Big[C_A\Big(-\frac{64}{9} + 28\zeta_3\Big) - \frac{56}{9}\beta_0\Big]\,, \\
\tilde{\gamma}_{\nu\,2}^i \equiv \tilde{\gamma}_{\nu\,(3,0)}^i &= 2C_i\Big[C_A^2\Big(-\frac{37871}{162} + \frac{620}{27}\zeta_2 + \frac{2548}{9}\zeta_3 + 144\zeta_4 - \frac{176}{3}\zeta_2\zeta_3 - 192\zeta_5\Big) \\
&\quad + C_A\beta_0\Big(\frac{3865}{54} + \frac{412}{27}\zeta_2 + \frac{220}{9}\zeta_3 - 50\zeta_4\Big) \\
&\quad + \beta_0^2\Big(-\frac{464}{81} - 8\zeta_3\Big) + \beta_1\Big(-\frac{1711}{54} + \frac{152}{9}\zeta_3 + 8\zeta_4\Big)\Big]\,.
\end{aligned}
\tag{B.26}
$$

The soft function coefficients are also known up to three loops [115, 119], and are given by

$$
\begin{aligned}
\tilde{s}_i^{(0)} \equiv \tilde{s}_i^{(0,0)} &= 1\,, \\
\tilde{s}_i^{(1)} \equiv \tilde{s}_i^{(1,0)} &= -C_i\, 2\zeta_2\,, \\
\tilde{s}_i^{(2)} \equiv \tilde{s}_i^{(2,0)} &= C_i\Big[C_i\, 5\zeta_4 + C_A\Big(\frac{208}{27} - 4\zeta_2 + 10\zeta_4\Big) + \beta_0\Big(\frac{164}{27} - 5\zeta_2 - \frac{14}{3}\zeta_3\Big)\Big]\,,
\end{aligned}
$$

$$\begin{aligned}\tilde{s}_i^{(3)} \equiv \tilde{s}_i^{(3,0)} = C_i\Big[&-C_i^2\,\frac{35}{6}\zeta_6 + C_iC_A\Big(-\frac{416}{27}\zeta_2 + 20\zeta_4 - 35\zeta_6\Big) + C_i\beta_0\Big(-\frac{328}{27}\zeta_2 + 25\zeta_4 + \frac{28}{3}\zeta_2\zeta_3\Big)\\ &+ C_A^2\Big(\frac{115895}{324} - \frac{51071}{486}\zeta_2 - \frac{23396}{81}\zeta_3 - 58\zeta_4 + 240\zeta_2\zeta_3 - 224\zeta_5 + \frac{928}{9}\zeta_3^2 - \frac{3086}{27}\zeta_6\Big)\\ &+ C_A\beta_0\Big(-\frac{363851}{2916} + \frac{2987}{486}\zeta_2 - \frac{428}{81}\zeta_3 + \frac{830}{9}\zeta_4 - \frac{220}{3}\zeta_2\zeta_3 + \frac{1388}{9}\zeta_5\Big)\\ &+ \beta_0^2\Big(-\frac{64}{729} - \frac{34}{3}\zeta_2 - \frac{140}{27}\zeta_3 - \frac{11}{3}\zeta_4\Big)\\ &+ \beta_1\Big(\frac{42727}{972} - \frac{275}{18}\zeta_2 - \frac{1744}{81}\zeta_3 - \frac{76}{9}\zeta_4 + \frac{40}{3}\zeta_2\zeta_3 - \frac{112}{9}\zeta_5\Big)\Big]\,. \end{aligned} \tag{B.27}$$

where $C_i = C_F$ for $i = q$ and $C_i = C_A$ for $i = g$.

B.5 RGE solutions

In this section we summarize the results for the higher-order analytic RGE solutions that are used in chapters 3, 4, and 5.

For the β-function RGE

$$\frac{\mathrm{d}\alpha(\mu)}{\mathrm{d}\ln\mu} \equiv \beta[\alpha(\mu)] = -2\alpha(\mu)\sum_{n=0}^{\infty}\epsilon^n\beta_n\Big[\frac{\alpha(\mu)}{4\pi}\Big]^{n+1}, \tag{B.28}$$

the iterative solution up to N^{3}LO, $\mathcal{O}(\epsilon^3)$, reads

$$\begin{aligned}\frac{\alpha(\mu_0)}{\alpha(\mu)} = X &+ \epsilon\,\frac{\alpha(\mu_0)}{4\pi}\,b_1\ln X + \epsilon^2\,\frac{\alpha(\mu_0)^2}{(4\pi)^2}\bigg(b_2\,\frac{X-1}{X} + b_1^2\,\frac{1-X+\ln X}{X}\bigg)\\ &+ \epsilon^3\,\frac{\alpha(\mu_0)^3}{(4\pi)^3}\bigg[b_3\,\frac{X^2-1}{2X^2} + b_2b_1\Big(\frac{1-X}{X} + \frac{\ln X}{X^2}\Big) + b_1^3\,\frac{(1-X)^2-\ln^2 X}{2X^2}\bigg], \end{aligned} \tag{B.29}$$

where $b_n = \beta_n/\beta_0$ and $X = 1 + \frac{\alpha(\mu_0)}{2\pi}\,\beta_0\,\ln(\mu/\mu_0)$.

The functions K_Γ^i, η_Γ^i, and K_γ^i appearing in the unexpanded analytic Sudakov exponents are defined as

$$K_\Gamma^i(\mu_0,\mu) = \frac{1}{\epsilon}\int_{\alpha(\mu_0)}^{\alpha(\mu)}\frac{\mathrm{d}\alpha}{\beta(\alpha)}\,\Gamma^i_{\mathrm{cusp}}(\alpha)\int_{\alpha(\mu_0)}^{\alpha}\frac{\mathrm{d}\alpha'}{\beta(\alpha')}\,, \tag{B.30}$$

$$\eta_\Gamma^i(\mu_0,\mu) = \frac{1}{\epsilon}\int_{\alpha(\mu_0)}^{\alpha(\mu)}\frac{\mathrm{d}\alpha}{\beta(\alpha)}\,\Gamma^i_{\mathrm{cusp}}(\alpha)\,, \tag{B.31}$$

$$K_{\gamma^i}(\mu_0,\mu) = \int_{\alpha(\mu_0)}^{\alpha(\mu)}\frac{\mathrm{d}\alpha}{\beta(\alpha)}\,\gamma^i(\alpha)\,, \tag{B.32}$$

and up to N^{3}LL, $\mathcal{O}(\epsilon^3)$, they are given by

$$\begin{aligned}
K^i_\Gamma(\mu_0,\mu) = &-\frac{\Gamma^i_0}{4\beta_0^2}\Bigg\{\frac{4\pi}{\alpha(\mu_0)}\Big(1-\frac{1}{r}-\ln r\Big)+\epsilon\Big[(\hat\Gamma^i_1-b_1)(1-r+\ln r)+\frac{b_1}{2}\ln^2 r\Big]\\
&+\epsilon^2\,\frac{\alpha(\mu_0)}{4\pi}\Bigg[(b_1^2-b_2)\Big(\frac{1-r^2}{2}+\ln r\Big)+(b_1\hat\Gamma^i_1-b_1^2)(1-r+r\ln r)\\
&-(\hat\Gamma^i_2-b_1\hat\Gamma^i_1)\frac{(1-r)^2}{2}\Bigg]+\epsilon^3\,\frac{\alpha(\mu_0)^2}{(4\pi)^2}\Bigg[(b_2-b_1^2)(\hat\Gamma^i_1-b_1)\frac{(1-r)^2(2+r)}{3}\\
&+(\hat\Gamma^i_3-b_3-b_1(\hat\Gamma^i_2-b_2))\Big(\frac{1-r^3}{3}-\frac{1-r^2}{2}\Big)\\
&+b_1(\hat\Gamma^i_2-b_2-b_1(\hat\Gamma^i_1-b_1))\Big(\frac{1-r^2}{4}+\frac{r^2\ln r}{2}\Big)\\
&+(-b_3+2b_1b_2-b_1^3)\Big(\frac{1-r^2}{4}+\frac{\ln r}{2}\Big)\Bigg]\Bigg\},
\end{aligned}\tag{B.33}$$

$$\begin{aligned}
\eta^i_\Gamma(\mu_0,\mu) = &-\frac{\Gamma^i_0}{2\beta_0}\Bigg[\ln r+\epsilon\,\frac{\alpha(\mu_0)}{4\pi}(\hat\Gamma^i_1-b_1)(r-1)+\epsilon^2\,\frac{\alpha(\mu_0)^2}{(4\pi)^2}(\hat\Gamma^i_2-b_1\hat\Gamma^i_1+b_1^2-b_2)\frac{r^2-1}{2}\\
&+\epsilon^3\,\frac{\alpha(\mu_0)^3}{(4\pi)^3}\Big[\hat\Gamma^i_3-b_3-b_1(\hat\Gamma^i_2-b_2)+(b_1^2-b_2)(\hat\Gamma^i_1-b_1)\Big]\frac{r^3-1}{3}\Bigg],
\end{aligned}\tag{B.34}$$

$$K_{\gamma^i}(\mu_0,\mu)=-\frac{\gamma^i_0}{2\beta_0}\Bigg[\epsilon\ln r+\epsilon^2\,\frac{\alpha(\mu_0)}{4\pi}(\hat\gamma^i_1-b_1)(r-1)+\epsilon^3\,\frac{\alpha(\mu_0)^2}{(4\pi)^2}(\hat\gamma^i_2-b_1\hat\gamma^i_1+b_1^2-b_2)\frac{r^2-1}{2}\Bigg],\tag{B.35}$$

where $b_n=\beta_n/\beta_0$, $\hat\Gamma^i_n=\Gamma^i_n/\Gamma^i_0$, $\hat\gamma^i_n=\gamma^i_n/\gamma^i_0$, and $r=\alpha(\mu)/\alpha(\mu_0)$.

The corresponding kernels for the expanded analytic method are obtained by inserting eq. (B.29) into the above and expanding the results to $\mathcal{O}(\epsilon^3)$.

Appendix C

Extraction of three-loop mixed QCD⊗QED coefficients

In this section, we discuss our extraction of the three-loop coefficients of the mixed QCD⊗QED β-functions from the results in ref. [143], which are required for the complete NNLO running in sections 3.3.2 and 3.5.

Ref. [143] considers the coupled β-function RGE for a generic gauge group given as the product of n simple groups, $G = G_1 \otimes G_2 \otimes \cdots \otimes G_n$. They explicitly calculate the case of three distinct simple groups $G = G_1 \otimes G_2 \otimes G_3$, since at most three gauge bosons can propagate simultaneously at three loops. They consider the case where each simple group G_i is nonabelian, but it is straightforward to apply their results to the abelian case by a proper modification of the Casimir invariants.

To obtain the QCD⊗QED coefficients, we specify ourselves to the product group $G = \mathrm{SU}(3)_c \otimes \mathrm{U}(1)_{\mathrm{em}} \otimes \mathbf{1}$, where $\mathbf{1}$ is the trivial identity group. In addition, we only keep fermionic matter couplings, setting the Yukawa and scalar (quartic) couplings and the Casimir invariants of the scalar representation S to zero, as they appear in eq. (3.1) of ref. [143]. We have explicitly checked that with this procedure we reproduce the pure QCD β-function coefficients.

Since we only have two couplings, namely α_i with $i = s, e$ for QCD and QED respectively, the usual Casimir invariants for the $\mathrm{SU}(3)_c$ gauge group are

$$\begin{aligned}
[T_F^A, T_F^B] &= \mathrm{i} f^{ABC} T_F^C \,, \\
\mathrm{Tr}\, T_F^A T_F^B &= \delta^{AB}\, T(F_s)\,, \\
(T_F^A)_{ab}(T_F^A)_{bc} &= \delta_{ac}\, C(F_s)\,, \\
f^{ABC} f^{DBC} &= \delta^{AD}\, C(G_s)\,, \\
\delta^{AA} &= d(G_s)\,,
\end{aligned} \tag{C.1}$$

where F_s and G_s stand for the fundamental and adjoint representations, so $C(F_s) \equiv C_F$ and $C(G_s) \equiv C_A$. For the case of $\mathrm{U}(1)_{\mathrm{em}}$, we take the abelian limit

$$C(F_e) \to Q_f^2\,, \qquad T(F_e) \to Q_f^2\,, \qquad C(G_e) \to 0\,, \tag{C.2}$$

with f representing quarks and leptons. Note that sums over fermion species do appear in the β-function coefficients that each gauge group involves, i.e. quarks for $\mathrm{SU}(3)_c$ and both

quarks and leptons for $\mathrm{U}(1)_{\mathrm{em}}$. Also, since ref. [143] decomposes Dirac fermions into chiral fermions, we have to substitute $n_f \to 2n_f$ for the number of quarks and $n_\ell \to 2n_\ell$ for the number of leptons in their results.

All of this considered, the β^e_{11} coefficient can be extracted from the generic results of ref. [143], finding[1]

$$\beta^e_{11} = \sum_F 2[2C(G_i) - C(F_i)]T(F_i)C(F_j)D(F_{ij})D(F_i)\,, \tag{C.3}$$

where $i = e$, since we are considering the $\mathrm{U}(1)_{\mathrm{em}}$ β-function, and $j = s$. These specifications then give

$$\beta^e_{11} = -2\sum_{F=q,\ell} C(F_e)T(F_e)C(F_s)D(F_{es})D(F_e) = -4C_F\,\overline{Q^4}\,N_c\,, \tag{C.4}$$

where the fermion sum over the leptons does not contribute due to the presence of $C(\ell_s) = 0$ and the multiplicity factors

$$D(F_{es}) = \prod_{k\neq e,s} d(F_k) = d(\mathbf{1}) = 1\,, \qquad D(F_e) = \prod_{k\neq e} d(F_k) = d(F_s)\,d(\mathbf{1}) = N_c \tag{C.5}$$

in our case correspond to the dimension of the trivial group factor and of the fundamental $\mathrm{SU}(3)_c$ representation.

We can also read off the β^e_{02} coefficient[2]

$$\begin{aligned}\beta^e_{02} = &\sum_F \Big(\frac{133}{18}C(G_j) - C(F_j)\Big)C(F_j)T(F_i)D(F_{ij})D(F_i)\\ &- \sum_{F_m,F_n}\frac{11}{9}C(F_{m,j})T(F_{n,j})T(F_{m,i})D(F_{m,ij})D(F_{n,j})D(F_{m,i})\,,\end{aligned} \tag{C.6}$$

where again $i = e$ and $j = s$. We therefore find

$$\begin{aligned}\beta^e_{02} &= \Big(\frac{133}{18}C_A - C_F\Big)C_F\,2\overline{Q^2}\,d(\mathbf{1})N_c - \sum_{F_m}\frac{11}{9}C(F_{m,s})T(F_{m,e})D(F_{m,es})D(F_{m,e})(2\,T_F\,n_f)\\ &= \Big(\frac{133}{18}C_A - C_F\Big)2C_F\,N_c\,\overline{Q^2} - \frac{44}{9}\,C_F\,T_F\,n_f\,N_c\,\overline{Q^2}\,.\end{aligned} \tag{C.7}$$

Observe that again only the sum over quarks contributes, since the leptonic sums include a $C(\ell_s) = T(\ell_s) = 0$.

Following the same procedure we also obtained the mixed QCD coefficients β^s_{11} and β^s_{02} as given in eq. (B.6), in agreement with the corresponding results given in ref. [412], where β^s_{11} was obtained from an explicit three-loop calculation.

[1] We found a typo in this term in eq. (3.1) of ref. [143], which is missing the last $D(F_i)$ factor. This is confirmed by comparing this term for the full SM gauge group with the results of refs. [409, 410].

[2] We also found a typo in these terms in eq. (3.1) of ref. [143], which are missing the last $D(F_i)$ and $D(F_{m,i})$ factors. This is confirmed by comparing the result for β^e_{02} with the results in ref. [411].

Appendix D

Extraction of beam functions in the eikonal limit

This appendix is based on ref. [2] and parts of it have also appeared in ref. [163] as a result of a close collaboration with the author.

D.1 Threshold soft function

In this section we discuss the double-differential threshold soft function $S_i^{\rm thr}(k^-, k^+, \mu)$, which appears in the soft threshold factorization for the inclusive cross section in eq. (4.39) and determines the eikonal limit of the $\mathcal{T}_0$ beam function in eq. (4.43). We give its complete N^{3}LO result in appendix D.1.2 in terms of a convenient plus distribution basis defined in appendix D.1.1. In appendix D.1.3, we discuss how the three-loop coefficients are extracted from the known three-loop results for the closely-related inclusive threshold soft function.

D.1.1 Plus distribution basis

A key property of the threshold soft function is that is invariant under the simultaneous rescaling $k^- \mapsto k^- e^{+y}$ and $k^+ \mapsto k^+ e^{-y}$, see eq. (4.40). To make this property manifest, we define a basis of plus distributions in $k^\pm$ that individually satisfy this property,

$$\begin{aligned}\frac{\theta(k^-)\theta(k^+)}{\mu^2}\Big(\frac{k^-k^+}{\mu^2}\Big)^{-1+a} &= \bigg[\frac{\delta(k^-)}{a} + \sum_{n=0}^{\infty}\frac{a^n}{n!}\mathcal{L}_n(k^-,\mu)\bigg]\bigg[\frac{\delta(k^+)}{a} + \sum_{m=0}^{\infty}\frac{a^m}{m!}\mathcal{L}_m(k^+,\mu)\bigg] \\ &\equiv \frac{\delta(k^-,k^+)}{a^2} + \sum_{n=0}^{\infty}\frac{a^{n-1}}{n!}\mathcal{L}_n(k^-,k^+,\mu)\,. \end{aligned} \tag{D.1}$$

Note that the leading $\delta(k^-, k^+)$ term multiplies a double pole in a. The second line implicitly defines the $\mathcal{L}_n(k^-, k^+, \mu)$ by the expansion of the first line in powers of a. They are by construction invariant under rescaling, because the left-hand side is. Explicitly, they are given by

$$\delta(k^-,k^+) = \delta(k^-)\,\delta(k^+)\,,$$

$$\mathcal{L}_n(k^-,k^+,\mu) = \delta(k^-)\,\mathcal{L}_n(k^+,\mu) + \mathcal{L}_n(k^-,\mu)\,\delta(k^+) + n\sum_{m=0}^{n-1}\binom{n-1}{m}\mathcal{L}_m(k^-,\mu)\,\mathcal{L}_{n-1-m}(k^+,\mu)\,. \tag{D.2}$$

D.1.2 Three-loop result

The threshold soft function satisfies the all-order RGE

$$\mu\frac{\mathrm{d}}{\mathrm{d}\mu}S_i^{\mathrm{thr}}(k^-,k^+,\mu) = \int \mathrm{d}\ell^-\mathrm{d}\ell^+\,\gamma_{\mathrm{thr}}^i(k^-\!-\ell^-,k^+\!-\ell^+,\mu)\,S_i^{\mathrm{thr}}(\ell^-,\ell^+,\mu)\,,$$
$$\gamma_{\mathrm{thr}}^i(k^-,k^+,\mu) = -2\Gamma^i_{\mathrm{cusp}}[\alpha_s(\mu)]\,\mathcal{L}_0(k^-,k^+,\mu) + \gamma^i_{\mathrm{thr}}[\alpha_s(\mu)]\,\delta(k^-,k^+)\,. \tag{D.3}$$

Expanding the threshold soft function in $\alpha_s/(4\pi)$ and suppressing all arguments for brevity, $S_i^{\mathrm{thr}(n)} \equiv S_i^{\mathrm{thr}(n)}(k^-,k^+,\mu)$, $\mathcal{L}_n \equiv \mathcal{L}_n(k^-,k^+,\mu)$, $\delta \equiv \delta(k^-,k^+)$, the three-loop solution of eq. (D.3) takes the form

$$\begin{aligned}
S_i^{\mathrm{thr}(0)} &= \delta\,,\\
S_i^{\mathrm{thr}(1)} &= \mathcal{L}_1\,\Gamma_0^i - \mathcal{L}_0\,\frac{\gamma^i_{\mathrm{thr}\,0}}{2} + \delta\,s_i^{\mathrm{thr}(1)}\,,\\
S_i^{\mathrm{thr}(2)} &= \mathcal{L}_3\frac{(\Gamma_0^i)^2}{2} - \mathcal{L}_2\frac{\Gamma_0^i}{2}\Big(\beta_0+\frac{3}{2}\gamma^i_{\mathrm{thr}\,0}\Big) + \mathcal{L}_1\Big[-2\zeta_2(\Gamma_0^i)^2 + \Big(\beta_0+\frac{\gamma^i_{\mathrm{thr}\,0}}{2}\Big)\frac{\gamma^i_{\mathrm{thr}\,0}}{2} + \Gamma_1^i + \Gamma_0^i s_i^{\mathrm{thr}(1)}\Big]\\
&\quad + \mathcal{L}_0\Big[\Gamma_0^i\big(2\zeta_3\Gamma_0^i + \zeta_2\gamma^i_{\mathrm{thr}\,0}\big) - \frac{\gamma^i_{\mathrm{thr}\,1}}{2} - \Big(\beta_0+\frac{\gamma^i_{\mathrm{thr}\,0}}{2}\Big)s_i^{\mathrm{thr}(1)}\Big] + \delta\,s_i^{\mathrm{thr}(2)}\,,\\
S_i^{\mathrm{thr}(3)} &= \mathcal{L}_5\,\frac{(\Gamma_0^i)^3}{8} - \mathcal{L}_4\,\frac{5}{8}(\Gamma_0^i)^2\Big(\frac{2}{3}\beta_0+\frac{\gamma^i_{\mathrm{thr}\,0}}{2}\Big)\\
&\quad + \mathcal{L}_3\,\Gamma_0^i\Big[-2\zeta_2(\Gamma_0^i)^2 + \frac{\beta_0^2}{3} + \Big(\frac{5}{3}\beta_0+\frac{\gamma^i_{\mathrm{thr}\,0}}{2}\Big)\frac{\gamma^i_{\mathrm{thr}\,0}}{2} + \Gamma_1^i + \frac{\Gamma_0^i}{2}s_i^{\mathrm{thr}(1)}\Big]\\
&\quad + \mathcal{L}_2\Big\{(\Gamma_0^i)^2\Big[5\zeta_3\Gamma_0^i + 3\zeta_2(\beta_0+\gamma^i_{\mathrm{thr}\,0})\Big] - \Big(\beta_0+\frac{3}{4}\gamma^i_{\mathrm{thr}\,0}\Big)\Big(\beta_0\frac{\gamma^i_{\mathrm{thr}\,0}}{2}+\Gamma_1^i\Big)\\
&\qquad - \frac{(\gamma^i_{\mathrm{thr}\,0})^3}{16} - \frac{\Gamma_0^i}{2}\Big[\beta_1 + \frac{3}{2}\gamma^i_{\mathrm{thr}\,1} + \Big(4\beta_0+\frac{3}{2}\gamma^i_{\mathrm{thr}\,0}\Big)s_i^{\mathrm{thr}(1)}\Big]\Big\}\\
&\quad + \mathcal{L}_1\Big\{(\Gamma_0^i)^2\big[4\zeta_4\Gamma_0^i - \zeta_3(6\beta_0+4\gamma^i_{\mathrm{thr}\,0})\big] - \zeta_2\Gamma_0^i\big[(3\beta_0+\gamma^i_{\mathrm{thr}\,0})\gamma^i_{\mathrm{thr}\,0} + 4\Gamma_1^i\big]\\
&\qquad + \beta_0\gamma^i_{\mathrm{thr}\,1} + \frac{\gamma^i_{\mathrm{thr}\,0}}{2}(\beta_1+\gamma^i_{\mathrm{thr}\,1}) + \Gamma_2^i\\
&\qquad + \Big[-2\zeta_2(\Gamma_0^i)^2 + 2\beta_0^2 + \Big(3\beta_0+\frac{\gamma^i_{\mathrm{thr}\,0}}{2}\Big)\frac{\gamma^i_{\mathrm{thr}\,0}}{2} + \Gamma_1^i\Big]s_i^{\mathrm{thr}(1)} + \Gamma_0^i\,s_i^{\mathrm{thr}(2)}\Big\}\\
&\quad + \mathcal{L}_0\Big\{(\Gamma_0^i)^2\big[-\Gamma_0^i(8\zeta_2\zeta_3 - 6\zeta_5) + 2\zeta_4(\beta_0-\gamma^i_{\mathrm{thr}\,0})\big] + \zeta_3\Gamma_0^i\Big[\Big(\beta_0+\frac{\gamma^i_{\mathrm{thr}\,0}}{2}\Big)\gamma^i_{\mathrm{thr}\,0}\\
&\qquad + 4\Gamma_1^i\Big] + \zeta_2\big(\gamma^i_{\mathrm{thr}\,0}\Gamma_1^i + \Gamma_0^i\gamma^i_{\mathrm{thr}\,1}\big) - \frac{\gamma^i_{\mathrm{thr}\,2}}{2} + \Big[(\Gamma_0^i)^2 2\zeta_3 + \Gamma_0^i\zeta_2(2\beta_0+\gamma^i_{\mathrm{thr}\,0})\\
&\qquad - \Big(\beta_1+\frac{\gamma^i_{\mathrm{thr}\,1}}{2}\Big)\Big]s_i^{\mathrm{thr}(1)} - \Big(2\beta_0+\frac{\gamma^i_{\mathrm{thr}\,0}}{2}\Big)s_i^{\mathrm{thr}(2)}\Big\} + \delta\,s_i^{\mathrm{thr}(3)}\,.
\end{aligned} \tag{D.4}$$

Consistency of the factorization theorems in eq. (4.5), (4.38), and (4.39) implies

$$2\gamma_B^i(\alpha_s) + \gamma_S^i(\alpha_s) = 2\gamma_f^i(\alpha_s) + \gamma_{\rm thr}^i(\alpha_s) = \gamma_f^i(\alpha_s) + \gamma_B^i(\alpha_s)\,, \tag{D.5}$$

because the hard function is the same in all cases. Here, $\gamma_f^i(\alpha_s)$ is the coefficient of $\delta(1-z)$ in the PDF anomalous dimension eq. (A.32). Solving eq. (D.5) for $\gamma_{\rm thr}^i(\alpha_s)$, we find

$$\gamma_{\rm thr}^i(\alpha_s) = -\gamma_S^i(\alpha_s)\,, \qquad \gamma_{{\rm thr}\,n}^i = -\gamma_{S\,n}^i\,, \tag{D.6}$$

where the soft anomalous dimension coefficients $\gamma_{S\,n}^i$ are given in eq. (B.23).

The boundary coefficients $s_i^{{\rm thr}(n)}$, which are defined as the coefficients of $\delta(k^-,k^+)$ in eq. (D.4), are given by [173, 174][1]

$$\begin{aligned}
s_i^{{\rm thr}(1)} &= -C_i\, 2\zeta_2\,,\\
s_i^{{\rm thr}(2)} &= C_i\Big[C_i\, 21\zeta_4 + C_A\Big(\frac{208}{27} - 4\zeta_2 - 10\zeta_4\Big) + \beta_0\Big(\frac{164}{27} - 5\zeta_2 - \frac{10\zeta_3}{3}\Big)\Big]\,,\\
s_i^{{\rm thr}(3)} &= C_i\Big[C_i^2\Big(\frac{640}{3}\zeta_3^2 - \frac{499}{6}\zeta_6\Big) + C_iC_A\Big(-\frac{416}{27}\zeta_2 - \frac{512}{9}\zeta_3 + \frac{188}{3}\zeta_4 + 224\zeta_3^2 - 77\zeta_6\Big)\\
&\quad + C_i\beta_0\Big(-\frac{328}{27}\zeta_2 - \frac{448}{9}\zeta_3 + \frac{235}{3}\zeta_4 + \frac{308}{3}\zeta_2\zeta_3 - 64\zeta_5\Big)\\
&\quad + C_A^2\Big(\frac{115895}{324} - \frac{45239}{486}\zeta_2 - \frac{23396}{81}\zeta_3 - \frac{334}{3}\zeta_4\\
&\qquad + 240\zeta_2\zeta_3 - 224\zeta_5 + \frac{1072}{9}\zeta_3^2 + \frac{4348}{27}\zeta_6\Big)\\
&\quad + C_A\beta_0\Big(-\frac{363851}{2916} + \frac{1043}{486}\zeta_2 - \frac{140}{81}\zeta_3 + \frac{230}{9}\zeta_4 - \frac{164}{3}\zeta_2\zeta_3 + \frac{632}{9}\zeta_5\Big)\\
&\quad + \beta_0^2\Big(-\frac{64}{729} - \frac{34}{3}\zeta_2 - \frac{20}{27}\zeta_3 + \frac{31}{3}\zeta_4\Big)\\
&\quad + \beta_1\Big(\frac{42727}{972} - \frac{275}{18}\zeta_2 - \frac{1636}{81}\zeta_3 - \frac{76}{9}\zeta_4 + \frac{40}{3}\zeta_2\zeta_3 - \frac{112}{9}\zeta_5\Big)\Big]\,.
\end{aligned} \tag{D.7}$$

where $C_i = C_F$ for $i = q$ and $C_i = C_A$ for $i = g$. We have also checked that inserting the above coefficients into eq. (D.4) and expanding against the Drell-Yan hard function, we reproduce the three-loop soft-virtual partonic cross section in refs. [176, 248] in terms of $1 - z_a = k^-/(Qe^{+Y})$ and $1 - z_b = k^+/(Qe^{-Y})$.

D.1.3 Extraction method

The double-differential threshold soft function depends on the total lightcone momentum components $k^\pm$ of the soft hadronic final state. Equivalently, its Fourier transform

$$\hat{S}_i^{\rm thr}(b^+,b^-,\mu) = \int {\rm d}k^-{\rm d}k^+\, e^{+{\rm i}(k^-b^+ + k^+b^-)/2}\, S_i^{\rm thr}(k^-,k^+,\mu)\,, \tag{D.8}$$

[1] We note that the coefficient of C_iC_A in the two-loop finite term disagrees with the $\vec{b}_T \to 0$ limit of the fully-differential soft function as reported in terms of $k^\pm$ and $\vec{b}_T$ in ref. [283]. This color structure only enters at two loops and thus is unaffected by non-Abelian exponentiation. We were unable to resolve this difference, but tend to attribute it to a typographical error in ref. [283] because refs. [76, 119] agreed with the pure position-space result of ref. [283] in terms of $b^\pm$ and $\vec{b}_T$.

depends on the time-like separation $(b^- n^\mu + b^+ \bar{n}^\mu)/2$ between the Wilson lines in the soft matrix element.

Importantly, $\hat{S}_i^{\rm thr}(b^+, b^-, \mu)$ only depends on the product $b^+ b^-$ by the rescaling relation eq. (4.40), and thus only depends on $b^+ b^- \mu^2$ by dimensional analysis. On the other hand, the dependence on μ is fully predicted by the RGE eq. (D.3), which in position space reads

$$\mu \frac{\mathrm{d}}{\mathrm{d}\mu} \hat{S}_i^{\rm thr}(b^+, b^-, \mu) = \Big\{ 2\Gamma^i_{\rm cusp}[\alpha_s(\mu)]\, L_{\rm thr}(b^+, b^-, \mu) + \gamma^i_{\rm thr}[\alpha_s(\mu)] \Big\}\, \hat{S}_i^{\rm thr}(b^+, b^-, \mu)\,. \quad \text{(D.9)}$$

This implies that at any given order in perturbation theory, $\hat{S}_i^{\rm thr}(b^+, b^-, \mu)$ is a polynomial in

$$L_{\rm thr}(b^+, b^-, \mu) \equiv \ln\Big(-\frac{b^+ b^- \mu^2 e^{2\gamma_E}}{4} - \mathrm{i}0 \Big)\,. \quad \text{(D.10)}$$

The relevant Fourier transforms between $L^n_{\rm thr}$ and $\mathcal{L}_n(k^-, k^+, \mu)$ follow from the one-dimensional Fourier transforms in appendix B of ref. [144], accounting for the relative factors of $-1/2$ in the Fourier exponent in eq. (D.8).

A factorization analogous to eq. (4.39) holds for the inclusive cross section $\mathrm{d}\sigma/\mathrm{d}Q^2$, where the corresponding inclusive threshold soft function $S_i^{\rm thr}(k^0, \mu)$ only depends on the total energy k^0 of soft radiation. In particular, $S_i^{\rm thr}(k^0, \mu)$ is the process-independent soft contribution to the inclusive partonic cross section $\sigma_{ab}(z)$ in the soft-virtual limit $z \to 1$, where $1 - z = 2k^0/Q$. In position space, the inclusive threshold soft function $\hat{S}_i^{\rm thr}(b^0, \mu)$ is defined in terms of Wilson lines separated by $b^0(n^\mu + \bar{n}^\mu)/2$, i.e., strictly along the time axis. This is a special case of eq. (D.8), so the two position-space threshold soft functions are simply related by

$$\hat{S}_i^{\rm thr}(b^0, b^0, \mu) = \hat{S}_i^{\rm thr}(b^0, \mu)\,. \quad \text{(D.11)}$$

This is of course equivalent to integrating over the longitudinal momentum k^3 of soft radiation. We stress that eq. (D.11) cannot be used to approximate $\hat{S}_i^{\rm thr}(b^+, b^-, \mu)$ by taking $b^+ = b^-$ in general. This is because in eq. (4.39) the k^+ and k^- dependences are separately convolved with the PDFs and thus the rescaling property eq. (4.40) is lost at the level of the cross section. See also Appendix D of ref. [241] for further discussion of this point.

Inserting eq. (D.11) into eq. (D.9) implies that both threshold soft functions have the same noncusp anomalous dimension given by eq. (D.6). Moreover, the position-space boundary coefficients of the double-differential soft function at $L_{\rm thr} = 0$, i.e., at $\mu = \mu_* \equiv +\mathrm{i}2e^{-\gamma_E}/b^0$, are equal to the inclusive ones at the same scale. Hence, the double-differential threshold soft function can be constructed from the inclusive one.

The inclusive threshold soft function was calculated to three loops in refs. [173, 174]. Here we use the results of ref. [174], where the three-loop soft function for $i = g$ is reported in exponentiated form,

$$\hat{S}_i^{\rm thr}(b^0, \mu_*) = \exp\Big\{ \frac{C_i}{C_A} \Big[\frac{\alpha_s(\mu_*)}{4\pi} c^H_{1\,\text{ref. [174]}} + \frac{\alpha_s^2(\mu_*)}{(4\pi)^2} \Delta c^H_{2\,\text{ref. [174]}} + \frac{\alpha_s^3(\mu_*)}{(4\pi)^3} \Delta c^H_{3\,\text{ref. [174]}} \Big] + \mathcal{O}(\alpha_s^4) \Big\}. \quad \text{(D.12)}$$

We have also exploited Casimir scaling to three loops to restore the dependence on C_i. Comparing eq. (D.12) to the position-space solution of eq. (D.9) at $L_{\text{thr}} = 0$, we obtain eq. (D.7) for the momentum-space boundary coefficients after performing the inverse Fourier transform.

D.2 Collinear-soft function for the exponential regulator

In this section we derive the all-order expression for the collinear-soft function using the exponential regulator, which leads to eq. (4.88) in the main text.

We start by defining the complete Fourier transform of the fully-differential threshold soft function

$$\hat{S}_i^{\text{thr}}(b^+, b^-, b_T, \mu) = \int \mathrm{d}^4k\, e^{+\mathrm{i}b\cdot k}\, S_i^{\text{thr}}(k^-, k^+, k_T, \mu)\,, \tag{D.13}$$

where $b^\mu = (b^+, b^-, \vec{b}_T)$ is the four-vector Fourier conjugate of $k^\mu = (k^+, k^-, \vec{k}_T)$ with $b \cdot k = b^+k^-/2 + b^-k^+/2 - \vec{b}_T \cdot \vec{k}_T$. Correspondingly, we define the Fourier transform of $\tilde{\mathcal{S}}_i(k^\pm, b_T, \mu, \nu)$ with respect to its lightcone momentum argument $k^\pm$ as

$$\hat{\mathcal{S}}_i(b^+, b_T, \mu, \nu) = \int \mathrm{d}k^-\, e^{+\mathrm{i}k^-b^+/2}\, \tilde{\mathcal{S}}_i(k^-, b_T, \mu, \nu)\,, \tag{D.14}$$

and analogously for $b^- \leftrightarrow b^+$ and $k^+ \leftrightarrow k^-$. Fully in position space, the consistency relation eq. (4.87) reads

$$\hat{S}_i^{\text{thr}}(b^+, b^-, b_T, \mu) = \hat{\mathcal{S}}_i(b^+, b_T, \mu, \nu)\, \hat{\mathcal{S}}_i(b^-, b_T, \mu, \nu)\, \tilde{S}_i(b_T, \mu, \nu) \left[1 + \mathcal{O}\Big(\frac{b^+b^-}{b_T^2}\Big)\right]. \tag{D.15}$$

In the exponential regulator scheme, the regulated q_T soft function is *defined* as [76, 119][2]

$$\tilde{S}_i(b_T, \mu, \nu') = \lim_{\nu'\to\infty} \hat{S}_i^{\text{thr}}\Big(\frac{\mathrm{i}b_0}{\nu'}, \frac{\mathrm{i}b_0}{\nu'}, b_T, \mu\Big)\,, \tag{D.16}$$

where we use ν' to distinguish it from the scale at which we later wish to evaluate the collinear-soft function. The prescription for taking the limit is to keep all nonvanishing terms. In particular, a logarithmic dependence of the right-hand side on ν' is to be kept. Inserting eq. (D.15), we have

$$\begin{aligned}
\tilde{S}_i(b_T, \mu, \nu') &= \lim_{\nu'\to\infty} \Big[\hat{\mathcal{S}}_i\Big(\frac{\mathrm{i}b_0}{\nu'}, b_T, \mu, \nu\Big)\, \hat{\mathcal{S}}_i\Big(\frac{\mathrm{i}b_0}{\nu'}, b_T, \mu, \nu\Big)\, \tilde{S}_i(b_T, \mu, \nu) + \mathcal{O}\Big(\frac{1}{\nu'^2 b_T^2}\Big)\Big] \\
&= \tilde{S}_i(b_T, \mu, \nu) \lim_{\nu'\to\infty} \Big[\hat{\mathcal{S}}_i\Big(\frac{\mathrm{i}b_0}{\nu'}, b_T, \mu, \nu\Big)\, \hat{\mathcal{S}}_i\Big(\frac{\mathrm{i}b_0}{\nu'}, b_T, \mu, \nu\Big)\Big] \\
&= \tilde{S}_i(b_T, \mu, \nu)\, \hat{\mathcal{S}}_i\Big(\frac{\mathrm{i}b_0}{\nu'}, b_T, \mu, \nu\Big)\, \hat{\mathcal{S}}_i\Big(\frac{\mathrm{i}b_0}{\nu'}, b_T, \mu, \nu\Big)\,.
\end{aligned} \tag{D.17}$$

In the second line we moved the q_T soft function out of the limit, since it does not depend on ν', and dropped the power corrections. On the third line we used that all dependence

[2] Comparing eq. (2) in ref. [119] to eq. (33) in ref. [76] suggests that the latter has a spurious factor of 2 in the denominator, noting that their $\tau = 1/\nu$.

of the $\hat{\mathcal{S}}_i$ on ν' is logarithmic, so the limit is trivial. Because the exponential regulator is symmetric under an interchange of collinear-soft directions, we find

$$\hat{\mathcal{S}}_i^2\Big(\frac{\mathrm{i}b_0}{\nu'}, b_T, \mu, \nu\Big) = \frac{\tilde{S}_i(b_T, \mu, \nu')}{\tilde{S}_i(b_T, \mu, \nu)} = \exp\Big[\tilde{\gamma}_\nu^i(b_T, \mu) \ln \frac{\nu'}{\nu}\Big]\,, \tag{D.18}$$

where the second equality follows from solving the rapidity RGE of the soft function between ν and ν' at fixed μ. Assuming we are dealing with the n_a-collinear-soft function that depends on b^+, we can analytically continue back to $\nu' = \mathrm{i}b_0/b^+ = 2\mathrm{i}/(b^+ e^{\gamma_E})$, leaving

$$\hat{\mathcal{S}}_i(b^+, b_T, \mu, \nu) = \exp\Big[-\frac{1}{2}\tilde{\gamma}_\nu^i(b_T, \mu) \ln(-\mathrm{i}b^+\nu e^{\gamma_E}/2)\Big]\,. \tag{D.19}$$

Evaluating the inverse Fourier transform using eq. (A.23), we find the following all-order relation for the momentum-space n_a-collinear-soft function in the exponential regulator scheme,

$$\tilde{\mathcal{S}}_i(k^-, b_T, \mu, \nu) = \mathcal{V}_{\tilde{\gamma}_\nu^i(b_T,\mu)/2}(k^-, \nu)\,, \tag{D.20}$$

and identically for the n_b-collinear one as a function of k^+. In other words, the collinear-soft function in the exponential regulator scheme is simply given by the rapidity RG evolution between its canonical rapidity scale $\nu_{\mathcal{S}} \sim k^-$ and ν, with trivial boundary condition at $\nu_{\mathcal{S}}$. Inserting this result into eq. (4.86) leads to eq. (4.88) in the main text.

References

Citing pages are listed in square brackets after each reference.

[1] G. Billis, F. J. Tackmann and J. Talbert, *Higher-Order Sudakov Resummation in Coupled Gauge Theories*, *JHEP* **03** (2020) 182 [1907.02971]. [pp. v, 45, and 149]

[2] G. Billis, M. A. Ebert, J. K. L. Michel and F. J. Tackmann, *A toolbox for q_T and 0-jettiness subtractions at N^3LO*, *Eur. Phys. J. Plus* **136** (2021) 214 [1909.00811]. [pp. v, 57, 85, 87, 97, 102, 113, 118, 140, 150, and 191]

[3] G. Billis, B. Dehnadi, M. A. Ebert, J. K. L. Michel and F. J. Tackmann, *Higgs pT Spectrum and Total Cross Section with Fiducial Cuts at Third Resummed and Fixed Order in QCD*, *Phys. Rev. Lett.* **127** (2021) 072001 [2102.08039]. [pp. v, 85, and 139]

[4] ATLAS collaboration, *Observation of a new particle in the search for the Standard Model Higgs boson with the ATLAS detector at the LHC*, *Phys. Lett. B* **716** (2012) 1 [1207.7214]. [pp. 1 and 139]

[5] CMS collaboration, *Observation of a New Boson at a Mass of 125 GeV with the CMS Experiment at the LHC*, *Phys. Lett. B* **716** (2012) 30 [1207.7235]. [pp. 1 and 139]

[6] A. Salam, *Weak and Electromagnetic Interactions*, *Conf. Proc. C* **680519** (1968) 367. [p. 1]

[7] S. Weinberg, *A Model of Leptons*, *Phys. Rev. Lett.* **19** (1967) 1264. [p. 1]

[8] S. L. Glashow, *Partial Symmetries of Weak Interactions*, *Nucl. Phys.* **22** (1961) 579. [p. 1]

[9] P. W. Higgs, *Broken Symmetries and the Masses of Gauge Bosons*, *Phys. Rev. Lett.* **13** (1964) 508. [p. 1]

[10] F. Englert and R. Brout, *Broken Symmetry and the Mass of Gauge Vector Mesons*, *Phys. Rev. Lett.* **13** (1964) 321. [p. 1]

[11] G. S. Guralnik, C. R. Hagen and T. W. B. Kibble, *Global Conservation Laws and Massless Particles*, *Phys. Rev. Lett.* **13** (1964) 585. [p. 1]

[12] Q. R. Ahmad, R. C. Allen, T. C. Andersen, J. D.Anglin, J. C. Barton, E. W. Beier et al., *Direct evidence for neutrino flavor transformation from neutral-current interactions in the sudbury neutrino observatory*, *Physical Review Letters* **89** (2002) . [p. 1]

[13] Y. Fukuda, T. Hayakawa, E. Ichihara, K. Inoue, K. Ishihara, H. Ishino et al., *Evidence for oscillation of atmospheric neutrinos*, *Physical Review Letters* **81** (1998) 1562–1567. [p. 1]

[14] A. D. Sakharov, *Violation of CP Invariance, C asymmetry, and baryon asymmetry of the universe*, *Pisma Zh. Eksp. Teor. Fiz.* **5** (1967) 32. [p. 1]

[15] Particle Data Group collaboration, M. Tanabashi, K. Hagiwara, K. Hikasa, K. Nakamura, Y. Sumino, F. Takahashi et al., *Review of particle physics*, *Phys. Rev. D* **98** (2018) 030001. [pp. 2, 12, 13, and 142]

[16] M. Grazzini, A. Ilnicka, M. Spira and M. Wiesemann, *Modeling BSM effects on the Higgs transverse-momentum spectrum in an EFT approach*, *Journal of High Energy Physics* **2017** (2017) . [p. 2]

[17] F. Bishara, U. Haisch, P. F. Monni and E. Re, *Constraining light-quark yukawa couplings from higgs distributions*, *Physical Review Letters* **118** (2017) . [p. 2]

[18] Y. Soreq, H. X. Zhu and J. Zupan, *Light quark Yukawa couplings from Higgs kinematics*, *JHEP* **12** (2016) 045 [1606.09621]. [p. 2]

[19] A. Sirunyan, A. Tumasyan, W. Adam, F. Ambrogi, E. Asilar, T. Bergauer et al., *Measurement and interpretation of differential cross sections for Higgs boson production at s=13TeV*, *Physics Letters B* **792** (2019) 369–396. [pp. 2 and 3]

[20] CMS Collaboration collaboration, *Sensitivity projections for Higgs boson properties measurements at the HL-LHC*, tech. rep., CERN, Geneva, 2018. [p. 3]

[21] ATLAS Collaboration collaboration, *Measurements of Higgs boson properties in the diphoton decay channel using 80 fb^{-1} of pp collision data at $\sqrt{s}$ = 13 TeV with the ATLAS detector*, tech. rep., CERN, Geneva, Jul, 2018. [pp. 2 and 3]

[22] ATLAS Collaboration collaboration, *Prospects for differential cross-section measurements of Higgs boson production measured in decays to ZZ and $\gamma\gamma$ with the ATLAS experiment at the High-Luminosity LHC*, tech. rep., CERN, Geneva, Dec, 2018. [p. 3]

[23] A. Dainese, M. Mangano, A. B. Meyer, A. Nisati, G. Salam and M. A. Vesterinen, *Report on the Physics at the HL-LHC, and Perspectives for the HE-LHC*, tech. rep., Geneva, Switzerland, 2019. 10.23731/CYRM-2019-007. [p. 3]

[24] ATLAS Collaboration collaboration, *Expected performance of the ATLAS detector at the High-Luminosity LHC*, tech. rep., CERN, Geneva, Jan, 2019. [p. 3]

[25] CMS Collaboration collaboration, T. C. Collaboration, *Expected performance of the physics objects with the upgraded CMS detector at the HL-LHC*, tech. rep., CERN, Geneva, Dec, 2018. [p. 3]

[26] S. D. Drell and T.-M. Yan, *Massive Lepton Pair Production in Hadron-Hadron Collisions at High-Energies*, *Phys. Rev. Lett.* **25** (1970) 316. [p. 5]

[27] M. Aaboud, G. Aad, B. Abbott, J. Abdallah, O. Abdinov, B. Abeloos et al., *Measurement of the W-boson mass in pp collisions at $\sqrt{s} = 7$ TeV with the ATLAS detector*, *The European Physical Journal C* **78** (2018) . [p. 5]

[28] G. Aad, B. Abbott, J. Abdallah, S. Abdel Khalek, O. Abdinov, R. Aben et al., *Measurement of the forward-backward asymmetry of electron and muon pair-production in pp collisions at $\sqrt{s} = 7$ TeV with the ATLAS detector*, *Journal of High Energy Physics* **2015** (2015) . [p. 5]

[29] A. M. Sirunyan, A. Tumasyan, W. Adam, F. Ambrogi, E. Asilar, T. Bergauer et al., *Measurement of the weak mixing angle using the forward–backward asymmetry of Drell–Yan events in pp collisions at 8 TeV*, *The European Physical Journal C* **78** (2018) . [p. 5]

[30] J. Rojo, A. Accardi, R. D. Ball, A. Cooper-Sarkar, A. d. Roeck, S. Farry et al., *The PDF4LHC report on PDFs and LHC data: results from Run I and preparation for Run II*, *Journal of Physics G: Nuclear and Particle Physics* **42** (2015) 103103. [p. 5]

[31] ATLAS collaboration, *Measurements of Higgs boson properties in the diphoton decay channel with 36 fb^{-1} of pp collision data at $\sqrt{s} = 13$ TeV with the ATLAS detector*, *Phys. Rev. D* **98** (2018) 052005 [1802.04146]. [pp. 6, 139, 155, and 163]

[32] ATLAS Collaboration, *Measurements and interpretations of Higgs-boson fiducial cross sections in the diphoton decay channel using 139 fb^{-1} of pp collision data at $\sqrt{s} = 13$ TeV with the ATLAS detector*, *ATLAS-CONF-2019-029* (2019) . [pp. 6, 155, 163, and 167]

[33] S. J. Brodsky and R. Shrock, *Maximum wavelength of confined quarks and gluons and properties of quantum chromodynamics*, *Physics Letters B* **666** (2008) 95–99. [p. 14]

[34] G. P. Salam, *Elements of qcd for hadron colliders*, 2011. [p. 14]

[35] J. Collins, *Foundations of perturbative QCD*, vol. 32. Cambridge University Press, 11, 2013. [pp. 14, 22, and 26]

[36] M. E. Peskin and D. V. Schroeder, *An Introduction to quantum field theory*. Addison-Wesley, Reading, USA, 1995. [pp. 14, 18, 31, and 35]

[37] F. Bloch and A. Nordsieck, *Note on the Radiation Field of the electron*, *Phys. Rev.* **52** (1937) 54. [p. 16]

[38] T. Kinoshita, *Mass singularities of Feynman amplitudes*, *J. Math. Phys.* **3** (1962) 650. [p. 16]

[39] T. D. Lee and M. Nauenberg, *Degenerate Systems and Mass Singularities*, *Phys. Rev.* **133** (1964) B1549. [p. 16]

[40] J. C. Collins, D. E. Soper and G. F. Sterman, *Factorization of Hard Processes in QCD*, *Adv. Ser. Direct. High Energy Phys.* **5** (1989) 1 [hep-ph/0409313]. [pp. 16, 22, and 26]

[41] Y. L. Dokshitzer, *Calculation of the Structure Functions for Deep Inelastic Scattering and e+ e- Annihilation by Perturbation Theory in Quantum Chromodynamics.*, *Sov. Phys. JETP* **46** (1977) 641. [p. 20]

[42] V. N. Gribov and L. N. Lipatov, *Deep inelastic e p scattering in perturbation theory*, *Sov. J. Nucl. Phys.* **15** (1972) 438. [p. 20]

[43] G. Altarelli and G. Parisi, *Asymptotic Freedom in Parton Language*, *Nucl. Phys. B* **126** (1977) 298. [p. 20]

[44] C. W. Bauer, S. Fleming and M. Luke, *Summing Sudakov logarithms in $\overrightarrow{B} X_s\gamma$ in effective field theory*, *Phys. Rev. D* **63** (2000) 014006. [pp. 21 and 22]

[45] C. W. Bauer and I. W. Stewart, *Invariant operators in collinear effective theory*, *Phys. Lett. B* **516** (2001) 134 [hep-ph/0107001]. [pp. 21, 22, 30, 31, and 146]

[46] C. W. Bauer, S. Fleming, D. Pirjol and I. W. Stewart, *An effective field theory for collinear and soft gluons: Heavy to light decays*, *Phys. Rev. D* **63** (2001) 114020. [pp. 21, 22, 30, 31, and 34]

[47] A. Banfi, G. P. Salam and G. Zanderighi, *Principles of general final-state resummation and automated implementation*, *Journal of High Energy Physics* **2005** (2005) 073–073. [p. 21]

[48] S. Catani, B. R. Webber and G. Marchesini, *QCD coherent branching and semiinclusive processes at large x*, *Nucl. Phys. B* **349** (1991) 635. [p. 21]

[49] M. A. Ebert, J. K. L. Michel, F. J. Tackmann et al., *SCETlib: A C++ Package for Numerical Calculations in QCD and Soft-Collinear Effective Theory*, *DESY-17-099* (2018) . [pp. 22, 123, 135, 146, and 156]

[50] G. Sterman, *Mass divergences in annihilation processes. I. Origin and nature of divergences in cut vacuum polarization diagrams*, *Phys. Rev. D* **17** (1978) 2773. [p. 22]

[51] C. W. Bauer and I. W. Stewart, "The Soft-Collinear Effective Theory." `https://courses.edx.org/c4x/MITx/8.EFTx/asset/notes_scetnotes.pdf`. [p. 22]

[52] C. W. Bauer, D. Pirjol and I. W. Stewart, *Factorization and end point singularities in heavy-to-light decays*, *Phys. Rev. D* **67** (2003) 071502. [p. 26]

[53] I. Z. Rothstein and I. W. Stewart, *An effective field theory for forward scattering and factorization violation*, *Journal of High Energy Physics* **2016** (2016) . [p. 26]

[54] J. C. Collins, D. E. Soper and G. F. Sterman, *Transverse Momentum Distribution in Drell-Yan Pair and W and Z Boson Production*, *Nucl. Phys. B* **250** (1985) 199. [pp. 26, 103, 104, and 109]

[55] A. V. Manohar and I. W. Stewart, *The Zero-Bin and Mode Factorization in Quantum Field Theory*, *Phys. Rev. D* **76** (2007) 074002 [`hep-ph/0605001`]. [p. 29]

[56] C. W. Bauer and I. W. Stewart, *Invariant operators in collinear effective theory*, *Physics Letters B* **516** (2001) 134–142. [p. 29]

[57] C. W. Bauer, D. Pirjol and I. W. Stewart, *Power suppressed operators and gauge invariance in soft-collinear effective theory*, *Phys. Rev. D* **68** (2003) 034021. [pp. 30, 31, and 32]

[58] C. W. Bauer, D. Pirjol and I. W. Stewart, *Soft collinear factorization in effective field theory*, *Phys. Rev. D* **65** (2002) 054022 [`hep-ph/0109045`]. [pp. 30, 31, 34, 35, 36, 41, 42, 49, and 146]

[59] A. V. Manohar, T. Mehen, D. Pirjol and I. W. Stewart, *Reparameterization invariance for collinear operators*, *Physics Letters B* **539** (2002) 59–66. [pp. 31, 32, 52, and 53]

[60] T. Becher, A. Broggio and A. Ferroglia, *Introduction to Soft-Collinear Effective Theory*, vol. 896. Springer, 2015, 10.1007/978-3-319-14848-9, [`1410.1892`]. [p. 33]

[61] C. Arzt, *Reduced effective Lagrangians*, *Phys. Lett. B* **342** (1995) 189 [`hep-ph/9304230`]. [p. 36]

[62] C. W. Bauer, S. Fleming, C. Lee and G. Sterman, *Factorization of e^+e event shape distributions with hadronic final states in soft collinear effective theory*, *Physical Review D* **78** (2008) . [p. 39]

[63] S. Fleming, A. H. Hoang, S. Mantry and I. W. Stewart, *Jets from massive unstable particles: Top-mass determination*, *Physical Review D* **77** (2008) . [pp. 39 and 91]

[64] C. W. Bauer, S. Fleming, D. Pirjol, I. Z. Rothstein and I. W. Stewart, *Hard scattering factorization from effective field theory*, *Phys. Rev. D* **66** (2002) 014017 [hep-ph/0202088]. [pp. 39, 40, 42, and 146]

[65] I. W. Stewart, F. J. Tackmann and W. J. Waalewijn, *Factorization at the LHC: From PDFs to Initial State Jets*, *Phys. Rev. D* **81** (2010) 094035 [0910.0467]. [pp. 40, 51, 58, 86, 88, 89, 93, and 186]

[66] C. Marcantonini and I. W. Stewart, *Reparameterization Invariant Collinear Operators*, *Phys. Rev. D* **79** (2009) 065028 [0809.1093]. [pp. 40, 41, and 98]

[67] Y. L. Dokshitzer, A. Lucenti, G. Marchesini and G. P. Salam, *On the QCD analysis of jet broadening*, *Journal of High Energy Physics* **1998** (1998) 011–011. [p. 41]

[68] C. W. Bauer, D. Pirjol and I. W. Stewart, *Factorization and endpoint singularities in heavy to light decays*, *Phys. Rev. D* **67** (2003) 071502 [hep-ph/0211069]. [pp. 42 and 49]

[69] J.-Y. Chiu, A. Jain, D. Neill and I. Z. Rothstein, *A formalism for the systematic treatment of rapidity logarithms in quantum field theory*, *Journal of High Energy Physics* **2012** (2012) . [pp. 42, 43, 54, and 55]

[70] J.-y. Chiu, A. Jain, D. Neill and I. Z. Rothstein, *Rapidity renormalization group*, *Phys. Rev. Lett.* **108** (2012) 151601. [pp. 42, 43, and 55]

[71] T. Becher and M. Neubert, *Drell-Yan Production at Small q_T, Transverse Parton Distributions and the Collinear Anomaly*, *Eur. Phys. J. C* **71** (2011) 1665 [1007.4005]. [pp. 42, 46, 54, 103, and 104]

[72] J. Collins and F. Tkachov, *Breakdown of dimensional regularization in the sudakov problem*, *Physics Letters B* **294** (1992) 403–411. [p. 42]

[73] T. Becher and G. Bell, *Analytic regularization in soft-collinear effective theory*, *Physics Letters B* **713** (2012) 41–46. [p. 42]

[74] M. G. Echevarría, A. Idilbi and I. Scimemi, *Factorization theorem for Drell-Yan at low q_T and transverse-momentum distributions on-the-light-cone*, *Journal of High Energy Physics* **2012** (2012) . [p. 42]

[75] J.-y. Chiu, A. Fuhrer, A. H. Hoang, R. Kelley and A. V. Manohar, *Soft-collinear factorization and zero-bin subtractions*, *Physical Review D* **79** (2009) . [p. 42]

[76] Y. Li, D. Neill and H. X. Zhu, *An exponential regulator for rapidity divergences*, *Nucl. Phys. B* **960** (2020) 115193 [1604.00392]. [pp. 42, 98, 103, 104, 114, 115, 146, 193, and 195]

[77] P. Ciafaloni and D. Comelli, *Sudakov enhancement of electroweak corrections*, *Phys. Lett.* **B446** (1999) 278 [hep-ph/9809321]. [p. 45]

[78] V. S. Fadin, L. N. Lipatov, A. D. Martin and M. Melles, *Resummation of double logarithms in electroweak high-energy processes*, *Phys. Rev.* **D61** (2000) 094002 [hep-ph/9910338]. [p. 45]

[79] J. H. Kuhn, A. A. Penin and V. A. Smirnov, *Summing up subleading Sudakov logarithms*, *Eur. Phys. J.* **C17** (2000) 97 [hep-ph/9912503]. [p. 45]

[80] B. Jantzen, J. H. Kuhn, A. A. Penin and V. A. Smirnov, *Two-loop electroweak logarithms in four-fermion processes at high energy*, *Nucl. Phys.* **B731** (2005) 188 [hep-ph/0509157]. [p. 45]

[81] A. Denner, B. Jantzen and S. Pozzorini, *Two-loop electroweak next-to-leading logarithmic corrections to massless fermionic processes*, *Nucl. Phys.* **B761** (2007) 1 [hep-ph/0608326]. [p. 45]

[82] J.-y. Chiu, F. Golf, R. Kelley and A. V. Manohar, *Electroweak Corrections in High Energy Processes using Effective Field Theory*, *Phys. Rev.* **D77** (2008) 053004 [0712.0396]. [pp. 45 and 80]

[83] J.-y. Chiu, R. Kelley and A. V. Manohar, *Electroweak Corrections using Effective Field Theory: Applications to the LHC*, *Phys. Rev.* **D78** (2008) 073006 [0806.1240]. [pp. 45, 83, and 183]

[84] G. Bell, J. H. Kuhn and J. Rittinger, *Electroweak Sudakov Logarithms and Real Gauge-Boson Radiation in the TeV Region*, *Eur. Phys. J.* **C70** (2010) 659 [1004.4117]. [p. 45]

[85] T. Becher and X. Garcia i Tormo, *Electroweak Sudakov effects in W, Z and γ production at large transverse momentum*, *Phys. Rev.* **D88** (2013) 013009 [1305.4202]. [p. 45]

[86] J. R. Christiansen and T. Sjöstrand, *Weak Gauge Boson Radiation in Parton Showers*, *JHEP* **04** (2014) 115 [1401.5238]. [p. 45]

[87] F. Krauss, P. Petrov, M. Schoenherr and M. Spannowsky, *Measuring collinear W emissions inside jets*, *Phys. Rev.* **D89** (2014) 114006 [1403.4788]. [p. 45]

[88] S. Jadach, B. F. L. Ward, Z. A. Was and S. A. Yost, *KK MC-hh: Resumed exact $O(\alpha^2 L)$ EW corrections in a hadronic MC event generator*, *Phys. Rev.* **D94** (2016) 074006 [1608.01260]. [p. 45]

[89] C. W. Bauer, N. Ferland and B. R. Webber, *Standard Model Parton Distributions at Very High Energies*, *JHEP* **08** (2017) 036 [1703.08562]. [p. 45]

[90] A. V. Manohar and W. J. Waalewijn, *Electroweak Logarithms in Inclusive Cross Sections*, *JHEP* **08** (2018) 137 [1802.08687]. [p. 45]

[91] M. L. Mangano et al., *Physics at a 100 TeV pp Collider: Standard Model Processes*, *CERN Yellow Rep.* (2017) 1 [1607.01831]. [p. 45]

[92] ATLAS collaboration, *Measurement of the Z/γ^* boson transverse momentum distribution in pp collisions at $\sqrt{s}$ = 7 TeV with the ATLAS detector*, *JHEP* **09** (2014) 145 [1406.3660]. [p. 45]

[93] ATLAS collaboration, *Measurement of the transverse momentum and ϕ^*_η distributions of Drell-Yan lepton pairs in proton-proton collisions at $\sqrt{s} = 8$ TeV with the ATLAS detector*, *Eur. Phys. J.* **C76** (2016) 291 [1512.02192]. [p. 45]

[94] ATLAS collaboration, *Measurement of the W-boson mass in pp collisions at $\sqrt{s} = 7$ TeV with the ATLAS detector*, *Eur. Phys. J.* **C78** (2018) 110 [1701.07240]. [pp. 45 and 85]

[95] CMS collaboration, *Measurement of the differential and double-differential Drell-Yan cross sections in proton-proton collisions at $\sqrt{s}$ = 7 TeV*, *JHEP* **12** (2013) 030 [1310.7291]. [p. 45]

[96] CMS collaboration, *Measurement of the Z boson differential cross section in transverse momentum and rapidity in proton–proton collisions at 8 TeV*, *Phys. Lett. B* **749** (2015) 187 [1504.03511]. [p. 45]

[97] CMS collaboration, *Measurements of differential Z boson production cross sections in pp collisions with CMS at $\sqrt{s} = 13$* TeV, Tech. Rep. CMS-PAS-SMP-17-010, CERN, Geneva, 2019. [p. 45]

[98] S. Dittmaier, A. Huss and C. Schwinn, *Dominant mixed QCD-electroweak $O(\alpha_s\alpha)$ corrections to Drell–Yan processes in the resonance region*, *Nucl. Phys.* **B904** (2016) 216 [1511.08016]. [p. 45]

[99] S. Alioli et al., *Precision studies of observables in $pp \to W \to l\nu_l$ and $pp \to \gamma, Z \to l^+l^-$ processes at the LHC*, *Eur. Phys. J.* **C77** (2017) 280 [1606.02330]. [p. 45]

[100] C. M. Carloni Calame, M. Chiesa, H. Martinez, G. Montagna, O. Nicrosini, F. Piccinini et al., *Precision Measurement of the W-Boson Mass: Theoretical Contributions and Uncertainties*, *Phys. Rev.* **D96** (2017) 093005 [1612.02841]. [p. 45]

[101] S. Jadach, B. F. L. Ward, Z. A. Was and S. A. Yost, *Systematic Studies of Exact $\mathcal{O}(\alpha^2 L)$ CEEX EW Corrections in a Hadronic MC for Precision Z/γ^* Physics at LHC Energies*, *Phys. Rev.* **D99** (2019) 076016 [1707.06502]. [p. 45]

[102] M. Roth and S. Weinzierl, *QED corrections to the evolution of parton distributions*, *Phys. Lett.* **B590** (2004) 190 [hep-ph/0403200]. [p. 45]

[103] A. D. Martin, R. G. Roberts, W. J. Stirling and R. S. Thorne, *Parton distributions incorporating QED contributions*, *Eur. Phys. J.* **C39** (2005) 155 [hep-ph/0411040]. [p. 45]

[104] NNPDF collaboration, R. D. Ball, V. Bertone, S. Carrazza, L. Del Debbio, S. Forte, A. Guffanti et al., *Parton distributions with QED corrections*, *Nucl. Phys.* **B877** (2013) 290 [1308.0598]. [p. 45]

[105] D. de Florian, G. F. R. Sborlini and G. Rodrigo, *QED corrections to the Altarelli-Parisi splitting functions*, *Eur. Phys. J.* **C76** (2016) 282 [1512.00612]. [pp. 45 and 184]

[106] D. de Florian, G. F. R. Sborlini and G. Rodrigo, *Two-loop QED corrections to the Altarelli-Parisi splitting functions*, *JHEP* **10** (2016) 056 [1606.02887]. [pp. 45, 57, and 184]

[107] M. Mottaghizadeh, F. Taghavi Shahri and P. Eslami, *Analytical solutions of the QED⊗QCD DGLAP evolution equations based on the Mellin transform technique*, *Phys. Lett.* **B773** (2017) 375 [1707.00108]. [p. 45]

[108] D. de Florian, M. Der and I. Fabre, *QCD⊕QED NNLO corrections to Drell Yan production*, *Phys. Rev.* **D98** (2018) 094008 [1805.12214]. [pp. 46, 57, 183, and 184]

[109] A. H. Ajjath, A. Chakraborty, P. K. Dhani, P. Mukherjee, N. Rana, V. Ravindran et al., *NNLO QCD⊕QED corrections to Higgs production in bottom quark annihilation*, 1906.09028. [p. 46]

[110] R. Abbate, M. Fickinger, A. H. Hoang, V. Mateu and I. W. Stewart, *Thrust at N^3LL with Power Corrections and a Precision Global Fit for $\alpha_s(m_Z)$*, *Phys. Rev.* **D83** (2011) 074021 [1006.3080]. [pp. 46, 71, 85, and 91]

[111] L. Cieri, G. Ferrera and G. F. Sborlini, *Combining QED and QCD transverse-momentum resummation for Z boson production at hadron colliders*, *JHEP* **08** (2018) 165 [1805.11948]. [pp. 46 and 81]

[112] A. Bacchetta and M. G. Echevarria, *QCD×QED evolution of TMDs*, *Phys. Lett. B* **788** (2019) 280 [1810.02297]. [pp. 46, 50, and 184]

[113] M. Ebert, *Precision Predictions for Higgs Differential Distributions at the LHC*, Ph.D. thesis, Hamburg U., Hamburg, 2017. 10.3204/PUBDB-2017-08764. [pp. 46 and 54]

[114] J. Oredsson, "Transverse Momentum Dependent Soft Function in SCET to NNLO." http://particle.thep.lu.se/pub/Preprints/15/lu_tp_15_32.pdf. [pp. 46 and 54]

[115] T. Lübbert, J. Oredsson and M. Stahlhofen, *Rapidity renormalized TMD soft and beam functions at two loops*, *JHEP* **03** (2016) 168 [1602.01829]. [pp. 57, 104, 105, 107, 111, 116, 150, and 186]

[116] S. Moch, J. A. M. Vermaseren and A. Vogt, *The Quark form-factor at higher orders*, *JHEP* **08** (2005) 049 [hep-ph/0507039]. [pp. 57, 86, and 182]

[117] R. Brüser, Z. L. Liu and M. Stahlhofen, *Three-loop quark jet function*, *Physical Review Letters* **121** (2018) . [p. 57]

[118] I. W. Stewart, F. J. Tackmann and W. J. Waalewijn, *The Quark Beam Function at NNLL*, *JHEP* **09** (2010) 005 [1002.2213]. [pp. 57, 89, 91, 93, 96, and 185]

[119] Y. Li and H. X. Zhu, *Bootstrapping Rapidity Anomalous Dimensions for Transverse-Momentum Resummation*, *Phys. Rev. Lett.* **118** (2017) 022004 [1604.01404]. [pp. 57, 98, 104, 105, 106, 107, 115, 124, 150, 186, 193, and 195]

[120] A. A. Vladimirov, *Correspondence between Soft and Rapidity Anomalous Dimensions*, *Phys. Rev. Lett.* **118** (2017) 062001 [1610.05791]. [pp. 57, 105, 150, and 186]

[121] G. P. Korchemsky and A. V. Radyushkin, *Renormalization of the Wilson Loops Beyond the Leading Order*, *Nucl. Phys.* **B283** (1987) 342. [pp. 57, 150, and 181]

[122] J. Henn, A. V. Smirnov, V. A. Smirnov, M. Steinhauser and R. N. Lee, *Four-loop photon quark form factor and cusp anomalous dimension in the large-N_c limit of QCD*, *JHEP* **03** (2017) 139 [1612.04389]. [p. 57]

[123] R. N. Lee, A. V. Smirnov, V. A. Smirnov and M. Steinhauser, *Four-loop quark form factor with quartic fundamental colour factor*, *JHEP* **02** (2019) 172 [1901.02898]. [pp. 57, 150, and 181]

[124] J. Henn, T. Peraro, M. Stahlhofen and P. Wasser, *Matter dependence of the four-loop cusp anomalous dimension*, *Phys. Rev. Lett.* **122** (2019) 201602 [1901.03693]. [pp. 57, 150, and 181]

[125] R. Brüser, A. Grozin, J. M. Henn and M. Stahlhofen, *Matter dependence of the four-loop QCD cusp anomalous dimension: from small angles to all angles*, *JHEP* **05** (2019) 186 [1902.05076]. [pp. 57, 150, and 181]

[126] J. M. Henn, G. P. Korchemsky and B. Mistlberger, *The full four-loop cusp anomalous dimension in $\mathcal{N} = 4$ super Yang-Mills and QCD*, *JHEP* **04** (2020) 018 [1911.10174]. [pp. 57 and 150]

[127] A. von Manteuffel, E. Panzer and R. M. Schabinger, *Analytic four-loop anomalous dimensions in massless QCD from form factors*, *Phys. Rev. Lett.* **124** (2020) 162001 [2002.04617]. [pp. 57 and 150]

[128] A. Vogt, S. Moch and J. A. M. Vermaseren, *The Three-loop splitting functions in QCD: The Singlet case*, *Nucl. Phys.* **B691** (2004) 129 [hep-ph/0404111]. [pp. 57, 150, 179, and 181]

[129] S. Moch, J. A. M. Vermaseren and A. Vogt, *The Three loop splitting functions in QCD: The Nonsinglet case*, *Nucl. Phys.* **B688** (2004) 101 [hep-ph/0403192]. [pp. 57, 179, and 181]

[130] S. Moch, B. Ruijl, T. Ueda, J. Vermaseren and A. Vogt, *Four-Loop Non-Singlet Splitting Functions in the Planar Limit and Beyond*, *JHEP* **10** (2017) 041 [1707.08315]. [pp. 57 and 181]

[131] O. V. Tarasov, A. A. Vladimirov and A. Yu. Zharkov, *The Gell-Mann-Low Function of QCD in the Three Loop Approximation*, *Phys. Lett.* **93B** (1980) 429. [pp. 57, 150, and 181]

[132] S. A. Larin and J. A. M. Vermaseren, *The Three loop QCD Beta function and anomalous dimensions*, *Phys. Lett.* **B303** (1993) 334 [hep-ph/9302208]. [pp. 57, 150, and 181]

[133] T. van Ritbergen, J. A. M. Vermaseren and S. A. Larin, *The Four loop beta function in quantum chromodynamics*, *Phys. Lett.* **B400** (1997) 379 [hep-ph/9701390]. [pp. 57, 150, and 181]

[134] M. Czakon, *The Four-loop QCD beta-function and anomalous dimensions*, *Nucl. Phys.* **B710** (2005) 485 [hep-ph/0411261]. [pp. 57, 150, and 181]

[135] M. A. Ebert, J. K. L. Michel and F. J. Tackmann, *Resummation Improved Rapidity Spectrum for Gluon Fusion Higgs Production*, *JHEP* **05** (2017) 088 [1702.00794]. [pp. 57, 71, 85, 86, 147, 148, 149, 150, 153, 154, 155, and 168]

[136] P. A. Baikov, K. G. Chetyrkin, A. V. Smirnov, V. A. Smirnov and M. Steinhauser, *Quark and gluon form factors to three loops*, *Phys. Rev. Lett.* **102** (2009) 212002 [0902.3519]. [pp. 57, 86, and 150]

[137] R. N. Lee, A. V. Smirnov and V. A. Smirnov, *Analytic Results for Massless Three-Loop Form Factors*, *JHEP* **04** (2010) 020 [1001.2887]. [pp. 57, 86, and 150]

[138] T. Gehrmann, E. W. N. Glover, T. Huber, N. Ikizlerli and C. Studerus, *Calculation of the quark and gluon form factors to three loops in QCD*, *JHEP* **06** (2010) 094 [1004.3653]. [pp. 57, 86, and 150]

[139] M. A. Ebert, B. Mistlberger and G. Vita, *Transverse momentum dependent PDFs at N^3LO*, *JHEP* **09** (2020) 146 [2006.05329]. [pp. 57, 87, 104, 111, 116, 118, 124, 135, 138, and 150]

[140] M.-x. Luo, T.-Z. Yang, H. X. Zhu and Y. J. Zhu, *Unpolarized Quark and Gluon TMD PDFs and FFs at N^3LO*, 2012.03256. [pp. 57, 104, 111, 116, 118, 124, 138, and 150]

[141] A. H. Ajjath, P. Mukherjee and V. Ravindran, *Infrared structure of $SU(N) \times U(1)$ gauge theory to three loops*, *JHEP* **08** (2020) 156 [1912.13386]. [pp. 57 and 184]

[142] C. F. Berger, C. Marcantonini, I. W. Stewart, F. J. Tackmann and W. J. Waalewijn, *Higgs Production with a Central Jet Veto at NNLL+NNLO*, *JHEP* **04** (2011) 092 [1012.4480]. [pp. 58, 71, 88, 91, 93, 94, 96, 149, 150, and 185]

[143] L. Mihaila, *Three-loop gauge beta function in non-simple gauge groups*, *PoS* **RADCOR2013** (2013) 060. [pp. 63, 189, and 190]

[144] M. A. Ebert and F. J. Tackmann, *Resummation of Transverse Momentum Distributions in Distribution Space*, *JHEP* **02** (2017) 110 [1611.08610]. [pp. 65, 89, 90, 147, 177, 178, and 194]

[145] S. Fleming, A. H. Hoang, S. Mantry and I. W. Stewart, *Top Jets in the Peak Region: Factorization Analysis with NLL Resummation*, *Phys. Rev.* **D77** (2008) 114003 [0711.2079]. [pp. 71 and 89]

[146] Z. Ligeti, I. W. Stewart and F. J. Tackmann, *Treating the b quark distribution function with reliable uncertainties*, *Phys. Rev.* **D78** (2008) 114014 [0807.1926]. [pp. 71, 90, and 176]

[147] I. W. Stewart, F. J. Tackmann, J. R. Walsh and S. Zuberi, *Jet p_T resummation in Higgs production at NNLL′+NNLO*, *Phys. Rev.* **D89** (2014) 054001 [1307.1808]. [pp. 71, 87, 149, 151, and 154]

[148] L. G. Almeida, S. D. Ellis, C. Lee, G. Sterman, I. Sung and J. R. Walsh, *Comparing and counting logs in direct and effective methods of QCD resummation*, *JHEP* **04** (2014) 174 [1401.4460]. [p. 71]

[149] A. Hornig, Y. Makris and T. Mehen, *Jet Shapes in Dijet Events at the LHC in SCET*, *JHEP* **04** (2016) 097 [1601.01319]. [p. 71]

[150] D. Kang, C. Lee and V. Vaidya, *A fast and accurate method for perturbative resummation of transverse momentum-dependent observables*, *JHEP* **04** (2018) 149 [1710.00078]. [p. 71]

[151] X. Chen, T. Gehrmann, E. W. N. Glover, A. Huss, Y. Li, D. Neill et al., *Precise QCD Description of the Higgs Boson Transverse Momentum Spectrum*, *Phys. Lett.* **B788** (2019) 425 [1805.00736]. [pp. 71, 85, 140, 156, and 159]

[152] M. Procura, W. J. Waalewijn and L. Zeune, *Joint resummation of two angularities at next-to-next-to-leading logarithmic order*, *JHEP* **10** (2018) 098 [1806.10622]. [p. 71]

[153] G. Bell, A. Hornig, C. Lee and J. Talbert, *e^+e^- angularity distributions at NNLL′ accuracy*, *JHEP* **01** (2019) 147 [1808.07867]. [pp. 71 and 75]

[154] M. Baumgart, T. Cohen, E. Moulin, I. Moult, L. Rinchiuso, N. L. Rodd et al., *Precision Photon Spectra for Wino Annihilation*, *JHEP* **01** (2019) 036 [1808.08956]. [p. 71]

[155] G. Lustermans, J. K. L. Michel, F. J. Tackmann and W. J. Waalewijn, *Joint two-dimensional resummation in q_T and 0-jettiness at NNLL*, *JHEP* **03** (2019) 124 [1901.03331]. [pp. 71, 87, 121, 150, and 151]

[156] S. Catani, D. de Florian, M. Grazzini and P. Nason, *Soft gluon resummation for Higgs boson production at hadron colliders*, *JHEP* **07** (2003) 028 [hep-ph/0306211]. [pp. 73 and 74]

[157] W. Bizon, P. F. Monni, E. Re, L. Rottoli and P. Torrielli, *Momentum-space resummation for transverse observables and the Higgs $p_\perp$ at N^3LL+NNLO*, *JHEP* **02** (2018) 108 [1705.09127]. [pp. 73, 74, and 140]

[158] S. Catani, D. de Florian and M. Grazzini, *Universality of nonleading logarithmic contributions in transverse momentum distributions*, *Nucl. Phys.* **B596** (2001) 299 [hep-ph/0008184]. [pp. 73, 74, 103, and 104]

[159] G. Bozzi, S. Catani, D. de Florian and M. Grazzini, *Transverse-momentum resummation and the spectrum of the Higgs boson at the LHC*, *Nucl. Phys.* **B737** (2006) 73 [hep-ph/0508068]. [pp. 73, 74, 123, 124, and 140]

[160] G. Bozzi, S. Catani, G. Ferrera, D. de Florian and M. Grazzini, *Production of Drell-Yan lepton pairs in hadron collisions: Transverse-momentum resummation at next-to-next-to-leading logarithmic accuracy*, *Phys. Lett. B* **696** (2011) 207 [1007.2351]. [pp. 73 and 74]

[161] A. Banfi, P. F. Monni, G. P. Salam and G. Zanderighi, *Higgs and Z-boson production with a jet veto*, *Phys. Rev. Lett.* **109** (2012) 202001 [1206.4998]. [pp. 73 and 74]

[162] A. Banfi, H. McAslan, P. F. Monni and G. Zanderighi, *A general method for the resummation of event-shape distributions in e^+e^- annihilation*, *JHEP* **05** (2015) 102 [1412.2126]. [pp. 73 and 74]

[163] J. Michel, *Factorization and Resummation for Precision Physics at the LHC*, Ph.D. thesis, Hamburg U., 2020. 10.3204/PUBDB-2020-03616. [pp. 85 and 191]

[164] ATLAS collaboration, *Measurement of the Drell-Yan triple-differential cross section in pp collisions at $\sqrt{s} = 8$ TeV*, *JHEP* **12** (2017) 059 [1710.05167]. [p. 85]

[165] CMS collaboration, *Measurement of the transverse momentum spectra of weak vector bosons produced in proton-proton collisions at $\sqrt{s} = 8$ TeV*, *JHEP* **02** (2017) 096 [1606.05864]. [p. 85]

[166] CMS collaboration, *Measurements of differential Z boson production cross sections in pp collisions with CMS at* $\sqrt{s} = 13$ TeV, Tech. Rep. CMS-PAS-SMP-17-010, CERN, Geneva, 2019. [p. 85]

[167] CMS collaboration, *Combined measurements of Higgs boson couplings in proton-proton collisions at* $\sqrt{s} = 13$ *TeV*, *Eur. Phys. J.* **C79** (2019) 421 [1809.10733]. [p. 85]

[168] ATLAS collaboration, *Combined measurements of Higgs boson production and decay using up to* 80 fb^{-1} *of proton-proton collision data at* $\sqrt{s} = 13$ *TeV collected with the ATLAS experiment*, Tech. Rep. ATLAS-CONF-2019-005, CERN, Geneva, 2019. [p. 85]

[169] ATLAS collaboration, *Measurements and interpretations of Higgs-boson fiducial cross sections in the diphoton decay channel using 139* fb^{-1} *of pp collision data at* $\sqrt{s} = 13$ *TeV with the ATLAS detector*, Tech. Rep. ATLAS-CONF-2019-029, CERN, Geneva, 2019. [p. 85]

[170] ATLAS collaboration, *Measurement of fiducial and differential* W^+W^- *production cross-sections at* $\sqrt{s} = 13$ *TeV with the ATLAS detector*, *Eur. Phys. J.* **C79** (2019) 884 [1905.04242]. [p. 85]

[171] ATLAS collaboration, *Measurement of ZZ production in the* $\ell\ell\nu\nu$ *final state with the ATLAS detector in pp collisions at* $\sqrt{s} = 13$ *TeV*, *JHEP* **10** (2019) 127 [1905.07163]. [p. 85]

[172] CMS collaboration, *Search for anomalous triple gauge couplings in WW and WZ production in lepton + jet events in proton-proton collisions at* $\sqrt{s} = 13$ *TeV*, *JHEP* **12** (2019) 062 [1907.08354]. [p. 85]

[173] C. Anastasiou, C. Duhr, F. Dulat, E. Furlan, T. Gehrmann, F. Herzog et al., *Higgs boson gluon-fusion production at threshold in* N^3LO *QCD*, *Phys. Lett.* **B737** (2014) 325 [1403.4616]. [pp. 85, 98, 193, and 194]

[174] Y. Li, A. von Manteuffel, R. M. Schabinger and H. X. Zhu, *Soft-virtual corrections to Higgs production at* N^3LO, *Phys. Rev.* **D91** (2015) 036008 [1412.2771]. [pp. 85, 98, 193, and 194]

[175] T. Ahmed, M. Mahakhud, N. Rana and V. Ravindran, *Drell-Yan Production at Threshold to Third Order in QCD*, *Phys. Rev. Lett.* **113** (2014) 112002 [1404.0366]. [p. 85]

[176] T. Ahmed, M. K. Mandal, N. Rana and V. Ravindran, *Rapidity Distributions in Drell-Yan and Higgs Productions at Threshold to Third Order in QCD*, *Phys. Rev. Lett.* **113** (2014) 212003 [1404.6504]. [pp. 85, 98, and 193]

[177] C. Anastasiou, C. Duhr, F. Dulat, F. Herzog and B. Mistlberger, *Higgs Boson Gluon-Fusion Production in QCD at Three Loops*, *Phys. Rev. Lett.* **114** (2015) 212001 [1503.06056]. [p. 85]

[178] F. A. Dreyer and A. Karlberg, *Vector-Boson Fusion Higgs Production at Three Loops in QCD*, *Phys. Rev. Lett.* **117** (2016) 072001 [1606.00840]. [p. 85]

[179] B. Mistlberger, *Higgs boson production at hadron colliders at N^3LO in QCD*, *JHEP* **05** (2018) 028 [1802.00833]. [pp. 85, 139, and 160]

[180] L. Cieri, X. Chen, T. Gehrmann, E. W. N. Glover and A. Huss, *Higgs boson production at the LHC using the q_T subtraction formalism at N^3LO QCD*, *JHEP* **02** (2019) 096 [1807.11501]. [pp. 85, 111, 119, 121, 124, and 140]

[181] F. Dulat, B. Mistlberger and A. Pelloni, *Precision predictions at N^3LO for the Higgs boson rapidity distribution at the LHC*, *Phys. Rev.* **D99** (2019) 034004 [1810.09462]. [pp. 85 and 98]

[182] C. Duhr, F. Dulat and B. Mistlberger, *Higgs Boson Production in Bottom-Quark Fusion to Third Order in the Strong Coupling*, *Phys. Rev. Lett.* **125** (2020) 051804 [1904.09990]. [p. 85]

[183] C. Duhr, F. Dulat and B. Mistlberger, *Charged current Drell-Yan production at N^3LO*, *JHEP* **11** (2020) 143 [2007.13313]. [p. 85]

[184] X. Chen, X. Chen, T. Gehrmann, E. W. N. Glover, A. Huss, B. Mistlberger et al., *Fully Differential Higgs Boson Production to Third Order in QCD*, 2102.07607. [p. 85]

[185] C. Duhr, F. Dulat and B. Mistlberger, *Drell-Yan Cross Section to Third Order in the Strong Coupling Constant*, *Phys. Rev. Lett.* **125** (2020) 172001 [2001.07717]. [p. 85]

[186] T. Becher and M. D. Schwartz, *A precise determination of α_s from LEP thrust data using effective field theory*, *JHEP* **07** (2008) 034 [0803.0342]. [p. 85]

[187] A. H. Hoang, D. W. Kolodrubetz, V. Mateu and I. W. Stewart, *Precise determination of α_s from the C-parameter distribution*, *Phys. Rev.* **D91** (2015) 094018 [1501.04111]. [p. 85]

[188] M. Bonvini and S. Marzani, *Resummed Higgs cross section at N^3LL*, *JHEP* **09** (2014) 007 [1405.3654]. [p. 85]

[189] T. Schmidt and M. Spira, *Higgs Boson Production via Gluon Fusion: Soft-Gluon Resummation including Mass Effects*, *Phys. Rev.* **D93** (2016) 014022 [1509.00195]. [p. 85]

[190] A. H. Ajjath, A. Chakraborty, G. Das, P. Mukherjee and V. Ravindran, *Resummed prediction for Higgs boson production through $b\bar{b}$ annihilation at N^3LL*, *JHEP* **11** (2019) 006 [1905.03771]. [p. 85]

[191] W. Bizon, X. Chen, A. Gehrmann-De Ridder, T. Gehrmann, N. Glover, A. Huss et al., *Fiducial distributions in Higgs and Drell-Yan production at N^3LL+NNLO*, *JHEP* **12** (2018) 132 [1805.05916]. [pp. 85, 140, 156, and 159]

[192] M. A. Ebert, B. Mistlberger and G. Vita, *The Energy-Energy Correlation in the back-to-back limit at N^3LO and N^3LL'*, 2012.07859. [p. 85]

[193] A. Gehrmann-De Ridder, T. Gehrmann and E. W. N. Glover, *Antenna subtraction at NNLO*, *JHEP* **09** (2005) 056 [hep-ph/0505111]. [p. 85]

[194] J. Currie, E. W. N. Glover and S. Wells, *Infrared Structure at NNLO Using Antenna Subtraction*, *JHEP* **04** (2013) 066 [1301.4693]. [p. 85]

[195] M. Czakon, *A novel subtraction scheme for double-real radiation at NNLO*, *Phys. Lett.* **B693** (2010) 259 [1005.0274]. [p. 85]

[196] M. Czakon and D. Heymes, *Four-dimensional formulation of the sector-improved residue subtraction scheme*, *Nucl. Phys.* **B890** (2014) 152 [1408.2500]. [p. 85]

[197] R. Boughezal, K. Melnikov and F. Petriello, *A subtraction scheme for NNLO computations*, *Phys. Rev.* **D85** (2012) 034025 [1111.7041]. [p. 85]

[198] S. Catani and M. Grazzini, *An NNLO subtraction formalism in hadron collisions and its application to Higgs boson production at the LHC*, *Phys. Rev. Lett.* **98** (2007) 222002 [hep-ph/0703012]. [pp. 85, 120, 123, and 165]

[199] V. Del Duca, C. Duhr, G. Somogyi, F. Tramontano and Z. Trócsányi, *Higgs boson decay into b-quarks at NNLO accuracy*, *JHEP* **04** (2015) 036 [1501.07226]. [p. 85]

[200] V. Del Duca, C. Duhr, A. Kardos, G. Somogyi and Z. Trócsányi, *Three-Jet Production in Electron-Positron Collisions at Next-to-Next-to-Leading Order Accuracy*, *Phys. Rev. Lett.* **117** (2016) 152004 [1603.08927]. [p. 85]

[201] R. Boughezal, C. Focke, X. Liu and F. Petriello, *W-boson production in association with a jet at next-to-next-to-leading order in perturbative QCD*, *Phys. Rev. Lett.* **115** (2015) 062002 [1504.02131]. [pp. 85, 120, and 121]

[202] J. Gaunt, M. Stahlhofen, F. J. Tackmann and J. R. Walsh, *N-jettiness Subtractions for NNLO QCD Calculations*, *JHEP* **09** (2015) 058 [1505.04794]. [pp. 85, 90, 94, 120, 121, and 123]

[203] M. Cacciari, F. A. Dreyer, A. Karlberg, G. P. Salam and G. Zanderighi, *Fully Differential Vector-Boson-Fusion Higgs Production at Next-to-Next-to-Leading Order*, *Phys. Rev. Lett.* **115** (2015) 082002 [1506.02660]. [p. 85]

[204] F. Caola, K. Melnikov and R. Röntsch, *Nested soft-collinear subtractions in NNLO QCD computations*, *Eur. Phys. J.* **C77** (2017) 248 [1702.01352]. [p. 85]

[205] F. Caola, K. Melnikov and R. Röntsch, *Analytic results for color-singlet production at NNLO QCD with the nested soft-collinear subtraction scheme*, *Eur. Phys. J.* **C79** (2019) 386 [1902.02081]. [p. 85]

[206] F. Herzog, *Geometric IR subtraction for final state real radiation*, *JHEP* **08** (2018) 006 [1804.07949]. [p. 85]

[207] L. Magnea, E. Maina, G. Pelliccioli, C. Signorile-Signorile, P. Torrielli and S. Uccirati, *Local analytic sector subtraction at NNLO*, *JHEP* **12** (2018) 107 [1806.09570]. [p. 85]

[208] L. Magnea, E. Maina, G. Pelliccioli, C. Signorile-Signorile, P. Torrielli and S. Uccirati, *Factorisation and Subtraction beyond NLO*, *JHEP* **12** (2018) 062 [1809.05444]. [p. 85]

[209] G. Kramer and B. Lampe, *Two Jet Cross-Section in e^+e^- Annihilation*, *Z. Phys.* **C34** (1987) 497. [pp. 86 and 182]

[210] T. Matsuura and W. L. van Neerven, *Second Order Logarithmic Corrections to the Drell-Yan Cross-section*, *Z. Phys.* **C38** (1988) 623. [pp. 86 and 182]

[211] T. Matsuura, S. C. van der Marck and W. L. van Neerven, *The Calculation of the Second Order Soft and Virtual Contributions to the Drell-Yan Cross-Section*, *Nucl. Phys.* **B319** (1989) 570. [pp. 86 and 182]

[212] R. V. Harlander, *Virtual corrections to $gg \to H$ to two loops in the heavy top limit*, *Phys. Lett.* **B492** (2000) 74 [hep-ph/0007289]. [pp. 86, 150, and 182]

[213] R. V. Harlander and W. B. Kilgore, *Higgs boson production in bottom quark fusion at next-to-next-to leading order*, *Phys. Rev.* **D68** (2003) 013001 [hep-ph/0304035]. [p. 86]

[214] T. Gehrmann, T. Huber and D. Maitre, *Two-loop quark and gluon form-factors in dimensional regularisation*, *Phys. Lett.* **B622** (2005) 295 [hep-ph/0507061]. [pp. 86 and 182]

[215] S. Moch, J. A. M. Vermaseren and A. Vogt, *Three-loop results for quark and gluon form-factors*, *Phys. Lett.* **B625** (2005) 245 [hep-ph/0508055]. [pp. 86, 150, and 182]

[216] V. Ravindran, *Higher-order threshold effects to inclusive processes in QCD*, *Nucl. Phys.* **B752** (2006) 173 [hep-ph/0603041]. [p. 86]

[217] C. Anastasiou, F. Herzog and A. Lazopoulos, *The fully differential decay rate of a Higgs boson to bottom-quarks at NNLO in QCD*, *JHEP* **03** (2012) 035 [1110.2368]. [p. 86]

[218] T. Gehrmann and D. Kara, *The $Hb\bar{b}$ form factor to three loops in QCD*, *JHEP* **09** (2014) 174 [1407.8114]. [p. 86]

[219] T. T. Jouttenus, I. W. Stewart, F. J. Tackmann and W. J. Waalewijn, *The Soft Function for Exclusive N-Jet Production at Hadron Colliders*, *Phys. Rev.* **D83** (2011) 114030 [1102.4344]. [pp. 87 and 88]

[220] T. Kasemets, W. J. Waalewijn and L. Zeune, *Calculating Soft Radiation at One Loop*, *JHEP* **03** (2016) 153 [1512.00857]. [p. 87]

[221] D. Bertolini, D. Kolodrubetz, D. Neill, P. Pietrulewicz, I. W. Stewart, F. J. Tackmann et al., *Soft Functions for Generic Jet Algorithms and Observables at Hadron Colliders*, *JHEP* **07** (2017) 099 [1704.08262]. [p. 87]

[222] G. Bell, R. Rahn and J. Talbert, *Generic dijet soft functions at two-loop order: correlated emissions*, *JHEP* **07** (2019) 101 [1812.08690]. [p. 87]

[223] A. Jain, M. Procura and W. J. Waalewijn, *Fully-Unintegrated Parton Distribution and Fragmentation Functions at Perturbative k_T*, *JHEP* **04** (2012) 132 [1110.0839]. [p. 87]

[224] M. Procura, W. J. Waalewijn and L. Zeune, *Resummation of Double-Differential Cross Sections and Fully-Unintegrated Parton Distribution Functions*, *JHEP* **02** (2015) 117 [1410.6483]. [pp. 87, 114, and 121]

[225] J. R. Gaunt and M. Stahlhofen, *The Fully-Differential Quark Beam Function at NNLO*, *JHEP* **12** (2014) 146 [1409.8281]. [p. 87]

[226] T. Becher, M. Neubert and L. Rothen, *Factorization and N^3LL_p+NNLO predictions for the Higgs cross section with a jet veto*, *JHEP* **10** (2013) 125 [1307.0025]. [p. 87]

[227] S. Gangal, J. R. Gaunt, M. Stahlhofen and F. J. Tackmann, *Two-Loop Beam and Soft Functions for Rapidity-Dependent Jet Vetoes*, *JHEP* **02** (2017) 026 [1608.01999]. [p. 87]

[228] J. K. L. Michel, P. Pietrulewicz and F. J. Tackmann, *Jet Veto Resummation with Jet Rapidity Cuts*, *JHEP* **04** (2019) 142 [1810.12911]. [p. 87]

[229] P. Pietrulewicz, D. Samitz, A. Spiering and F. J. Tackmann, *Factorization and Resummation for Massive Quark Effects in Exclusive Drell-Yan*, *JHEP* **08** (2017) 114 [1703.09702]. [p. 87]

[230] M. A. Ebert, B. Mistlberger and G. Vita, *N-jettiness beam functions at N^3LO*, *JHEP* **09** (2020) 143 [2006.03056]. [pp. 87 and 124]

[231] M.-x. Luo, T.-Z. Yang, H. X. Zhu and Y. J. Zhu, *Quark Transverse Parton Distribution at the Next-to-Next-to-Next-to-Leading Order*, *Phys. Rev. Lett.* **124** (2020) 092001 [1912.05778]. [pp. 87, 104, 111, 116, 118, 124, and 138]

[232] I. W. Stewart, F. J. Tackmann and W. J. Waalewijn, *N-Jettiness: An Inclusive Event Shape to Veto Jets*, *Phys. Rev. Lett.* **105** (2010) 092002 [1004.2489]. [pp. 88 and 93]

[233] J. R. Gaunt, *Glauber Gluons and Multiple Parton Interactions*, *JHEP* **07** (2014) 110 [1405.2080]. [p. 88]

[234] M. Zeng, *Drell-Yan process with jet vetoes: breaking of generalized factorization*, *JHEP* **10** (2015) 189 [1507.01652]. [p. 88]

[235] M. D. Schwartz, *Resummation and NLO matching of event shapes with effective field theory*, *Phys. Rev.* **D77** (2008) 014026 [0709.2709]. [p. 89]

[236] R. Kelley, M. D. Schwartz, R. M. Schabinger and H. X. Zhu, *The two-loop hemisphere soft function*, *Phys. Rev.* **D84** (2011) 045022 [1105.3676]. [pp. 89 and 186]

[237] P. F. Monni, T. Gehrmann and G. Luisoni, *Two-Loop Soft Corrections and Resummation of the Thrust Distribution in the Dijet Region*, *JHEP* **08** (2011) 010 [1105.4560]. [pp. 89 and 186]

[238] A. Hornig, C. Lee, I. W. Stewart, J. R. Walsh and S. Zuberi, *Non-global Structure of the $O(\alpha_s^2)$ Dijet Soft Function*, *JHEP* **08** (2011) 054 [1105.4628]. [pp. 89 and 186]

[239] D. Kang, O. Z. Labun and C. Lee, *Equality of hemisphere soft functions for e^+e^-, DIS and pp collisions at $\mathcal{O}(\alpha_s^2)$*, *Phys. Lett.* **B748** (2015) 45 [1504.04006]. [pp. 89 and 186]

[240] D. Kang, C. Lee and I. W. Stewart, *Using 1-Jettiness to Measure 2 Jets in DIS 3 Ways*, *Phys. Rev.* **D88** (2013) 054004 [1303.6952]. [p. 93]

[241] G. Lustermans, J. K. L. Michel and F. J. Tackmann, *Generalized Threshold Factorization with Full Collinear Dynamics*, 1908.00985. [pp. 93, 97, 98, 99, and 194]

[242] J. R. Gaunt, M. Stahlhofen and F. J. Tackmann, *The Quark Beam Function at Two Loops*, *JHEP* **04** (2014) 113 [1401.5478]. [pp. 93, 94, 97, and 99]

[243] J. Gaunt, M. Stahlhofen and F. J. Tackmann, *The Gluon Beam Function at Two Loops*, *JHEP* **08** (2014) 020 [1405.1044]. [pp. 93, 94, 97, and 99]

[244] M. A. Ebert, B. Mistlberger and G. Vita, *N-jettiness beam functions at N3LO*, *Journal of High Energy Physics* **2020** (2020) . [pp. 93, 99, 102, and 138]

[245] M. Höschele, J. Hoff, A. Pak, M. Steinhauser and T. Ueda, *MT: A Mathematica package to compute convolutions*, *Comput. Phys. Commun.* **185** (2014) 528 [1307.6925]. [pp. 95 and 111]

[246] L. A. Harland-Lang, A. D. Martin, P. Motylinski and R. S. Thorne, *Parton distributions in the LHC era: MMHT 2014 PDFs*, *Eur. Phys. J.* **C75** (2015) 204 [1412.3989]. [pp. 97 and 113]

[247] S. Catani and L. Trentadue, *Resummation of the QCD Perturbative Series for Hard Processes*, *Nucl. Phys.* **B327** (1989) 323. [p. 98]

[248] V. Ravindran, J. Smith and W. L. van Neerven, *QCD threshold corrections to di-lepton and Higgs rapidity distributions beyond N^2 LO*, *Nucl. Phys.* **B767** (2007) 100 [hep-ph/0608308]. [pp. 98 and 193]

[249] D. Westmark and J. F. Owens, *Enhanced threshold resummation formalism for lepton pair production and its effects in the determination of parton distribution functions*, *Phys. Rev.* **D95** (2017) 056024 [1701.06716]. [p. 98]

[250] P. Banerjee, G. Das, P. K. Dhani and V. Ravindran, *Threshold resummation of the rapidity distribution for Higgs production at NNLO+NNLL*, *Phys. Rev.* **D97** (2018) 054024 [1708.05706]. [p. 98]

[251] P. Banerjee, G. Das, P. K. Dhani and V. Ravindran, *Threshold resummation of the rapidity distribution for Drell-Yan production at NNLO+NNLL*, *Phys. Rev.* **D98** (2018) 054018 [1805.01186]. [p. 98]

[252] A. V. Manohar, T. Mehen, D. Pirjol and I. W. Stewart, *Reparameterization invariance for collinear operators*, *Phys. Lett.* **B539** (2002) 59 [hep-ph/0204229]. [p. 98]

[253] M. Procura and W. J. Waalewijn, *Fragmentation in Jets: Cone and Threshold Effects*, *Phys. Rev.* **D85** (2012) 114041 [1111.6605]. [p. 99]

[254] J. C. Collins and D. E. Soper, *Back-To-Back Jets in QCD*, *Nucl. Phys.* **B193** (1981) 381. [pp. 103, 104, and 150]

[255] J. C. Collins and D. E. Soper, *Back-To-Back Jets: Fourier Transform from B to K-Transverse*, *Nucl. Phys.* **B197** (1982) 446. [pp. 103, 104, and 150]

[256] D. de Florian and M. Grazzini, *The Structure of large logarithmic corrections at small transverse momentum in hadronic collisions*, *Nucl. Phys.* **B616** (2001) 247 [hep-ph/0108273]. [pp. 103 and 104]

[257] S. Catani and M. Grazzini, *QCD transverse-momentum resummation in gluon fusion processes*, *Nucl. Phys.* **B845** (2011) 297 [1011.3918]. [pp. 103 and 104]

[258] J. Collins, *Foundations of perturbative QCD*, Cambridge monographs on particle physics, nuclear physics, and cosmology. Cambridge Univ. Press, New York, NY, 2011. [pp. 103 and 104]

[259] M. G. Echevarria, A. Idilbi and I. Scimemi, *Factorization Theorem For Drell-Yan At Low q_T And Transverse Momentum Distributions On-The-Light-Cone*, *JHEP* **07** (2012) 002 [1111.4996]. [pp. 103 and 104]

[260] J.-Y. Chiu, A. Jain, D. Neill and I. Z. Rothstein, *A Formalism for the Systematic Treatment of Rapidity Logarithms in Quantum Field Theory*, *JHEP* **05** (2012) 084 [1202.0814]. [pp. 103, 104, and 146]

[261] M. A. Ebert and F. J. Tackmann, *Impact of isolation and fiducial cuts on q_T and N-jettiness subtractions*, *JHEP* **03** (2020) 158 [1911.08486]. [pp. 103, 122, 140, 144, 145, and 166]

[262] M. A. Ebert, J. K. Michel, I. W. Stewart and F. J. Tackmann, *Drell-Yan q_T Resummation of Fiducial Power Corrections at N^3LL*, 2006.11382. [pp. 103, 122, 140, 144, 145, 146, 148, 150, 151, 153, 156, and 166]

[263] J.-y. Chiu, A. Jain, D. Neill and I. Z. Rothstein, *The Rapidity Renormalization Group*, *Phys. Rev. Lett.* **108** (2012) 151601 [1104.0881]. [pp. 104 and 146]

[264] M. G. A. Buffing, Z.-B. Kang, K. Lee and X. Liu, *A transverse momentum dependent framework for back-to-back photon+jet production*, 1812.07549. [p. 104]

[265] Y.-T. Chien, D. Y. Shao and B. Wu, *Resummation of Boson-Jet Correlation at Hadron Colliders*, *JHEP* **11** (2019) 025 [1905.01335]. [p. 104]

[266] S. Catani and M. Grazzini, *Higgs Boson Production at Hadron Colliders: Hard-Collinear Coefficients at the NNLO*, *Eur. Phys. J.* **C72** (2012) 2013 [1106.4652]. [p. 104]

[267] S. Catani, L. Cieri, D. de Florian, G. Ferrera and M. Grazzini, *Vector boson production at hadron colliders: hard-collinear coefficients at the NNLO*, *Eur. Phys. J.* **C72** (2012) 2195 [1209.0158]. [p. 104]

[268] T. Gehrmann, T. Lübbert and L. L. Yang, *Transverse parton distribution functions at next-to-next-to-leading order: the quark-to-quark case*, *Phys. Rev. Lett.* **109** (2012) 242003 [1209.0682]. [p. 104]

[269] T. Gehrmann, T. Lübbert and L. L. Yang, *Calculation of the transverse parton distribution functions at next-to-next-to-leading order*, *JHEP* **06** (2014) 155 [1403.6451]. [pp. 104 and 111]

[270] M. G. Echevarria, I. Scimemi and A. Vladimirov, *Universal transverse momentum dependent soft function at NNLO*, *Phys. Rev.* **D93** (2016) 054004 [1511.05590]. [p. 104]

[271] M. G. Echevarria, I. Scimemi and A. Vladimirov, *Unpolarized Transverse Momentum Dependent Parton Distribution and Fragmentation Functions at next-to-next-to-leading order*, *JHEP* **09** (2016) 004 [1604.07869]. [pp. 104 and 116]

[272] M.-X. Luo, X. Wang, X. Xu, L. L. Yang, T.-Z. Yang and H. X. Zhu, *Transverse Parton Distribution and Fragmentation Functions at NNLO: the Quark Case*, *JHEP* **10** (2019) 083 [1908.03831]. [pp. 104 and 111]

[273] M. A. Ebert, I. W. Stewart and Y. Zhao, *Determining the Nonperturbative Collins-Soper Kernel From Lattice QCD*, *Phys. Rev.* **D99** (2019) 034505 [1811.00026]. [p. 105]

[274] M. A. Ebert, I. W. Stewart and Y. Zhao, *Towards Quasi-Transverse Momentum Dependent PDFs Computable on the Lattice*, *JHEP* **09** (2019) 037 [1901.03685]. [p. 105]

[275] M.-X. Luo, T.-Z. Yang, H. X. Zhu and Y. J. Zhu, *Transverse Parton Distribution and Fragmentation Functions at NNLO: the Gluon Case*, *JHEP* **01** (2020) 040 [1909.13820]. [pp. 112 and 150]

[276] D. Gutierrez-Reyes, S. Leal-Gomez, I. Scimemi and A. Vladimirov, *Linearly polarized gluons at next-to-next-to leading order and the Higgs transverse momentum distribution*, *JHEP* **11** (2019) 121 [1907.03780]. [pp. 112 and 140]

[277] H.-n. Li, *Unification of the k(T) and threshold resummations*, *Phys. Lett.* **B454** (1999) 328 [hep-ph/9812363]. [p. 113]

[278] E. Laenen, G. F. Sterman and W. Vogelsang, *Recoil and threshold corrections in short distance cross-sections*, *Phys. Rev.* **D63** (2001) 114018 [hep-ph/0010080]. [p. 113]

[279] A. Kulesza, G. F. Sterman and W. Vogelsang, *Joint resummation in electroweak boson production*, *Phys. Rev.* **D66** (2002) 014011 [hep-ph/0202251]. [p. 113]

[280] A. Kulesza, G. F. Sterman and W. Vogelsang, *Joint resummation for Higgs production*, *Phys. Rev.* **D69** (2004) 014012 [hep-ph/0309264]. [p. 113]

[281] G. Lustermans, W. J. Waalewijn and L. Zeune, *Joint transverse momentum and threshold resummation beyond NLL*, *Phys. Lett.* **B762** (2016) 447 [1605.02740]. [pp. 114, 115, and 116]

[282] C. W. Bauer, F. J. Tackmann, J. R. Walsh and S. Zuberi, *Factorization and Resummation for Dijet Invariant Mass Spectra*, *Phys. Rev.* **D85** (2012) 074006 [1106.6047]. [p. 114]

[283] Y. Li, S. Mantry and F. Petriello, *An Exclusive Soft Function for Drell-Yan at Next-to-Next-to-Leading Order*, *Phys. Rev.* **D84** (2011) 094014 [1105.5171]. [pp. 115 and 193]

[284] H. X. Zhu, C. S. Li, H. T. Li, D. Y. Shao and L. L. Yang, *Transverse-momentum resummation for top-quark pairs at hadron colliders*, *Phys. Rev. Lett.* **110** (2013) 082001 [1208.5774]. [p. 120]

[285] J. Gao, C. S. Li and H. X. Zhu, *Top Quark Decay at Next-to-Next-to Leading Order in QCD*, *Phys. Rev. Lett.* **110** (2013) 042001 [1210.2808]. [p. 120]

[286] S. Catani, M. Grazzini and A. Torre, *Transverse-momentum resummation for heavy-quark hadroproduction*, *Nucl.Phys.* **B890** (2014) 518 [1408.4564]. [p. 120]

[287] J. Gao and H. X. Zhu, *Electroweak prodution of top-quark pairs in e^+e^- annihilation at NNLO in QCD: the vector contributions*, *Phys. Rev. D* **90** (2014) 114022 [1408.5150]. [p. 120]

[288] J. Gao and H. X. Zhu, *Top Quark Forward-Backward Asymmetry in e^+e^- Annihilation at Next-to-Next-to-Leading Order in QCD*, *Phys. Rev. Lett.* **113** (2014) 262001 [1410.3165]. [p. 120]

[289] S. Gangal, M. Stahlhofen and F. J. Tackmann, *Rapidity-Dependent Jet Vetoes*, *Phys. Rev. D* **91** (2015) 054023 [1412.4792]. [p. 120]

[290] S. Alioli, C. W. Bauer, C. J. Berggren, A. Hornig, F. J. Tackmann, C. K. Vermilion et al., *Combining Higher-Order Resummation with Multiple NLO Calculations and Parton Showers in GENEVA*, *JHEP* **09** (2013) 120 [1211.7049]. [p. 121]

[291] S. Alioli, C. W. Bauer, C. Berggren, F. J. Tackmann, J. R. Walsh and S. Zuberi, *Matching Fully Differential NNLO Calculations and Parton Showers*, *JHEP* **06** (2014) 089 [1311.0286]. [p. 121]

[292] S. Alioli, C. W. Bauer, C. Berggren, F. J. Tackmann and J. R. Walsh, *Drell-Yan production at NNLL′+NNLO matched to parton showers*, *Phys. Rev.* **D92** (2015) 094020 [1508.01475]. [p. 121]

[293] M. Grazzini, *NNLO predictions for the Higgs boson signal in the $H \to WW \to \ell\nu\ell\nu$ and $H \to ZZ \to 4\ell$ decay channels*, *JHEP* **0802** (2008) 043 [0801.3232]. [p. 121]

[294] S. Catani, L. Cieri, G. Ferrera, D. de Florian and M. Grazzini, *Vector boson production at hadron colliders: a fully exclusive QCD calculation at NNLO*, *Phys. Rev. Lett.* **103** (2009) 082001 [0903.2120]. [p. 121]

[295] M. Grazzini, S. Kallweit and M. Wiesemann, *Fully differential NNLO computations with MATRIX*, *Eur. Phys. J.* **C78** (2018) 537 [1711.06631]. [pp. 121 and 124]

[296] J. M. Campbell, R. K. Ellis and C. Williams, *Associated production of a Higgs boson at NNLO*, *JHEP* **06** (2016) 179 [1601.00658]. [p. 121]

[297] R. Boughezal, J. M. Campbell, R. K. Ellis, C. Focke, W. Giele, X. Liu et al., *Color singlet production at NNLO in MCFM*, *Eur. Phys. J.* **C77** (2017) 7 [1605.08011]. [p. 121]

[298] G. Heinrich, S. Jahn, S. P. Jones, M. Kerner and J. Pires, *NNLO predictions for Z-boson pair production at the LHC*, *JHEP* **03** (2018) 142 [1710.06294]. [p. 121]

[299] J. M. Campbell, R. K. Ellis and S. Seth, *H + 1 jet production revisited*, *JHEP* **10** (2019) 136 [1906.01020]. [pp. 121 and 139]

[300] I. Moult, L. Rothen, I. W. Stewart, F. J. Tackmann and H. X. Zhu, *Subleading Power Corrections for N-Jettiness Subtractions*, *Phys. Rev.* **D95** (2017) 074023 [1612.00450]. [pp. 122 and 157]

[301] I. Moult, L. Rothen, I. W. Stewart, F. J. Tackmann and H. X. Zhu, *N-jettiness subtractions for $gg \to H$ at subleading power*, *Phys. Rev.* **D97** (2018) 014013 [1710.03227]. [pp. 122 and 157]

[302] M. A. Ebert, I. Moult, I. W. Stewart, F. J. Tackmann, G. Vita and H. X. Zhu, *Power Corrections for N-Jettiness Subtractions at $\mathcal{O}(\alpha_s)$*, *JHEP* **12** (2018) 084 [1807.10764]. [p. 122]

[303] R. Boughezal, X. Liu and F. Petriello, *Power Corrections in the N-jettiness Subtraction Scheme*, *JHEP* **03** (2017) 160 [1612.02911]. [p. 122]

[304] R. Boughezal, A. Isgrò and F. Petriello, *Next-to-leading-logarithmic power corrections for N-jettiness subtraction in color-singlet production*, *Phys. Rev.* **D97** (2018) 076006 [1802.00456]. [p. 122]

[305] R. Boughezal, A. Isgrò and F. Petriello, *Next-to-leading power corrections to $V + 1$ jet production in N-jettiness subtraction*, *Phys. Rev.* **D101** (2020) 016005 [1907.12213]. [p. 122]

[306] M. A. Ebert, I. Moult, I. W. Stewart, F. J. Tackmann, G. Vita and H. X. Zhu, *Subleading power rapidity divergences and power corrections for q_T*, *JHEP* **04** (2019) 123 [1812.08189]. [pp. 122 and 144]

[307] L. Cieri, C. Oleari and M. Rocco, *Higher-order power corrections in a transverse-momentum cut for colour-singlet production at NLO*, *Eur. Phys. J.* **C79** (2019) 852 [1906.09044]. [p. 122]

[308] A. Behring, K. Melnikov, R. Rietkerk, L. Tancredi and C. Wever, *Quark beam function at next-to-next-to-next-to-leading order in perturbative QCD in the generalized large-N_c approximation*, *Phys. Rev. D* **100** (2019) 114034 [1910.10059]. [p. 124]

[309] E. REMIDDI and J. A. M. VERMASEREN, *Harmonic polylogarithms*, *International Journal of Modern Physics A* **15** (2000) 725–754. [pp. 124, 125, 126, and 127]

[310] T. Gehrmann and E. Remiddi, *Numerical evaluation of harmonic polylogarithms*, *Computer Physics Communications* **141** (2001) 296–312. [pp. 124, 128, 130, and 135]

[311] J. Ablinger, J. Blümlein, M. Round and C. Schneider, *Numerical implementation of harmonic polylogarithms to weight $w = 8$*, *Computer Physics Communications* **240** (2019) 189–201. [p. 124]

[312] S. Buehler and C. Duhr, *Chaplin - complex harmonic polylogarithms in fortran*, 2011. [p. 124]

[313] J. Vollinga and S. Weinzierl, *Numerical evaluation of multiple polylogarithms*, *Computer Physics Communications* **167** (2005) 177–194. [p. 124]

[314] D. Maître, *Hpl, a mathematica implementation of the harmonic polylogarithms*, *Computer Physics Communications* **174** (2006) 222–240. [pp. 124 and 135]

[315] D. Maître, *Extension of hpl to complex arguments*, *Computer Physics Communications* **183** (2012) 846. [p. 124]

[316] C. Duhr and F. Dulat, *Polylogtools — polylogs for the masses*, *Journal of High Energy Physics* **2019** (2019) . [p. 124]

[317] A. B. Goncharov, *Multiple polylogarithms and mixed Tate motives*, `math/0103059`. [p. 125]

[318] N. Nielsen, *Der eulersche dilogarithmus und seine verallgemeinerungen, nova acta 90, nr.3, halle 1909.*, . [p. 126]

[319] G. 't Hooft and M. J. G. Veltman, *Scalar One Loop Integrals*, *Nucl. Phys. B* **153** (1979) 365. [p. 130]

[320] C. Duhr and F. Dulat, *PolyLogTools — polylogs for the masses*, *JHEP* **08** (2019) 135 [`1904.07279`]. [p. 134]

[321] W. R. Inc., "Mathematica, Version 12.3.1." [p. 135]

[322] ATLAS collaboration, *Measurements of Higgs boson production and couplings in diboson final states with the ATLAS detector at the LHC*, *Phys. Lett. B* **726** (2013) 88 [`1307.1427`]. [p. 139]

[323] ATLAS collaboration, *Measurements of fiducial and differential cross sections for Higgs boson production in the diphoton decay channel at* $\sqrt{s} = 8$ *TeV with ATLAS*, *JHEP* **09** (2014) 112 [`1407.4222`]. [p. 139]

[324] ATLAS collaboration, *Fiducial and differential cross sections of Higgs boson production measured in the four-lepton decay channel in pp collisions at* $\sqrt{s}$*=8 TeV with the ATLAS detector*, *Phys. Lett. B* **738** (2014) 234 [`1408.3226`]. [p. 139]

[325] ATLAS collaboration, *Measurement of fiducial differential cross sections of gluon-fusion production of Higgs bosons decaying to* $WW^* \to e\nu\mu\nu$ *with the ATLAS detector at* $\sqrt{s} = 8$ *TeV*, *JHEP* **08** (2016) 104 [`1604.02997`]. [p. 139]

[326] ATLAS collaboration, *Measurement of inclusive and differential cross sections in the* $H \to ZZ^* \to 4\ell$ *decay channel in pp collisions at* $\sqrt{s} = 13$ *TeV with the ATLAS detector*, *JHEP* **10** (2017) 132 [`1708.02810`]. [p. 139]

[327] ATLAS collaboration, *Measurements of the Higgs boson inclusive and differential fiducial cross sections in the 4ℓ decay channel at $\sqrt{s}$ = 13 TeV*, *Eur. Phys. J. C* **80** (2020) 942 [2004.03969]. [p. 139]

[328] CMS collaboration, *Measurement of differential cross sections for Higgs boson production in the diphoton decay channel in pp collisions at $\sqrt{s} = 8$ TeV*, *Eur. Phys. J. C* **76** (2016) 13 [1508.07819]. [p. 139]

[329] CMS collaboration, *Measurement of differential and integrated fiducial cross sections for Higgs boson production in the four-lepton decay channel in pp collisions at $\sqrt{s} = 7$ and 8 TeV*, *JHEP* **04** (2016) 005 [1512.08377]. [p. 139]

[330] CMS collaboration, *Measurement of the transverse momentum spectrum of the Higgs boson produced in pp collisions at $\sqrt{s} = 8$ TeV using $H \to WW$ decays*, *JHEP* **03** (2017) 032 [1606.01522]. [p. 139]

[331] CMS collaboration, *Measurement of inclusive and differential Higgs boson production cross sections in the diphoton decay channel in proton-proton collisions at $\sqrt{s} = 13$ TeV*, *JHEP* **01** (2019) 183 [1807.03825]. [p. 139]

[332] CMS collaboration, *Measurement and interpretation of differential cross sections for Higgs boson production at $\sqrt{s} = 13$ TeV*, *Phys. Lett. B* **792** (2019) 369 [1812.06504]. [p. 139]

[333] CMS collaboration, *Measurement of the inclusive and differential Higgs boson production cross sections in the leptonic WW decay mode at $\sqrt{s} = 13$ TeV*, 2007.01984. [p. 139]

[334] M. Cepeda et al., *Report from Working Group 2: Higgs Physics at the HL-LHC and HE-LHC*, *CERN Yellow Rep. Monogr.* **7** (2019) 221 [1902.00134]. [p. 139]

[335] S. Dawson, *Radiative corrections to Higgs boson production*, *Nucl. Phys.* **B359** (1991) 283. [p. 139]

[336] A. Djouadi, M. Spira and P. M. Zerwas, *Production of Higgs bosons in proton colliders: QCD corrections*, *Phys. Lett. B* **264** (1991) 440. [p. 139]

[337] M. Spira, A. Djouadi, D. Graudenz and P. M. Zerwas, *Higgs boson production at the LHC*, *Nucl. Phys.* **B453** (1995) 17 [hep-ph/9504378]. [p. 139]

[338] R. V. Harlander and W. B. Kilgore, *Next-to-next-to-leading order Higgs production at hadron colliders*, *Phys. Rev. Lett.* **88** (2002) 201801 [hep-ph/0201206]. [p. 139]

[339] C. Anastasiou and K. Melnikov, *Higgs boson production at hadron colliders in NNLO QCD*, *Nucl. Phys. B* **646** (2002) 220 [hep-ph/0207004]. [p. 139]

[340] V. Ravindran, J. Smith and W. L. van Neerven, *NNLO corrections to the total cross-section for Higgs boson production in hadron hadron collisions*, *Nucl. Phys. B* **665** (2003) 325 [hep-ph/0302135]. [p. 139]

[341] C. Anastasiou, C. Duhr, F. Dulat, F. Herzog and B. Mistlberger, *Higgs Boson Gluon-Fusion Production in QCD at Three Loops*, *Phys. Rev. Lett.* **114** (2015) 212001 [1503.06056]. [p. 139]

[342] C. Anastasiou, C. Duhr, F. Dulat, E. Furlan, T. Gehrmann, F. Herzog et al., *High precision determination of the gluon fusion Higgs boson cross-section at the LHC*, *JHEP* **05** (2016) 058 [1602.00695]. [pp. 139 and 168]

[343] D. de Florian, M. Grazzini and Z. Kunszt, *Higgs production with large transverse momentum in hadronic collisions at next-to-leading order*, *Phys. Rev. Lett.* **82** (1999) 5209 [hep-ph/9902483]. [p. 139]

[344] V. Ravindran, J. Smith and W. L. Van Neerven, *Next-to-leading order QCD corrections to differential distributions of Higgs boson production in hadron hadron collisions*, *Nucl. Phys. B* **634** (2002) 247 [hep-ph/0201114]. [p. 139]

[345] C. J. Glosser and C. R. Schmidt, *Next-to-leading corrections to the Higgs boson transverse momentum spectrum in gluon fusion*, *JHEP* **12** (2002) 016 [hep-ph/0209248]. [pp. 139 and 156]

[346] X. Chen, T. Gehrmann, E. W. N. Glover and M. Jaquier, *Precise QCD predictions for the production of Higgs + jet final states*, *Phys. Lett. B* **740** (2015) 147 [1408.5325]. [pp. 139 and 156]

[347] R. Boughezal, C. Focke, W. Giele, X. Liu and F. Petriello, *Higgs boson production in association with a jet at NNLO using jettiness subtraction*, *Phys. Lett.* **B748** (2015) 5 [1505.03893]. [p. 139]

[348] R. Boughezal, F. Caola, K. Melnikov, F. Petriello and M. Schulze, *Higgs boson production in association with a jet at next-to-next-to-leading order*, *Phys. Rev. Lett.* **115** (2015) 082003 [1504.07922]. [p. 139]

[349] F. Caola, K. Melnikov and M. Schulze, *Fiducial cross sections for Higgs boson production in association with a jet at next-to-next-to-leading order in QCD*, *Phys. Rev. D* **92** (2015) 074032 [1508.02684]. [p. 139]

[350] X. Chen, J. Cruz-Martinez, T. Gehrmann, E. W. N. Glover and M. Jaquier, *NNLO QCD corrections to Higgs boson production at large transverse momentum*, *JHEP* **10** (2016) 066 [1607.08817]. [pp. 139 and 156]

[351] X. Chen, T. Gehrmann, E. W. N. Glover and A. Huss, *Fiducial cross sections for the four-lepton decay mode in Higgs-plus-jet production up to NNLO QCD*, *JHEP* **07** (2019) 052 [1905.13738]. [p. 139]

[352] T. Becher, M. Neubert and D. Wilhelm, *Higgs-Boson Production at Small Transverse Momentum*, *JHEP* **05** (2013) 110 [1212.2621]. [p. 140]

[353] D. Neill, I. Z. Rothstein and V. Vaidya, *The Higgs Transverse Momentum Distribution at NNLL and its Theoretical Errors*, *JHEP* **12** (2015) 097 [1503.00005]. [p. 140]

[354] T. Becher and T. Neumann, *Fiducial q_T resummation of color-singlet processes at N^3LL+NNLO*, 2009.11437. [p. 140]

[355] S. Camarda, L. Cieri and G. Ferrera, *Drell-yan lepton-pair production: q_t resummation at n^3ll accuracy and fiducial cross sections at n^3lo*, 2021. [p. 140]

[356] F. Wilczek, *Decays of heavy vector mesons into higgs particles*, *Phys. Rev. Lett.* **39** (1977) 1304. [p. 141]

[357] M. A. Shifman, A. I. Vainshtein and V. I. Zakharov, *Remarks on Higgs Boson Interactions with Nucleons*, *Phys. Lett. B* **78** (1978) 443. [p. 141]

[358] T. Inami, T. Kubota and Y. Okada, *Effective Gauge Theory and the Effect of Heavy Quarks in Higgs Boson Decays*, *Z. Phys. C* **18** (1983) 69. [p. 141]

[359] K. G. Chetyrkin, B. A. Kniehl and M. Steinhauser, *Decoupling relations to O (alpha-s**3) and their connection to low-energy theorems*, *Nucl. Phys. B* **510** (1998) 61 [hep-ph/9708255]. [p. 141]

[360] Y. Schröder and M. Steinhauser, *Four-loop decoupling relations for the strong coupling*, *Journal of High Energy Physics* **2006** (2006) 051–051. [p. 141]

[361] K. Chetyrkin, J. Kühn and C. Sturm, *Qcd decoupling at four loops*, *Nuclear Physics B* **744** (2006) 121–135. [p. 141]

[362] H. M. Georgi, S. L. Glashow, M. E. Machacek and D. V. Nanopoulos, *Higgs bosons from two-gluon annihilation in proton-proton collisions*, *Phys. Rev. Lett.* **40** (1978) 692. [p. 141]

[363] D. Graudenz, M. Spira and P. M. Zerwas, *Qcd corrections to higgs-boson production at proton-proton colliders*, *Phys. Rev. Lett.* **70** (1993) 1372. [p. 141]

[364] S. Dawson and R. P. Kauffman, *Qcd corrections to higgs boson production: Nonleading terms in the heavy quark limit*, *Physical Review D* **49** (1994) 2298–2309. [p. 141]

[365] M. Spira, A. Djouadi, D. Graudenz and R. Zerwas, *Higgs boson production at the lhc*, *Nuclear Physics B* **453** (1995) 17–82. [p. 141]

[366] R. V. Harlander and K. J. Ozeren, *Top mass effects in higgs production at next-to-next-to-leading order qcd: Virtual corrections*, *Physics Letters B* **679** (2009) 467–472. [p. 141]

[367] A. Pak, M. Rogal and M. Steinhauser, *Virtual three-loop corrections to higgs boson production in gluon fusion for finite top quark mass*, *Physics Letters B* **679** (2009) 473–477. [p. 141]

[368] A. Pak, M. Rogal and M. Steinhauser, *Finite top quark mass effects in nnlo higgs boson production at lhc*, *Journal of High Energy Physics* **2010** (2010) . [p. 141]

[369] R. V. Harlander, H. Mantler, S. Marzani and K. J. Ozeren, *Higgs production in gluon fusion at next-to-next-to-leading order qcd for finite top mass*, *The European Physical Journal C* **66** (2010) 359–372. [p. 141]

[370] S. Alekhin, A. Kardos, S. Moch and Z. Trócsányi, *Precision studies for Drell-Yan processes at NNLO*, 2021. [pp. 144 and 166]

[371] G. P. Salam and E. Slade, *Cuts for two-body decays at colliders*, `2106.08329`. [p. 144]

[372] R. Boughezal, J. M. Campbell, R. K. Ellis, C. Focke, W. Giele, X. Liu et al., *Color-singlet production at nnlo in mcfm*, *The European Physical Journal C* **77** (2016) . [p. 146]

[373] C. W. Bauer, S. Fleming and M. E. Luke, *Summing Sudakov logarithms in $B \to X_s\gamma$ in effective field theory*, *Phys. Rev.* **D63** (2000) 014006 [`hep-ph/0005275`]. [p. 146]

[374] C. W. Bauer, S. Fleming, D. Pirjol and I. W. Stewart, *An Effective field theory for collinear and soft gluons: Heavy to light decays*, *Phys. Rev.* **D63** (2001) 114020 [`hep-ph/0011336`]. [p. 146]

[375] P. F. Monni, E. Re and P. Torrielli, *Higgs transverse-momentum resummation in direct space*, *Physical Review Letters* **116** (2016) . [p. 147]

[376] C. F. Berger, C. Marcantonini, I. W. Stewart, F. J. Tackmann and W. J. Waalewijn, *Higgs production with a central jet veto at nnll+nnlo*, *Journal of High Energy Physics* **2011** (2011) . [p. 147]

[377] R. V. Harlander, *Virtual corrections to ggh to two loops in the heavy top limit*, *Physics Letters B* **492** (2000) 74–80. [p. 147]

[378] T. Gehrmann, T. Huber and D. Maître, *Two-loop quark and gluon form factors in dimensional regularisation*, *Physics Letters B* **622** (2005) 295–302. [p. 147]

[379] S. Moch, J. Vermaseren and A. Vogt, *Three-loop results for quark and gluon form factors*, *Physics Letters B* **625** (2005) 245–252. [pp. 147 and 182]

[380] P. A. Baikov, K. G. Chetyrkin, A. V. Smirnov, V. A. Smirnov and M. Steinhauser, *Quark and gluon form factors to three loops*, *Physical Review Letters* **102** (2009) . [p. 147]

[381] R. N. Lee, A. V. Smirnov and V. A. Smirnov, *Analytic results for massless three-loop form factors*, *Journal of High Energy Physics* **2010** (2010) . [p. 147]

[382] T. Gehrmann, E. W. N. Glover, T. Huber, N. Ikizlerli and C. Studerus, *Calculation of the quark and gluon form factors to three loops in qcd*, *Journal of High Energy Physics* **2010** (2010) . [p. 147]

[383] V. Ahrens, T. Becher, M. Neubert and L. L. Yang, *Origin of the large perturbative corrections to higgs production at hadron colliders*, *Physical Review D* **79** (2009) . [p. 149]

[384] G. Parisi, *Summing Large Perturbative Corrections in QCD*, *Phys. Lett. B* **90** (1980) 295. [p. 149]

[385] G. F. Sterman, *Summation of Large Corrections to Short Distance Hadronic Cross-Sections*, *Nucl. Phys. B* **281** (1987) 310. [p. 149]

[386] L. Magnea and G. F. Sterman, *Analytic continuation of the Sudakov form-factor in QCD*, *Phys. Rev. D* **42** (1990) 4222. [p. 149]

[387] T. O. Eynck, E. Laenen and L. Magnea, *Exponentiation of the Drell-Yan cross-section near partonic threshold in the DIS and MS-bar schemes*, *JHEP* **06** (2003) 057 [hep-ph/0305179]. [p. 149]

[388] V. Ahrens, T. Becher, M. Neubert and L. L. Yang, *Origin of the Large Perturbative Corrections to Higgs Production at Hadron Colliders*, *Phys. Rev.* **D79** (2009) 033013 [0808.3008]. [p. 149]

[389] A. Idilbi, X.-d. Ji, J.-P. Ma and F. Yuan, *Threshold resummation for Higgs production in effective field theory*, *Phys. Rev.* **D73** (2006) 077501 [hep-ph/0509294]. [p. 150]

[390] J. Butterworth et al., *PDF4LHC recommendations for LHC Run II*, *J. Phys. G* **43** (2016) 023001 [1510.03865]. [p. 155]

[391] J. C. Collins and D. E. Soper, *Angular Distribution of Dileptons in High-Energy Hadron Collisions*, *Phys. Rev. D* **16** (1977) 2219. [p. 156]

[392] H. Takahasi and M. Mori, *Double exponential formulas for numerical integration*, *Pub. RIMS* **9** (1974) 721. [p. 156]

[393] T. Ooura, *A continuous euler transformation and its application to the fourier transform of a slowly decaying function*, *J. Comput. Appl. Math.* **130** (2001) 259–270. [p. 156]

[394] T. Ooura, *Study on numerical integration of Fourier type integrals*, Ph.D. thesis, University of Tokyo, 1997. [p. 156]

[395] T. Hahn, *Cuba—a library for multidimensional numerical integration*, *Computer Physics Communications* **168** (2005) 78–95. [p. 156]

[396] T. Hahn, *Concurrent cuba*, 2014. [p. 156]

[397] F. Dulat, S. Lionetti, B. Mistlberger, A. Pelloni and C. Specchia, *Higgs-differential cross section at NNLO in dimensional regularisation*, *JHEP* **07** (2017) 017 [1704.08220]. [p. 156]

[398] M. Bonvini, S. Marzani, C. Muselli and L. Rottoli, *On the Higgs cross section at N^3LO+N^3LL and its uncertainty*, *JHEP* **08** (2016) 105 [1603.08000]. [p. 160]

[399] A. Djouadi, J. Kalinowski and M. Spira, *HDECAY: A Program for Higgs boson decays in the standard model and its supersymmetric extension*, *Comput. Phys. Commun.* **108** (1998) 56 [hep-ph/9704448]. [p. 168]

[400] A. Bredenstein, A. Denner, S. Dittmaier and M. M. Weber, *Precise predictions for the Higgs-boson decay $H \to WW/ZZ \to 4$ leptons*, *Phys. Rev. D* **74** (2006) 013004 [hep-ph/0604011]. [p. 168]

[401] LHC Higgs Cross Section Working Group collaboration, D. de Florian et al., *Handbook of LHC Higgs Cross Sections: 4. Deciphering the Nature of the Higgs Sector*, 1610.07922. [p. 168]

[402] S. Actis, G. Passarino, C. Sturm and S. Uccirati, *NLO Electroweak Corrections to Higgs Boson Production at Hadron Colliders*, *Phys. Lett. B* **670** (2008) 12 [0809.1301]. [p. 168]

[403] A. Grozin, *Four-loop cusp anomalous dimension in QED*, *JHEP* **06** (2018) 073 [1805.05050]. [p. 181]

[404] A. von Manteuffel, E. Panzer and R. M. Schabinger, *Cusp and collinear anomalous dimensions in four-loop qcd from form factors*, *Physical Review Letters* **124** (2020) . [p. 181]

[405] A. Idilbi, X.-d. Ji and F. Yuan, *Resummation of threshold logarithms in effective field theory for DIS, Drell-Yan and Higgs production*, *Nucl. Phys.* **B753** (2006) 42 [hep-ph/0605068]. [p. 182]

[406] T. Becher, M. Neubert and B. D. Pecjak, *Factorization and Momentum-Space Resummation in Deep-Inelastic Scattering*, *JHEP* **01** (2007) 076 [hep-ph/0607228]. [p. 182]

[407] R. Brüser, Z. L. Liu and M. Stahlhofen, *Three-Loop Quark Jet Function*, *Phys. Rev. Lett.* **121** (2018) 072003 [1804.09722]. [p. 185]

[408] P. Banerjee, P. K. Dhani and V. Ravindran, *Gluon jet function at three loops in QCD*, *Phys. Rev.* **D98** (2018) 094016 [1805.02637]. [p. 185]

[409] L. N. Mihaila, J. Salomon and M. Steinhauser, *Gauge Coupling Beta Functions in the Standard Model to Three Loops*, *Phys. Rev. Lett.* **108** (2012) 151602 [1201.5868]. [p. 190]

[410] A. V. Bednyakov, A. F. Pikelner and V. N. Velizhanin, *Anomalous dimensions of gauge fields and gauge coupling beta-functions in the Standard Model at three loops*, *JHEP* **01** (2013) 017 [1210.6873]. [p. 190]

[411] P. A. Baikov, K. G. Chetyrkin, J. H. Kuhn and J. Rittinger, *Vector Correlator in Massless QCD at Order $O(\alpha_s^4)$ and the QED beta-function at Five Loop*, *JHEP* **07** (2012) 017 [1206.1284]. [p. 190]

[412] T. Huber, E. Lunghi, M. Misiak and D. Wyler, *Electromagnetic logarithms in $\bar{B} \to X_s l^+ l^-$*, *Nucl. Phys.* **B740** (2006) 105 [hep-ph/0512066]. [p. 190]

Eidesstattliche Versicherung

Hiermit versichere ich an Eides statt, die vorliegende Dissertationsschrift selbst verfasst und keine anderen als die angegebenen Hilfsmittel und Quellen benutzt zu haben.

Die eingereichte schriftliche Fassung entspricht der auf dem elektronischen Speichermedium.

Die Dissertation wurde in der vorgelegten oder einer ähnlichen Form nicht schon einmal in einem früheren Promotionsverfahren angenommen oder als ungenügend beurteilt.

Hamburg, den 6.8.2021

Georgios Billis